EERL 2003-01
Earthquake Engineering
Research Laboratory

Three-Dimensional Nonlinear Analysis of Tall Irregular Steel Buildings Subject to Strong Ground Motion

Thesis by

Swaminathan Krishnan

In Partial Fulfillment of the Requirements

for the Degree of

Doctor of Philosophy

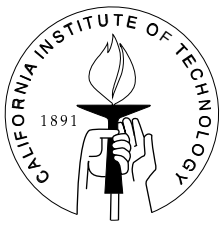

California Institute of Technology

Pasadena, California

2004

(Submitted September 8, 2003)

Acknowledgements

I would like to acknowledge my advisor, Professor John Hall's guidance, encouragement and support during my years at Caltech. His open doors are truly reflective of his commitment to education and to his students and I am grateful for the many walk-in discussions that I have had with him. I have tried to imbibe many great qualities from him – patience and the willingness to listen being the foremost among them. He has taught me to analyze problems in a very clear, methodical and logical manner. I will try to reflect the lessons learnt from him in my personal as well as professional life.

I wish to thank the members of my thesis defense committee, Professors James Beck, Thomas Heaton, Wilfred Iwan, and G. Ravichandran. I am grateful to California Institute of Technology for the excellent education that I have received and the great research environment that I have cherished, and its generous financial support through the course of my stay here.

My thanks go to my fellow graduate students, Andy Guyader, Isaac Chenchiah, Prashant Purohit, and John Clinton for helping me get through the Candidacy examination. I would also like to acknowledge the good times I have had with Georgia Cua, Samuel Bradford, Peter Clinton, Kelvin Yuen, Steve Alves, Matt Muto, Julie Wolf, Jeff Scruggs, the staff at Thomas Lab, and the many many Indian graduate students who have come and gone during my years at Caltech.

Above all, I am deeply thankful to my wonderful family. It is their love and affection that have given me the strength and conviction to pursue my goals in life.

Abstract

Strong ground motion from a nearby fault has frequency content in the same range as the natural frequencies of tall buildings. This may have serious repercussions and is the topic of this dissertation. Buildings are designed per building code standards. But, are the code provisions adequate? Strong motion from large earthquakes has been recorded only in recent times in the near-source region. Have the current codes used this information to update tall structure design guidelines? Considerable damage has been observed in tall buildings from the Northridge, Kobe, Turkey, and Taiwan earthquakes. How will tall buildings designed per the latest code regulations perform if they were to be shaken by any of these earthquakes? This thesis attempts to answer these questions.

Tall buildings by their nature are computationally intensive to analyze. They consist of thousands of degrees of freedom and when subjected to strong ground motion from a nearby source, exhibit inelastic response. Modeling this inelastic response requires an iterative approach that is computationally expensive. Furthermore, a large class of buildings, classified as irregular, exhibits complex behavior that can be studied only when the structures are modeled in their entirety. To this end, a three-dimensional analysis program, FRAME3D, has been developed incorporating two special beam-column elements – the plastic hinge element and the elastofiber element that can model beams and columns in buildings accurately and efficiently, a beam-column joint element that can model inelastic joint deformation, and 4-noded elastic plane-stress elements to model floor slabs acting as diaphragms forcing the lateral force resisting frames in a building to act as one unit. The program is capable of performing time-history analyses of buildings in their entirety.

Six 19-story irregular steel moment frame buildings (with buildings 2A and 3A being variants of buildings 2 and 3, respectively) have been designed per the latest code (Uniform Building Code, 1997). Two of these buildings have reentrant corners and the other two have torsional irregularity. Their strength and ductility are assessed by performing pushover analyses on them. To assess their performance under strong shaking, FRAME3D models of these buildings are subjected to near-source strong motion records from the Iran earthquake ($M_w = 7.3$, Tabas Station) of 1978, the Northridge earthquake ($M_w = 6.7$, Syl-

mar Station) of 1994 and the Kobe earthquake ($M_w = 6.9$, Takatori Station) of 1995. None of the buildings collapsed under these strong events in the computer analyses. However, when compared against the acceptable limits for various performance levels in FEMA 356 document, the damage in terms of plastic deformation at the ends of beams and columns and at joints would render the buildings inadequate in terms of life safety in quite a few cases and would even indicate possible collapse in a couple of cases. Thus, in these terms, the code falls short of achieving its life safety objective, and the near-source factors introduced in the code in 1997 in recognition of the special features of near-source ground motion seem to be inadequate.

The ductility demand, in terms of plastic rotation at the ends of beams and columns and in joints, on these buildings during this class of earthquakes is up to 6% of a radian, which is far greater than a typical limiting plastic rotation of 3% associated with fracture and consequent failure of large wide-flanged steel sections during experiments. Thus, if strength degradation due to fractures, local buckling, etc., were to be included in the analysis, then the results would likely to be worse, as far as the ability of these buildings to withstand these earthquakes without collapse is concerned.

Due to damage localization, the peak drifts observed in the structure far exceeded the inelastic drift limit in the code of 0.02 (in some cases up to 3 times). This points to serious non-structural damage to facades, interior dry wall, etc. Furthermore, large roof permanent offsets after the events indicate significant post-earthquake repair requiring considerable disruption and building closure.

Column yielding was minimal thus validating the strong-column weak-beam criterion in the code. Redundancy factors used to assess the redundancy in the system need to take into account the case of torsionally sensitive structures where frames in both principal directions are simultaneously activated. Stress concentration was not observed at the reentrant corners in L-shaped buildings.

Finally, the data catalogued in this work could be useful for future code development and tall structure design guidelines.

Contents

List of Figures

List of Tables

Chapter 1 Introduction

Strong ground motion from a nearby source has frequency content in the same range as the natural frequencies of tall buildings. This may have serious repercussions and is the topic of this dissertation. Buildings are designed per code standards. But, are the code provisions adequate? Near-source strong motion from large earthquakes has been recorded only in recent times. What is the implication of this information with respect to updating tall structure design guidelines? Considerable damage has been observed in tall buildings from the Northridge, Kobe, Turkey & Taiwan earthquakes. How will tall buildings designed per the latest code regulations perform if they were to be shaken with an intensity, frequency content and duration similar to these earthquakes? These are some of the questions that can be answered through finite element models of tall buildings.

The next three sections give some background on near-source ground motion, tall irregular buildings, and finite-element models for modeling tall structures, followed by a brief description of the analysis of four 19-story irregular buildings designed per the latest codes and subjected to strong ground motion records.

1.1 Near-Source Ground Motion

Near-source ground motion is characterized by rapidly occurring (i.e., high velocity) displacement pulses [34, 30]. Both the static component of the displacement that occurs along the surface trace of the fault and the shear wave component of the displacement associated with the seismic waves generated at the fault during rupture and oriented normal to the fault attain large amplitudes in the near-source region. Large displacements would be of little consequence if they occurred slowly (unless a structure straddled the fault). It turns out that the duration of these displacements is closely related to the characteristic slip time of a point on the fault, and there is compelling evidence that this slip is rapid [31]. Both the static and shear wave displacements can occur as pulses. Further, a shear-wave displacement pulse can have both a forward and back phase which can be more damaging to a structure than the forward-only static pulse. The rapid velocity at which these displace-

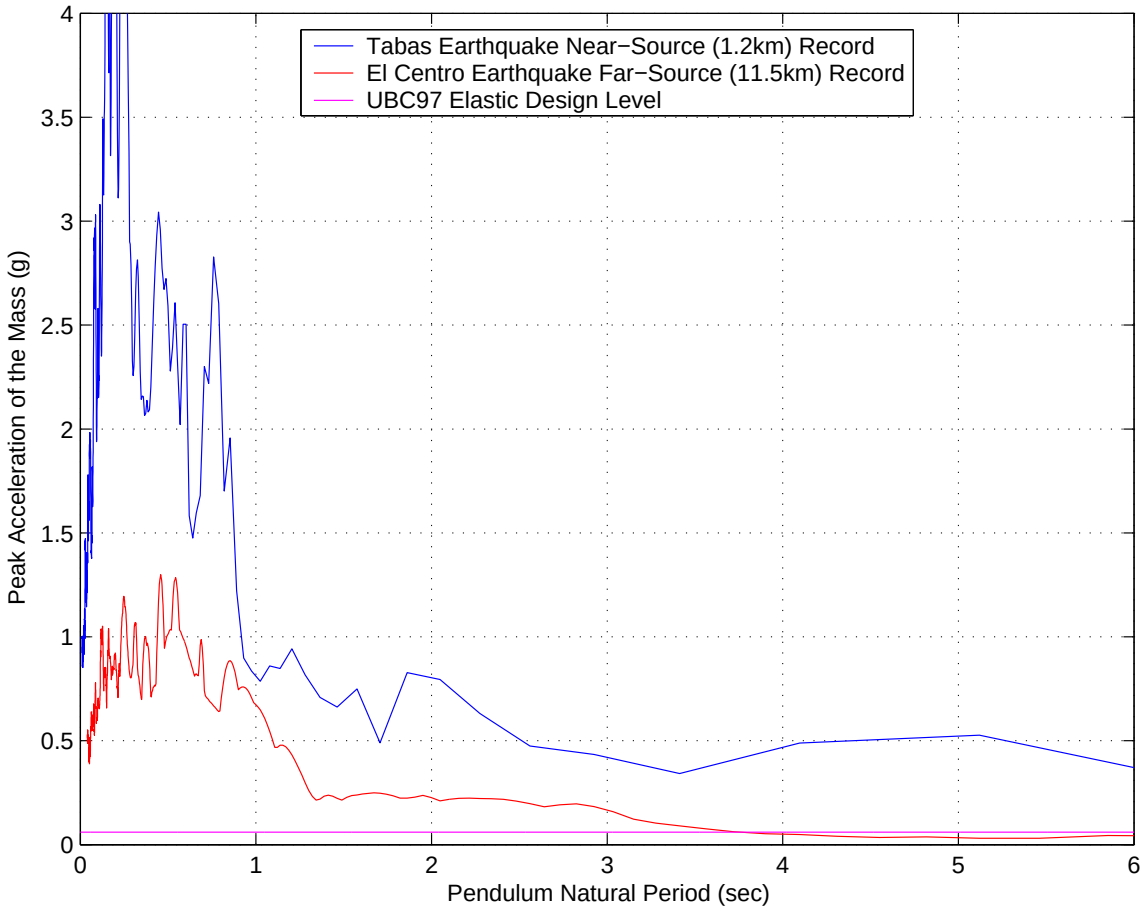

Figure 1.1: Comparison of Response Spectra of Tabas Near-Source Record and El Centro Far-Source Record

ments occur lead to pulses in the velocity time-histories as well. The characteristic period of these pulses is typically in the range of 2-6 *seconds* which corresponds to the fundamental natural period range of 20-60 story structures.

To bring out the difference between near-source and far-source records, plotted in Figure 1.1 are the response spectra of the Tabas near-source (1.2 km from the fault rupture) record from the Iran earthquake ($M_w = 7.3$) of 1978 and that of the Imperial Valley far-source (11.5 km from the fault rupture) record from the El Centro earthquake ($M_w = 6.9$) of 1940. Observe that while for short buildings, the structure response to the Tabas record is on the average 2.5 times its response to the El Centro record, this ratio varies from 3-10 for tall buildings.

In the simple analysis above, it was assumed that the structure remains elastic and in addition, vibrates purely in the fundamental mode. Of course both these assumptions

may be incorrect. In a large event, that is the focus of this study, almost all structures are bound to yield leading to lengthening of periods and significantly altered structure displaced configurations. A more rational way to approach this problem is by taking the velocity pulse from a near-source record and study its propagation through the height of the structure as a wave. This velocity pulse produces a shear wave that causes a velocity-proportional strain in the structure [30].

The wave has a forward pulse and a reverse pulse. The forward pulse gets the building going in one direction. Now the reverse pulse comes in and imparts a velocity to the base in the opposite direction. This causes large strains in the building. It turns out that if the period of the pulse is close to the building period then there is constructive interference between the forward pulse reflecting off the free surface and the reverse pulse that is entering the building. This will lead to localization of strains in the region of interference and consequently severe yielding. The yielding remains localized as the wave slows down because of the reduction of the stiffness in the structure due to yielding. Depending upon the gravity load distribution, P-Delta effects could cause instability in the building, significant enough to lead to collapse.

In a uniform shear building, it is easy to predict when and where along the height of the building the yield localization would occur. This is not the case, however, in real buildings that are bound to exhibit nonlinear behavior at discrete locations in beams, columns and joints. Hence, a detailed analytical model is necessary to study the impact of near-source motions in real buildings.

1.2 Tall Irregular Buildings

Buildings with 10 stories or more can be classified as tall buildings. Fundamental natural periods of tall buildings vary from about 0.8 *seconds* for a 10-story building ($\approxeq$ 40 m height) to 10-15 *seconds* for a 100 story building ($\approxeq$ 400-450 m height). In the traditional forms of construction, three classical lateral force resisting systems have been utilized to resist wind and earthquake forces in tall buildings - the moment frame system, the braced frame system and the shear wall system. In very tall buildings ($>$ 40 stories), combinations of any two of these three systems, aptly termed dual systems, have been utilized successfully. Reinforced concrete and steel have been the popular materials of construction. Composite

columns with concrete-filled steel tubes with nominal reinforcement are quite common in super-highrise construction. Four building characteristics that dictate the performance of the structure during earthquakes are strength, stiffness, ductility and damping. This study focuses on a set of 19-story steel moment-frame structures.

A large class of tall structures, classified as irregular, exhibits complex behavior that can be studied only when the structures are modeled in their entirety, i.e., we need to have a program capable of performing 3-D analysis. Tall buildings are classified as being irregular when any one of a number of special features are present in the design. Such features include but are not limited to torsional plan irregularity (wherein the center of mass does not coincide with the center of resistance, causing the building to have a significant twisting component in its response to seismic loading), reentrant corner irregularity (wings in L-shaped buildings have a tendency to flap causing twisting in the building if they flap in phase and causing stress concentration at the reentrant corner if they flap out-of-phase), vertical stiffness discontinuity (when the stiffness of a given story is much higher or lower than the story immediately above or below), vertical mass discontinuity (large mass difference between consecutive stories), etc.

This study focuses on tall irregular buildings with either a torsional plan irregularity or a reentrant corner irregularity.

1.3 Finite Element Models: Joints (Panel Zones)

A joint in a moment frame consists of a length of column within the depth of the connecting beams at the beam-column intersection. A typical beam-column joint consists of plates in two orthogonal directions, termed panel zones. The load on a panel zone is a double couple derived from the end moments and shears of the connected beams and columns, one couple coming from the beam end moments and column shears and the other coming from the column end moments and beam shears. The 3-D joint element developed herein consists of two orthogonal panel zones, one assimilated by combining all the column flange plates and the other combining all the column web plates including any doubler plates added to strengthen the joint. The two orthogonal panels form a cruciform section. Behavior of each panel zone is governed by either a bilinear or a linear-quadratic hysteretic relation between this moment and the resulting shear strain. The mathematical formulation of this element

is presented in Chapter 3.

1.4 Finite Element Models: Beam-Columns

Finite element models developed for beam-columns in buildings can be classified broadly in two categories - the plastic hinge type [38, 29, 11, 3, 36, 50, 51] and the fiber element type [8, 29, 11, 69, 68, 35, 46]. The plastic hinge element is a stiffness-based standard cubic-interpolated beam element (with cubic Hermitian polynomials for the transverse displacement and linear shape functions for the axial displacement, both of which represent the exact solution for a linear elastic prismatic beam) with material nonlinearity lumped into discrete locations at the ends of the element called plastic hinges. When the moment reaches the moment capacity of the section at these locations, the material yields and the element develops a kink. Attala, Deierlein, and McGuire [5] have proposed a concentrated hinge model that accurately captures the spread of plasticity with the computational ease of an elastic-plastic hinge model and without the need to discretize across the section or length of a member. They use nonlinear force-strain relations for the cross-section that are calibrated to data from inelastic analyses and numerical integration of the cross-section model along the element length to obtain inelastic flexibility coefficients for the member. The flexibility coefficients are employed in generating an inelastic stiffness matrix in which geometric nonlinearity is also accounted for.

The fiber element is a heavily discretized element designed to replicate true nonlinear beam behavior in flexure to the largest possible extent. The element is subdivided into a number of segments along its length and each segment is further subdivided into a number of fibers in the cross-section. The forces in the segment are computed as a summation of the forces in all the fibers. The axial force in the segment is the sum of the axial forces in all the fibers while the moment in the segment about either major or minor axis is the sum of the product of the axial force and the distance of each fiber from the corresponding neutral axis of the cross-section. The axial stress-strain relation of each fiber includes yielding and strain-hardening. This element is computationally expensive and has been used primarily to analyze two-dimensional frames in tall buildings.

Over the last 5-10 years research has been focussed on extending 2 dimensional formulations of these two element types to 3 dimensions as well as developing new, fast and efficient

finite elements for use in modeling complex structural systems.

To handle non-prismatic members (especially concrete sections with varying reinforcement along the length of the element), flexibility-based elements that utilize interpolation functions for the internal forces are more convenient [48, 49, 62, 63, 64, 24, 9, 10, 61, 60].

In this work, the 2-D plastic-hinge beam-column element [29] has been extended to 3 dimensions. The mathematical formulation of this element is given in Chapter 4. To overcome the inherent weaknesses of the plastic-hinge element and the heavy computational requirements of the fiber element, a new hybrid element called the elastofiber element is introduced in this work. It combines the attractive features of the plastic-hinge and fiber elements. An element is subdivided into three segments - two end fiber segments that exhibit nonlinear behavior and an interior segment that remains elastic. This element is suitable for applications such as moment frames where nonlinearity/damage is restricted to the ends of elements. End fiber segments are meant to include nonlinear behavior at the ends of the beam-column element and also in the beam to column connection. The two fiber segments are subdivided in cross-section into a number of fibers and the behavior of these fibers is governed by a cubic-ellipsoidal (nonlinear) stress-strain law with appropriate hysteretic rules to describe the fiber stress-strain state during unloading. Rupture and fracture are included in the fiber segment formulation. The elastic segment is modeled as a standard cubic-interpolated stiffness-based beam element. The mathematical formulation of this element is presented in Chapter 5. Three examples validating the elastofiber and joint elements are presented in Chapter 7.

1.5 FRAME3D: Program for Nonlinear 3-D Building Analysis

A number of nonlinear analysis programs incorporating various types of beam and column elements have been developed by research groups in seismic engineering. These include ANDERS [8], CU-DYNAMIX [17], DRAIN2DX [3], DRAIN3DX [56, 55], FEDEAS [24], IDARC [52, 43, 42], IDARC3D [44], and ISTAR-ST [45]. A summary of their capabilities is provided in Reference [8].

The programs capable of 3-D modeling are ANDERS, DRAIN3DX, and IDARC3D. ANDERS models buildings using planar frames arranged in an orthogonal pattern. Two-

dimensional multi-segment fiber elements are employed except at the intersections of the frames where three-dimensional fiber elements are needed to model bi-axial behavior. The orthogonal frames are constrained to move together at floor levels using a master-slave constraint. DRAIN3DX includes a fully discretized fiber element with a trilinear axial stress-strain law for the fibers. $P-\Delta$ effects are included by adding a geometric stiffness matrix to the tangent stiffness matrix for each element and accounting for second order effects in the resisting force computation. Geometric updating of the model nodes is not done. Thus, equilibrium is checked in the original configuration and not in the updated configuration. IDARC3D is a program developed for the modeling of reinforced concrete structures in which beams and columns are modeled as inelastic single component elements with distributed flexibility. Beam-column elements are modeled as simple flexural springs in which shear deformation effects are included. During the time-history analysis, updating of stiffness matrices is carried out only in the event of a stiffness change. A single-step force-equilibrium correction procedure is used. $P-\Delta$ effects are accounted for by a simple equivalent force method.

In this work, the computational challenges posed by three-dimensional seismic analysis of tall buildings are addressed here by the development of a comprehensive nonlinear Finite Element Analysis program, FRAME3D, that is capable of performing time-history analysis. The focus is on steel moment frames, although braced frames can also be modeled with slight modifications.

There are two distinguishing features of the program. First, a geometric updating feature is provided to accommodate large nodal translations and rotations. This automatically accounts for $P-\Delta$ effects and allows the analysis to follow a building's response well into collapse. Second is the use of computationally efficient elements which incorporate the important types of nonlinear behavior. Full three-dimensional analysis can be made of large, complex structures. At the present time, the element library of FRAME3D includes the following finite elements: (1) 3-D plastic hinge element to model beam-columns, (2) 3-D elastofiber element to model beam-columns, (3) 3-D joint element to model panel zones in beam-to-column joints of frames and (4) elastic plane-stress element to model floors in buildings that act as diaphragms tying the frames together (Chapter 6). The first three element types contain material nonlinearity, and the plastic hinge and elastofiber elements include geometric stiffness. An overview of the analysis procedure which is the basis for

this program is presented in Chapter 2.

1.6 Tall Building Analysis

To address the questions regarding the safety of tall irregular structures raised at the beginning of this chapter, two 19-story torsionally irregular structures and two 19-story irregular structures with reentrant corners are designed per the 1997 Uniform Building Code, UBC97 [33], and analyzed for strong shaking from three near-source ground motion records from the Northridge earthquake ($M_w = 6.7$) of 1994, the Iran earthquake ($M_w = 7.3$) of 1978, and the Kobe earthquake ($M_w = 6.9$) of 1995. The designs of these buildings and results from the analyses are presented in Chapters 8 and 9. The irregular features in buildings 2 and 3 were such that the frames had to be considerably stiffened (and as a result strengthened) to satisfy empirical wind drift limits. Such limits are generally imposed by practicing engineers to ensure occupant comfort and the safety of non-structural components since the codes do not specify a wind drift limit. Hence it is of interest to study the behavior of these two structures if they were not designed to satisfy any wind drift limit criterion. Thus, buildings 2A and 3A were designed to withstand earthquake and wind loads, but only the earthquake drifts were controlled to code-specified values.

The conclusions of this study and future work in this area are summarized in Chapter 10. Built-up sections were used in the design of the six buildings and their dimensions are tabulated in Appendix B. Moment frame elevations with beam and column sizes are presented in Appendix C. Maps indicating the location of the centers of mass and stiffness of all the six buildings are presented in Appendix D. Important data from the pushover and ground-motion analyses including pushover curves, displacement and drift time-histories, bar diagrams of peak drifts, damage maps of beam-columns and joints, floor diaphragm stress maps, and element response time-histories that could be valuable for future work involving code modifications is catalogued in Appendices E, F, G, H, I, and J.

Chapter 2 Overview of Analysis Procedure

2.1 Description of Model

This work deals with the modeling of 3-D frame structures consisting of grids of beams and columns. The structural model is comprised of three element types: panel zone elements, beam elements for beams and columns, and diaphragm elements (See Figure 2.1).

2.1.1 Panel Zone Element

This element models nonlinear shear deformation in the region of the joint where the beams and columns intersect. The joint region consists of a length of column within the depth of the connecting beams. The shear deformation is due primarily to opposing moments from the beams and columns at the joint caused by the frame being subjected to lateral loads (Figure 2.2). Each panel zone element is associated with a global node J, K, etc. at the center of the joint and where the global degrees of freedom (DOF) are defined. Each panel zone element consists of two orthogonal panels ① and ② which always remain planar and orthogonal. Edges of these panels contain attachment points a, b, c, and d, where beams attach and e and f on the top and bottom where columns attach. Details of the panel zone element are presented in Chapter 3.

2.1.2 Beam Element

This element is used to model beams and columns. Two types of beam elements have been developed: plastic hinge type and elastofiber type. The plastic hinge element has 2 nodes with local node numbers 1 and 2, while the elastofiber element consists of 3 segments with 4 nodes. The exterior nodes at the ends of the element are numbered 1 and 2, while the interior nodes are numbered 3 and 4. Both types of beam elements consider nonlinear behavior for flexural and axial deformations. Details of the plastic hinge element and the elastofiber element are presented in Chapters 4 and 5, respectively.

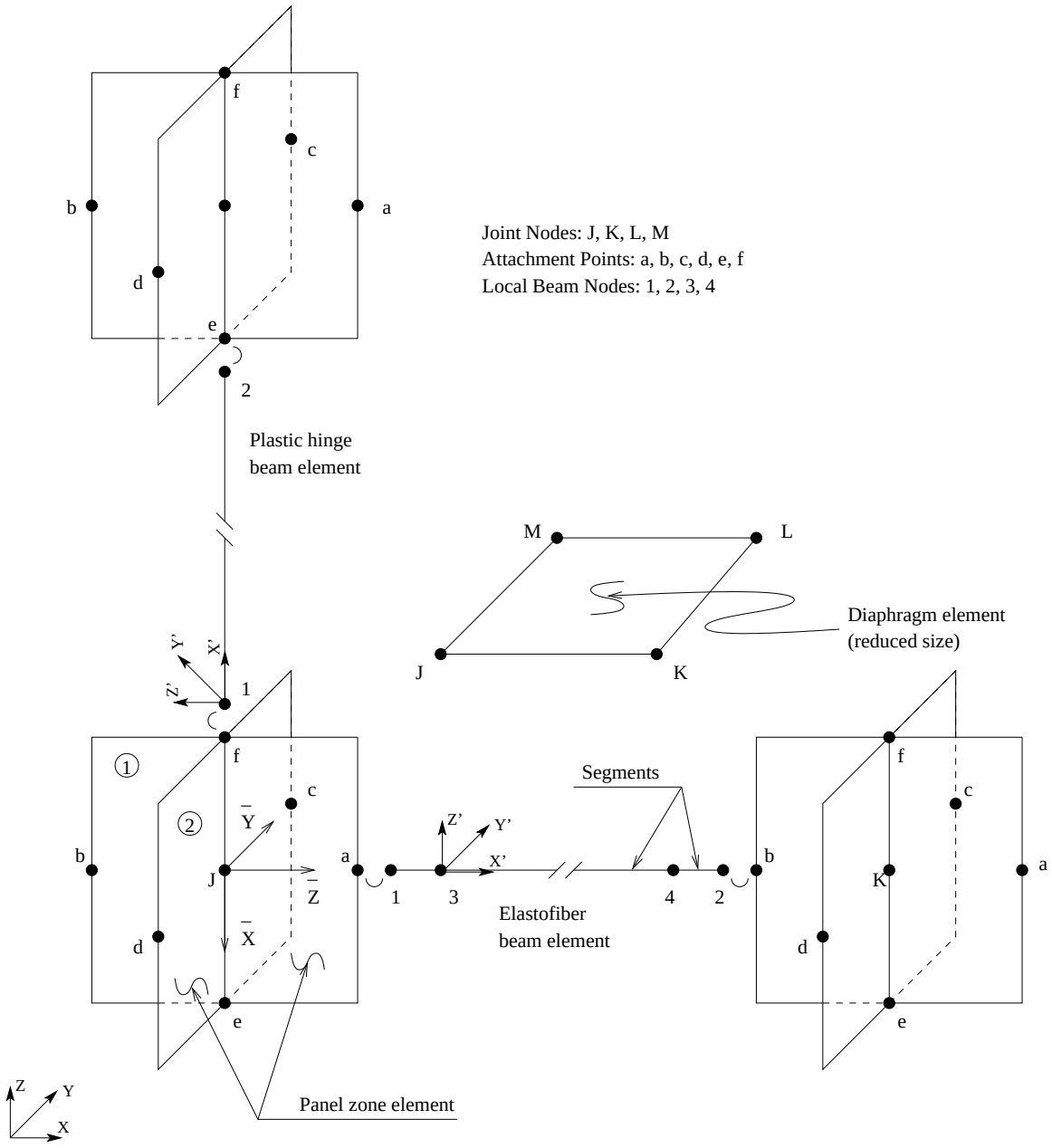

Figure 2.1: Element Arrangement in Frame Model, Showing Nodes, Attachment Points, and Coordinate Systems

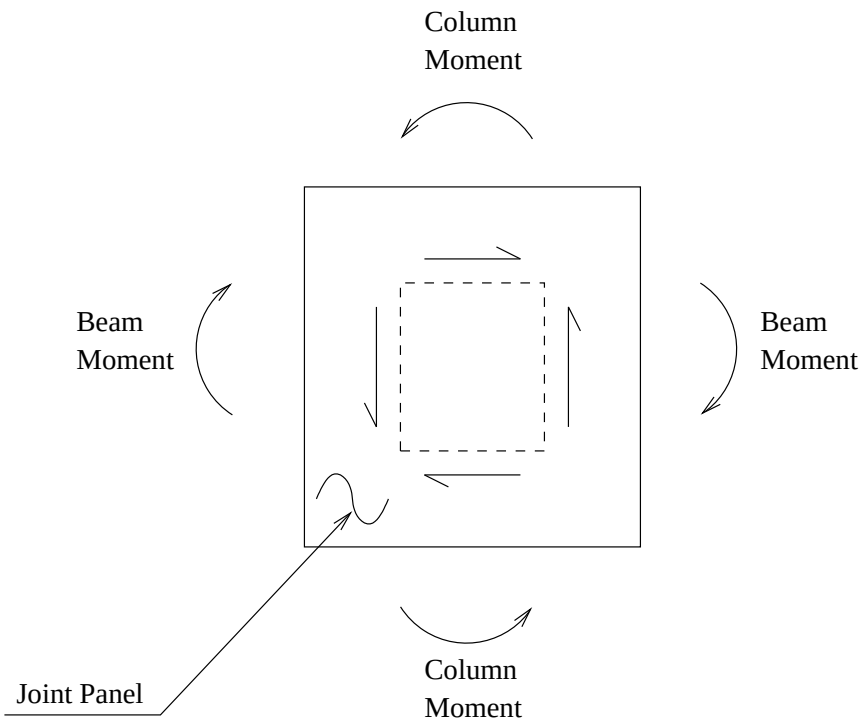

Figure 2.2: Panel zone shear caused by beam and column moments at the joint

2.1.3 Diaphragm Element

This element is used to model the in-plane stiffness of floor slabs. It is essentially a 4-noded plane-stress element connecting to global nodes J, K, L, and M. Details of the diaphragm element are presented in Chapter 6.

2.1.4 Coordinate Systems

The following are the various coordinate systems used in the structural model:

1. XYZ: The global coordinate system, XYZ, is the fixed coordinate system that is used to define the structure in space. The coordinates of the nodes defined by the user are in this coordinate system. For the building analysis presented in this work, Z axis is taken to be vertical (direction of gravity) and the X and Y axes are oriented in the two principal directions of the building.

2. $\bar{X}\bar{Y}\bar{Z}$: This coordinate system is local to the panel zone element. $\bar{X}$ lies along the line connecting attachment points e and f, in the direction of a vector running from f to e. $\bar{X}-\bar{Z}$ is the plane of panel ① and $\bar{X}-\bar{Y}$ is the plane of panel ②. This coordinate

system translates and rotates with the panel zone element.

3. $X'Y'Z'$: This coordinate system is local to the plastic hinge beam element. X' lies along the longitudinal axis of the beam running from node 1 to node 2. $Y' - Z'$ is the cross-sectional plane of the beam. Y' is the major principal axis of the cross-section while Z' is the minor axis. This coordinate system translates and rotates with the beam element.

4. $X'Y'Z'$: This coordinate system is local to each segment of the elastofiber beam element. Its orientation is similar to the plastic hinge beam element except that each segment has its own $X'Y'Z'$ system. Each translates and rotates with the corresponding segment of the element.

5. $X'Y'$: This coordinate system is local to the plane of the diaphragm element with nodes J, K, L, and M. Its origin lies at the center of the element. X' axis is in the direction of the vector running from node K to L and Y' is perpendicular to X' and in the plane of the element.

2.1.5 Structure Degrees of Freedom

The global degrees of freedom (DOF) are associated only with the nodes J, K, etc. at the centers of joints. The structural model consists of 8 global DOF at each node, J. These DOF are listed below:

1. U_{JX}: Translation in the X direction.

2. U_{JY}: Translation in the Y direction.

3. U_{JZ}: Translation in the Z direction.

4. $\theta_{J\bar{X}}$: Rotation of panel zone element as a rigid body about the $\bar{X}$ axis.

5. $\theta^B_{J\bar{Y}}$: Rotation of the line $e - f$ about the $\bar{Y}$ axis. It corresponds to deformation of panel ① into the shape of a parallelogram (Figure 2.3a). The B indicates that the rotating panel edges are connected to beams.

6. $\theta^C_{J\bar{Y}}$: Rotation of the line $a - b$ about the $\bar{Y}$ axis. It corresponds to deformation of panel ① into the shape of a parallelogram (Figure 2.3b). The C indicates that

the rotating panel edges are connected to columns. Note that $\theta^B_{J\bar{Y}}$ and $\theta^C_{J\bar{Y}}$ together accommodate a rigid rotation of panel ① about $\bar{Y}$ plus its shear deformation.

7. $\theta^B_{J\bar{Z}}$: Rotation of the line $e-f$ about the $\bar{Z}$ axis. It corresponds to deformation of panel ② into the shape of a parallelogram (Figure 2.3c). The B indicates that the rotating panel edges are connected to beams.

8. $\theta^C_{J\bar{Z}}$: Rotation of the line $c-d$ about the $\bar{Z}$ axis. It corresponds to deformation of panel ② into the shape of a parallelogram (Figure 2.3d). The C indicates that the rotating panel edges are connected to columns. Note that $\theta^B_{J\bar{Z}}$ and $\theta^C_{J\bar{Z}}$ together accommodate a rigid rotation of panel ② about $\bar{Z}$ plus its shear deformation.

Panel zone elements contribute stiffness directly to the four global DOF, $\theta^B_{J\bar{Y}}$, $\theta^C_{J\bar{Y}}$, $\theta^B_{J\bar{Z}}$, and $\theta^C_{J\bar{Z}}$. Beam elements are formulated in terms of 3 translational and 3 rotational DOF at each of the local nodes (1 and 2 for plastic hinge element and 1, 2, 3, and 4 for elastofiber element). However, none of these DOF appear in the global equations. Appropriate stiffness terms are assembled into the global DOF through transformation matrices based on the geometry of the deformed panel zone elements at nodes 1 and 2.

In addition to material nonlinearity, geometric stiffness (effect of axial force on flexural stiffness) is included with the beam elements. In addition, as the building deforms, locations of global nodes, local beam nodes and attachment points are updated, as are all the local coordinate systems. This ensures that $P-\Delta$ effects are accounted for accurately.

Mass is lumped into the global translational DOF at nodes J, K, etc. Damping is assumed to be of the Rayleigh type (stiffness and mass proportional). Building foundation is assumed to be rigid.

2.2 Equations of Motion and Solution Process

The matrix equation of motion of the building [16, 13] as a function of time, t, is

$$[M]\left\{\ddot{U}(t)\right\} + [C]\left\{\dot{U}(t)\right\} + \{R(t)\} = \{f_g\} - [M]\,[r]\left\{\ddot{U}_g(t)\right\} \tag{2.1}$$

In the above,

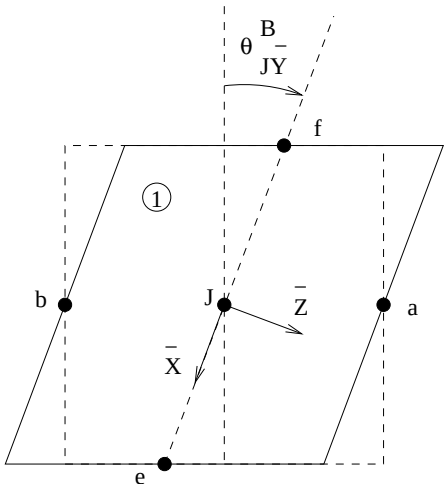

(a) $\theta^B_{J\bar{Y}}$ DOF

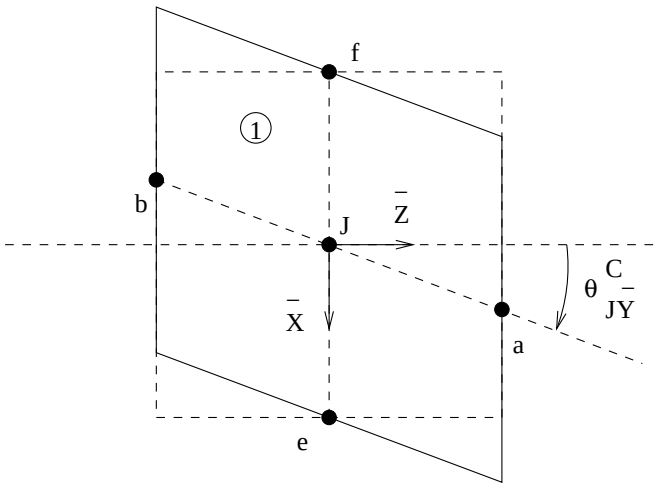

(b) $\theta^C_{J\bar{Y}}$ DOF

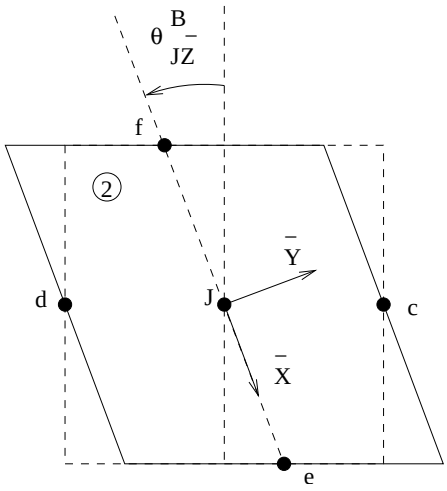

(c) $\theta^B_{J\bar{Z}}$ DOF

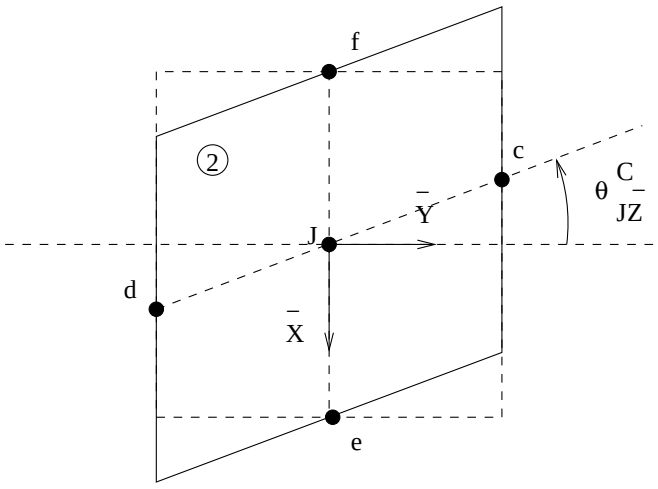

(d) $\theta^C_{J\bar{Z}}$ DOF

Figure 2.3: Degrees of Freedom of Panel Zone Element

1. $\{U(t)\}$ = Vector of global displacements at time, t, comprising of the set of 8 global translations and rotations at each node, J, K, etc.

2. $\left\{\dot{U}(t)\right\}$, $\left\{\ddot{U}(t)\right\}$ = Vectors of nodal velocities and accelerations, respectively corresponding to the 8 global translations and rotations at each node.

3. $[M]$ = Structure mass matrix. The mass in the structural system is lumped into the translational degrees of freedom at the joint nodes rendering the mass matrix diagonal. Further, the rotary inertia of the lumped nodal masses is neglected, and so the only non-zero terms of the mass matrix are the diagonal terms corresponding to the translational degrees of freedom.

4. $[C]$ = Structure damping matrix.

   Damping is assumed to be of the Rayleigh type (stiffness and mass proportional). Thus, the damping matrix is computed as

$$[C] = \alpha_0 [M] + \alpha_1 [K] \tag{2.2}$$

   where a_0 and a_1 are user defined proportionality constants. The initial elastic stiffness matrix is used in the above computation.

   In the linear elastic case, where modal superposition is valid, if Rayleigh damping is assumed, the modal damping in the i^{th} mode can be written in terms of the corresponding modal frequency as

$$\zeta_i = \frac{1}{2}\left(\alpha_0 \omega_i + \frac{\alpha_1}{\omega_i}\right) \tag{2.3}$$

   If we plot ω_i vs ζ_i, the curve is found to be reasonably flat in the intermediate frequency range. Assuming that the structure exhibits approximately equal damping values in all the modes, two frequencies, ω and $R\omega$, are picked covering the frequency range of interest and the desired amount of modal damping. Then a_0 and a_1 can be computed

as

$$\alpha_0 = \frac{2\zeta\omega R}{1+R} \tag{2.4a}$$

$$\alpha_1 = \frac{2\zeta}{\omega\,(1+R)} \tag{2.4b}$$

5. $\{R(t)\}$ = Vector of stiffness forces corresponding to the configuration, $\{U(t)\}$. It is computed considering all material and geometric nonlinear effects.

6. $\{f_g\}$ = Vector of static gravity loads for which a static analysis is performed first.

7. $\left\{\ddot{U}_g(t)\right\}$ = Vector consisting of two horizontal components (X and Y) and one vertical component (Z) of the free-field ground acceleration at time t. The ground motion is assumed uniform.

8. $[r]$ = A 3-column matrix of zeroes except for ones in the first, second, and third columns in the positions corresponding to the X, Y, and Z DOF, respectively.

9. The base DOF are fixed and are not included.

The nonlinear effects contained in $\{R(t)\}$ can be linearized over the time interval between t and $t+\Delta t$ as:

$$\{R(t+\Delta t)\} = [K_T]\,\{\Delta U\} + \{R(t)\} \tag{2.5}$$

where $[K_T]$ is the tangent stiffness matrix corresponding to the configuration, $\{U(t)\}$. Eq. 2.5 will be substituted into eq. 2.1 written at time, $t+\Delta t$, along with the following relations representing a constant average acceleration over the time step, Δt:

$$\left\{\dot{U}(t+\Delta t)\right\} = \left\{\dot{U}(t)\right\} + \left\{\ddot{U}(t) + \ddot{U}(t+\Delta t)\right\}\frac{\Delta t}{2} \tag{2.6a}$$

$$\left\{\ddot{U}(t+\Delta t)\right\} = \frac{4}{(\Delta t)^2}\{U(t+\Delta t) - U(t)\} - \frac{4}{\Delta t}\left\{\dot{U}(t)\right\} - \left\{\ddot{U}(t)\right\} \tag{2.6b}$$

The result is

$$\left[\frac{4}{(\Delta t)^2}M + \frac{2}{\Delta t}C + K_T\right]\{\Delta U\} = \{f_g\} - \{R(t)\} - [M][r]\left\{\ddot{U}_g(t)\right\} + [M]\left\{\frac{4}{\Delta t}\dot{U}(t) + \ddot{U}(t)\right\} + [C]\left\{\dot{U(t)}\right\} \tag{2.7}$$

Solution of eq. 2.7 for $\{\Delta U\}$ leads to the new displacements via

$$\{U(t+\Delta t)\} = \{U(t)\} + \{\Delta U\} \tag{2.8}$$

Once $[K_T]$ and R are updated to time $t+\Delta t$ and $\left\{\dot{U}(t+\Delta t)\right\}$ and $\left\{\ddot{U}(t+\Delta t)\right\}$ are determined from eqs. 2.6a and 2.6b, the next time step can commence. This process continues forward in time step by step.

However, since its unlikely that the linearization in 2.5 will hold throughout the entire time step without $[K_T]$ changing, iterations are used within each time step. In iteration l, displacement configuration $\left\{U^l\right\}$ has been reached, and the equation to be solved uses $\left[K_T^l\right]$ and $\left\{R^l\right\}$ corresponding to this configuration:

$$\begin{aligned}\left[\frac{4}{(\Delta t)^2}M + \frac{2}{\Delta t}C + K_T^l\right]\{\Delta U\} = \; & \{f_g\} - \left\{R^l\right\} - [M][r]\left\{\ddot{U}_g(t)\right\} + \\ & [M]\left\{\frac{4}{(\Delta t)^2}U(t) + \frac{4}{\Delta t}\dot{U}(t) + \ddot{U}(t)\right\} + \\ & [C]\left\{\frac{2}{\Delta t}U(t) + \dot{U}(t)\right\} - \left[\frac{4}{(\Delta t)^2}M + \frac{2}{\Delta t}C\right]\left\{U^l\right\}\end{aligned} \tag{2.9}$$

Solution of eq. 2.9 leads to $\{\Delta U\}$ which adds to $\left\{U^l\right\}$ to give $\left\{U^{l+1}\right\}$. The next iteration uses the updated values of $\left[K_T^{l+1}\right]$ and $\left\{R^{l+1}\right\}$ corresponding to configuration U^{l+1}. Iterations continue until convergence, and then the next time step begins. Convergence is determined based on user-defined tolerances on the force imbalance represented by the right-hand-side of eq. 2.9.

For nonlinear problems, the basic computational task is to update $\left[K_T^l\right]$ and $\left\{R^l\right\}$ using $\{\Delta U\}$. It should be mentioned that $\left[K_T^{l+1}\right]$ generally includes only linearization of material nonlinearities, not geometric ones. This omission is not very important, however, and any inaccuracy in $\left[K_T^{l+1}\right]$ gets removed in the iteration process as long as all nonlinear effects are properly included in $\left\{R^{l+1}\right\}$. In fact, even material nonlinearities will not be correct in $\left[K_T^{l+1}\right]$ if loading and unloading behaviors of the material differ because it will not be possible to foresee which parts of the structure will be loading and which will be unloading. This is one reason why iterations are performed.

Element assembly is used to construct $\left[K_T^{l+1}\right]$ and $\left\{R^{l+1}\right\}$, i.e., contributions to $\left[K_T^{l+1}\right]$ are the element matrices, $\left[K_{pz}^{l+1}\right]$, $\left[K_{ph}^{l+1}\right]$, $\left[K_{ef}^{l+1}\right]$ and $\left[K_d^{l+1}\right]$, and contributions to $\left\{R^{l+1}\right\}$ are the element vectors, $\left\{R_{pz}^{l+1}\right\}$, $\left\{R_{ph}^{l+1}\right\}$, $\left\{R_{ef}^{l+1}\right\}$, and $\left\{R_d^{l+1}\right\}$. The subscripts stand for panel zone element, plastic hinge beam element, elastofiber beam element, and diaphragm element, respectively.

Take, for example, computation of the updated $\left[K_{ph}^{l+1}\right]$ and $\left\{R_{ph}^{l+1}\right\}$ for a plastic hinge element. The following steps are performed:

1. The 16 global displacement increments from $\{\Delta U\}$ computed by eq. 2.9 for the nodes J and K associated with the plastic hinge element are extracted and placed in the vector $\{\Delta U_{ph}\}$.

2. Using a matrix $\left[T_{ph}^{l}\right]$, vector $\{\Delta U_{ph}\}$ is transformed into $\left\{\Delta U'_{ph}\right\}_L$ which contains displacement increments for the element's 12 degrees of freedom at nodes 1 and 2 in the $X'Y'Z'$ coordinate system:

$$\left\{\Delta U'_{ph}\right\}_L = \left[T_{ph}^{l}\right]\{\Delta U_{ph}\} \tag{2.10}$$

   The subscript, L, indicates that the vector contains terms for the element's 12 DOF at its local nodes 1 and 2.

3. The element's displacement increments $\left\{\Delta U'_{ph}\right\}_L$ are used to first compute $\left[K'^{l+1}_{ph}\right]_L$ and $\left\{R'^{l+1}_{ph}\right\}_L$, which are in terms of the element's 12 DOF.

4. Then, $\left[K'^{l+1}_{ph}\right]_L$ and $\left\{R'^{l+1}_{ph}\right\}_L$ are transformed to the global DOF at nodes J and K using the matrix $\left[T_{ph}^{l+1}\right]$ updated to the $l+1$ configuration:

$$\left[K_{ph}^{l+1}\right] = \left[T_{ph}^{l+1}\right]^T \left[K'^{l+1}_{ph}\right]_L \left[T_{ph}^{l+1}\right] \tag{2.11}$$

$$\left\{R_{ph}^{l+1}\right\} = \left[T_{ph}^{l+1}\right]^T \left\{R'^{l+1}_{ph}\right\}_L \tag{2.12}$$

The updating process is a little different for the other element types. Since the θ^B and θ^C degrees of freedom for the panel zone element are also global degrees of freedom, no transformation with a T matrix is necessary. Some additional steps are necessary for the elastofiber element because the presence of interior nodes means that a nonlinear structural

analysis problem must be solved for each element, using iterations. These iterations are within those performed during the global solution process. Details for the panel zone, plastic hinge, elastofiber, and diaphragm elements are provided in Chapters 3, 4, 5, and 6, respectively. Parts dealing with the element tangent stiffness matrices use a differential notation since tangent is a limit concept.

Chapter 3 Panel Zone Element

Each joint is modeled by a panel zone element consisting of a length of column within the depth of the connecting beams. This implies that one column, the associated column of the joint (ACJ) runs continuously through the height of the joint. The panel zone element is an idealization of the joint region of this column. It consists of two rectangular panels which are perpendicular to each other, panel ① in the $\bar{X} - \bar{Z}$ plane and panel ② in the $\bar{X} - \bar{Y}$ plane, forming a cruciform section (Figure 3.1). The thicknesses of all web plates and web doubler plates of the ACJ are combined to form the thickness of panel ①, $t_p^{①}$, while the thicknesses of all flange plates of the ACJ are combined to form the thickness of panel ②, $t_p^{②}$. The depth, D, of the joint is taken to be equal to the depth (dimension along the minor axis, Z') of the ACJ. The width, W, of the joint is taken to be equal to the width (dimension along the major axis, Y') of the ACJ. The height, H, of the joint is taken to be equal to the depth of the deepest beam framing into that joint. Beams and columns modeled using beam elements connect to the panel zone element at the mid-points of the edges of the two panels. These connection points are henceforth referred to as attachment points. There are six attachment points, a through f. Attachment points a, b, c, and d are reserved for beams, while attachment points e and f are reserved for columns.

The panels are assumed to deform only in shear as a result of the end moments and shears of the attached beams and columns. However, they remain planar and perpendicular to each other at all times. The relation between the shear stress, τ, and the shear strain, γ, can be a nonlinear relation. Detailed experimental [37, 40, 54, 7] and analytical [53, 39, 37, 54, 23] studies have been carried out on steel-frame joints and have resulted in a much better understanding of their hysteretic behavior. Two material shear stress-strain models (bilinear and linear-quadratic [11, 29]) are implemented in this work.

Each panel has two degrees of freedom as shown in Figure 2.3: $\theta^B_{J\bar{Y}}$ and $\theta^C_{J\bar{Y}}$ for panel ①, and $\theta^B_{J\bar{Z}}$ and $\theta^C_{J\bar{Z}}$ for panel ②, where J is the global node at the center of the joint. These DOF are also global DOF. Strain or rotation in one of the panels causes a rigid body rotation but no strain in the orthogonal panel.

The joint coordinate system with origin at the center of the joint (at the node), $\bar{X}\bar{Y}\bar{Z}$

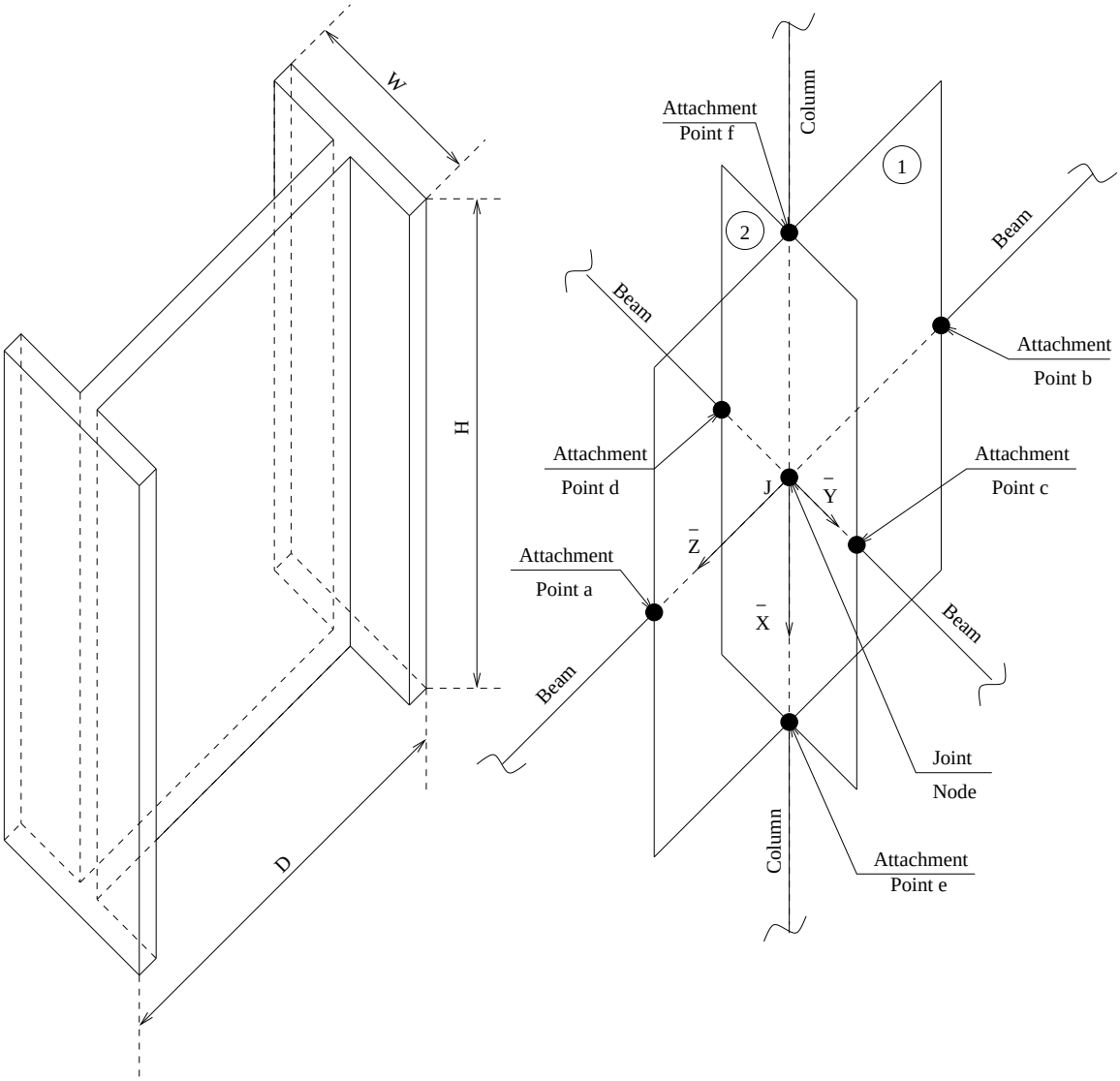

Figure 3.1: Panel Zone Element

is defined as follows:

1. $\bar{X}$ axis: Defined as the vector from attachment point f to attachment point e of the joint.

2. $\bar{Y}$ axis: It is a vector normal to the plane consisting of attachment points a, b, e and f. A unit vector in the direction of $\bar{Y}$ axis is computed as a cross-product of the vector going from point b to point a with the vector going from point f to point e and dividing by the length of the resulting vector.

3. $\bar{Z}$ axis: It is a vector normal to the plane consisting of attachment points c, d, e, and f. A unit vector in the direction of $\bar{Y}$ axis is computed as a cross-product of the vector going from point d to point c with the vector going from point f to point e and dividing by the length of the resulting vector.

Thus, at the beginning of the analysis, the joint coordinate system is the same as the local element coordinate system of the associated column of the joint (ACJ). The direction cosines of the $\bar{X}$ axis *w.r.t.*the Global Coordinate System (XYZ) are given by

$$\bar{p}_x = \frac{X_e - X_f}{\sqrt{(X_e - X_f)^2 + (Y_e - Y_f)^2 + (Z_e - Z_f)^2}} \tag{3.1a}$$

$$\bar{p}_y = \frac{Y_e - Y_f}{\sqrt{(X_e - X_f)^2 + (Y_e - Y_f)^2 + (Z_e - Z_f)^2}} \tag{3.1b}$$

$$\bar{p}_z = \frac{Z_e - Z_f}{\sqrt{(X_e - X_f)^2 + (Y_e - Y_f)^2 + (Z_e - Z_f)^2}} \tag{3.1c}$$

Noting that the $\bar{Y}$ axis is normal to the plane consisting vectors $\vec{V}_{ab}$ and $\vec{V}_{ef}$, a vector,

$\vec{V}_{\bar{Y}}$, in the direction of the $\bar{Y}$ axis is computed as follows:

$$\begin{aligned}
\vec{V}_{\bar{Y}} &= \vec{V}_{ab} \times \vec{V}_{ef} \\
&= \begin{vmatrix} \vec{i} & \vec{j} & \vec{k} \\ X_a - X_b & Y_a - Y_b & Z_a - Z_b \\ X_e - X_f & Y_e - Y_f & Z_e - Z_f \end{vmatrix} \\
&= [(Y_a - Y_b)(Z_e - Z_f) - (Y_e - Y_f)(Z_a - Z_b)]\,\vec{i} \\
&\quad + [(X_e - X_f)(Z_a - Z_b) - (X_a - X_b)(Z_e - Z_f)]\,\vec{j} \\
&\quad + [(X_a - X_b)(Y_e - Y_f) - (X_e - X_f)(Y_a - Y_b)]\,\vec{k}
\end{aligned} \tag{3.2}$$

Now, the direction cosines of the $\bar{Y}$ axis *w.r.t.*the Global Coordinate System (XYZ) are given by

$$\bar{q}_x = \frac{(Y_a - Y_b)(Z_e - Z_f) - (Y_e - Y_f)(Z_a - Z_b)}{L_{\bar{y}}} \tag{3.3a}$$

$$\bar{q}_y = \frac{(X_e - X_f)(Z_a - Z_b) - (X_a - X_b)(Z_e - Z_f)}{L_{\bar{y}}} \tag{3.3b}$$

$$\bar{q}_z = \frac{(X_a - X_b)(Y_e - Y_f) - (X_e - X_f)(Y_a - Y_b)}{L_{\bar{y}}} \tag{3.3c}$$

where

$$\begin{aligned}
L_{\bar{y}} = \{\ & [(Y_a - Y_b)(Z_e - Z_f) - (Y_e - Y_f)(Z_a - Z_b)]^2 \\
& + [(X_e - X_f)(Z_a - Z_b) - (X_a - X_b)(Z_e - Z_f)]^2 \\
& + [(X_a - X_b)(Y_e - Y_f) - (X_e - X_f)(Y_a - Y_b)]^2\ \}^{\frac{1}{2}}
\end{aligned} \tag{3.3d}$$

Similarly, noting that the $\bar{Z}$ axis is normal to the plane consisting vectors $\vec{V}_{ef}$ and $\vec{V}_{cd}$,

a vector, $\vec{V}_{\bar{Z}}$, in the direction of the $\bar{Z}$ axis is computed as follows:

$$\begin{aligned}
\vec{V}_{\bar{Z}} &= \vec{V}_{ef} \times \vec{V}_{cd} \\
&= \begin{vmatrix} \vec{i} & \vec{j} & \vec{k} \\ X_e - X_f & Y_e - Y_f & Z_e - Z_f \\ X_c - X_d & Y_c - Y_d & Z_c - Z_d \end{vmatrix} \\
&= [(Y_e - Y_f)(Z_c - Z_d) - (Y_c - Y_d)(Z_e - Z_f)]\,\vec{i} \\
&\quad + [(X_c - X_d)(Z_e - Z_f) - (X_e - X_f)(Z_c - Z_d)]\,\vec{j} \\
&\quad + [(X_e - X_f)(Y_c - Y_d) - (X_c - X_d)(Y_e - Y_f)]\,\vec{k}
\end{aligned} \tag{3.4}$$

Now, the direction cosines of the $\bar{Z}$ axis *w.r.t.*the Global Coordinate System (XYZ) are given by

$$\bar{r}_x = \frac{(Y_e - Y_f)(Z_c - Z_d) - (Y_c - Y_d)(Z_e - Z_f)}{L_{\bar{z}}} \tag{3.5a}$$

$$\bar{r}_y = \frac{(X_c - X_d)(Z_e - Z_f) - (X_e - X_f)(Z_c - Z_d)}{L_{\bar{z}}} \tag{3.5b}$$

$$\bar{r}_z = \frac{(X_e - X_f)(Y_c - Y_d) - (X_c - X_d)(Y_e - Y_f)}{L_{\bar{z}}} \tag{3.5c}$$

where

$$\begin{aligned}
L_{\bar{z}} = \{\ & [(Y_e - Y_f)(Z_c - Z_d) - (Y_c - Y_d)(Z_e - Z_f)]^2 \\
& + [(X_c - X_d)(Z_e - Z_f) - (X_e - X_f)(Z_c - Z_d)]^2 \\
& + [(X_e - X_f)(Y_c - Y_d) - (X_c - X_d)(Y_e - Y_f)]^2\ \}^{\frac{1}{2}}
\end{aligned} \tag{3.5d}$$

Finally, the panel zone direction cosine matrix is given by

$$\left[\bar{C}_J\right] = \begin{bmatrix} \bar{p}_x & \bar{p}_y & \bar{p}_z \\ \bar{q}_x & \bar{q}_y & \bar{q}_z \\ \bar{r}_x & \bar{r}_y & \bar{r}_z \end{bmatrix} \tag{3.6}$$

3.1 Material Models for Panel Shear

3.1.1 Bilinear Model

The bilinear model was first proposed by Fielding and Chen [23]. The virgin shear stress-strain curve for the joint hysteresis behavior in this model is bilinear (Figure 3.2). The virgin curves for positive and negative shears are identical. The shear yield stress, τ_y, is given by the von Mises yield criterion:

$$\tau_y = \frac{\sigma_y}{\sqrt{3}} \tag{3.7}$$

where σ_y is the axial yield stress of the material. The yield strain is given by

$$\gamma_y = \frac{\tau_y}{G} \qquad \textit{where} \qquad G = \frac{E}{2(1+\nu)} \tag{3.8}$$

In the above, E is the Young's modulus, G is the shear modulus, and ν is the Poisson's ratio of the material. For a panel zone with the bilinear material model, the tangent shear modulus is given by:

$$G_T = G \text{ if panel zone has not yielded} \tag{3.9a}$$

$$G_T = \alpha_{pz}^s G \text{ if panel zone has yielded} \tag{3.9b}$$

Unloading occurs linearly until zero stress is reached at a rate equal to the elastic modulus and further loading in the reverse direction follows a bilinear stress-strain relation in the opposite direction shifted suitably.

3.1.2 Linear-Quadratic Ellipsoidal Model

The linear-quadratic ellipsoidal joint hysteresis model proposed by Challa and Hall [11, 29] defines a virgin curve for the joint hysteresis behavior as shown in Figure 3.3. The shear stress-strain is assumed to be linear until a stress of $0.8\tau_y$ is reached corresponding to a strain of $0.8\gamma_y$, where, as before, τ_y and γ_y are the yield shear stress and strain, respectively. The ultimate shear stress, τ_u, of the panel zone is assumed to be equal to $2.35\tau_y$, corresponding to an ultimate shear strain, γ_u, of $100\gamma_y$. The post-ultimate behavior is assumed to be perfectly plastic. The curve between the joint shear strain limits of $0.8\gamma_y$ and $100\gamma_y$ is

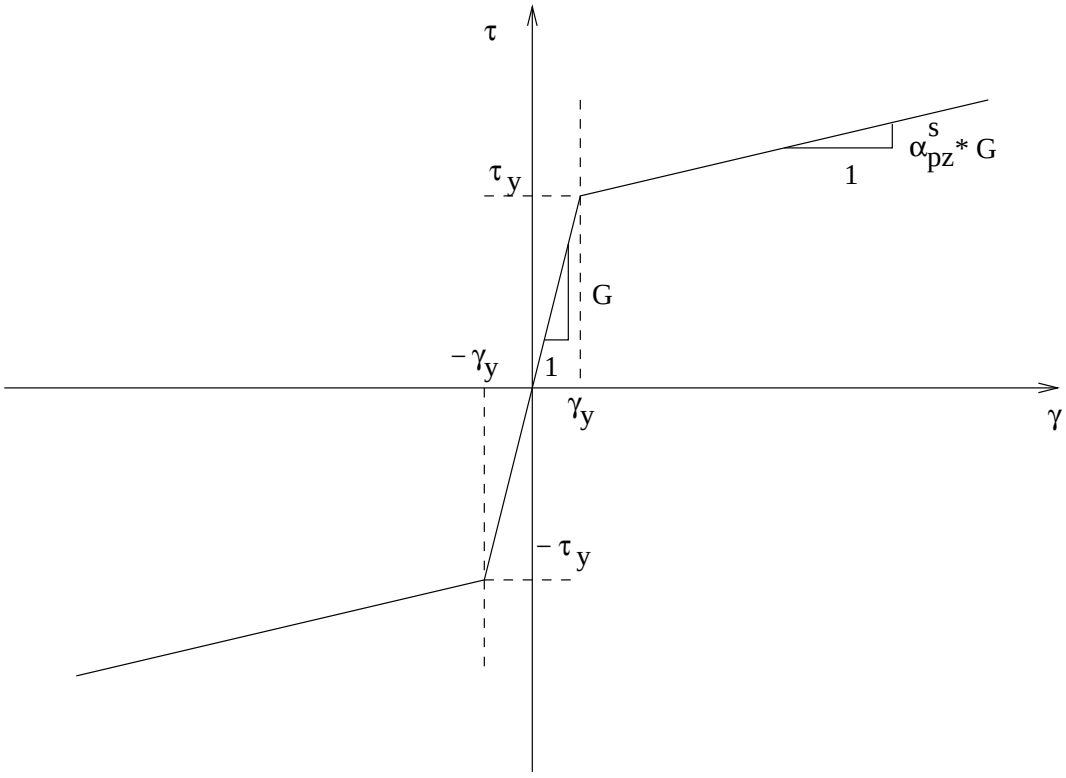

Bilinear shear stress−strain law for a panel zone

Figure 3.2: Shear Stress-Strain Model for a Bilinear Panel Zone Element

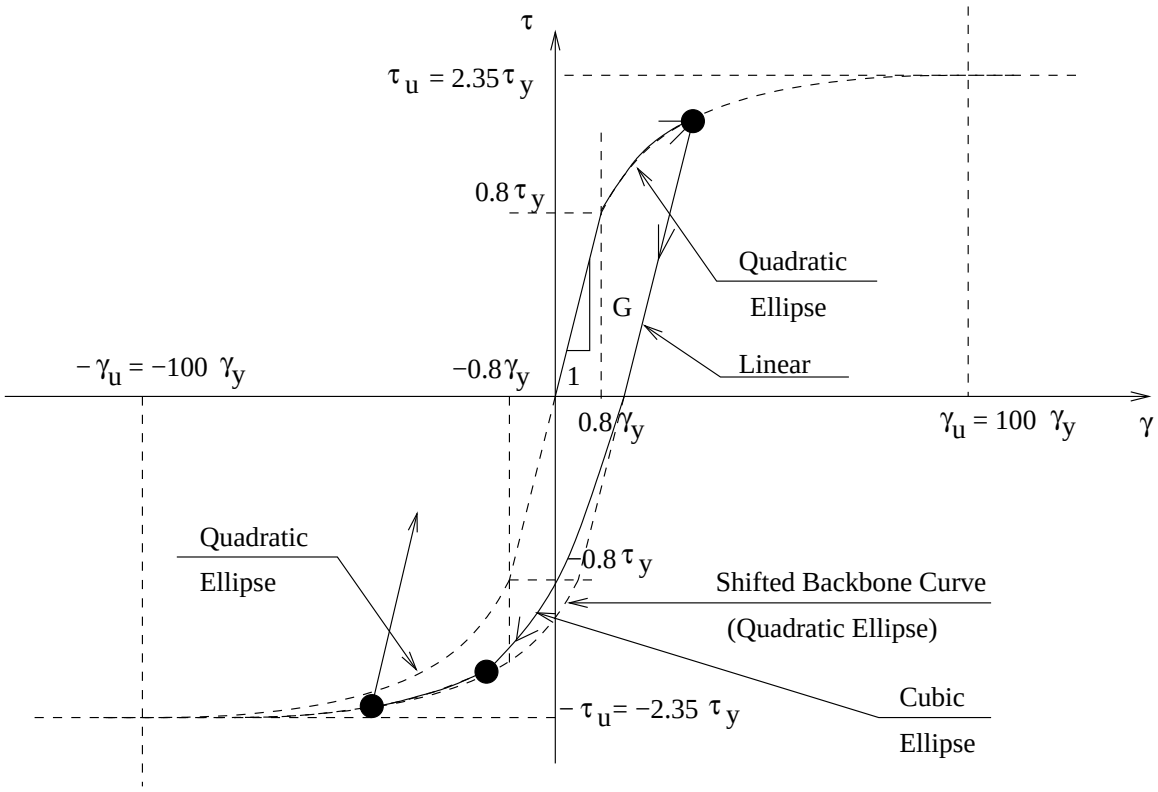

Figure 3.3: Shear Stress-Strain Model for a Linear-Quadratic Panel Zone Element

defined by a quadratic ellipse given by:

$$\frac{(\gamma-\gamma_0)^2}{a^2}+\frac{(\tau-\tau_0)^2}{b^2}=1 \tag{3.10}$$

where σ_0 and γ_0 are the coordinates of the center of the ellipse whose semi-major and semi-minor axes are a and b, respectively. The hysteresis loops or the branch curves are defined by cubic ellipses given by:

$$-\frac{(\gamma-\gamma_0)^3}{a^3}+\frac{(\tau-\tau_0)^3}{b^3}=1 \text{ for positive curve} \tag{3.11a}$$

$$\text{and } \frac{(\gamma-\gamma_0)^3}{a^3}-\frac{(\tau-\tau_0)^3}{b^3}=1 \text{ for negative curve} \tag{3.11b}$$

The hysteresis rules to define the cyclic response of each panel are given in Reference [11]. For a panel zone with the linear-quadratic ellipsoidal material model, the tangent shear modulus, G_T, is given by the slope of the curve (Figure 3.3) at the current state which is determined from the stress-strain history and current strain increment.

3.2 Theory of the Panel Zone Element

Figure 3.4 shows panels ① and ② with their dimensions, degrees of freedom, and shear forces acting on the panel edges. The shear forces come from the end moments and shears from the connected beam elements modeling beams and columns. Each panel is under a uniform state of shear stress: $\tau^{①}$ for panel ① and $\tau^{②}$ for panel ②.

Consider panel ① with its degrees of freedom, $\theta^B_{J\bar{Y}}$ and $\theta^C_{J\bar{Y}}$. The four edge forces form a double couple of amplitude, $\tau^{①} t_p^{①} HD$. The halves of this double couple are the panel moments which correspond to the two rotational DOF and can be written as

$$M^C_{J\bar{Y}} = -M^B_{J\bar{Y}} = \tau^{①} t_p^{①} HD \tag{3.12}$$

The shear stress, $\tau^{①}$, is related to the shear strain, $\gamma^{①}$, by the incremental relation,

$$d\tau^{①} = G_T^{①} d\gamma^{①} \tag{3.13}$$

according to the formulation of the previous section, where $G_T^{①}$ is the tangent shear modulus of the previous section. The incremental shear strain is related to the degrees of freedom by

$$d\gamma^{①} = d\theta^C_{J\bar{Y}} - d\theta^B_{J\bar{Y}} \tag{3.14}$$

Combining eqs. 3.13 and 3.14 with the incremental version of eq. 3.12:

$$\begin{Bmatrix} dM^B_{J\bar{Y}} \\ dM^C_{J\bar{Y}} \end{Bmatrix} = G_T^{①} t_p^{①} HD \begin{bmatrix} 1 & -1 \\ -1 & 1 \end{bmatrix} \begin{Bmatrix} d\theta^B_{J\bar{Y}} \\ d\theta^C_{J\bar{Y}} \end{Bmatrix} \tag{3.15}$$

which is the tangent stiffness relation for panel ①.

A similar treatment for panel ② results in the following tangent stiffness relation:

$$\begin{Bmatrix} dM^B_{J\bar{Z}} \\ dM^C_{J\bar{Z}} \end{Bmatrix} = G_T^{②} t_p^{②} HW \begin{bmatrix} 1 & -1 \\ -1 & 1 \end{bmatrix} \begin{Bmatrix} d\theta^B_{J\bar{Z}} \\ d\theta^C_{J\bar{Z}} \end{Bmatrix} \tag{3.16}$$

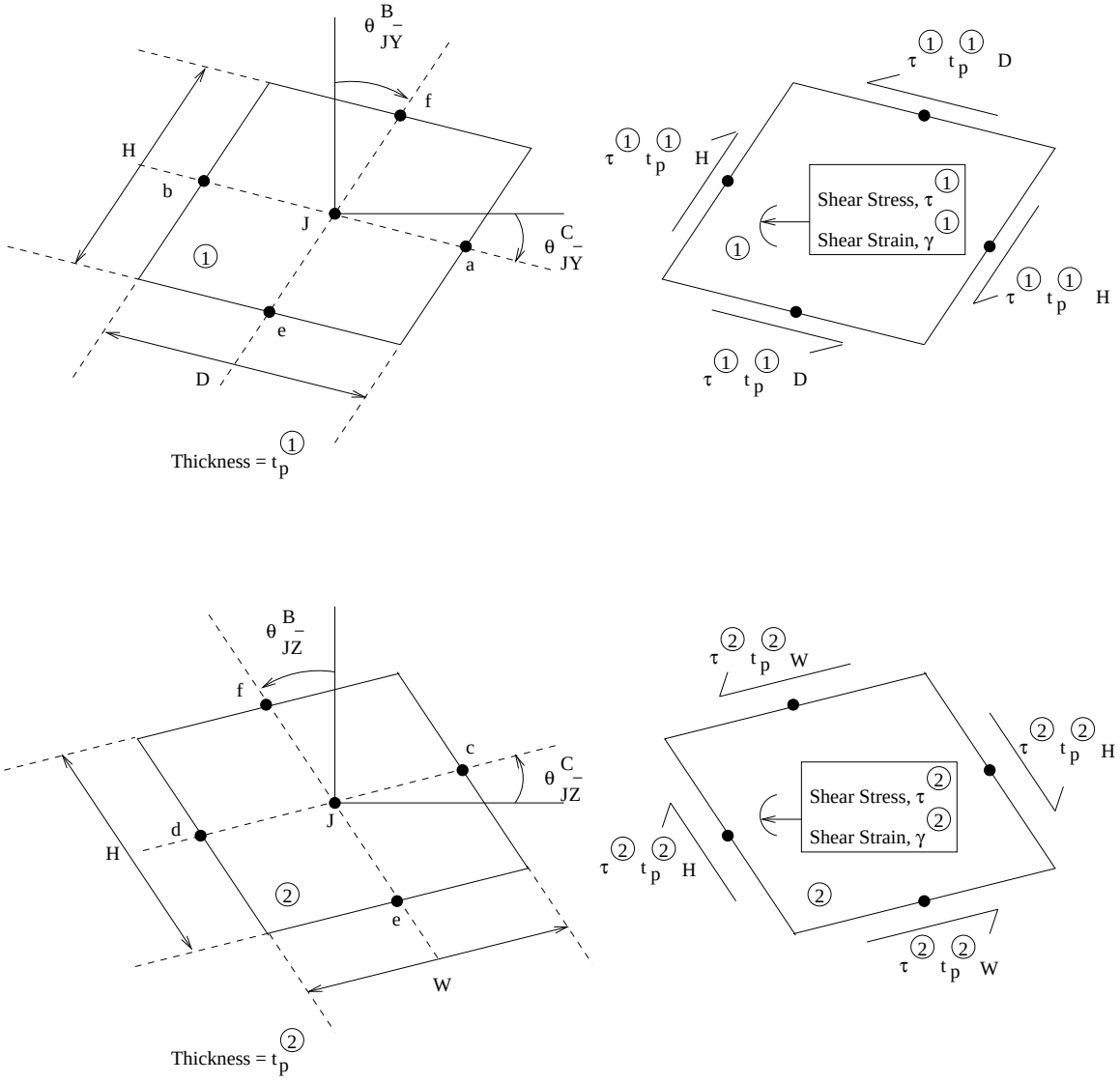

Figure 3.4: Panels ① (Top) and ② (Bottom) Showing Dimensions and Degrees of Freedom (Left) and Edge Shear Forces (Right)

Combining eqs. 3.15 and 3.16 leads to

$$\{dR_{pz}\} = [K_{T,pz}]\,\{dU_{pz}\} \tag{3.17}$$

where $\{dR_{pz}\}$ is the incremental version of

$$\langle R_{pz} \rangle = \langle\ M^B_{J\bar{Y}} \quad M^C_{J\bar{Y}} \quad M^B_{J\bar{Z}} \quad M^C_{J\bar{Z}}\ \rangle \tag{3.18}$$

$[K_{T,pz}]$ is the 4x4 tangent stiffness matrix for the panel zone element, and

$$\langle dU_{pz} \rangle = \langle\ d\theta^B_{J\bar{Y}} \quad d\theta^C_{J\bar{Y}} \quad d\theta^B_{J\bar{Z}} \quad d\theta^C_{J\bar{Z}}\ \rangle \tag{3.19}$$

3.3 Updating Process

In global iteration l, $\{\Delta U\}$ is computed from eq. 2.9. The four rotation increments for a panel zone element, $\Delta\theta^B_{J\bar{Y}}$, $\Delta\theta^C_{J\bar{Y}}$, $\Delta\theta^B_{J\bar{Z}}$, and $\Delta\theta^C_{J\bar{Z}}$, are extracted from $\{\Delta U\}$ and placed in $\{\Delta U_{pz}\}$. The coordinates of node J of the panel zone element are updated using ΔU_{JX}, ΔU_{JY}, and ΔU_{JZ}, also obtained from $\{\Delta U\}$. Using the new location of node J and the incremental rotations, $\{\Delta U_{pz}\}$, the updated coordinates for attachment points a through f and the updated orientations for $\bar{X}$, $\bar{Y}$, and $\bar{Z}$ axes are found. The procedure for this geometry updating is given in Appendix A. In addition, the angles, $\xi^{①}$ and $\xi^{②}$, used in Chapter 4 are updated.

The shear strain increments in the two panels are computed as

$$\Delta\gamma^{①} = \Delta\theta^C_{J\bar{Y}} - \Delta\theta^B_{J\bar{Y}} \tag{3.20a}$$

$$\Delta\gamma^{②} = \Delta\theta^B_{J\bar{Z}} - \Delta\theta^C_{J\bar{Z}} \tag{3.20b}$$

from which the updated shear strains are

$$\gamma^{①,l+1} = \gamma^{①,l} + \Delta\gamma^{①} \tag{3.21a}$$

$$\gamma^{②,l+1} = \gamma^{②,l} + \Delta\gamma^{②} \tag{3.21b}$$

Using the formulation of Section 3.1, the updated shear stresses, $\tau^{①,l+1}$ and $\tau^{②,l+1}$, can

now be found. From eq. 3.12, the moments for panel ① are

$$M_{J\bar{Y}}^{C,l+1} = -M_{J\bar{Y}}^{B,l+1} = \tau^{①,l+1} t_p^{①} HD \tag{3.22}$$

Similarly, the moments for panel ② are given by

$$M_{J\bar{Z}}^{C,l+1} = -M_{J\bar{Z}}^{B,l+1} = -\tau^{②,l+1} t_p^{②} HW \tag{3.23}$$

Then, as in eq. 3.18,

$$\langle R_{pz}^{l+1} \rangle = \langle \; M_{J\bar{Y}}^{B,l+1} \quad M_{J\bar{Y}}^{C,l+1} \quad M_{J\bar{Z}}^{B,l+1} \quad M_{J\bar{Z}}^{C,l+1} \; \rangle \tag{3.24}$$

The element tangent stiffness matrix can be updated once the tangent shear moduli, $G_T^{①,l+1}$ and $G_T^{②,l+1}$, are found for each panel. This information is available as a result of computing $\left\{R_{pz}^{l+1}\right\}$, after which $\left[K_{T,pz}^{l+1}\right]$ can be found from the formulae in the previous section.

Since the rotational DOF of the panel zone element are also global DOF, no transformations of $\left\{R_{pz}^{l+1}\right\}$ and $\left[K_{T,pz}^{l+1}\right]$ are necessary before they are assembled into the global equations.

Chapter 4 Three-Dimensional Plastic-Hinge Element

4.1 General Description

The following assumptions are made in the formulation of this element:

1. The cross-section is assumed uniform along the length of the element.
2. The cross-section is assumed to be doubly symmetric (with shear center at the centroid).
3. Plane sections remain plane; however, they do not have to remain normal to the beam axis. Thus, shear deformations are included.
4. Strains in the element are small.
5. Lateral deflections relative to the chord are small. This means that the effect of bowing [50, 51, 36] on axial stiffness is neglected. This effect is important only for very slender members or during post-buckling of compression members such as braces in braced frames.
6. Warping restraint under twisting is neglected.
7. The element is loaded only at its ends.
8. Composite action with the slab is not included.
9. Local buckling is not included.

The plastic hinge beam element has two nodes which connect to the attachment points a through f of the panel zone element. This element can model beams and columns in framed structures. Columns connect to attachment points e and f while beams connect to attachment points a through d. The beam element along with its degrees of freedom is shown in Figure4.1. Original length of the element is L_0.

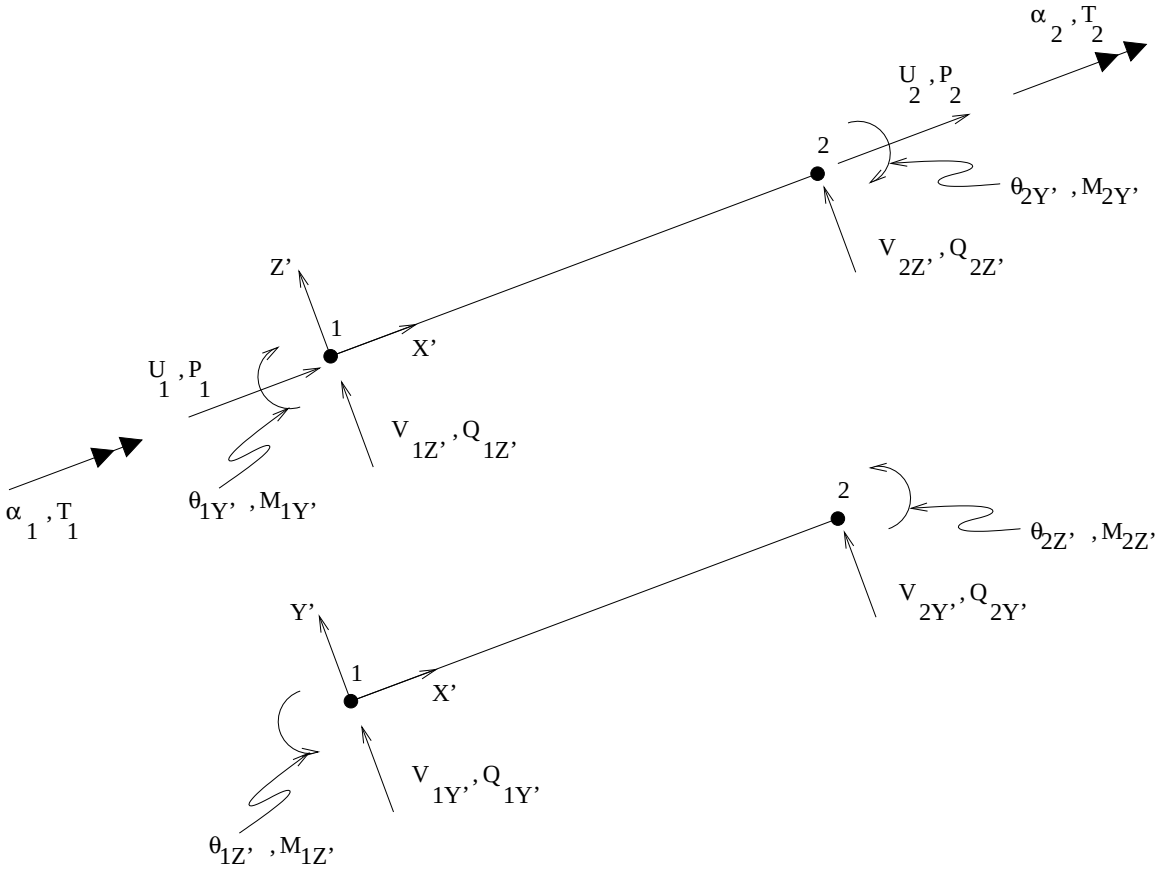

Figure 4.1: DOF of the Plastic Hinge Beam Element Showing Nodal Translations and Rotations and Nodal Forces and Moments

The plastic hinge element local coordinate system, $X'Y'Z'$, is a right-handed, orthogonal system and is defined as follows:

1. X' axis: It runs along the longitudinal axis of the element at the centroid of the cross-section. It is defined as a vector from node 1 to node 2 which are also located at the centroid.

2. Y' axis: Y' axis is orthogonal to X' and is the major principal axis of the cross-section of the element.

3. Z' axis: Z' axis is the minor principal axis of the cross-section of the element.

The major and minor principal axes, Y' and Z', of the cross-section are oriented using a user-defined orientation angle, α_{or}, that is defined differently for beams and columns as described below. Also described in the following subsections is the procedure used to compute the direction cosine matrix, $[C']$, for beams and columns, using α_{or}.

4.1.1 Direction Cosine Matrix for Columns

For columns, α_{or} is the angle made by the Z' axis with a plane passing through the longitudinal axis of the element, X' and the global X axis (See Figure 4.2). The direction of α_{or} is defined using the right-hand-thumb rule and is positive if it is in the positive direction of X' axis. It is updated after every iteration during each time step of the analysis based on the twist (torsional deformation) in the element. See section 4.4 for the updating strategy.

Using Euler angles, the column direction cosine matrix, $[C']$ can be derived as the product of three transformations as follows (See Figure 4.3):

1. $XYZ \rightarrow XY_1Z_1$: Rotate XYZ frame about the X axis through angle β. This rotation

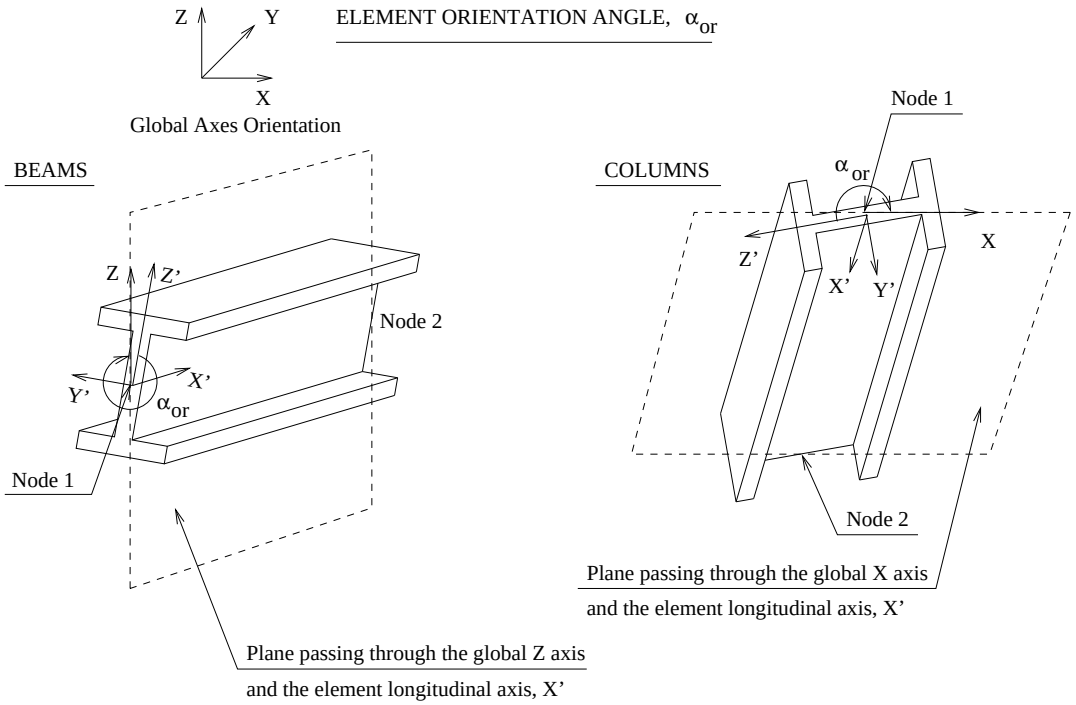

BEAMS: α_{or} = Angle made by the Z' axis with a plane passing through the global Z axis and the element longitudinal axis, X'; it is measured using the right−hand−thumb rule with the thumb pointing in the positive direction of the X' axis, which runs from node 1 to node 2 of the element

COLUMNS: α_{or} = Angle made by the Z' axis with a plane passing through the global X axis and the element longitudinal axis, X'; it is measured using the right−hand−thumb rule with the thumb pointing in the positive direction of the X' axis, which runs from node 1 to node 2 of the element

Figure 4.2: Element Orientation Angle, α_{or}

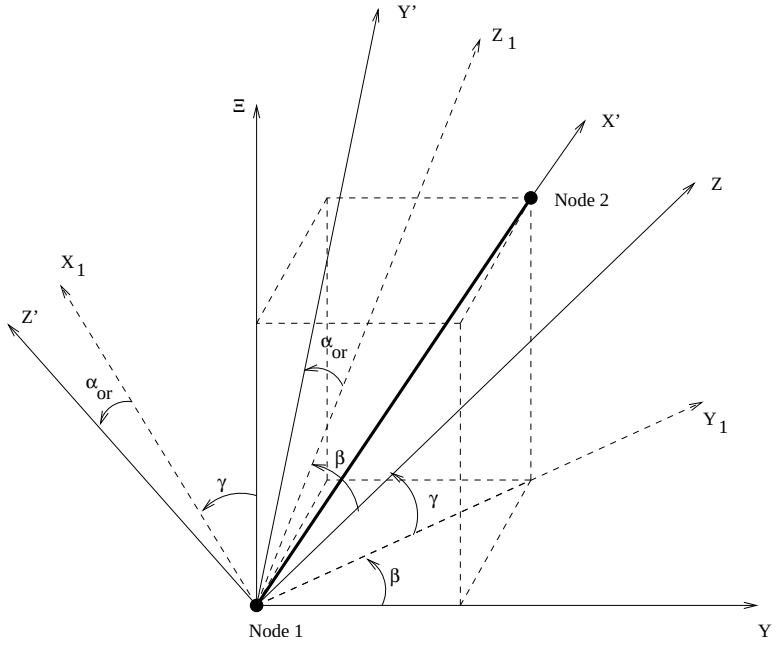

Figure 4.3: Rotations Used to Transform Global Axes to Column Element Local Axes

is achieved with the transformation matrix, $[L]_\beta$ given below.

$$\cos\beta = \frac{c_y}{\sqrt{c_y^2 + c_z^2}} \tag{4.1a}$$

$$\sin\beta = \frac{c_z}{\sqrt{c_y^2 + c_z^2}} \tag{4.1b}$$

$$c_x = \frac{X_2 - X_1}{L};\ c_y = \frac{Y_2 - Y_1}{L};\ c_z = \frac{Z_2 - Z_1}{L} \tag{4.1c}$$

$$L = \sqrt{(X_2 - X_1)^2 + (Y_2 - Y_1)^2 + (Z_2 - Z_1)^2} \tag{4.1d}$$

$$[L_\beta] = \begin{bmatrix} 1 & 0 & 0 \\ 0 & \cos\beta & \sin\beta \\ 0 & -\sin\beta & \cos\beta \end{bmatrix} \tag{4.1e}$$

2. $XY_1Z_1 \rightarrow X_1X'Z_1$: Rotate XY_1Z_1 frame about $-Z_1$ axis through an angle γ such that Y_1 axis coincides with X' axis. This rotation is achieved with the transformation matrix, $[L]_\gamma$ given below.

$$\cos\gamma = \sqrt{c_y^2 + c_z^2} \tag{4.1f}$$

$$\sin\gamma = c_x \tag{4.1g}$$

$$[L_\gamma] = \begin{bmatrix} \cos\gamma & -\sin\gamma & 0 \\ \sin\gamma & \cos\gamma & 0 \\ 0 & 0 & 1 \end{bmatrix} \tag{4.1h}$$

3. $X_1X'Z_1 \rightarrow Z'X'Y'$: Rotate $X_1X'Z_1$ frame about the X' axis through an angle α_{or} such that the X_1 axis coincides with the Z' axis and the Z_1 axis coincides with the Y' axis. This rotation is achieved with the transformation matrix, $[L]_\alpha$ given below.

$$[L_\alpha] = \begin{bmatrix} \cos\alpha_{or} & 0 & \sin\alpha_{or} \\ 0 & 1 & 0 \\ -\sin\alpha_{or} & 0 & \cos\alpha_{or} \end{bmatrix} \tag{4.1i}$$

4. $Z'X'Y' \rightarrow X'Y'Z'$; Shift the rows of the transformation matrix resulting from the previous steps.

Finally, the column direction cosine matrix is given by

$$[C']^{Z'X'Y'} = [L_\alpha]\,[L_\gamma]\,[L_\beta] \tag{4.1j}$$

$$[C']^{X'Y'Z'} == \begin{bmatrix} s_\gamma & c_\gamma c_\beta & c_\gamma s_\beta \\ -s_{\alpha_{or}} c_\gamma & s_{\alpha_{or}} s_\gamma c_\beta - c_{\alpha_{or}} s_\beta & s_{\alpha_{or}} s_\gamma s_\beta + c_{\alpha_{or}} c_\beta \\ c_{\alpha_{or}} c_\gamma & -c_{\alpha_{or}} s_\gamma c_\beta - s_{\alpha_{or}} s_\beta & -c_{\alpha_{or}} s_\gamma s_\beta + s_{\alpha_{or}} c_\beta \end{bmatrix} \tag{4.1k}$$

where c and s refer to cos and sin, respectively.

4.1.2 Direction Cosine Matrix for Beams

For beams, α_{or} is the angle made by the Z' axis with a plane passing through the longitudinal axis of the element, X' and the global Z axis (See Figure 4.2). When the global Z axis is the vertical axis, this plane is a global vertical plane passing through the longitudinal axis of the element. The direction of α_{or} is defined using the right-hand-thumb rule and is positive if it is in the positive direction of X' axis. It is updated after every iteration during each time step of the analysis based on the twist (torsional deformation) in the element. See section 4.4 for the updating strategy.

Using Euler angles, the beam direction cosine matrix, $[L]_{beam}$ can be derived as the product of three transformations as follows (See Figure 4.4):

1. $XYZ \rightarrow X_1Y_1Z$: Rotate XYZ frame about the Z axis through angle β. This rotation is achieved with the transformation matrix, $[L]_\beta$ given below.

$$\cos\beta = \frac{c_x}{\sqrt{c_x^2 + c_y^2}} \tag{4.2a}$$

$$\sin\beta = \frac{c_y}{\sqrt{c_x^2 + c_y^2}} \tag{4.2b}$$

$$c_x = \frac{X_2 - X_1}{L};\ c_y = \frac{Y_2 - Y_1}{L};\ c_z = \frac{Z_2 - Z_1}{L} \tag{4.2c}$$

$$L = \sqrt{(X_2 - X_1)^2 + (Y_2 - Y_1)^2 + (Z_2 - Z_1)^2} \tag{4.2d}$$

$$[L_\beta] = \begin{bmatrix} \cos\beta & \sin\beta & 0 \\ -\sin\beta & \cos\beta & 0 \\ 0 & 0 & 1 \end{bmatrix} \tag{4.2e}$$

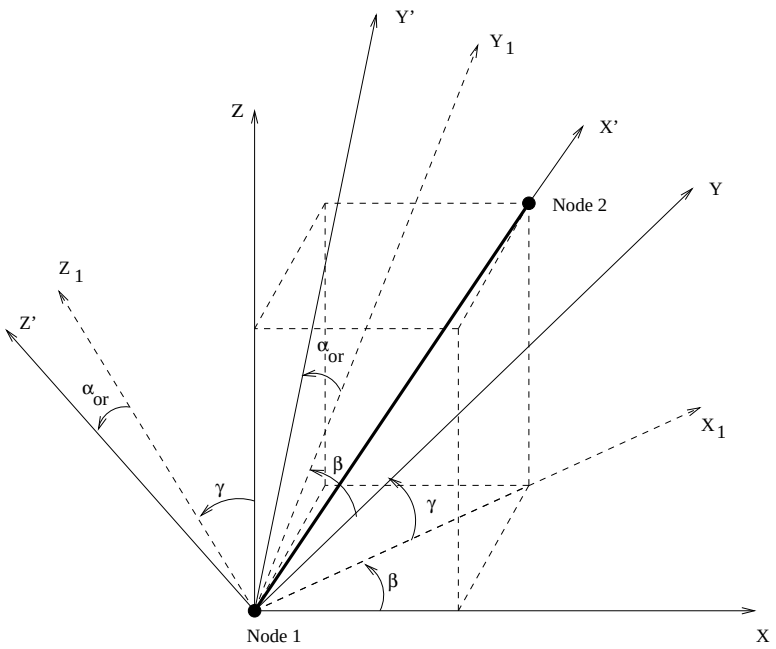

Figure 4.4: Rotations Used to Transform Global Axes to Beam Element Local Axes

2. $X_1Y_1Z \rightarrow X'Y_1Z_1$: Rotate X_1Y_1Z frame about Y_1 axis through an angle γ such that X_1 axis coincides with X' axis. This rotation is achieved with the transformation matrix, $[L]_\gamma$ given below.

$$\cos\gamma = \sqrt{c_x^2 + c_y^2} \tag{4.2f}$$

$$\sin\gamma = c_z \tag{4.2g}$$

$$[L_\gamma] = \begin{bmatrix} \cos\gamma & 0 & \sin\gamma \\ 0 & 1 & 0 \\ -\sin\gamma & 0 & \cos\gamma \end{bmatrix} \tag{4.2h}$$

3. $X'Y_1Z_1 \rightarrow X'Y'Z'$: Rotate $X'Y_1Z_1$ frame about the X' axis through an angle α_{or} such that the Y_1 axis coincides with the Y' axis and the Z_1 axis coincides with the Z' axis. This rotation is achieved with the transformation matrix, $[L]_\alpha$ given below.

$$[L_\alpha] = \begin{bmatrix} 1 & 0 & 0 \\ 0 & \cos\alpha_{or} & \sin\alpha_{or} \\ 0 & -\sin\alpha_{or} & \cos\alpha_{or} \end{bmatrix} \tag{4.2i}$$

Finally, the beam direction cosine matrix is given by

$$[C'] = [L_\alpha][L_\gamma][L_\beta] = \begin{bmatrix} c_\gamma c_\beta & c_\gamma s_\beta & s_\gamma \\ -s_{\alpha_{or}} s_\gamma c_\beta - c_{\alpha_{or}} s_\beta & -s_{\alpha_{or}} s_\gamma s_\beta + c_{\alpha_{or}} c_\beta & s_{\alpha_{or}} c_\gamma \\ -c_{\alpha_{or}} s_\gamma c_\beta + s_{\alpha_{or}} s_\beta & -c_{\alpha_{or}} s_\gamma s_\beta - s_{\alpha_{or}} c_\beta & c_{\alpha_{or}} c_\gamma \end{bmatrix} \tag{4.2j}$$

where c and s refer to cos and sin, respectively.

4.1.3 Degrees of Freedom, and Nodal Forces and Moments

The degrees of freedom (Figure 4.1) of the plastic hinge element are:

1. U_1, $U_2 = X'$ translations of nodes 1 and 2, respectively.
2. $V_{1Y'}$, $V_{2Y'} = Y'$ translations of nodes 1 and 2, respectively.
3. $V_{1Z'}$, $V_{2Z'} = Z'$ translations of nodes 1 and 2, respectively.
4. α_1, α_2 = Rotations of the element about X' at nodes 1 and 2, respectively.
5. $\theta_{1Y'}$, $\theta_{2Y'}$ = Rotations of the element about Y' at nodes 1 and 2, respectively.
6. $\theta_{1Z'}$, $\theta_{2Z'}$ = Rotations of the element about Z' at nodes 1 and 2, respectively.

Corresponding to these DOF are nodal forces and moments (Figure 4.1):

1. P_1, P_2 = Forces in X' direction at nodes 1 and 2, respectively.
2. $Q_{1Y'}$, $Q_{2Y'}$ = Forces in Y' direction at nodes 1 and 2, respectively.
3. $Q_{1Z'}$, $Q_{2Z'}$ = Forces in Z' direction at nodes 1 and 2, respectively.
4. T_1, T_2 = Moments about X' at nodes 1 and 2, respectively.
5. $M_{1Y'}$, $M_{2Y'}$ = Moments about Y' at nodes 1 and 2, respectively.
6. $M_{1Z'}$, $M_{2Z'}$ = Moments about Z' at nodes 1 and 2, respectively.

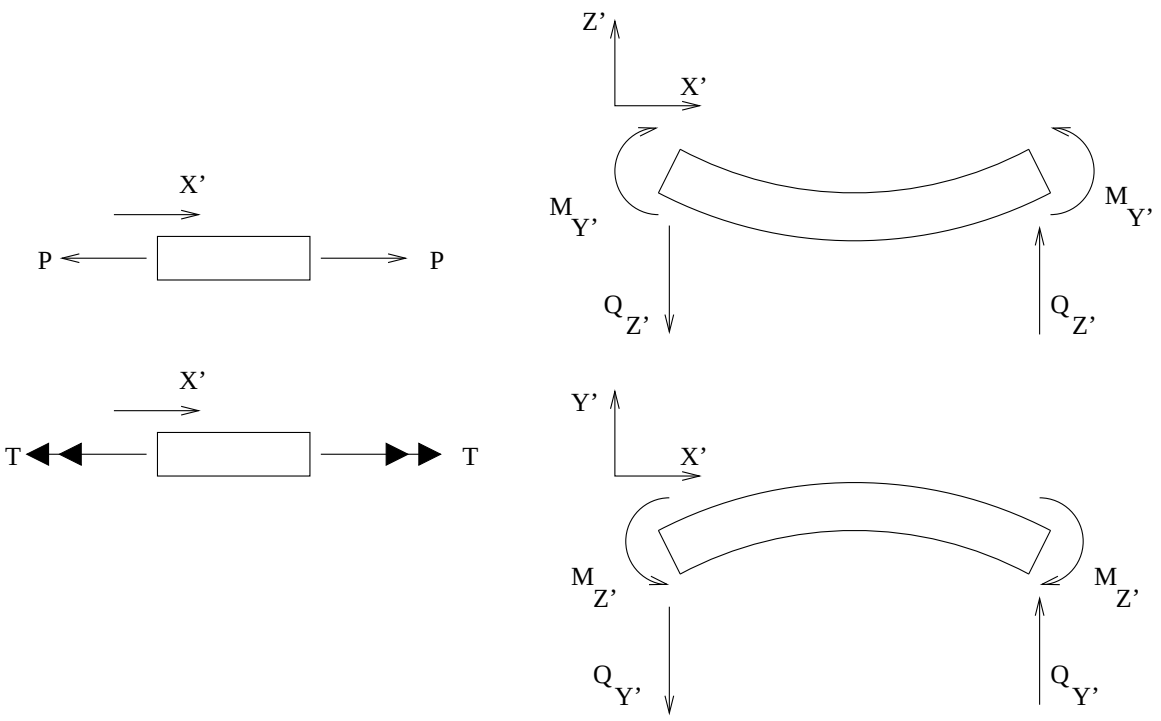

Figure 4.5: Sign Convention for Internal Forces and Moments in a Plastic Hinge Beam Element

4.1.4 Internal Forces and Moments

The set of internal forces and moments in the plastic hinge beam element are as follows:

1. P = Axial force in the element.

2. $Q_{Y'}$, $Q_{Z'}$ = Shear forces in the element in the Y' and Z' directions, respectively.

3. T = Twisting moment (torque) in the element.

4. $M_{Y'}$, $M_{Z'}$ = Moments in the element about the Y' and Z' axes, respectively.

The sign convention (positive directions) for these forces and moments is shown in Figure 4.5.

4.1.5 Material Nonlinearity

Two types of material nonlinearity are considered.

1. Axial yielding when axial force, P, in the element reaches the yield axial force, P_y,

which is given by:

$$P_y = \sigma_y A \tag{4.3}$$

where σ_y is the yield stress of the material and A is the area of the cross-section.

2. Flexural yielding when the bending moment, $M_{Y'}$ or $M_{Z'}$ at the ends of the element reaches the plastic moment capacity, $M_{pY'}$ or $M_{pZ'}$, which depend on the axial force, P, as shown in Figure 4.6. The plastic moment capacities when $P = 0$, denoted by $M^0_{pY'}$ and $M^0_{pZ'}$, are given by

$$M^0_{pY'} = \sigma_y Z_{Y'} \tag{4.4a}$$

$$M^0_{pZ'} = \sigma_y Z_{Z'} \tag{4.4b}$$

where $Z_{Y'}$ and $Z_{Z'}$ are the plastic moduli of the cross-section of the element about its major and minor axes respectively. Once $|M_{Y'}|$ or $|M_{Z'}|$ reaches $M_{pY'}$ or $M_{pZ'}$ at node 1 or node 2, further loading loading causes a kink, termed a plastic hinge to form in the beam at that node. Between these plastic hinge locations, the beam behaves elastically. To approximate the effect of strain hardening, elastic rotational springs are mounted across the plastic hinges to exert moments proportional to the kink angles about Y' and Z' axes.

4.2 Transformation Matrix, $[T_{ph}]$

$[T_{ph}]$ is the transformation matrix between the 16 global DOF at the nodes J and K of the joints and the 12 local degrees of freedom at nodes 1 and 2. The transformation is carried out in four steps for displacement increments:

$\{\Delta U_{ph}\} \xrightarrow{1} \left\{\Delta \bar{U}_{ph}\right\} \xrightarrow{2} \left\{\Delta \bar{U}_{ph}\right\}_L \xrightarrow{3} \{\Delta U_{ph}\}_L \xrightarrow{4} \left\{\Delta U'_{ph}\right\}_L$ where $\left\{\Delta U'_{ph}\right\}_L$ contains the 12 terms for the local nodes 1 and 2 (indicated by the L subscript) in the $X'Y'Z'$ coordinate system and $\{\Delta U_{ph}\}$ contains the 16 global DOF at the nodes J and K of the joints with translational DOF in XYZ and rotational DOF in $\bar{X}\bar{Y}\bar{Z}$ of nodes J and K.

$$\langle \Delta U_{ph} \rangle = \begin{matrix} \langle \Delta U_{JX} & \Delta U_{JY} & \Delta U_{JZ} & \Delta \theta_{J\bar{X}} & \Delta \theta^B_{J\bar{Y}} & \Delta \theta^C_{J\bar{Y}} & \Delta \theta^B_{J\bar{Z}} & \Delta \theta^C_{J\bar{Z}} \\ \Delta U_{KX} & \Delta U_{KY} & \Delta U_{KZ} & \Delta \theta_{K\bar{X}} & \Delta \theta^B_{K\bar{Y}} & \Delta \theta^C_{K\bar{Y}} & \Delta \theta^B_{K\bar{Z}} & \Delta \theta^C_{K\bar{Z}} \rangle \end{matrix} \tag{4.5}$$

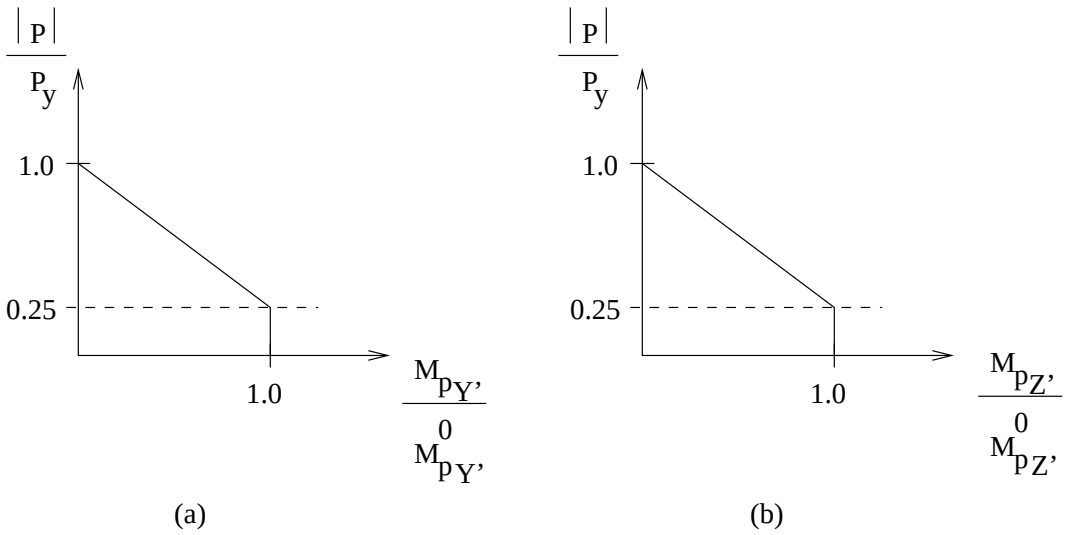

Figure 4.6: $P - M_{pY'} - M_{pZ'}$ Interaction Diagrams Used for the Plastic Hinge Element

The first transformation

$$\left\{\Delta\bar{U}_{ph}\right\} = [T_1]\left\{\Delta U_{ph}\right\} \tag{4.6a}$$

produces

$$\langle\Delta\bar{U}_{ph}\rangle = \begin{matrix}\langle\Delta U_{J\bar{X}} & \Delta U_{J\bar{Y}} & \Delta U_{J\bar{Z}} & \Delta\theta_{J\bar{X}} & \Delta\theta^B_{J\bar{Y}} & \Delta\theta^C_{J\bar{Y}} & \Delta\theta^B_{J\bar{Z}} & \Delta\theta^C_{J\bar{Z}} \\ \Delta U_{K\bar{X}} & \Delta U_{K\bar{Y}} & \Delta U_{K\bar{Z}} & \Delta\theta_{K\bar{X}} & \Delta\theta^B_{K\bar{Y}} & \Delta\theta^C_{K\bar{Y}} & \Delta\theta^B_{K\bar{Z}} & \Delta\theta^C_{K\bar{Z}}\rangle\end{matrix} \tag{4.6b}$$

where the translational DOF are now in $\bar{X}\bar{Y}\bar{Z}$. Note that the $\bar{X}\bar{Y}\bar{Z}$ for node 1 belongs to node J to which node 1 is connected through one of the attachment points, and the $\bar{X}\bar{Y}\bar{Z}$ for node 2 belongs to node K to which node 2 is connected to an attachment point there.

The second transformation

$$\left\{\Delta\bar{U}_{ph}\right\}_L = [T_2]\left\{\Delta\bar{U}_{ph}\right\} \tag{4.7a}$$

produces

$$\langle\Delta\bar{U}_{ph}\rangle_L = \langle\Delta U_{1\bar{X}} \quad \Delta U_{1\bar{Y}} \quad \Delta U_{1\bar{Z}} \quad \Delta\theta_{1\bar{X}} \quad \Delta\theta_{1\bar{Y}} \quad \Delta\theta_{1\bar{Z}} \quad \Delta U_{2\bar{X}} \quad \Delta U_{2\bar{Y}} \quad \Delta U_{2\bar{Z}} \quad \Delta\theta_{2\bar{X}} \quad \Delta\theta_{2\bar{Y}} \quad \Delta\theta_{2\bar{Z}}\rangle \tag{4.7b}$$

where the 8 DOF at node J have been transformed to the 6 local beam DOF at node 1

(still in node J's $\bar{X}\bar{Y}\bar{Z}$) and the 8 DOF at node K have been transformed to the 6 local beam DOF at node 2 (still in node K's $\bar{X}\bar{Y}\bar{Z}$).

The third transformation

$$\{\Delta U_{ph}\}_L = [T_3]\left\{\Delta \bar{U}_{ph}\right\}_L \tag{4.8a}$$

produces

$$\langle \Delta U_{ph}\rangle_L = \langle \Delta U_{1X} \quad \Delta U_{1Y} \quad \Delta U_{1Z} \quad \Delta\theta_{1X} \quad \Delta\theta_{1Y} \quad \Delta\theta_{1Z} \quad \Delta U_{2X} \quad \Delta U_{2Y} \quad \Delta U_{2Z} \quad \Delta\theta_{2X} \quad \Delta\theta_{2Y} \quad \Delta\theta_{2Z}\rangle \tag{4.8b}$$

where all DOF are now in XYZ.

Finally, the fourth transformation

$$\left\{\Delta U'_{ph}\right\}_L = [T_4]\left\{\Delta U_{ph}\right\}_L \tag{4.9a}$$

produces

$$\langle \Delta U'_{ph}\rangle_L = \langle \Delta U_1 \quad \Delta V_{1Y'} \quad \Delta V_{1Z'} \quad \Delta\alpha_1 \quad \Delta\theta_{1Y'} \quad \Delta\theta_{1Z'} \quad \Delta U_2 \quad \Delta V_{2Y'} \quad \Delta V_{2Z'} \quad \Delta\alpha_2 \quad \Delta\theta_{2Y'} \quad \Delta\theta_{2Z'}\rangle \tag{4.9b}$$

where all DOF are now in the beam element's local $X'Y'Z'$.

Combining the above leads to

$$\left\{\Delta U'_{ph}\right\}_L = [T_{ph}]\left\{\Delta U_{ph}\right\} \tag{4.10a}$$

where

$$[T_{ph}] = [T_4]\,[T_3]\,[T_2]\,[T_1] \tag{4.10b}$$

The components, $[T_1], [T_2], [T_3], and\, [T_4]$ are defined below.

$$[T_1]^{(16\times16)} = \begin{bmatrix} \left[\bar{C}_J\right]^{(3\times3)} & [0]^{(3\times5)} & [0]^{(3\times3)} & [0]^{(3\times5)} \\ [0]^{(5\times3)} & [I]^{(5\times5)} & [0]^{(5\times3)} & [0]^{(5\times5)} \\ [0]^{(3\times3)} & [0]^{(3\times5)} & \left[\bar{C}_K\right]^{(3\times3)} & [0]^{(3\times5)} \\ [0]^{(5\times3)} & [0]^{(5\times5)} & [0]^{(5\times3)} & [I]^{(5\times5)} \end{bmatrix} \tag{4.11}$$

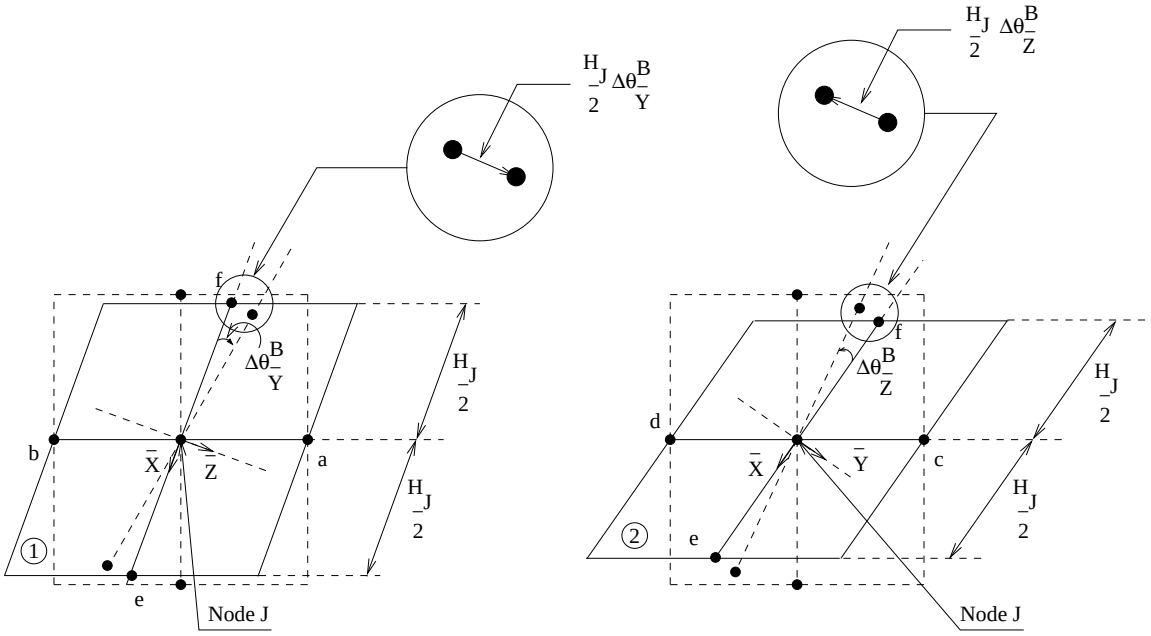

Figure 4.7: Panel Zone Deformation Geometry for Construction of $[T_2]$ for a Column

where $[I]$ is the 5×5 identity matrix.

$[T_2]$ is different for beams and columns. It also depends on the attachment points to which the element local nodes 1 and 2 are connected at nodes J and K. As an example, the following matrix is derived for a column whose local node 1 connects to attachment point f at node J and local node 2 connects to attachment point e at node K. The source of some of the terms of this matrix is graphically shown in Figure 4.7.

$$[T]_2^{col-f-e(12\times16)} = \left[\begin{array}{cccccccc|cccccccc}
1.0 & 0.0 & 0.0 & 0.0 & 0.0 & 0.0 & 0.0 & 0.0 & 0.0 & 0.0 & 0.0 & 0.0 & 0.0 & 0.0 & 0.0 & 0.0 \\
0.0 & 1.0 & 0.0 & 0.0 & 0.0 & 0.0 & -0.5H_J & 0.0 & 0.0 & 0.0 & 0.0 & 0.0 & 0.0 & 0.0 & 0.0 & 0.0 \\
0.0 & 0.0 & 1.0 & 0.0 & 0.5H_J & 0.0 & 0.0 & 0.0 & 0.0 & 0.0 & 0.0 & 0.0 & 0.0 & 0.0 & 0.0 & 0.0 \\
0.0 & 0.0 & 0.0 & 1.0 & 0.0 & 0.0 & 0.0 & 0.0 & 0.0 & 0.0 & 0.0 & 0.0 & 0.0 & 0.0 & 0.0 & 0.0 \\
0.0 & 0.0 & 0.0 & 0.0 & 0.0 & 1.0 & 0.0 & 0.0 & 0.0 & 0.0 & 0.0 & 0.0 & 0.0 & 0.0 & 0.0 & 0.0 \\
0.0 & 0.0 & 0.0 & 0.0 & 0.0 & 0.0 & 0.0 & 1.0 & 0.0 & 0.0 & 0.0 & 0.0 & 0.0 & 0.0 & 0.0 & 0.0 \\
\hline
0.0 & 0.0 & 0.0 & 0.0 & 0.0 & 0.0 & 0.0 & 0.0 & 1.0 & 0.0 & 0.0 & 0.0 & 0.0 & 0.0 & 0.0 & 0.0 \\
0.0 & 0.0 & 0.0 & 0.0 & 0.0 & 0.0 & 0.0 & 0.0 & 0.0 & 1.0 & 0.0 & 0.0 & 0.0 & 0.0 & 0.5H_K & 0.0 \\
0.0 & 0.0 & 0.0 & 0.0 & 0.0 & 0.0 & 0.0 & 0.0 & 0.0 & 0.0 & 1.0 & 0.0 & -0.5H_K & 0.0 & 0.0 & 0.0 \\
0.0 & 0.0 & 0.0 & 0.0 & 0.0 & 0.0 & 0.0 & 0.0 & 0.0 & 0.0 & 0.0 & 1.0 & 0.0 & 0.0 & 0.0 & 0.0 \\
0.0 & 0.0 & 0.0 & 0.0 & 0.0 & 0.0 & 0.0 & 0.0 & 0.0 & 0.0 & 0.0 & 0.0 & 0.0 & 1.0 & 0.0 & 0.0 \\
0.0 & 0.0 & 0.0 & 0.0 & 0.0 & 0.0 & 0.0 & 0.0 & 0.0 & 0.0 & 0.0 & 0.0 & 0.0 & 0.0 & 0.0 & 1.0
\end{array}\right] \tag{4.12}$$

The deformed panel zone geometry for calculating some of the terms of $[T_2]$ for a beam is shown in Figures 4.8 and 4.9. As an example, the following matrix is derived for a beam whose local node 1 connects to attachment point a at node J and local node 2 connects to

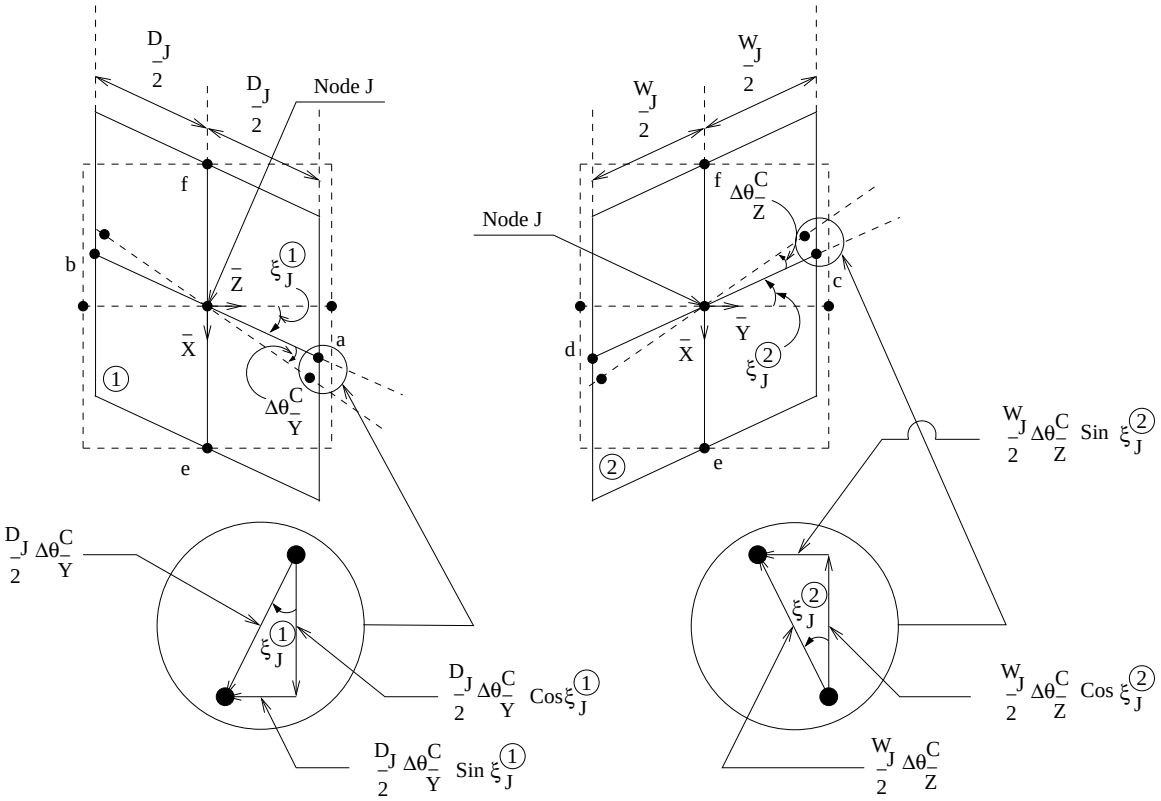

Figure 4.8: Panel Zone Deformation Geometry for Construction of $[T_2]$ for a Beam

attachment point b at node K.

$$[T]_2^{bm-a-b(12\times16)} =$$

$$\left[\begin{array}{cccccccc|cccccccc}
1.0 & 0.0 & 0.0 & 0.0 & 0.0 & 0.5D_J\cos\xi_J^{①} & 0.0 & 0.0 & 0.0 & 0.0 & 0.0 & 0.0 & 0.0 & 0.0 & 0.0 & 0.0 \\
0.0 & 1.0 & 0.0 & -0.5D_J\cos\xi_J^{①} & 0.0 & 0.0 & 0.0 & 0.0 & 0.0 & 0.0 & 0.0 & 0.0 & 0.0 & 0.0 & 0.0 & 0.0 \\
0.0 & 0.0 & 1.0 & 0.0 & 0.0 & -0.5D_J\sin\xi_J^{①} & 0.0 & 0.0 & 0.0 & 0.0 & 0.0 & 0.0 & 0.0 & 0.0 & 0.0 & 0.0 \\
0.0 & 0.0 & 0.0 & 1.0 & 0.0 & 0.0 & 0.0 & 0.0 & 0.0 & 0.0 & 0.0 & 0.0 & 0.0 & 0.0 & 0.0 & 0.0 \\
0.0 & 0.0 & 0.0 & 0.0 & 1.0 & 0.0 & 0.0 & 0.0 & 0.0 & 0.0 & 0.0 & 0.0 & 0.0 & 0.0 & 0.0 & 0.0 \\
0.0 & 0.0 & 0.0 & 0.0 & 0.0 & 0.0 & 0.5 & 0.5 & 0.0 & 0.0 & 0.0 & 0.0 & 0.0 & 0.0 & 0.0 & 0.0 \\
\hline
0.0 & 0.0 & 0.0 & 0.0 & 0.0 & 0.0 & 0.0 & 0.0 & 1.0 & 0.0 & 0.0 & 0.0 & 0.0 & -0.5D_K\cos\xi_K^{①} & 0.0 & 0.0 \\
0.0 & 0.0 & 0.0 & 0.0 & 0.0 & 0.0 & 0.0 & 0.0 & 0.0 & 1.0 & 0.0 & 0.5D_K\cos\xi_K^{①} & 0.0 & 0.0 & 0.0 & 0.0 \\
0.0 & 0.0 & 0.0 & 0.0 & 0.0 & 0.0 & 0.0 & 0.0 & 0.0 & 0.0 & 1.0 & 0.0 & 0.0 & 0.5D_K\sin\xi_K^{①} & 0.0 & 0.0 \\
0.0 & 0.0 & 0.0 & 0.0 & 0.0 & 0.0 & 0.0 & 0.0 & 0.0 & 0.0 & 0.0 & 1.0 & 0.0 & 0.0 & 0.0 & 0.0 \\
0.0 & 0.0 & 0.0 & 0.0 & 0.0 & 0.0 & 0.0 & 0.0 & 0.0 & 0.0 & 0.0 & 0.0 & 1.0 & 0.0 & 0.0 & 0.0 \\
0.0 & 0.0 & 0.0 & 0.0 & 0.0 & 0.0 & 0.0 & 0.0 & 0.0 & 0.0 & 0.0 & 0.0 & 0.0 & 0.0 & 0.5 & 0.5
\end{array}\right] \tag{4.13}$$

The following matrix is derived for a beam where local node 1 connects to attachment point c at node J and local node 2 connects to attachment point d at node K. The derivation of the non-zero and non-unity terms of this matrix is graphically shown in Figure 4.8.

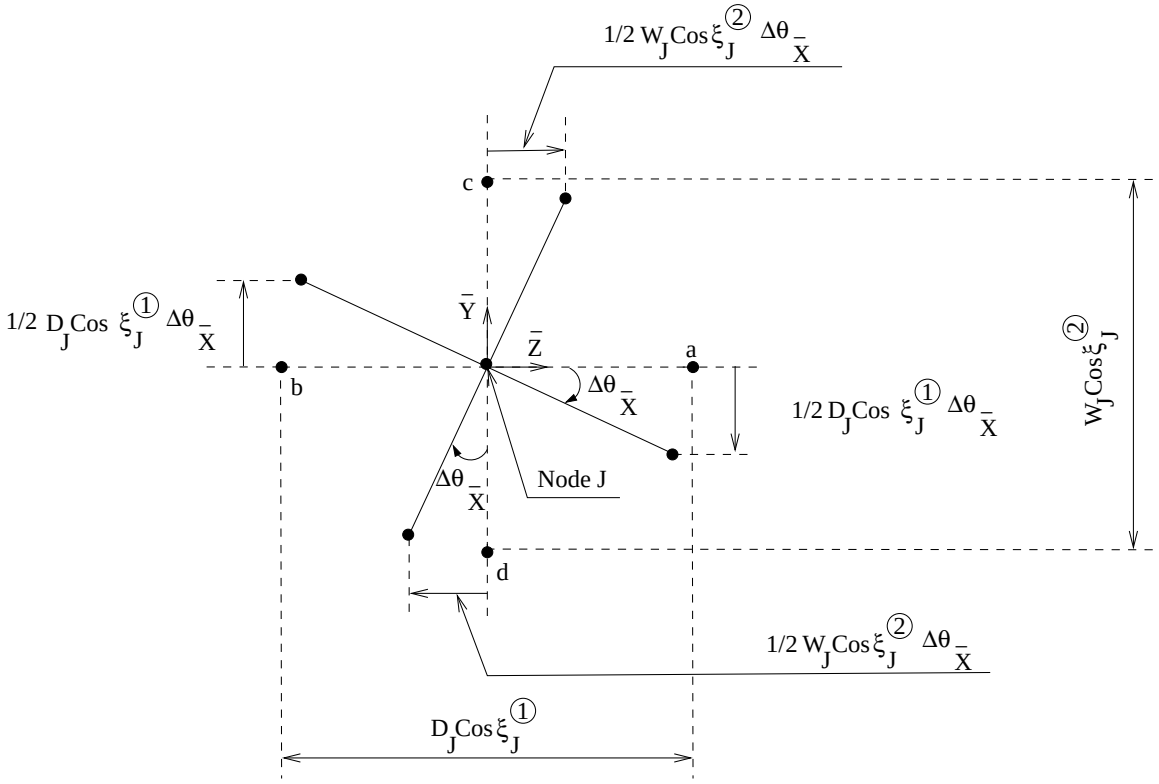

Figure 4.9: Panel Zone Deformation Geometry for Construction of $[T_2]$ for a Beam (Contd.)

$$[T]_2^{bm-c-d(12\times16)} =$$

$$\left[\begin{array}{cccccccc|cccccccc}
1.0 & 0.0 & 0.0 & 0.0 & 0.0 & 0.0 & 0.0 & -0.5W_J\cos\xi_J^{②} & 0.0 & 0.0 & 0.0 & 0.0 & 0.0 & 0.0 & 0.0 & 0.0 \\
0.0 & 1.0 & 0.0 & 0.0 & 0.0 & 0.0 & 0.0 & -0.5W_J\sin\xi_J^{②} & 0.0 & 0.0 & 0.0 & 0.0 & 0.0 & 0.0 & 0.0 & 0.0 \\
0.0 & 0.0 & 1.0 & 0.5W_J\cos\xi_J^{②} & 0.0 & 0.0 & 0.0 & 0.0 & 0.0 & 0.0 & 0.0 & 0.0 & 0.0 & 0.0 & 0.0 & 0.0 \\
0.0 & 0.0 & 0.0 & 1.0 & 0.0 & 0.0 & 0.0 & 0.0 & 0.0 & 0.0 & 0.0 & 0.0 & 0.0 & 0.0 & 0.0 & 0.0 \\
0.0 & 0.0 & 0.0 & 0.0 & 0.5 & 0.5 & 0.0 & 0.0 & 0.0 & 0.0 & 0.0 & 0.0 & 0.0 & 0.0 & 0.0 & 0.0 \\
0.0 & 0.0 & 0.0 & 0.0 & 0.0 & 0.0 & 1.0 & 0.0 & 0.0 & 0.0 & 0.0 & 0.0 & 0.0 & 0.0 & 0.0 & 0.0 \\
\hline
0.0 & 0.0 & 0.0 & 0.0 & 0.0 & 0.0 & 0.0 & 0.0 & 1.0 & 0.0 & 0.0 & 0.0 & 0.0 & 0.0 & 0.0 & 0.5W_K\cos\xi_K^{②} \\
0.0 & 0.0 & 0.0 & 0.0 & 0.0 & 0.0 & 0.0 & 0.0 & 0.0 & 1.0 & 0.0 & 0.0 & 0.0 & 0.0 & 0.0 & 0.5W_K\sin\xi_K^{②} \\
0.0 & 0.0 & 0.0 & 0.0 & 0.0 & 0.0 & 0.0 & 0.0 & 0.0 & 0.0 & 1.0 & -0.5W_K\cos\xi_K^{②} & 0.0 & 0.0 & 0.0 & 0.0 \\
0.0 & 0.0 & 0.0 & 0.0 & 0.0 & 0.0 & 0.0 & 0.0 & 0.0 & 0.0 & 0.0 & 1.0 & 0.0 & 0.0 & 0.0 & 0.0 \\
0.0 & 0.0 & 0.0 & 0.0 & 0.0 & 0.0 & 0.0 & 0.0 & 0.0 & 0.0 & 0.0 & 0.0 & 0.5 & 0.5 & 0.0 & 0.0 \\
0.0 & 0.0 & 0.0 & 0.0 & 0.0 & 0.0 & 0.0 & 0.0 & 0.0 & 0.0 & 0.0 & 0.0 & 0.0 & 0.0 & 1.0 & 0.0
\end{array}\right] \tag{4.14}$$

In the above matrices,

$$\cos \xi_J^{①} = \frac{\vec{V}_{J,ab}}{\left|\vec{V}_{J,ab}\right|} \cdot \frac{\vec{V}_{J\bar{Z}}}{\left|\vec{V}_{J\bar{Z}}\right|} \tag{4.15a}$$

$$\sin \xi_J^{①} = \frac{\vec{V}_{J,ab}}{\left|\vec{V}_{J,ab}\right|} \cdot \frac{\vec{V}_{J,ef}}{\left|\vec{V}_{J,ef}\right|} \tag{4.15b}$$

$$\cos \xi_J^{②} = \frac{\vec{V}_{J\bar{Y}}}{\left|\vec{V}_{J\bar{Y}}\right|} \cdot \frac{\vec{V}_{J,cd}}{\left|\vec{V}_{J,cd}\right|} \tag{4.15c}$$

$$\sin \xi_J^{②} = -\frac{\vec{V}_{J,cd}}{\left|\vec{V}_{J,cd}\right|} \cdot \frac{\vec{V}_{J,ef}}{\left|\vec{V}_{J,ef}\right|} \tag{4.15d}$$

where $\vec{V}_{J,ab}$ is a vector from attachment point b to attachment point a at node J and so on.

Each of the above three $[T]_2$ matrices is partitioned into four submatrices, $[T]_2^{11}$, $[T]_2^{12}$, $[T]_2^{21}$, and $[T]_2^{22}$. The submatrices $[T]_2^{12}$ & $[T]_2^{21}$ are zero matrices. The other two matrices, $[T]_2^{11}$ & $[T]_2^{22}$, depend upon which attachment points the local nodes 1 and 2 of the element in question is attached to. For example, if an element local node 1 is connected to attachment point d and its local node 2 is connected to attachment point b, then the $[T]_2^{11}$ matrix for that element would be the $[T]_2^{22}$ matrix from eq. 4.14 with the K subscript replaced by J and its $[T]_2^{22}$ matrix would be the $[T]_2^{11}$ matrix from eq. 4.13 with the J subscript replaced by K.

$$[T_3]^{(12\times12)} = \begin{bmatrix} \left[\bar{C}_J\right]^{T(3\times3)} & [0]^{(3\times3)} & [0]^{(3\times3)} & [0]^{(3\times3)} \\ [0]^{(3\times3)} & \left[\bar{C}_J\right]^{T(3\times3)} & [0]^{(3\times3)} & [0]^{(3\times3)} \\ [0]^{(3\times3)} & [0]^{(3\times3)} & \left[\bar{C}_K\right]^{T(3\times3)} & [0]^{(3\times3)} \\ [0]^{(3\times3)} & [0]^{(3\times3)} & [0]^{(3\times3)} & \left[\bar{C}_K\right]^{T(3\times3)} \end{bmatrix} \tag{4.16}$$

where $\left[\bar{C}_J\right]$ is given by eq. 3.6.

$$[T_4]^{(12\times12)} = \begin{bmatrix} [C']^{(3\times3)} & [0]^{(3\times3)} & [0]^{(3\times3)} & [0]^{(3\times3)} \\ [0]^{(3\times3)} & [C']^{(3\times3)} & [0]^{(3\times3)} & [0]^{(3\times3)} \\ [0]^{(3\times3)} & [0]^{(3\times3)} & [C']^{(3\times3)} & [0]^{(3\times3)} \\ [0]^{(3\times3)} & [0]^{(3\times3)} & [0]^{(3\times3)} & [C']^{(3\times3)} \end{bmatrix} \tag{4.17}$$

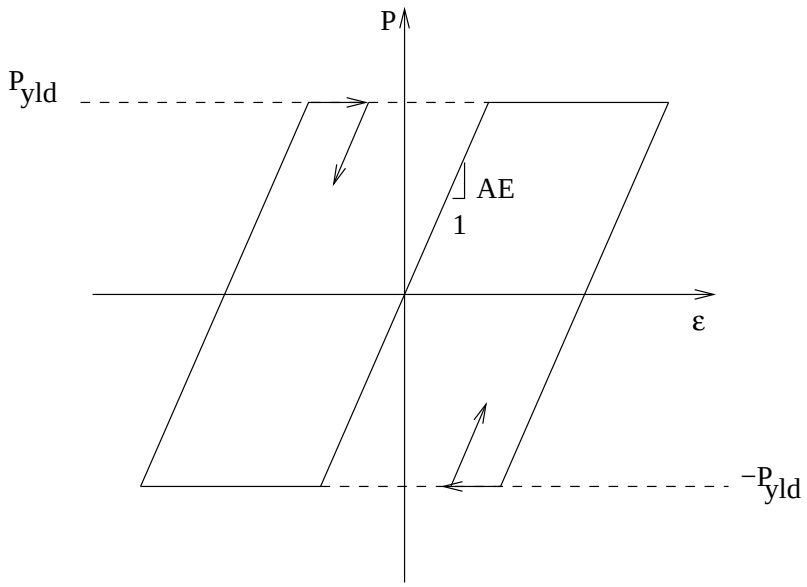

Figure 4.10: $P - \epsilon$ Relation for Plastic Hinge Element

where $[C']$ is defined in Sections 4.1.1 and 4.1.2 for columns and beams, respectively.

4.3 Theory of the Plastic Hinge Beam Element

4.3.1 Axial Deformation

The axial force, P, in the element is a function of the axial strain, ϵ as shown in Figure 4.10. ϵ is the axial strain at the centroid of the cross-section. Increments in P and ϵ are related by

$$dP = E_T A d\epsilon \tag{4.18a}$$

where E_T is the tangent modulus, either Young's modulus, E, or zero as shown in Figure 4.10, and A is the area of the cross-section.

In terms of P, the nodal forces are

$$P_1 = -P_2 = P \tag{4.18b}$$

In terms of dU_1 and dU_2, $d\epsilon$ is given by

$$d\epsilon = \frac{dU_2 - dU_1}{L_0} \tag{4.18c}$$

Combining the above eqs.,

$$\left\{ \begin{array}{c} dP_1 \\ dP_2 \end{array} \right\} = \frac{E_T A}{L_0} \left[\begin{array}{cc} 1 & -1 \\ -1 & 1 \end{array} \right] \left\{ \begin{array}{c} dU_1 \\ dU_2 \end{array} \right\} \tag{4.18d}$$

which is the tangent stiffness relation for the nodal quantities associated with axial deformation. Note that the effect of bowing (effect of bending moments on axial stiffness) is not included explicitly.

4.3.2 Twisting

Twisting is assumed to be linearly elastic with increments in torque, T, and twisting strain, ω (twist per unit length), related by

$$dT = GJd\omega \tag{4.19a}$$

where G is the shear modulus and J is the torsional constant of the cross-section.

In terms of T, the nodal forces are

$$T_1 = -T_2 = T \tag{4.19b}$$

In terms of $d\alpha_1$ and $d\alpha_2$, $d\omega$ is given by

$$d\omega = \frac{d\alpha_2 - d\alpha_1}{L_0} \tag{4.19c}$$

Combining the above eqs.,

$$\left\{ \begin{array}{c} dT_1 \\ dT_2 \end{array} \right\} = \frac{GJ}{L_0} \left[\begin{array}{cc} 1 & -1 \\ -1 & 1 \end{array} \right] \left\{ \begin{array}{c} d\alpha_1 \\ d\alpha_2 \end{array} \right\} \tag{4.19d}$$

which is the tangent stiffness relation for the nodal quantities associated with twisting.

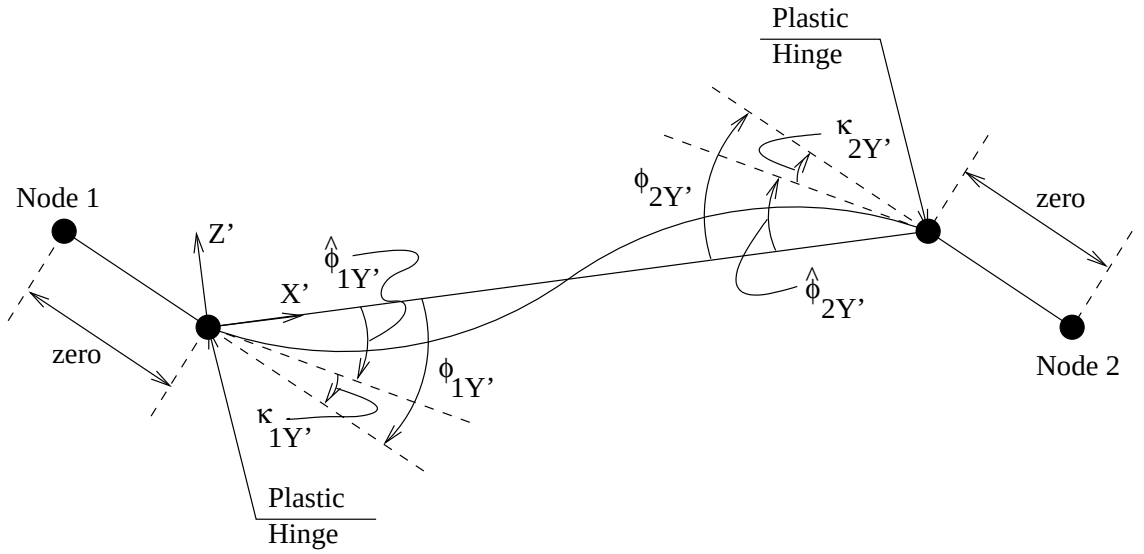

Figure 4.11: Geometry of Plastic Hinge Beam Element for Bending and Shearing in the $X' - Z'$ Plane

4.3.3 Bending and Shearing in the $X' - Z'$ Plane (Bending about the Major Axis of the Cross-Section)

Figure 4.11 shows the plastic hinge beam element with the plastic hinges located along the beam just inside the nodes ("inside" means the side towards the middle of the beam). $\phi_{1Y'}$ and $\phi_{2Y'}$ are the rotations of the cross-section about Y' between the plastic hinges and the nodes, and $\hat{\phi}_{1Y'}$ and $\hat{\phi}_{2Y'}$ are the rotations of the cross-section about Y' just inside the plastic hinges. These rotations are relative to the chord (straight line connecting nodes 1 and 2). Since the behavior between the plastic hinges is elastic,

$$\left\{ \begin{array}{c} M_{1Y'} \\ M_{2Y'} \end{array} \right\} = \left[\begin{array}{cc} a & b \\ b & c \end{array} \right] \left\{ \begin{array}{c} \hat{\phi}_{1Y'} \\ \hat{\phi}_{2Y'} \end{array} \right\} \tag{4.20}$$

where a, b, and c depend on E, the moment of inertia, $I_{Y'}$ about the major axis, G (since shear deformations will be included [57]), the effective shear area, $A_{SZ'}$ as shown in Figure 4.12, and P (since effect of axial load on stiffness will be included [59]). For convenience, subscripts denoting the $X' - Z'$ plane will be omitted on a, b, and c.

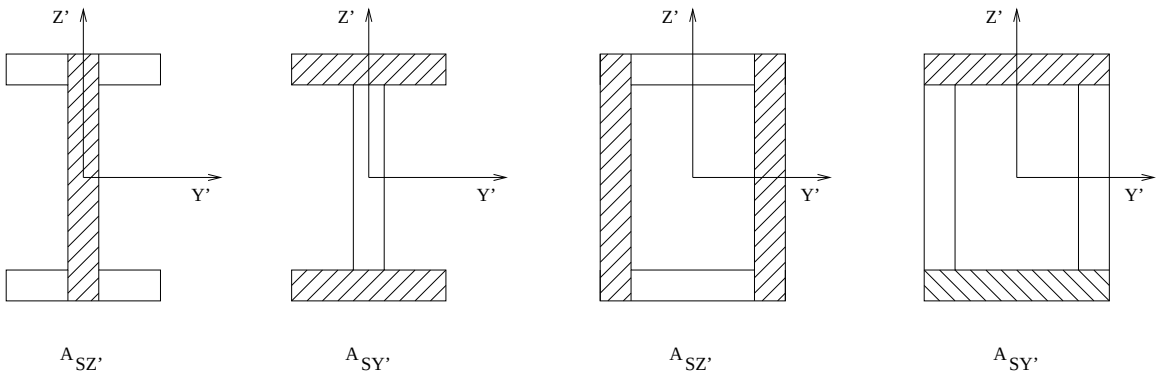

Figure 4.12: Effective Shear Areas for Wide-Flanged and Box Sections

Solutions for a, b, and c come from the following differential equations:

$$\frac{d^2 M_{Y'}}{dX'^2} + Q_{Z'} = P\frac{d^2 V_{Z'}}{dX'^2} \tag{4.21a}$$

$$\frac{dQ_{Z'}}{dX'} = 0 \tag{4.21b}$$

$$M_{Y'} = -EI_{Y'}\frac{d\hat{\phi}_{Y'}}{dX'} \tag{4.21c}$$

$$Q_{Z'} = GA_{SZ'}\left(\frac{dV_{Z'}}{dX'} + \hat{\phi}_{Y'}\right) \tag{4.21d}$$

subject to $V_{Z'} = 0$ at nodes 1 and 2, and $\hat{\phi}_{Y'} = \hat{\phi}_{1Y'}$ at node 1, and $\hat{\phi}_{Y'} = \hat{\phi}_{2Y'}$ at node 2.

In these equations, $V_{Z'}$ is the Z' translation along the beam relative to the chord, and $\hat{\phi}_{Y'}$ is the rotation of the cross-section about Y' along the beam relative to the chord.

Results are as follows [29, 11]:

1. $P = 0$

$$a = \frac{EI_{Y'}}{L_0}\left(\frac{4+\beta}{1+\beta}\right) \tag{4.22a}$$

$$b = \frac{EI_{Y'}}{L_0}\left(\frac{2-\beta}{1+\beta}\right) \tag{4.22b}$$

$$c = a \tag{4.22c}$$

2. $P < 0$

$$a = \frac{EI_{Y'}}{L_0}\left[\frac{\left(1+\frac{1}{12}\rho^2\beta\right)\rho\sin\rho - \rho^2\cos\rho}{2\left(1+\frac{1}{12}\rho^2\beta\right)(1-\cos\rho) - \rho\sin\rho}\right] \tag{4.23a}$$

$$b = \frac{EI_{Y'}}{L_0}\left[\frac{-\left(1+\frac{1}{12}\rho^2\beta\right)\rho\sin\rho + \rho^2}{2\left(1+\frac{1}{12}\rho^2\beta\right)(1-\cos\rho) - \rho\sin\rho}\right] \tag{4.23b}$$

$$c = a \tag{4.23c}$$

3. $P > 0$

$$a = \frac{EI_{Y'}}{L_0}\left[\frac{-\left(1-\frac{1}{12}\rho^2\beta\right)\rho\sinh\rho + \rho^2\cosh\rho}{2\left(1-\frac{1}{12}\rho^2\beta\right)(1-\cosh\rho) + \rho\sinh\rho}\right] \tag{4.24a}$$

$$b = \frac{EI_{Y'}}{L_0}\left[\frac{\left(1-\frac{1}{12}\rho^2\beta\right)\rho\sinh\rho - \rho^2}{2\left(1-\frac{1}{12}\rho^2\beta\right)(1-\cosh\rho) + \rho\sinh\rho}\right] \tag{4.24b}$$

$$c = a \tag{4.24c}$$

In the above equations,

$$\beta = \frac{12EI_{Y'}}{GA_{SZ'}L_0^2} \qquad \rho = \pi\sqrt{\frac{|P|}{P_E}} \qquad P_E = \frac{\pi^2 EI_{Y'}}{L_0^2} \tag{4.25}$$

Each moment, $M_{1Y'}$ and $M_{2Y'}$, consists of a part carried by the plastic hinge and a part carried by the rotational spring:

$$M_{1Y'} = M_{1Y'}^h + M_{1Y'}^s \tag{4.26a}$$

$$M_{2Y'} = M_{2Y'}^h + M_{2Y'}^s. \tag{4.26b}$$

The hinge contribution is a rigid-plastic function of the kink rotation as shown in Figure 4.13 and the spring contribution is a linear function of the kink rotation:

$$M_{1Y'}^s = k_1\kappa_{1Y'} \tag{4.27a}$$

$$M_{2Y'}^s = k_2\kappa_{2Y'} \tag{4.27b}$$

where the rotational spring constants at the two ends of the element are k_1 and k_2 (subscripts to indicate $X'-Z'$ plane are omitted for convenience), and $\kappa_{1Y'}$ and $\kappa_{2Y'}$ are the kink angles

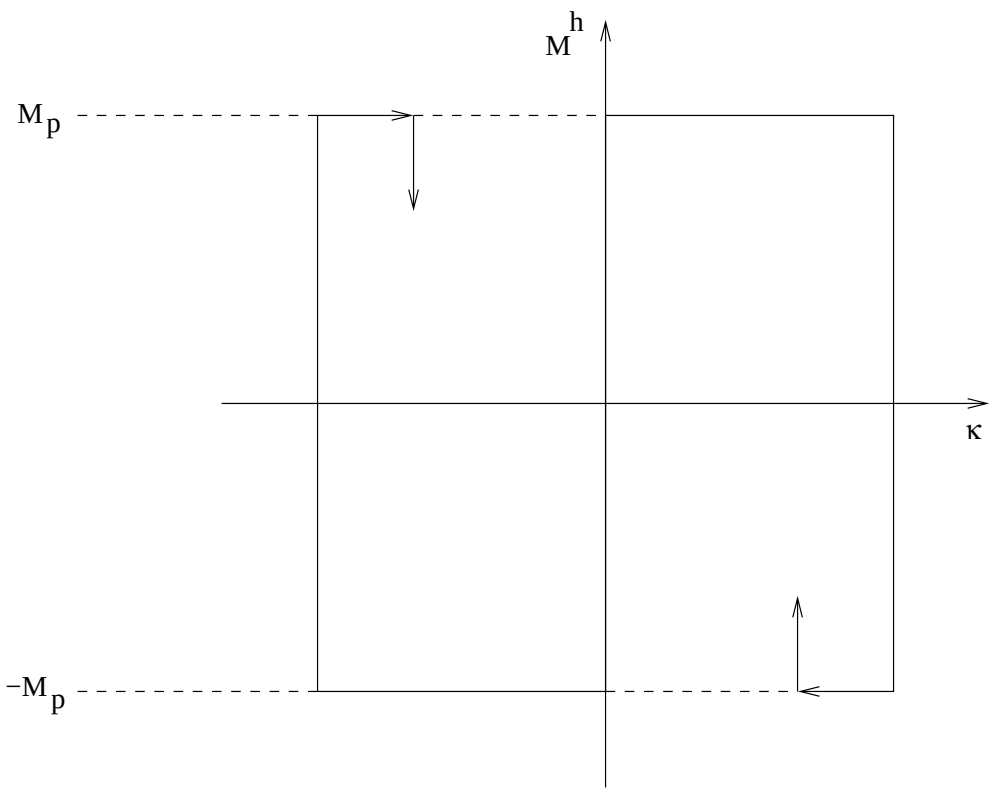

Figure 4.13: $M^h - \kappa$ Relation at a Plastic Hinge

given by

$$\kappa_{1Y'} = \phi_{1Y'} - \hat{\phi}_{1Y'} \tag{4.28a}$$

$$\kappa_{2Y'} = \phi_{2Y'} - \hat{\phi}_{2Y'}. \tag{4.28b}$$

Substituting eqs. 4.28 into eq. 4.20:

$$\left\{ \begin{array}{c} M_{1Y'} \\ M_{2Y'} \end{array} \right\} = \left[\begin{array}{cc} a & b \\ b & c \end{array} \right] \left\{ \begin{array}{c} \phi_{1Y'} - \kappa_{1Y'} \\ \phi_{2Y'} - \kappa_{2Y'} \end{array} \right\} \tag{4.29}$$

and taking the differential form gives

$$\left\{ \begin{array}{c} dM_{1Y'} \\ dM_{2Y'} \end{array} \right\} = \left[\begin{array}{cc} a & b \\ b & c \end{array} \right] \left\{ \begin{array}{c} d\phi_{1Y'} - d\kappa_{1Y'} \\ d\phi_{2Y'} - d\kappa_{2Y'} \end{array} \right\} \tag{4.30}$$

where terms containing dP have been dropped. With appropriate substitutions from above,

this equation can be rewritten as

$$\begin{Bmatrix} dM_{1Y'} \\ dM_{2Y'} \end{Bmatrix} = \begin{bmatrix} a_T & b_T \\ b_T & c_T \end{bmatrix} \begin{Bmatrix} d\phi_{1Y'} \\ d\phi_{2Y'} \end{Bmatrix} \tag{4.31}$$

where a_T, b_T, and c_T are tangent stiffness coefficients which depend on whether plastic hinges are active during the increment.

1. If no plastic hinges are active, $d\kappa_{1Y'} = d\kappa_{2Y'} = 0$ and

$$a_T = a \tag{4.32a}$$

$$b_T = b \tag{4.32b}$$

$$c_T = c \tag{4.32c}$$

2. If an active hinge exists at node 1 only, $d\kappa_{1Y'} = \frac{dM_{1Y'}}{k_1}$ and $d\kappa_{2Y'} = 0$ and eqs. 4.30 and 4.31 lead to

$$a_T = a\frac{k_1}{k_1 + a} \tag{4.33a}$$

$$b_T = b\frac{k_1}{k_1 + a} \tag{4.33b}$$

$$c_T = c - \frac{b^2}{k_1 + a} \tag{4.33c}$$

3. If an active hinge exists at node 2 only, $d\kappa_{1Y'} = 0$ and $d\kappa_{2Y'} = \frac{dM_{2Y'}}{k_2}$ and eqs. 4.30 and 4.31 lead to

$$a_T = a - \frac{b^2}{k_2 + c} \tag{4.34a}$$

$$b_T = b\frac{k_2}{k_2 + c} \tag{4.34b}$$

$$c_T = c\frac{k_2}{k_2 + c} \tag{4.34c}$$

4. If active hinges exist at both nodes 1 and 2, $d\kappa_{1Y'} = \frac{dM_{1Y'}}{k_1}$ and $d\kappa_{2Y'} = \frac{dM_{2Y'}}{k_2}$ and

eqs. 4.30 and 4.31 lead to

$$a_T = \frac{k_1\left[a(k_2+c)-b^2\right]}{(k_1+a)(k_2+c)-b^2} \tag{4.35a}$$

$$b_T = \frac{bk_1k_2}{(k_1+a)(k_2+c)-b^2} \tag{4.35b}$$

$$c_T = \frac{k_2\left[c(k_1+a)-b^2\right]}{(k_1+a)(k_2+c)-b^2} \tag{4.35c}$$

Equation 4.31 needs to be transformed and expanded to the nodal degrees of freedom. The following equations are employed:

$$\left\{\begin{array}{c} d\phi_{1Y'} \\ d\phi_{2Y'} \end{array}\right\} = [S]\left\{\begin{array}{c} dV_{1Z'} \\ d\theta_{1Y'} \\ dV_{2Z'} \\ d\theta_{2Y'} \end{array}\right\} \tag{4.36a}$$

$$\left\{\begin{array}{c} dQ_{1Z'} \\ dM_{1Y'} \\ dQ_{2Z'} \\ dM_{2Y'} \end{array}\right\} = [S]^T\left\{\begin{array}{c} dM_{1Y'} \\ dM_{2Y'} \end{array}\right\} + \frac{P}{L_0}\left[\begin{array}{cccc} 1 & 0 & -1 & 0 \\ 0 & 0 & 0 & 0 \\ -1 & 0 & 1 & 0 \\ 0 & 0 & 0 & 0 \end{array}\right]\left\{\begin{array}{c} dV_{1Z'} \\ d\theta_{1Y'} \\ dV_{2Z'} \\ d\theta_{2Y'} \end{array}\right\} \tag{4.36b}$$

where

$$[S] = \left[\begin{array}{cccc} -\frac{1}{L_0} & 1 & \frac{1}{L_0} & 0 \\ -\frac{1}{L_0} & 0 & \frac{1}{L_0} & 1 \end{array}\right]$$

and the $\frac{P}{L_0}$ term is additional geometric stiffness. The $\frac{1}{L_0}$ terms in $[S]$ come from chord rotations.

Combining with eq. 4.31 leads to

$$\left\{\begin{array}{c} dQ_{1Z'} \\ dM_{1Y'} \\ dQ_{2Z'} \\ dM_{2Y'} \end{array}\right\} = \left[[S]^T\left[\begin{array}{cc} a_T & b_T \\ b_T & c_T \end{array}\right][S] + \frac{P}{L_0}\left[\begin{array}{cccc} 1 & 0 & -1 & 0 \\ 0 & 0 & 0 & 0 \\ -1 & 0 & 1 & 0 \\ 0 & 0 & 0 & 0 \end{array}\right]\right]\left\{\begin{array}{c} dV_{1Z'} \\ d\theta_{1Y'} \\ dV_{2Z'} \\ d\theta_{2Y'} \end{array}\right\} \tag{4.37}$$

which is the tangent stiffness relation for the nodal quantities associated with bending and

shearing in the $X' - Z'$ plane.

4.3.4 Bending and Shearing in the $X' - Y'$ Plane (Bending about the Minor Axis of the Cross-Section)

A formulation similar to the preceding section leads to

$$\begin{Bmatrix} dQ_{1Y'} \\ dM_{1Z'} \\ dQ_{2Y'} \\ dM_{2Z'} \end{Bmatrix} = \left[[S]^T \begin{bmatrix} a_T & b_T \\ b_T & c_T \end{bmatrix} [S] + \frac{P}{L_0} \begin{bmatrix} 1 & 0 & -1 & 0 \\ 0 & 0 & 0 & 0 \\ -1 & 0 & 1 & 0 \\ 0 & 0 & 0 & 0 \end{bmatrix} \right] \begin{Bmatrix} dV_{1Y'} \\ d\theta_{1Z'} \\ dV_{2Y'} \\ d\theta_{2Z'} \end{Bmatrix} \tag{4.38}$$

where

$$[S] = \begin{bmatrix} \frac{1}{L_0} & 1 & -\frac{1}{L_0} & 0 \\ \frac{1}{L_0} & 0 & -\frac{1}{L_0} & 1 \end{bmatrix}$$

and a_T, b_T, and c_T in terms of a, b, and c are as described previously except that a, b, and c use the minor axis moment of inertia, $I_{Z'}$, and the effective shear area, $A_{SY'}$ (Figure 4.12).

4.3.5 Combined Results

The tangent stiffness relations in eqs. 4.18d, 4.19d, 4.37, and 4.38 are combined into

$$\left\{dR'_{ph}\right\}_L = \left[K'_{T,ph}\right]_L \left\{dU'_{ph}\right\}_L \tag{4.39}$$

where L refers to local nodes 1 and 2, $\left\{dR'_{ph}\right\}_L$ is the incremental version of

$$\langle R'_{ph} \rangle_L = \langle \; P_1 \quad Q_{1Y'} \quad Q_{1Z'} \quad T_1 \quad M_{1Y'} \quad M_{1Z'} \quad P_2 \quad Q_{2Y'} \quad Q_{2Z'} \quad T_2 \quad M_{2Y'} \quad M_{2Z'} \; \rangle, \tag{4.40a}$$

$\left[K'_{T,ph}\right]_L$ is the 12×12 tangent stiffness matrix for the plastic hinge element, and $\left\{dU'_{ph}\right\}_L$ is the incremental version of

$$\langle U'_{ph} \rangle_L = \langle \; U_1 \quad V_{1Y'} \quad V_{1Z'} \quad \alpha_1 \quad \theta_{1Y'} \quad \theta_{1Z'} \quad U_2 \quad V_{2Y'} \quad V_{2Z'} \quad \alpha_2 \quad \theta_{2Y'} \quad \theta_{2Z'} \; \rangle. \tag{4.40b}$$

4.4 Updating Process

In global iteration l, $\{\Delta U\}$ is computed from eq. 2.9. The 12 displacement increments in $X'Y'Z'$ at nodes 1 and 2 for a plastic hinge element are found as

$$\left\{\Delta U'_{ph}\right\}_L = \left[T^l_{ph}\right]\{\Delta U_{ph}\} \tag{4.41}$$

where $\{\Delta U_{ph}\}$ contains the 16 terms extracted from $\{\Delta U\}$ corresponding to the joint nodes J and K connected to element nodes 1 and 2, and $\left[T^l_{ph}\right]$ is the transformation matrix representing configuration l.

Updating the panel zone element geometries as discussed in Section 3.3 will produce new locations for the attachment points, from which new $\bar{X}$, $\bar{Y}$, and $\bar{Z}$ orientations can be found, leading to $\left[\bar{C}^{l+1}_J\right]$ and $\left[\bar{C}^{l+1}_K\right]$ and then $\left[T^{l+1}_1\right]$ and $\left[T^{l+1}_3\right]$ by eqs. 4.11 and 4.16, respectively. Updating $\xi^{①}$ and $\xi^{②}$ leads to $\left[T^{l+1}_2\right]$ for a beam (for example, eq. 4.13 for an $a-b$ beam, eq. 4.14 for a $c-d$ beam); $\left[T^{l+1}_2\right]$ for a column does not need updating (eq. 4.12, for example). The new attachment point locations also give the new locations for nodes 1 and 2 and these will give the updated direction for the X' axis. Next, the updated value for α_{or} is found as

$$\alpha^{l+1}_{or} = \alpha^l_{or} + \frac{\Delta\alpha_1 + \Delta\alpha_2}{2} \tag{4.42}$$

from which the new directions for Y' and Z' are found. The updated direction cosine matrix $\left[C'^{l+1}\right]$ is then used to form $\left[T^{l+1}_4\right]$ by eq. 4.17. Then,

$$\left[T^{l+1}_{ph}\right] = \left[T^{l+1}_4\right]\left[T^{l+1}_3\right]\left[T^{l+1}_2\right]\left[T^{l+1}_1\right] \tag{4.43}$$

Now $\left\{R'^{l+1}_{ph}\right\}_L$ is found from $\left\{R'^{l}_{ph}\right\}_L$ and $\left\{\Delta U'_{ph}\right\}_L$. Consider first the nodal axial forces P^{l+1}_1 and P^{l+1}_2. Once the locations for nodes 1 and 2 are determined, the new element length, L^{l+1}, can be found. Then

$$\epsilon^{l+1} = \frac{L^{l+1} - L_0}{L_0} \tag{4.44a}$$

$$\text{and} \quad \Delta\epsilon = \epsilon^{l+1} - \epsilon^l. \tag{4.44b}$$

Using ϵ^l and $\Delta\epsilon$, P^{l+1} can be found from Figure 4.10. Then,

$$P_1^{l+1} = -P_2^{l+1} = P^{l+1} \tag{4.44c}$$

Next consider the nodal torques T_1^{l+1} and T_2^{l+1}. The increment in twisting strain is

$$\Delta\omega = \frac{\Delta\alpha_2 - \Delta\alpha_1}{L_0} \tag{4.45a}$$

and then

$$T^{l+1} = T^l + GJ\Delta\omega. \tag{4.45b}$$

Nodal values are

$$T_1^{l+1} = -T_2^{l+1} = T^{l+1}. \tag{4.45c}$$

Next is the $X' - Z'$ plane bending and shearing. The $l+1$ state will correspond to one of nine plastic hinge cases which are listed in Table 4.1. The procedure is as follows. The nodal ϕ rotations are first updated as

$$\phi_{1Y'}^{l+1} = \phi_{1Y'}^l + \Delta\theta_{1Y'} + \frac{\Delta V_{2Z'} - \Delta V_{1Z'}}{L_0} \tag{4.46a}$$

$$\phi_{2Y'}^{l+1} = \phi_{2Y'}^l + \Delta\theta_{2Y'} + \frac{\Delta V_{2Z'} - \Delta V_{1Z'}}{L_0} \tag{4.46b}$$

Second, the plastic moment capacity is updated to $M_{pY'}^{l+1}$ according to Figure 4.6 using P^{l+1}. Then each case is examined using eqn. **??** written for state $l+1$. Then each case is examined using eq. 4.29 written for state $l+1$:

$$\begin{Bmatrix} M_{1Y'}^{l+1} \\ M_{2Y'}^{l+1} \end{Bmatrix} = \begin{bmatrix} a^{l+1} & b^{l+1} \\ b^{l+1} & c^{l+1} \end{bmatrix} \begin{Bmatrix} \phi_{1Y'}^{l+1} - \kappa_{1Y'}^{l+1} \\ \phi_{2Y'}^{l+1} - \kappa_{2Y'}^{l+1} \end{Bmatrix} \tag{4.47}$$

where a^{l+1}, b^{l+1}, and c^{l+1} are computed using P^{l+1}.

To examine Case 1, $\kappa_{1Y'}^{l+1} = \kappa_{1Y'}^l$ and $\kappa_{2Y'}^{l+1} = \kappa_{2Y'}^l$ are substituted into eq. 4.47, and $M_{1Y'}^{l+1}$ and $M_{2Y'}^{l+1}$ are computed. Then, if $M_{1Y'}^{l+1} < \left|M_{pY'}^{l+1}\right|$ and $M_{2Y'}^{l+1} < \left|M_{pY'}^{l+1}\right|$, the current state corresponds to Case 1 and the updated moments are accepted. If Case 1 does not

Table 4.1: Nine Plastic Hinge Cases Used for Determining $\left\{R'^{l+1}_{ph}\right\}_L$

Case	**Plastic Hinges**	M_1^{l+1}	M_1^{l+2}	κ_1^{l+1}	κ_2^{l+1}
1	None	$\lvert*\rvert < M_p^{l+1}$	$\lvert*\rvert < M_p^{l+1}$	$= \kappa_1^l$	$= \kappa_2^l$
2	Node 1	$= M_p^{l+1}$	$\lvert*\rvert < M_p^{l+1}$	$> \kappa_1^l$	$= \kappa_2^l$
3	Node 1	$= -M_p^{l+1}$	$\lvert*\rvert < M_p^{l+1}$	$< \kappa_1^l$	$= \kappa_2^l$
4	Node 2	$\lvert*\rvert < M_p^{l+1}$	$= M_p^{l+1}$	$= \kappa_1^l$	$> \kappa_2^l$
5	Node 2	$\lvert*\rvert < M_p^{l+1}$	$= -M_p^{l+1}$	$= \kappa_1^l$	$< \kappa_2^l$
6	Nodes 1 and 2	$= M_p^{l+1}$	$= M_p^{l+1}$	$> \kappa_1^l$	$> \kappa_2^l$
7	Nodes 1 and 2	$= M_p^{l+1}$	$= -M_p^{l+1}$	$> \kappa_1^l$	$< \kappa_2^l$
8	Nodes 1 and 2	$= -M_p^{l+1}$	$= M_p^{l+1}$	$< \kappa_1^l$	$> \kappa_2^l$
9	Nodes 1 and 2	$= -M_p^{l+1}$	$= -M_p^{l+1}$	$< \kappa_1^l$	$< \kappa_2^l$

check, Case 2 is examined. $M_{1Y'}^{l+1} = M_{pY'}^{l+1}$ and $\kappa_{2Y'}^{l+1} = \kappa_{2Y'}^{l}$ are substituted into eq. 4.47, and the set of eqs. is solved for $M_{2Y'}^{l+1}$ and $\kappa_{1Y'}^{l+1}$. If $\left|M_{2Y'}^{l+1}\right| < M_{pY'}^{l+1}$ and $\kappa_{1Y'}^{l+1} > \kappa_{1Y'}^{l}$, the current state corresponds to Case 2 and the updated moments are accepted. If not, Case 3 is examined, and so on. Only one out of the nine cases will check. Finally,

$$-Q_{1Z'}^{l+1} = Q_{2Z'}^{l+1} = \frac{M_{1Y'}^{l+1} + M_{2Y'}^{l+1}}{L^{l+1}}. \tag{4.48}$$

For $X' - Y'$ plane bending, $Q_{1Y'}^{l+1}$, $M_{1Z'}^{l+1}$, $Q_{2Y'}^{l+1}$, and $M_{2Z'}^{l+1}$ are found by a procedure similar to the one just described. Then the 12 updated nodal forces and moments are assembled into $\left\{R'^{l+1}_{ph}\right\}_L$.

The element tangent stiffness matrix can be updated once the updated axial force P^{l+1} and the appropriate plastic hinge cases for the $X' - Z'$ and $X' - Y'$ planes are determined. This information is available as a result of computing $\left\{R'^{l+1}_{ph}\right\}_L$, after which $\left[K'^{l+1}_{T,ph}\right]_L$ can be found from the formulae in the preceding section.

The final step is the transformation to the global DOF.

$$\left[K_{T,ph}^{l+1}\right] = \left[T_{ph}^{l+1}\right]^T \left[K'^{l+1}_{T,ph}\right]_L \left[T_{ph}^{l+1}\right] \tag{4.49a}$$

$$\left\{R_{ph}^{l+1}\right\} = \left[T_{ph}^{l+1}\right]^T \left\{R'^{l+1}_{ph}\right\}_L \tag{4.49b}$$

and then assembly into $\left[K_T^{l+1}\right]$ and $\left\{R^{l+1}\right\}$.

Chapter 5 Three-Dimensional Elastofiber Element

5.1 General Description

The following assumptions are made in the formulation of this element:

1. The cross-section is assumed uniform along the length of the element.
2. The cross-section is assumed to be doubly symmetric (with shear center at the centroid).
3. Plane sections remain plane; however, they do not have to remain normal to the beam axis. Thus, shear deformations are included.
4. Strains in the element are small.
5. Lateral deflections relative to the chord are small. This means that the effect of bowing [50, 51, 36] on axial stiffness is neglected. This effect is important only for very slender members or during post-buckling of compression members such as braces in braced frames.
6. Warping restraint under twisting is neglected.
7. The element is loaded only at its ends.
8. Composite action with the slab is not included.
9. Local buckling is not included.

The elastofiber beam element has 3 segments and 4 nodes. Two nodes numbered 1 and 2 are located at the ends and connect to the attachment points a through f of the panel zone element. The other two nodes are interior and are numbered 3 and 4 (See Figure 5.1). This element can model beams and columns in framed structures. As in the case of the plastic hinge element, columns connect to attachment points e and/or f while beams

connect to attachment points a through d. Original length of a segment is denoted by L_{s0}. Segment 1 goes from node 1 to node 3, segment 2 from node 3 to node 4, and segment 3 from node 4 to node 2.

Each segment has its own local coordinate system, $X'Y'Z'$, which is a right-handed, orthogonal system and is defined as follows:

1. X' axis: It runs along the longitudinal axis of the segment at the centroid of the cross-section. It is defined as a vector from node 1 to node 3 for segment 1, from node 3 to node 4 for segment 2, and from node 4 to node 2 for segment 3. All the nodes are located at the centroid of the cross-section.

2. Y' axis: Y' axis is orthogonal to X' and is the major principal axis of the cross-section of the segment.

3. Z' axis: Z' axis is the minor principal axis of the cross-section of the segment.

Initially, beam element is straight and each of the three $X'Y'Z'$ systems has the same orientation. Y' and Z' axes are oriented in the same way as for the plastic hinge element using the orientation angle, α_{or}, defined differently for beams and columns as described in Sections 4.1.1 and 4.1.2. The matrix of direction cosines, $[C']$, is computed as described in those sections for segments in beams and columns.

5.1.1 Degrees of Freedom of a Segment, and Nodal Forces and Moments

The degrees of freedom (Figure 5.2) of a segment of the elastofiber element are:

1. U_i, U_j = X' translations at nodes i and j of the segment, respectively.

2. $V_{iY'}$, $V_{jY'}$ = Y' translations at nodes i and j, respectively.

3. $V_{iZ'}$, $V_{jZ'}$ = Z' translations at nodes i and j, respectively.

4. α_i, α_j = Rotations of the segment about X' at nodes i and j, respectively.

5. $\theta_{iY'}$, $\theta_{jY'}$ = Rotations of the segment about Y' at nodes i and j, respectively.

6. $\theta_{iZ'}$, $\theta_{jZ'}$ = Rotations of the segment about Z' at nodes i and j, respectively.

Corresponding to these DOF are nodal forces and moments (Figure 5.2):

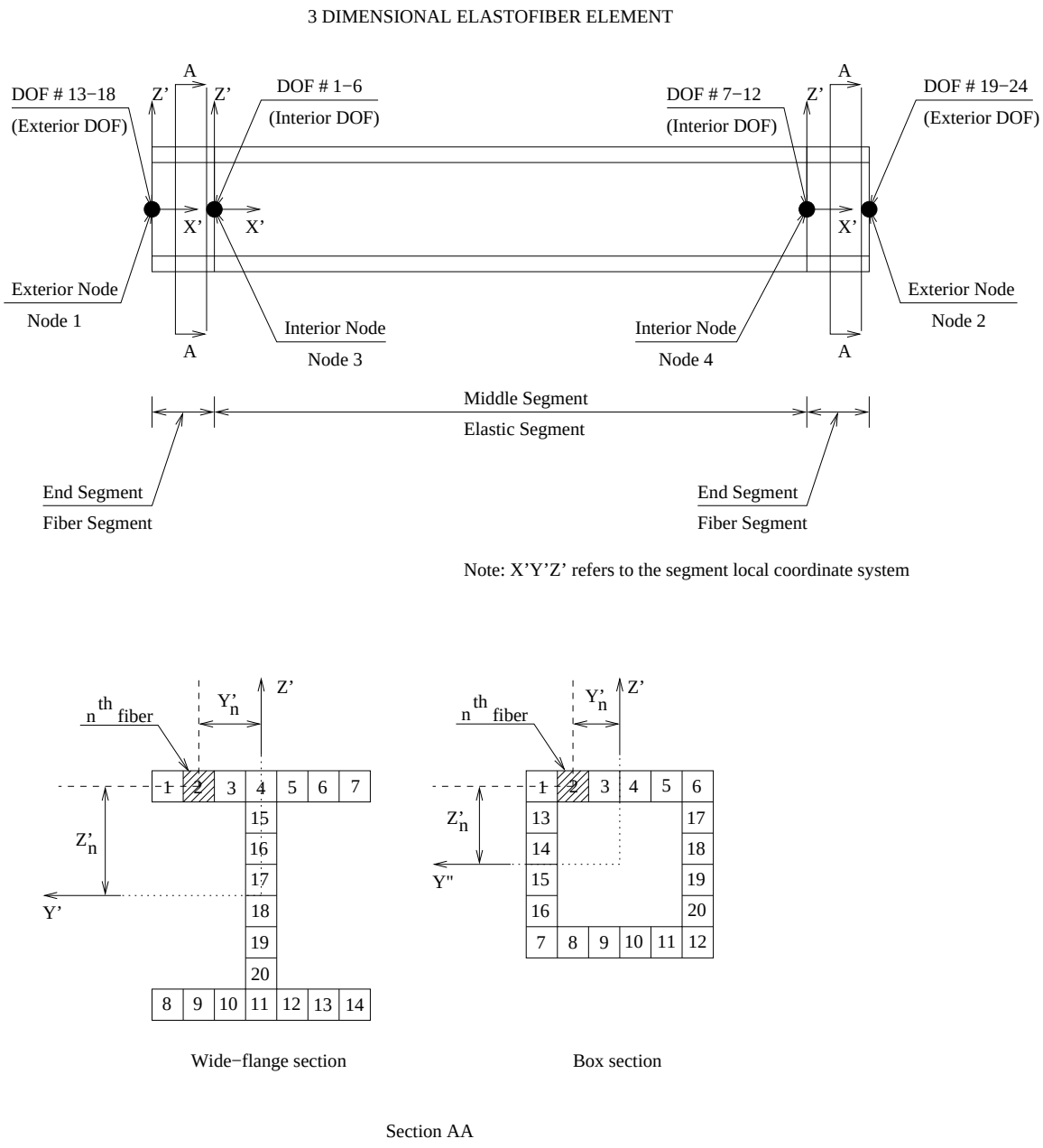

Figure 5.1: Layout of the 3-Segment Elastofiber Element

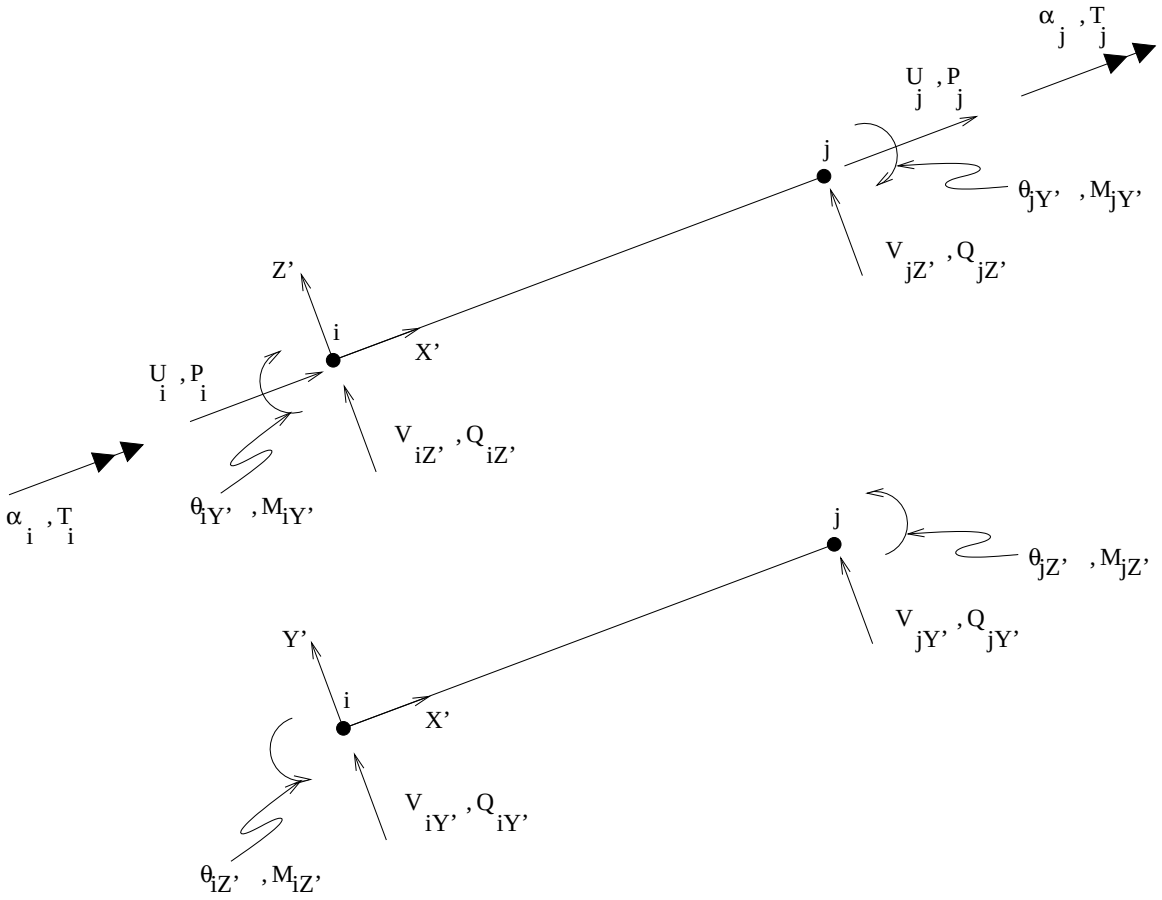

Figure 5.2: DOF of a Segment of the Elastofiber Beam Element Showing Nodal Translations and Rotations and Nodal Forces and Moments

1. P_i, P_j = Forces in X' direction at nodes i and j, respectively.

2. $Q_{iY'}$, $Q_{jY'}$ = Forces in Y' direction at nodes i and j, respectively.

3. $Q_{iZ'}$, $Q_{jZ'}$ = Forces in Z' direction at nodes i and j, respectively.

4. T_i, T_j = Moments about X' at nodes i and j, respectively.

5. $M_{iY'}$, $M_{jY'}$ = Moments about Y' at nodes i and j, respectively.

6. $M_{iZ'}$, $M_{jZ'}$ = Moments about Z' at nodes i and j, respectively.

5.1.2 Internal Forces and Moments in a Segment

The set of internal forces and moments in a segment of the elastofiber element are as follows:

1. P = Axial force in the segment.

2. $Q_{Y'}$, $Q_{Z'}$ = Shear forces in the segment in the Y' and Z' directions, respectively.

3. T = Twisting moment in the segment.

4. $M_{Y'}$, $M_{Z'}$ = Moments in the segment about the Y' and Z' axes, respectively.

The sign convention (positive directions) for these forces and moments is shown in Figure 4.5.

The middle segment of the elastofiber beam element is an elastic version of the plastic hinge beam element, i.e., no axial yielding and no plastic hinging. End segments are fiber segments. As shown in Figure 5.1, fiber segment cross-sections are divided into N fibers; each fiber runs the length of the segment. Associated with each fiber is a nonlinear hysteretic stress-strain law for axial stress, σ_n, and axial strain, ϵ_n, where n denotes the n^{th} fiber. This accounts for nonlinear coupling between bending about the Y' (major) and Z' (minor) axes, and axial deformation.

The fiber segment is based on finite element methodology whereby the beam translations and rotations are interpolated linearly and independently from their nodal values. This requires a one-point integration on the shear terms to prevent locking.

Because of the presence of the interior nodes, the updating process for each elastofiber beam element requires a nonlinear structural analysis. Iterations for each element are

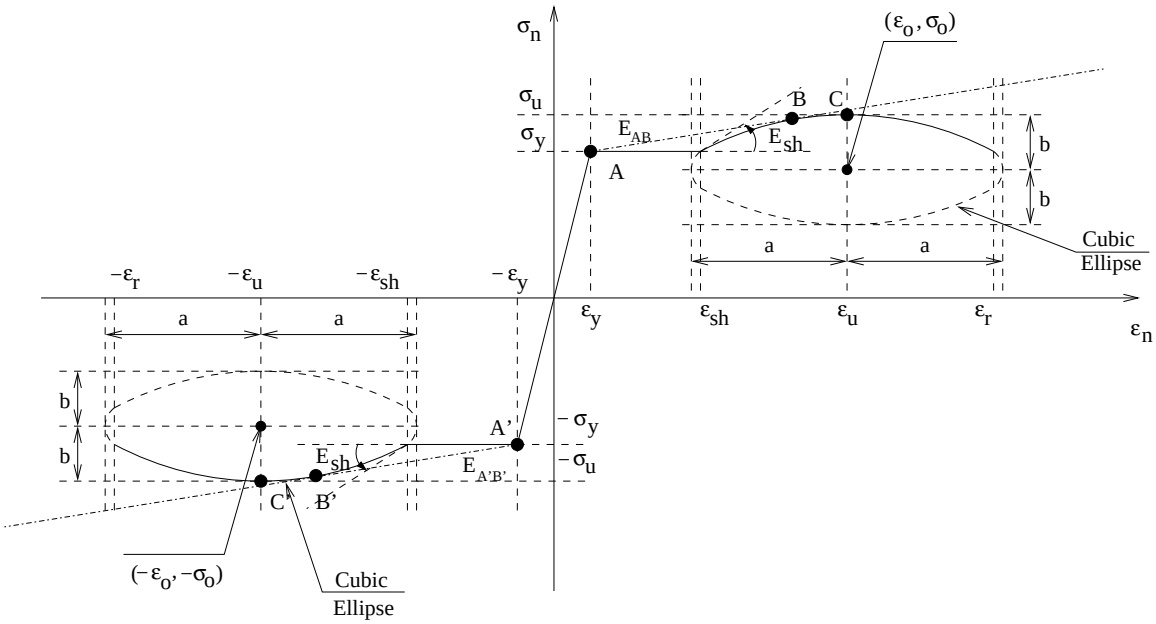

Figure 5.3: Stress-Strain Model for a Typical Fiber in a Fiber Segment of an Elastofiber Element

performed within each global iteration. The multi-segment element analyses are performed with degrees of freedom transformed to the global coordinate system, XYZ.

5.2 Material Model for Fiber Axial Stress-Strain

The axial stress-strain behavior of the fiber is governed by the hysteretic uniaxial cubic-ellipsoidal law proposed by Challa [11, 29]. The stress-strain curve for monotonic loading, shown in Figure 5.3, is symmetric about both the strain and stress axes. It consists of an elastic portion, a yield plateau and a strain-hardening region which is described by a cubic ellipse. The monotonic stress-strain curve is characterized by seven parameters: the yield stress, σ_y, the ultimate stress, σ_u, the yield strain, ϵ_y, the strain at initiation of strain hardening, ϵ_{sh}, the strain at ultimate stress, ϵ_u, the rupture strain, ϵ_r, and the tangent modulus at the initiation of strain hardening, E_{sh}. The cubic ellipse describing the strain hardening region is assumed to be centered at $(\epsilon_0 = \epsilon_u, \sigma_0)$ with radii, a and b:

$$\frac{(\epsilon_n - \epsilon_0)^3}{a^3} + \frac{(\sigma_n - \sigma_0)^3}{b^3} = 1 \tag{5.1}$$

Parameters, σ_0, a, and b, are determined from the user-defined properties, ϵ_{sh}, ϵ_u, E_{sh}, σ_y, and σ_u.

The hysterysis laws required to describe the stress-strain behavior under cyclic loading or reversal of loading are described in [11] and [29]. Although not included here, a fiber fracture capability can be added to approximately represent fracture of welded beam-to-column connections [26].

5.3 Transformation Matrix $[T_{ef}]$

$[T_{ef}]$ is the transformation matrix between the 16 DOF at the nodes, J and K, of the joints and the 12 degrees of freedom at nodes 1 and 2 of the elastofiber element. Because the element computations are done for DOF transformed to the XYZ coordinate system, only the first, second and third transformation steps, discussed in Section 4.2 in the context of the plastic hinge beam element, is necessary. The displacement vectors, $\{U_{ph}\}_L$, $\left\{\bar{U}_{ph}\right\}_L$, $\left\{\bar{U}_{ph}\right\}$, and $\{U_{ph}\}$ mentioned there contain the same terms as the elastofiber element, and can be renamed $\{U_{ef}\}_L$, $\left\{\bar{U}_{ef}\right\}_L$, $\left\{\bar{U}_{ef}\right\}$, and $\{U_{ef}\}$, respectively. The transformation matrix is

$$[T_{ef}] = [T_3]\,[T_2]\,[T_1] \tag{5.2}$$

5.4 Theory of the Fiber Segment

Because of the linear interpolation, the axial strain ϵ_n in fiber n is constant along the length of the segment. A strain increment $d\epsilon_n$ is caused by nodal displacement increments as follows:

$$d\epsilon_n = \frac{dU_j - dU_i}{L_{s0}} + \frac{Z'_n\left(d\phi_{jY'} - d\phi_{iY'}\right)}{L_{s0}} - \frac{Y'_n\left(d\phi_{jZ'} - d\phi_{iZ'}\right)}{L_{s0}} \tag{5.3}$$

where the rotations of the cross-section, $\phi_{iY'}$, $\phi_{jY'}$, $\phi_{iZ'}$, and $\phi_{jZ'}$, about Y' and Z' at the nodes are relative to the chord (straight line connecting nodes i and j of the segment), and Y'_n and Z'_n are the Y' and Z' coordinates of fiber n. Figure 5.1 shows the actual fiber layouts for wide-flange sections (I-sections) and box sections. The axial stress σ_n is related

to the axial strain ϵ_n by the incremental relation

$$d\sigma_n = E_{T,n} d\epsilon_n \tag{5.4}$$

according to the formulation of Section 5.2, where $E_{T,n}$ is the tangent modulus of the fiber. The internal axial force, P, and bending moments $M_{Y'}$ and $M_{Z'}$ are expressed in terms of σ_n as follows.

$$P = \sum_{n=1}^{N} \sigma_n A_n \tag{5.5}$$

$$\bar{M}_{Y'} = -\sum_{n=1}^{N} \sigma_n A_n Z'_n \tag{5.6a}$$

$$\bar{M}_{Z'} = \sum_{n=1}^{N} \sigma_n A_n Y'_n \tag{5.6b}$$

where A_n is the cross-sectional area of fiber n. The two moment expressions will only be used for the moments at mid-length of the segment, and this is denoted by $\bar{}$.

Expressions for the internal shear forces are expressed using elastic theory and properties of the entire cross-section:

$$Q_{Y'} = -A_{SY'} G \phi_{Z'} \tag{5.7a}$$

$$Q_{Z'} = A_{SZ'} G \phi_{Y'} \tag{5.7b}$$

where $A_{SY'}$ and $A_{SZ'}$ are the effective shear areas of the cross-section in the Y' and Z' directions (Figure 4.12) and $\phi_{Y'}$ and $\phi_{Z'}$ are the rotations of the cross-section about Y' and Z' along the beam relative to the chord. The shear forces will be assumed constant along the beam at their values at mid-length to prevent shear locking. Using the $\bar{}$ notation,

$$\bar{Q}_{Y'} = -A_{SY'} G \frac{\phi_{iZ'} + \phi_{jZ'}}{2} \tag{5.8a}$$

$$\bar{Q}_{Z'} = A_{SZ'} G \frac{\phi_{iY'} + \phi_{jY'}}{2} \tag{5.8b}$$

Incremental versions of eqs. 5.5, 5.6, and 5.8, are as follows:

$$dP = \sum_{n=1}^{N} E_{T,n} A_n d\epsilon_n \tag{5.9}$$

$$d\bar{M}_{Y'} = -\sum_{n=1}^{N} E_{T,n} A_n Z'_n d\epsilon_n \tag{5.10a}$$

$$d\bar{M}_{Z'} = \sum_{n=1}^{N} E_{T,n} A_n Y'_n d\epsilon_n \tag{5.10b}$$

using eq. 5.4 and

$$d\bar{Q}_{Y'} = -A_{SY'} G \frac{d\phi_{iZ'} + d\phi_{jZ'}}{2} \tag{5.11a}$$

$$d\bar{Q}_{Z'} = A_{SZ'} G \frac{d\phi_{iY'} + d\phi_{jY'}}{2} \tag{5.11b}$$

For twisting, similar to the plastic hinge element (Section 4.3.2),

$$dT = GJ d\omega \tag{5.12a}$$

$$d\omega = \frac{d\alpha_j - d\alpha_i}{L_{s0}} \tag{5.12b}$$

$$dT = GJ \frac{d\alpha_j - d\alpha_i}{L_{s0}} \tag{5.12c}$$

Substituting eq. 5.3 into eqs. 5.9 through 5.12, the incremental relations can be written in matrix form as

$$\begin{Bmatrix} dP \\ d\bar{M}_{Y'} \\ d\bar{M}_{Z'} \\ d\bar{Q}_{Y'} \\ d\bar{Q}_{Z'} \\ dT \end{Bmatrix} = [C_T] \begin{Bmatrix} \frac{dU_j - dU_i}{L_{s0}} \\ -\frac{\left(d\phi_{jY'} - d\phi_{iY'}\right)}{L_{s0}} \\ -\frac{\left(d\phi_{jZ'} - d\phi_{iZ'}\right)}{L_{s0}} \\ -\frac{d\phi_{iZ'} + d\phi_{jZ'}}{2} \\ \frac{d\phi_{iY'} + d\phi_{jY'}}{2} \\ \frac{d\alpha_j - d\alpha_i}{L_{s0}} \end{Bmatrix} \tag{5.13}$$

where

$$[C_T] = \begin{bmatrix} \sum_{n=1}^{N} E_{T,n}A_n & -\sum_{n=1}^{N} E_{T,n}A_nZ'_n & \sum_{n=1}^{N} E_{T,n}A_nY'_n & 0 & 0 & 0 \\ & \sum_{n=1}^{N} E_{T,n}A_nZ'^2_n & -\sum_{n=1}^{N} E_{T,n}A_nY'_nZ'_n & 0 & 0 & 0 \\ & & \sum_{n=1}^{N} E_{T,n}A_nY'^2_n & 0 & 0 & 0 \\ & symmetric & & A_{SY'}G & 0 & 0 \\ & & & & A_{SZ'}G & 0 \\ & & & & & GJ \end{bmatrix} \tag{5.14}$$

The right-hand side vector of eq. 5.13 is expressed in terms of nodal degrees of freedom as

$$\begin{Bmatrix} \frac{dU_j - dU_i}{L_{s0}} \\ -\frac{\left(d\phi_{jY'} - d\phi_{iY'}\right)}{L_{s0}} \\ -\frac{\left(d\phi_{jZ'} - d\phi_{iZ'}\right)}{L_{s0}} \\ -\frac{d\phi_{iZ'} + d\phi_{jZ'}}{2} \\ \frac{d\phi_{iY'} + d\phi_{jY'}}{2} \\ \frac{d\alpha_j - d\alpha_i}{L_{s0}} \end{Bmatrix} = \frac{1}{L_{s0}} [S] \begin{Bmatrix} dU_i \\ dV_{iY'} \\ dV_{iZ'} \\ d\alpha_i \\ d\theta_{iY'} \\ d\theta_{iZ'} \\ dU_j \\ dV_{jY'} \\ dV_{jZ'} \\ d\alpha_j \\ d\theta_{jY'} \\ d\theta_{jZ'} \end{Bmatrix} \tag{5.15}$$

where

$$[S] = \begin{bmatrix} -1 & 0 & 0 & 0 & 0 & 0 & 1 & 0 & 0 & 0 & 0 & 0 \\ 0 & 0 & 0 & 0 & 1 & 0 & 0 & 0 & 0 & 0 & -1 & 0 \\ 0 & 0 & 0 & 0 & 0 & 1 & 0 & 0 & 0 & 0 & 0 & -1 \\ 0 & -1 & 0 & 0 & 0 & -\frac{L_{s0}}{2} & 0 & 1 & 0 & 0 & 0 & -\frac{L_{s0}}{2} \\ 0 & 0 & -1 & 0 & \frac{L_{s0}}{2} & 0 & 0 & 0 & 1 & 0 & \frac{L_{s0}}{2} & 0 \\ 0 & 0 & 0 & -1 & 0 & 0 & 0 & 0 & 0 & 1 & 0 & 0 \end{bmatrix} \tag{5.16}$$

In incremental form, the nodal forces and moments are expressed in terms of the internal ones as

$$\begin{Bmatrix} dP_i \\ dQ_{iY'} \\ dQ_{iZ'} \\ dT_i \\ dM_{iY'} \\ dM_{iZ'} \\ dP_j \\ dQ_{jY'} \\ dQ_{jZ'} \\ dT_j \\ dM_{jY'} \\ dM_{jZ'} \end{Bmatrix} = [S]^T \begin{Bmatrix} dP \\ d\bar{M}_{Y'} \\ d\bar{M}_{Z'} \\ d\bar{Q}_{Y'} \\ d\bar{Q}_{Z'} \\ dT \end{Bmatrix} + \frac{P}{L_{s0}} \begin{bmatrix} 0 & 0 & 0 & 0 & 0 & 0 & 0 & 0 & 0 & 0 & 0 & 0 \\ 0 & 1 & 0 & 0 & 0 & 0 & 0 & -1 & 0 & 0 & 0 & 0 \\ 0 & 0 & 1 & 0 & 0 & 0 & 0 & 0 & -1 & 0 & 0 & 0 \\ 0 & 0 & 0 & 0 & 0 & 0 & 0 & 0 & 0 & 0 & 0 & 0 \\ 0 & 0 & 0 & 0 & 0 & 0 & 0 & 0 & 0 & 0 & 0 & 0 \\ 0 & 0 & 0 & 0 & 0 & 0 & 0 & 0 & 0 & 0 & 0 & 0 \\ 0 & 0 & 0 & 0 & 0 & 0 & 0 & 0 & 0 & 0 & 0 & 0 \\ 0 & -1 & 0 & 0 & 0 & 0 & 0 & 1 & 0 & 0 & 0 & 0 \\ 0 & 0 & -1 & 0 & 0 & 0 & 0 & 0 & 1 & 0 & 0 & 0 \\ 0 & 0 & 0 & 0 & 0 & 0 & 0 & 0 & 0 & 0 & 0 & 0 \\ 0 & 0 & 0 & 0 & 0 & 0 & 0 & 0 & 0 & 0 & 0 & 0 \\ 0 & 0 & 0 & 0 & 0 & 0 & 0 & 0 & 0 & 0 & 0 & 0 \end{bmatrix} \begin{Bmatrix} dU_i \\ dV_{iY'} \\ dV_{iZ'} \\ d\alpha_i \\ d\theta_{iY'} \\ d\theta_{iZ'} \\ dU_j \\ dV_{jY'} \\ dV_{jZ'} \\ d\alpha_j \\ d\theta_{jY'} \\ d\theta_{jZ'} \end{Bmatrix} \tag{5.17}$$

where the matrix consisting of $\frac{P}{L_{s0}}$ terms is the geometric stiffness matrix, $[G]$. Combining the above leads to

$$\left\{dR'_s\right\} = \left[K'_{T,s}\right] \left\{dU'_s\right\} \tag{5.18}$$

where $\{dR'_s\}$ is the incremental version of

$$\langle R'_s \rangle = \langle \; P_i \quad Q_{iY'} \quad Q_{iZ'} \quad T_i \quad M_{iY'} \quad M_{iZ'} \quad P_j \quad Q_{jY'} \quad Q_{jZ'} \quad T_j \quad M_{jY'} \quad M_{jZ'} \; \rangle \tag{5.19}$$

$\left[K'_{T,s}\right]$ is the 12×12 tangent stiffness matrix for a fiber segment:

$$\left[K'_{T,s}\right] = \frac{1}{L_{s0}} [S]^T [C_T] [S] + [G] \tag{5.20}$$

and

$$\langle dU'_s \rangle = \langle \; dU_i \quad dV_{iY'} \quad dV_{iZ'} \quad d\alpha_i \quad d\theta_{iY'} \quad d\theta_{iZ'} \quad dU_j \quad dV_{jY'} \quad dV_{jZ'} \quad d\alpha_j \quad d\theta_{jY'} \quad d\theta_{jZ'} \; \rangle \tag{5.21}$$

5.5 Updating Process

In global iteration l, $\{\Delta U\}$ is computed from eq. 2.9. The 12 displacement increments in the XYZ coordinate system at nodes 1 and 2 for an elastofiber element are found as

$$\{\Delta U_{ef}\}_L = \left[T_{ef}^l\right] \{\Delta U_{ef}\} \tag{5.22}$$

where $\{\Delta U_{ef}\}$ contains the 16 terms extracted from $\{\Delta U\}$ corresponding to the nodes J and K connected to nodes 1 and 2, and $\left[T_{ef}^l\right]$ is the transformation matrix representing configuration l.

Updating the panel zone element geometries as discussed in Section 3.3 will produce new locations for the attachment points, from which new $\bar{X}$, $\bar{Y}$, and $\bar{Z}$ orientations can be found, leading to $\left[\bar{C}_J^{l+1}\right]$ and $\left[\bar{C}_K^{l+1}\right]$ and then $\left[T_3^{l+1}\right]$ and $\left[T_1^{l+1}\right]$ by eqs. 4.16 and 4.11, respectively. Updating $\xi^{①}$ and $\xi^{②}$ leads to $\left[T_2^{l+1}\right]$ by eqs. 4.12, 4.13, and 4.14. Then,

$$\left[T_{ef}^{l+1}\right] = \left[T_3^{l+1}\right] \left[T_2^{l+1}\right] \left[T_1^{l+1}\right] \tag{5.23}$$

Next, the displacement increments, $\{\Delta U_{ef}\}_L$ are applied to nodes 1 and 2 of the elastofiber element, and the resulting displacements of nodes 3 and 4 computed by an iterative structural analysis. In the k^{th} iteration of this process (iteration (k) where the $()$ denotes element iterations within global iteration l), the equation to be solved is

$$\begin{bmatrix} K_{T,II}^{(k)} & K_{T,IE}^{(k)} \\ K_{T,EI}^{(k)} & K_{T,EE}^{(k)} \end{bmatrix} \begin{Bmatrix} \Delta U_I \\ \Delta U_E \end{Bmatrix} = \begin{Bmatrix} 0 \\ F_E \end{Bmatrix} - \begin{Bmatrix} R_I^{(k)} \\ R_E^{(k)} \end{Bmatrix} \tag{5.24}$$

which has been partitioned into the 12 DOF group I at the interior nodes 3 and 4, and the

12 DOF group E at the end nodes 1 and 2, where

$$\begin{bmatrix} K_{T,II}^{(k)} & K_{T,IE}^{(k)} \\ K_{T,EI}^{(k)} & K_{T,EE}^{(k)} \end{bmatrix} \text{and} \begin{Bmatrix} R_I^{(k)} \\ R_E^{(k)} \end{Bmatrix}$$

are the tangent stiffness matrix and stiffness force vector for configuration (k), respectively; $\{F_E\}$ is a vector of unknown loads applied to the element through nodes 1 and 2 by the surrounding structure; and $\{\Delta U_E\}$ is set to $\{\Delta U_{ef}\}_L$ for iteration $(k) = 1$ and to 0 for iteration $(k) > 1$. Eq. 5.24 can be solved for $\{\Delta U_I\}$ by substituting in the known vector $\{\Delta U_E\}$ and then solving the upper partitioned equation, which does not involve $\{F_E\}$. Iterations continue to convergence to the global $l+1$ state when the tangent stiffness matrix and stiffness force vector are denoted by

$$\begin{bmatrix} K_{T,II}^{l+1} & K_{T,IE}^{l+1} \\ K_{T,EI}^{l+1} & K_{T,EE}^{l+1} \end{bmatrix} \text{and} \begin{Bmatrix} R_I^{l+1} \\ R_E^{l+1} \end{Bmatrix}$$

These are used to start the beam analysis at $(k) = 1$ after global iteration $l + 1$.

The contributions to the global $\left[K_T^{l+1}\right]$ and $\left\{R^{l+1}\right\}$ are obtained from the $l+1$ tangent stiffness matrix and stiffness force vector by condensing out the I degrees of freedom:

$$\left[K_{T,ef}^{l+1}\right]_L = \left[K_{T,EE}^{l+1}\right] - \left[K_{T,EI}^{l+1}\right]\left[K_{T,II}^{l+1}\right]^{-1}\left[K_{T,IE}^{l+1}\right] \tag{5.25}$$

$$\left\{R_{ef}^{l+1}\right\}_L = \left\{R_E^{l+1}\right\} - \left[K_{T,EI}^{l+1}\right]\left[K_{T,II}^{l+1}\right]^{-1}\left\{R_I^{l+1}\right\} \tag{5.26}$$

and then transformation to

$$\left[K_{T,ef}^{l+1}\right] = \left[T_{ef}^{l+1}\right]^T\left[K_{T,ef}^{l+1}\right]_L\left[T_{ef}^{l+1}\right] \tag{5.27a}$$

$$\left\{R_{ef}^{l+1}\right\} = \left[T_{ef}^{l+1}\right]^T\left\{R_{ef}^{l+1}\right\}_L \tag{5.27b}$$

These are assembled into $\left[K_T^{l+1}\right]$ and $\left\{R^{l+1}\right\}$.

The element matrix, $\begin{bmatrix} K_{T,II} & K_{T,IE} \\ K_{T,EI} & K_{T,EE} \end{bmatrix}$ and vector $\begin{Bmatrix} R_I \\ R_E \end{Bmatrix}$ are assembled from the segment quantities $\left[K'_{T,s}\right]$ and $\{R'_s\}$ defined in Section 5.4 after transformation to the XYZ

coordinate system by

$$[K_{T,s}] = [T_s]^T \left[K'_{T,s}\right] [T_s] \tag{5.28}$$

$$\{R_s\} = [T_s]^T \left\{R'_s\right\} \tag{5.29}$$

where $[T_s]$ is similar to $[T_4]$ from Section 4.2,

$$[T_s]^{(12\times12)} = \begin{bmatrix} [C']^{(3\times3)} & [0]^{(3\times3)} & [0]^{(3\times3)} & [0]^{(3\times3)} \\ [0]^{(3\times3)} & [C']^{(3\times3)} & [0]^{(3\times3)} & [0]^{(3\times3)} \\ [0]^{(3\times3)} & [0]^{(3\times3)} & [C']^{(3\times3)} & [0]^{(3\times3)} \\ [0]^{(3\times3)} & [0]^{(3\times3)} & [0]^{(3\times3)} & [C']^{(3\times3)} \end{bmatrix} \tag{5.30}$$

The updating process for $[T_s]$, $\{R'_s\}$, and $\left[K'_{T,s}\right]$ during the element iterations is described now. The initial $\{\Delta U_E\}$ and the $\{\Delta U_I\}$ computed in iteration (k) are used to update the locations of the four element nodes. This leads to a new direction for the X' axis for each segment. Then terms from $\{\Delta U_E\}$ and $\{\Delta U_I\}$ are extracted and stored in $\{\Delta U_s\}$ for each segment, and then transformed to the $X'Y'Z'$ coordinate system by

$$\left\{\Delta U'_s\right\} = \left[T_s^{(k)}\right] \{\Delta U_s\} \tag{5.31}$$

Using $\Delta\alpha_i$ and $\Delta\alpha_j$, α_{or} is updated and then $\left[T_s^{(k+1)}\right]$ is found as discussed in Section 4.4.

For the middle segment, $\left\{R_s^{'(k+1)}\right\}$, and $\left[K_{T,s}^{'(k+1)}\right]$ are found by the procedure described in Section 4.4 for the plastic hinge element except that no plastic hinges are allowed to form.

The end segments are fiber segments. Consider $\left\{R_s^{'(k+1)}\right\}$. The $\Delta\phi$ rotation increments are computed as

$$\Delta\phi_{iY'} = \Delta\theta_{iY'} + \frac{\Delta V_{jZ'} - \Delta V_{iZ'}}{L_{s0}} \tag{5.32a}$$

$$\Delta\phi_{jY'} = \Delta\theta_{jY'} + \frac{\Delta V_{jZ'} - \Delta V_{iZ'}}{L_{s0}} \tag{5.32b}$$

$$\Delta\phi_{iZ'} = \Delta\theta_{iZ'} - \frac{\Delta V_{jY'} - \Delta V_{iY'}}{L_{s0}} \tag{5.32c}$$

$$\Delta\phi_{jZ'} = \Delta\theta_{jZ'} - \frac{\Delta V_{jY'} - \Delta V_{iY'}}{L_{s0}} \tag{5.32d}$$

where the right-side terms are from $\{\Delta U'_s\}$. Along with ΔU_i and ΔU_j, also from $\{\Delta U'_s\}$,

$\Delta\epsilon_n$ is found for each fiber from eq. 5.3. Then, using the formulation of Section 5.2, the updated stresses, $\sigma_n^{(k+1)}$ are found, and from eqs. 5.5 and 5.6:

$$P^{(k+1)} = \sum_{n=1}^{N} \sigma_n^{(k+1)} A_n \tag{5.33}$$

$$\bar{M}_{Y'}^{(k+1)} = -\sum_{n=1}^{N} \sigma_n^{(k+1)} A_n Z_n' \tag{5.34a}$$

$$\bar{M}_{Z'}^{(k+1)} = \sum_{n=1}^{N} \sigma_n^{(k+1)} A_n Y_n' \tag{5.34b}$$

The internal shear forces are updated as

$$\bar{Q}_{Y'}^{(k+1)} = \bar{Q}_{Y'}^{(k)} - A_{SY'} G \frac{\Delta\phi_{iZ'} + \Delta\phi_{jZ'}}{2} \tag{5.35a}$$

$$\bar{Q}_{Z'}^{(k+1)} = \bar{Q}_{Z'}^{(k)} + A_{SZ'} G \frac{\Delta\phi_{iY'} + \Delta\phi_{jY'}}{2} \tag{5.35b}$$

and the internal twisting moment is updated as

$$T^{(k+1)} = T^{(k)} + GJ \frac{\Delta\alpha_j - \Delta\alpha_i}{L_{s0}} \tag{5.36}$$

The nodal forces and moments can now be computed using the $[S]$ matrix as in eq. 5.17:

$$P_j^{(k+1)} = -P_i^{(k+1)} = P^{(k+1)} \tag{5.37a}$$

$$Q_{jY'}^{(k+1)} = -Q_{iY'}^{(k+1)} = \bar{Q}_{Y'}^{(k+1)} \tag{5.37b}$$

$$Q_{jZ'}^{(k+1)} = -Q_{iZ'}^{(k+1)} = \bar{Q}_{Z'}^{(k+1)} \tag{5.37c}$$

$$T_j^{(k+1)} = -T_i^{(k+1)} = T^{(k+1)} \tag{5.37d}$$

$$M_{iY'}^{(k+1)} = \bar{M}_{Y'}^{(k+1)} + \bar{Q}_{Z'}^{(k+1)} \frac{L_{s0}}{2} \tag{5.37e}$$

$$M_{iZ'}^{(k+1)} = \bar{M}_{Z'}^{(k+1)} - \bar{Q}_{Y'}^{(k+1)} \frac{L_{s0}}{2} \tag{5.37f}$$

$$M_{jY'}^{(k+1)} = -\bar{M}_{Y'}^{(k+1)} + \bar{Q}_{Z'}^{(k+1)} \frac{L_{s0}}{2} \tag{5.37g}$$

$$M_{jZ'}^{(k+1)} = -\bar{M}_{Z'}^{(k+1)} - \bar{Q}_{Y'}^{(k+1)} \frac{L_{s0}}{2} \tag{5.37h}$$

These are assembled into $\left\{R_s^{\prime(k+1)}\right\}$.

After $\left\{R_s^{\prime(k+1)}\right\}$ is computed for a fiber segment, $P^{(k+1)}$ for the segment and $E_{T,n}^{(k+1)}$ for each fiber will be known. Then, $\left[K_{T,s}^{\prime(k+1)}\right]$ can be computed using the formulae of Section 5.4.

5.6 Elastofiber Element Calibration Using Fiber Element

The length of the fiber segment in relation to the total clear length of the elastofiber element has to be calibrated for so as to provide a basis for subdividing the element into the three segments in the most suitable proportion. This calibration is carried out on a single element model of a simply supported beam ($W30\times116$, Figure 5.4) that is 20 feet (about 6.1 meters) long. A572-Grade 50 steel with an yield stress of 50 ksi and an ultimate stress of 65 ksi is used. The elastofiber element is calibrated against a fully discretized 8-segment fiber element model. This element is a two-dimensional element described in references, [11], [12] and [27]. The element is subjected to the rotation history shown in Figure 5.5 at both ends. The specified end rotations force the beam into double curvature similar to the situation of a beam or column that is part of a frame subjected to lateral loading in an earthquake. It is assumed that there exists no axial restraint in the beam. Results using a fiber segment length of 3% of the clear span of the beam are presented in Figures 5.5 through 5.8. These include the moment histories, $M_1(t)$ and $M_2(t)$ generated at the right and left ends of the beam, the axial force history, $F(t)$, the moment plotted against the rotation at one of the two ends of the beam, and the stress-strain history of a typical fiber in the top and bottom flanges of one of the two end fiber segments. These results for the elastofiber element are compared against those for the 2-D fiber element. There is good agreement between the elastofiber element with fiber segments of length, 3%L, and the fiber element [28, 27] even after significant loss of capacity due to the rupture of a few fibers. All the analyses in this work utilize A572-Grade 50 steel and hence adopt fiber segment lengths of 3% of the clear span. The results of this analysis demonstrate that there is very little spread of plasticity into the interior segments of the fully discretized fiber element in the case of A572-Grade 50 steel.

In the case of $A36$ steel with an yield stress of 36 ksi and an ultimate stress of 58 ksi, the yielding spreads into the interior segment of the fiber element prior to strain hardening in

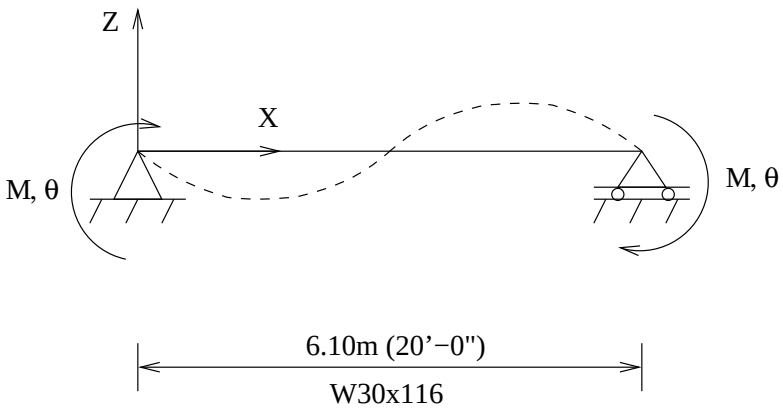

Figure 5.4: Simply Supported Beam Used for Calibration Studies

the end segment. To capture the true behavior in such cases using the elastofiber element, it is observed that an end fiber segment length of 11% of the clear span of the beam gives accurate results (Figures 5.9 and 5.10). Thus, it is recommended that for materials with low ultimate stress-to-yield stress ratios (less than 1.4) such as A572-Grade 50 steels, end segment lengths of 3% of the clear span be used while for materials with high ultimate stress-to-yield stress ratios (greater than 1.4) such as A36 steels, end segment lengths of 11% of the clear span be used.

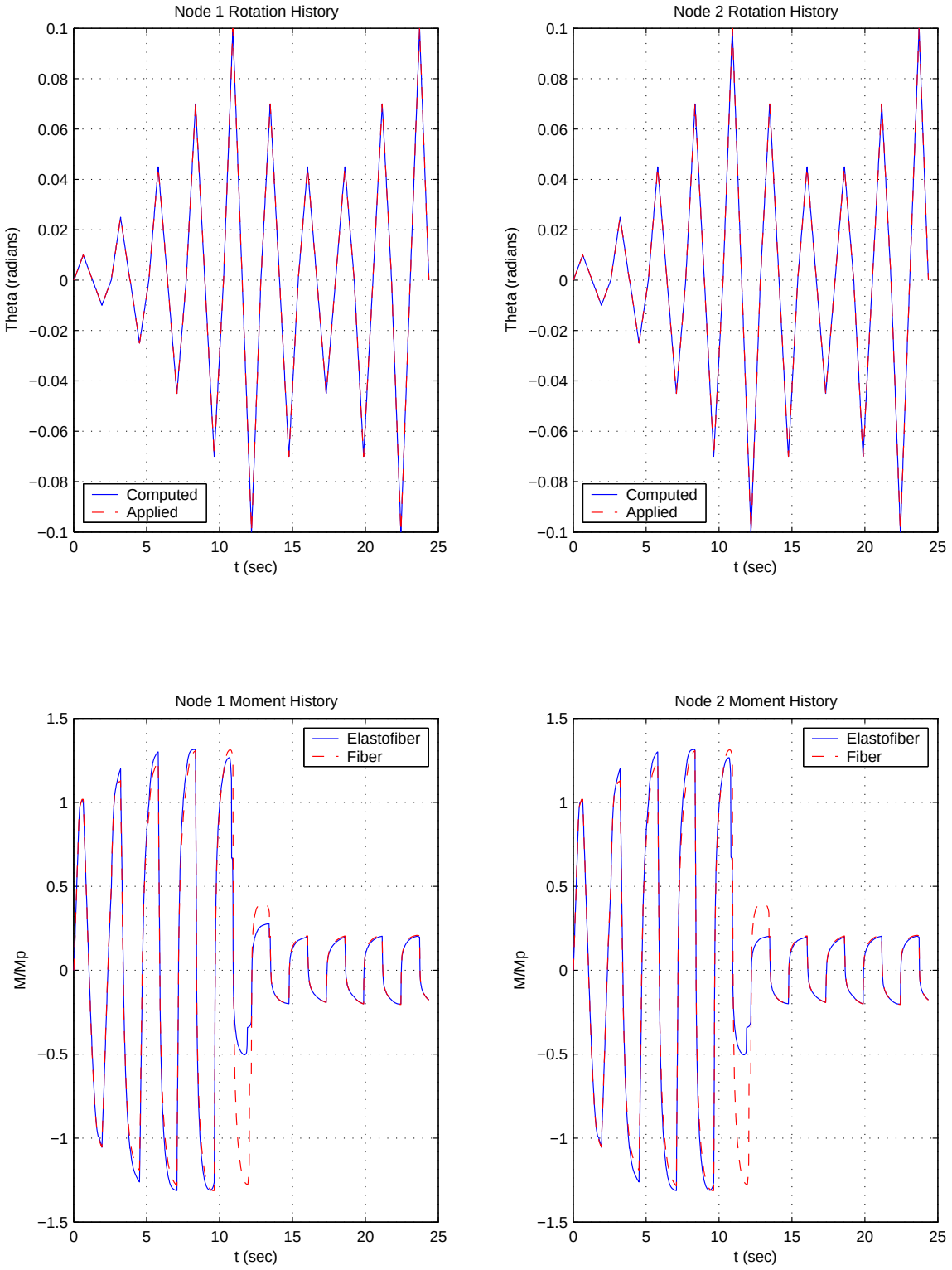

Figure 5.5: Comparison of Elastofiber Element with a Fully Discretized Fiber Elements ($\sigma_y = 50\ ksi; \sigma_u = 65\ ksi$)

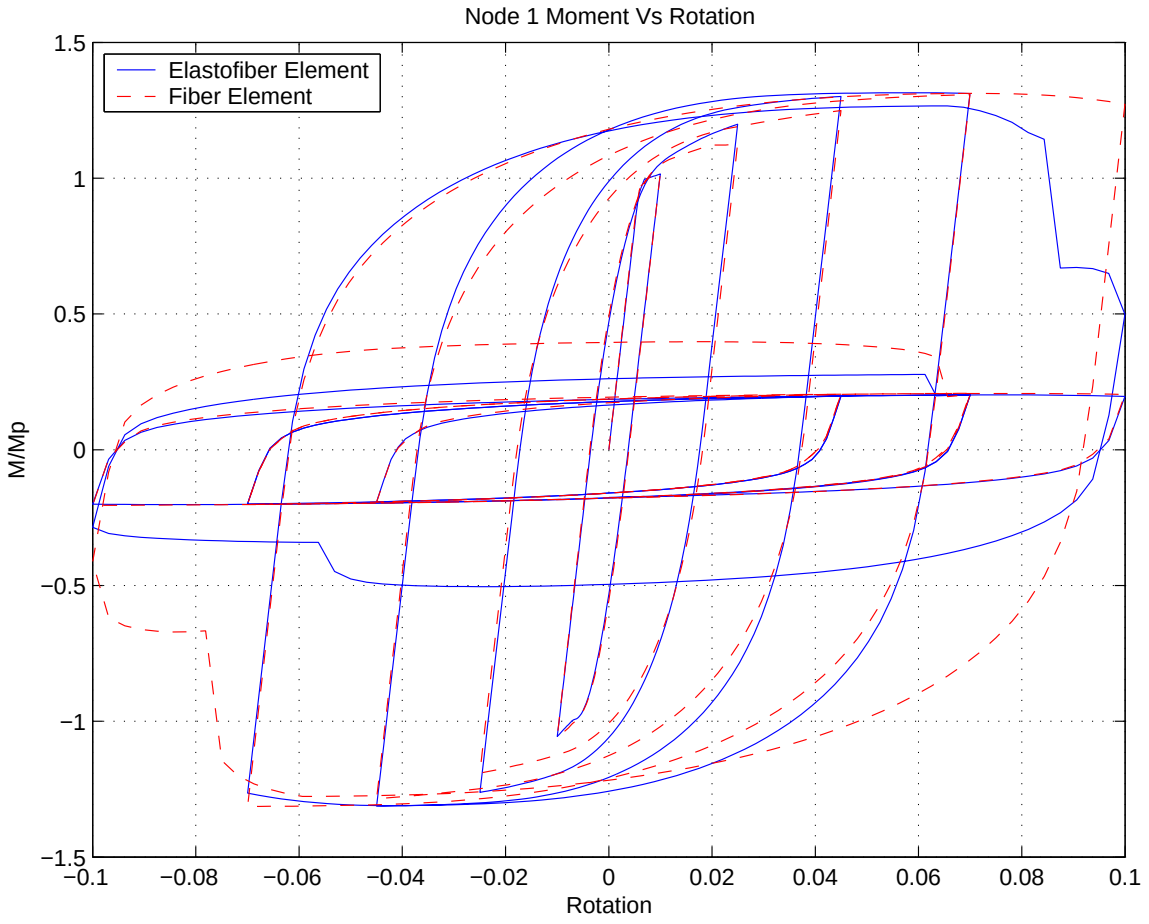

Figure 5.6: Comparison of Elastofiber Element with a Fully Discretized Fiber Elements ($\sigma_y = 50\ ksi; \sigma_u = 65\ ksi$)

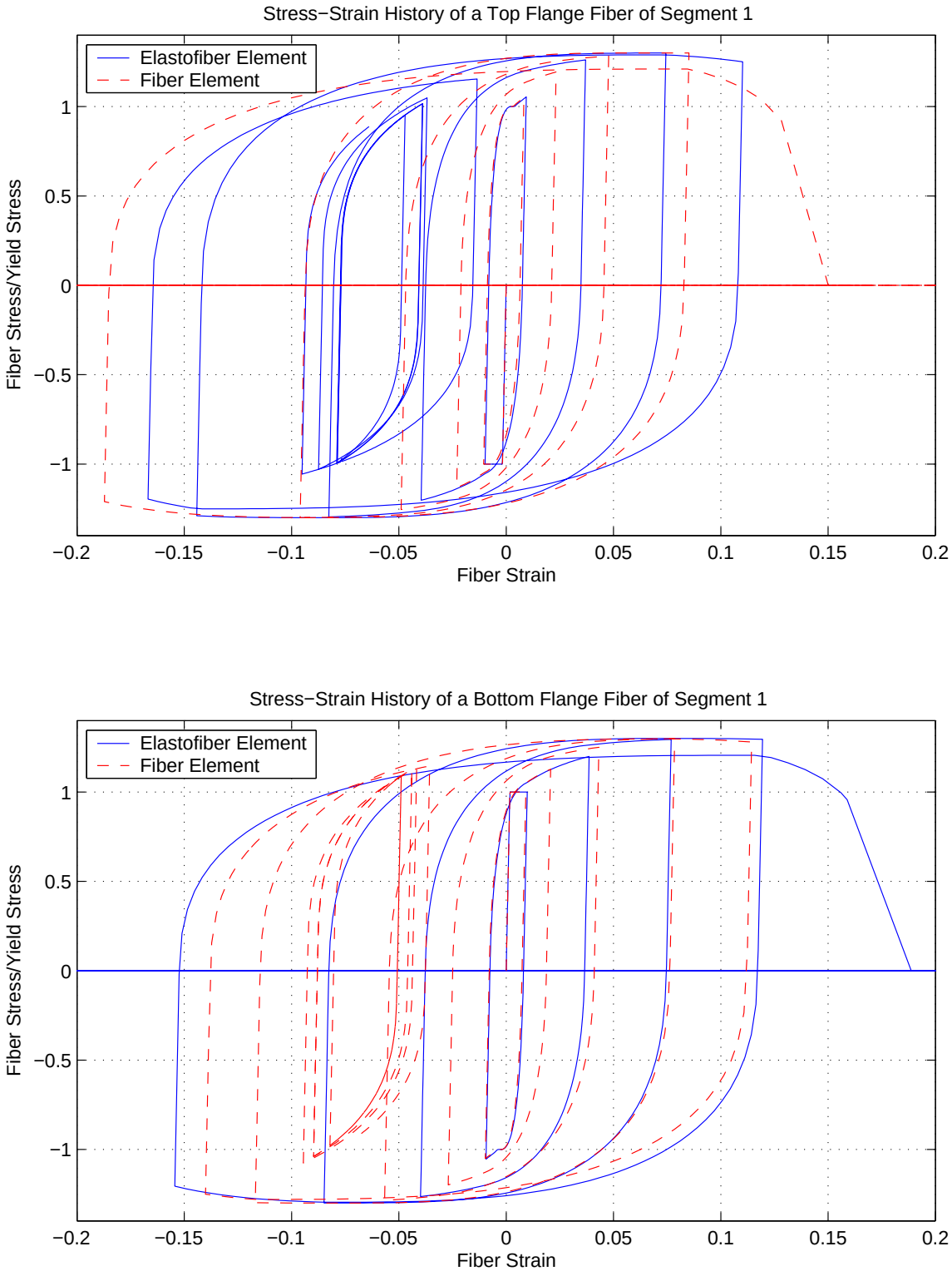

Figure 5.7: Comparison of Elastofiber Element with a Fully Discretized Fiber Elements ($\sigma_y = 50\ ksi; \sigma_u = 65\ ksi$)

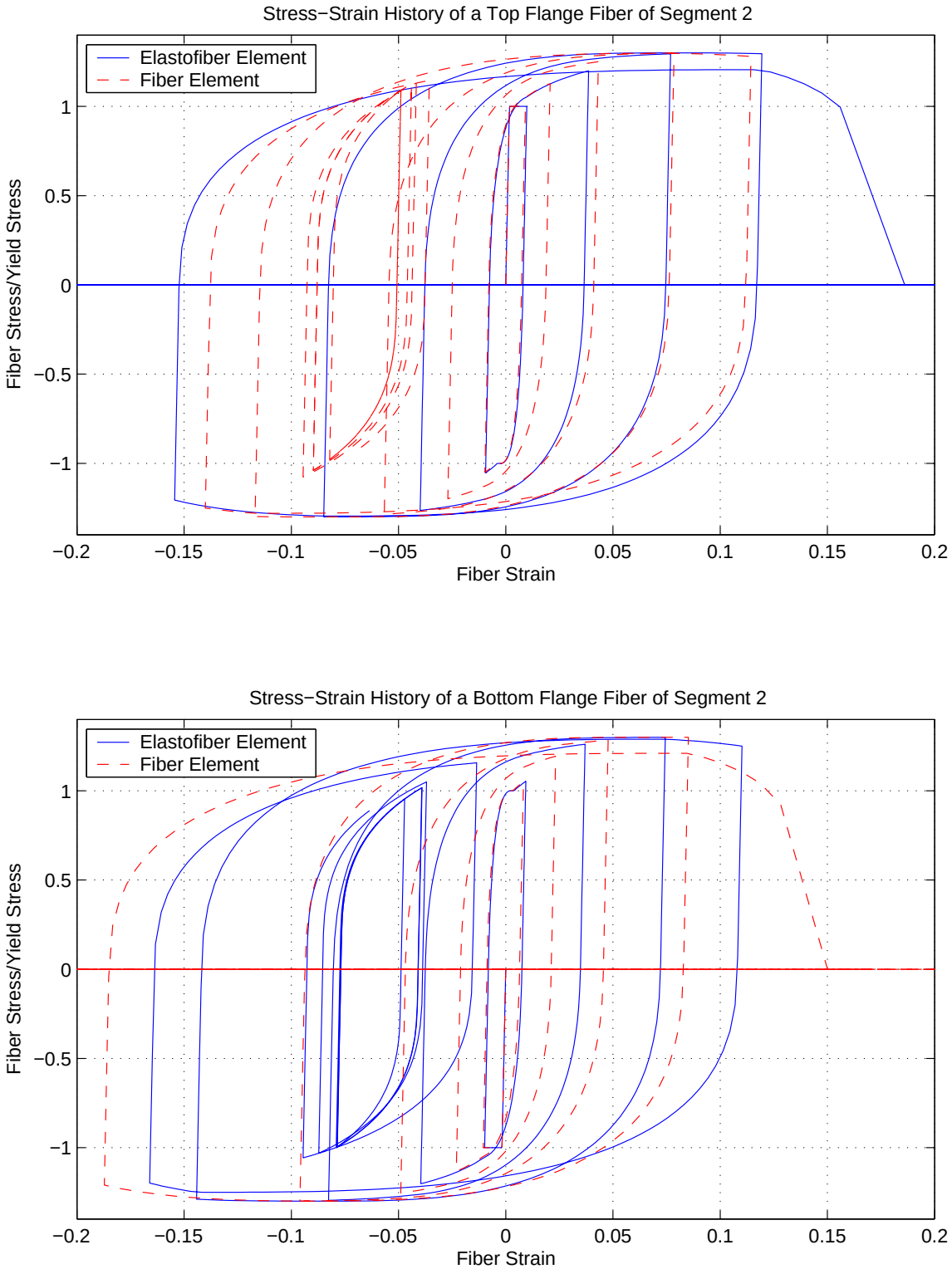

Figure 5.8: Comparison of Elastofiber Element with a Fully Discretized Fiber Elements ($\sigma_y = 50\ ksi; \sigma_u = 65\ ksi$)

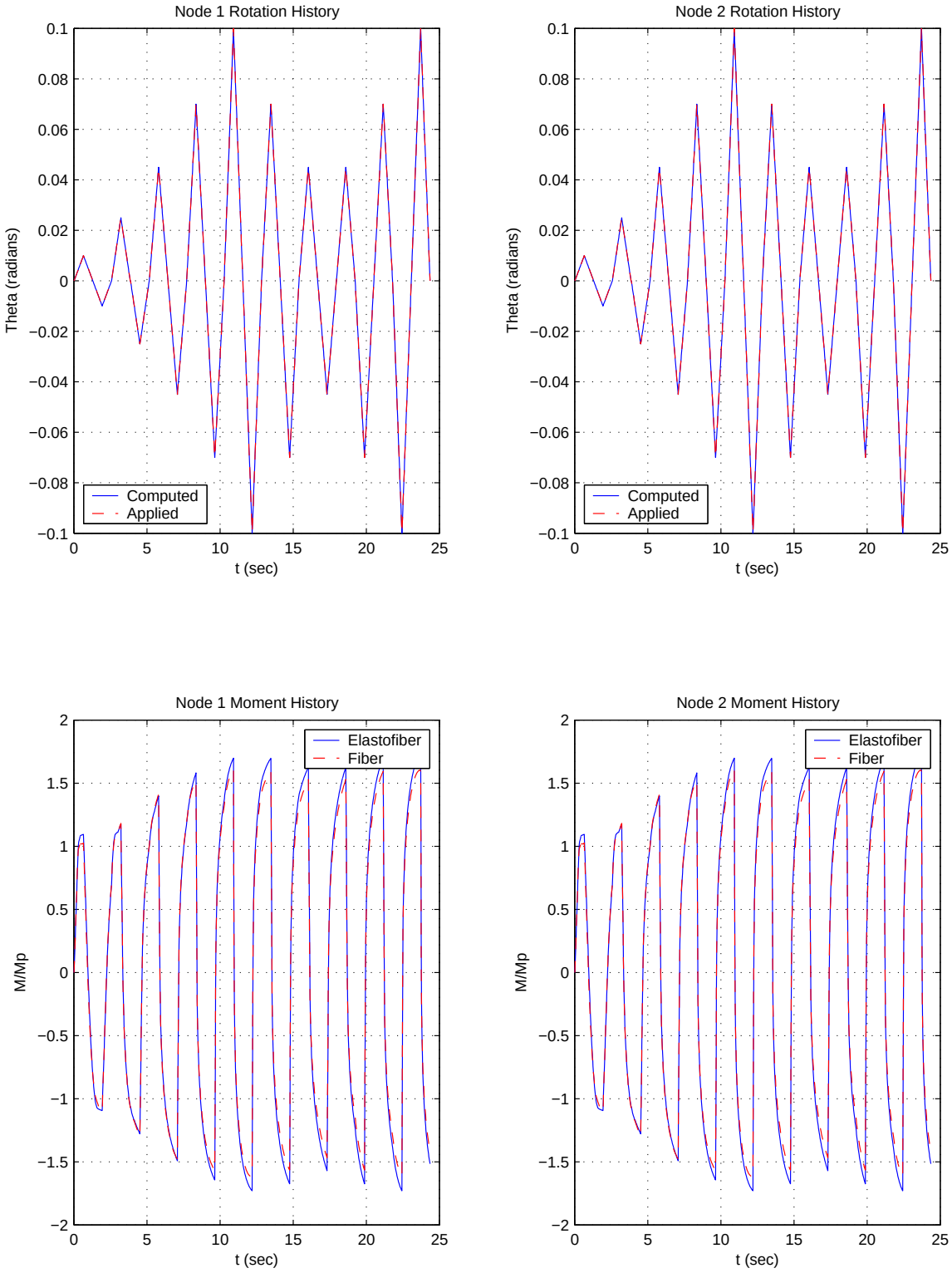

Figure 5.9: Comparison of Elastofiber Element with a Fully Discretized Fiber Elements ($\sigma_y = 36\ ksi; \sigma_u = 58\ ksi$)

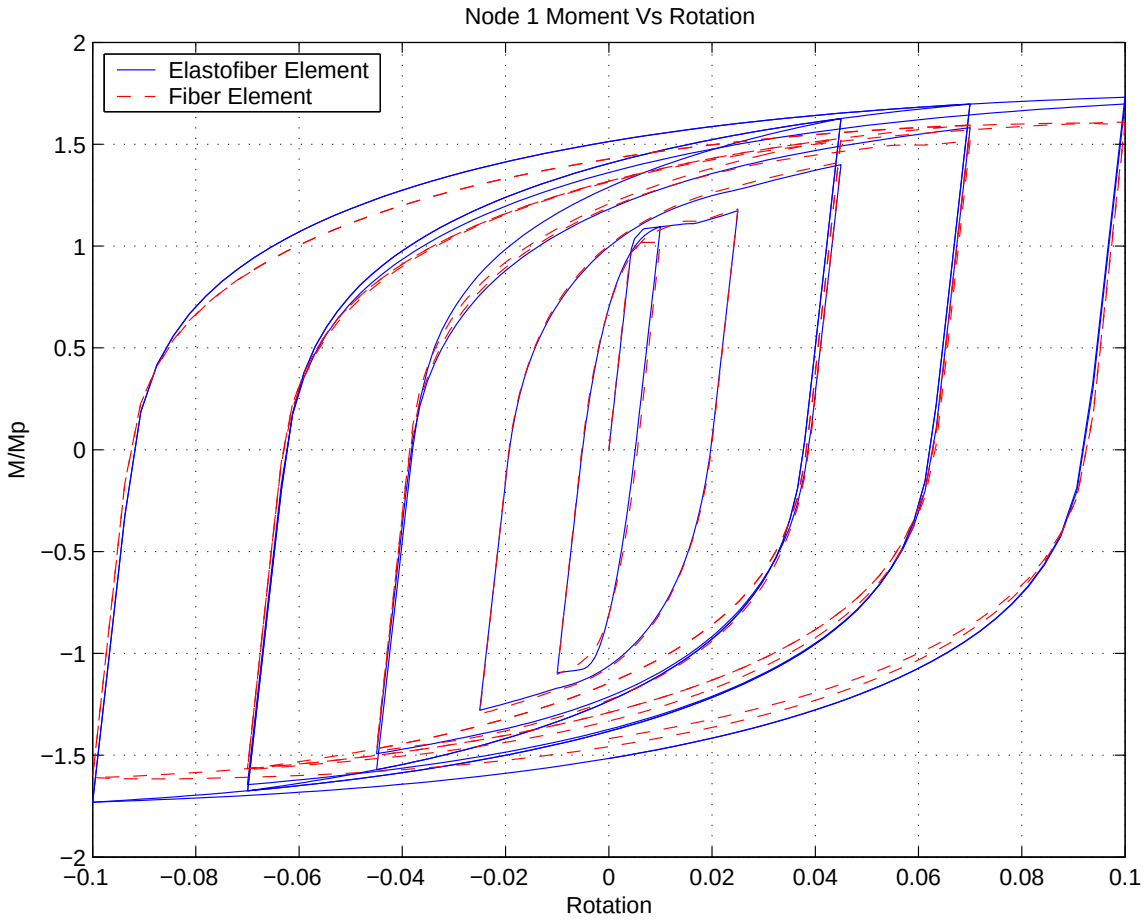

Figure 5.10: Comparison of Elastofiber Element with a Fully Discretized Fiber Elements ($\sigma_y = 36\ ksi; \sigma_u = 58\ ksi$)

Chapter 6 Diaphragm Element

6.1 General Description

The diaphragm element is a 4-noded linear-elastic plane element that can take a quadrilateral form in 3-D spatial coordinates, XYZ. It is used to provide translational restraint caused by floor slabs to columns in buildings. The following assumptions are made in the formulation of this element:

1. Material is isotropic and linear-elastic, with Young's modulus, E, shear modulus, G, and Poisson's ratio, ν.

2. Warping is not considered.

3. A state of plane-stress is assumed in the element.

4. The element continues to provide the same restraint (in magnitude and direction) as in the original configuration even though during the course of the analysis the nodes of the element may have translated causing the geometry of the element to change.

5. The element is not externally loaded and all the stresses in the element are generated by stiffness forces due to the translation of the nodes during the course of the analysis.

The nodes of the element are labeled i, j, m, and n. Each element has its own local coordinate system, $X'Y'$, which lies in the plane of the element and is defined as follows:

1. X' is in the direction of a vector from node j to node k.

2. Y' is orthogonal to X' and lies in the plane of the 4 nodes.

6.1.1 Degrees of Freedom, and Nodal Forces

The degrees of freedom (Figure 6.1) of a diaphragm element are:

1. $V_{iX'}$, $V_{jX'}$, $V_{mX'}$, $V_{nX'} = X'$ translations at nodes i, j, m, and n of the element, respectively.

2. $V_{iY'}$, $V_{jY'}$, $V_{mY'}$, $V_{nY'}$ = Y' translations at nodes i, j, m, and n of the element, respectively.

Corresponding to these degrees of freedom are nodal forces:

1. $Q_{iX'}$, $Q_{jX'}$, $Q_{mX'}$, $Q_{nX'}$ = X' forces at nodes i, j, m, and n of the element, respectively.

2. $Q_{iY'}$, $Q_{jY'}$, $Q_{mY'}$, $Q_{nY'}$ = Y' forces at nodes i, j, m, and n of the element, respectively.

6.1.2 Internal Stresses in a Diaphragm Element

The internal stresses in the diaphragm element are:

1. $\sigma_{X'X'}$ = Normal stress in X' direction.

2. $\sigma_{Y'Y'}$ = Normal stress in Y' direction.

3. $\sigma_{X'Y'}$ = Shear stress in the element.

These can be transformed to principal tensile and compressive stresses, σ_1 and σ_2, respectively, using Mohr's circle.

6.2 Theory of the Diaphragm Element

The diaphragm element is a plane-stress element based on the Finite Element Method. The theory for this element can be found in standard textbooks on FEM [6, 70, 71]. In the finite element method, the displacement field within an element is defined in terms of prescribed functions of position called shape functions and the displacements at the discrete node points of the element. The element is formulated as a planar element in the element local coordinate system, $X'Y'Z'$, with 8 degrees of freedom. The stiffness matrix, $[K'_{dia}]_L$, and the stiffness force vector, $\{R'_{dia}\}_L$, are then transformed to the global translational DOF in the global directions X, Y, and Z, using a transformation matrix $[T_{dia}]$. These are then assembled into the appropriate locations of the global structure stiffness matrix and stiffness force vector, respectively.

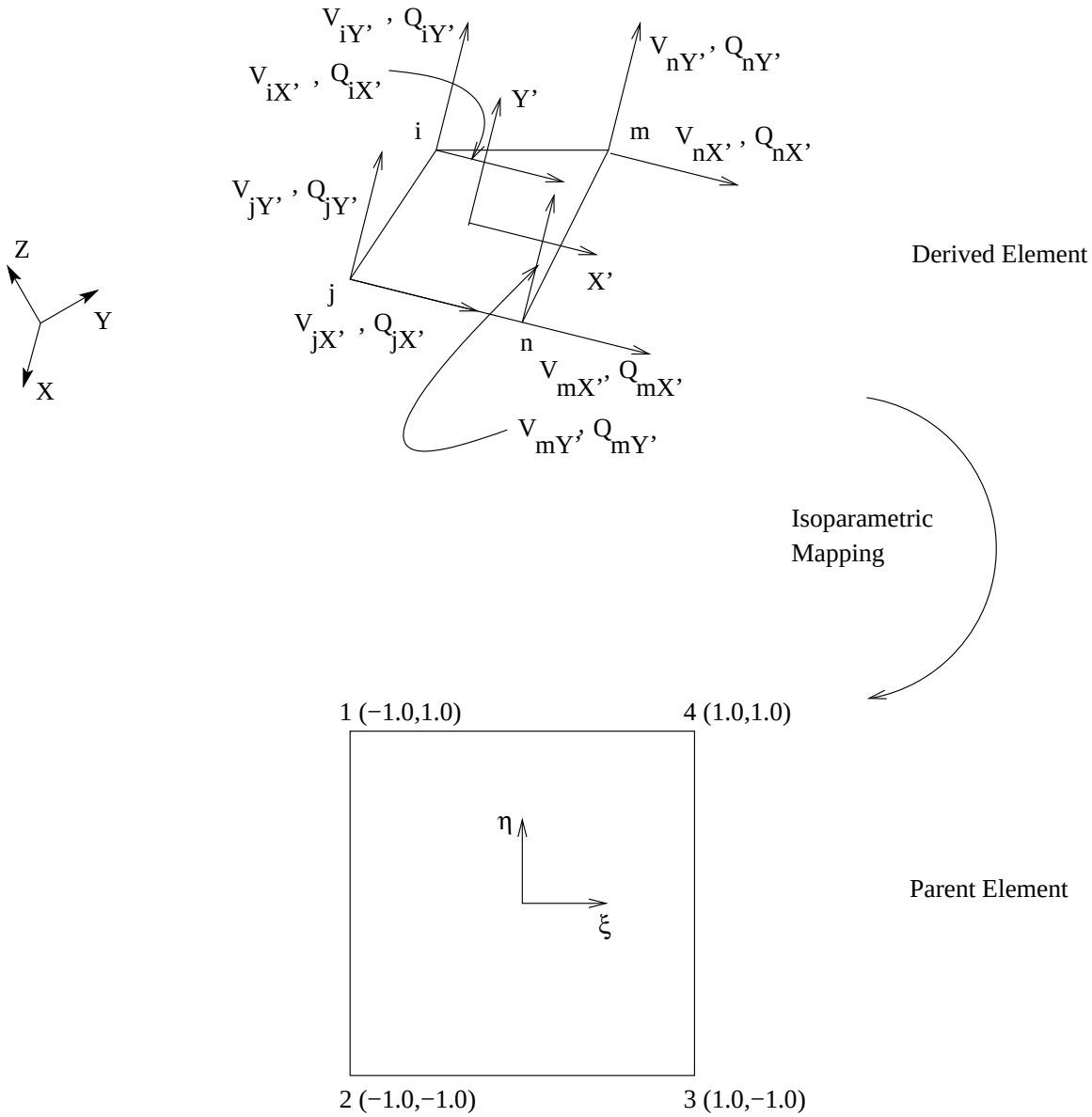

Figure 6.1: DOF of the Diaphragm Element Showing Nodal Translations and Rotations and Nodal Forces and the Isoparametric Mapping from a Square Parent Element

Based on the assumptions described previously, the element force-displacement relation can be written as

$$\left[K'_{dia}\right]_L \left\{U'_{dia}\right\}_L = \left\{R'_{dia}\right\}_L \tag{6.1}$$

where the nodal force and displacement vectors are

$$\langle R'_{dia}\rangle_L = \langle \; Q_{iX'} \quad Q_{iY'} \quad Q_{jX'} \quad Q_{jY'} \quad Q_{mX'} \quad Q_{mY'} \quad Q_{nX'} \quad Q_{nY'} \; \rangle \tag{6.2a}$$

$$\langle U'_{dia}\rangle_L = \langle \; V_{iX'} \quad V_{iY'} \quad V_{jX'} \quad V_{jY'} \quad V_{mX'} \quad V_{mY'} \quad V_{nX'} \quad V_{nY'} \; \rangle \tag{6.2b}$$

The stiffness matrix, $[K'_{dia}]_L$, is given by

$$\left[K'_{dia}\right]_L = t_{dia} \iint\limits_{A_{dia}} [B]^T [D] [B] \, dX' \, dY' \tag{6.3}$$

where t_{dia} and A_{dia} are the thickness and area of the element, $[B]$ is a matrix consisting of the derivatives of the shape functions, and $[D]$ is the material constitutive matrix and is given below for the case of plane-stress.

$$[D] = \frac{E}{1-\nu^2} \begin{bmatrix} 1 & \nu & 0 \\ \nu & 1 & 0 \\ 0 & 0 & \frac{1-\nu}{2} \end{bmatrix} \tag{6.4}$$

In order to compute the double integral in eq. 6.3 for a diaphragm element that can take the shape of a quadrilateral, the element will be derived (mapped) from a standard 4-noded parent element, whose displacement field is described with the same shape functions as the derived element (hence the parent and the derived elements are isoparametric). The parent element is a square element with its own coordinate system, $\xi - \eta$ (Figure 6.1). The coordinates of nodes 1, 2, 3, and 4 of the parent element in the $\xi - \eta$ coordinate system are (-1,1), (-1,-1), (1,-1), and (1,1), respectively. The Jacobian of this transformation is given by

$$[J] = \begin{bmatrix} \frac{\partial X'}{\partial \xi} & \frac{\partial Y'}{\partial \xi} \\ \frac{\partial X'}{\partial \eta} & \frac{\partial Y'}{\partial \eta} \end{bmatrix} \tag{6.5}$$

Making a change of variables ($X' \rightarrow \xi$ and $Y' \rightarrow \eta$) in the double integral,

$$\left[K'_{dia}\right]_L = t_{dia}\,|J| \int_{-1}^{1}\int_{-1}^{1} [B]^T\,[D]\,[B]\;d\xi\,d\eta \tag{6.6}$$

To solve this double integral, Gauss quadrature will be used.

$$\left[K'_{dia}\right]_L = t_{dia}\,|J| \sum_{q}^{N_q} [B]_q^T\,[D]\,[B]_q\,w_q \tag{6.7}$$

where N_q is the number of quadrature points, w_q is the weight at quadrature point q, and $[B]_q$ is the $[B]$ matrix evaluated at quadrature point q.

The shape functions, N_1, N_2, N_3, and N_4, and the $[B]$ matrix are

$$N_1 = \frac{1}{4}\,(1-\xi)\,(1+\eta) \tag{6.8}$$

$$N_2 = \frac{1}{4}\,(1-\xi)\,(1-\eta) \tag{6.9}$$

$$N_3 = \frac{1}{4}\,(1+\xi)\,(1-\eta) \tag{6.10}$$

$$N_4 = \frac{1}{4}\,(1+\xi)\,(1+\eta) \tag{6.11}$$

$$[B] = \begin{bmatrix} \frac{\partial N_i}{\partial \xi} & 0 & \frac{\partial N_j}{\partial \xi} & 0 & \frac{\partial N_m}{\partial \xi} & 0 & \frac{\partial N_n}{\partial \xi} & 0 \\ 0 & \frac{\partial N_i}{\partial \eta} & 0 & \frac{\partial N_j}{\partial \eta} & 0 & \frac{\partial N_m}{\partial \eta} & 0 & \frac{\partial N_n}{\partial \eta} \\ \frac{\partial N_i}{\partial \eta} & \frac{\partial N_i}{\partial \xi} & \frac{\partial N_j}{\partial \eta} & \frac{\partial N_j}{\partial \xi} & \frac{\partial N_m}{\partial \eta} & \frac{\partial N_m}{\partial \xi} & \frac{\partial N_n}{\partial \eta} & \frac{\partial N_n}{\partial \xi} \end{bmatrix} \tag{6.12}$$

At the beginning of the analysis the local stiffness matrix (8 DOF) for each diaphragm element is computed. Then it is transformed to the 12 translational global DOF associated with the 4 nodes of the element using the transformation matrix T_{dia}.

$$[K_{dia}]^{(12\times12)} = [T_{dia}]^{T(8\times12)}\,\left[K'_{dia}\right]_L^{(8\times8)}\,[T_{dia}]^{(8\times12)} \tag{6.13}$$

The transformation matrix, T_{dia}, is given by

$$[T_{dia}] = \begin{bmatrix} [C_{dia}]^{(2\times3)} & [0]^{(2\times3)} & [0]^{(2\times3)} & [0]^{(2\times3)} \\ [0]^{(2\times3)} & [C_{dia}]^{(2\times3)} & [0]^{(2\times3)} & [0]^{(2\times3)} \\ [0]^{(2\times3)} & [0]^{(2\times3)} & [C_{dia}]^{(2\times3)} & [0]^{(2\times3)} \\ [0]^{(2\times3)} & [0]^{(2\times3)} & [0]^{(2\times3)} & [C_{dia}]^{(2\times3)} \end{bmatrix} \tag{6.14}$$

where $[C_{dia}]$ is a matrix consisting of the direction cosines of the X' and Y' axes with respect to the X, Y, and Z axes.

$$[C_{dia}] = \begin{bmatrix} p'_x & p'_y & p'_z \\ q'_x & q'_y & q'_z \end{bmatrix} \tag{6.15}$$

The $[K_{dia}]$ matrices for all diaphragm elements are stored and used for the entire analysis. Unlike the stiffness matrices of the other type of elements, these are not updated in accordance with the assumptions described previously.

6.3 Updating Process

In global iteration l, $\{\Delta U\}$ is computed from eq. 2.9. The contribution of the stiffness forces in each diaphragm element, $\left\{R^l_{dia}\right\}$, to the $\left\{R^l\right\}$ vector is computed from

$$[K_{dia}]\left\{U^{tot}_{dia}\right\} = \left\{R^l_{dia}\right\} \tag{6.16}$$

where $\left\{U^{tot}_{dia}\right\}$ consists of the total displacements of the 4 nodes of the element in X, Y, and Z directions from the beginning of the analysis.

The internal stress vector, $\{\sigma'_{dia}\}$ (See Section 6.1.2), is given by

$$\left\{\sigma'_{dia}\right\} = [D]\,[B]\,[T_{dia}]\left\{U^{tot}_{dia}\right\} \tag{6.17}$$

where $[T_{dia}]$, $[B]$ and $[D]$ are the matrices computed and stored at the beginning of the analysis.

Chapter 7 Validation of 3-D Elastofiber and Panel Zone Elements

In this chapter, the ability of the FRAME3D program to model real structures is validated by way of three examples: (1) Elastic large deflection of a long cantilever beam, (2) Cyclic loading of a cantilever beam and (3) Comparison of the pushover analysis of a structural model of a 20-story building consisting of 3-D elastofiber and joint elements against one consisting of 2-D fully discretized 8-segment fiber elements [11, 29] and 2-D panel zone elements.

7.1 Large Deflection of an Elastic Cantilever Beam

The problem of the large deflection of an elastic cantilever beam with a transversely acting point load at the free end has been analyzed by [47]. It has probably been the "test problem" most commonly used in the examination of finite element procedures for geometrically nonlinear beam and frame analysis. The cantilever beam is illustrated in Figure 7.1. Also illustrated on that figure is the comparison of the numerical solution using elliptic integrals [47] and the finite element solution using the elastofiber element. The beam was discretized into 10 elastofiber elements. The load, P, was increased gradually from 0 to 155.74 kN (35 Kips) and the horizontal (u) and vertical (w) deflections of the free end were computed. These displacements are normalized by the length, L, and plotted against the load, P, normalized by $\frac{EI}{L^2}$. The close match indicates the ability of the elastofiber element to solve large deflection problems accurately.

7.2 Cyclic Loading of a Cantilever Beam

The second example consists of a $W21\times57$ cantilever beam (Figure 7.2) of length 2.44 m (96 in) subjected to a specified cyclic vertical displacement, w, at the free end as also shown in the figure. Two cases are considered - the first without any axial load for which experimental results are available [18, 19, 38] and the second with a constant axial compressive load of

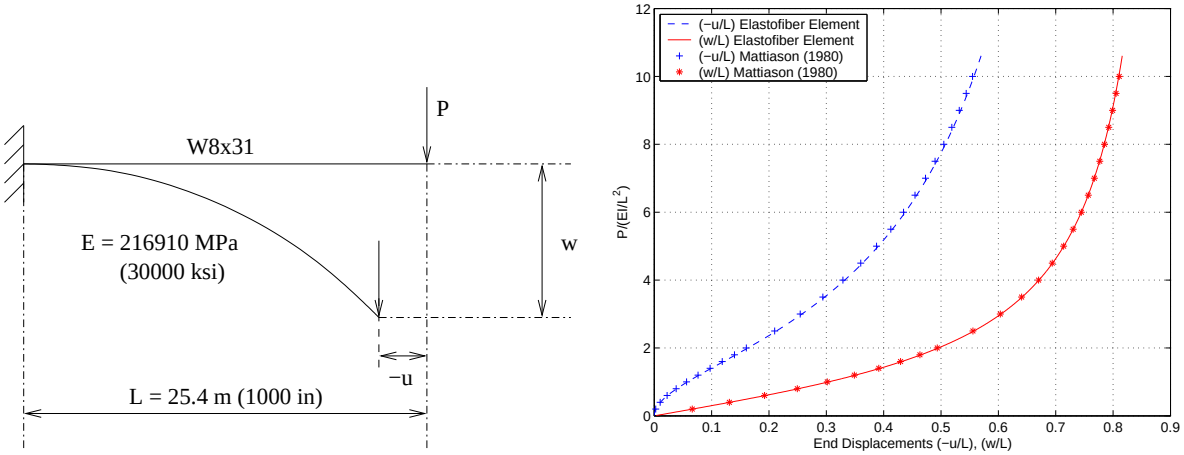

Figure 7.1: Large Deflection of a Cantilever Beam

$0.3P_y = 909.5\ kN$ $(204.4\ Kips)$. Measured values of σ_y of 281.4 MPa (40.8 ksi) and σ_u of 415.2 MPa (60.2 ksi) were employed in the analysis, along with assumed values of $E = 2 \times 10^5\ MPa$ (29000 ksi), $\epsilon_{sh} = 0.012$, $\epsilon_u = 0.160$, $\epsilon_r = 0.308$, $E_{sh} = 4000\ MPa$ (580 ksi), and $G = 8 \times 10^4\ MPa$ (11600 ksi). The experimental setup is given in Figure 7.2). Analysis was carried out using three elastofiber elements with fiber segment length of $11\%L$ for the two elements modeling the column and $22\%L$ for the element modeling the cantilever beam as well as using three 2-dimensional, 8-segment fiber elements [29] for comparison with the experimental data. Shown in Figure 7.3 are results for the first case: the history of the beam shear force Q resulting from the specified displacement, and a plot of Q versus the free-end vertical displacement w. Results for the two beam elements match quite well, and they also agree with the experimental data up to the time that local flange buckling decreases the moment capacity of the test specimen. Even before this time, the response is well into the nonlinear range.

In Figure 7.4, results using elastofiber elements are compared to those using 2-dimensional 8-segment elements for the case with axial load present. Included in the figure are plots of the history of Q, Q versus w, and Q versus the axial displacement u. The constant axial load causes a greater moment to be reached and an axial displacement which continues to increase as the beam cycles up and down. Agreement between the two elements for the Q history and Q versus w curves is very good, comparable to the case without axial load. Axial displacements predicted using the elastofiber elements are within 20% of those using

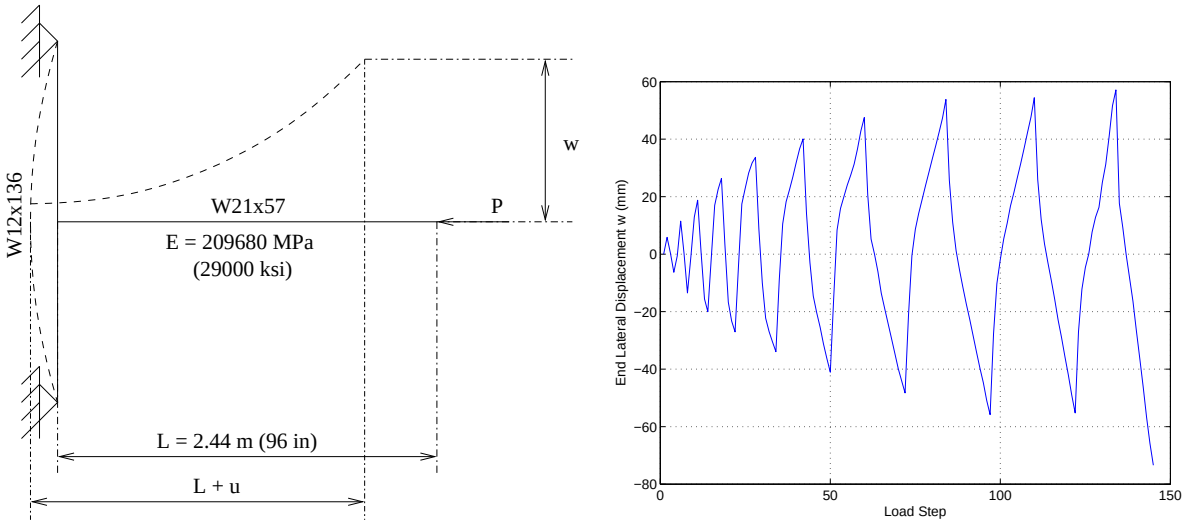

Figure 7.2: Cantilever Beam and Applied Displacement History, w, Used for Cyclic Loading Example

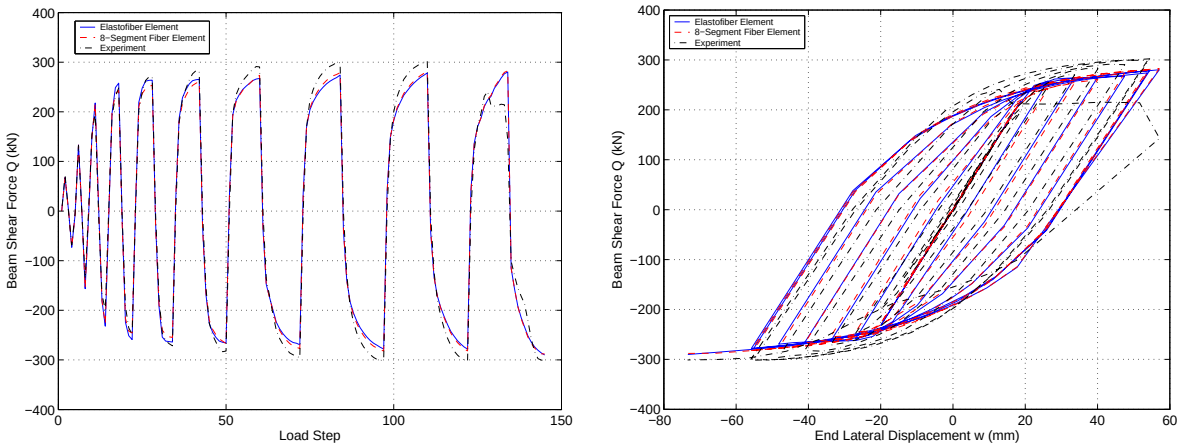

Figure 7.3: Cycled Cantilever Beam: Comparison of Experiment, Elastofiber Element and 8-Segment Fiber Element

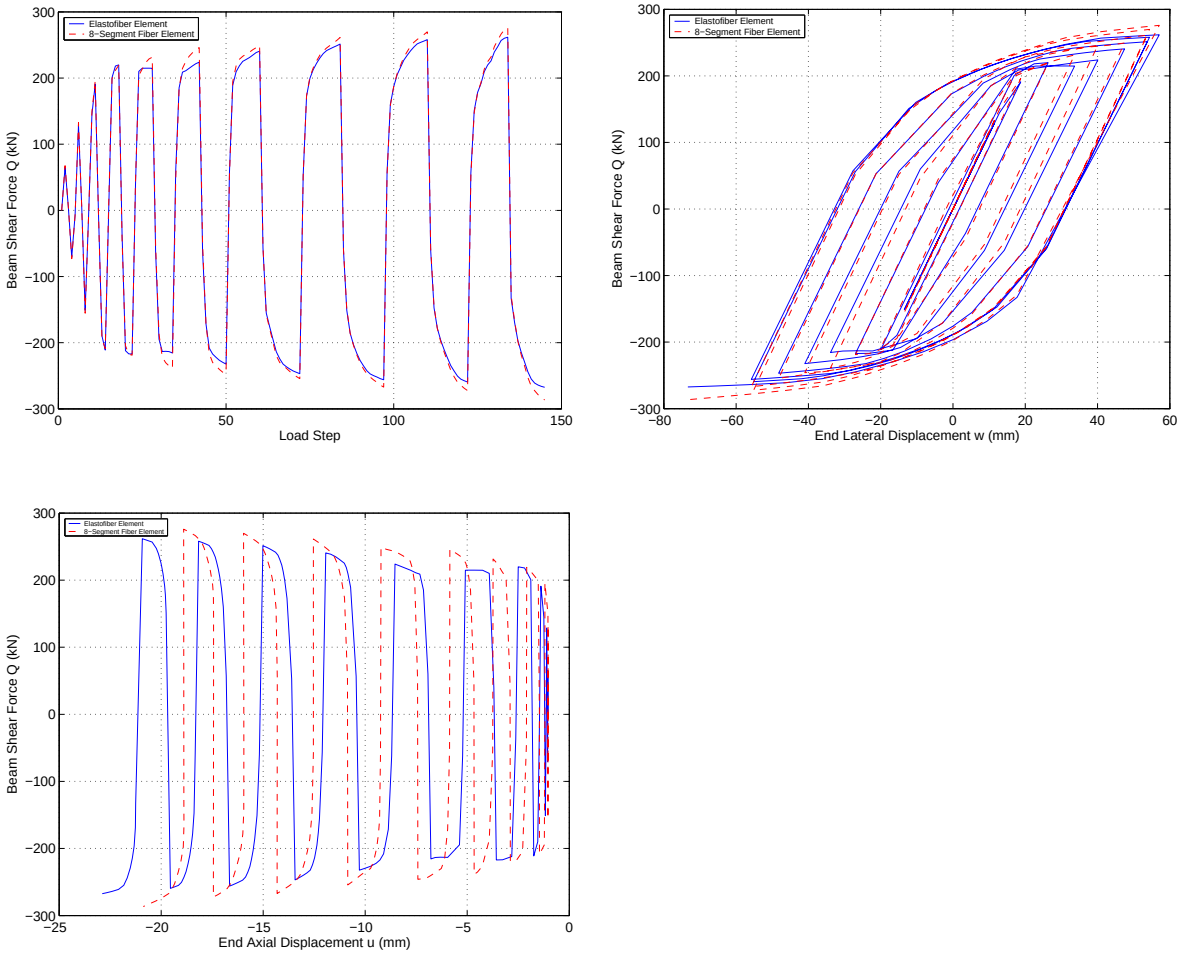

Figure 7.4: Cycled Cantilever Beam with Axial Load: Comparison of Elastofiber and 8-Segment Fiber Element

the more accurate 8-segment fiber elements.

7.3 Pushover Analysis of a 20-Story Building

In 1997, a study comparing buildings designed per UBC94 [32] and the Japanese code provisions at that time was done by Hall [28, 27]. As part of this study, a pushover analysis was performed on a 20-story building (referred to as U20 in that study) designed per the UBC94 code [32] in the X-direction in order to quantify the actual strength of the building. This building was originally designed by Tsai and Popov [66] and later used in earthquake collapse analysis of steel frames by Challa and Hall [12]. The fully discretized 2-D fiber element [11, 29] was used to model the beams and columns along with a two-dimensional

panel-zone element to model joints. This model is picked as the reference against which a FRAME3D model of the structure is compared.

The typical floor plan of this building is reproduced here for convenience (Figure 7.5). The sizes of the exterior moment-resisting frames and the interior gravity columns are given in Figures 7.6 and 7.7. ASTM-A36 steel is used for the beams and columns. The loading criteria are specified in Table 7.1. The steel material properties used in FRAME3D analysis are specified in Table 7.2. The remaining design parameters may be obtained from Reference [27]. The analysis of this model using the elements in that study is repeated here with three changes from the original Hall analysis - no residual stresses are included, no doubler plates are included in the panel zones, and slab contribution to beam strength and stiffness is not included (these changes lead to results that are slightly different from the original study).

To demonstrate the effectiveness of the elastofiber element under severe deformations (highly nonlinear), a 3-D model of this building (Figure 7.8) is analyzed using elastofiber beam-column elements and the 3-D panel-zone element to model joints. In this analysis, the building is subjected to a slow, ramped, horizontal ground acceleration that increases by $0.3\frac{g}{minute}$, and the building response is computed dynamically. This approach enables the modeling of the structure after the ultimate strength is reached and $P-\Delta$ effects cause the building to lose stability and it starts tipping over. As the building collapses, the inertial and damping forces proportional to the building acceleration and velocity become significant and a dynamic analysis is required to follow the structure response. The masses for the horizontal and vertical degrees of freedom are computed such that the total mass equals the total seismic mass with a distribution proportional to the UBC97 [33] static seismic design loads. The pushover analysis results are compared against those using the fully discretized 2-D fiber element in Figure 7.9. Note that since the structure is biaxially symmetric on plan, 3-D effects are negligible. Hence the results from the two analyses can be compared. Horizontal springs are included at the base of all columns in order to extract the reaction forces that are then used to compute the total base shear at any instant in time.

The good match in the base-shear and roof displacement plots between the analysis using elastofiber elements and the one using fully discretized fiber elements till imminent structural collapse demonstrates the robustness of the elastofiber elements. Since the elastofiber elements utilize far less computational time than the fiber elements, we have now con-

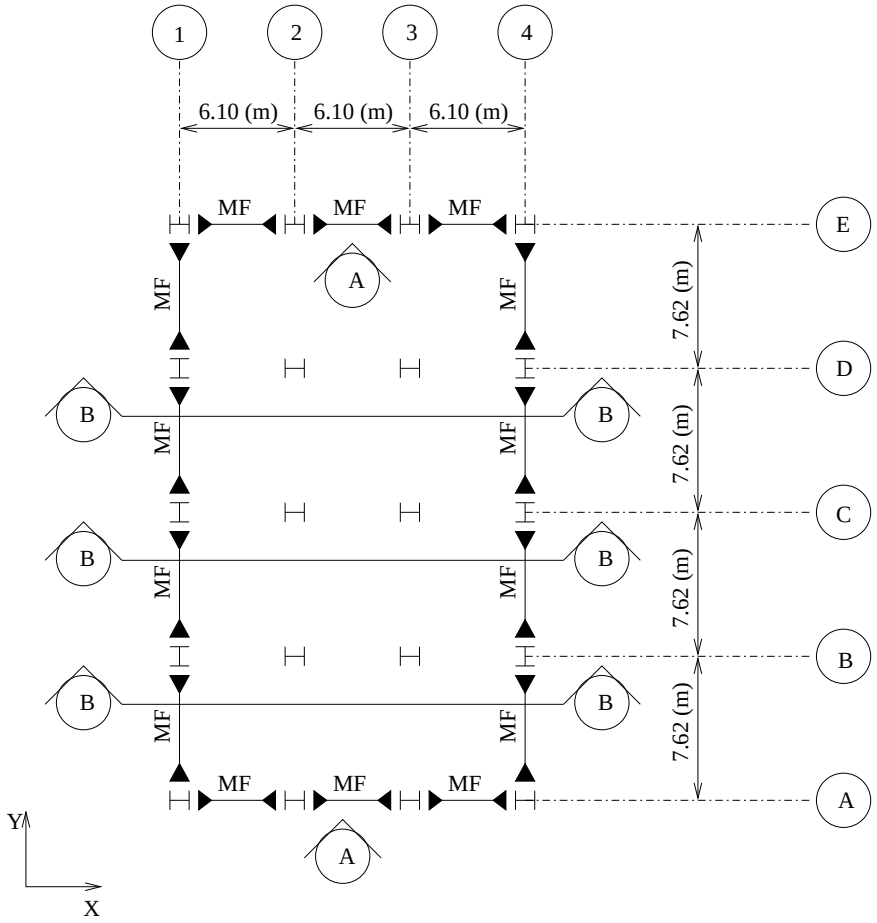

Figure 7.5: Typical Floor Plan of U20 Building

structed an efficient finite element that is accurate as well as fast enough to analyze large structures in three dimensions. In addition, this analysis also validates the correctness of the formulation of the 3-D joint element at least when its two-dimensional behavior is compared against the 2-D joint element described in References [11] and [29].

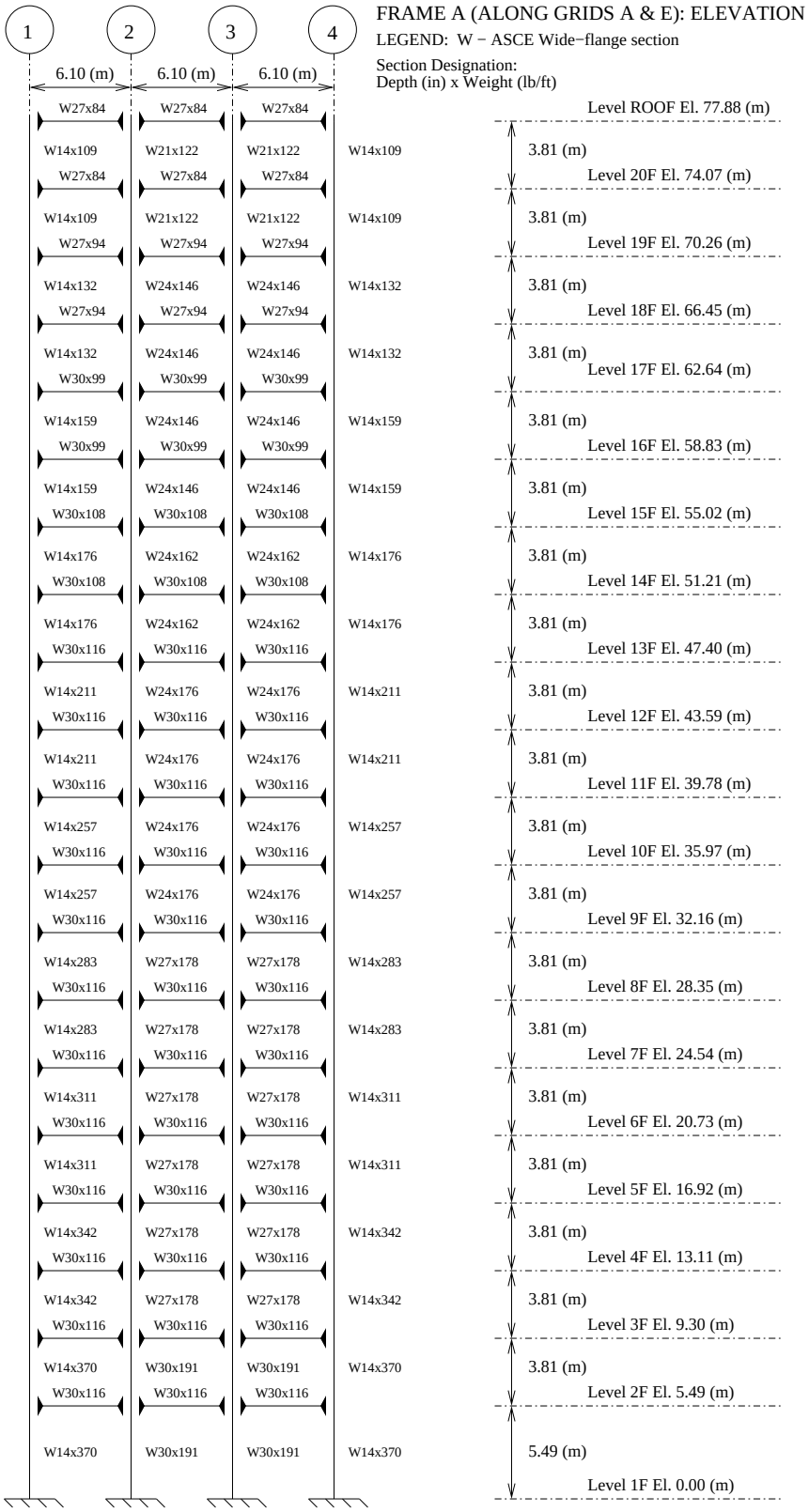

Figure 7.6: Elevation of Frame A: U20 Building

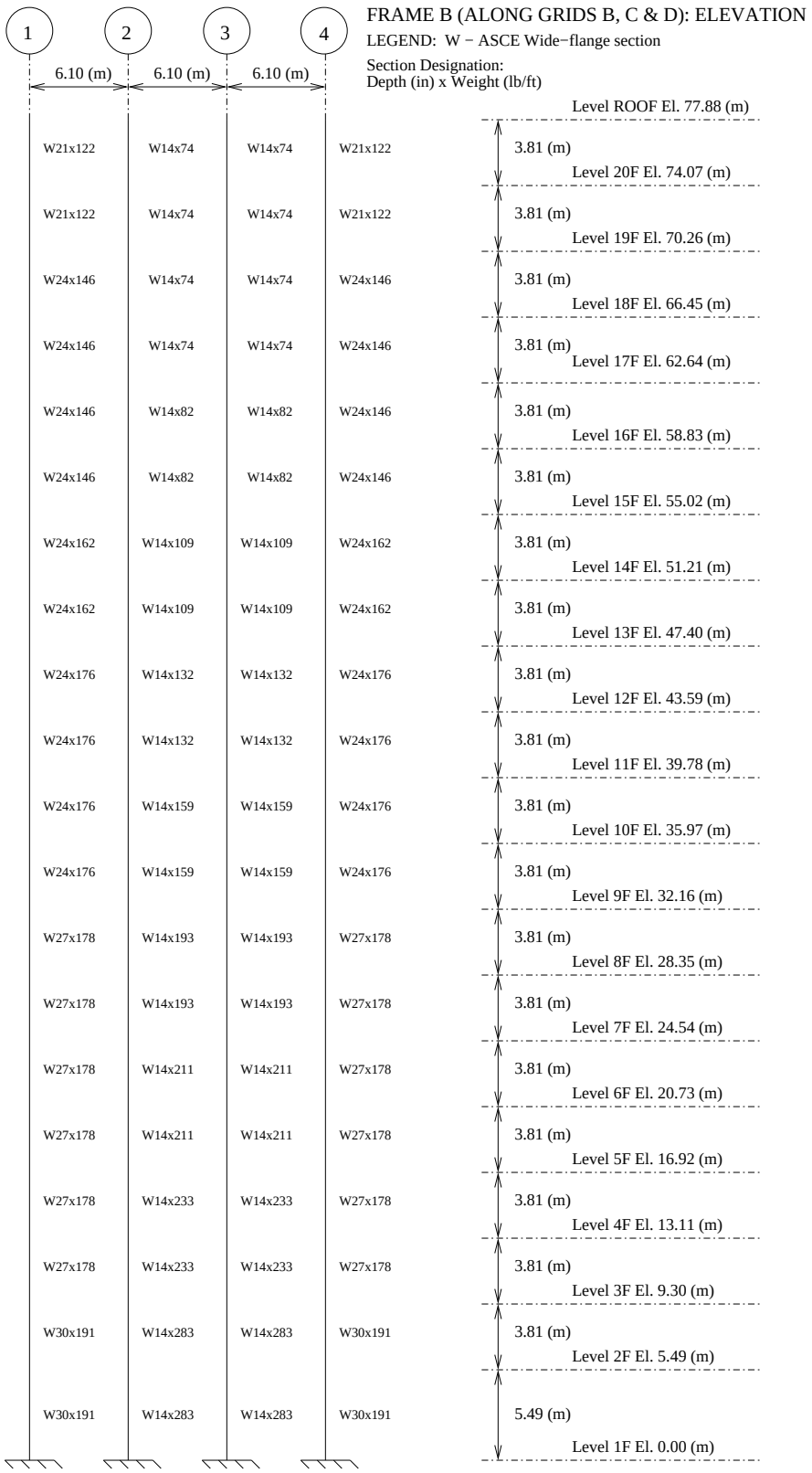

Figure 7.7: Elevation of Frame B: U20 Building

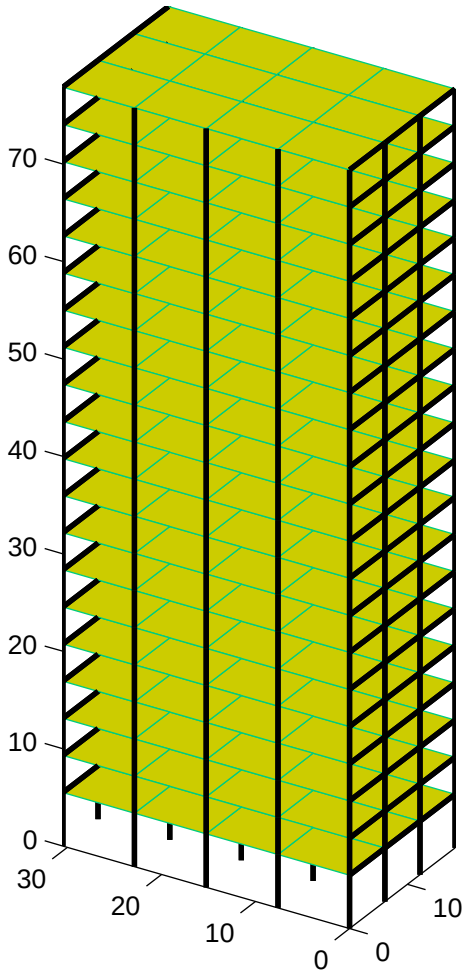

Figure 7.8: 3-D Model of U20 Building (using Elastofiber beam-column elements)

Table 7.1: Building U20 Loading Criteria (UBC94)

Occupancy	**Item #**	**Item**	**Load Type**	**Load ($\frac{kg}{m^2}$)**
Typical Floor	1	Dead Load	DL	464.00
	2	Live Load	LL	244.00 (30% used in analysis)
Roof	1	Dead Load	DL	391.00
	2	Live Load	LL	244.00 (30% used in analysis)
Cladding	1	Stone Cladding	DL	120.00

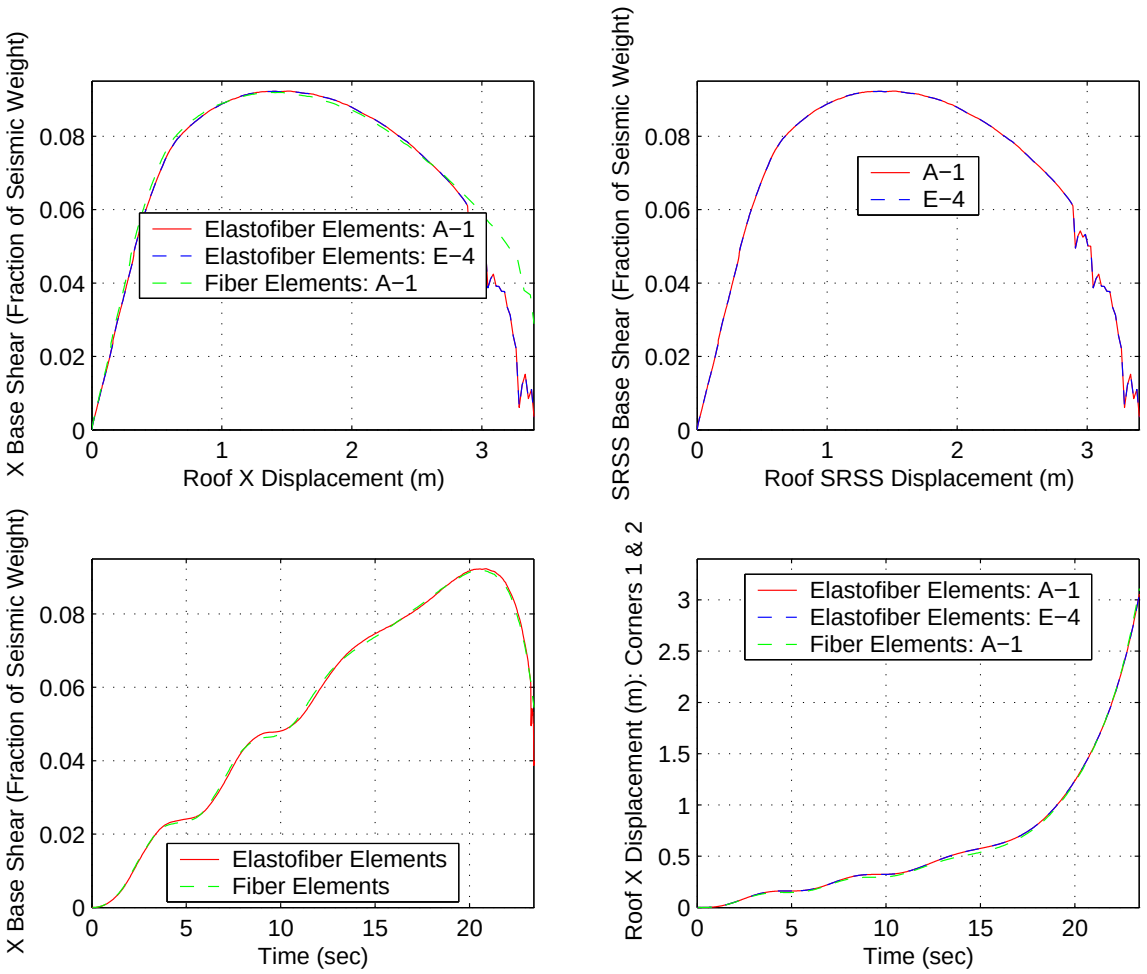

Figure 7.9: Pushover of U20 Building in the X-Direction (comparison of 3-D elastofiber element and 2-D fiber element models)

Table 7.2: Steel Material Properties Used in the Analysis

Usage	**Property**	$kgf-m$ **Units**	$Kip-in$ **Units**
Beam-Columns	Elastic Modulus, E	20388731162.41 $\frac{kg}{m^2}$	29000.00 ksi
	Shear Modulus, G	8155492464.96 $\frac{kg}{m^2}$	11600.00 ksi
	Yield Stress, σ_y	29528507.20 $\frac{kg}{m^2}$	42.00 ksi
	Yield Strain, ϵ_y	0.00145	0.00145
	Slope at Initiation of Strain Hardening, E_s, for Elastofiber Elements	407774623.25 $\frac{kg}{m^2}$	580.00 ksi
	Ultimate Stress, σ_u, for Elastofiber Elements	35152984.76 $\frac{kg}{m^2}$	50.00 ksi
	Strain at Initiation of Strain Hardening, ϵ_y, for Elastofiber Elements	0.0120	0.0120
	Ultimate Strain, ϵ_u, for Elastofiber Elements	0.1600	0.1600
Panel Zones	Shear Modulus, G	8155492464.96 $\frac{kg}{m^2}$	11600.00 ksi
	Shear Yield Stress, τ_y	16873432.69 $\frac{kg}{m^2}$	24.00 ksi

Chapter 8 Building Design

8.1 Introduction

Buildings are designed per building code regulations. These regulations provide minimum standards for use in building design to maintain public safety in the extreme ground shaking likely to occur during an earthquake. The Uniform Building Code (UBC97, [33]) is the standard code of practice adopted in the state of California and many Western states of the U.S., and is generally considered as one of the premier codes in the world for the design of earthquake-resistant construction. The code requirements are intended primarily to safeguard against major failures and loss of life, not to limit damage, maintain function, or provide for easy repair. The purpose of these recommended design procedures is to provide buildings that are *expected* to meet this "life safety objective" [15].

To achieve this objective, the code specifies a linear elastic design procedure to resist lateral forces from an earthquake. The specified design forces are based on the assumption that a significant amount of inelastic behavior may take place in the structure when subjected to significant ground shaking. As a result, these design forces and related elastic deformations are much lower than those that would be required if the structure were to remain elastic. For a given structural system, the design requirements outlined in the code are intended to provide for the necessary inelastic behavior. Representations of the element force levels and deformations in the fully responding inelastic structure are given as appropriate multiples of the values that would be determined by linear elastic analysis of the structure using the design forces specified in the code.

Structures designed in conformance with the code requirements should, in general, be able to:

1. Resist a minor level of earthquake ground motion without damage.

2. Resist a moderate level of earthquake ground motion without structural damage, but possibly experience some non-structural damage.

3. Resist a major level of earthquake ground motion - of an intensity equal to the

strongest earthquake, either experienced or forecast, for the building site - without collapse, but possibly with some structural as well as non-structural damage.

It is expected that structural damage, even in a major design level earthquake, will be limited to a repairable level for most structures that meet the code requirements. In some instances, damage may not be economically repairable. The level of damage depends upon a number of factors, including the intensity and duration of ground shaking, structure configuration, type of lateral force resisting system, materials used in the construction, and construction workmanship.

Unfortunately, conformance to the code requirements does not constitute any kind of guarantee or assurance that significant structural damage will not occur in the event of design level earthquake ground motion. To fulfill the life safety objective of the code, there are requirements that provide for structural stability in the event of extreme structural deformations and requirements that protect the vertical load-carrying system from fracture or buckling at these extreme states. While damage to the primary structural system may be either negligible or significant, repairable or virtually irreparable, it is reasonable to expect that a well-planned and constructed structure will not collapse in a major earthquake. The protection of life is reasonably provided, but not with complete assurance.

The code requirements provide minimum design criteria in specific categories stated in broad general terms. It is the responsibility of the engineer to interpret and adapt these basic principles to each structure using experience and good judgment. Because of the great variability and complexity of individual structures, it is impractical and beyond the scope of the code to go into the detail necessary to specifically cover all of the possible variations in structure response. The dynamic characteristics of the structure, behavior of structural elements, the variability in ground motion, and the types of soil all affect building response. Thus, both latitude and responsibility for the exercise of judgment are given to the engineer.

Where damage control is desired, the design must not only provide sufficient strength to resist the specified seismic forces, but also provide the proper stiffness or rigidity. Control of damage is very complex. Some structural elements are sensitive to acceleration, making floor acceleration the key design consideration, while others are sensitive to inter-story deformations, making drift the key design consideration. Damage to non-structural elements may be minimized by proper limitation of deformations, by careful attention to detail, and

by providing proper clearances for exterior cladding, glazing, partitions, and wall panels. It must be recognized that major earthquake ground motion can cause inter-story deformations several times larger than those calculated with the seismic design forces given in the code.

In addition to designing the structure for earthquake forces, the structure needs to be designed for wind forces. Wind and seismic forces are fundamentally different. Wind force results from aerodynamic pressures applied to an exterior surface of a structure, whereas seismic forces result from the inertial response of a structure to accelerations and displacements from earthquake ground shaking. Seismic ground shaking is cyclic in nature and the structure can be allowed to yield and traverse well into the inelastic regime without danger of collapse. However, since wind forces are unidirectional, if the structure is allowed to yield, then, as the wind keeps blowing, the structure will continue to deform rapidly in the down-wind direction and will ultimately lose stability and collapse. Thus, buildings are designed to remain elastic under design wind storms. Since the structure is allowed to deform inelastically during an earthquake, the structural lateral force resisting system must conform to special detailing requirements in order to accommodate these large deformations. These detailing requirements are intended to allow the lateral force resisting system to deform inelastically without catastrophic failure and to provide the necessary inelastic energy absorption and toughness necessary to resist actual seismic forces, which, as mentioned before, far exceed the specified seismic design forces.

8.2 Key Aspects of Code Design

8.2.1 Basis for Design

The procedures and the limitations for the design of structures are determined considering seismic zoning, site characteristics, occupancy, configuration, structural system and height. Structures are required to be designed with adequate strength to withstand the lateral displacements induced by the Design Basis Ground Motion, considering the inelastic response of the structure and the inherent redundancy, over-strength and ductility of the lateral-force-resisting system. The minimum design strength is based on the Design Seismic Forces determined in accordance with a static lateral force procedure.

8.2.2 Seismic Zones and Seismic Zone Coefficient, Z

Every region in the US is categorized under one of four seismic zones based on the effective peak ground acceleration (EPA) projected for the region in question. The EPA is the acceleration that a perfectly rigid structure, having a period of 0 *seconds*, would effectively experience if subjected to the ground motion. The EPA, when presented in units of "g", corresponds in value to the seismic zone coefficient, Z, and takes into account geographical variations in the expected levels of earthquake ground shaking. Evidence for such variations can be found both in the historical record of earthquake effects, and also in the distribution of the major fault systems considered likely to produce significant earthquakes. The seismic zone map for California is based primarily on historical seismicity and was derived from the Applied Technology Council (ATC) zoning maps [4], which are based on probabilistic maps by Algermissien and Perkins [2]. These probabilistic maps estimated peak horizontal acceleration on rock that has a 10% probability of being exceeded in a 50-year period. This level of ground motion roughly corresponds to that which would be exceeded roughly once every 500 years. The seismic zone map presents effective peak acceleration values (or Z values) in units of "g". The Z values for Zones 3 and 4 are 0.3 and 0.4, respectively indicating that the EPA for seismic zones 3 and 4 is expected to be 0.3g and 0.4g, respectively. The Z coefficient directly enters the design base shear formulation.

8.2.3 Near-Source Factors and Seismic Source Types

Ground motion in Zone 4 near major faults requires special attention, particularly for structures with periods greater than about 0.3 *seconds*. In 1978, the authors of ATC 3-06 Commentary [4] acknowledged the possibility of near-fault ground motion higher than that corresponding to $Z = 0.4$. True to their judgment, horizontal components of ground acceleration during the 1994 Northridge earthquake recorded approximately 5 km from the fault rupture have instrumental peak ground acceleration (PGA) values over 0.7 g, and the average acceleration response at a period of 1.0 *second* is typically over 0.9 g. In contrast, the UBC spectrum anchored to an EPA of 0.4 g, corresponding to Zone 4, has 1-*second* acceleration response of 0.4 g for rock sites and about 0.6 g for soil sites. Response decreases with distance and at about a distance of 10 km from the fault rupture, values are approximately consistent with the UBC spectrum (anchored to an EPA of 0.4 g).

Similar features were observed during the Kobe earthquake of 1995. Ground shaking in Kobe was intense, but of relatively short duration and typical of ground motion recorded close to fault rupture. Soil effects contributed to the intense shaking in certain areas, but the primary cause of strong ground shaking felt throughout Kobe was the proximity of the city to fault rupture. 90% of the buildings that collapsed or were severely damaged were located within 5 km of the fault rupture. Ground motion records indicate that the near-source factor is best described by distinguishing between the short-period (acceleration) and long-period (velocity) domains since the effect is substantially greater at longer periods. This distinction is made through the use of two near-source factors, N_a and N_v. The values for the N_a factor are based on the ratio of 0.3 *second* response predicted by the median estimates of ground motion attenuation functions to the 0.3 *second* response of the UBC spectrum for stiff soil anchored at an EPA of $0.4g$. The N_v factor is derived similarly for the 1.0 *second* period. The near-source factors represent typical horizontal ground shaking and are not intended to account for higher levels of shaking that occur due to the inherent variability of ground motion. Similarly, they are not intended to bound ground motion in the strongest possible (e.g., fault normal) direction of shaking.

Seismic source types are classified based on the maximum magnitude, M, and the slip rate, SR, on the fault. Type A sources are faults that have a moment magnitude potential of $M >= 7.0$ and a slip rate SR equal to greater than 5 $\frac{mm}{year}$. These types of faults are considered to be active and capable of producing large magnitude events. Most segments of the San Andreas fault are classified as a Type A fault. Type C sources are faults that have a moment magnitude potential of M less than 6.5 and a slip rate SR less than or equal to 2 $\frac{mm}{year}$. These types of faults are considered to be sufficiently inactive and not capable of producing large magnitude events such that potential near-source ground shaking effects can be ignored. Most faults outside of California are of Type C. Type B sources are all faults that are not either Type A or Type C, and include most of the faults in California. Magnitude and slip rate information for faults may be obtained from the USGS or the California Geological Survey (CGS). For example, a recent compilation of data on all faults in the Western US has been made by the USGS as a part of Project 97, a national seismic hazard mapping project [25].

8.2.4 Site Categorization

Local geology and soil characteristics influence the ground motions at a site. The significance of this influence varies from essentially nil to very large. Data from the 1985 Mexico City earthquake and the 1989 Loma Prieta earthquake show that the motions can be significantly amplified for soft soil sites and moderate accelerations. The largest amplification typically occurs at the natural period of the soft soil deposit. For example, in the Mexico City shaking, the rock acceleration was amplified four times by the soft clay deposit at T=0 *seconds* while the spectral amplitude at approximately T=2 *seconds* indicated an amplification of 15-20 times the rock acceleration. Data from the Loma Prieta earthquake also indicate an amplification at long-period spectral amplitudes of 3-6 times, and the largest amplification occurred at the natural period of the soil deposit. However, at stronger levels of ground shaking, the earthquake motions are attenuated as they propagate through a soft soil layer as the strength of the soil is exceeded and the soil behaves in a highly nonlinear manner.

As the ground motion propagates from rock through the overlying soil medium, the rock motion is amplified or attenuated as discussed above. Non-homogeneous layered sites with a soft layer between rock and the stiffer soils complicate the problem. The parameters necessary to characterize the site and determine analytically the amplification or attenuation and frequency modification are the thickness of the soft and stiff soil layers, the shear wave velocities of the rock and soil layers, the soil/rock impedance ratio (which is a function of the shear wave velocity), the layering and properties of the soil layers including modulus and damping properties. The impedance contrast must consider the whole soil profile and thus both the soft and stiff soil layers play a role in determining the damping and the amplification (or attenuation). The maximum amplification generally occurs at or close to the natural frequency of the soil deposit, but may occur at the natural frequency of the soft layer, the natural frequency of the whole soil deposit, or some other frequency. In all cases, the shear wave velocity of the rock and the soil deposit has a dominant role. Hence, the code characterizes the site primarily by the shear wave velocity. In shallow or moderate soil depth sites, where the soil depth is less than 30m, the entire soil deposit is important to the overall response. In deep soil (greater than 30m) sites having thick (35m) soft-medium stiff clays, or highly plastic or organic clays and peats of any thickness, cannot be characterized in this manner and must be evaluated on a site-specific basis. Similarly,

sites having liquefiable soils, e.g., loose sands, or highly sensitive soils that may lose strength during an earthquake, e.g., bay muds, must be evaluated on a site-specific basis.

The code characterizes soil profiles into six categories S_A through S_F. S_A corresponds to hard rock sites (with shear wave velocity, $V_s > 1500\frac{m}{sec}$), S_B to rock sites ($760 < V_s < 1500\frac{m}{sec}$), S_C to very dense soil and soft rock sites ($360 < V_s < 760\frac{m}{sec}$), S_D to stiff soil sites ($180 < V_s < 360\frac{m}{sec}$), S_E to soft soil sites ($V_s < 180\frac{m}{sec}$), and S_F to soils requiring site-specific evaluation. Soil profile type, S_A (hard rock) is appropriate for classification of sites in the eastern United States only.

8.2.5 Seismic Coefficients, C_a and C_v

Seismic coefficients, C_a and C_v, are used to construct the design response spectrum, C_a corresponds to the EPA and C_v corresponds to the value of the acceleration response at a structure period of 1.0 *second*. They are also used to determine the static design base shear. These coefficients depend on the soil profile type, the seismic zone factor, and the near-source factors, N_a and N_v. For soil profile type, S_B, C_a and C_v are equivalent to the seismic zone factor, Z, except in the case of seismic zone 4 where they are equivalent to ZN_a and ZN_v, respectively. For soil types S_C through S_E, C_a and C_v are amplified while for soil type, S_A, they are attenuated when compared to soil type, S_B. Seismic coefficients are not provided for soil profile type, S_F, and must be determined by a site-specific hazard analysis.

8.2.6 Occupancy Categories

For purposes of earthquake-resistant and wind-resistant design, structures are categorized into one of five occupancy categories. Each category is assigned a seismic importance factor, I, and a wind importance factor, I_w, in addition to special requirements such as independent design review and an appropriate program of testing and inspection, and construction observation. The I and I_w factors are used to scale up the design base shear. The five occupancy categories include essential facilities, hazardous facilities, special occupancy structures, standard occupancy structures and miscellaneous structures. All the structures studied in this work fall under Category IV (standard occupancy structures with $I = 1.0$ and $I_w = 1.0$).

8.2.7 Configuration Requirements (Regular and Irregular Structures)

Irregularities in load paths and in structural configuration are major contributors to structural damage and failure due to strong earthquake ground motion [65]. Vertical and plan irregularities can result in loads and deformations significantly different from those assumed by equivalent static design procedures prescribed by the code. Those distributions of mass, stiffness, or strength that result in earthquake forces and/or deformations over the height of the structure, which are significantly different from linearly varying distributions, are designated as vertical irregularities. Those plan or diaphragm characteristics that result in significant amounts of torsional response, diaphragm deformations, or diaphragm stress concentrations are designated as plan irregularities. The lack of a direct path for force transfer is referred to as an irregularity in force transfer, and an example would be where a lateral force resisting element is offset or discontinuous. This condition can cause a concentration of inelastic demand, and can occur even when no irregularities in plan or elevation exist. In such cases, the Commentary to the code [15] suggests that the irregularities or discontinuities and resulting concentrations of inelastic behavior must either be corrected or strengthened, or the R value (Section 8.2.8) must be decreased to reflect the limited and concentrated amount of inelastic behavior in the structural system. For structures with plan or vertical irregularities, the code imposes a penalty of about 11% on the design base shear. In addition, the code requires the use of dynamic analysis for irregular structures taller than 19.8 m with the design forces scaled down by scaling the dynamic base shear from the analysis results to 100% of the static design base shear (Section 8.2.11). If a dynamic analysis procedure is adopted for a regular structure, the dynamic base shear is allowed to be scaled down to 90% of the static design base shear. Thus, this constitutes a penalty of about 11% on the design of irregular structures.

The code classifies vertical structural irregularities into 5 types:

1. Stiffness irregularity (soft story) – A soft story is one in which the lateral stiffness is less than 70% of that in the story above or less than 80% of the average stiffness of the three stories above.

2. Weight (mass) irregularity – Mass irregularity is considered to exist where the effective mass of any story is more than 150% of the effective mass of an adjacent story. A roof that is lighter than the floor below need not be considered.

3. Vertical geometric irregularity – Vertical geometric irregularity is considered to exist where the horizontal dimension of the lateral-force-resisting system in any story is more than 130% of that in an adjacent story.

4. In-plane discontinuity in vertical lateral-force-resisting element – An in-plane offset of the lateral-load-resisting elements greater than the length of these elements.

5. Discontinuity in capacity (weak story) – A weak story is one in which the story strength is less than 80% of that in the story above. The story strength is the total strength of all seismic-resisting elements sharing the story shear for the direction under consideration.

The code classifies plan structural irregularities into 5 types as well:

1. Torsional irregularity to be considered when diaphragms are not flexible – Torsional irregularity is considered to exist when the maximum story drift, computed including accidental torsion, at one end of the structure transverse to an axis is more than 1.2 times the average of the story drifts of the two ends of the structure.

2. Reentrant corners – Plan configurations of a structure and its lateral-force-resisting system contain reentrant corners, where both projections of the structure beyond a reentrant corner are greater than 15% of the plan dimension of the structure in the given direction.

3. Diaphragm discontinuity – Diaphragms with abrupt discontinuities or variations in stiffness, including those having cutout or open areas greater than 50% of the gross enclosed area of the diaphragm, or changes in effective diaphragm stiffness of more than 50% from one story to the next.

4. Out-of-plane offsets – Discontinuities in a lateral force path, such as out-of-plane offsets of the vertical elements.

5. Non-parallel systems – The vertical lateral-load-resisting elements are not parallel to or symmetric about the major orthogonal axes of the lateral-force-resisting system.

8.2.8 Structural Systems and R-factor

Structural systems used in buildings and other structures to resist gravity, wind, and earthquake loads are classified into one of six categories: bearing wall system, building frame system, moment-resisting frame system, dual system, cantilever column system, and "undefined" structural system. The R-factor defines the numerical coefficient representative of the inherent over-strength and global ductility capacity of lateral force resisting systems. The code provides R-factors for each of the 6 structural systems. For special moment resisting frame systems (Section 8.2.20), the ductility factor is 3.4 and the over-strength factor is 2.5, giving an R-factor of 8.5. As explained before, structures are designed based on the assumption that a significant amount of inelastic behavior may be exhibited by the structure when subjected to significant ground shaking. As a result, the design forces are much lower than those that would be required if the structure were to remain elastic. The factor by which the design base shear differs from the actual elastic base shear during the design earthquake is in fact the R-factor. This will be apparent in the code formulae for the design base shear (Section 8.2.11).

8.2.9 Redundancy/Reliability Factor, ρ

Redundancy is a characteristic of structures in which multiple paths of resistance to loads are provided. It has long been recognized as a desirable attribute, especially in cases where loads are likely to exceed service levels, as with earthquakes. The code design philosophy assumes inelastic action of structures during a major seismic event. In order to prevent collapse of structures undergoing inelastic deformations, it is essential to limit strength degradation. An important part of limiting the strength degradation is to provide multiple paths for the lateral loads. As portions of the structure yield, increases in loading may be distributed to other resisting elements and the energy absorbing inelastic action is distributed through the structure. Redundancy also decreases the probability that flaws in construction or design will have catastrophic results. Non-redundant structures are those for which failure of a small number of lateral force resisting components would result in the formation of a collapse mechanism for the structure. The Redundancy/Reliability factor, ρ, is intended to encourage engineers to design redundant structures. If the engineer is not able to achieve a redundant design, an increase in the seismic design loads are required in an attempt to

reduce the magnitude of the inelastic response and therefore the ductility demand. The ρ-factor is dependent upon the number of lateral load resisting elements provided, the plan area of the building and the initial distribution of lateral load in the resisting elements. In SI units, it is given by:

$$\rho = 2 - \frac{6.1}{r_{max}\sqrt{A_B}} \tag{8.1}$$

where r_{max} is given by the maximum element-story-shear ratio and A_B is the ground floor area in square meters. For a given direction of loading, the element-story-shear ratio is the ratio of the design story shear in the most heavily loaded single element divided by the total design story shear. For any given story level, i, the element-story-shear ratio is denoted as r_i. The maximum element-story-shear ratio, r_{max}, is defined as the largest of the element-story-shear ratios, r_i, which occurs in any of the story levels at or below the two-thirds height level of the building. For moment frames, r_i is taken as the maximum of the sum of the shears in any two adjacent columns in a moment frame bay divided by the story shear. For columns common to two bays with moment-resisting connections on opposite sides at Level i in the direction under consideration, 70% of the shear in that column is to be used in the column shear summation. For special moment resisting frames (SMRF, Section 8.2.20), ρ cannot exceed 1.25. The number of bays of SMRFs are required to be increased to reduce r, such that ρ is less than or equal to 1.25. When calculating drifts, ρ can be taken to be 1.00.

8.2.10 Load Combinations (Allowable Stress Design) and Earthquake loads

Allowable stress design is used for the design of all the buildings in this work. The code requires structures to be designed for the most critical effects resulting from the following load combinations. When using these load combinations, a one-third increase is permitted in allowable stresses for all combinations including W or E.

$$D + L + L_r \tag{8.2a}$$

$$D + L + \left(W or \frac{E}{1.4}\right) \tag{8.2b}$$

where D stands for the dead load, L stands for the live load, L_r stands for the roof live load, W stands for the wind load, and E stands for the earthquake load. The code allows the design live load to be reduced on any structural member supporting more than 13.94 m^2 of floor area, in accordance with the following formula:

$$R^L = r(A - 13.94) \tag{8.3a}$$

where R^L is the reduction in percentage and r is the rate of reduction equal to 0.08% for floors. The reduction should not exceed 40% for members receiving load from one level only, 60% for other members or R^L as defined by the following formula:

$$R^L_{max} = 23.1\left(1 + \frac{D}{L}\right) \tag{8.3b}$$

In addition, in Seismic Zones 3 and 4, columns in frames are required to have the strength to resist the axial loads resulting from the following load combinations:

$$1.0P_{DL} + 0.7P_{LL} + \Omega_0 P_E \qquad \text{in axial compression} \tag{8.4a}$$

$$0.85P_{DL} \pm \Omega_0 P_E \qquad \text{in axial tension} \tag{8.4b}$$

where P_{DL}, P_{LL}, and P_E are the axial loads in the column from the dead, live and earthquake loads, respectively, and Ω_0 is the Seismic Force Amplification Factor, which is required to account for structural over-strength.

These axial load combinations need not exceed either the maximum force that can be transferred to the column, by elements of the structure, or the limit as determined by the overturning uplift which the foundation is capable of resisting. They need not apply to columns in moment-resisting frames that comply with the strong column-weak beam criteria where the axial stress, f_a, is less than or equal to $0.3F_y$ for the load combinations in eqs. 8.2, where F_y is the yield stress.

The code requires structures to be designed for ground motion producing structural response and seismic forces in any horizontal direction. The earthquake load, E, is given by:

$$E = \rho E_h + E_v \tag{8.5}$$

where ρ is the reliability/redundancy factor, E_h is the earthquake load due to the design base shear, V, described in the next section and E_v is the load effect resulting from the vertical component of the earthquake ground motion and may be taken to be zero for Allowable Stress Design.

8.2.11 Design Base Shear - Static Force Procedure

The design base shear, V, provides the level of seismic design forces for a given structural system. The resulting force level is based on the assumption that the structure will undergo several cycles of inelastic deformation during major earthquake ground motion, and, therefore, the level is related to the type of structural system and its estimated ability to sustain these deformations and dissipate energy without collapse. The total design base shear, V, in a given direction is given by

$$V = \frac{C_v I}{RT} W \tag{8.6a}$$

It need not exceed

$$V_{max} = \frac{2.5 C_a I}{R} W \tag{8.6b}$$

It cannot be less than

$$V = 0.11 C_a I W \tag{8.6c}$$

In addition, for Seismic Zone 4, it cannot be less than

$$V = \frac{0.8 Z N_v I}{R} W \tag{8.6d}$$

In the above equations, C_a and C_v are the seismic coefficients, I is the structure Importance factor, R is the R-factor, T is the structure fundamental period computed as described below, Z is the Seismic Zone coefficient, N_a and N_v are the near-source factors, and W is the seismic weight of the building which includes only the dead weight of the structure (self-weight, interior partitions, floor fill, equipment, and cladding) and does not include the live load of the structure. The force level defined above is used not only for the static

lateral force procedure, but also as the lower bound for the dynamic lateral force procedure.

The code provides an approximate method to compute the structure fundamental period based on its type and height, $h_n(m)$:

$$T = C_t h_n^{\frac{3}{4}} \tag{8.7}$$

The value of C_t depends on the structure type and the code specifies a value of 0.0853 for steel moment-resisting frames. The period may also be computed using a full dynamic modal analysis of the structure. However, for the purpose of computation of the base shear in a structure located in Seismic Zone 4, the code requires limiting the value of T from this analysis to 130% of the T computed using the formula above.

8.2.12 Vertical Distribution of Shear - Static Force Procedure

The total design base shear, V, is distributed over the height of the structure in accordance with the following formulae:

$$V = F_t + \sum_{i=1}^{n} F_i \tag{8.8a}$$

$$F_i = \frac{(V - F_t)\, w_i h_i}{\sum_{j=1}^{n} w_j h_j} \tag{8.8b}$$

where n is the number of stories, F_i is the force at the i^{th} story applied over the area of the building in accordance with the mass distribution at that story, w_i is the seismic weight of the i^{th} story, h_i is the height of the i^{th} story, and F_t is a concentrated force at the top of the structure given by

$$F_t = 0.07TV \tag{8.8c}$$

where T is the period used in the computation of the base shear, V. F_t need not exceed 25% of V and may be considered as zero where T is 0.7 *second* or less.

This vertical distribution of the base shear is based on a linear mode shape of the structure, with the force at the top, F_t, accounting for higher modal effects.

8.2.13 Horizontal Distribution of Shear - Static Force Procedure

The design story shear, V_i, in any story is the sum of the forces, F_t and F_i above that story. The code requires V_i to be distributed to the various elements of the vertical lateral-force-resisting system in proportion to their rigidities, considering the rigidity of the floor diaphragm.

Where diaphragms are not flexible, the mass at each level is required to be displaced from the calculated center of mass in each direction a distance equal to 5% of the building dimension at that level perpendicular to the direction of the force under consideration. The effect of this accidental eccentricity of the center of mass on the story shear distribution needs to be considered.

The accidental eccentricity of the center of mass results in horizontal torsion leading to increased shears. Thus, the torsional design moment at a given story is the moment resulting from eccentricities between applied design lateral forces at levels above that story and the vertical-resisting elements in that story plus the accidental torsion resulting from the accidental eccentricity of the center of mass.

In the case of torsionally irregular buildings, the accidental torsion at each level is required to be increased by an Amplification factor, A_i, determined from the following formula:

$$A_i = \left[\frac{\delta^i_{max}}{1.2\delta^i_{avg}}\right]^2 \tag{8.9}$$

where δ^i_{avg} is the average of the displacements at the extreme points of the structure at the i^{th} level and δ^i_{max} is the maximum displacement at the i^{th} level.

8.2.14 Seismic Drift Ratio

Inter-story drift ratio is defined as the difference in the displacements of the top and bottom of story normalized by the story height. Drift is associated with damage to non-structural components including the exterior facade of the building, dry wall interior, and windows, in addition to being associated with occupant comfort. The drift, Δ_s, corresponding to the design seismic forces is determined at all critical locations of the structure using an elastic analysis of the lateral-force-resisting system. The calculated drift should include translational and torsional deflections. The code extrapolates the Maximum Inelastic Response

Drift, Δ_M, of the structure caused by the Design Basis Ground Motion from the elastic drift ratio, Δ_s, as follows:

$$\Delta_M = 0.7R\Delta_s \tag{8.10}$$

The code requires that the calculated story drift, Δ_M, shall not exceed 0.025 for structures having a fundamental period of less than 0.7 *seconds* and 0.02 for structures with greater periods.

The design lateral forces used to determine the calculated drift are based solely on formulae 8.6a and 8.6b. The code allows the limitations of formulae 8.6c and 8.6d to be disregarded for drift computation. In addition, for the purpose of computing this design base shear for drift computation, there is no restriction on the period computed from a full dynamic modal analysis to 130% of the period computed using the code formula, 8.7.

8.2.15 $P-\Delta$ Effects

When the lateral forces from an earthquake displace a building laterally, the gravity loads acting vertically downward cause an overturning moment on the structure about its base, in addition to the overturning moment caused by the lateral forces themselves. This second order effect which can lead to global instability of the building is termed the $P-\Delta$ effect. The code requires that the resulting member forces and moments and the story drifts induced by $P-\Delta$ effects be considered in the evaluation of overall structural frame stability.

8.2.16 Dynamic Analysis

The distribution of seismic forces on a number of structures is often considerably different from those that would be given by the static lateral force procedure described in previous sections. Such differences can occur in buildings with severe setbacks, buildings with irregular/unusual configuration, and buildings with significant variation in drift from one story to another. In such instances, a dynamic analysis can bring out the effects of the structure's dynamic characteristics on the distribution of lateral forces along its height, the effects of the structure's higher modes of response that could contribute substantially to individual story shears and deformations and the effects of the existence of normal modes with significant components of torsional motion that can lead to increased demand on the

structure's lateral force resisting system.

Implementation of dynamic lateral force procedures involves:

1. Identification of appropriate ground motion representations for use as input to the analysis.

2. Development of an elastic mathematical model of the structure that represents its important geometric, stiffness, inertial and damping characteristics.

3. Computation of the model's dynamic response to the seismic input motion, using response spectrum or time-history methods and an established structural analysis computer program, such as ETABS.

4. Careful interpretation and application of the results of the analysis.

The requirements of the horizontal distribution of shear (including accidental eccentricity and torsion), seismic drift ratio and $P-\Delta$ effects described previously are applicable to the Dynamic Analysis procedure as well.

8.2.17 Response Spectrum Method - Dynamic Analysis Procedures

A response spectrum of an earthquake is the plot of the time period of a single degree of freedom (SDOF) system with varying natural period, versus the peak acceleration experienced by the mass during the earthquake. In the elastic range, a building response can be decomposed into a number of modes, each mode corresponding to a period and a deformed shape (mode shape).

During an earthquake, if a building responds purely in one of its modes, then its peak acceleration during the earthquake will be the same as the acceleration value on the response spectrum corresponding to a SDOF system period equal to the building modal period.

A design response spectrum is usually an idealized average spectrum derived from the spectra of past earthquakes in a region. The UBC97 [33] design response spectrum is shown in Figure 8.1.

The Response Spectrum Method requires dynamic analysis of a mathematical model of the building to establish modal frequencies and mode shapes. Using standard mathematical procedures [14] and a design response spectrum corresponding to the damping in the building, the modal frequencies and shapes are used to establish spectral demands. The

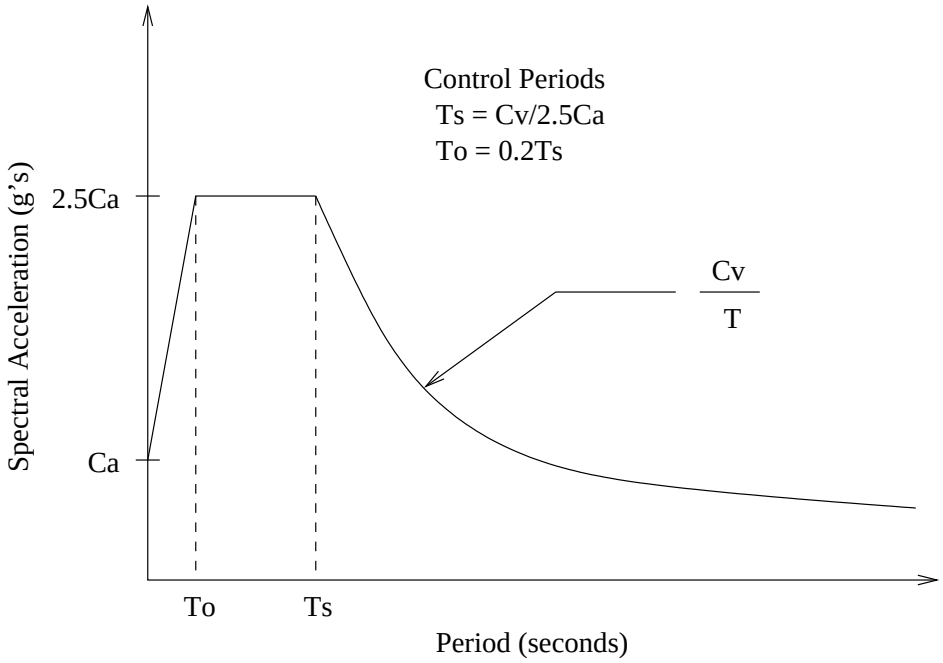

Figure 8.1: 1997 Uniform Building Code [33] Response Spectrum

spectral demands are then used to calculate member forces, displacements, story forces, story shears, and base reactions for each mode of response considered. These forces and displacements represent the maximum responses of the structure when it is vibrating in that mode. However, because these maximum modal responses will not occur at the same time during the earthquake ground motion, it is necessary to combine these maximum modal responses in a statistical manner in order to estimate the maximum composite response of the structure. Such procedures are typically based on an appropriate combination of the maximum individual modal responses, and should account for possible interaction between any closely spaced modal responses that may exist. A simple and accurate modal combination approach that satisfies this requirement is the Complete Quadratic Combination (CQC) method [67]. This approach is based on random vibration concepts and assumes that the duration of the earthquake shaking is long when compared to the fundamental period of the structure and the design response spectrum exhibits slowly varying amplitudes over a wide range of periods that include the dominant modes of the structure. In the CQC combination, all the significant modes of the structure need to be included. The code requires that at least 90% of the participating mass of the structure be included in the calculation of dynamic response for each principal horizontal direction.

8.2.18 Reduction of Elastic Response Parameters for Design

The earthquake force levels corresponding to the static analysis procedure described previously reflect the influence of structural period, ductility, and damping for various structural systems. Because it is difficult to reflect these influences on a consistent basis for design using the dynamic procedure, the code allows the Elastic Response Parameters (which are the results of the response spectrum analysis that is based on an unreduced spectrum and a linear elastic structural model) to be reduced for purposes of design with the limitation that in no case shall the Elastic Response Parameters be reduced such that the corresponding design base shear is less than the Elastic Response Base Shear divided by the value of R. This scaling is used to make dynamic analysis consistent with the results of the static design approach. For regular structures, the response parameters may be reduced to 80% (if site-specific spectrum is used in the dynamic analysis) or 90% (if the generic UBC97 code spectrum (Figure 8.1) is used in the dynamic analysis) of the corresponding parameters determined using the static lateral force procedure. For irregular structures, the scaling down could be up to 100% of the responses from the static lateral force procedure.

8.2.19 Orthogonal Effects

In the case of certain irregular buildings (Plan Types 1 and 5), all building components in Seismic Zones 2, 3 and 4 are required by the code to be designed to resist the effects of the seismic forces considering the effects of earthquake forces acting in a direction other than the principal directions. In addition, the corner columns of all regular and irregular buildings that are part of two or more intersecting lateral-force-resisting systems are required to be designed considering orthogonal effects. The requirement that orthogonal effects be considered may be satisfied by designing such elements for 100% of the prescribed design seismic forces in one direction plus 30% of the prescribed design seismic forces in the perpendicular direction. Alternatively, the effects of the two orthogonal directions may be combined on a square root of the sum of the squares (SRSS) basis.

8.2.20 Special Moment Resisting Frames (SMRF)

The basic philosophy of the design of SMRFs is simply that non-ductile failure modes should be prevented, and that inelastic deformations should be concentrated in regions that

have a capacity for ductile behavior. Thus, column buckling and connection failures are to be avoided. At the same time, frame stiffness and therefore, frame stability, must be maintained. The code thus specifies some special requirements for the design of SMRFs intended to minimize the possibility of premature failure of non-ductile elements.

Ductile behavior and inelastic energy absorption are allowed to occur in three elements of a moment frame - the beams and the columns in which flexural yielding may occur and the joint panel zones in which shear yielding may occur. Within limits, inelastic behavior of any or a combination of these three elements is permitted. Some of the special requirements for steel SMRF design are as follows:

1. The girder-to-columns connection is required to be adequate to develop the lesser of the strength of the girder in flexure and the moment corresponding to development of the panel zone shear strength.

2. Connection configurations utilizing welds or high-strength bolts are required to demonstrate the ability to sustain inelastic rotation and develop the required strength by approved cyclic test results or calculations, considering the effect of steel over-strength and strain hardening.

3. The panel zone of the joint is required to be capable of resisting the shear induced by beam bending moments due to gravity loads plus 1.85 times the prescribed seismic forces, but the shear strength need not exceed that required to develop $0.8 \sum M_s$ of the girders framing into the column flanges at the joint. To satisfy this requirement, doubler plates can be added to strengthen the panel zone. However, the thickness of the panel zone (not including doubler plates) is required to be not less than $\frac{1}{45}$ of the average of the panel zone depth and width.

4. Beam flange width-thickness ratio, $\frac{b_f}{2t_f}$, cannot exceed $\frac{52}{\sqrt{F_y}}$ in addition to satisfying compactness requirements. The outside wall width-thickness ratio of rectangular tubes used for columns cannot exceed $\frac{110}{\sqrt{F_y}}$, unless otherwise stiffened. F_y is the yield stress in ksi units.

5. Most engineers believe that it is better to have flexural hinges form in the girders than in columns [58]. If flexural hinges form in the columns, additional concerns include concentration of inelastic behavior in the columns of a story leading to a weak story

condition and excessive inelastic deformations leading to column failure under the possible high axial loads that could occur due to maximum expected ground motion. The strong column-weak beam concept is addressed with the introduction of two simple formulae that require the potential for yielding at a beam-column joint to be located in the beam or the joint panel zone.

8.2.21 Wind Design

The forces from wind that a building can be subjected to, depend on the terrain of the region in which the building is located, the configuration of neighboring structures, the basic wind speed, height of the building, plan configuration of the building, and the extent of structure enclosure (extent of openings in the structure). The basic wind speed is defined as the fastest-mile wind speed associated with an annual probability of 0.02 measured at a point 10 m above the ground for an area having exposure category C. The code classifies terrains into three exposure categories, B, C and D. Exposure B has terrain with buildings, forest or surface irregularities, covering at least 20% of the ground level area extending 1 mile or more from the site. Exposure C has terrain that is flat and generally open, extending $\frac{1}{2}$ mile or more from the site in any full quadrant. Exposure D represents the most severe exposure in areas with basic wind speeds of 80 miles per hour (mph) or greater and has terrain that is flat and unobstructed facing large bodies of water over 1 mile or more in width relative to any quadrant of the building site. Exposure D extends inland from the shoreline $\frac{1}{4}$ mile or 10 times the building height whichever is greater.

The design wind pressures for buildings are determined for any height in accordance with the following formula:

$$P = C_e C_q q_s I_w \tag{8.11}$$

where C_e is a combined height, exposure, and gust factor coefficient, C_q is a pressure coefficient for the structure, q_s is the wind stagnation pressure at the standard height of 10 m and I_w is the building importance factor similar to the importance factor used in seismic design. The wind stagnation pressure is a function of the basic wind speed. The C_e coefficient is a function of the height and the exposure category. The pressure coefficient, C_q, varies based on the structural component being designed, for example, primary frames

and systems, chimneys, tanks, etc. It is different for the windward and leeward faces of the building.

The primary frames or load-resisting system of every structure are required by the code to be designed for the pressure, P, using a Normal Force Method or a Projected Area Method. For tall buildings, the Normal Force Method is to be applied. In this method, the wind pressures are assumed to act simultaneously normal to all exterior surfaces. For pressures on roofs and leeward walls, C_e is required to be evaluated at the mean roof height. Since C_q, q_s and I_w are constants over the height of the building, it is the coefficient, C_e, that dictates the profile of the wind load on the structure. On the windward face, this profile is quadratic with zero at the street level and maximum at the roof level. On the leeward face, since a constant C_e evaluated at the mean roof height is to be used, the load profile is uniform as well. This is based on the fact that suction pressures are usually uniform.

The structural elements are designed for the forces resulting from these wind pressures in conjunction with the gravity loads per the load combinations set forth in eqs. 8.2. Unlike seismic design where the structure is allowed and expected to behave in an inelastic manner, in wind design, the code requires the structure to remain elastic at all times (See Section 8.1 for explanation). While the code specifies a limit on the inelastic drift experienced by the building during the design basis earthquake, it does not specify any limit on the wind drifts. As explained previously, the primary objective of the code is life-safety. In the case of earthquakes, where the building is expected to behave in an inelastic manner, the drift ratio limit of 0.02 serves to define the threshold of deformation beyond which the $P-\Delta$ effects could become significant enough to threaten the stability of the structure. The code-writers believe that this level of drift is extremely large and represents possibly the physical drift capacity of many structural systems. Thus, in this case, the code perceives drift as being a life-safety issue. However, in the case of wind design, where the structure is designed to remain elastic, the actual drifts would be small enough that there would be no risk to the stability of the structure. Thus, wind drift is considered as a serviceability issue, not a life-safety issue and so the code does not impose any limits on the wind drifts. However, it is standard practice among engineers to restrict the elastic wind drift ratio to 0.0025. Non-structural components such as the facade and partition walls are then designed to accommodate this movement during design wind-storms.

8.3 Selection Criteria, Geometry and Design Criteria for the 6 Buildings

8.3.1 Building Selection Criteria: Philosophy and Motivation

In the event of a large earthquake, strength and stiffness are important, but perhaps the most important issue is that of ductility. Ductility is a measure of the ability of the structure to go through multiple inelastic cycles until collapse. Different measures of ductility have been used in the past. These include ductility ratios, plastic rotations, and energy dissipation (calculated as the area enclosed by the hysteretic loops). Whatever measure is chosen to judge ductility, an estimate for actual ductility demands on structural components and connections in actual earthquakes is needed. Unfortunately, this information is rather limited. Since strong ground motion from near-source earthquakes has been recorded only in recent times, data on ductility demands in such cases is even more limited. One means for estimating plastic rotation demands in beams, columns, and joints is to conduct inelastic dynamic time-history analyses of structural models using past earthquake records. To gather such data for irregular buildings requires modeling the buildings in 3 dimensions and for this reason, seismic demand data for irregular structures is almost non-existent. One of the primary motivations of this study is to gather such data for a carefully selected suite of irregular buildings by analyzing structural models of these buildings for strong ground motion from a suite of near-source earthquake records.

Further motivation for this study comes from the fact that codes have been changing constantly and there has not been a great amount of data to calibrate and verify a number of design requirements in the code. The question of how a building designed today per the current code requirements would perform in the event of a major earthquake on a nearby fault can be answered at least in part by performing these types of analyses using similar earthquake records. Performance of these buildings can be compared against ad-hoc performance criteria developed by the National Earthquake Hazard Reduction Program (NEHRP) of the Federal Emergency Management Agency (FEMA). Unfortunately, these criteria may not be necessarily accurate since they have been developed from past experience with limited data from large earthquakes, nevertheless, they provide a basis for such performance evaluation.

As described previously, there are a number of potential plan and vertical irregularities that could occur in structures. Of particular interest are buildings with two types of irregularity that occur quite frequently - a reentrant corner irregularity and a plan torsion irregularity wherein the centers of mass and stiffness do not coincide. To keep the study focussed, it was decided to limit this study to buildings with these two types of irregularity. There are a number of 20-story steel moment frame buildings in Los Angeles and other seismically active regions of the US close to major faults. It was further decided to limit the study to this class of buildings. In addition, the fundamental period of all the buildings was strictly constrained to lie between 3.2 and 3.5 *seconds* during the design process, so that it would be reasonable to compare the performance of the buildings against each other. Also, the conclusions drawn from this data set collected for this narrow range of buildings would be reliable.

Four distinct buildings, numbered 1 through 4, were planned and designed, two of them with reentrant corners (Buildings 1 and 2), and the other two with plan torsion irregularity (Buildings 3 and 4). The design of buildings 2 and 3 were governed to some extent by the wind drift ratio limit of 0.0025 accepted in practice and since this is not a limit imposed by the code, it was decided to design alternate versions of these two buildings (Buildings 2A and 3A) disregarding this limit on wind drift ratios. In the case of buildings 2A and 3A, the fundamental natural period has been allowed to go well beyond the 3.2-3.5 *second* range. These buildings are compared solely against their parent versions, 2 and 3. The following sections describe the geometry and design criteria for the 6 buildings, and the design process using a commercial program, ETABS. The next chapter describes the analyses of these buildings subjected to strong ground motion from near-source earthquakes.

8.3.2 Description of the Buildings

The first building is a 19-story residential tower (70.8m tall) designed using the 1997 Uniform Building Code [33]. It has a typical floor area of 1810m^2 and a perimeter of 248m. It is dumb-bell shaped in plan (Figure 8.2) with two elevator cores to serve the two spines of the building. The key irregular feature in this building is the presence of reentrant corners. The primary lateral system consists of moment frames. The presence of setbacks precludes multiple-bay moment frames along the perimeter. However, there are two 3-bay moment frames (along grids C and D) in the building long direction (X) and one 5-bay moment

frame (along grid 4) in the building short direction (Y). The floor is made of concrete slab on metal-deck ($5\frac{1}{2}''$ thick with $1''$ topping) supported by steel beams framing into interior gravity columns and exterior moment frame columns. All interior beams are pinned at both ends and their sizes are not relevant to this study. The building is covered with stone cladding (facade). Partitions are made up of dry wall supported by metal studs. The floor is carpeted. Typical story height is $3.6m$ with variations at the lobby level and the mechanical stories. The isometric view of the building is illustrated in Figure 8.3. The dark lines represent the moment-frame beams and columns. The gray rectangles represent the floor slab.

Building 2 is a 19-story office tower ($78.3m$ tall) with a typical floor area of $1024m^2$ and a perimeter of $160m$. It is L-shaped in plan (Figure 8.4) with one elevator core serving both wings of the building. The key irregular feature in this building is the presence of a reentrant corner. The primary lateral system consists of a perimeter moment frame. In L-shaped buildings such as this, the wings, with fewer moment frame bays, being less stiff have a tendency to flap during strong shaking. As shown in Figure 8.6, out-of-phase shaking of the wings leads to stress concentration at the reentrant corner and potential failure in a tearing mode. In-phase shaking of the wings leads to twisting in the building and potential failure in a torsional mode. There is a great need for data on the behavior of such buildings during strong ground shaking and this work is an effort in that direction. The floor is made of concrete slab on metal deck ($5\frac{1}{2}''$ thick total) supported by steel beams and girders framing into interior gravity columns and exterior moment frame columns. The building is covered with stone cladding (facade). Partitions are made up of dry wall supported by metal studs. The floor is carpeted. Typical story height is $4.0m$ with variations at the lobby level and the mechanical stories. Building 2A has the same plan and elevation as building 2, except that it has been designed without any imposed wind drift limit. The isometric view of the two buildings is illustrated in Figure 8.5.

Building 3 is a 19-story office tower ($78.3m$ tall) with a typical floor area of $696m^2$ and a perimeter of $106m$. It is rectangular shaped in plan (Figure 8.7) with the elevators and stairs located along one face of the building. The ocean-view on the building face along grid 5 precludes the use of deep beams that would restrict the view on that face. Thus, the moment frame on that face had to be shifted to lie along grid 2. This creates a large open layout with maximum headroom for the offices between grids 2 & 5, and A & D with

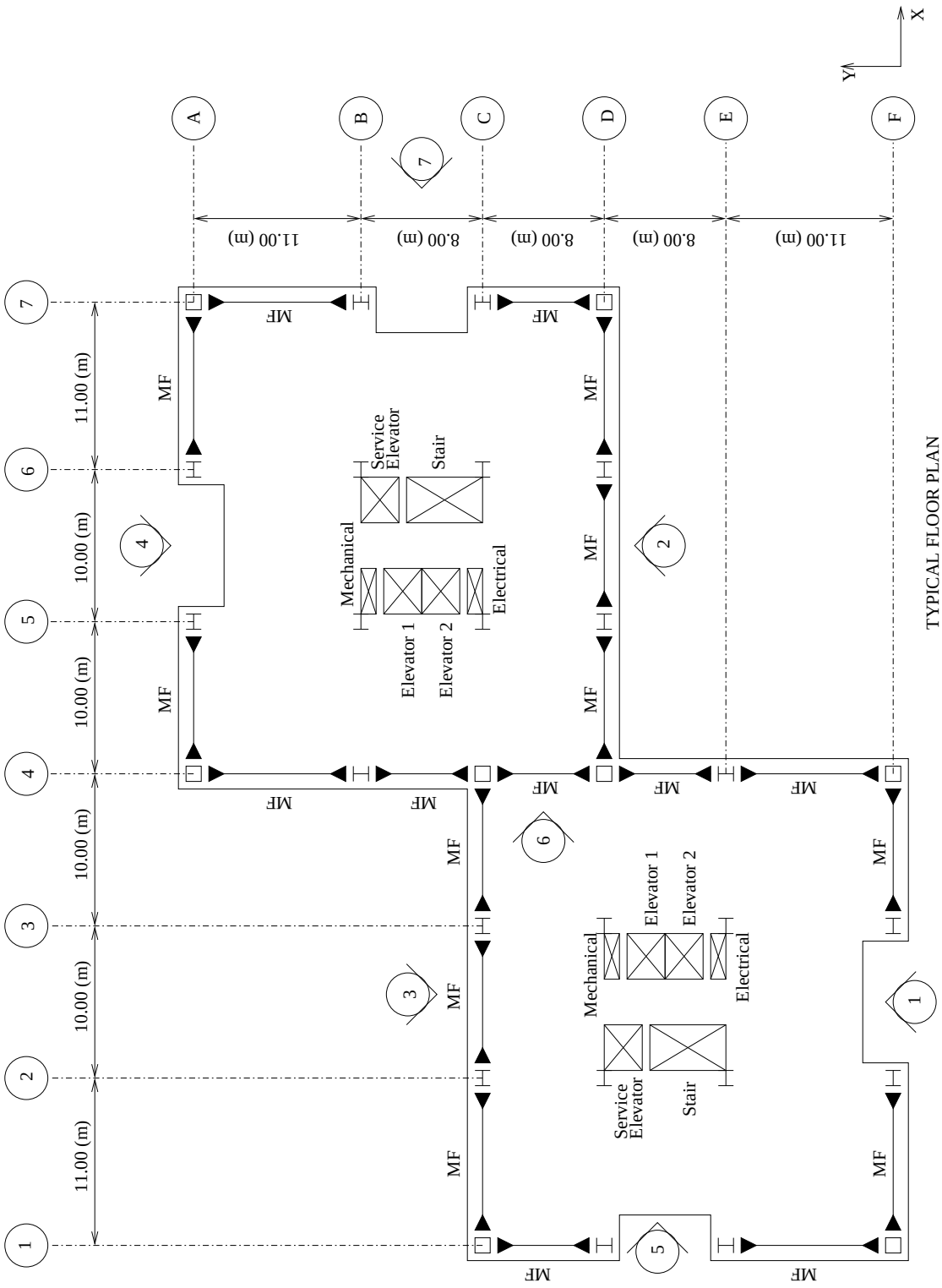

Figure 8.2: Typical Floor Plan: Building 1

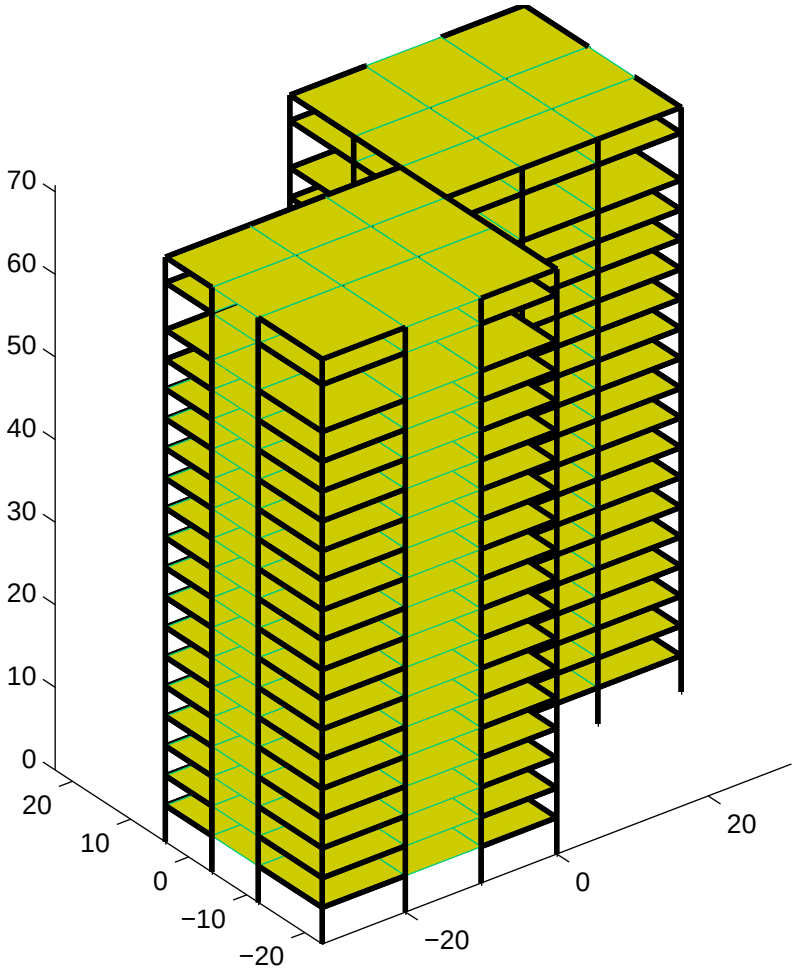

Figure 8.3: Isometric View: Building 1

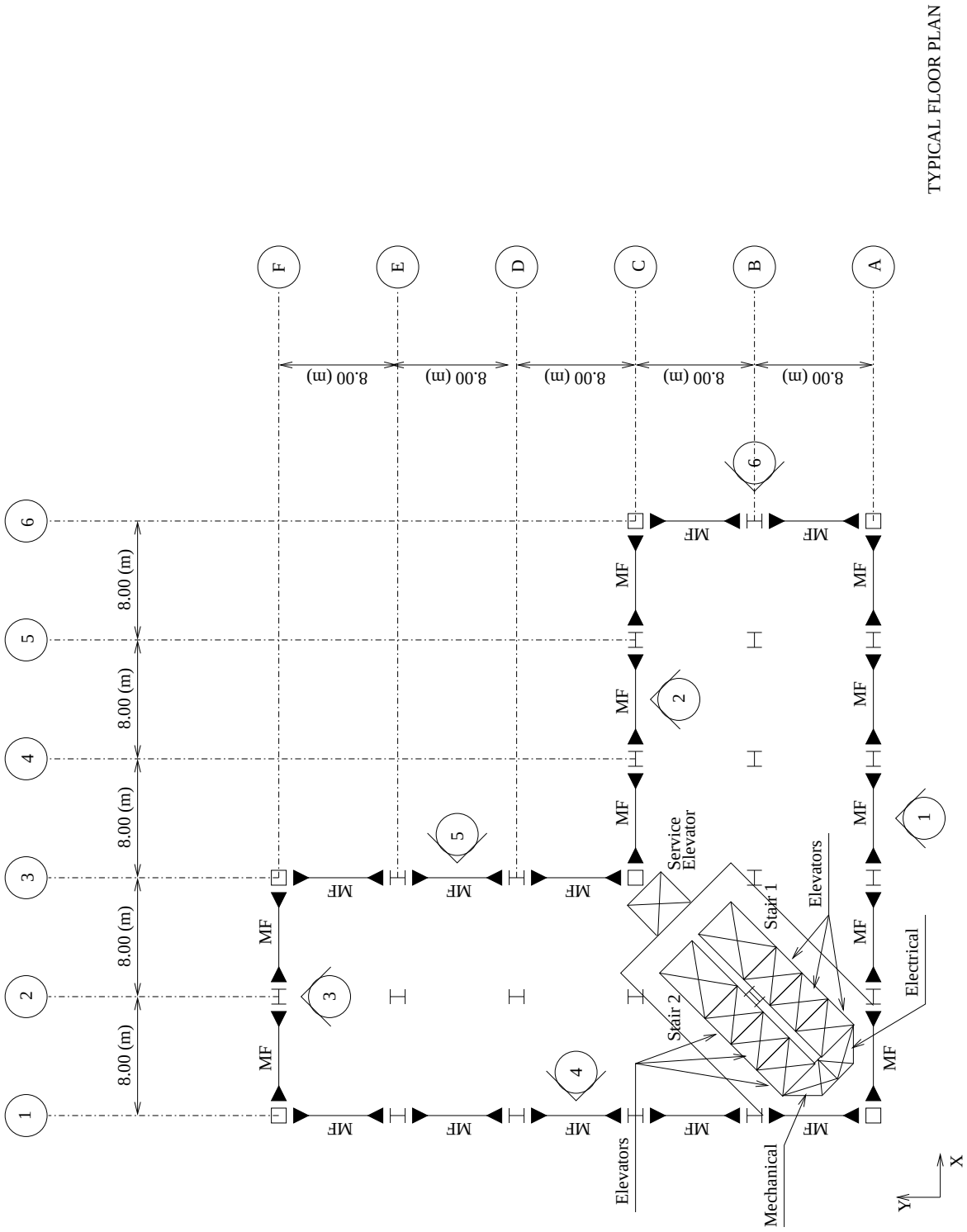

Figure 8.4: Typical Floor Plan: Buildings 2 and 2A

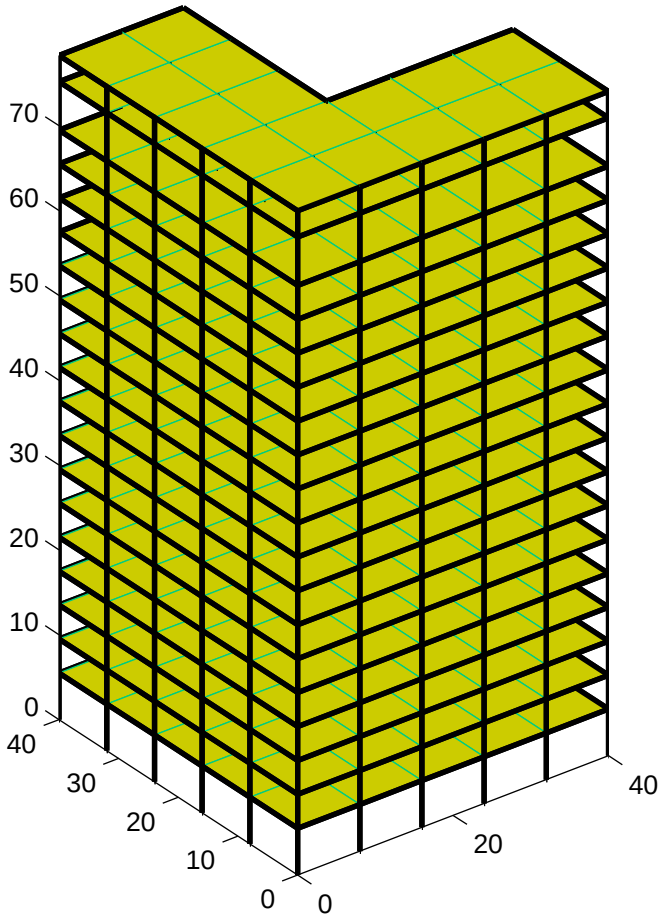

Figure 8.5: Isometric View: Buildings 2 and 2A

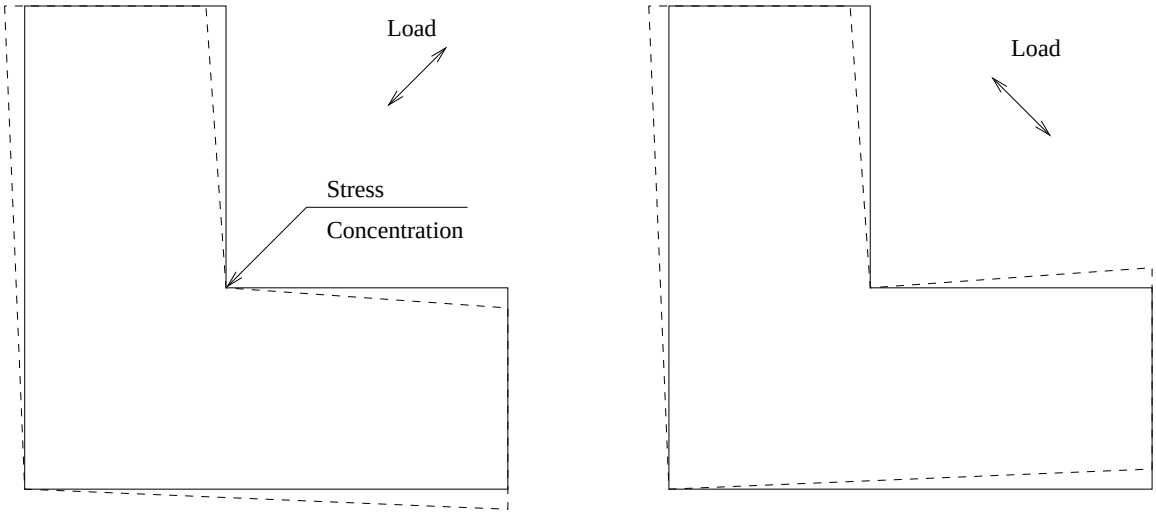

Figure 8.6: In-Phase and Out-of-Phase Shaking of L-Shaped Building

maximum beam depths being governed by gravity loads. The shifting of the moment frame away from the face of the building shifts the center of stiffness towards grid 2. On plan, the center of mass is close to the center of the building. This eccentricity between the locations of the center of mass and the center of resistance leads to torsional sensitivity in the building. During an earthquake, there will be a significant contribution from the torsional mode to the building response. Such torsionally sensitive buildings are classified as irregular in the code and there is a premium of about 10% placed on the seismic force used for their design. Torsion in buildings has been the cause of catastrophic failures during earthquakes and there is a great need for data on the behavior of such buildings during strong ground shaking. In most cases, since architecture drives the design and often defines the layout, such irregular designs cannot be avoided. So, a comprehensive effort is needed to understand the behavior of such structures so that the best possible designs are implemented. The floor is made of concrete slab on metal deck ($5\frac{1}{2}''$ thick total) supported by steel beams and girders framing into interior gravity columns and exterior moment frame columns. The building is covered with stone cladding (facade). Partitions are made up of dry wall supported by metal studs. The floor is carpeted. Typical story height is $4.0m$ with variations at the lobby level and the mechanical stories. Building 3A has the same plan and elevation as building 3, except that it has been designed without any imposed wind drift limit. The isometric view of the

two buildings is illustrated in Figure 8.8.

Building 4 is a 19-story mixed-use tower ($75.1m$ tall) with a hotel on the lower 10 stories and an office on the upper 9 stories. The hotel floors (Figure 8.9) contain a large atrium. The presence of this opening shifts the center of mass to one side. Furthermore, the beams on the atrium face are limited to a depth of 500 mm. This shifts the center of stiffness away from the atrium face, a greater distance than the shift in the center of the mass, leading to a torsional eccentricity. The mass on the upper (office) floors is also distributed unevenly to accentuate the atrium effect below (Figure 8.10). In addition, the glass cladding on the atrium face, along with stone cladding on the other faces adds to the non-uniform distribution of the mass. During an earthquake, there will be a significant contribution from the torsional mode to the building response. As described before, per the code (UBC97 [33]), torsional irregularity shall be considered to exist when the maximum story drift, computed including accidental torsion, at one end of the structure transverse to an axis is more than 1.2 times the average of the story drifts of the two ends of the structure. A premium of 10% is placed on the seismic design base shear used for the design of such a torsionally irregular structure. From a linear dynamic analysis using the commercial program, ETABS, it was determined that the building did not satisfy this irregularity criterion in spite of all the seemingly irregular features, in other words, per the code, the building is deemed regular and its design forces need not be increased by 10%. So here's a building that seems highly irregular but is not classified as such by the code and it should be of great interest to study its performance under strong earthquake events.

The building has a typical floor area of $1216m^2$ at the hotel levels and $1600m^2$ at the office levels, with a perimeter of $160m$. The building is rectangular shaped in plan (Figures 8.9 and 8.10) with separate elevators and stairs servicing the hotel and office levels. Typical hotel story height is $3.6m$ while the typical office story height is $4.0m$ with variations at the lobby level and the mechanical stories.

The primary lateral system consists of a perimeter moment frame. The atrium at the lower (hotel) levels requires the termination of columns at grid intersections C-2 and D-2. The loads from these columns are transferred to the adjacent columns by way of single story-deep trusses along grids C and D with two bays from grids 1 to 3. The elevation of these two transfer trusses is shown in Figure C.26. The truss members are assumed to be pinned at their ends. At the atrium (hotel) levels, the columns of the moment frame along

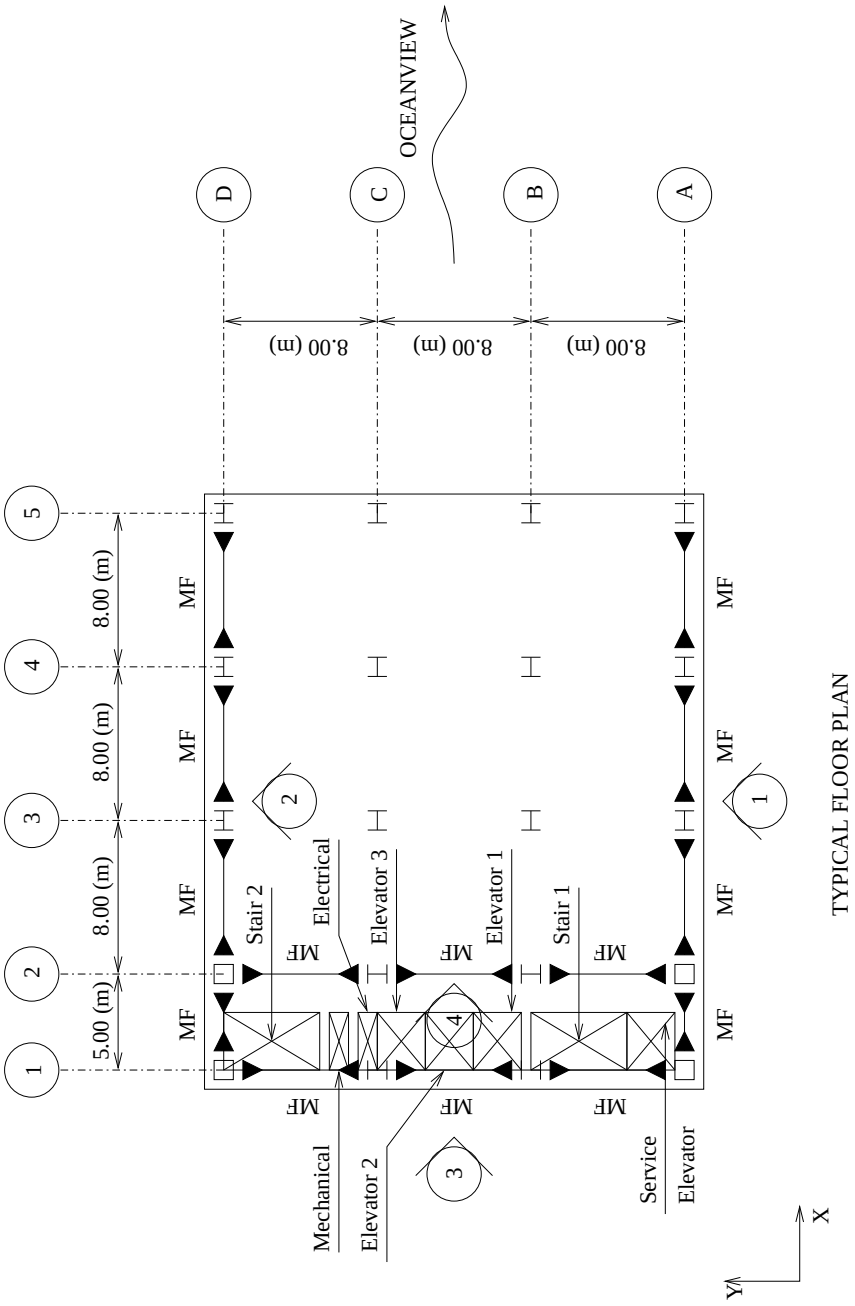

Figure 8.7: Typical Floor Plan: Buildings 3 and 3A

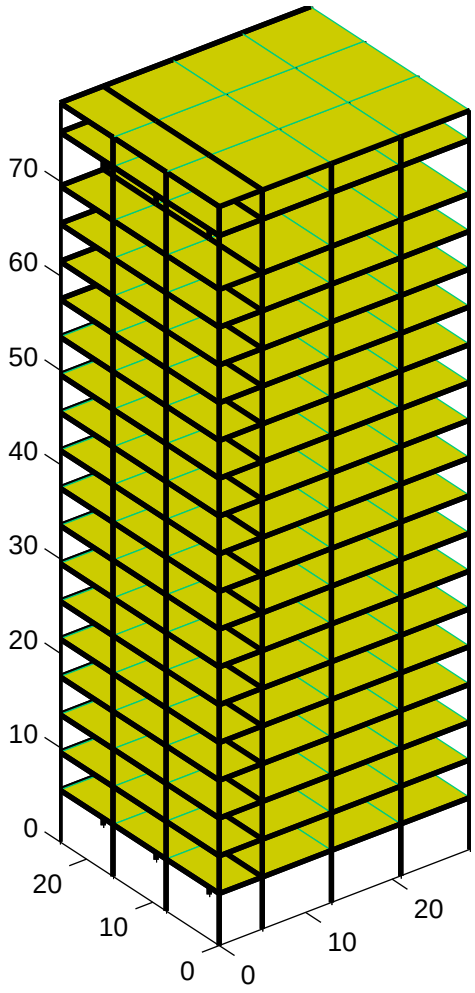

Figure 8.8: Isometric View: Buildings 3 and 3A

grid 1 are laterally braced by horizontal braces extending from columns at grid intersections, B-2 and E-2 (Figure 8.9). These braces also serve to transfer some of the diaphragm forces to this frame. Thus, to some extent, they make up for the lack of diaphragms at the atrium. The braces are pin-connected at their ends. These braces are also shown along with the moment frame beams and columns in the isometric view of the building shown in Figure 8.11. The floor is made of concrete slab on metal deck ($5\frac{1}{2}''$ thick total) supported by steel beams and girders framing into interior gravity columns and exterior moment frame columns. The building is covered with a glass facade on the atrium face (along grid 1) and stone cladding (facade) on the other three faces. Partitions are made up of dry wall supported by metal studs. The hotel floors are completely carpeted whereas a portion of the office floors consists of marble finish with the rest being carpeted (Figure 8.10).

ASTM-A572, Grade 50 steel is used for all the buildings. It is assumed that the nominal yield stress is 50 ksi and the nominal ultimate stress is 65 ksi.

8.3.3 Gravity Load Criteria

The gravity loading criteria for all the buildings are given in Table 8.1. The loads are based on the occupancy of a particular floor. For example, building 1 is primarily a residential tower with two mechanical floors and a roof. Thus, the loads on the typical floor of this building correspond to the "Residential" occupancy category in this table while the loads on the mechanical floors and the roof correspond to those listed in the "Mechanical" and "Roof" occupancy categories. Note that in addition to these loads, the self-weight of the lateral-force-resisting-system (Moment frame beams and columns) and the gravity columns is to be included. This is computed internally in the ETABS program and added on to the seismic mass and the dead load.

8.3.4 Seismic Criteria

All the buildings are assumed to be located in Seismic Zone 4 (UBC97 [33]) at a distance of 5 km from a Type A fault. The soil at the site is assumed to be of Type S_b per the UBC97 [33] soil classification. The seismic design criteria for all the buildings are given in Table 8.2. Based on these criteria, the UBC97 response spectrum is computed and is shown in Figure 8.12.

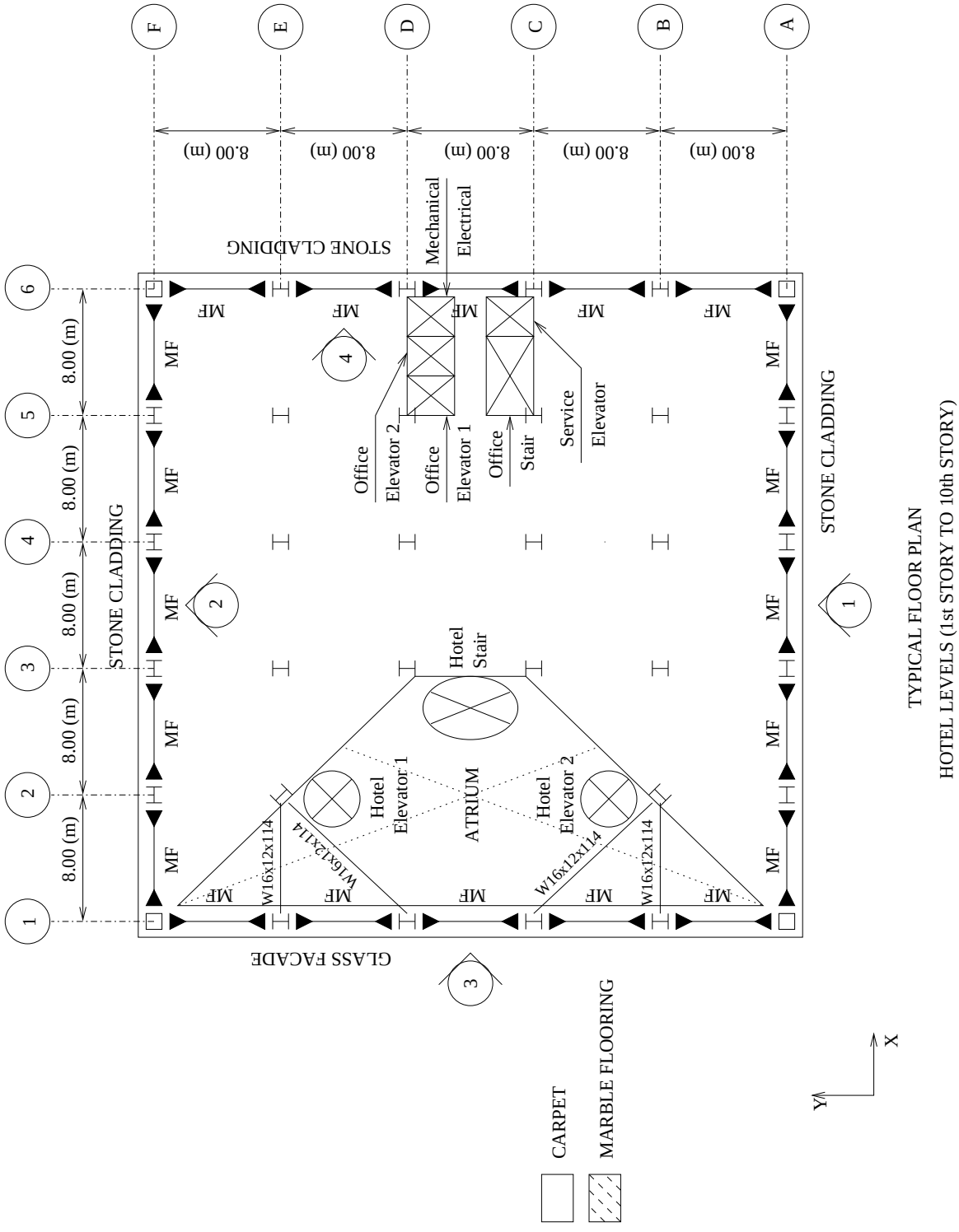

Figure 8.9: Typical Hotel Floor Plan: Building 4

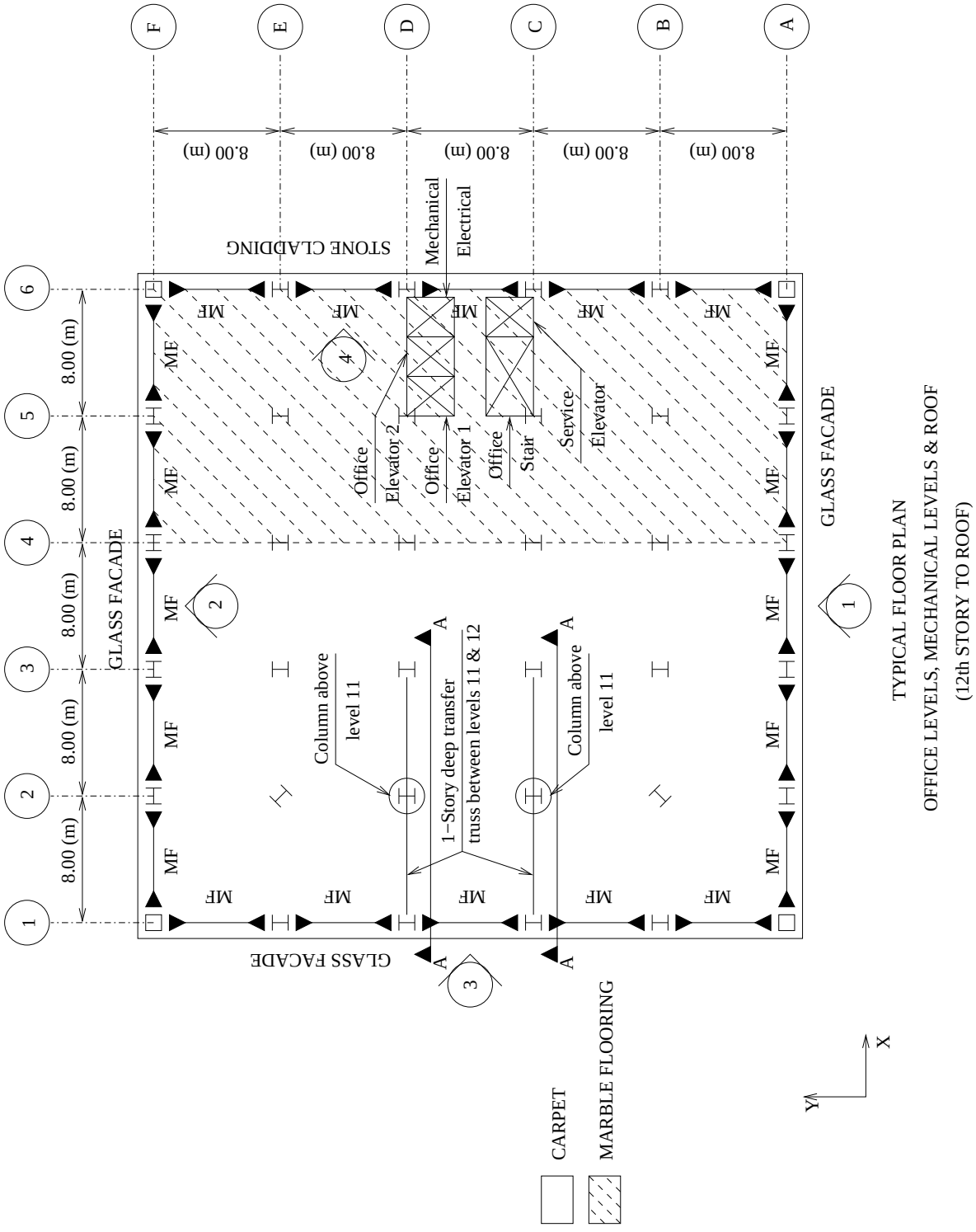

Figure 8.10: Typical Office Floor Plan: Building 4

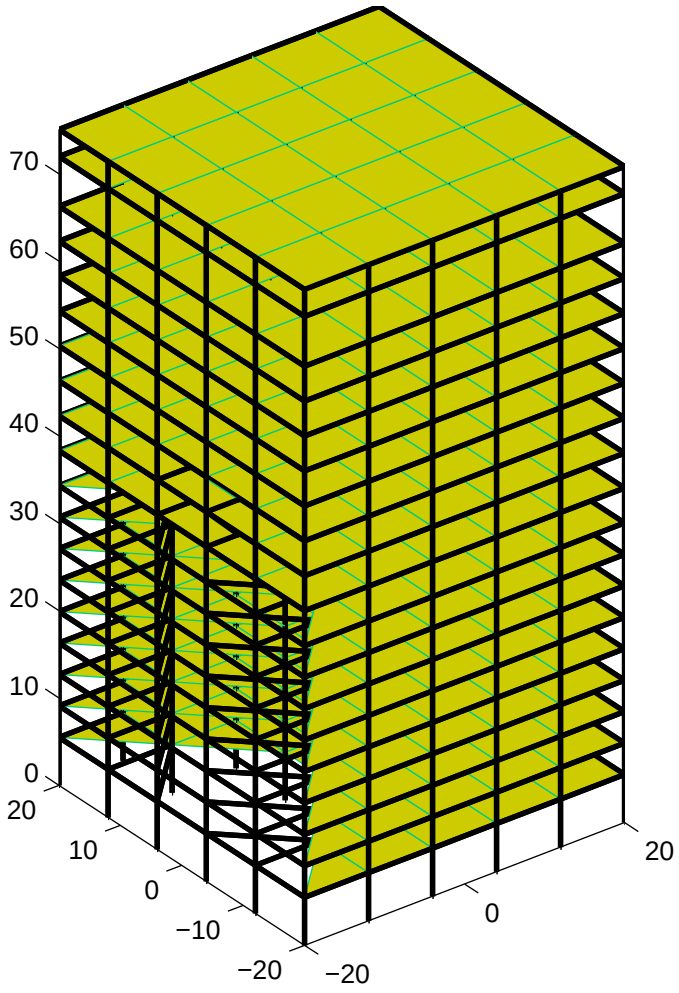

Figure 8.11: Isometric View: Building 4

Table 8.1: Gravity Loading Criteria (UBC97 [33])

Occupancy	**Item**	**Load ($\frac{kg}{m^2}$)**
Residential	Concrete Slab on Metal Deck Floor Fill (Carpet) Partitions (Metal Stud & Dry Wall) Mechanical Floor Framing Live Load	315.00 10.00 100.00 50.00 15.00 200.00
Office	Concrete Slab on Metal Deck Floor Fill (Carpet) Floor Fill (Marble, Building 4 only) Partitions (Metal Stud & Dry Wall) Mechanical Floor Framing Live Load	255.00 10.00 120.00 100.00 35.00 15.00 250.00
Hotel	Concrete Slab on Metal Deck Floor Fill (Carpet) Partitions (Metal Stud & Dry Wall) Mechanical Floor Framing Live Load	255.00 10.00 100.00 50.00 15.00 200.00
Mechanical	Concrete Slab on Metal Deck Floor Fill Mechanical Floor Framing Live Load	255.00 120.00 35.00 40.00 1200.00
Roof	Concrete Slab on Metal Deck Waterproofing Mechanical Floor Framing Live Load (Residential Tower) Live Load (Office & Hotel Towers)	255.00 10.00 35.00 15.00 200.00 250.00
Cladding	Stone Cladding Glass Cladding	120.00 40.00

Table 8.2: Seismic Design Criteria (UBC97 [33])

Seismic Zone Factor (Z)	0.400
Seismic Source Type	A
Closest Distance to Source	5.000 km
Soil Type	Sb
Importance Factor (I)	1.000
Structural System Factor (R)	8.500
Structural Over-strength Factor (Ω_0)	2.800
Near-Source Factor (N_a)	1.200
Near-Source Factor (N_v)	1.600
Seismic Coefficient (C_a)	0.480
Seismic Coefficient (C_v)	0.640
Lateral System Type Factor (C_t)	0.085

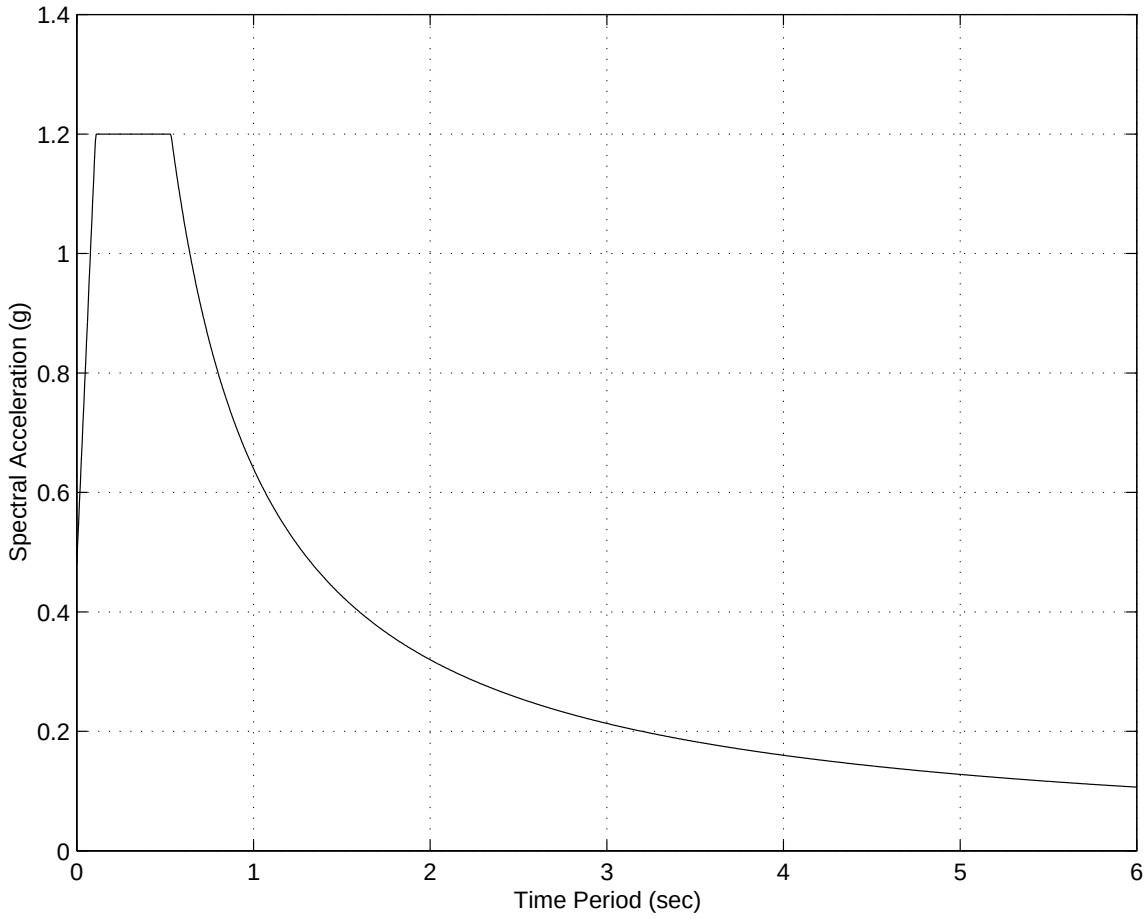

Figure 8.12: 1997 Uniform Building Code [33] Response Spectrum Used in Design ($C_a = 0.48$ and $C_v = 0.64$)

Table 8.3: Wind Design Criteria (UBC97 [33])

Exposure	B
Basic Wind Speed (v)	70.00 mph
Importance Factor (I_w)	1.00
Windward Coefficient (C_q)	0.80
Leeward Coefficient (C_q)	0.50

8.3.5 Wind Criteria

All the buildings are assumed to be located in an area that is categorized as Exposure B in UBC97 [33] for wind design. The wind design criteria for all the buildings are given in Table 8.3.

8.4 Design of the Buildings per UBC97 Using the Commercial Program, ETABS

A three-dimensional linear elastic model of the building is built using the commercial program ETABS. In addition to the design of beams and columns, the program is capable of checking for the strong column-weak beam criterion in the code. $P-\Delta$ effects are included in the analysis. The program accounts for the $P-\Delta$ effects from only the seismic weight (Dead Load). However, there is a provision to specify a scaling factor for these effects. This factor can be used to include the $P-\Delta$ effects from Live Load. Assuming that during an earthquake, the building is loaded with 30% of the design Live Load (which on the average works out to about 15% of the design Dead Load for all the buildings), a value of 1.15 is used for this scale factor for all buildings. The design procedure is outlined below. A rigid foundation is assumed.

- After the structural model (with preliminary member sizes) including masses and loads is built, a linear dynamic response spectrum analysis is performed. For this purpose, the UBC97 [33] response spectrum (Figure 8.12) corresponding to the seismic parameters of the site given in Table 8.2 is used.

- The program computes the frame element weights and these are added on to the dead weight of the structure to arrive at the total seismic weight. The code static base shear is then computed based on this total seismic weight.

- The program computes the dynamic spectral base shear. Per the code, this base shear can be scaled down to 100% of the static base shear for the design of irregular buildings and 90% of the static base shear for the design of regular buildings.

- The program also computes the center of mass for each floor. Per the code accidental eccentricity criterion, the center of mass is shifted by 5% of the building dimension in each of the two principal directions. An eccentricity in the location of the center of mass would generate a torsional component in the response and the intent of the code is to ensure some torsional resistance in the design to account for modeling and real-world errors in locating the center of mass (such as openings in the floor slab that may not been incorporated into the model).

- The analysis is repeated with the new center of mass and the spectral scaling factor. The member forces from this analysis are scaled up by the frame redundancy factors, ρ_x and ρ_y, in the two horizontal directions. The code requires that there be a minimum number of bays of moment frames in each of the two principal directions and it penalizes those buildings that have insufficient redundancy by scaling up the member forces by ρ_x and ρ_y ([33], Section 1630.1.1).

- The scaled member forces are used to check the stresses in the beams and columns. If the members are inadequate, the sizes are increased and the process is repeated. This iterative process is carried out until the design is satisfactory. Similarly the drifts are checked against allowable limits and the stiffness of the structure is adjusted to satisfy the drift limits.

- ETABS also computes the required doubler plates at joints as per UBC97 ([33], Section 2213.7.2). The thicknesses of these doubler plates are rounded to the nearest eighth of an inch.

- The building is then checked for wind forces. The wind pressure is computed per UBC97 [33] in conjunction with the Wind Design Criteria specified in Table 8.3. The wind drifts are restricted to the limit specified therein.

The seismic design parameters and the wind design parameters specific to each building are given in Tables 8.4 and 8.5, respectively.

Table 8.4: Seismic Design Parameters for All the Buildings

Seismic Parameter	**Building ID**					
	B-1	**B-2**	**B-2A**	**B-3**	**B-3A**	**B-4**
Height of Building (H_n in meters)	70.800	78.300	78.300	78.300	78.300	75.100
Code Fundamental Period (sec)	2.08	2.25	2.25	2.25	2.25	2.18
Base Shear (V^*)	6.024%	6.024%	6.024%	6.024%	6.024%	6.024%$^+$
Static Base Shear (metric Tonnes)	1253.41	659.27	656.17	481.76	465.23	837.61$^+$
Base Shear for X-Drift Computation*	2.234%	2.215%	1.814%	3.765%	2.734%	2.202%
Base Shear for Y-Drift Computation*	2.164%	2.215%	1.814%	2.331%	1.588%	2.145%
System Redundancy Factor (ρ_x)	1.064	1.000	1.000	1.000	1.000	1.000
System Redundancy Factor (ρ_y)	1.086	1.000	1.000	1.241	1.217	1.125
Irregular Building?	Yes	Yes	Yes	Yes	Yes	No
Seismic Inelastic Drift Ratio Limit, Δ_M^{max}	0.02	0.02	0.02	0.02	0.02	0.02

** % of Seismic Weight*
+ Only 90% of this is used for design

Table 8.5: Wind Design Parameters for All the Buildings

Wind Parameter	**Building ID**					
	B-1	**B-2**	**B-2A**	**B-3**	**B-3A**	**B-4**
X-Direction Base Shear (metric Tonnes)	334.00	332.00	332.00	199.06	199.06	313.77
Y-Direction Base Shear (metric Tonnes)	450.00	332.00	332.00	240.53	240.53	313.77
Drift Ratio Limit	0.0025	0.0025	None	0.0025	None	0.0025

The elevations of the moment frames (see plans for location) and gravity columns of all buildings are given in Appendix C. The section sizes shown correspond to the final design arrived at after multiple iterations of the design process described above. The section dimensions are given in the section database in Appendix B. The centers of mass and stiffness at three floors along the height of each building are shown on maps in Appendix D. The location of the center of mass in relation to the center of stiffness determines the extent of twisting in the building during an earthquake.

Building 1 moment frame elevations with beam and column sizes are given in Figures C.1 through C.4. The gravity column sizes are given in Figure C.5. The average weight of steel in the structure is 84.1 $\frac{kg}{m^2}$ of plan area.

The building design using ETABS gives good insight into its behavior. The 5% shift in the center of mass activates the torsional mode. The induced twisting is sufficiently large for the building to be classified as a torsionally irregular building. Of course, the presence of reentrant corners in itself is a necessary criterion for the building to be designed as an irregular building. The single-bay frames on the building perimeter lead to the building being torsionally soft in addition to reducing the redundancy in the system by forcing the 5-bay frame in the Y-direction and the two 3-bay frames in the X-direction to carry majority of the seismic shear. Although the building does not have any axis of symmetry, it does possess a certain kind of geometric symmetry. If mass is uniformly distributed in plan (as is the case here), both the center of mass and the center of stiffness will lie at the mid-point of column line 4 (Figure D.1). This precludes twisting under seismic loading, unless the building yields unsymmetrically, which is possible because the two horizontal components of ground motion applied simultaneously will cause an unsymmetric load pattern on the beams and columns. Wind loads should not cause twisting

The design of columns was governed by strength requirements, including the strong column-weak beam criterion of the code (Section 8.2.20). The design of the moment frame beams was governed by the stiffness required to maintain the fundamental period between 3.2 *seconds* and 3.5 *seconds*.

Building 2 moment frame elevations with beam and column sizes are given in Figures C.6 through C.8 and the gravity column sizes are given in Figure C.9. The average weight of steel in the structure is 89.5 $\frac{kg}{m^2}$ of plan area.

The wings have only two bays of moment frames each across their ends and as a result, tend to be softer than the spine of the building. Wind forces controlled the design for the moment frames at the wings. Wind forces are applied along the vertical centroidal axes of the windward and leeward faces of the building. Since the center of resistance (on plan) of the building is closer to the reentrant corner than to this mid-point, wind forces lead to twisting in the building. Since the wings are soft, this torsion leads to large drifts at the far corners (at grid intersections F-1, F-3, C-6 and A-6 in Figure 8.4). Reduction in the drift due to building translation (sway) was achieved by stiffening all moment frames. To reduce the drift in the short direction of the wings, the beams and columns in the 2-bay moment frames at the wings (frames 3 and 6 along grids F and 6 in Figure 8.4) were considerably stiffened compared to those in the 3-bay and 5-bay moment frames (frames 1, 2, 4 and 5 along grids 1, 3, A and C). The beam depths in the 3-bay and 5-bay frames vary from 400 *mm* at the roof to 600 *mm* at the second floor while they vary from 650 *mm* at the roof to 750 *mm* at the second floor in the case of the 2-bay frames at the wings (Figures C.6 through C.8). This moves the center of stiffness from within the spine to a location very close to the reentrant corner (Figure D.2). However, this remedial measure to distribute the stiffness (on plan) more uniformly is still not sufficient to eliminate twisting in the building under wind forces. But the reduction in the translational drift (sway) allows the wind drift at the far corners (at grid intersections F-1, F-3, C-6 and A-6 in Figure 8.4) to be restricted to within the 0.0025 limit.

As in building 1, the design of columns was governed by strength requirements including the strong column-weak beam criterion of the code (Section 8.2.20). In this case, the design of the moment frame beams was governed by the stiffness required to keep the wind-drifts below 0.0025.

As described above, at least some aspects of the design of building 2 are governed by the wind drifts. Since no wind drift limit is imposed by the code (UBC97 [33]), it is of interest to study the performance of a building that does not satisfy any limits on the wind drift, but designed to withstand wind forces and earthquake forces with imposed seismic drift limits alone. Such a building (labeled building 2A) is designed and its performance under strong ground motion is analyzed.

To arrive at the design of Building 2A starting from Building 2, the stiffness of the wing moment frames as well as the spine moment frames has been reduced in the same

proportion. Thus, as in building 2, the beams in the 2-bay moment frames are deeper than the beams in the 3-bay and 5-bay moment frames to compensate for the fewer bays. The average weight of steel used in the structure is lower at 86.9 $\frac{kg}{m^2}$ of plan area compared to building 2 at 89.5 $\frac{kg}{m^2}$.

Since the fundamental period of building 2A is higher than that of building 2, the static base shear, to which the dynamic base shear is scaled down for use in the analysis to compute the seismic drifts, is lower (1.814% of seismic weight compared to 2.215% for building 2).

Building 2A moment frame elevations with beam and columns sizes are given in Figures C.10 through C.12 and the gravity column sizes are given in Figure C.13.

No wind drift limit is imposed and this allows for lower frame stiffnesses. Thus, the beam depths in the 3-bay and 5-bay frames (frames 1, 2, 4, and 5 along grids, 1, 3, A and C in Figure 8.4) in the spine vary from 400 mm at the roof to 500 mm at the second floor while they vary from 500 mm at the roof to 600 mm at the second floor in the case of the 2-bay frames (frames 3 and 6, along grids, F and 6). In addition the depth of the middle column in the 2-bay frame has been reduced by 100 mm. By retaining the higher relative stiffness of the 2-bay frame in relation to the 3-bay and 5-bay frames, the center of resistance is held close to the reentrant corner even though there is a greater eccentricity in the locations of the center of mass and center of resistance relative to each other (Figure D.3). Some columns are heavier than in building 2 because of the increased $P - \Delta$ effects resulting from the reduction in the stiffness of the structure.

Some amount of twisting can be observed from the wind drifts. This is due to the fact that the center of application of wind forces is along the vertical centroidal axis of the face of the building while the center of resistance/stiffness is closer to the reentrant corner leading to torsional eccentricity in as far as wind loading is concerned. However, in the case of seismic forces, there is very little twisting observed consistent with the fact that the centers of mass and stiffness are located close to each other.

Building 3 moment frame elevations with beam and column sizes are given in Figures C.14 through C.16 and the gravity column sizes are given in Figure C.17. The average weight of steel in the structure is 133.7 $\frac{kg}{m^2}$ of plan area.

Wind forces are applied in X or Y direction along the vertical centroidal axes of the windward and leeward faces of the building. For Y-direction wind analysis, the center of resistance does not coincide with the center of applied force (Figure D.4) and this leads

to twisting in the building. There is considerably greater drift at the soft corners, A-5 and D-5, when compared to the stiff corners, A-1 and D-1. The drift at these two corners has two components, one coming from translation in the Y-direction and the other from the twisting in the building. While the translational component of the wind drift is resisted by the Y-direction moment frames along grids 1 and 2, the twisting component is primarily resisted by the X-direction moment frames along grids A and D. Thus, in order to restrict the overall drift to the generally accepted elastic wind drift limit of 0.0025 (in consideration of occupant comfort), all four moment frames had to be stiffened (and as a result strengthened). However, since this limit is not imposed by the code (UBC97 [33]), it is of interest to study the performance of a building that does not satisfy any limits on the wind drift, but designed to withstand wind forces and earthquake forces with imposed seismic drift limits alone. Such a building (labeled building 3A) is designed and its performance under strong ground motion is analyzed.

The design of columns was governed by strength requirements, including the strong column-weak beam criterion of the code (Section 8.2.20). As in building 2, the design of the moment frame beams was governed by the stiffness required to keep the wind-drifts below 0.0025.

Building 3A has the same plan and elevation as building 3, except that it has been designed without any imposed wind drift limit. Thus, building 3A (with fundamental period of 4.74 *sec*) is far softer than building 3 (with fundamental period of 3.21 *sec*). The stiffness of all four frames in building 3A is reduced. Beam depths in building 3A vary from 450 *mm* at the roof to 650 *mm* at the second floor as opposed to beam depths of 600 *mm* at the roof to 1000 *mm* at the second floor in building 3. The interior columns in the frames were reduced in depth from 1000 *mm* in building 3 to 700 *mm* in building 3A. The average steel weight used in the structure is lower at 112.9 $\frac{kg}{m^2}$ of plan area compared to building 3 at 133.7 $\frac{kg}{m^2}$.

The reduction in the steel frame weight leads to a reduction in the seismic static base shear (465.23T compared to 481.76T for building 3). Furthermore, since the building fundamental period is higher compared to building 3, the static base shear, to which the dynamic base shear is scaled down for use in the analysis to compute the seismic drifts, is lower (2.734% of seismic weight compared to 3.765% for building 3 for the X direction wind drift and 1.588% of seismic weight compared to 2.331% for building 3 for the Y direction wind

drift).

Building 3A moment frame elevations with beam and columns sizes are given in Figures C.18 through C.20 and the gravity column sizes are given in Figure C.21.

The building is designed for wind forces applied in X or Y direction along the vertical centroidal axes of the windward and leeward faces of the building. As in building 3, for Y direction wind, there is considerable twisting as a result of the center of resistance not coinciding with the center of the applied force (Figure D.5). Once again, there is considerably greater drift at the soft corners, A-5 and D-5, when compared to the stiff corners, A-1 and D-1. Of course, this is not of much concern or consequence since no wind drift limit is imposed in the design of this building.

Building 4 moment frame elevations with beam and column sizes are given in Figures C.22 through C.24 and the gravity column sizes are given in Figure C.25. The average weight of steel in the structure is 75.7 $\frac{kg}{m^2}$ of plan area. The lower amount of steel used compared to buildings 1 and 2 comes from two sources - the lower design forces (10%) due to the "regular" classification of this building, and the efficient continuous perimeter tube moment frame system adopted for the lateral resistance.

Since the centers of mass and stiffness (Figure D.6) do not coincide, there is some amount of twisting observed during the earthquakes.

Wind forces are applied in X or Y direction at the mid-points of the windward and leeward faces of the building. In this case, the center of resistance coincides with the center of the applied wind force in the X direction. In the Y direction, there is a slight eccentricity between the centers of force and resistance resulting from a 500 *mm* limit on the beam depth (architectural requirement) in the moment frame adjacent to the atrium (along grid 1) that moves the center of resistance away from the atrium towards grid 6. The small eccentricity does not lead to significant twisting due to wind.

As in building 1, the design of columns was governed by strength requirements, including the strong column-weak beam criterion of the code (Section 8.2.20). The design of the moment frame beams was governed by the stiffness required to maintain the fundamental period between 3.2 *seconds* and 3.5 *seconds*.

The computed natural periods and the modal directions for all six buildings are given in Table 8.6. The modal direction factors identify the predominant direction of excitation associated with each of the modes. The factors are percentages associated with the X and

Y translational and Z-rotational directions. The sum of the three values add up to 100. The factors of a particular mode are given by:

$$\%X = 100 \sum_i M_i \phi_{X,i}^2 \tag{8.12}$$

$$\%Y = 100 \sum_i M_i \phi_{Y,i}^2 \tag{8.13}$$

$$\%Z = 100 \sum_i M_{\theta,i} \phi_{\theta Z,i}^2 \tag{8.14}$$

where all summations are over all the stories, M_i and $M_{\theta,i}$ represent the translational mass and the mass moment of inertia of the i^{th} story, $\phi_{X,i}$ and $\phi_{Y,i}$ represent the X and Y-translational mode shape components at the i^{th} story, and $\phi_{\theta Z,i}$ represents the corresponding Z-rotational mode shape component.

The computed drift ratios from the response spectral analyses for all the buildings are given in Table 8.7. The X and Y drifts corresponding to two cases - spectral direction corresponding to building X and Y directions - are listed. The elastic drift, Δ_s, is computed for each case by taking the square root of the sum of the squares (SRSS) of these drifts. As described in Section 8.2.14, this elastic drift ratio is converted to an inelastic drift ratio, Δ_M, which is then compared against the code limit, Δ_M^{max}.

The computed drift ratios from the wind analyses for all the buildings are given in Table 8.8.

Table 8.6: Building Natural Periods and Modal Directions (first 3 modes)

Building ID	**Mode Number**	**Period** (*sec*)	**Modal Direction Factors**		
			X-Trans	**Y-Trans**	**Z-Rotn**
B-1	1	3.50	91.55	3.61	4.84
	2	3.41	5.67	89.52	4.81
	3	2.69	2.77	6.88	90.35
B-2	1	3.39	50.00	50.00	0.00
	2	3.32	49.89	49.89	0.22
	3	2.33	0.12	0.12	99.76
B-2A	1	4.15	50.00	50.00	0.00
	2	4.11	49.93	49.93	0.14
	3	2.78	0.08	0.08	99.84
B-3	1	3.21	0.00	72.64	27.36
	2	2.03	100.00	0.00	0.00
	3	1.22	0.00	30.99	69.01
B-3A	1	4.74	0.00	79.16	20.84
	2	2.75	100.00	0.00	0.00
	3	1.85	0.00	20.91	79.09
B-4	1	3.51	0.00	95.49	4.51
	2	3.42	100.00	0.00	0.00
	3	2.02	0.00	4.67	95.33

Table 8.7: Building Seismic Drift Ratios

Building ID	**Spectral Direction**	**X-Drift**	**Y-Drift**	**SRSS Δ_s**	**SRSS Δ_M**	Δ_M^{max}
B-1	X Y	0.0026 0.0008	0.0007 0.0025	0.0027 0.0027	0.0159 0.0159	0.0200 0.0200
B-2	X Y	0.0018 0.0003	0.0003 0.0018	0.0018 0.0018	0.0108 0.0108	0.0200 0.0200
B-2A	X Y	0.0025 0.0003	0.0003 0.0025	0.0025 0.0025	0.0147 0.0147	0.0200 0.0200
B-3	X Y	0.0011 0.0007	0.0003 0.0018	0.0011 0.0020	0.0065 0.0117	0.0200 0.0200
B-3A	X Y	0.0014 0.0011	0.0004 0.0030	0.0015 0.0031	0.0088 0.0187	0.0200 0.0200
B-4	X Y	0.0021 0.0007	0.0004 0.0022	0.0022 0.0023	0.0129 0.0140	0.0200 0.0200

Table 8.8: Building Wind Drift Ratios

Building ID	**Wind Direction**	**X-Drift**	**Y-Drift**	**SRSS Δ_w**	Δ_w^{max}
B-1	X Y	0.00139 0.00003	0.00002 0.00173	0.00139 0.00173	0.00250 0.00250
B-2	X Y	0.00249 0.00029	0.00029 0.00249	0.00251 0.00251	0.00250 0.00250
B-2A	X Y	0.00366 0.00004	0.00004 0.00366	0.00366 0.00366	- -
B-3	X Y	0.00060 0.00076	0.00000 0.00244	0.00060 0.00256	0.00250 0.00250
B-3A	X Y	0.00121 0.00162	0.00002 0.00575	0.00121 0.00597	- -
B-4	X Y	0.00167 0.00022	0.00000 0.00184	0.00167 0.00185	0.00250 0.00250

Chapter 9 Building Analysis

9.1 Introduction

In the last chapter, the planning and design, based on current codes, of six irregular buildings was described. As mentioned there, the motivation for this was to study their performance under strong ground motion from near-source earthquakes and to gather data on the strength and ductility demands on these structures during such events. To this end, structural models of all the six buildings are built using elastofiber elements for moment-frame beams and columns, panel zone elements (with linear-quadratic material model) for joints and elastic plane-stress elements for floor diaphragms. Gravity columns are modeled using plastic hinge elements. The loads on these columns which contribute to the $P-\Delta$ effects on the building are included. Gravity beams that are used for supporting the floor slab and are pin-connected are not included in the model as they do not contribute to the lateral force resisting system. Doubler plates as computed by ETABS rounded to the nearest eighth of an inch are included at panel zone locations. In order to compute reactions at the base of the buildings, translational springs with large stiffness are placed at the base of all the columns. Two sets of analyses were performed on each building using the program, FRAME3D [41] - pushover analyses to quantify the strength and ductility of the buildings and ground motion analyses to study their performance in actual events and to gather structure ductility demand data in these events.

9.2 Analyses Assumptions

The following are the assumptions made in these analyses:

1. A rigid foundation is assumed with the base of all columns assumed fixed. Structure-foundation interaction is not included.

2. Strength degradation in the various elements from weld fracture or other means is not included. Thus, collapse of the structure can occur only through $P-\Delta$ effects.

Table 9.1: Steel Material Properties Used in the Analysis

Usage	**Property**	$kgf-m$ **Units**	$Kip-in$ **Units**
Beam-Columns	Elastic Modulus, E	20388731162.41 $\frac{kg}{m^2}$	29000.00 ksi
	Shear Modulus, G	8155492464.96 $\frac{kg}{m^2}$	11600.00 ksi
	α^s_{ph} for Plastic Hinge Elements	0.02	0.02
	Yield Stress, σ_y	35152984.76 $\frac{kg}{m^2}$	50.00 ksi
	Yield Strain, ϵ_y	0.0017	0.0017
	Slope at Initiation of Strain Hardening, E_s, for Elastofiber Elements	407774623.25 $\frac{kg}{m^2}$	580.00 ksi
	Ultimate Stress, σ_u, for Elastofiber Elements	45698880.19 $\frac{kg}{m^2}$	65.00 ksi
	Strain at Initiation of Strain Hardening, ϵ_y, for Elastofiber Elements	0.0120	0.0120
	Ultimate Strain, ϵ_u, for Elastofiber Elements	0.1600	0.1600
Panel Zones	Shear Modulus, G	8155492464.96 $\frac{kg}{m^2}$	11600.00 ksi
	Shear Yield Stress, τ_y	20295585.22 $\frac{kg}{m^2}$	28.87 ksi

3. Composite action arising out of the shear connection between the concrete slab on metal deck and the moment frame beams is not included.

4. At each level, the story mass is lumped at the location, on plan, of each column based on its tributary plan area.

5. 30% of the Live Load is included along with the Dead Load in the lumped masses.

6. An average of 30% of the Live Load is included in the gravity loads for ground motion analyses.

7. Gravity columns are modeled using plastic hinge elements and their contribution to the $P-\Delta$ effects are automatically included. They are assumed continuous over the height of the building.

8. Trusses and horizontal braces are modeled using plastic hinge elements with pinned-end conditions.

9. Detailed material properties used in the analysis are given in Table 9.1.

10. An effective thickness of $4''$ is assumed for the plane-stress elements representing the concrete slab on metal deck.

11. The concrete elastic modulus is taken to be 3605 ksi corresponding to a compressive strength of $f'_c = 4000\ psi$.

12. Poisson's ratio for the plane-stress elements is taken to be 0.3.

9.3 Pushover Analyses of Buildings

To quantify the actual strength and ductility (deformation potential) of each building in the two principal directions, pushover analyses are performed in either direction. In these analyses, the building is subjected to a slow, ramped, horizontal ground acceleration that increases by $0.3\frac{g}{minute}$, and the building response is computed dynamically. The structural model is identical to that used in the earthquake analyses except that masses for the horizontal degrees of freedom are recalculated to total the seismic-design mass, $\frac{W}{g}$, with a distribution that is proportional to the UBC97 [33] seismic static design loads. Thus, in this analysis technique, the lateral loads are essentially the horizontal seismic design forces proportionally increasing with time at a slow rate. With this analysis, the ductility of the building can also be quantified in terms of its post-yield displacement capacity.

The results of the pushover analyses of all six buildings are presented in Appendix E. Pushover curves for each building in both X and Y directions (except for buildings 2 and 2A which are symmetric) are plotted in Figures E.1, E.4, E.7, E.10, E.13, E.15, E.17, E.19, E.21, and E.23. Four plots are shown in each figure. These correspond to the results from pushover analysis in the building X direction or the Y direction. The four plots are:

1. The base shear in the direction of pushing as a percentage of the seismic weight of the building plotted against the roof displacement. The roof displacements at two diagonally opposite corners of the building (for example, grid intersections A-7 and F-1 for building 1) are used for this purpose so that any twisting occurring in the building can be observed. This plot is usually referred to as the "pushover curve" in literature.

2. The square root of the sum of the squares (SRSS) of the base shear in X and Y directions as a percentage of the seismic weight of the building plotted against the

roof displacements at the two diagonally opposite corners of the building.

3. The base shear in the direction of pushing as a percentage of the seismic weight of the building plotted against time. This plot should essentially be linear indicating a static (or slow) rate of loading. Of course, since the analysis is carried out dynamically, some deviation from linearity is unavoidable. This should have only a negligible effect on the analysis results.

4. The roof displacements at the two diagonally opposite corners of the building plotted against time. This plot gives some insight into the rate of post-yield lead-up to the collapse of the building.

In addition to the pushover plots, plastic hinge maps showing the location and extent of plastic hinges in the building frames when ultimate strength is reached during the pushover analyses are also presented in Appendix E (Figures E.2, E.3, E.5, E.6, E.8, E.9, E.11, E.12, E.14, E.16, E.18, E.20, E.22, and E.24).

From the pushover plots, the following quantities can be extracted:

1. The yield strength of the building and the yield roof displacement, in the direction of pushing, corresponding to the point on the pushover curve at which the curve ceases to be linear.

2. The ultimate strength of the building and the ultimate roof displacement, in the direction of pushing, corresponding to the point on the pushover curve at which the peak base shear occurs.

These quantities are listed for all 6 buildings in Table 9.2. The design strength listed in this table corresponds to the design base shear computed using eqs. 8.6a through 8.6d. Note that for allowable stress design this base shear is scaled down by a factor of 1.4 when combining with gravity loads (Section 8.2.10).

The ratio of the ultimate strength to the design strength can be viewed upon as an "over-strength" factor. This over-strength factor varies from 1.5 to 2.3 for all buildings except buildings 3 and 3A which are torsionally extremely sensitive. The over-strength factor is as high as 5.5 for building 3 and 2.5 for building 3A.

The ratio of the roof ultimate displacement to its yield displacement is a measure of the

Table 9.2: Building Pushover Results

Building ID	**Pushover Direction**	**Strength***			**Roof Displacement (m)**	
		Yield	**Ultimate**	**Design+**	**Yield (m)**	**Ultimate(m)**
B-1	X Y	11.0 11.2	13.4 13.8	6.0 6.0	0.9 0.9	3.2 2.8
B-2	X Y	9.0 9.0	13.6 13.6	6.0 6.0	0.8 0.8	3.0 3.0
B-2A	X Y	8.0 8.0	10.0 10.0	6.0 6.0	0.9 0.9	2.2 2.2
B-3	X Y	22.0 20.0	36.5 33.0	6.0 6.0	0.8 0.7	4.5 5.2
B-3A	X Y	17.0 10.0	25.0 15.1	6.0 6.0	0.8 0.7	3.8 3.4
B-4	X Y	6.5 6.5	8.2 8.4	5.4 5.4	0.9 0.9	3.2 2.7

** % of Seismic Weight*

+ Corresponding to strength design (divide by 1.4 for allowable stress design)

ductility of the building. This varies from 2.4 to 3.8 for all buildings except buildings 3 and 3A. Ductility of buildings 3 and 3A are 5.6 and 4.9, respectively.

For buildings 2 and 2A, pushover analysis is carried out in the building X direction only. Since the two wings of these L-shaped buildings are identical, switching the pushover direction to the building Y direction will simply have the effect of swapping the responses of the two wings. As expected, both the ultimate strength and the ultimate roof displacement for building 2A are smaller than for building 2. However, they seem to be disproportionately smaller when compared to the ratio of the steel weights used in the two cases ($\frac{89.5}{86.9} = 1.03$ compared to ultimate strength ratio of $\frac{13.6}{10.0} = 1.36$ and ultimate roof displacement ratio of $\frac{3.0}{2.2} = 1.36$). This is because only a fraction of this steel actually goes into beams with the rest going into columns and floor framing that are more or less the same in the two cases. The performance of building 2A is not necessarily worse than that of building 2 and in fact it is the other way around when the peak displacements and permanent roof offsets are compared. Thus, pushover analyses while giving a good benchmark for structure strength and ductility could be quite misleading when used to compare building performance and should be used with great care and discretion.

The ultimate strength of building 3A in the X direction was 25% of its seismic weight (compared to 37% in the case of building 3) while it was just 15% in the Y direction (compared to 33% in the case of building 3). This is consistent with the lower amount of steel used in building 3A compared to building 3. As expected, twisting was observed in both buildings in the Y direction pushover while it was not observed in the X direction pushover.

The lower ultimate strengths of about 8.2% in the X direction and 8.4% in the Y direction of building 4 are consistent with the fact that a lower amount of steel was used as a result of smaller design forces arising out of the "regularity" classification of the structure.

Significant twisting is observed only in the case of buildings 3, 3A and 4 when pushed in the building Y direction, consistent with the torsional eccentricity in these buildings.

9.4 Description of Ground Motion Records

The ground motions used in this work include the January 17, 1994, Northridge earthquake ($M_w = 6.7$) Sylmar station record, the September 16, 1978, Iran earthquake ($M_w = 7.3$)

Tabas record, and the January 17, 1995, Kobe earthquake ($M_w = 6.9$) Takatori record. These records were picked for the analysis as all three are near-source records with a distance to source of less than 5 km. In addition, these records are representative of the potential magnitude 7.0 earthquake that could occur on the Elysian Park fault running underneath Los Angeles downtown which has many moment frame buildings in the height range of interest ($\cong$ 20 stories). The displacement and velocity plots of the strong horizontal component of each of these three near-source earthquakes consist of large-amplitude, long-period pulses. The effect of these pulses on tall buildings is of great interest and this was the primary motivation for selecting these records for performance analysis of the 6 buildings. Plots of the acceleration, velocity, and displacement time histories are given in Figures 9.1 through 9.3. Also plotted on these figures are the spectra of the pseudo-acceleration response [14] of a single degree of freedom oscillator with 2% and 5% damping and the UBC97 [33] response spectrum used in the design for comparison. Since the strong component of the horizontal ground motion could be oriented in any direction, two sets of analyses were carried out for each ground motion, one with the strong component oriented in the building X-direction and the other with the strong component oriented in the building Y-direction. In each instance, the building was accelerated by all three components of the ground motion simultaneously. The strong components are NS for the Sylmar record, 74° Azimuth (approximately EW) for the Tabas record and EW for the Takatori record.

9.5 Description of Output Quantities and Performance Criteria

There are various performance indicators that can be used to judge the performance of buildings during earthquakes. Two of the most common performance indicators are the maximum inter-story drift ratio and the plastic rotations observed at the ends of beams and columns and at panel-zones.

As described in the previous chapter, inter-story drift ratio is the difference in the displacements of the top and bottom of the story normalized by the story height. Large drifts indicate a greater potential for damage to non-structural components. During large earthquakes, the code requires the inelastic drift to be less than 0.02 to prevent excessive $P - \Delta$ effects from threatening the stability of the structure. The time-histories of the

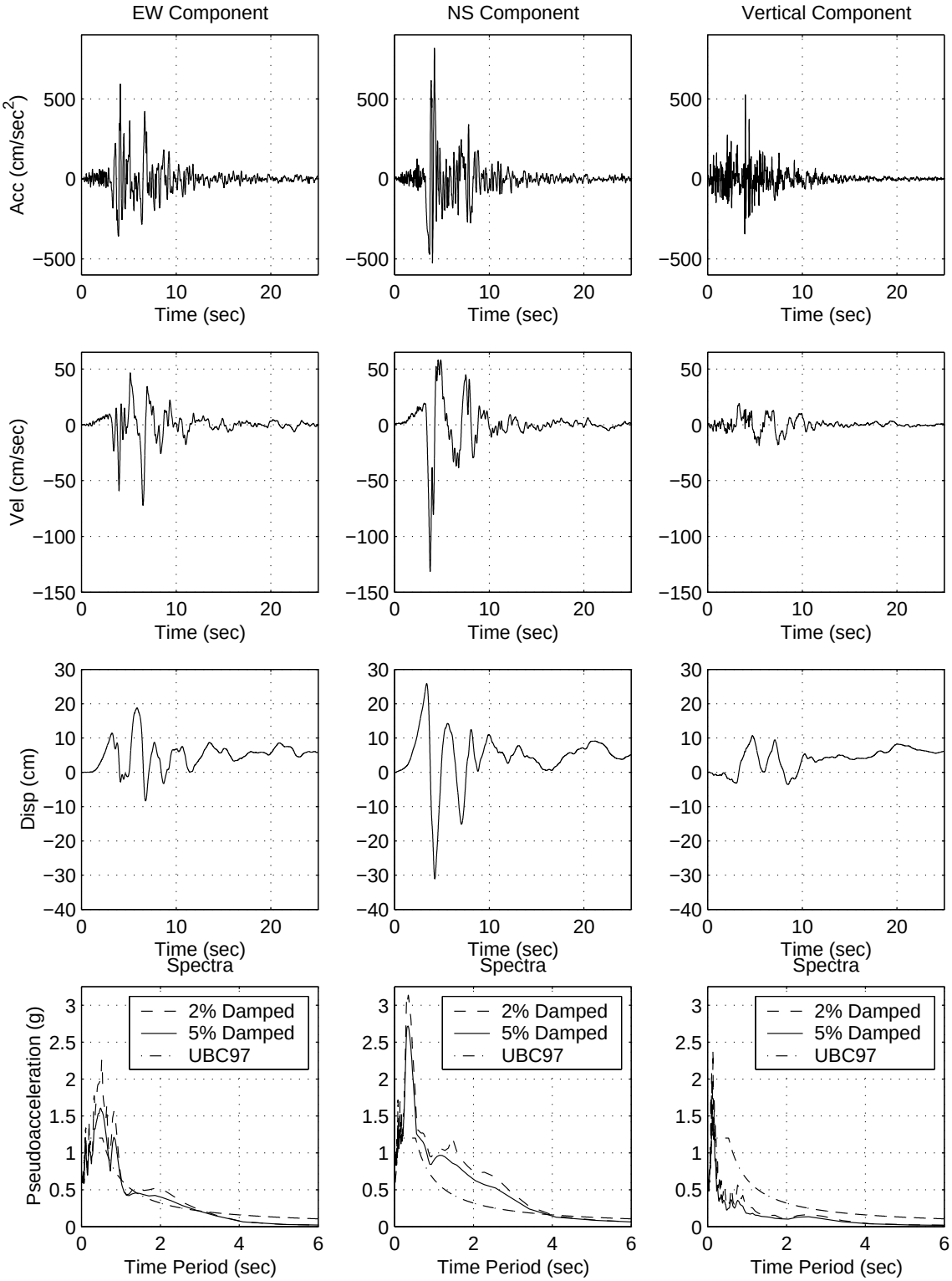

Figure 9.1: 1994 Northridge Earthquake Sylmar Station Acceleration, Velocity, Displacement and Response Spectra

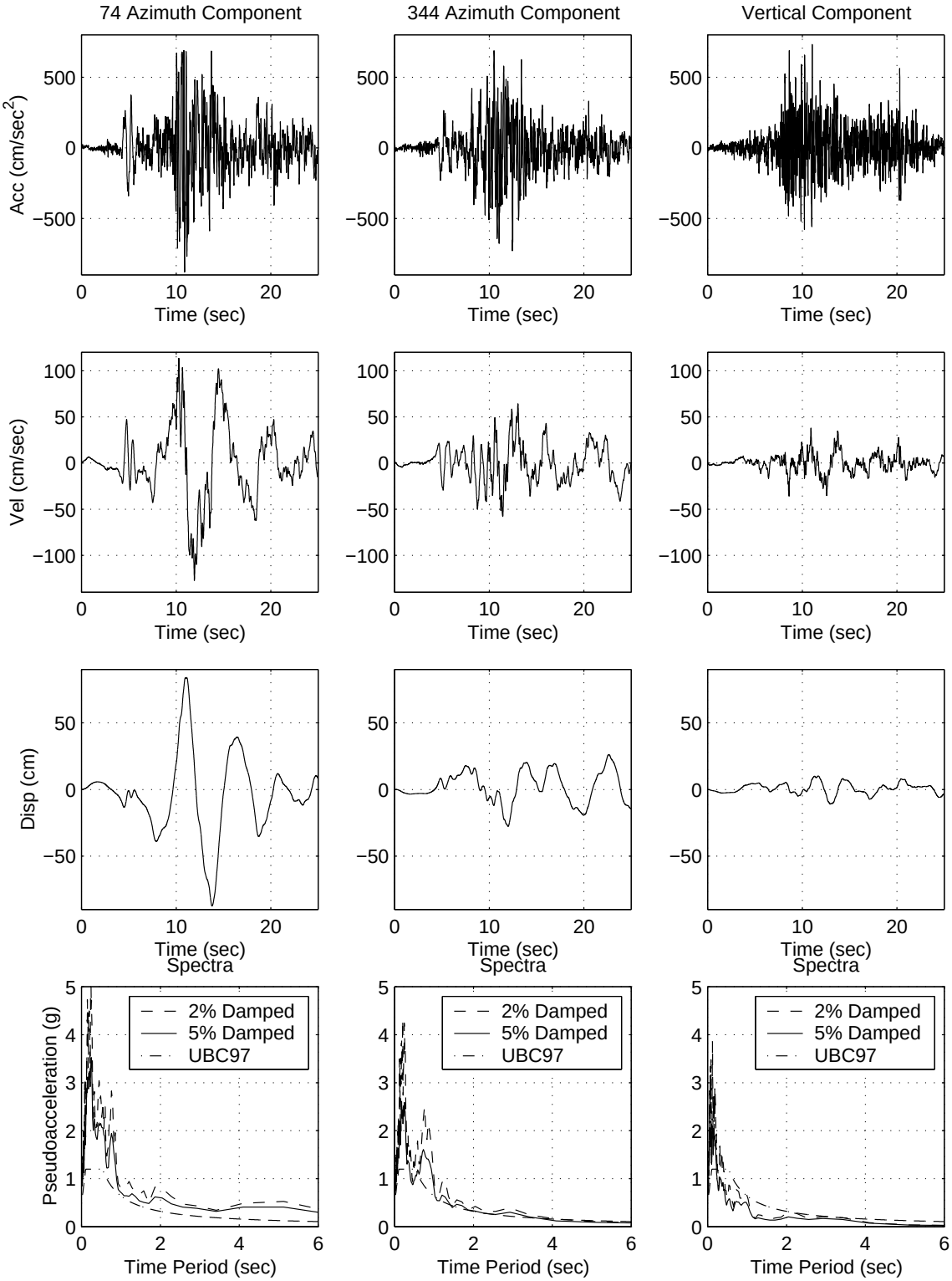

Figure 9.2: 1978 Iran Earthquake Tabas Station Acceleration, Velocity, Displacement and Response Spectra

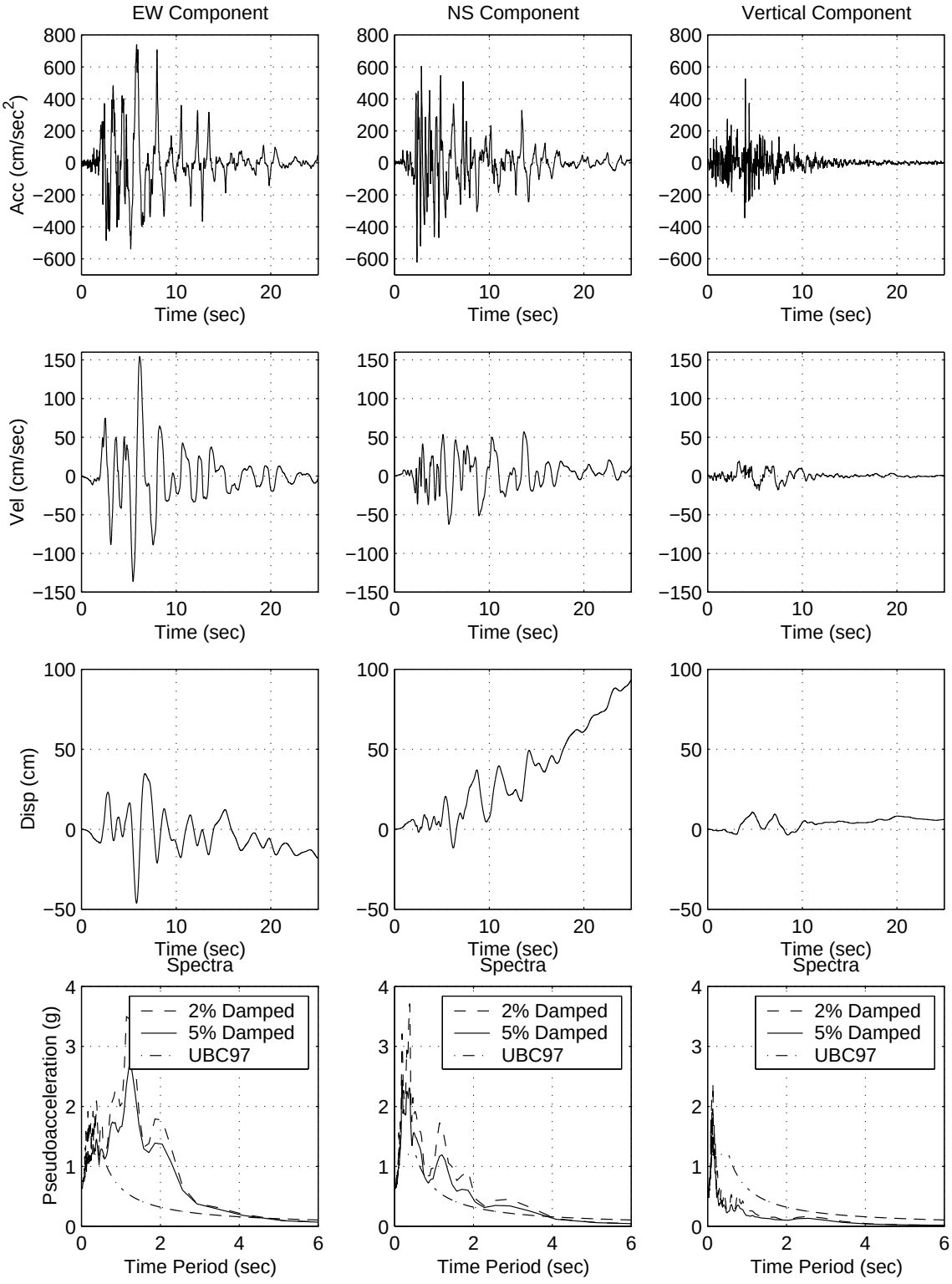

Figure 9.3: 1995 Kobe Earthquake Takatori Station Acceleration, Velocity, Displacement and Response Spectra

floor/roof displacements and inter-story drift ratios observed at two diagonally opposite corners of the building (for example, grid-line intersections F-1 and A-7 in the case of building 1) are presented in Appendix F for each analysis of the 6 buildings. The multiple plots shown in each plot-box of the figures correspond to the 19 above-ground floor/roof levels in the case of displacements and the 19 stories in the case of drifts. The peak roof displacements, peak inter-story drift ratios and the permanent roof displacements extracted from these figures are listed in Table 9.3 for each building and each ground motion record.

The peak X and Y drifts occurring over the height of each building during each analysis run are depicted in bar diagrams in Appendix G. These diagrams give an insight into regions of maximum strain in the buildings during these earthquakes.

Plastic rotation at the ends of beams and columns is defined as the permanent rotation after unloading the element that has yielded in flexure and is measured in *radians* or % of a *radian*. Panel-zone plastic rotation is defined as the unrecoverable permanent shear strain in the joint and is also measured in *radians* or % of a *radian*. Excessive plastic rotations in the panel zones, beams and columns indicate damage and structural degradation (not included in the present analysis), important factors in collapse potential. These plastic rotations can be compared against the structural performance levels set by the Federal Emergency Management Agency in its document titled "Seismic Rehabilitation Prestandard", FEMA-356 [22], formerly FEMA-273 [21] and FEMA-274 [20]. Even though this document is meant for the seismic rehabilitation of existing buildings, the performance standards are applicable to new structures as well and these are utilized here for comparison in the absence of more suitable specifications regarding damage levels. The three structural performance levels specified in FEMA-356 are Collapse Prevention, Life Safety, and Immediate Occupancy in decreasing order of structural damage. The acceptable limits, prescribed in FEMA-356 [22], for plastic rotations in beams, columns, and panel zones in steel moment frames for each of the performance levels are given in Table 9.4. In Table 9.4, b is flange width, t_f if flange thickness, h is section depth, t_w is web thickness, F_{ye} is expected yield strength of material, Z is plastic section modulus, l_b and I_b are beam length and moment of inertia, respectively, l_c and I_c are column length and moment of inertia, respectively, E and G are the material elastic and shear moduli, P is axial load on column, P_{CL} is the lower bound compression strength of the column, P_{ye} is expected axial yield force of column and τ_y is the shear yield stress of the panel zone. The ranges indicated in the table for the yield

Table 9.3: Building Peak Roof Displacements^{+} (δ_{peak}^{roof}), Peak Inter-Story Drift Ratios^{+} (Δ_{peak}) & Permanent Roof Displacements^{+} (δ_{perm}^{roof})

Building ID	**Response Quantity**	**Ground Motion Record**					
		Sylmar $[X]^{*}$	**Sylmar** $[Y]^{**}$	**Tabas** $[X]^{*}$	**Tabas** $[Y]^{**}$	**Takatori** $[X]^{*}$	**Takatori** $[Y]^{**}$
B-1	$\delta_{peak}^{roof}(m)$	0.80	0.90	2.00	1.90	1.30	1.20
	Δ_{peak}	0.030	0.028	0.054	0.048	0.054	0.046
	δ_{perm}^{roof}	0.2	0.2	0.9	0.9	0.7	0.5
B-2	$\delta_{peak}^{roof}(m)$	0.80	0.80	2.10	2.10	1.10	1.10
	Δ_{peak}	0.026	0.026	0.050	0.050	0.042	0.042
	δ_{perm}^{roof}	0.1	0.1	0.9	0.9	0.5	0.5
B-2A	$\delta_{peak}^{roof}(m)$	0.75	0.75	2.30	2.30	0.85	0.85
	Δ_{peak}	0.030	0.030	0.053	0.053	0.047	0.047
	δ_{perm}^{roof}	0.1	0.1	0.8	0.8	0.2	0.2
B-3	$\delta_{peak}^{roof}(m)$	0.95	1.20	1.20	2.00	1.40	1.50
	Δ_{peak}	0.024	0.033	0.023	0.033	0.043	0.040
	δ_{perm}^{roof}	0.1	0.3	0.3	0.3	0.4	0.4
B-3A	$\delta_{peak}^{roof}(m)$	1.10	1.30	1.30	2.60	1.00	1.10
	Δ_{peak}	0.028	0.046	0.030	0.056	0.052	0.062
	δ_{perm}^{roof}	0.2	0.1	0.4	0.8	0.4	0.4
B-4	$\delta_{peak}^{roof}(m)$	0.85	0.90	2.40	2.60	1.00	1.00
	Δ_{peak}	0.034	0.037	0.061	0.065	0.047	0.053
	δ_{perm}^{roof}	0.2	0.2	0.9	1.2	0.3	0.5

** Strong ground motion component in building X direction*
*** Strong ground motion component in building Y direction*
+ In the direction of the strong component of the earthquake

Table 9.4: Acceptance Criteria for Structural Elements at Various Structural Performance Levels

Component	Yield Rotation, θ_y	Plastic Rotation Limits [22]		
		Immediate Occupancy S-5 (IO)	Life Safety S-3 (LS)	Collapse Prevention S-1 (CP)
Beams with $\frac{b}{2t_f} < \frac{52}{\sqrt{F_{ye}}}$ and $\frac{h}{t_w} <= \frac{418}{\sqrt{F_{ye}}}$	$\frac{ZF_{ye}l_b}{6EI_b} = 0.5 - 1.1\%$	θ_y	$6\theta_y$	$8\theta_y$
Columns with $\frac{b}{2t_f} < \frac{52}{\sqrt{F_{ye}}}$, $\frac{h}{t_w} < \frac{300}{\sqrt{F_{ye}}}$ & $\frac{P}{P_{CL}} < 0.20$	$\frac{ZF_{ye}l_c}{6EI_c(1-\frac{P}{P_{ye}})} = 0.3 - 0.5\%$	θ_y	$6\theta_y$	$8\theta_y$
Columns with $\frac{b}{2t_f} < \frac{52}{\sqrt{F_{ye}}}$, $\frac{h}{t_w} < \frac{300}{\sqrt{F_{ye}}}$ & $0.2 <= \frac{P}{P_{CL}} < 0.50$	$\frac{ZF_{ye}l_c}{6EI_c(1-\frac{P}{P_{ye}})} = 0.15 - 0.4\%$	$0.25\theta_y$	$8\theta_y\,(1 - 1.7\frac{P}{P_{CL}})$	$14\theta_y\,(1 - 1.7\frac{P}{P_{CL}})$
Panel Zones	$\frac{\tau_y}{G} = 0.25\%$	θ_y	$8\theta_y$	$11\theta_y$

rotation, θ_y, correspond to the beam and column sections used in the 6 buildings.

For each moment frame in each building, plastic rotation maps are presented in Appendix H corresponding to each analysis run. Each map consists of a moment frame depicting peak plastic rotations occurring at the ends of beams and columns (solid black squares) and panel zones (plain white squares) in % of a *radian*. Each map also depicts a scale showing the size of these squares corresponding to 1%, 2%, 3%, 4% and 5% plastic rotations. The moment frames are labeled on the plans of the six buildings (Figures 8.2, 8.4, 8.7, 8.9 and 8.10). Also presented in Appendix H are tables listing the plastic hinges in beams and columns about their major and minor axes, and in panel zones. The tables list the number of plastic hinges with peak plastic rotations in the following ranges: $< 0.1\%, (0.1-1.0]\%, (1.0-2.0]\%, (2.0-3.0]\%, (3.0-4.0]\%, (4.0-5.0]\%, and (5.0-6.0]\%$. For example, building 1 has a total of 361 moment frame beams, with a total of 1444 possible beam hinges, half of these due to bending about the major axis and the other half due to bending about the minor axis. The peak plastic rotations observed in these 1444 possible hinges are summarized in Tables H.1 (major axis bending) and H.2 (minor axis bending).

In the case of corner columns, peak plastic rotations due to biaxial bending, about both axes of symmetry of the box section are included in the table corresponding to major axis bending. For example, building 1 has a total of 570 columns (including gravity columns), with a total of 2280 possible column hinges. Out of these 570 columns, 152 are corner columns with box sections undergoing biaxial bending. Thus, there are 1444 possible major

axis hinges and 836 possible minor axis hinges. The peak plastic rotations observed in these 2280 possible hinges are summarized in Tables H.3 (major axis bending) and H.4 (minor axis bending).

Each joint could have a single panel zone or two panel zones based on whether the column is undergoing uniaxial or biaxial bending. In the case of building 1, there are 570 panel zones and the peak plastic rotations observed in these are summarized in Table H.5. Similar data is presented for the remaining five buildings as well in Tables H.10 through H.30.

As seen in the plastic hinge maps and the plastic rotation tables, there is very little column yielding in all the cases. Thus, it is the beam and panel zone peak plastic rotations that dictate the building performance level in accordance with the FEMA criteria (Table 9.4). To this end, Tables 9.5 and 9.6 summarize the number of beam and panel zone hinge locations with plastic rotations in various ranges in relation to the yield rotation, θ_y, for all six buildings. Finally, comparing this data with the FEMA performance criteria (Table 9.4), the performance of each building is classified as IO (Immediate Occupancy), LS (Life-Safe), CP (Collapse Prevention), or CO (Collapsed).

Table 9.5: Classification of Building Performance Based on Beam Major Axis Yielding: Number of locations with peak plastic rotation in each of six ranges

Bldg. ID	Ground Motion	Plastic Rotation						Perf. Level
		IO#	LS#			CP#	CO#	
		$\leqslant \theta_y$	$(\theta_y, 3\theta_y]$	$(3\theta_y, 5\theta_y]$	$(5\theta_y, 6\theta_y]$	$(6\theta_y, 8\theta_y]$	$> 8\theta_y$	
B-1	Sylmar $[X]^*$	702	20	0	0	0	0	LS
	Sylmar $[Y]^+$	642	80	0	0	0	0	LS
	Tabas $[X]^*$	491	161	70	0	0	0	LS
	Tabas $[Y]^+$	512	120	75	13	2	0	CP
	Takatori $[X]^*$	479	241	2	0	0	0	LS
	Takatori $[Y]^+$	509	207	6	0	0	0	LS
B-2	Sylmar $[X]^*$	736	24	0	0	0	0	LS
	Tabas $[X]^*$	579	135	37	9	0	0	LS
	Takatori $[X]^*$	642	112	6	0	0	0	LS
B-2A	Sylmar $[X]^*$	744	16	0	0	0	0	LS
	Tabas $[X]^*$	517	196	47	0	0	0	LS
	Takatori $[X]^*$	511	248	1	0	0	0	LS
B-3	Sylmar $[X]^*$	518	14	0	0	0	0	LS
	Sylmar $[Y]^+$	503	25	4	0	0	0	LS
	Tabas $[X]^*$	468	64	0	0	0	0	LS
	Tabas $[Y]^+$	490	36	6	0	0	0	LS
	Takatori $[X]^*$	457	60	9	0	6	0	CP
	Takatori $[Y]^+$	465	59	8	0	0	0	LS

** Strong ground motion component in building X direction*

+ Strong ground motion component in building Y direction

 # IO:Immediate Occupancy LS:Life-Safe CP:Collapse Prevented CO:Collapsed

Table 9.5: Classification of Building Performance Based on Beam Major Axis Yielding: Number of locations with peak plastic rotation in each of six ranges

Bldg. ID	Ground Motion	Plastic Rotation						Perf. Level
		IO#	LS#			CP#	CO#	
		$\leqslant \theta_y$	$(\theta_y, 3\theta_y]$	$(3\theta_y, 5\theta_y]$	$(5\theta_y, 6\theta_y]$	$(6\theta_y, 8\theta_y]$	$> 8\theta_y$	
B-3A	Sylmar $[X]^*$	514	18	0	0	0	0	LS
	Sylmar $[Y]^+$	520	12	0	0	0	0	LS
	Tabas $[X]^*$	476	56	0	0	0	0	LS
	Tabas $[Y]^+$	412	117	3	0	0	0	LS
	Takatori $[X]^*$	449	72	6	2	3	0	CP
	Takatori $[Y]^+$	428	97	6	1	0	0	LS
B-4	Sylmar $[X]^*$	673	87	0	0	0	0	LS
	Sylmar $[Y]^+$	694	66	0	0	0	0	LS
	Tabas $[X]^*$	486	149	118	6	1	0	CP
	Tabas $[Y]^+$	462	191	100	7	0	0	LS
	Takatori $[X]^*$	512	235	13	0	0	0	LS
	Takatori $[Y]^+$	541	206	13	0	0	0	LS

** Strong ground motion component in building X direction*

+ Strong ground motion component in building Y direction

 # IO:Immediate Occupancy LS:Life-Safe CP:Collapse Prevented CO:Collapsed

Table 9.6: Classification of Building Performance Based on Panel Zone Yielding: Number of locations with peak plastic rotation in each of six ranges

Bldg. ID	Ground Motion	Plastic Rotation						Perf. Level
		IO#	LS#			CP#	CO#	
		$\leqslant \theta_y$	$(\theta_y, 3\theta_y]$	$(3\theta_y, 6\theta_y]$	$(6\theta_y, 8\theta_y]$	$(8\theta_y, 11\theta_y]$	$> 11\theta_y$	
B-1	Sylmar $[X]^*$	379	149	42	0	0	0	LS
	Sylmar $[Y]^+$	413	131	26	0	0	0	LS
	Tabas $[X]^*$	365	100	105	0	0	0	LS
	Tabas $[Y]^+$	368	125	75	2	0	0	LS
	Takatori $[X]^*$	374	115	66	11	4	0	CP
	Takatori $[Y]^+$	402	84	78	6	0	0	LS
B-2	Sylmar $[X]^*$	297	126	67	4	0	0	LS
	Tabas $[X]^*$	261	106	54	42	24	7	CO
	Takatori $[X]^*$	277	84	112	12	6	3	CO
B-2A	Sylmar $[X]^*$	330	135	29	0	0	0	LS
	Tabas $[X]^*$	253	157	84	0	0	0	LS
	Takatori $[X]^*$	283	149	49	8	5	0	CP
B-3	Sylmar $[X]^*$	237	53	46	4	2	0	CP
	Sylmar $[Y]^+$	206	102	21	7	6	0	CP
	Tabas $[X]^*$	232	19	74	17	0	0	LS
	Tabas $[Y]^+$	168	69	95	10	0	0	LS
	Takatori $[X]^*$	188	73	54	11	7	9	CO
	Takatori $[Y]^+$	186	63	56	26	3	8	CO

** Strong ground motion component in building X direction*

+ Strong ground motion component in building Y direction

 # IO:Immediate Occupancy LS:Life-Safe CP:Collapse Prevented CO:Collapsed

Table 9.6: Classification of Building Performance Based on Panel Zone Yielding: Number of locations with peak plastic rotation in each of six ranges

Bldg. ID	Ground Motion	Plastic Rotation						Perf. Level
		IO#	LS#			CP#	CO#	
		$\leqslant \theta_y$	$(\theta_y, 3\theta_y]$	$(3\theta_y, 6\theta_y]$	$(6\theta_y, 8\theta_y]$	$(8\theta_y, 11\theta_y]$	$> 11\theta_y$	
B-3A	Sylmar $[X]^*$	207	107	28	0	0	0	LS
	Sylmar $[Y]^+$	239	96	7	0	0	0	LS
	Tabas $[X]^*$	197	88	57	0	0	0	LS
	Tabas $[Y]^+$	137	105	67	19	8	6	CO
	Takatori $[X]^*$	197	82	45	10	8	0	CP
	Takatori $[Y]^+$	143	119	71	9	0	0	LS
B-4	Sylmar $[X]^*$	248	165	43	0	0	0	LS
	Sylmar $[Y]^+$	227	177	52	0	0	0	LS
	Tabas $[X]^*$	202	106	136	12	0	0	LS
	Tabas $[Y]^+$	188	128	110	25	5	0	CP
	Takatori $[X]^*$	203	194	59	0	0	0	LS
	Takatori $[Y]^+$	206	143	107	0	0	0	LS

** Strong ground motion component in building X direction*

+ Strong ground motion component in building Y direction

 # IO:Immediate Occupancy LS:Life-Safe CP:Collapse Prevented CO:Collapsed

In the case of buildings with reentrant corners, it has been hypothesized that there could be stress concentration in the horizontal diaphragms in the vicinity of the reentrant corners. So, it is of interest to study the stress-distribution in the plane-stress elements and the beams in buildings 1, 2 and 2A. The principal tensile and compressive occurring in the plane-stress elements at the second, ninth and Lower Mechanical floors in these buildings during each earthquake are shown in stress maps in Appendix I. To further see whether there is stress concentration, the peak slab stress at the reentrant corner (comprising of the 3 plane-stress elements that create the corner) is compared against the peak slab stress elsewhere. Similarly, the peak axial stress ($\frac{P}{A}$) in the two moment frame beams at the reentrant corner is compared against the peak axial stress in the remaining moment frame beams. This data is listed in Table 9.7 for each building, for each ground motion.

Table 9.7: Building Stresses at Reentrant Corners

Bldg. ID	Ground Motion	Stresses (psi)							
		Peak Principal Stresses in Slab				Peak Axial Stress in MF Beam			
		Tensile		Compressive		Tensile		Compressive	
		Corner	Elsewhere	Corner	Elsewhere	Corner	Elsewhere	Corner	Elsewhere
B-1	Sylmar $[X]^*$	286.1	194.1	322.0	207.5	3504.4	1951.8	3314.5	1888.1
	Sylmar $[Y]^+$	279.9	183.8	291.5	199.3	2987.1	1816.1	2994.8	1875.8
	Tabas $[X]^*$	471.1	276.9	569.0	278.6	4604.8	2899.9	4292.2	2352.5
	Tabas $[Y]^+$	348.9	354.6	399.4	339.8	4278.13	3003.78	4021.3	1835.1
	Takatori $[X]^*$	364.8	256.8	388.1	255.3	4160.8	2931.9	3979.5	1949.4
	Takatori $[Y]^+$	391.4	245.0	401.2	247.8	3560.4	3053.4	3380.5	2175.6
B-2	Sylmar $[X]^*$	209.7	223.6	246.4	431.8	2592.6	10707.2	2510.0	2191.7
	Tabas $[X]^*$	249.0	257.4	298.8	496.5	10310.3	14221.8	2773.1	2361.1
	Takatori $[X]^*$	221.7	258.7	306.7	264.3	3006.7	10154.9	3506.5	2577.9
B-2A	Sylmar $[X]^*$	259.8	249.7	247.2	212.4	3006.3	2467.1	2184.8	1989.6
	Tabas $[X]^*$	245.4	236.2	246.6	594.1	2957.7	12584.9	2287.2	1808.5
	Takatori $[X]^*$	277.2	237.2	213.3	254.8	3850.11	6916.8	2404.1	2240.9

** Strong ground motion component in building X direction*
+ Strong ground motion component in building Y direction

Key element and structure response time histories are plotted for various ground motion cases in Appendix J. Response quantities include structure base shear in X and Y directions, beam and column end moments, panel zone moments, and column axial forces.

9.6 Analyses Results

In this section, the results of the ground motion analyses of the six buildings are discussed in terms of plastic rotations, drifts, and stress concentration. In addition, the performance of buildings 2A and 3A is compared against buildings 2 and 3, respectively.

9.6.1 Plastic Rotations and Building Performance

Significant yielding was observed in beams and panel zones in almost all cases. Column yielding was minimal validating the strong column-weak beam criterion of the code (Section 8.2.20). The yielding in the beams and panel zones indicate that in a number of instances, the buildings were not deemed life-safe. In fact, in a few cases such as building 2 subjected

to the Tabas and Takatori records, the panel zone plastic rotations exceeded collapse prevention limits. Thus, on the whole the code may not achieve its Life Safety objective for 20-story moment frame buildings subjected to these near-source magnitude 6.7-7.3 earthquakes. This also indicates that the near-source factors (Section 8.2.3) to account for the special features of near-source ground motion, incorporated into the code recently, may be inadequate. It should be noted that these conclusions are based on analyses that do not include any strength degradation from weld fractures, etc. This is significant since experiments performed on large beam sections [18] indicate fractures and consequent failure of section at plastic rotations of less than 3% of a *radian* (pre-Northridge moment connections were used in these experiments). The plastic rotation demands on these buildings during these large earthquakes from these analyses are far greater and vary up to 6% of a *radian*.

Of all the buildings, buildings 1 and 2A perform the best (Life-safe in all cases except one) while buildings 2 and 3 perform the worst (Collapse in two cases) going purely by the magnitude of the plastic rotation compared against the FEMA performance criteria. Buildings 1 and 2A exhibit an equitable distribution of yielding between beams and panel zones, while yielding in panel zones is much greater than in beams in the remaining buildings.

Of the three records, the Tabas record is the most damaging to buildings 1, 2, 3A, and 4 while the Takatori record is the most damaging to buildings 2, 2A, 3 and 3A. Sylmar record is quite severe on building 3.

In almost all the cases, the nonlinear response in terms of plastic rotations in beams, columns and panel zones gets localized in one or two regions over the height of the building. This yield localization leads to a kink in the building and it oscillates about a skewed axis instead of the vertical axis, leading to a permanent tilt in the building at the end of the event. This focussed severe demand on certain portions (stories) of the building during these near-source earthquakes is not accounted for by the code, at present. The seismic drift criterion (Section 8.2.14) indirectly addresses this issue since excessive yielding is bound to lead to excessive drifts. However, the elastic response spectral analysis required by the code cannot capture this localization effect and although the spectral drifts are restricted to the specified limit, this effect leads to far greater yields during real events as discussed in the next section.

Buildings 3 and 3A have a torsional plan irregularity. This leads to considerable twisting especially when the strong component is in the building Y direction. The greater damage

observed in just two of the four frames (along grids A & D) in all the cases indicates that the twisting component of the structure response is far greater than the translational component. Thus, these frames (along grids A & D) are performing double duty of resisting the translation from the X component of the ground motion and the translation resulting from twisting generated by the Y component of the ground motion. This implies a smaller effective redundancy in the system. The code (UBC97 [33]) has a redundancy requirement that ensures a minimum number of moment frame bays in each direction. It fails, however, to account for torsional sensitivity in the structure where the redundancy in each of the two principal directions is satisfactory but the effective redundancy when torsion is taken into account may be smaller than in each of the two principal directions. This redundancy criterion in the code needs to be extended to include torsionally sensitive buildings.

In general, the damage to building 4 in the cases with the strong component of the ground motion in the building Y direction is more severe. This is expected for two reasons - firstly, the eccentricity due to the uneven mass and stiffness distribution causes twisting in the building that is proportional to the Y direction accelerations and the stronger component being in Y direction would cause greater twisting; secondly, lateral loads cannot be transferred as efficiently to the atrium frame along grid 1 (in the Y direction) through the horizontal bracing when compared with a floor diaphragm. Therefore, a greater proportion of the lateral load is carried by the frame along grid 6, thus making it more susceptible to damage. This problem does not exist in the X direction since both the frames (along grids A and F) are well connected into a diaphragm and hence load transfer is efficient.

9.6.2 Building Drifts

Peak inter-story drift ratios in all the buildings vary between 0.028 and 0.046 in the case of the Sylmar record, between 0.023 and 0.065 in the case of the Tabas record, and between 0.040 and 0.062 in the case of the Takatori record. These drifts are all far greater than the inelastic drift limit of 0.02 prescribed by the code. These large drifts can be expected to cause severe damage to non-structural components such as facades and interior dry wall, and could lead to alignment problems for doors and windows. All buildings exhibit permanent offsets from the vertical line of plumb due to severe yielding. The permanent offsets at the roof vary between $0.1m$ and $1.0m$. Significant twisting is observed in buildings 3, 3A, and 4 as evident from the difference in the drifts observed at two diagonally opposite corners

of the buildings. An interesting observation in the case of building 4 is that in the case of the Sylmar record analysis with strong component in the Y direction, the peak drift at one corner (A-1) is 0.037 while it is 0.02 at the diagonally opposite corner (F-6). Thus, the drift at A-1 is 1.3 times the average of the story drifts at A-1 and F-6 which is greater than the factor of 1.2 beyond which the code would classify this building to be irregular. Thus, the linear dynamic analysis of this structure does not really capture the torsional plan irregularity. Recall that this building was classified as regular per the code and designed as such to a smaller design force.

9.6.3 Stress Concentration at Reentrant Corners

Based on the analyses results, there is no evidence of any significant stress concentration at the reentrant corners in the L-shaped buildings, 2 and 2A. In general the axial stresses in the moment frame beams are far greater than the membrane stresses in the plane-stress elements. The corner elements in building 1 do experience greater stresses than the other elements, but this is most likely due to the necking (narrowing/pinching) of the plan area at the corner locations. Thus, stress concentration observed at corners in solid elements does not apply to building structures with corners, since the force transfer mechanism in a solid continuum is completely different from that in buildings which is primarily achieved through discrete lateral-load-resisting systems.

9.6.4 Performance of Building 2A in Relation to Building 2

As described in the previous chapter, building 2A has the same plan and elevation as building 2, except that it has been designed without any imposed wind drift limits. Thus, it is softer than building 2 with a longer fundamental period (4.15 *sec* compared to 3.39 *sec* for building 2). While the Tabas record seems to be slightly more severe on building 2A than on building 2 as far as peak drifts are concerned, the Sylmar and Takatori records seem to be distinctly less severe. This is because, while building 2A is softer than building 2, this also implies that its response is lower when subjected to the Sylmar and Takatori records due to the frequency content of these earthquakes not matching the softer characteristic frequency of building 2A as can be seen in the response spectra of these earthquakes (Figures 9.1 through 9.3). However, the Tabas record has a bump in its response spectrum beyond a structure period of 4 *seconds*. Of course, these spectra are based on elastic structural

response, nevertheless, they give a qualitative insight into the differences in the response of buildings 2 and 2A.

A key difference between the performance of buildings 2 and 2A is that, there is hardly any panel zone yielding observed in building 2A, but considerably greater yielding at the ends of beams. This is a direct result of reducing the moment frame beam strengths in building 2A while maintaining more or less similar columns sizes as in building 2 (Note that the reduction in seismic moments and axial forces are compensated for by the increase in $P - \Delta$ effects leading to column sizes remaining the same or even slightly bigger than in building 2). The yielding has essentially shifted from the beam-column joints to the interior of beams. The roof permanent offsets at the end of the events for building 2A are consistently less than those for building 2. This can be attributed to the greater amount of panel zone yielding in building 2 as compared to building 2A. The hypothesis that panel zone yielding leads to greater roof offsets when compared with beam-end yielding could seem intuitive and the data here certainly seems to validate this theory. However, it needs to be corroborated with lot more data. It should be mentioned here that a greater effort might be required to repair panel zones at the end of an event, since they are part of columns that carry loads many times greater than loads carried by beams. The temporary shoring of columns is in general much more expensive than that of beams. In this sense, it might be better if all the damage is sustained in the beams. However, in the case of larger earthquakes that test the structure to the ultimate limit state of collapse, it would definitely be better if the yielding is well distributed between beams, panel zones and columns. During such catastrophic events if the beams get overloaded, then they could fail completely and there could be sudden loss of stiffness in the building leading to instability and premature collapse. Thus the designer needs to carefully assess the seismic hazard of the site before making a choice one way or another.

In the worst case scenario, the overall performance of building 2 in terms of plastic rotations is beyond the Collapse Prevention limit while that of building 2A borders the Collapse Prevention limit. In this sense, building 2A seems to have performed better than building 2 for the records chosen.

9.6.5 Performance of Building 3A in Relation to Building 3

As described in the previous chapter, building 3A has the same plan and elevation as building 3, except that it has been designed without any imposed wind drift limits. Thus, it is softer than building 3 with a longer fundamental period (4.74 *sec* compared to 3.21 *sec* for building 2). Since both beam and column strengths were considerably reduced in building 3A, there is far greater yielding observed in beams, columns and panel zones in building 3A. This greater yielding is what is responsible for the far greater drifts and permanent roof offsets observed in building 3A. This is unlike in buildings 2 and 2A where the beam-stiffness and strength were reduced while maintaining the column sizes, shifting the yielding from panel zones to the ends of beams and resulting in lower permanent roof offsets in building 2A.

In both buildings, twisting as a result of the torsional eccentricity causes much greater damage than translation. This is evident from the fact that even when the strong component of the earthquake is in the building Y-direction, there is greater yielding observed in the two X-direction frames than in the Y-direction frames.

In the case of the Tabas record, the yielding is uniformly distributed in building 3, whereas there is some yield localization observed in building 3A. This is probably because there is a bump in the Tabas response spectrum about the structure period of 4.74 *sec*, i.e., the frequency characteristics of the structure match more closely with the frequency content of the Tabas record in the case of building 3A.

9.6.6 Building Yield Pattern: Pushover Analyses Vs Ground Motion Analyses

The yield patterns in the building frames during the pushover analyses (Appendix E) can be compared against the yield patterns observed in the building frames during the ground motion analyses to judge the ability of pushover analyses to predict the performance of buildings. In the case of buildings 1 and 2, the yield patterns observed in the pushover analyses compare well against those observed during the Tabas record ground motion analyses, but do not match well against those observed during the Sylmar and Takatori record ground motion analyses. In the case of building 2A, the peak yielding occurs in the height range of 18-38 m during the pushover analysis, while it occurs in the height range of 30-50

m during the Tabas record ground motion analysis. The pusohver analysis yield pattern does not match the Sylmar and Talatori ground motion analyses either. Similarly, in the case of buildings 3, 3A and 4, there is no significant correlation between the yield pattern during pushover analyses and ground motion analyses. Thus, it can be concluded that using pushover analyses to predict the performance of tall irregular buildings during strong near-source earthquakes or to check their adequacy during such events may be misleading.

Chapter 10 Summary, Conclusions and Future Direction

10.1 Summary of Research

This thesis is essentially divided into two parts. The first part (Chapters 2 through 7) describes the development of realistic and efficient computational tools to study the three-dimensional behavior of tall buildings under strong ground motion from a nearby source. The second part (Chapters 8 through 9) deals with the performance of four irregular 19-story buildings designed per the latest code (UBC97 [33]) under measured near-source strong ground motion records. The following is the summary of this thesis:

1. The theory for a three-dimensional cubic-interpolated plastic hinge element with material nonlinearity lumped at its two ends is developed. The moment-rotation relation at the plastic hinge locations is bilinear to include strain-hardening. Shear deformation is included in the formulation. The element is suitable for modeling beam-columns in framed structures where damage is localized primarily at the ends of beams and columns. Damage to the interior of the beam-columns can be modeled by dividing the member into an appropriate number of elements thus introducing plastic hinges in the interior. The element is assumed to remain elastic under shear and torsion.

2. The theory for a three-dimensional elastofiber element is developed. The elastofiber element is divided into 3 segments - two end nonlinear segments and an interior elastic segment. The nonlinear segments are further subdivided in the cross-section into a number of fibers. The axial stress-strain law of the fiber is a cubic-ellipsoidal hysteretic model that includes yielding and strain-hardening. The axial force in the segment is the sum of the axial forces in all the fibers while the moment in the segment about either major or minor axis is the sum of the product of the axial force and the distance of each fiber from the corresponding neutral axis of the cross-section. The degrees of freedom at the two interior nodes of the element are not included in the global system of equations. Instead, a local member iterative technique is adopted

to determine the displacements and rotations at these degrees of freedom from the imposed displacements and rotations at the exterior nodes, based on the extent of yielding in the fibers of the fiber segments. Once the interior degrees of freedom displacements and rotations are known, the forces in the elastic interior segment are determined by linear-elastic constitutive laws. The member iterative technique checks for force equilibrium at the two interior nodes at each iteration step. Thus, force equilibrium is maintained between the fiber segments and the elastic segment. Shear deformation is included in the formulation. The element is assumed to remain elastic under shear and torsion.

3. The theory for a three-dimensional joint element is developed. The element idealizes a joint into two orthogonal panels that form a cruciform section. All the web plates from the column that the joint is part of (the associated column) are combined into a single panel and all the flange plates from the associated column are combined to form an orthogonal panel. Apart from the node located at the center of the joint, the joint element consists of 6 attachment points at the mid-points of each side of the two panels. It is at these attachment points that beams and columns connect to the joint. The end moments and shears from the beams and columns cause a state of shear in each of the two panels and the panels can yield in shear. Two hysteretic shear stress-strain models (bilinear and linear-quadratic) are used to characterize the material behavior of the panel zones.

4. A comprehensive three-dimensional building analysis program, FRAME3D, is developed incorporating all the elements described above. The program is capable of performing nonlinear time-history analysis. Geometric nonlinearity is included in the formulation through an updated Lagrangian scheme that updates the coordinates of all the nodes and attachment points at every stage of the analysis process. In this way, $P-\Delta$ effects are automatically included. Four-noded elastic plane-stress elements are used to model floor slabs that act as diaphragms constraining the lateral force resisting frames to act as one unit. The program utilizes a global Newton-Raphson iterative scheme to march along a nonlinear path dictated by material and geometric nonlinearity to arrive at the true solution. Equilibrium is maintained at the nodes at each stage of the iteration process, within a specified force tolerance.

5. Four irregular 19-story moment frame buildings have been designed using the current building code (UBC97 [33]). Building 1 is a dumb-bell shaped residential tower with two reentrant corners. Building 2 is an L-shaped office tower with one reentrant corner. Building 3 is a rectangular office tower with torsional irregularity. The center of mass is near the center of the building while the center of resistance is located away from the center of mass, creating a torsional eccentricity. Building 4 is a rectangular mixed-use (hotel/office) tower, once again with torsional irregularity. The presence of an atrium and the $500mm$ restriction on the beam depth on the atrium face of the building causes a torsional eccentricity in the structure. Buildings 2A and 3A have the same plans and elevations as buildings 2 and 3, respectively, except that they have been designed without any limits being imposed on the wind drifts. Thus, these buildings are softer than the base buildings, 2 and 3.

6. Pushover analyses are performed on each of the six buildings and their strength and ductility are quantified. There is considerable variability in the ultimate strengths and ultimate displacements of the six buildings. Over-strength factors (defined as the ratio of the ultimate strength to the design strength) vary from 1.5 to 2.3 for all buildings except buildings 3 and 3A (over-strength factors of 5.5 and 2.5, respectively) which are torsionally sensitive. Ductility (defined here as the ratio of the roof ultimate displacement to its yield displacement) varies from 2.4 to 3.8 for all buildings except buildings 3 and 3A (ductility of 5.6 and 4.8, respectively).

7. The six buildings are subjected to strong ground motion recorded from the Iran earthquake ($M_w = 7.3$, Tabas Station) of 1978, the Northridge earthquake ($M_w = 6.7$, Sylmar Station) of 1994 and the Kobe earthquake ($M_w = 6.9$, Takatori Station) of 1995, and their performance is studied using the FRAME3D program. The data from these analyses include damage in the buildings in terms of plastic deformations at the ends of beams and columns and at joints, the nodal displacement time-histories which are used to determine the inter-story drift time-histories, the base-shear time-histories, the beam, column and joint element force histories, and diaphragm element principal stress time-histories and peak values. This data in conjunction with the pushover analyses data could be extremely useful in reviewing, validating and upgrading code design guidelines for this class of structures.

10.2 Conclusions

The conclusions of this research are as follows:

1. The plastic-hinge element is a very efficient beam-column element and can be used to perform quick preliminary nonlinear analysis of buildings and other structures. It can also be used for modeling gravity columns even in buildings where greater accuracy is desired as the gravity columns are generally not expected to experience severe strains in the nonlinear regime.

2. The elastofiber element is able to simulate true beam behavior as well as a fully discretized fiber element, as evident from calibration studies performed on the two elements, while maintaining a relatively low computational demand. In these studies, it was found that the extent of plasticity spreading into the interior segments of the fiber element depends upon the ratio of the material ultimate stress to its yield stress. When this ratio is low, there is not much plasticity spreading into the interior segments. When this ratio is high, yielding is observed in the first interior segment at each end of the element. In such cases, the response of the elastofiber element can be tuned to be as accurate as the fiber element by increasing the fiber segment length of the elastofiber element. The calibration studies indicate that for materials with low ultimate stress to yield stress ratios (less than 1.4) such as A572-Grade 50 steels, end segment lengths of 3% of the clear span are suitable while for materials with high ultimate stress to yield stress ratios (greater than 1.4) such as A36 steels, end segment lengths of 11% of the clear span are appropriate.

3. Results from a pushover analysis on a 20-story building performed using elastofiber elements for moment frame beam-columns, plastic hinge elements for gravity columns and 3-D joint elements for beam-column joints, match very well with similar analysis in two dimensions performed using fully discretized fiber elements and 2-D panel zone elements (similar to the joint elements in this work, only these are in two dimensions), thus validating the various finite elements developed in this work.

4. Results of the ground motion analyses of six 19-story buildings indicate large amounts of beam and panel zone yielding, deeming most buildings inadequate in as far as life-safety is concerned. In fact, in a few cases, such as building 2 subjected to the

Tabas and Takatori records, the panel zone plastic rotations exceed collapse prevention limits given in the FEMA-356 document [22]. Thus, on the whole, based on the FEMA performance criteria (Table 9.4), the code may not achieve its Life-Safety objective for this class of 19-story irregular steel moment-frame buildings subjected to these near-source magnitude 6.7-7.3 earthquakes. The near-source factors in the form of two numbers to account for the special features of near-source ground motion, incorporated into the code (UBC97) recently, may be inadequate to characterize the complete nature of such motion. Increasing the design forces may be an incomplete solution to handle such ground motion.

5. The ductility demand, in terms of plastic rotation at the ends of beams and columns and joints, on these buildings during this class of earthquakes is up to 6% of a radian which is far greater than a typical limiting plastic rotation of 3% associated with fracture and consequent failure of large wide-flanged steel sections during experiments (pre-Northridge moment connections were used in these experiments). If strength degradation due to fractures, etc. were to be included in the analysis, then the results would likely to be worse, as far as the ability of these buildings to withstand these earthquakes without collapse is concerned.

6. There is considerable localized yielding in almost all the cases leading to large drifts (two to three times the code inelastic drift limit of 0.02). These large drifts can be expected to cause damage to non-structural components such as facades and interior dry wall and could lead to alignment problems for doors and windows.

7. The large drifts cause significant permanent offsets at the roofs of the buildings. Post-earthquake repair in such cases would require considerable disruption and building closure is inevitable.

8. There was very little yielding observed in the columns which validates the strong-column weak-beam criterion in the code.

9. There is no evidence of any significant stress concentration at the reentrant corners in the L-shaped buildings. The corner elements in building 1 (dumb-bell shaped in plan) do experience greater stresses than the interior elements, but this is most likely due to the necking (narrowing/pinching) of the plan area at the corner locations.

10. In buildings that are L-shaped, twisting is an important factor in building response to wind since the center of action of wind forces does not coincide with the center of reaction of the resisting stiffness forces. However, this is not necessarily the case when it comes to ground shaking, since it is highly likely (from geometric considerations) that the center of action of seismic forces (the center of mass) is very close to the center of resisting (stiffness) forces, leading to minimal torsional eccentricity. In fact, a designer of an L-shaped building with a severe seismic hazard should give special consideration to this issue and distribute the lateral system stiffness such that the centers of mass and stiffness coincide.

11. In buildings that are torsionally sensitive, the engineer needs to ascertain the structural redundancy taking into account the fact that twisting activates frames in both directions simultaneously. In fact, the code redundancy requirement fails to account for torsional sensitivity in the structure while accounting for redundancy in each of the two principal directions. The greater damage observed in just two of the four frames (along grids A & D) of building 3 in all the ground motion cases indicates that these frames are performing double duty of resisting the translation from the X component of the ground motion and the translation resulting from twisting generated by the Y component of the ground motion, implying a smaller effective redundancy in the system. While the redundancy of this system may be adequate in the two principal directions as per the code guideline, when torsion is considered, this redundancy is smaller. Thus, the code criterion needs to be extended to include torsionally sensitive buildings.

12. In certain irregular buildings (such as building 4 in this study), a linear dynamic analysis does not bring out detrimental effects of the irregular features in the structure (such as the effect of the atrium, the effect of the transfer columns, etc.). For example, in the linear dynamic analysis performed on building 4, the twisting was not significant enough to deem the building "irregular" per the code criterion. But in the nonlinear analysis, the various irregular features in the building lead to greater twisting in the structural response and uneven damage on the building moment frames. Thus, a nonlinear analysis could bring out the effect of these features on structural response and a designer must use engineering judgment in deciding to go for a full-blown

analysis in cases that have a number of obvious irregular features.

13. The large differences in the yield patterns in the building frames during pushover analyses and ground motion analyses illustrate the inadequacy of pushover analysis as a tool for the performance analysis of tall irregular buildings subject to strong ground motion from large near-source earthquakes.

14. The data catalogued in this work could go a long way in understanding the nonlinear behavior of tall buildings under near-source ground motion. These data can be used in the development of future codes and tall structure design guidelines.

15. The analyses were performed on Sun Unix machines (SunOS 5.7) with 360 MHz CPU and 256 MB RAM. Buildings 1, 2, 2A, 3, 3A, and 4, consist of 4050, 3626, 3626, 2662, 2662, and 4572 degrees of freedom, respectively. Analyses were performed using 25 seconds of ground motion record spaced at 0.005 second interval (5000 dynamic steps). The computing time varied considerably for each building and each ground motion record, from 14.5 hours for building 3 subjected to the Sylmar record (with strong component in the Y direction) to about 130 hours for building 4 subjected to the Takatori record (with strong component in the Y direction).

10.3 Future Directions

1. The current study focuses on the class of 19-story moment frame buildings. Future work should be focussed on studying buildings; for example, buildings that are 40 stories high, 60 stories high, 80 stories high and 100 stories high.

2. A comprehensive database of tall buildings and their response to strong ground motion created from all these studies will help guide the future development of code documents that will ensure safer structures than the current state of the art.

3. Each of these four classes of buildings mentioned above utilize different lateral systems. To be able to realistically model these systems, the element library of FRAME3D needs to be considerably expanded. Elements for modeling braces, composite columns, reinforced concrete columns, and walls need to be developed in order to study the various tall building types.

4. Parallel computing may be required for the analysis of the super-highrise buildings within realistic computing times.

5. Improvements to the plastic hinge element would include a more realistic axial force, biaxial moment interaction relation with interaction between the major and minor axes moments considered as well and a trilinear or higher-order material model to better model the moment-rotation relation.

Appendix A Updating the Coordinates of Node and Attachment Points at a Joint

A.0.1 Node Point J

The coordinates of the node J, corresponding to the center of the joint are updated during every iteration of the solution process as follows:

$$X_J^{(l+1)}(t+\Delta t) = X_J^{(l)}(t+\Delta t) + \Delta U_{JX} \tag{A.1a}$$

$$Y_J^{(l+1)}(t+\Delta t) = Y_J^{(l)}(t+\Delta t) + \Delta U_{JY} \tag{A.1b}$$

$$Z_J^{(l+1)}(t+\Delta t) = Z_J^{(l)}(t+\Delta t) + \Delta U_{JZ} \tag{A.1c}$$

In the above, l and $l+1$ refer to the iteration number during the solution process for time step, $t+\Delta t$. The procedure for updating the coordinates of the attachment points associated with a joint is described in the next few subsections.

A.0.2 Attachment Point f

$$L_x^{(f)} = X_f^{(l)}(t+\Delta t) - X_J^{(l)}(t+\Delta t) \tag{A.2a}$$

$$L_y^{(f)} = Y_f^{(l)}(t+\Delta t) - Y_J^{(l)}(t+\Delta t) \tag{A.2b}$$

$$L_z^{(f)} = Z_f^{(l)}(t+\Delta t) - Z_J^{(l)}(t+\Delta t) \tag{A.2c}$$

$$\vec{r}_{Jf}^{(l)}(t+\Delta t) = L_x^{(f)}\vec{i} + L_y^{(f)}\vec{j} + L_z^{(f)}\vec{k} \tag{A.2d}$$

The panel zone $\bar{Y}$ and $\bar{Z}$ axes are defined by the following unit vectors:

$$\frac{\vec{V}_{\bar{Y}}}{\left|\vec{V}_{\bar{Y}}\right|} = \bar{q}_x\vec{i} + \bar{q}_y\vec{j} + \bar{q}_z\vec{k} \tag{A.3a}$$

$$\frac{\vec{V}_{\bar{Z}}}{\left|\vec{V}_{\bar{Z}}\right|} = \bar{r}_x\vec{i} + \bar{r}_y\vec{j} + \bar{r}_z\vec{k} \tag{A.3b}$$

where $\bar{q}_x$, $\bar{q}_y$ and $\bar{q}_z$ are the direction cosines of the $\bar{Y}$ axis given by equations 3.3, and $\bar{r}_x$,

$\bar{r}_y$ and $\bar{r}_z$ are the direction cosines of the $\bar{Z}$ axis given by equations 3.5.

$$\vec{\Delta\theta}_{J\bar{Y}} = \Delta\theta^B_{J\bar{Y}} \frac{\vec{V}_{\bar{Y}}}{\left|\vec{V}_{\bar{Y}}\right|} \tag{A.4a}$$

$$\vec{\Delta\theta}_{J\bar{Z}} = \Delta\theta^B_{J\bar{Z}} \frac{\vec{V}_{\bar{Z}}}{\left|\vec{V}_{\bar{Z}}\right|} \tag{A.4b}$$

Using small angle approximation,

$$\begin{aligned}\vec{r}^{(l+1)}_{Jf}(t+\Delta t) &= \vec{r}^{(l)}_{Jf}(t+\Delta t) + \vec{\Delta\theta}_{J\bar{Y}} \times \vec{r}^{(l)}_{Jf}(t+\Delta t) + \vec{\Delta\theta}_{J\bar{Z}} \times \vec{r}^{(l)}_{Jf}(t+\Delta t) \\ &= \vec{r}^{(l)}_{Jf}(t+\Delta t) + \begin{vmatrix} \vec{i} & \vec{j} & \vec{k} \\ \bar{q}_x \cdot \Delta\theta^B_{J\bar{Y}} & \bar{q}_y \cdot \Delta\theta^B_{J\bar{Y}} & \bar{q}_z \cdot \Delta\theta^B_{J\bar{Y}} \\ L^{(f)}_x & L^{(f)}_y & L^{(f)}_z \end{vmatrix} + \begin{vmatrix} \vec{i} & \vec{j} & \vec{k} \\ \bar{r}_x \cdot \Delta\theta^B_{J\bar{Z}} & \bar{r}_y \cdot \Delta\theta^B_{J\bar{Z}} & \bar{r}_z \cdot \Delta\theta^B_{J\bar{Z}} \\ L^{(f)}_x & L^{(f)}_y & L^{(f)}_z \end{vmatrix}\end{aligned} \tag{A.5}$$

Simplifying the above, we obtain

$$\begin{Bmatrix} X^{(l+1)}_f(t+\Delta t) \\ Y^{(l+1)}_f(t+\Delta t) \\ Z^{(l+1)}_f(t+\Delta t) \end{Bmatrix} = \begin{Bmatrix} X^{(l+1)}_J(t+\Delta t) \\ Y^{(l+1)}_J(t+\Delta t) \\ Z^{(l+1)}_J(t+\Delta t) \end{Bmatrix} + \left[U^{(f)}\right] \begin{Bmatrix} X^{(l)}_f(t+\Delta t) - X^{(l)}_J(t+\Delta t) \\ Y^{(l)}_f(t+\Delta t) - Y^{(l)}_J(t+\Delta t) \\ Z^{(l)}_f(t+\Delta t) - Z^{(l)}_J(t+\Delta t) \end{Bmatrix} \tag{A.6a}$$

where the coordinate update matrix $[U^{(f)}]$ is given by

$$\left[U^{(f)}\right] = \begin{bmatrix} 1 & -\bar{q}_z \cdot \Delta\theta^B_{J\bar{Y}} - \bar{r}_z \cdot \Delta\theta^B_{J\bar{Z}} & \bar{q}_y \cdot \Delta\theta^B_{J\bar{Y}} + \bar{r}_y \cdot \Delta\theta^B_{J\bar{Z}} \\ \bar{q}_z \cdot \Delta\theta^B_{J\bar{Y}} + \bar{r}_z \cdot \Delta\theta^B_{J\bar{Z}} & 1 & -\bar{q}_x \cdot \Delta\theta^B_{J\bar{Y}} - \bar{r}_x \cdot \Delta\theta^B_{J\bar{Z}} \\ -\bar{q}_y \cdot \Delta\theta^B_{J\bar{Y}} - \bar{r}_y \cdot \Delta\theta^B_{J\bar{Z}} & \bar{q}_x \cdot \Delta\theta^B_{J\bar{Y}} + \bar{r}_x \cdot \Delta\theta^B_{J\bar{Z}} & 1 \end{bmatrix} \tag{A.6b}$$

A.0.3 Attachment Point e

Similarly, the updated coordinates of attachment point e are given by

$$\begin{Bmatrix} X^{(l+1)}_e(t+\Delta t) \\ Y^{(l+1)}_e(t+\Delta t) \\ Z^{(l+1)}_e(t+\Delta t) \end{Bmatrix} = \begin{Bmatrix} X^{(l+1)}_J(t+\Delta t) \\ Y^{(l+1)}_J(t+\Delta t) \\ Z^{(l+1)}_J(t+\Delta t) \end{Bmatrix} + \left[U^{(e)}\right] \begin{Bmatrix} X^{(l)}_e(t+\Delta t) - X^{(l)}_J(t+\Delta t) \\ Y^{(l)}_e(t+\Delta t) - Y^{(l)}_J(t+\Delta t) \\ Z^{(l)}_e(t+\Delta t) - Z^{(l)}_J(t+\Delta t) \end{Bmatrix} \tag{A.7a}$$

where the coordinate update matrix $[U^{(e)}]$ is given by

$$\left[U^{(e)}\right] = \left[U^{(f)}\right] \tag{A.7b}$$

since the points e, f, and J lie on the same straight line (based on the assumption that the panel zone remains planar).

A.0.4 Attachment Points c & d

$$L_x^{(d)} = X_d^{(l)}(t+\Delta t) - X_J^{(l)}(t+\Delta t) \tag{A.8a}$$

$$L_y^{(d)} = Y_d^{(l)}(t+\Delta t) - Y_J^{(l)}(t+\Delta t) \tag{A.8b}$$

$$L_z^{(d)} = Z_d^{(l)}(t+\Delta t) - Z_J^{(l)}(t+\Delta t) \tag{A.8c}$$

$$\vec{r}_{Jd}^{(l)}(t+\Delta t) = L_x^{(d)}\vec{i} + L_y^{(d)}\vec{j} + L_z^{(d)}\vec{k} \tag{A.8d}$$

$$\vec{\Delta\theta}_{J\bar{Z}} = \Delta\theta_{J\bar{Z}}^{C}\frac{\vec{V}_{\bar{Z}}}{\left|\vec{V}_{\bar{Z}}\right|} \tag{A.9a}$$

$$\vec{\Delta\theta}_{J\bar{X}} = \Delta\theta_{J\bar{X}}\frac{\vec{V}_{\bar{X}}}{\left|\vec{V}_{\bar{X}}\right|} \tag{A.9b}$$

Using small angle approximation,

$$\begin{aligned}\vec{r}_{Jd}^{(l+1)}(t+\Delta t) &= \vec{r}_{Jd}^{(l)}(t+\Delta t) + \vec{\Delta\theta}_{J\bar{Z}} \times \vec{r}_{Jd}^{(l)}(t+\Delta t) + \vec{\Delta\theta}_{J\bar{X}} \times \vec{r}_{Jd}^{(l)}(t+\Delta t) \\ &= \vec{r}_{Jd}^{(l)}(t+\Delta t) + \begin{vmatrix} \vec{i} & \vec{j} & \vec{k} \\ \bar{r}_x \cdot \Delta\theta_{J\bar{Z}}^{C} & \bar{r}_y \cdot \Delta\theta_{J\bar{Z}}^{C} & \bar{r}_z \cdot \Delta\theta_{J\bar{Z}}^{C} \\ L_x^{(d)} & L_y^{(d)} & L_z^{(d)} \end{vmatrix} + \begin{vmatrix} \vec{i} & \vec{j} & \vec{k} \\ \bar{p}_x \cdot \Delta\theta_{J\bar{X}} & \bar{p}_y \cdot \Delta\theta_{J\bar{X}} & \bar{p}_z \cdot \Delta\theta_{J\bar{X}} \\ L_x^{(d)} & L_y^{(d)} & L_z^{(d)} \end{vmatrix}\end{aligned} \tag{A.10}$$

Simplifying the above, we obtain,

$$\begin{Bmatrix} X_d^{(l+1)}(t+\Delta t) \\ Y_d^{(l+1)}(t+\Delta t) \\ Z_d^{(l+1)}(t+\Delta t) \end{Bmatrix} = \begin{Bmatrix} X_J^{(l+1)}(t+\Delta t) \\ Y_J^{(l+1)}(t+\Delta t) \\ Z_J^{(l+1)}(t+\Delta t) \end{Bmatrix} + \left[U^{(d)}\right] \begin{Bmatrix} X_d^{(l)}(t+\Delta t) - X_J^{(l)}(t+\Delta t) \\ Y_d^{(l)}(t+\Delta t) - Y_J^{(l)}(t+\Delta t) \\ Z_d^{(l)}(t+\Delta t) - Z_J^{(l)}(t+\Delta t) \end{Bmatrix} \tag{A.11a}$$

where the coordinate update matrix $[U^{(d)}]$ is given by

$$\left[U^{(d)}\right] = \begin{bmatrix} 1 & -\bar{r}_z \cdot \Delta\theta^C_{J\bar{Z}} - \bar{p}_z \cdot \Delta\theta_{J\bar{X}} & \bar{r}_y \cdot \Delta\theta^C_{J\bar{Z}} + \bar{p}_y \cdot \Delta\theta_{J\bar{X}} \\ \bar{r}_z \cdot \Delta\theta^C_{J\bar{Z}} + \bar{p}_z \cdot \Delta\theta_{J\bar{X}} & 1 & -\bar{r}_x \cdot \Delta\theta^C_{J\bar{Z}} - \bar{p}_x \cdot \Delta\theta_{J\bar{X}} \\ -\bar{r}_y \cdot \Delta\theta^C_{J\bar{Z}} - \bar{p}_y \cdot \Delta\theta_{J\bar{X}} & \bar{r}_x \cdot \Delta\theta^C_{J\bar{Z}} + \bar{p}_x \cdot \Delta\theta_{J\bar{X}} & 1 \end{bmatrix} \tag{A.11b}$$

The updated coordinates of attachment point c are given by

$$\begin{Bmatrix} X_c^{(l+1)}(t+\Delta t) \\ Y_c^{(l+1)}(t+\Delta t) \\ Z_c^{(l+1)}(t+\Delta t) \end{Bmatrix} = \begin{Bmatrix} X_J^{(l+1)}(t+\Delta t) \\ Y_J^{(l+1)}(t+\Delta t) \\ Z_J^{(l+1)}(t+\Delta t) \end{Bmatrix} + \left[U^{(c)}\right] \begin{Bmatrix} X_c^{(l)}(t+\Delta t) - X_J^{(l)}(t+\Delta t) \\ Y_c^{(l)}(t+\Delta t) - Y_J^{(l)}(t+\Delta t) \\ Z_c^{(l)}(t+\Delta t) - Z_J^{(l)}(t+\Delta t) \end{Bmatrix} \tag{A.12a}$$

where the coordinate update matrix $[U^{(c)}]$ is given by

$$\left[U^{(c)}\right] = \left[U^{(d)}\right] \tag{A.12b}$$

since the points c, d, and J lie on the same straight line (based on the assumption that the panel zone remains planar).

A.0.5 Attachment Points a & b

By analogy to attachment points, c & d, the updated coordinates of attachment points a & b are given by

$$\begin{Bmatrix} X_a^{(l+1)}(t+\Delta t) \\ Y_a^{(l+1)}(t+\Delta t) \\ Z_a^{(l+1)}(t+\Delta t) \end{Bmatrix} = \begin{Bmatrix} X_J^{(l+1)}(t+\Delta t) \\ Y_J^{(l+1)}(t+\Delta t) \\ Z_J^{(l+1)}(t+\Delta t) \end{Bmatrix} + \left[U^{(a)}\right] \begin{Bmatrix} X_a^{(l)}(t+\Delta t) - X_J^{(l)}(t+\Delta t) \\ Y_a^{(l)}(t+\Delta t) - Y_J^{(l)}(t+\Delta t) \\ Z_a^{(l)}(t+\Delta t) - Z_J^{(l)}(t+\Delta t) \end{Bmatrix} \tag{A.13a}$$

and

$$\begin{Bmatrix} X_b^{(l+1)}(t+\Delta t) \\ Y_b^{(l+1)}(t+\Delta t) \\ Z_b^{(l+1)}(t+\Delta t) \end{Bmatrix} = \begin{Bmatrix} X_J^{(l+1)}(t+\Delta t) \\ Y_J^{(l+1)}(t+\Delta t) \\ Z_J^{(l+1)}(t+\Delta t) \end{Bmatrix} + \left[U^{(b)}\right] \begin{Bmatrix} X_b^{(l)}(t+\Delta t) - X_J^{(l)}(t+\Delta t) \\ Y_b^{(l)}(t+\Delta t) - Y_J^{(l)}(t+\Delta t) \\ Z_b^{(l)}(t+\Delta t) - Z_J^{(l)}(t+\Delta t) \end{Bmatrix} \tag{A.13b}$$

where the coordinate update matrices $[U^{(a)}]$ and $[U^{(b)}]$ are given by

$$\left[U^{(a,b)}\right] = \begin{bmatrix} 1 & -\bar{p}_z \cdot \Delta\theta_{J\bar{X}} - \bar{q}_z \cdot \Delta\theta^C_{J\bar{Y}} & \bar{p}_y \cdot \Delta\theta_{J\bar{X}} + \bar{q}_y \cdot \Delta\theta^C_{J\bar{Y}} \\ \bar{p}_z \cdot \Delta\theta_{J\bar{X}} + \bar{q}_z \cdot \Delta\theta^C_{J\bar{Y}} & 1 & -\bar{p}_x \cdot \Delta\theta_{J\bar{X}} - \bar{q}_x \cdot \Delta\theta^C_{J\bar{Y}} \\ -\bar{p}_y \cdot \Delta\theta_{J\bar{X}} - \bar{q}_y \cdot \Delta\theta^C_{J\bar{Y}} & \bar{p}_x \cdot \Delta\theta_{J\bar{X}} + \bar{q}_x \cdot \Delta\theta^C_{J\bar{Y}} & 1 \end{bmatrix} \tag{A.13c}$$

Appendix B Section Database

Section Designation	H (m)	B (m)	T_f (m)	T_w (m)	Closest AISC [1] Section
W39x20x526	1.000	0.500	0.075	0.029	W36x527
W39x20x451	1.000	0.500	0.060	0.029	W40x480
W39x20x407	1.000	0.500	0.055	0.025	W40x397
W37x20x493	0.950	0.500	0.070	0.029	W33x515
W37x20x419	0.950	0.500	0.055	0.029	W36x439
W36x20x369	0.900	0.500	0.050	0.025	W33x387
W35x24x934	0.900	0.600	0.120	0.050	Built-up
W35x24x876	0.900	0.600	0.110	0.050	Built-up
W35x20x526	0.900	0.500	0.065	0.045	W33x515
W35x20x411	0.900	0.500	0.055	0.029	W33x424
W35x20x386	0.900	0.500	0.050	0.029	W33x387
W35x20x361	0.900	0.500	0.045	0.029	W33x354
W34x20x490	0.850	0.500	0.060	0.045	W30x526
W34x20x326	0.850	0.500	0.045	0.022	W33x318
W33x20x586	0.850	0.500	0.080	0.045	W33x567
W33x20x338	0.850	0.500	0.045	0.025	W33x318
W33x18x291	0.850	0.450	0.040	0.025	W33x291
W33x18x274	0.850	0.450	0.036	0.025	W33x263
W32x20x654	0.800	0.500	0.100	0.040	Built-up
W32x20x533	0.800	0.500	0.075	0.040	W27x539
W32x20x421	0.800	0.500	0.060	0.029	W30x433
W32x20x411	0.800	0.500	0.050	0.040	W30x391
W32x20x346	0.800	0.500	0.045	0.029	W30x357
W32x20x306	0.800	0.500	0.040	0.025	W30x326
W32x16x303	0.800	0.400	0.050	0.025	W27x336
W32x18x267	0.800	0.450	0.036	0.025	W30x261
W32x16x248	0.800	0.400	0.036	0.025	W30x261
W32x16x232	0.800	0.400	0.032	0.025	W30x235
W30x20x436	0.750	0.500	0.060	0.036	W27x448
W30x20x324	0.750	0.500	0.045	0.025	W27x336
W30x20x299	0.750	0.500	0.040	0.025	W30x292
W30x16x297	0.750	0.400	0.050	0.025	W27x307

Section Designation	H (m)	B (m)	T_f (m)	T_w (m)	**Closest AISC [1] Section**
W30x20x289	0.750	0.500	0.040	0.022	W30x292
W30x20x279	0.750	0.500	0.036	0.025	W27x307
W30x16x231	0.750	0.400	0.036	0.022	W30x211
W28x20x633	0.700	0.500	0.100	0.040	Built-up
W28x20x439	0.700	0.500	0.065	0.032	W24x450
W28x20x430	0.700	0.500	0.065	0.029	W27x407
W28x20x405	0.700	0.500	0.060	0.029	W27x407
W28x20x390	0.700	0.500	0.055	0.032	W24x408
W28x20x380	0.700	0.500	0.055	0.029	W27x368
W28x20x356	0.700	0.500	0.050	0.029	W27x368
W28x22x354	0.700	0.550	0.045	0.029	W27x368
W28x18x317	0.700	0.450	0.045	0.032	W27x307
W28x18x307	0.700	0.450	0.050	0.022	W27x307
W28x20x306	0.700	0.500	0.040	0.029	W24x335
W28x20x293	0.700	0.500	0.040	0.025	W24x335
W28x16x281	0.700	0.400	0.050	0.022	W27x281
W28x20x273	0.700	0.500	0.036	0.025	W27x258
W28x20x263	0.700	0.500	0.036	0.022	W27x258
W28x18x244	0.700	0.450	0.036	0.022	W27x235
W28x16x199	0.700	0.400	0.032	0.019	W27x194
W28x14x171	0.700	0.350	0.029	0.019	W27x161
W26x20x336	0.650	0.500	0.050	0.025	W24x335
W26x20x311	0.650	0.500	0.045	0.025	W24x306
W26x18x301	0.650	0.450	0.050	0.022	W24x306
W26x18x287	0.650	0.450	0.045	0.025	W24x279
W26x20x286	0.650	0.500	0.040	0.025	W24x279
W26x16x284	0.650	0.400	0.050	0.025	W24x279
W26x20x266	0.650	0.500	0.036	0.025	W24x279
W26x18x247	0.650	0.450	0.036	0.025	W24x250
W26x16x219	0.650	0.400	0.036	0.022	W24x229
W26x18x211	0.650	0.450	0.032	0.019	W24x229
W26x16x203	0.650	0.400	0.032	0.022	W24x207
W26x16x182	0.650	0.400	0.029	0.019	W24x192
W26x14x177	0.650	0.350	0.032	0.019	W24x176
W26x14x143	0.650	0.350	0.025	0.016	W24x146
W26x12x108	0.650	0.300	0.022	0.012	W24x117
W24x24x590	0.600	0.600	0.080	0.036	W14x605
W24x24x530	0.600	0.600	0.070	0.036	W14x550

Section Designation	H (m)	B (m)	T_f (m)	T_w (m)	Closest AISC [1] Section
W24x24x423	0.600	0.600	0.055	0.029	W21x408
W24x20x297	0.600	0.500	0.045	0.022	W24x306
W24x20x271	0.600	0.500	0.040	0.022	W21x279
W24x20x260	0.600	0.500	0.036	0.025	W21x275
W24x16x257	0.600	0.400	0.045	0.025	W24x250
W24x18x250	0.600	0.450	0.040	0.022	W21x248
W24x16x249	0.600	0.400	0.045	0.022	W21x248
W24x18x241	0.600	0.450	0.036	0.025	W21x248
W24x18x232	0.600	0.450	0.036	0.022	W21x248
W24x18x223	0.600	0.450	0.032	0.025	W21x223
W24x16x213	0.600	0.400	0.036	0.022	W21x223
W24x18x206	0.600	0.450	0.032	0.019	W21x223
W24x16x205	0.600	0.400	0.036	0.019	W24x207
W24x16x189	0.600	0.400	0.032	0.019	W21x201
W24x16x177	0.600	0.400	0.029	0.019	W24x162
W24x14x172	0.600	0.350	0.032	0.019	W24x162
W24x14x161	0.600	0.350	0.029	0.019	W21x166
W22x22x457	0.550	0.550	0.065	0.036	W14x455
W22x22x393	0.550	0.550	0.055	0.032	W14x398
W22x22x349	0.550	0.550	0.050	0.025	W21x333
W22x22x294	0.550	0.550	0.040	0.025	W21x300
W22x20x253	0.550	0.500	0.036	0.025	W21x248
W22x18x237	0.550	0.450	0.040	0.019	W21x248
W22x18x234	0.550	0.450	0.036	0.025	W21x223
W22x18x219	0.550	0.450	0.036	0.019	W21x223
W22x16x223	0.550	0.400	0.040	0.022	W21x223
W22x16x216	0.550	0.400	0.040	0.019	W21x223
W22x16x200	0.550	0.400	0.036	0.019	W21x201
W22x16x184	0.550	0.400	0.032	0.019	W21x182
W22x16x172	0.550	0.400	0.029	0.019	W21x166
W22x14x156	0.550	0.350	0.029	0.019	W21x147
W22x12x150	0.550	0.300	0.032	0.019	W21x147
W20x20x389	0.500	0.500	0.060	0.036	W14x370
W20x20x381	0.500	0.500	0.060	0.032	W14x370
W20x20x364	0.500	0.500	0.055	0.036	W21x364
W20x20x356	0.500	0.500	0.055	0.032	W14x398
W20x20x324	0.500	0.500	0.045	0.040	W14x311
W20x20x307	0.500	0.500	0.045	0.032	W14x311

Section Designation	H (m)	B (m)	T_f (m)	T_w (m)	**Closest AISC [1] Section**
W20x20x285	0.500	0.500	0.045	0.022	W18x283
W20x20x266	0.500	0.500	0.040	0.025	W18x258
W20x16x202	0.500	0.400	0.036	0.022	W18x192
W20x18x196	0.500	0.450	0.032	0.019	W18x211
W20x16x195	0.500	0.400	0.036	0.019	W18x192
W20x16x188	0.500	0.400	0.036	0.016	W18x192
W20x16x172	0.500	0.400	0.032	0.016	W18x175
W20x16x167	0.500	0.400	0.029	0.019	W18x175
W20x12x164	0.500	0.300	0.036	0.022	W18x158
W20x14x155	0.500	0.350	0.032	0.016	W18x158
W20x14x144	0.500	0.350	0.029	0.016	W18x143
W20x14x130	0.500	0.350	0.025	0.016	W21x122
W20x12x98	0.500	0.300	0.022	0.012	W21x93
W18x18x291	0.450	0.450	0.050	0.029	W18x283
W18x18x274	0.450	0.450	0.045	0.032	W14x311
W18x18x247	0.450	0.450	0.040	0.029	W14x257
W18x18x215	0.450	0.450	0.036	0.022	W18x211
W18x16x174	0.450	0.400	0.032	0.019	W18x158
W18x16x162	0.450	0.400	0.029	0.019	W18x143
W18x12x152	0.450	0.300	0.036	0.019	W18x143
W18x14x140	0.450	0.350	0.029	0.016	W18x130
W18x12x140	0.450	0.300	0.032	0.019	W18x130
W18x12x131	0.450	0.300	0.029	0.019	W18x119
W16x16x281	0.400	0.400	0.055	0.032	W14x283
W16x16x249	0.400	0.400	0.045	0.036	W14x257
W16x16x211	0.400	0.400	0.040	0.025	W14x211
W16x16x195	0.400	0.400	0.036	0.025	W14x193
W16x16x190	0.400	0.400	0.036	0.022	W14x193
W16x16x174	0.400	0.400	0.032	0.022	W14x176
W16x16x169	0.400	0.400	0.032	0.019	W14x176
W16x12x114	0.400	0.300	0.025	0.019	W18x119
W16x12x109	0.400	0.300	0.025	0.016	W16x100
W16x12x92	0.400	0.300	0.022	0.012	W16x89
W14x14x175	0.350	0.350	0.036	0.029	W12x170
W14x14x165	0.350	0.350	0.036	0.022	W14x159
W14x14x156	0.350	0.350	0.032	0.025	W12x152
W14x14x151	0.350	0.350	0.032	0.022	W12x152

Section Designation	H (m)	B (m)	T_f (m)	T_w (m)	Closest AISC [1] Section
W14x14x136	0.350	0.350	0.029	0.019	W14x132
W12x12x144	0.300	0.300	0.036	0.025	W12x136
W12x12x140	0.300	0.300	0.036	0.022	W12x136
W12x12x125	0.300	0.300	0.032	0.019	W12x120
W12x12x120	0.300	0.300	0.029	0.022	W12x120
W12x12x104	0.300	0.300	0.025	0.019	W10x112
W12x12x100	0.300	0.300	0.025	0.016	W12x96
W12x12x95	0.300	0.300	0.022	0.019	W10x100
B32x32x865	0.800	0.800	0.055	0.055	Built-up
B30x30x739	0.750	0.750	0.050	0.050	Built-up
B28x28x1158	0.700	0.700	0.090	0.090	Built-up
B28x28x1103	0.700	0.700	0.085	0.085	Built-up
B28x28x871	0.700	0.700	0.065	0.065	Built-up
B28x28x749	0.700	0.700	0.055	0.055	Built-up
B28x28x622	0.700	0.700	0.045	0.045	Built-up
B26x26x802	0.650	0.650	0.065	0.065	Built-up
B26x26x747	0.650	0.650	0.060	0.060	Built-up
B26x26x690	0.650	0.650	0.055	0.055	Built-up
B26x26x633	0.650	0.650	0.050	0.050	Built-up
B26x26x574	0.650	0.650	0.045	0.045	Built-up
B24x24x632	0.600	0.600	0.055	0.055	Built-up
B24x24x580	0.600	0.600	0.050	0.050	Built-up
B24x24x527	0.600	0.600	0.045	0.045	Built-up
B24x24x473	0.600	0.600	0.040	0.040	Built-up
B22x22x479	0.550	0.550	0.045	0.045	Built-up
B22x22x455	0.550	0.550	0.045	0.040	Built-up
B22x22x430	0.550	0.550	0.040	0.040	Built-up
B20x20x388	0.500	0.500	0.040	0.040	Built-up
B20x20x366	0.500	0.500	0.040	0.035	Built-up
B20x20x352	0.500	0.500	0.036	0.036	Built-up
B20x20x348	0.500	0.500	0.036	0.035	Built-up
B18x18x346	0.450	0.450	0.040	0.040	Built-up
B18x18x282	0.450	0.450	0.032	0.032	Built-up
B18x18x258	0.450	0.450	0.029	0.029	Built-up
B16x16x276	0.400	0.400	0.036	0.036	Built-up
B16x16x248	0.400	0.400	0.032	0.032	Built-up
B16x16x227	0.400	0.400	0.029	0.029	Built-up

Section Designation	H (m)	B (m)	T_f (m)	T_w (m)	**Closest AISC [1] Section**
B14x14x196	0.350	0.350	0.029	0.029	Built-up
B14x14x171	0.350	0.350	0.025	0.025	Built-up

Appendix C Building Frame Elevations and Beam-Column Sizes

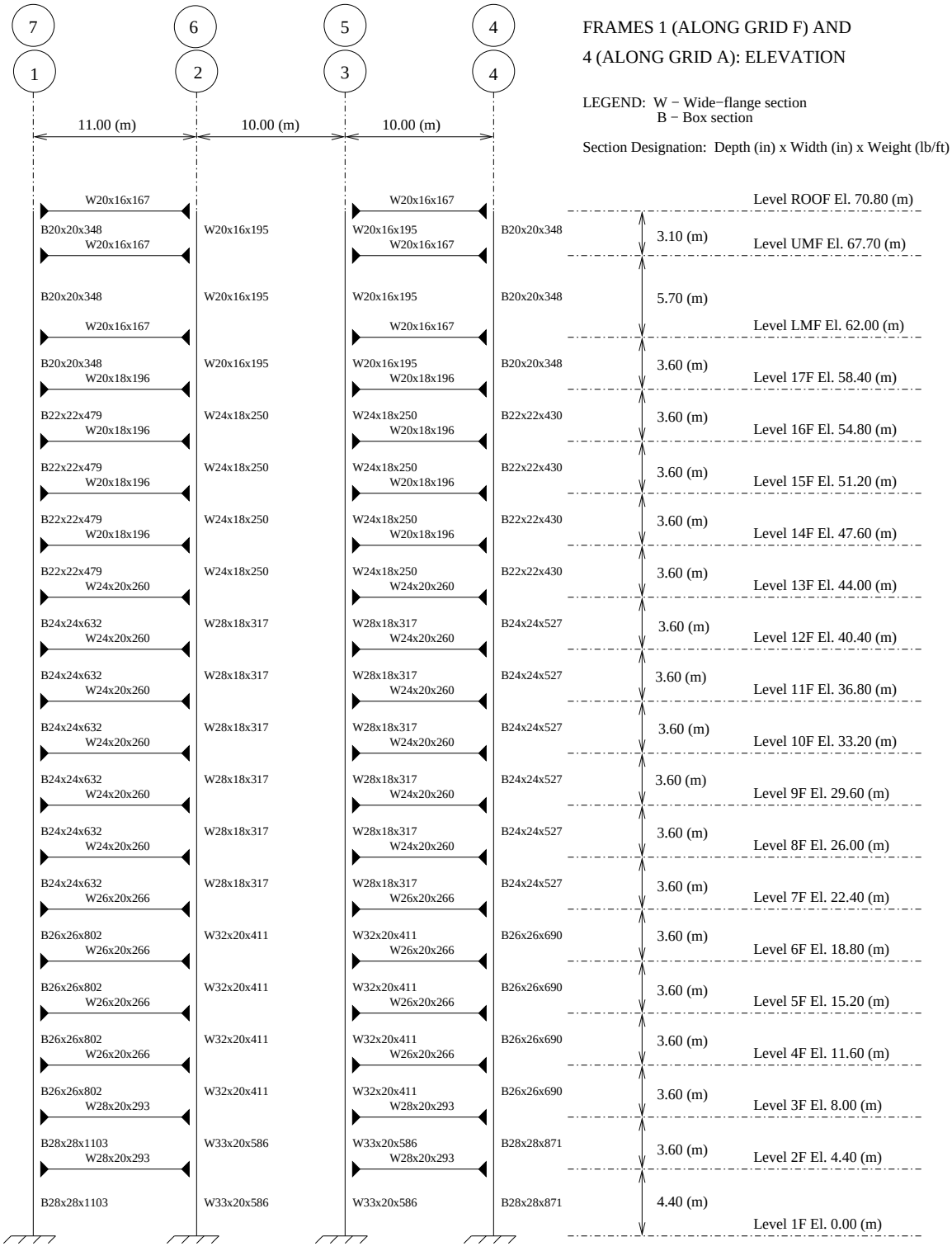

Figure C.1: Frames 1 & 4 Elevation: Building 1

Figure C.2: Frames 2 & 3 Elevation: Building 1

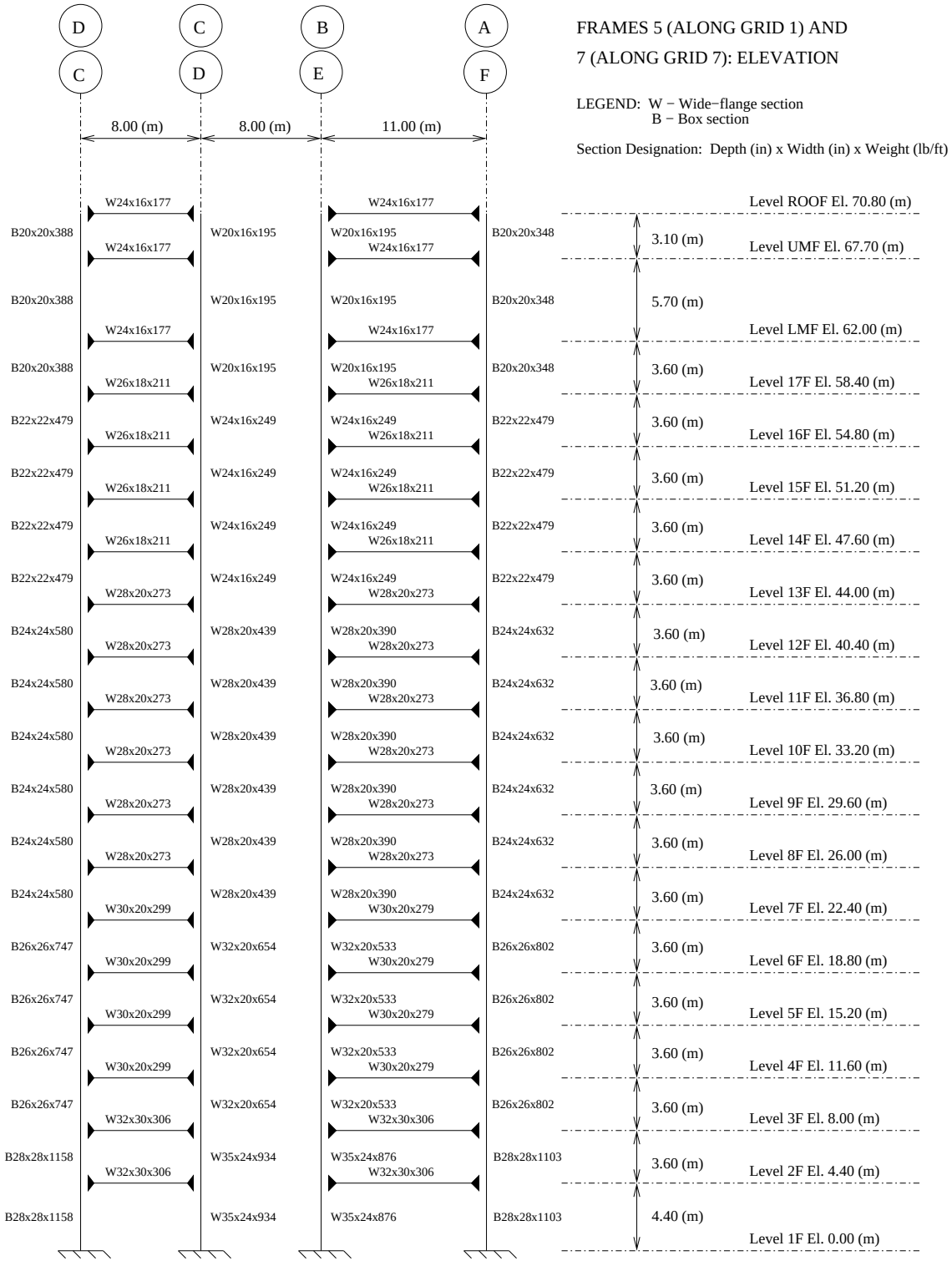

Figure C.3: Frames 5 & 7 Elevation: Building 1

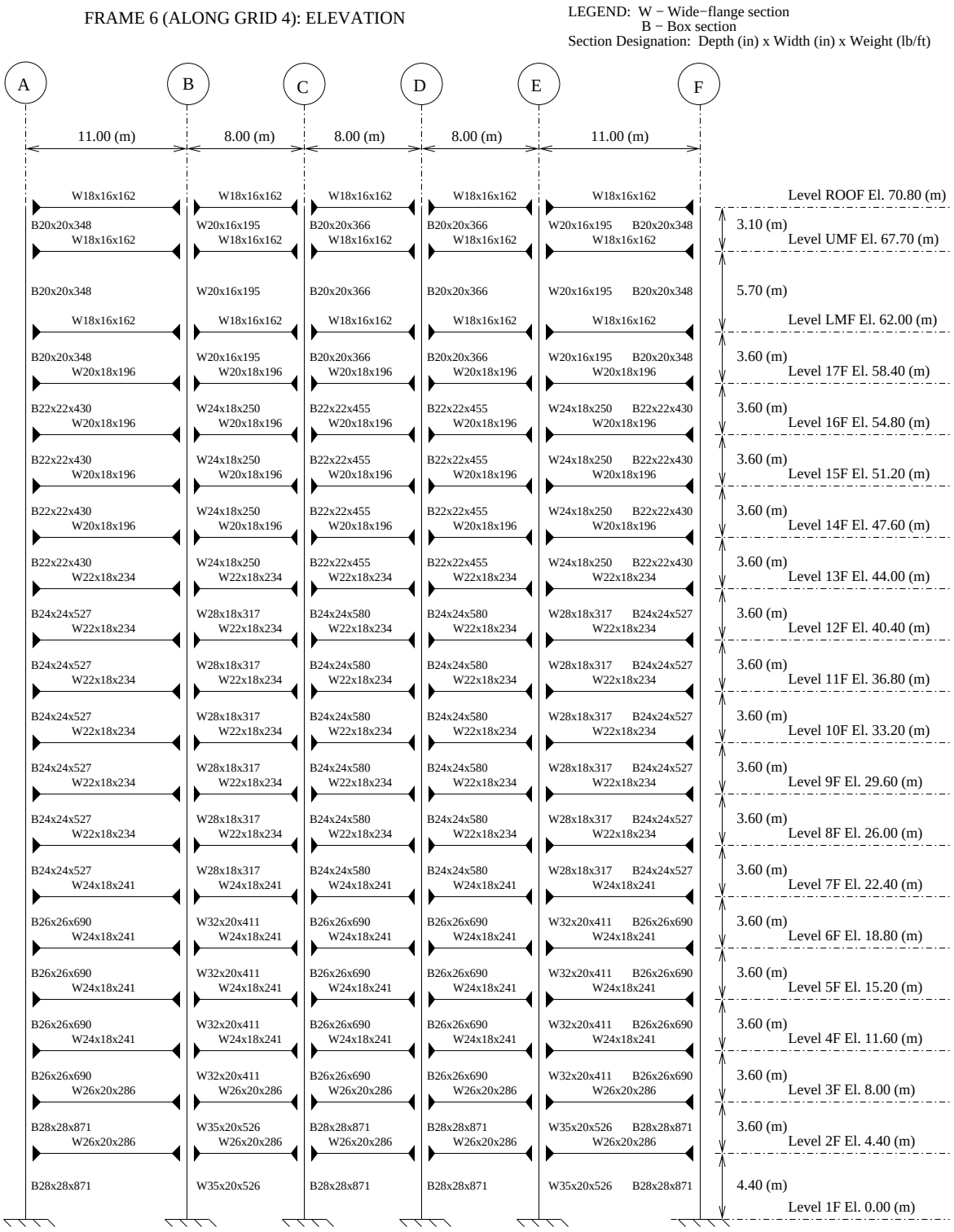

Figure C.4: Frame 6 Elevation: Building 1

Figure C.5: Gravity Columns Elevation: Building 1

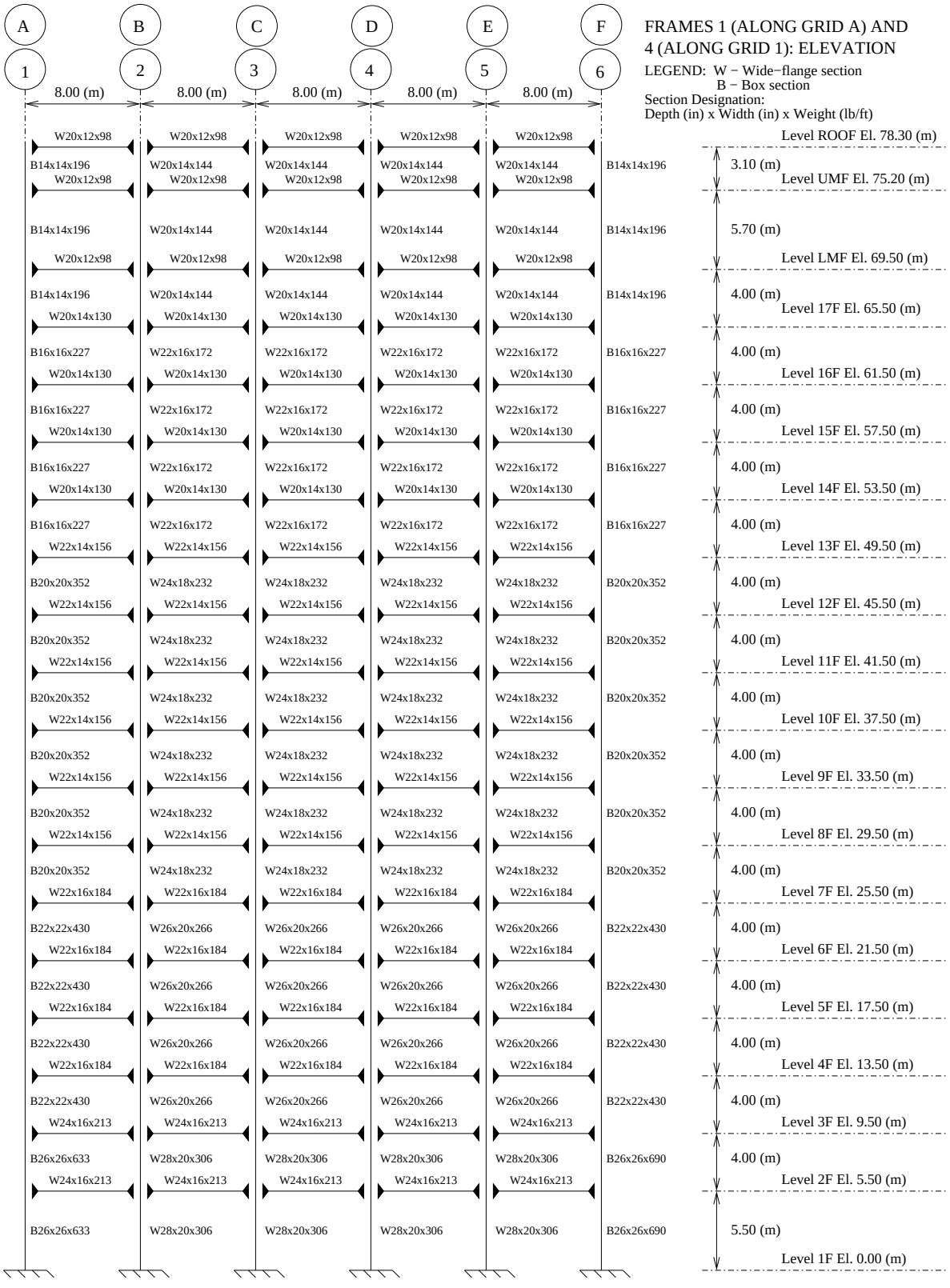

Figure C.6: Frames 1 & 4 Elevation: Building 2

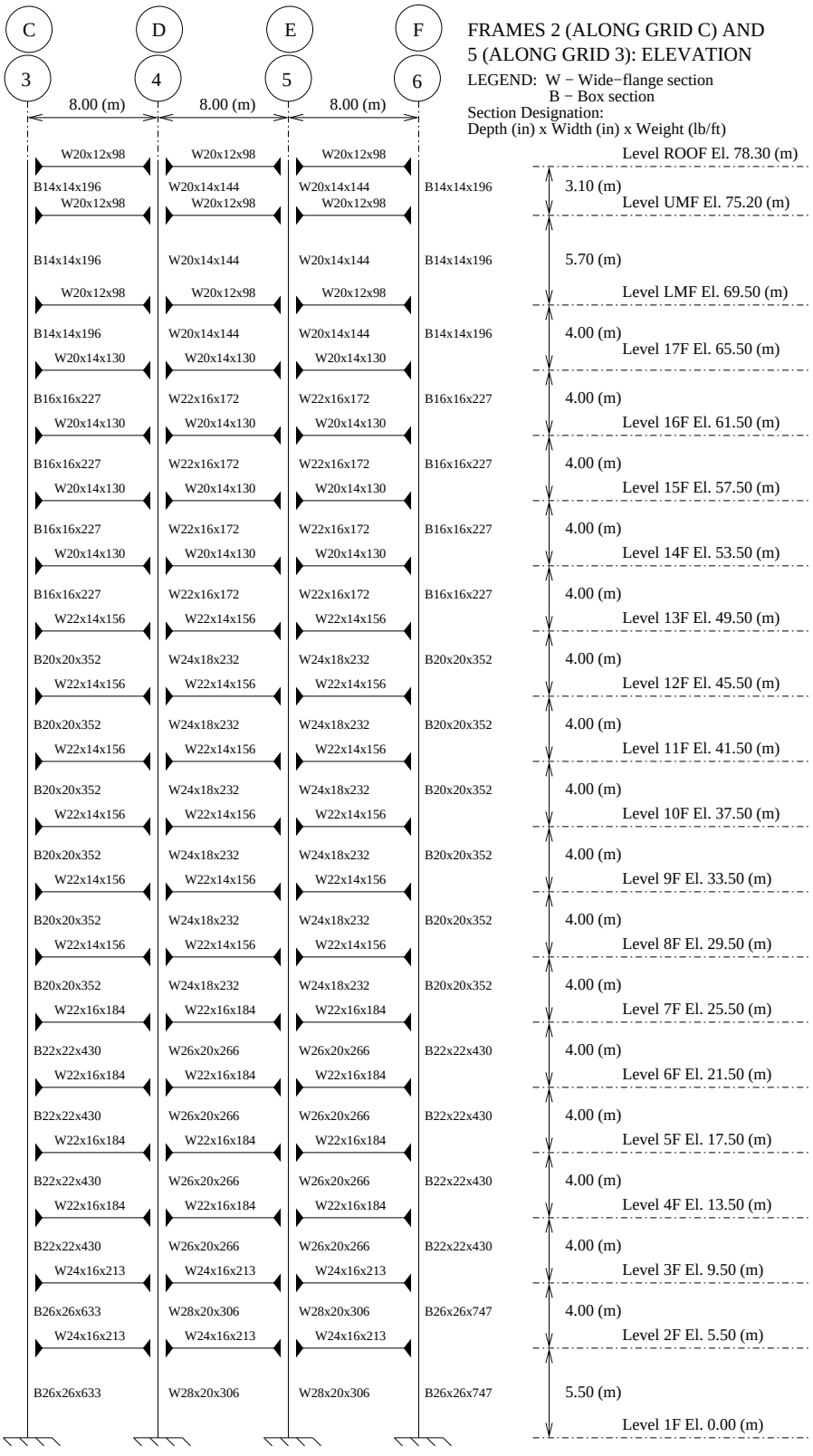

Figure C.7: Frames 2 & 5 Elevation: Building 2

Figure C.8: Frames 3 & 6 Elevation: Building 2

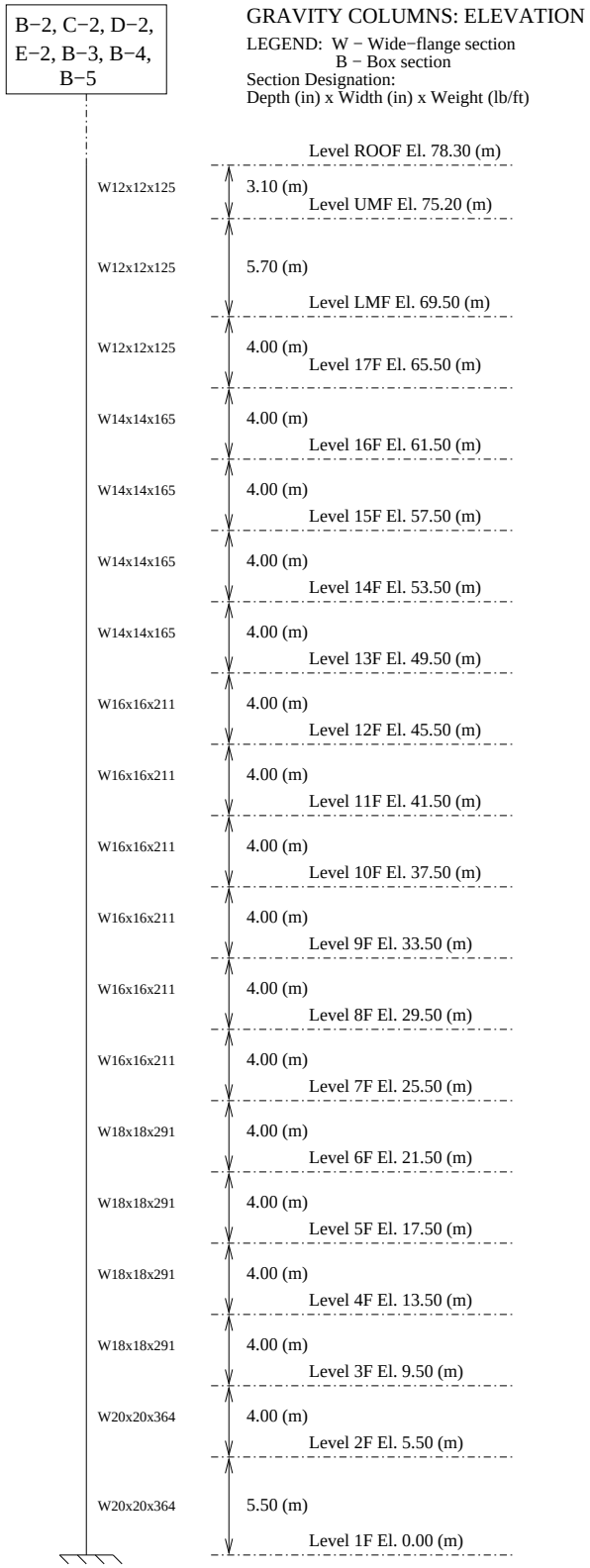

Figure C.9: Gravity Columns Elevation: Building 2

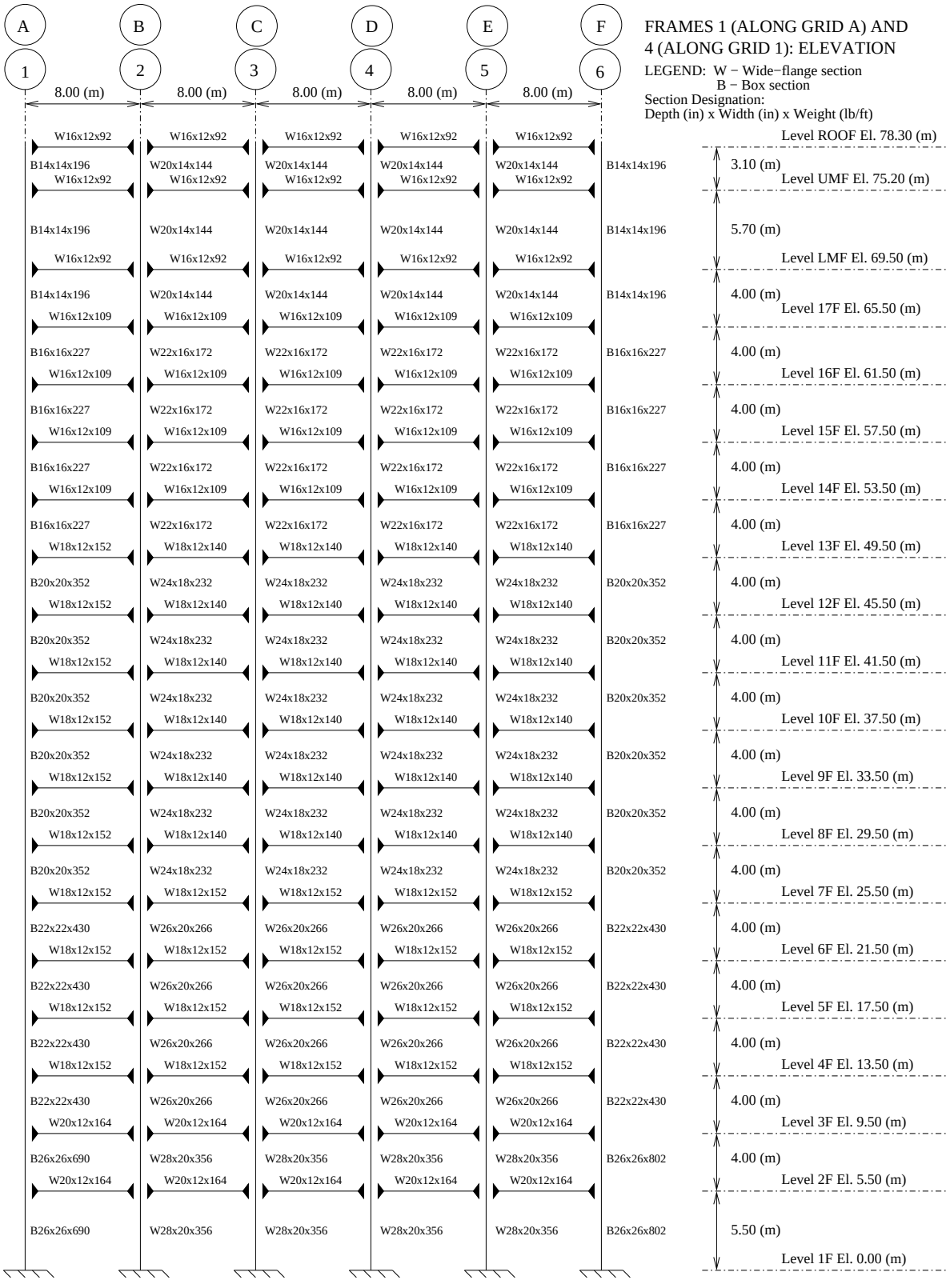

Figure C.10: Frames 1 & 4 Elevation: Building 2A

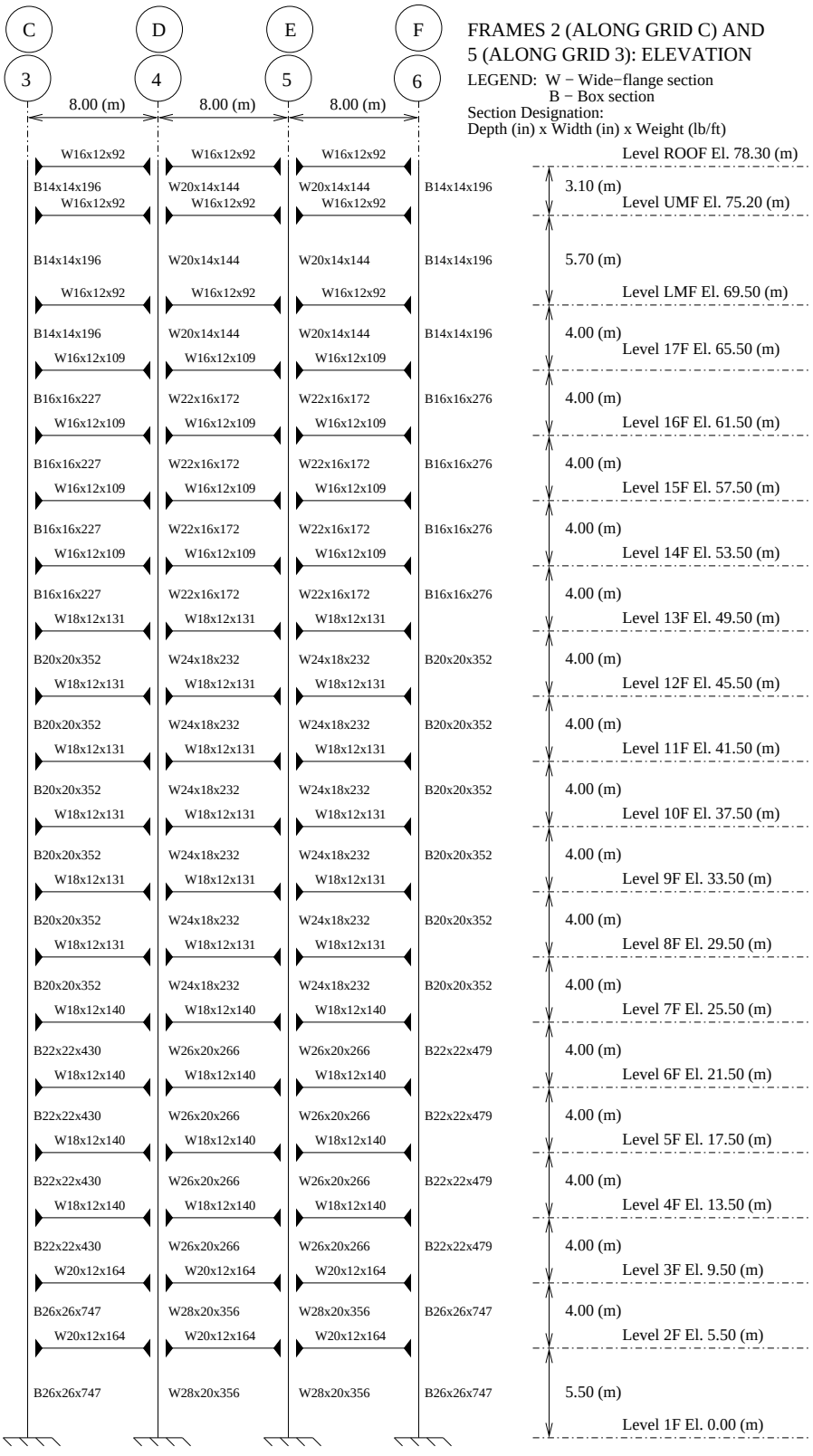

Figure C.11: Frames 2 & 5 Elevation: Building 2A

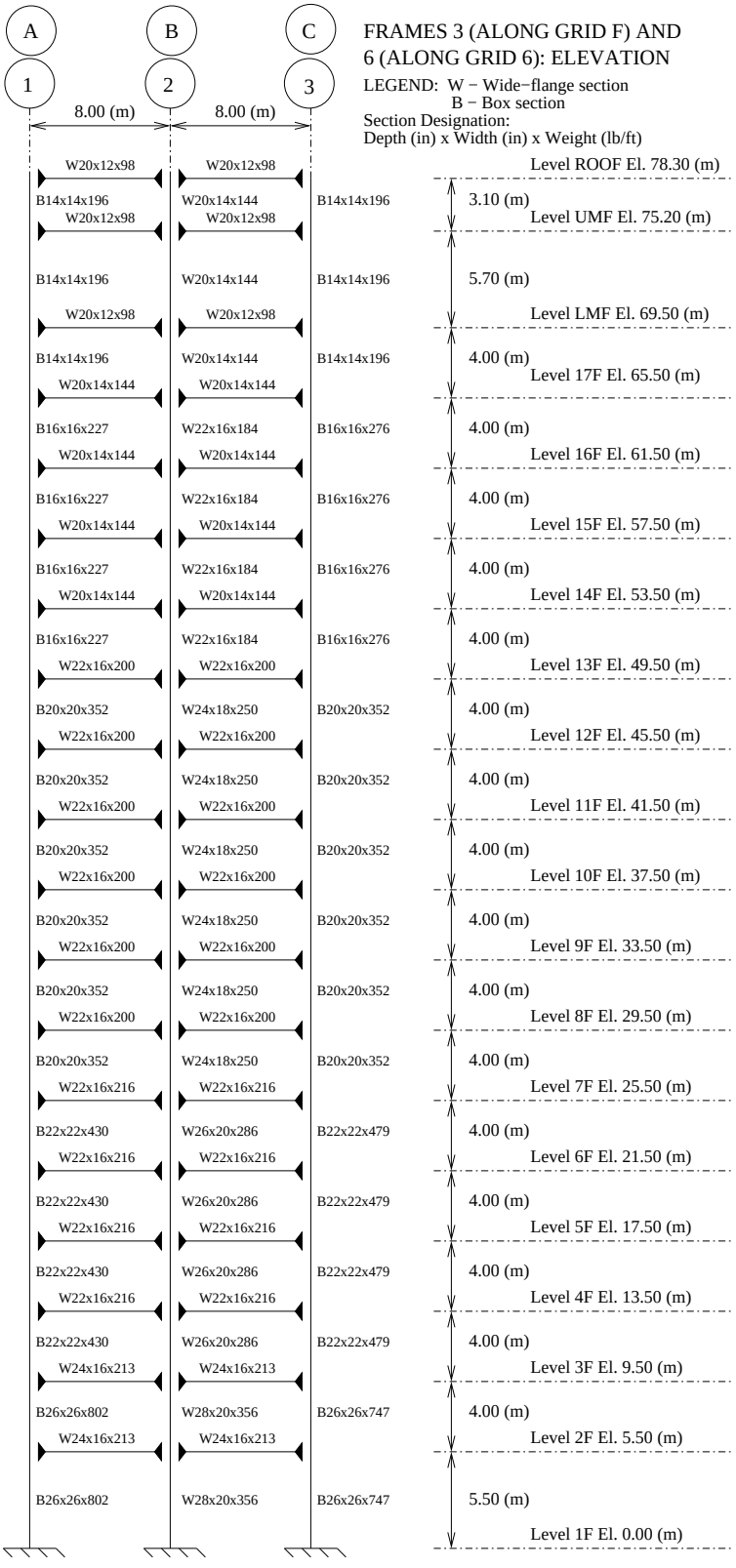

Figure C.12: Frames 3 & 6 Elevation: Building 2A

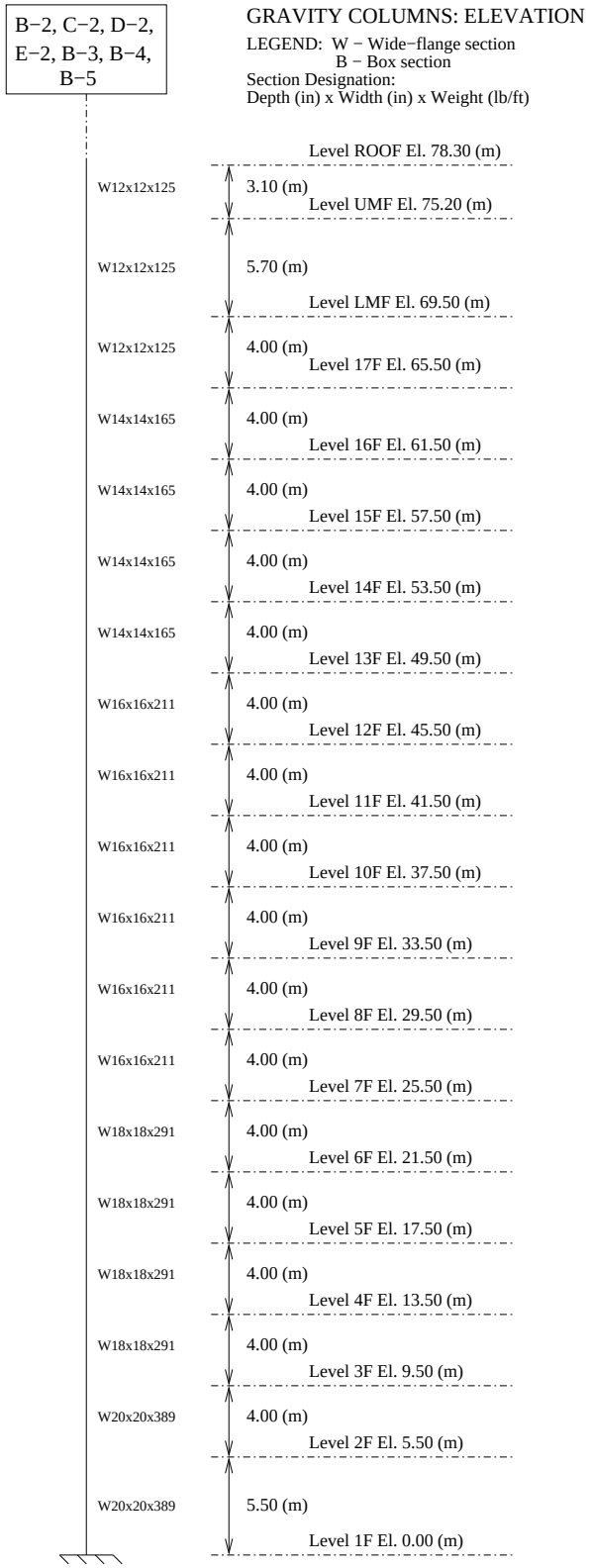

Figure C.13: Gravity Columns Elevation: Building 2A

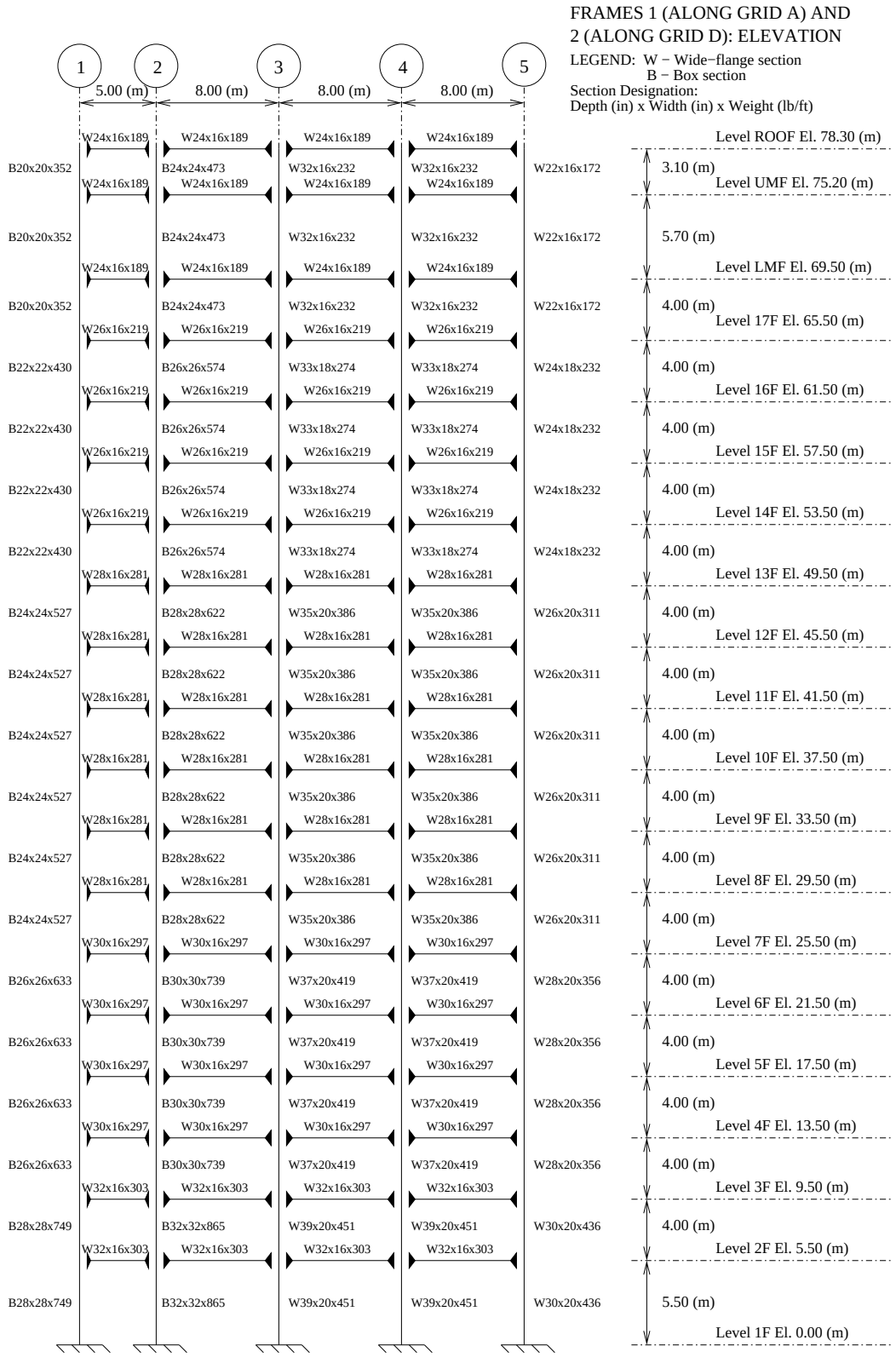

Figure C.14: Frames 1 & 2 Elevation: Building 3

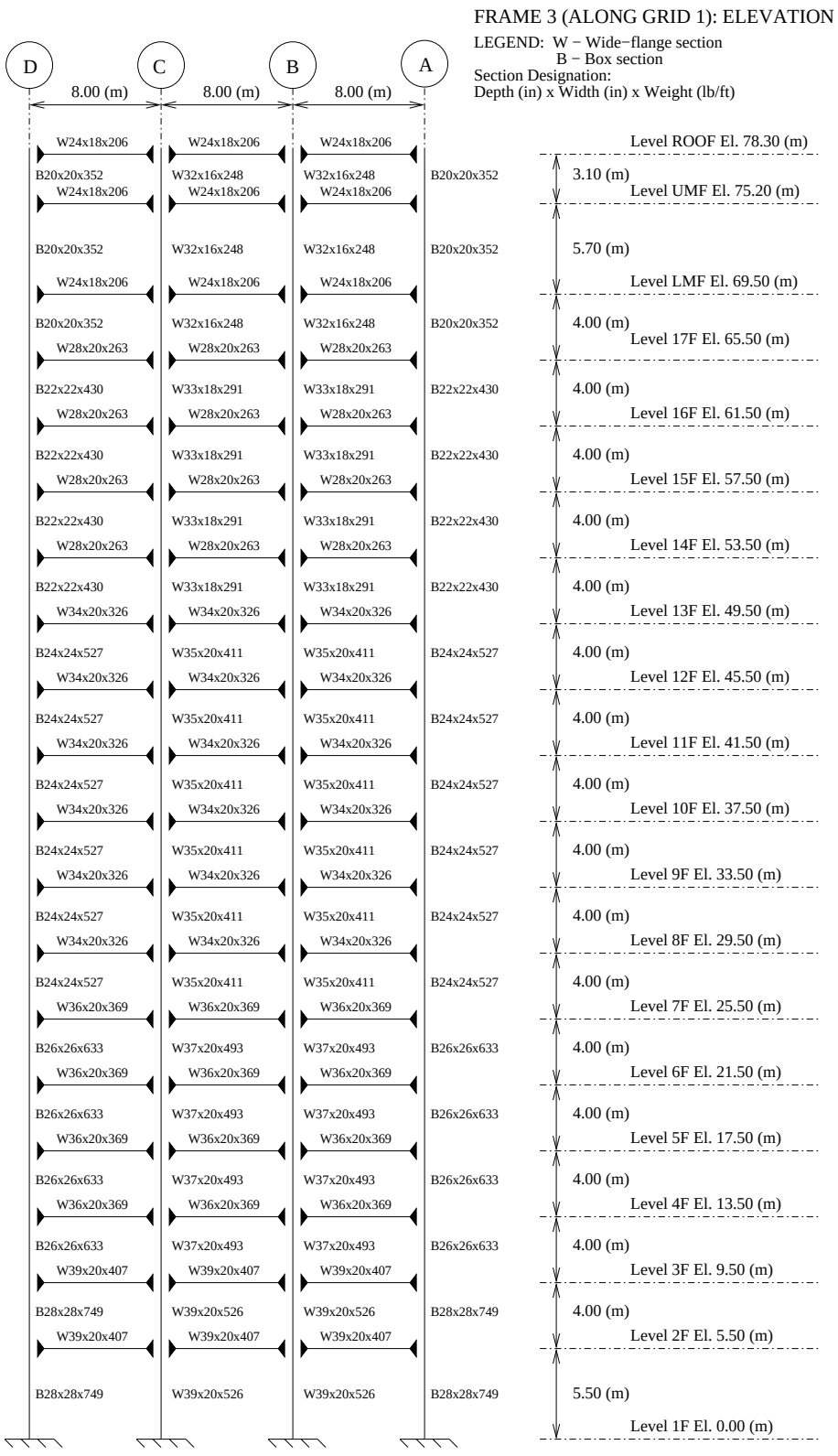

Figure C.15: Frame 3 Elevation: Building 3

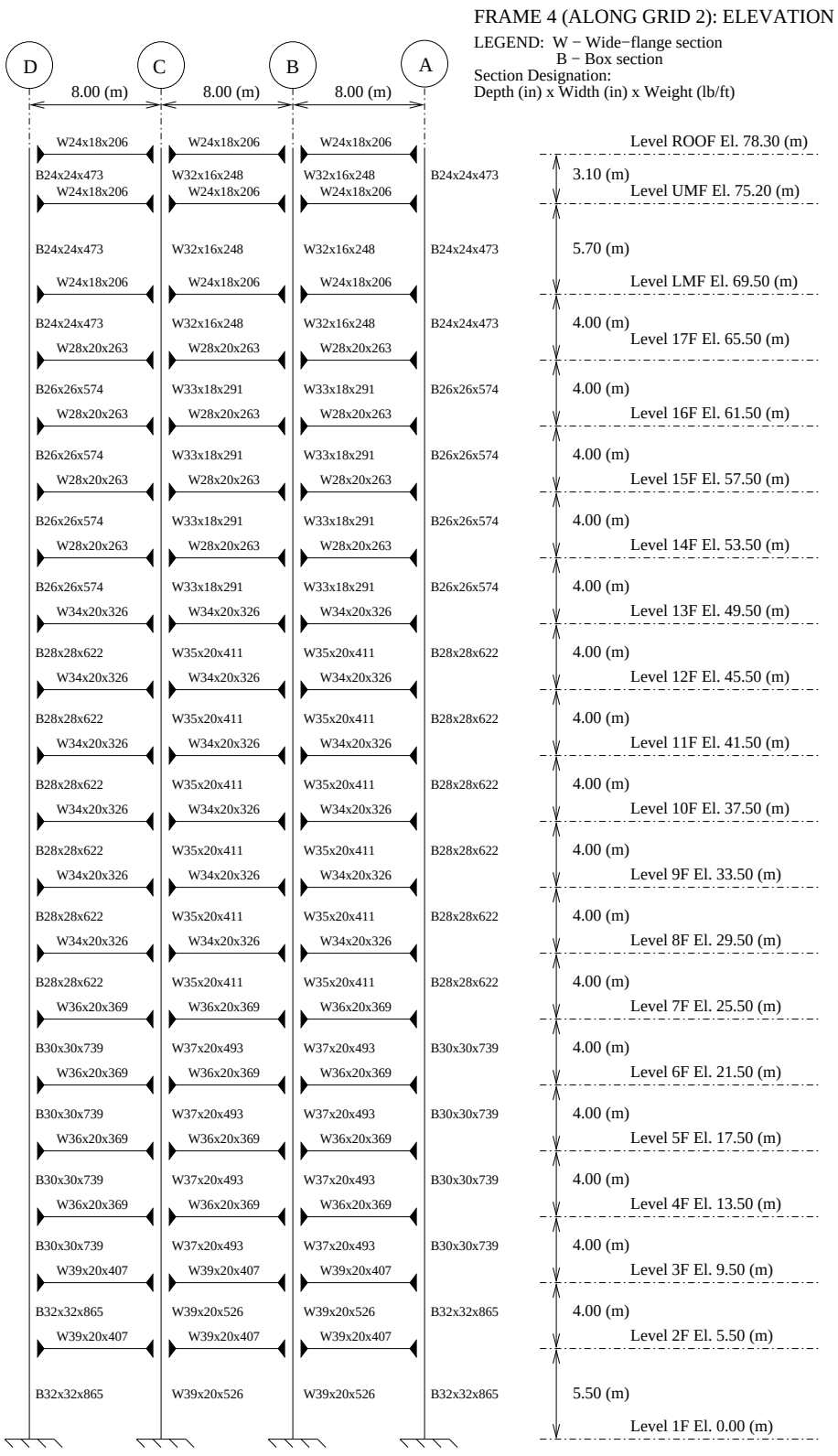

Figure C.16: Frame 4 Elevation: Building 3

Figure C.17: Gravity Columns Elevation: Building 3

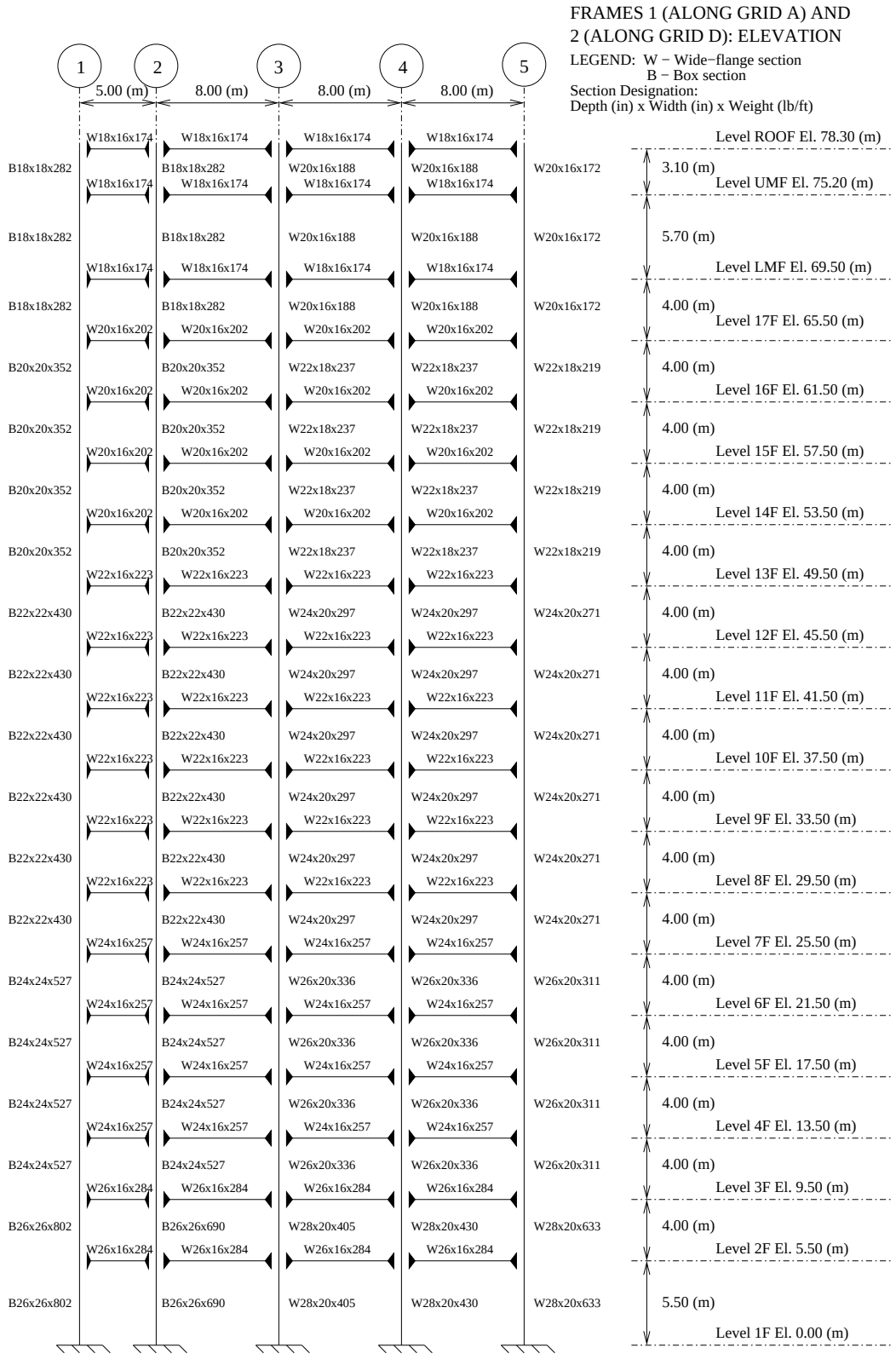

Figure C.18: Frames 1 & 2 Elevation: Building 3A

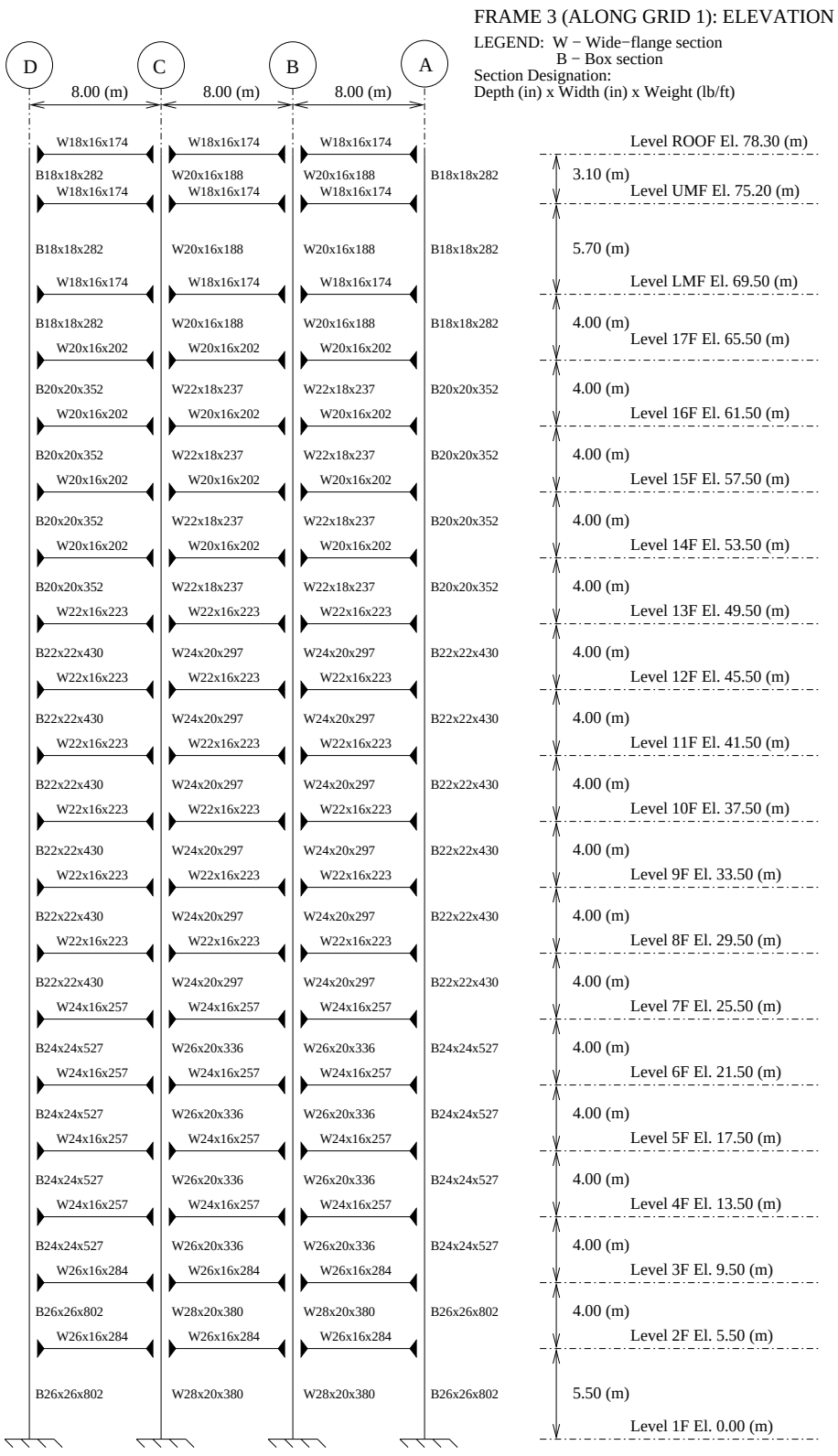

Figure C.19: Frame 3 Elevation: Building 3A

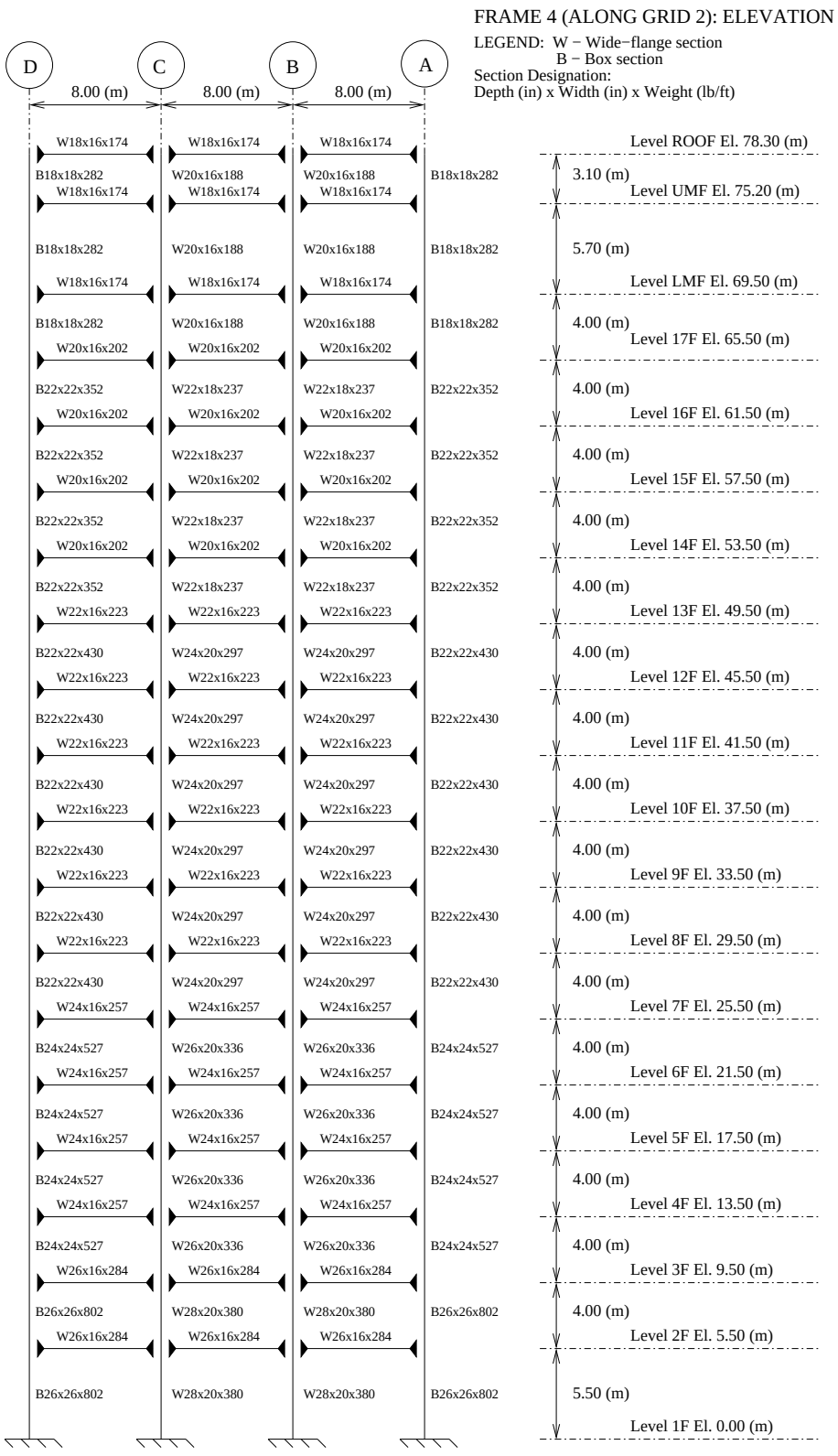

Figure C.20: Frame 4 Elevation: Building 3A

Figure C.21: Gravity Columns Elevation: Building 3A

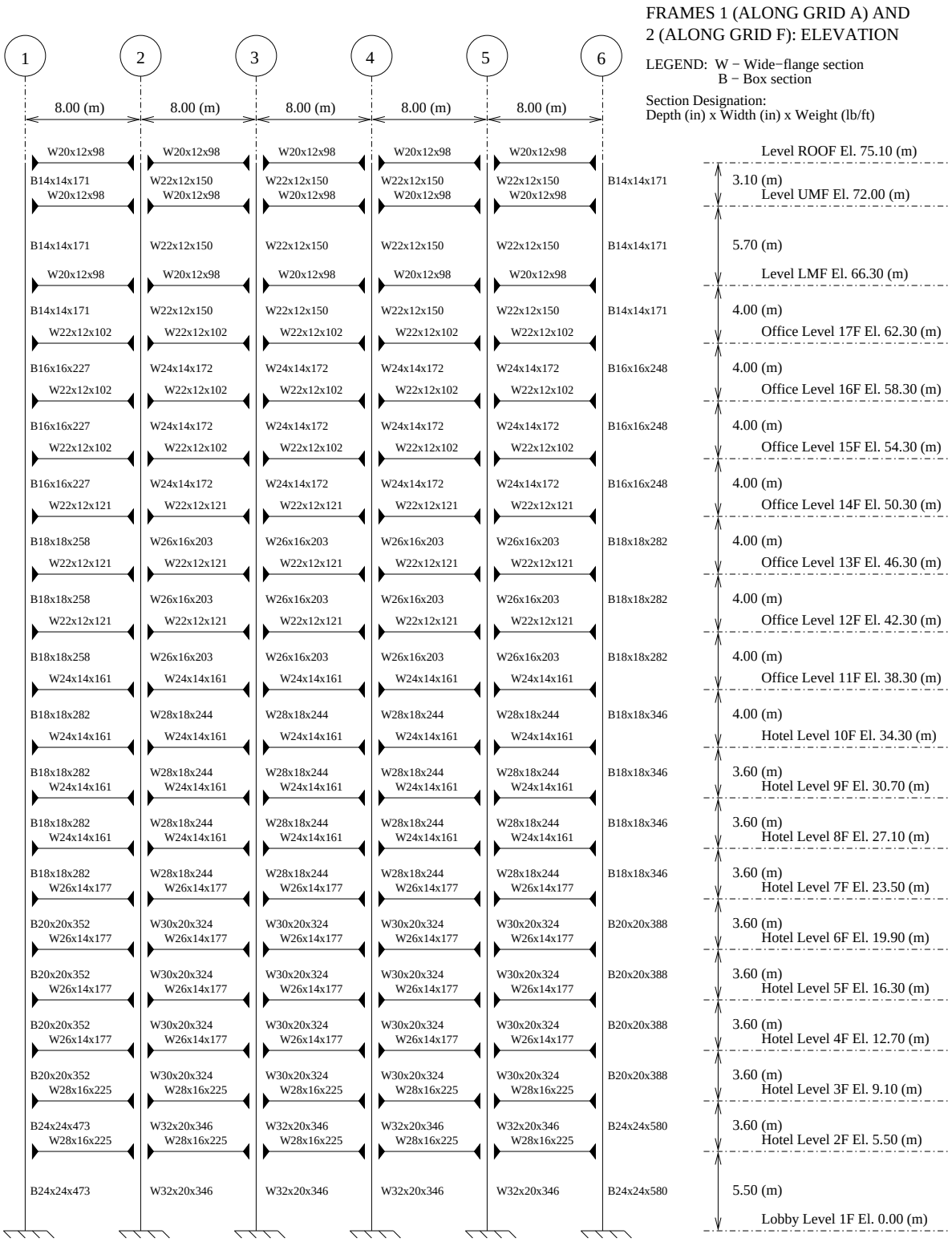

Figure C.22: Frames 1 & 2 Elevation: Building 4

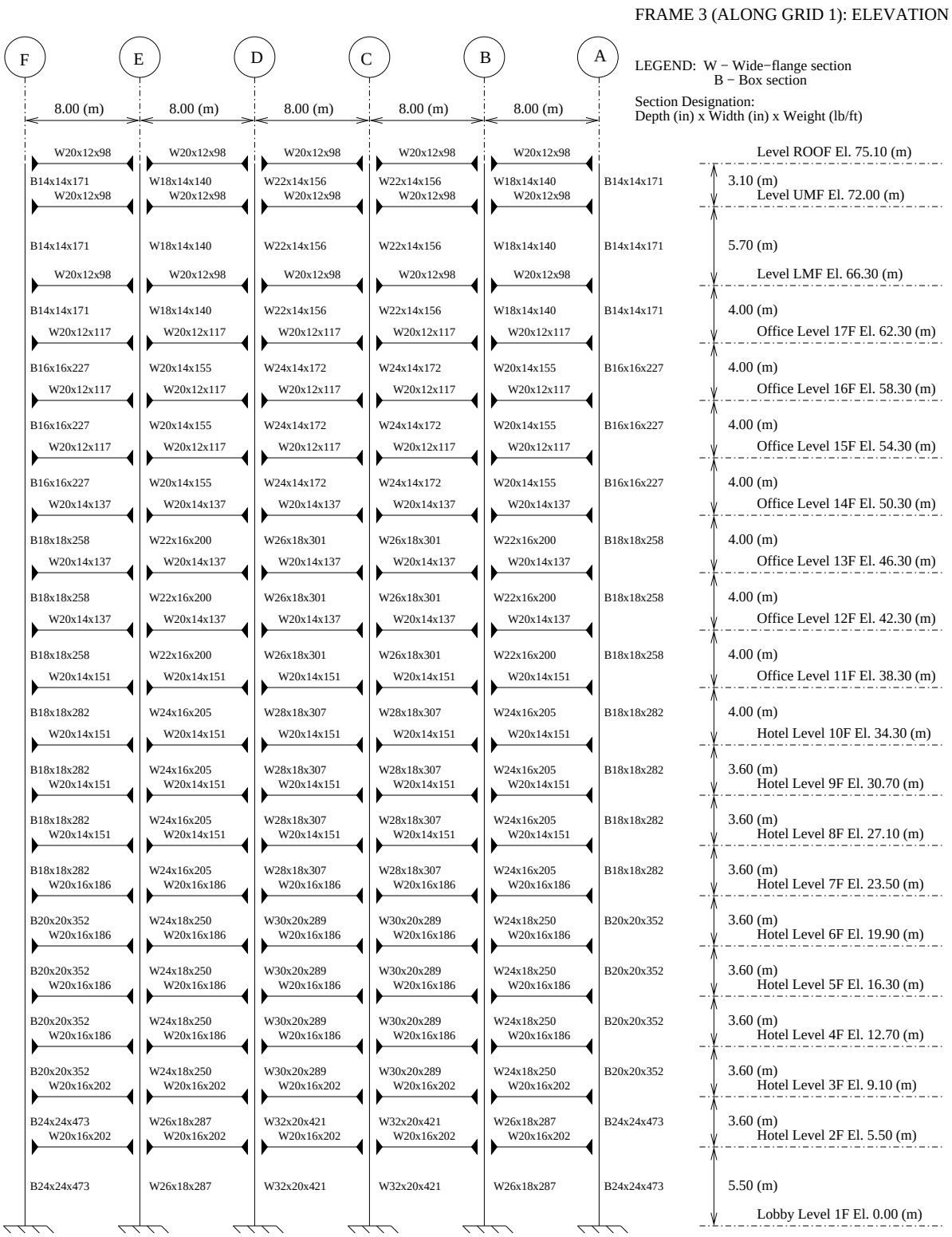

Figure C.23: Frame 3 Elevation: Building 4

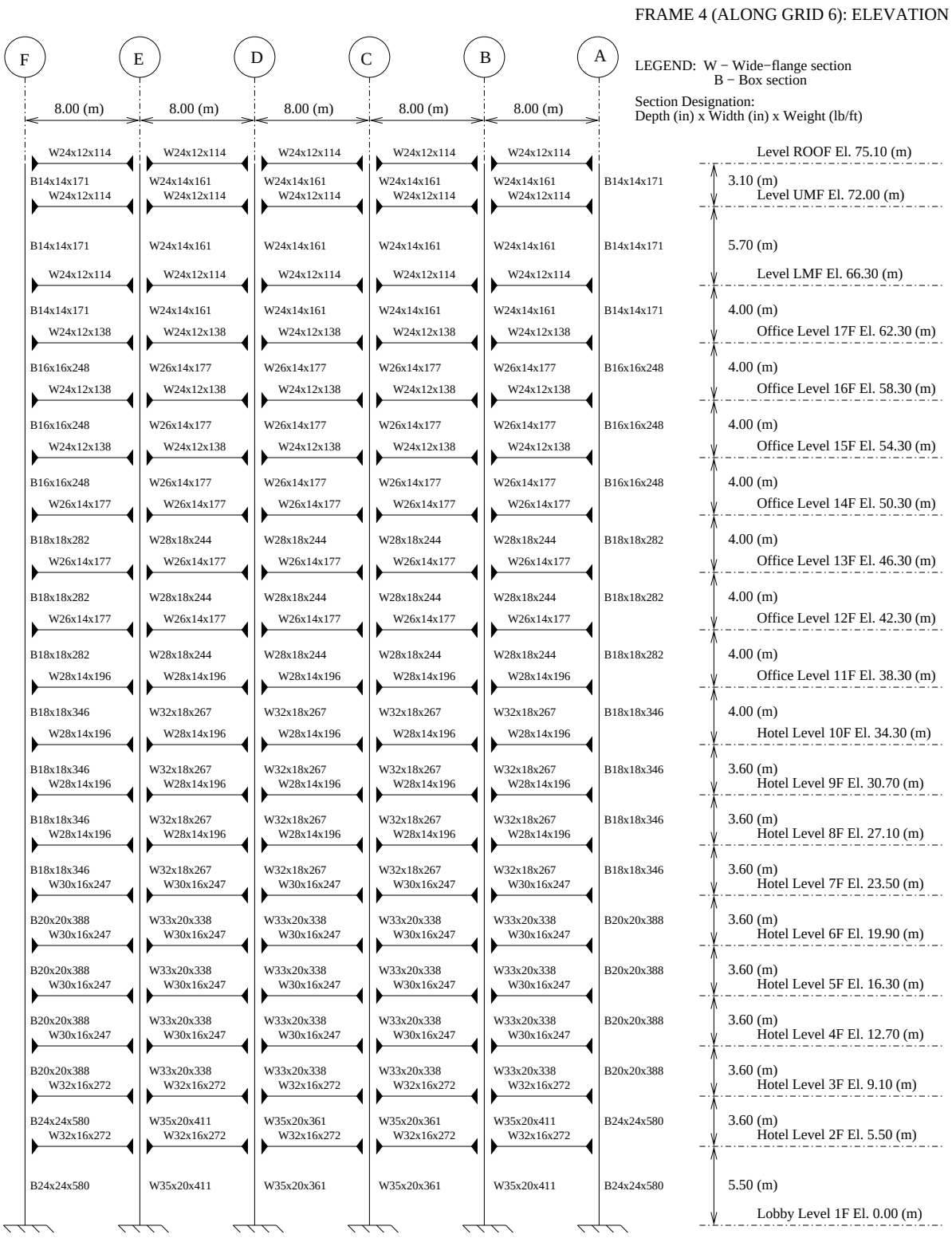

Figure C.24: Frame 4 Elevation: Building 4

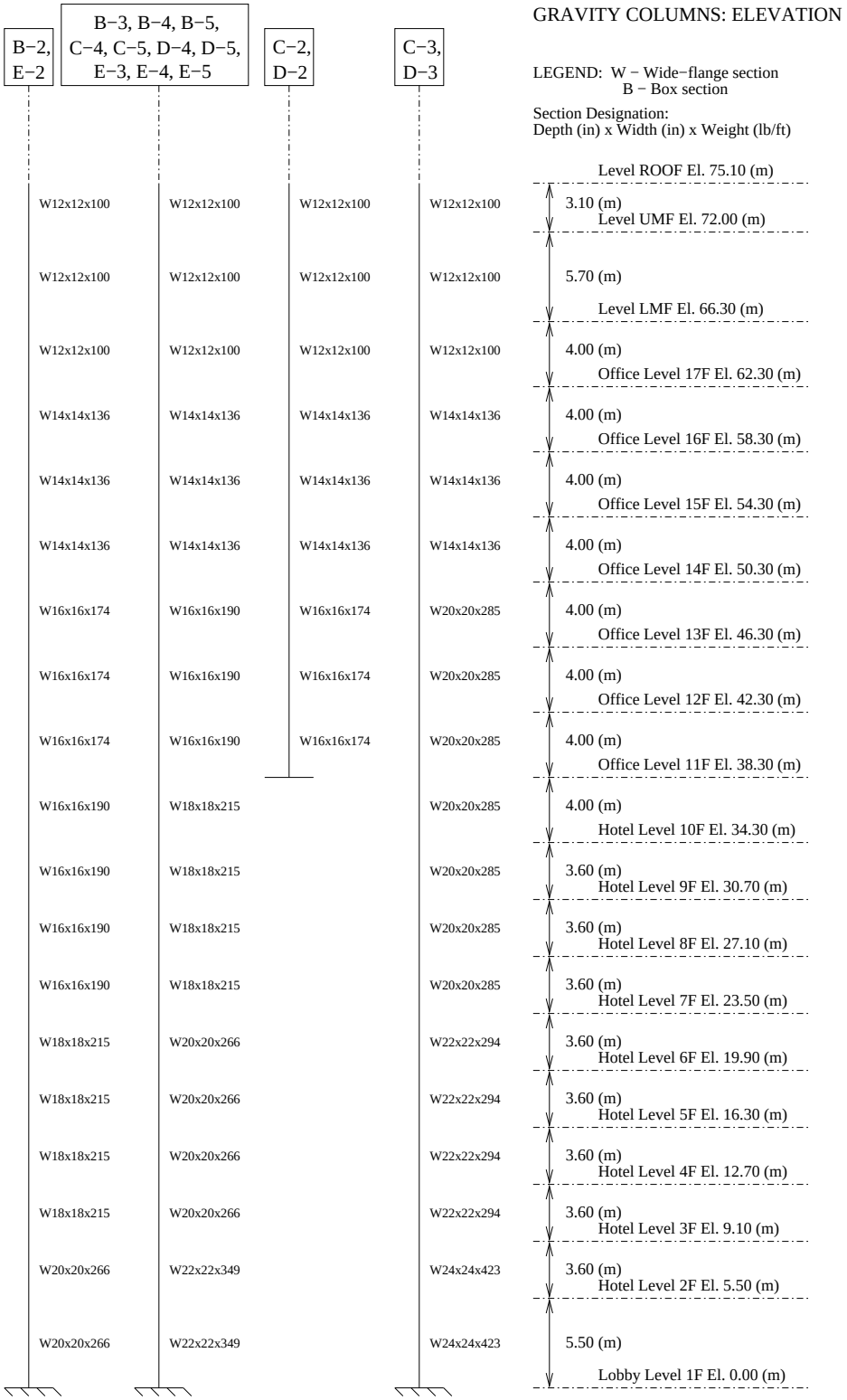

Figure C.25: Gravity Columns Elevation: Building 4

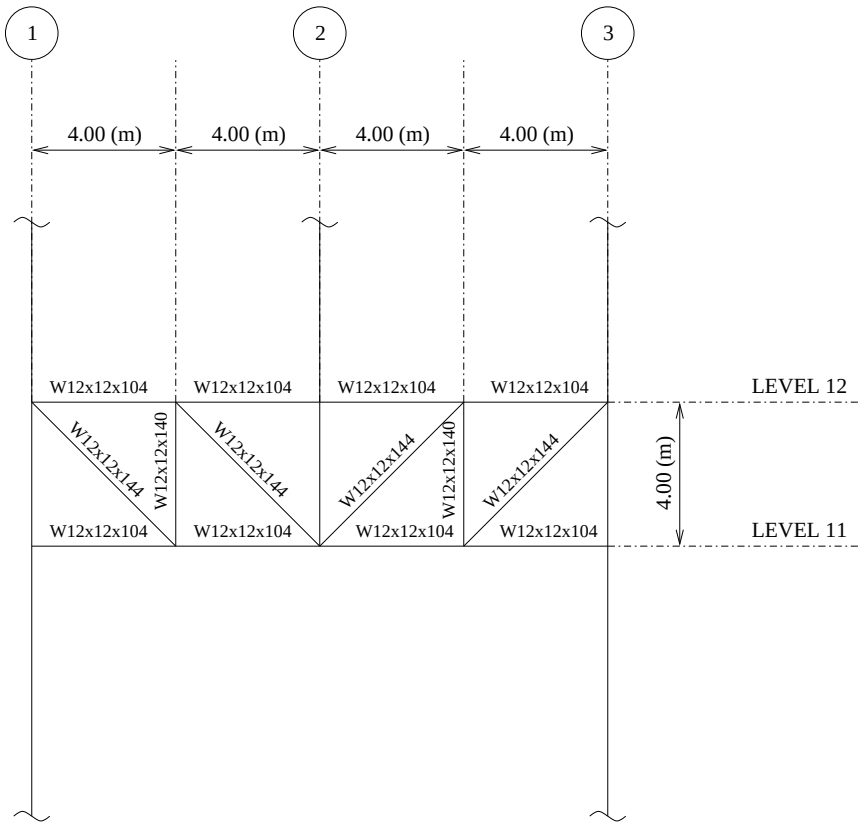

SECTION AA
1−STORY DEEP TRANSFER TRUSSES
AT GRIDS C AND E, BETWEEN LEVELS 11 & 12

Figure C.26: Transfer Truss Elevation: Building 4

Appendix D Building Centers of Mass and Stiffness

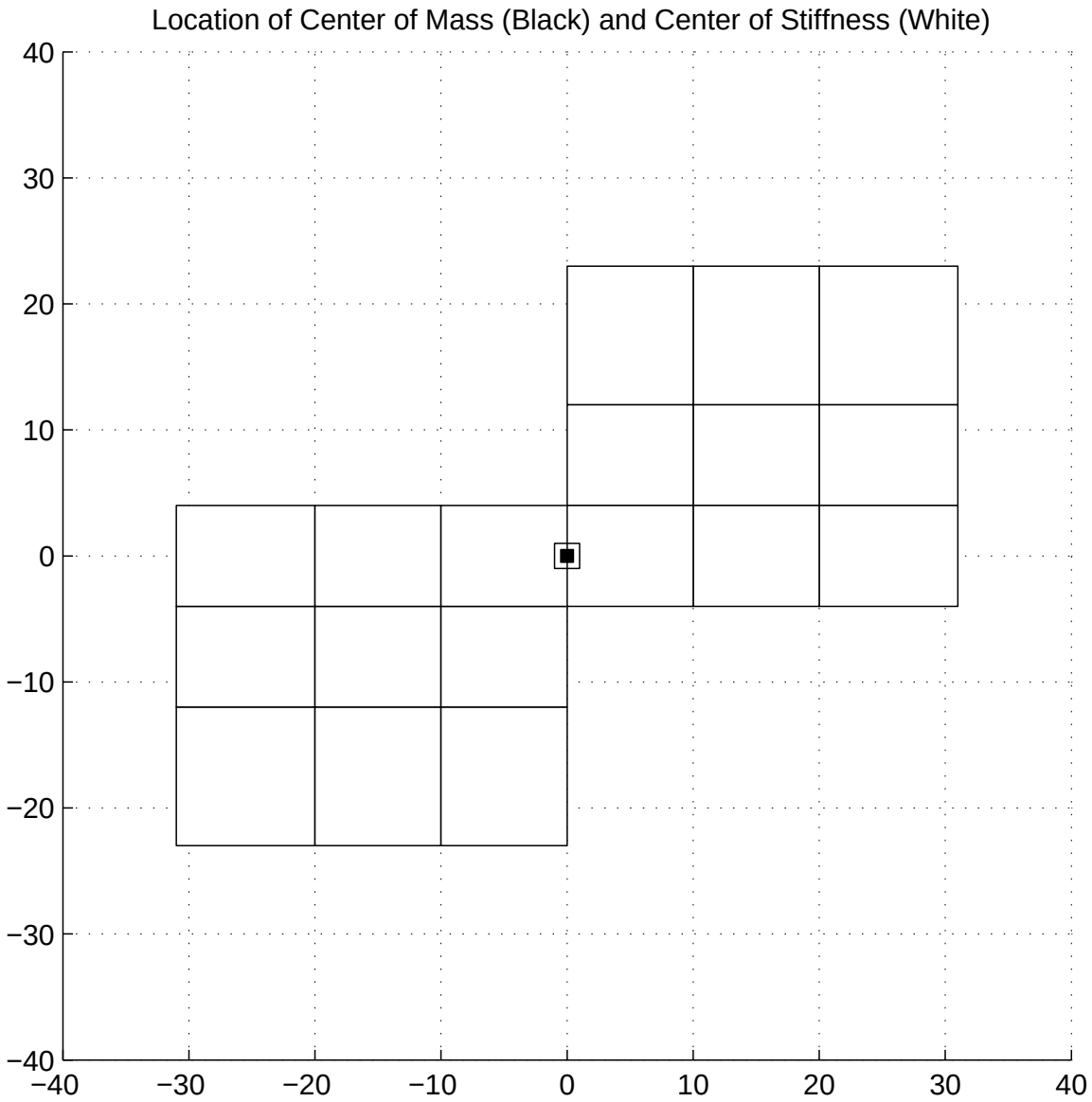

Figure D.1: Building 1: Location of Centers of Mass and Stiffness - All Floors

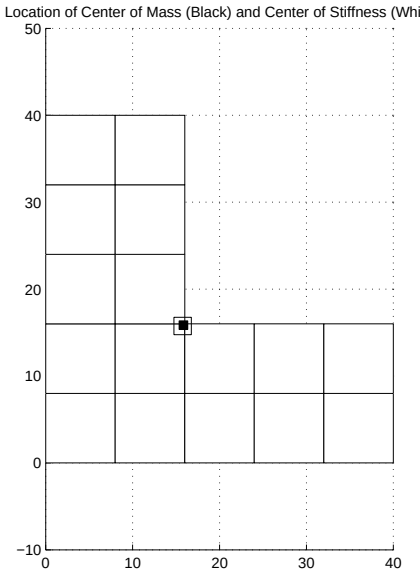

(a) Second Floor

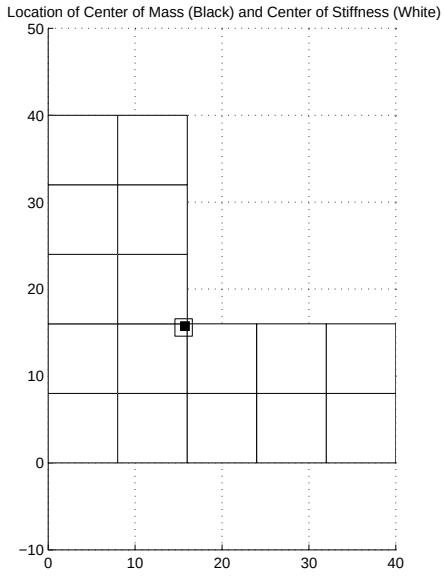

(b) Ninth Floor

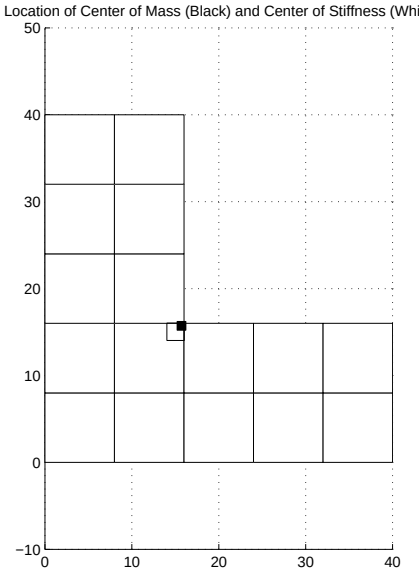

(c) Lower Mechanical Floor

Figure D.2: Building 2: Location of Centers of Mass and Stiffness

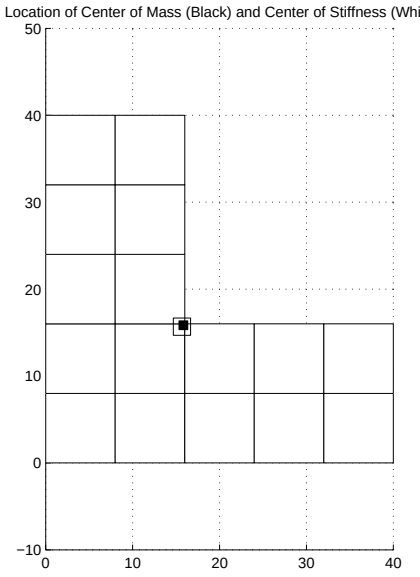

(a) Second Floor

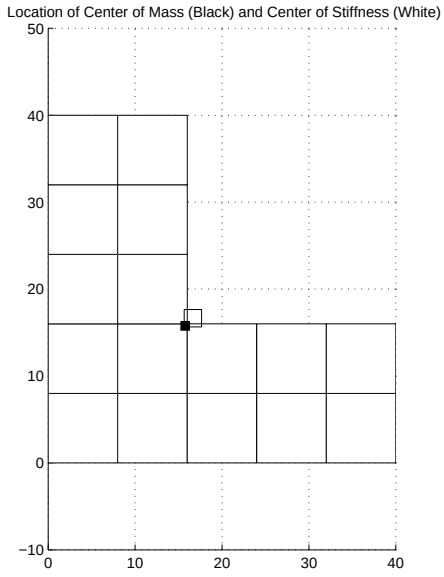

(b) Ninth Floor

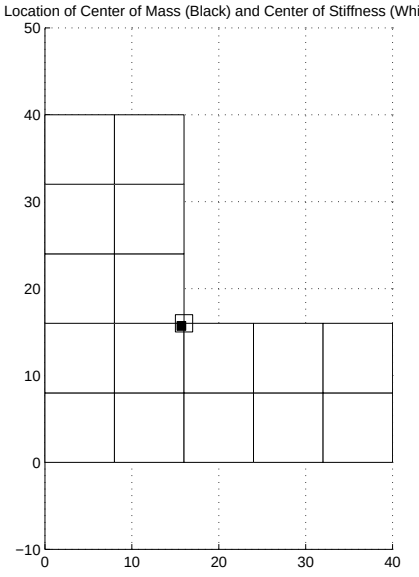

(c) Lower Mechanical Floor

Figure D.3: Building 2A: Location of Centers of Mass and Stiffness

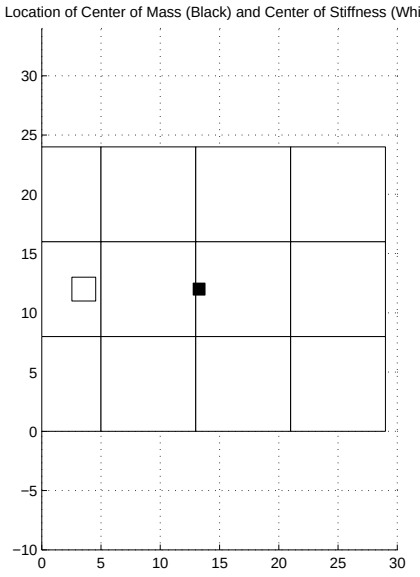

(a) Second Floor

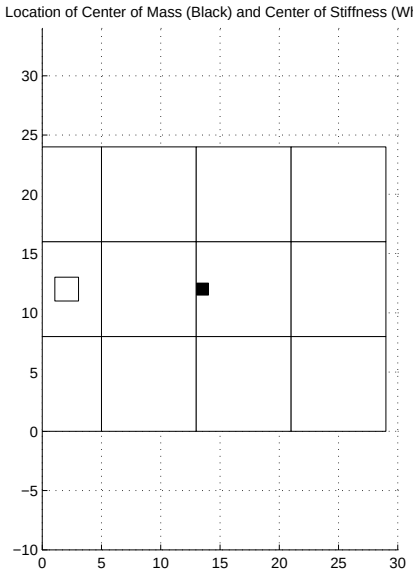

(b) Ninth Floor

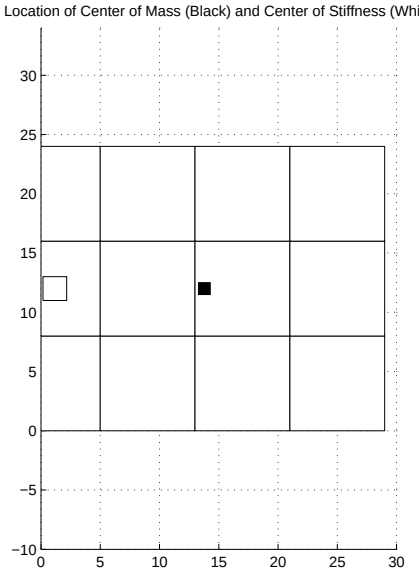

(c) Lower Mechanical Floor

Figure D.4: Building 3: Location of Centers of Mass and Stiffness

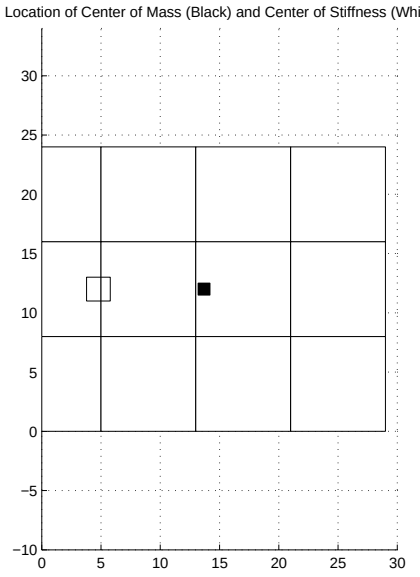

(a) Second Floor

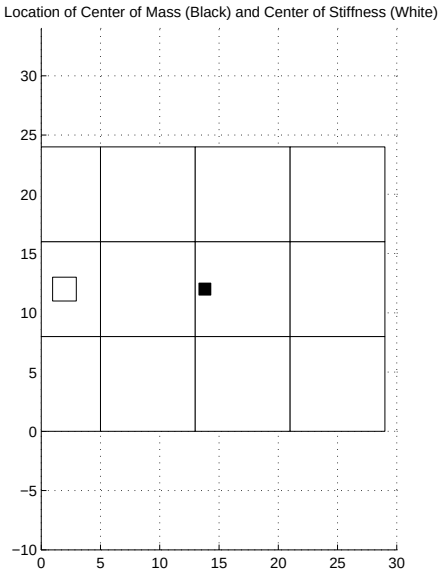

(b) Ninth Floor

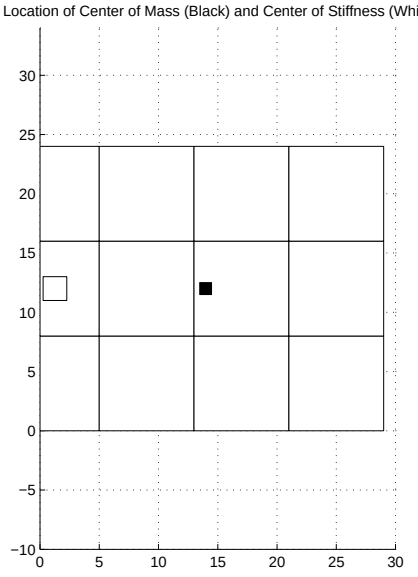

(c) Lower Mechanical Floor

Figure D.5: Building 3A: Location of Centers of Mass and Stiffness

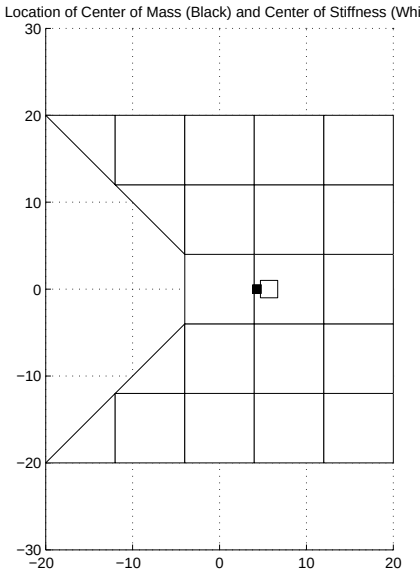

(a) Second Floor

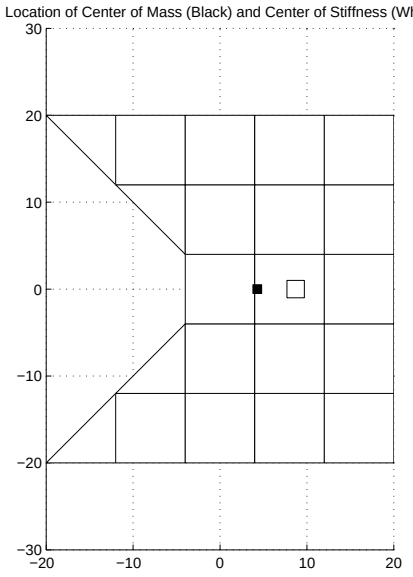

(b) Ninth Floor

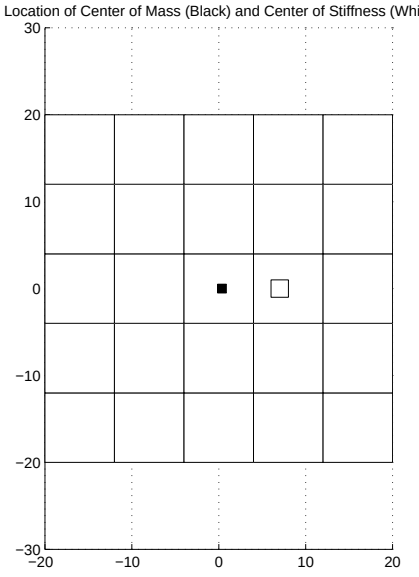

(c) Lower Mechanical Floor

Figure D.6: Building 4: Location of Centers of Mass and Stiffness

Appendix E Pushover Analysis of Buildings: Roof Displacement Plotted Against Base Shear

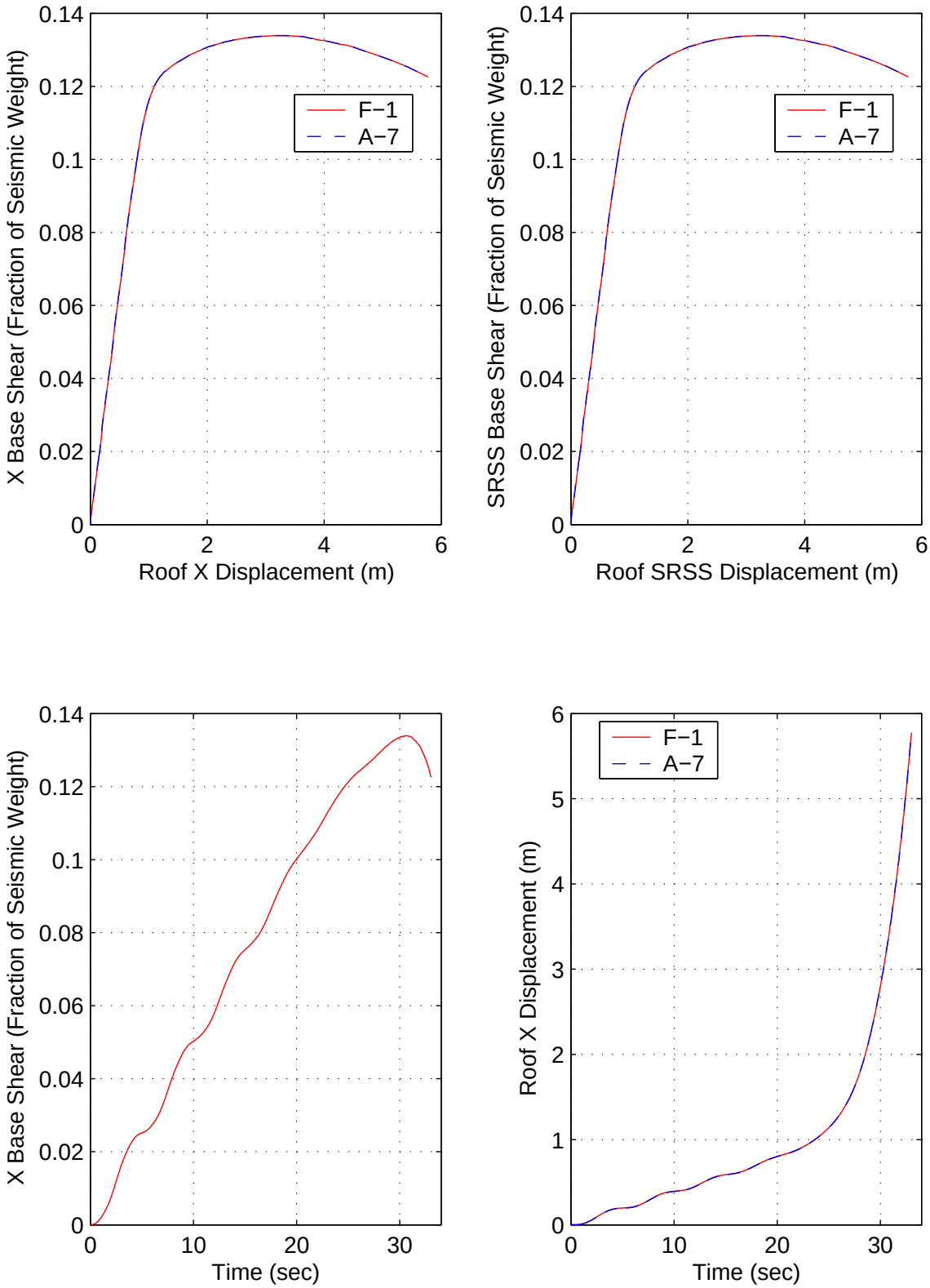

Figure E.1: Building 1 X-Direction Pushover Results

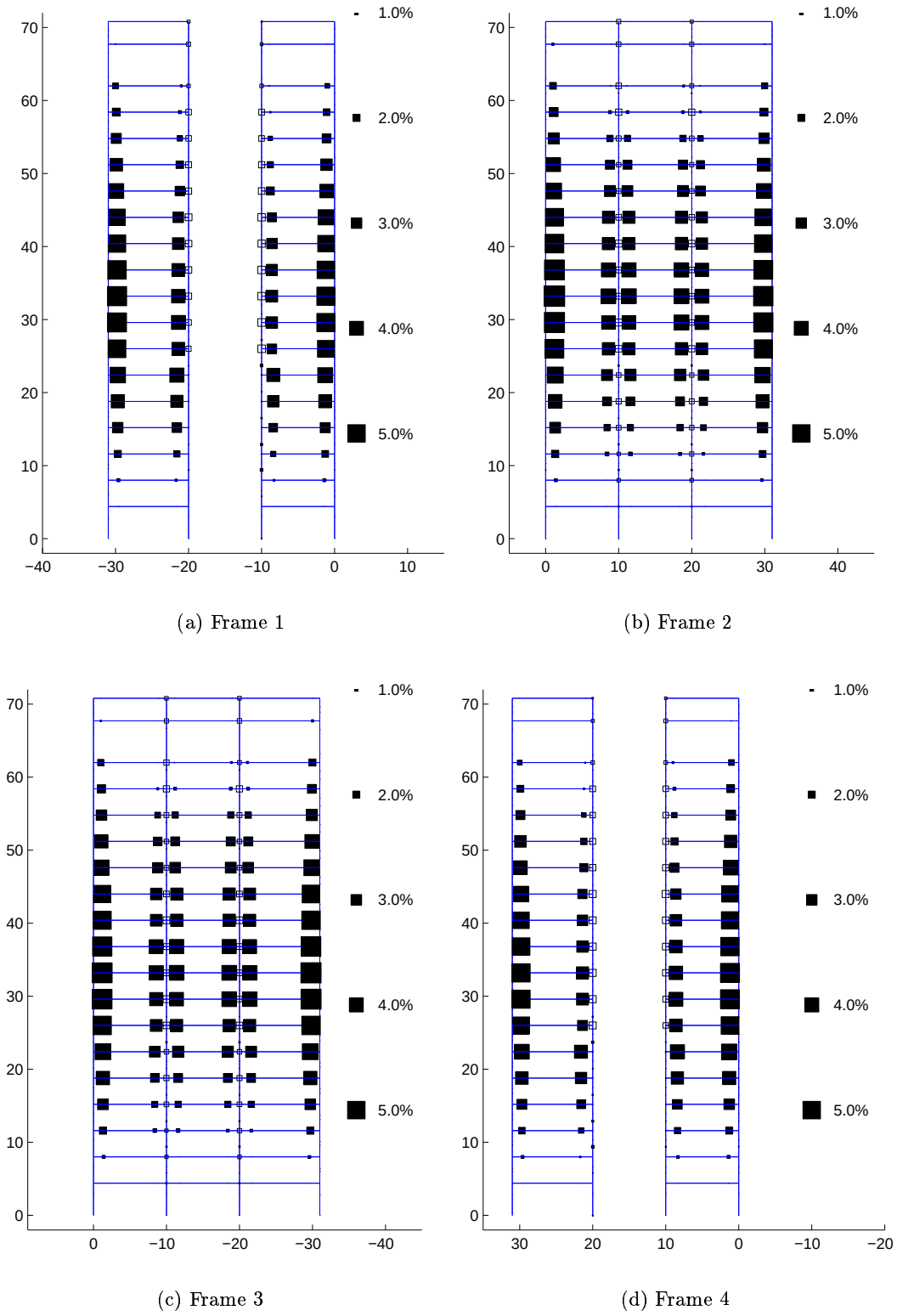

(a) Frame 1

(b) Frame 2

(c) Frame 3

(d) Frame 4

Figure E.2: Plastic Rotations (Black:Beam-Columns White:Panel Zones) at Ultimate Roof Displacement in Building 1 Frames 1-4: Pushover in X Direction

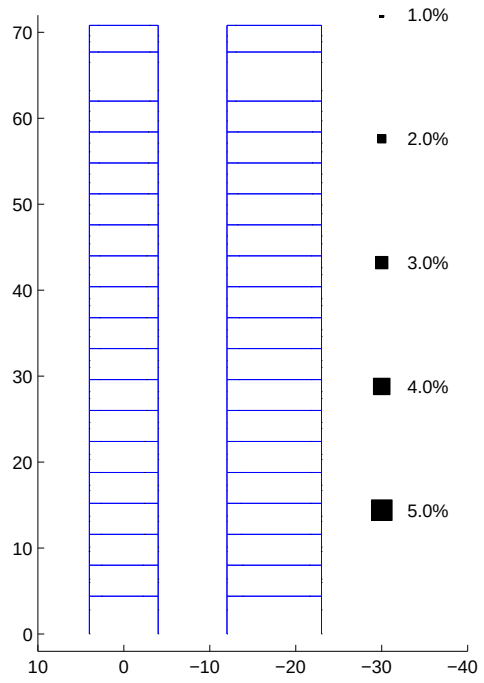

(a) Frame 5

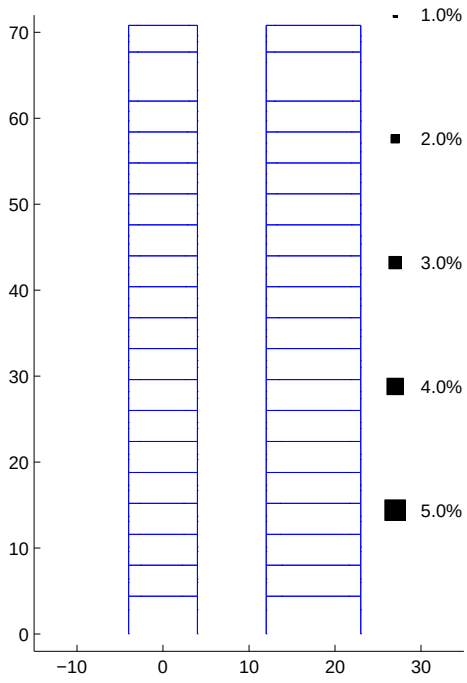

(b) Frame 7

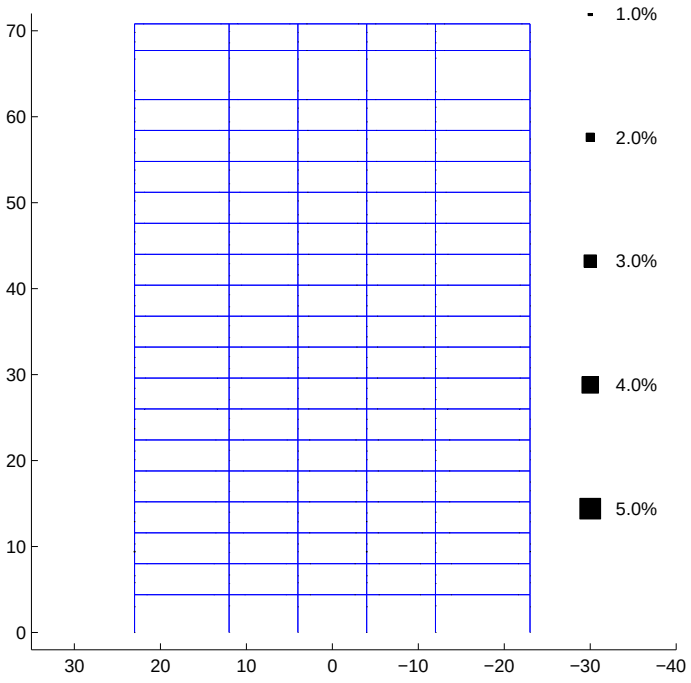

(c) Frame 6

Figure E.3: Plastic Rotations (Black:Beam-Columns White:Panel Zones) at Ultimate Roof Displacement in Building 1 Frames 5-7: Pushover in X Direction

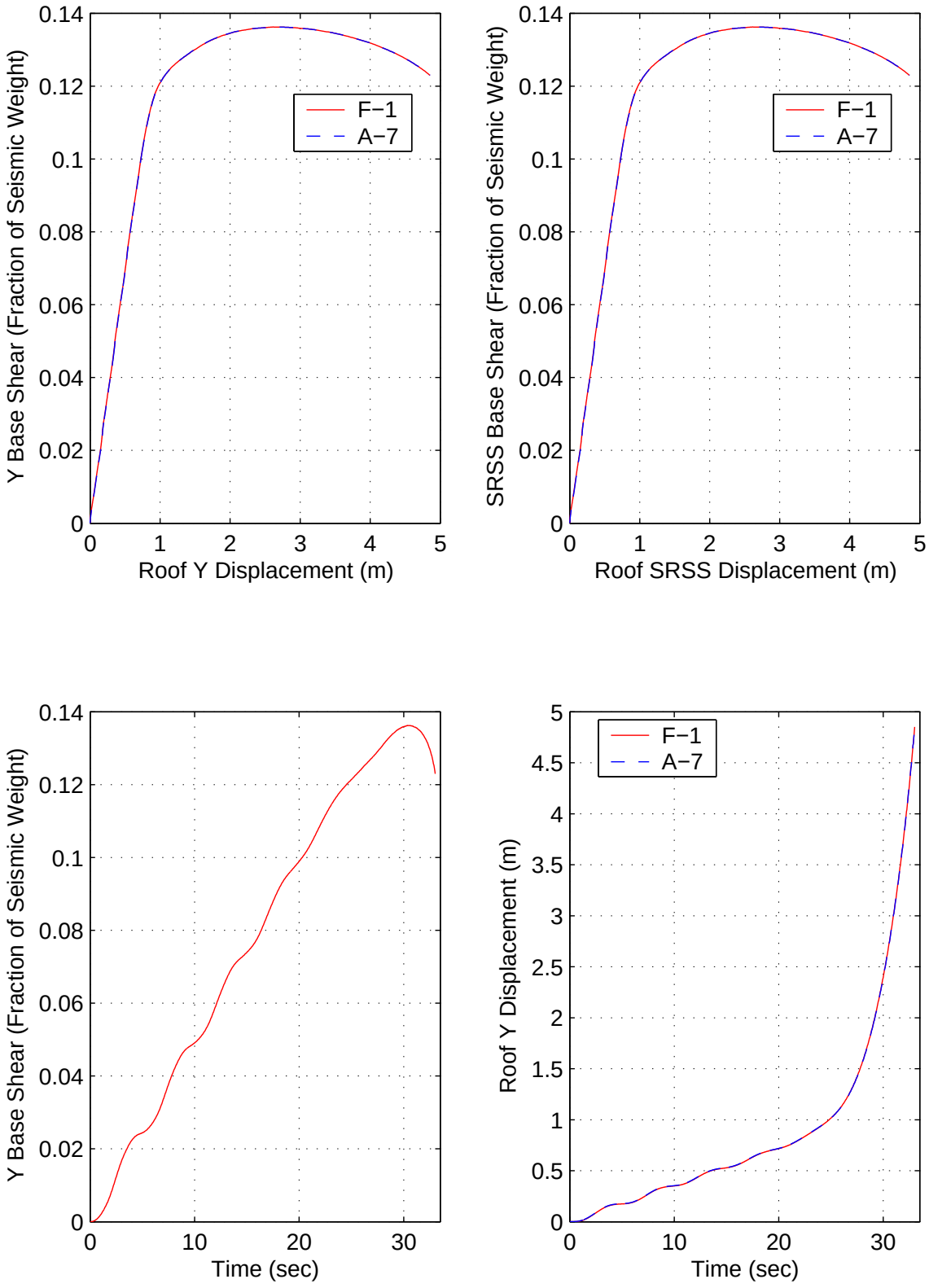

Figure E.4: Building 1 Y-Direction Pushover Results

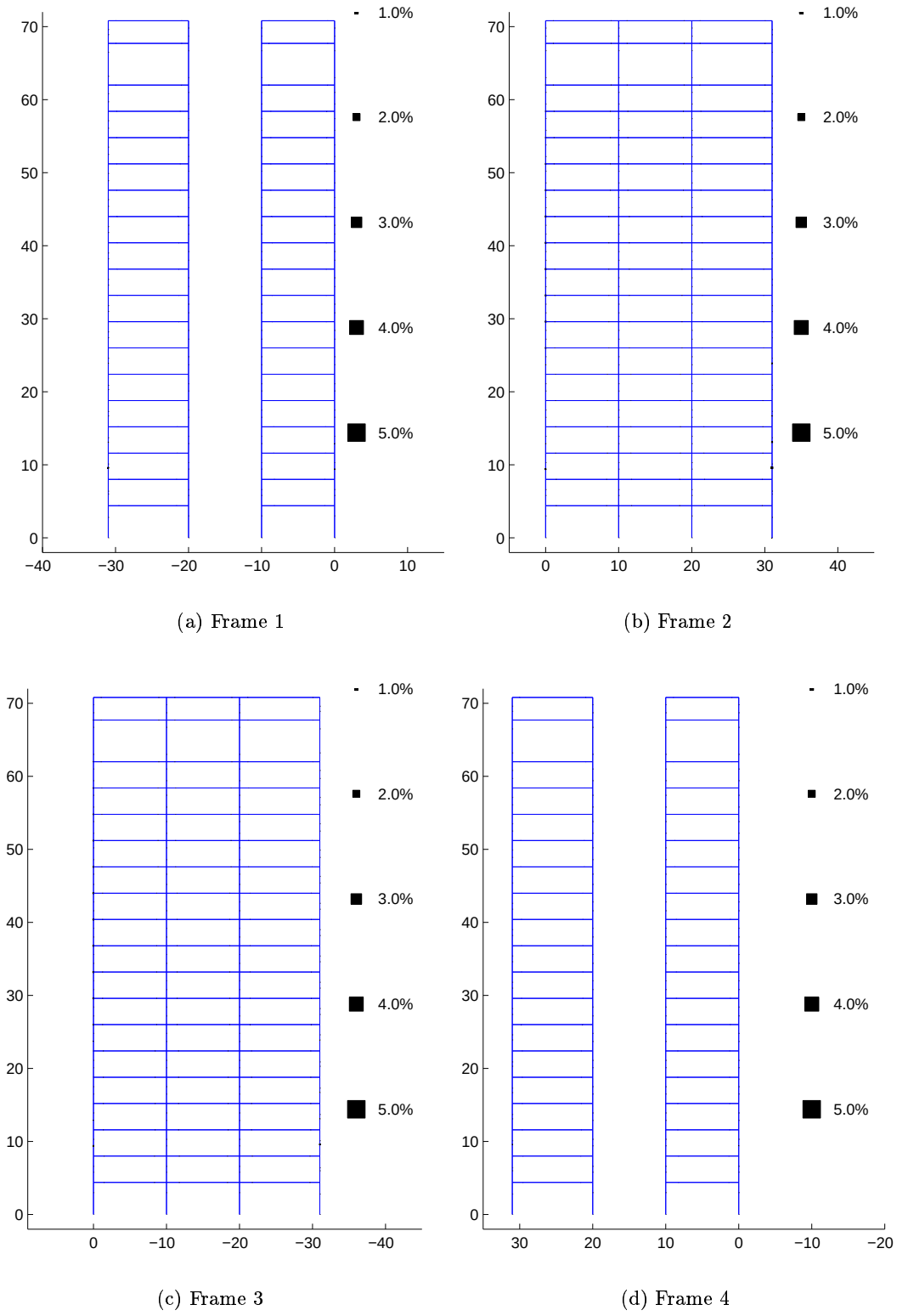

(a) Frame 1

(b) Frame 2

(c) Frame 3

(d) Frame 4

Figure E.5: Plastic Rotations (Black:Beam-Columns White:Panel Zones) at Ultimate Roof Displacement in Building 1 Frames 1-4: Pushover in Y Direction)

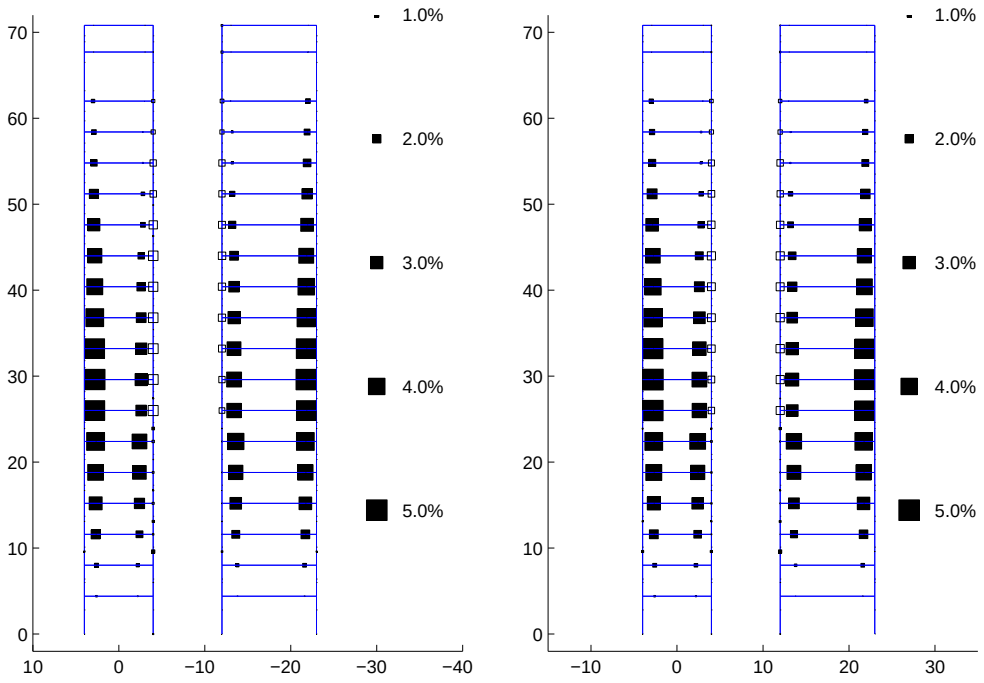

(a) Frame 5

(b) Frame 7

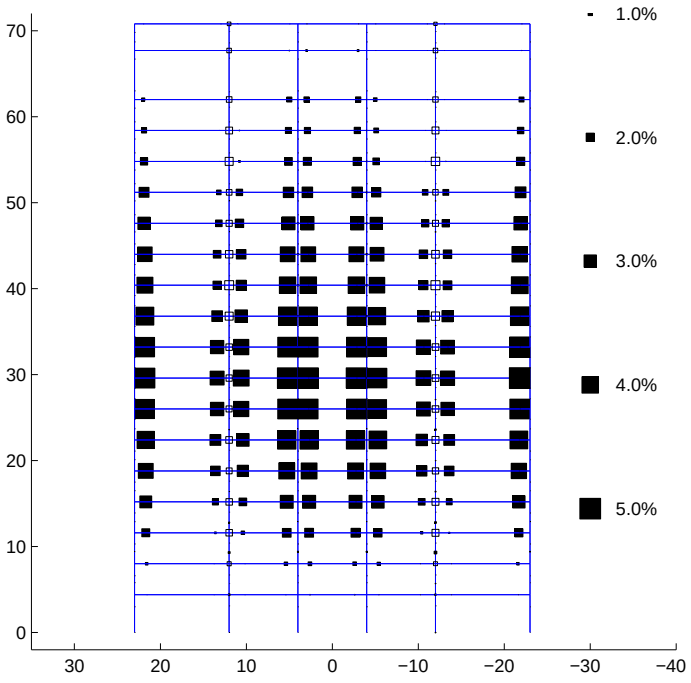

(c) Frame 6

Figure E.6: Plastic Rotations (Black:Beam-Columns White:Panel Zones) at Ultimate Roof Displacement in Building 1 Frames 5-7: Pushover in Y Direction

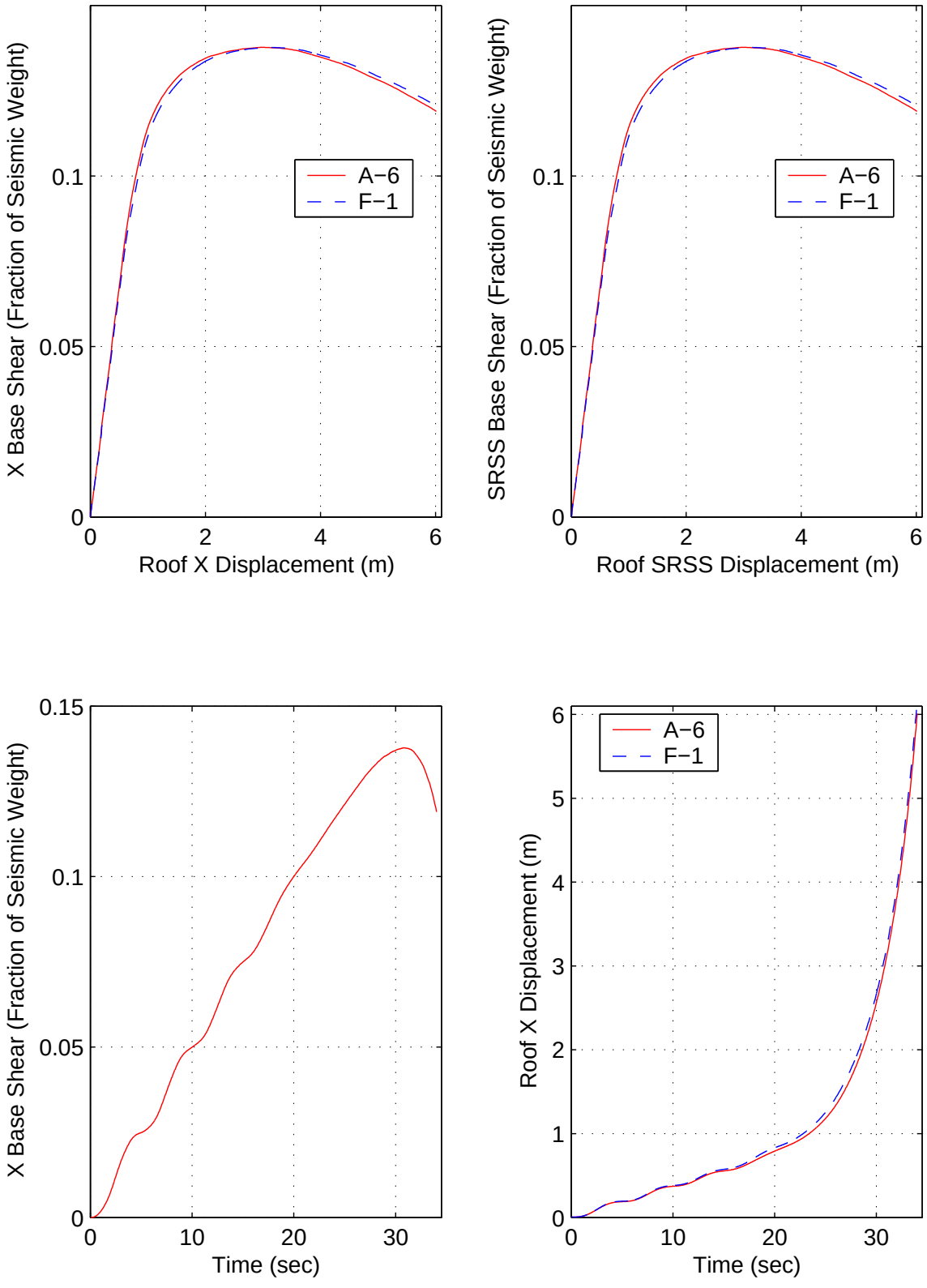

Figure E.7: Building 2 X-Direction Pushover Results

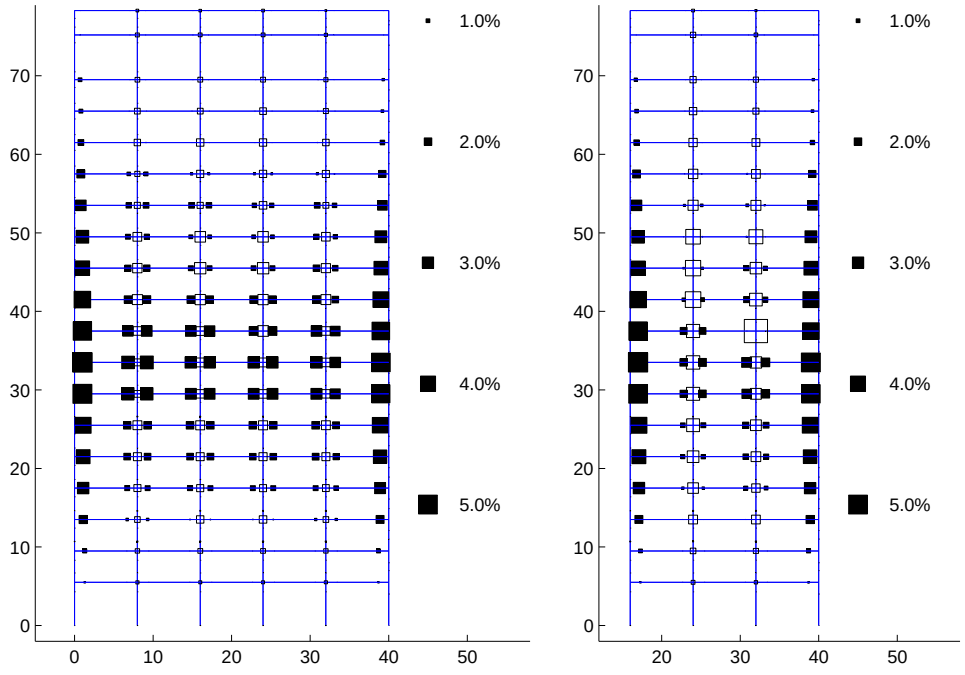

(a) Frame 1

(b) Frame 2

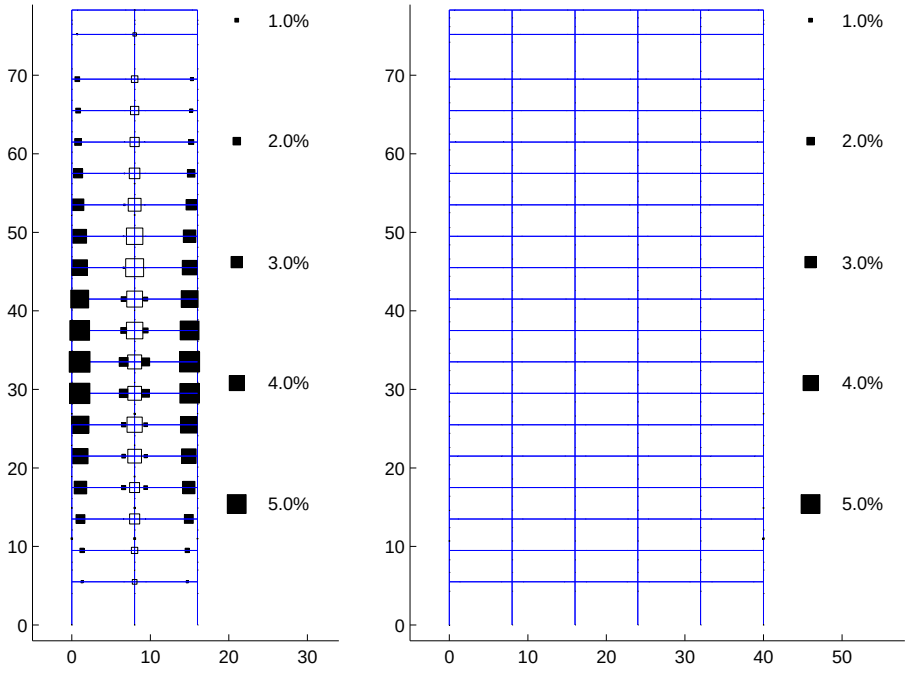

(c) Frame 3

(d) Frame 4

Figure E.8: Plastic Rotations (Black:Beam-Columns White:Panel Zones) at Ultimate Roof Displacement in Building 2 Frames 1-4: Pushover in X Direction

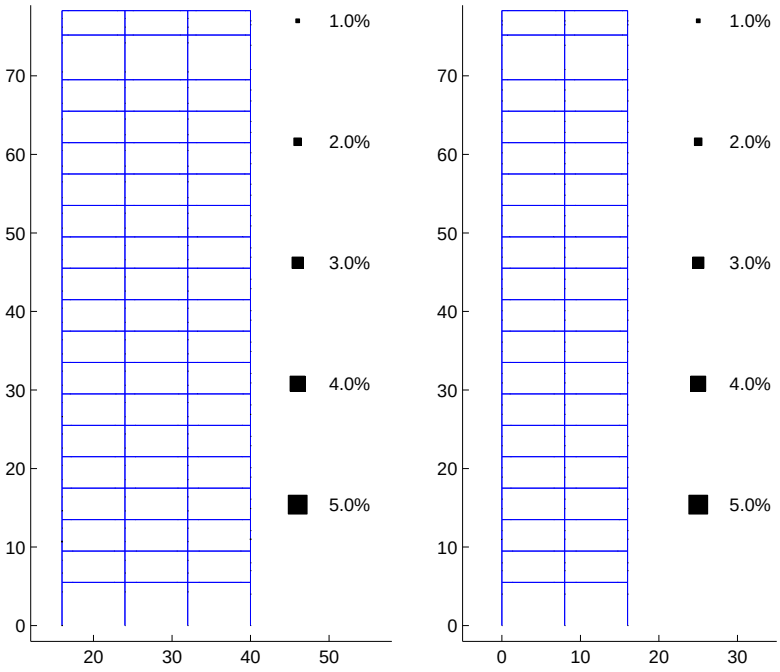

(a) Frame 5

(b) Frame 6

Figure E.9: Plastic Rotations (Black:Beam-Columns White:Panel Zones) at Ultimate Roof Displacement in Building 2 Frames 5-6: Pushover in X Direction

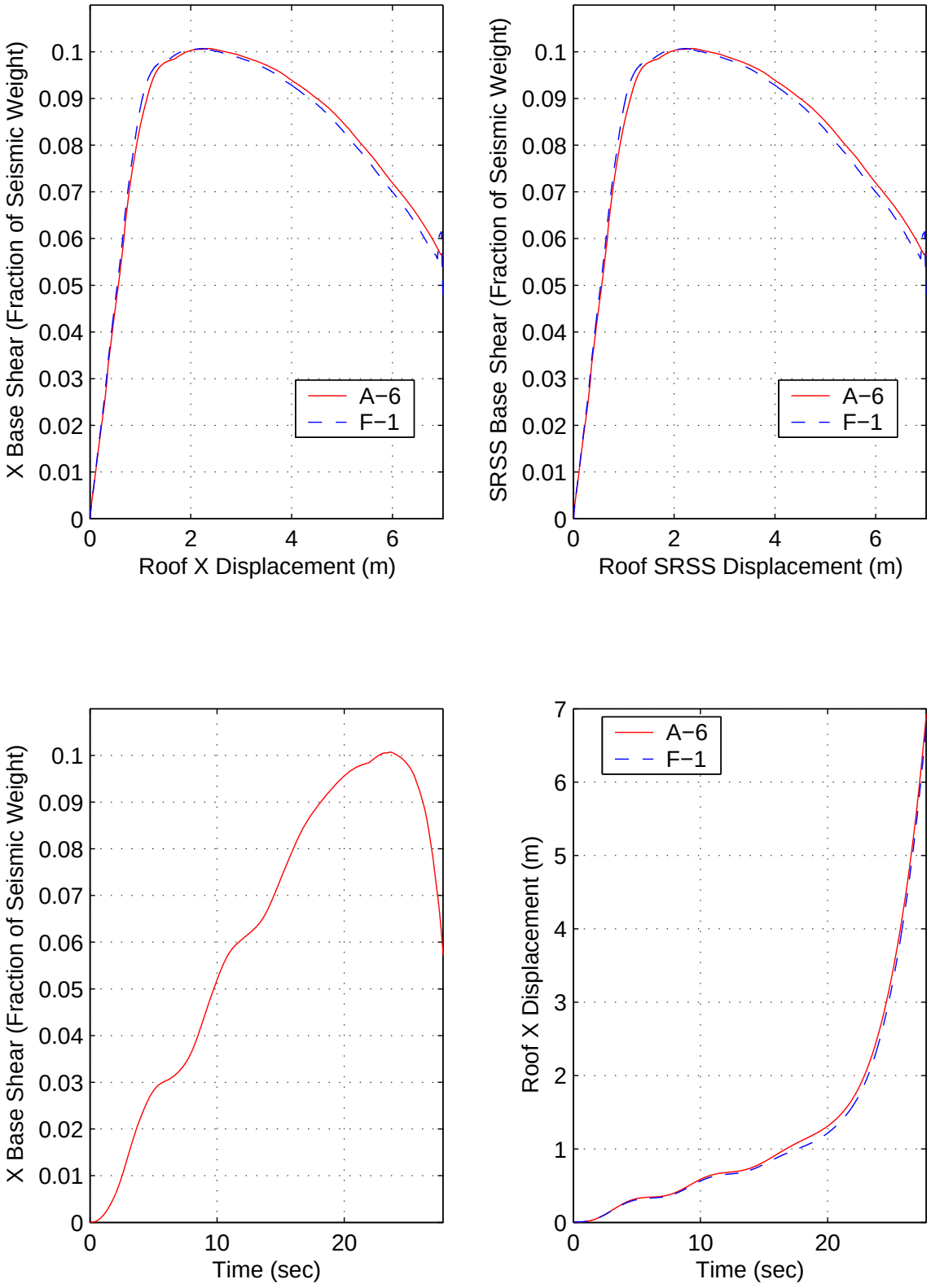

Figure E.10: Building 2A X-Direction Pushover Results

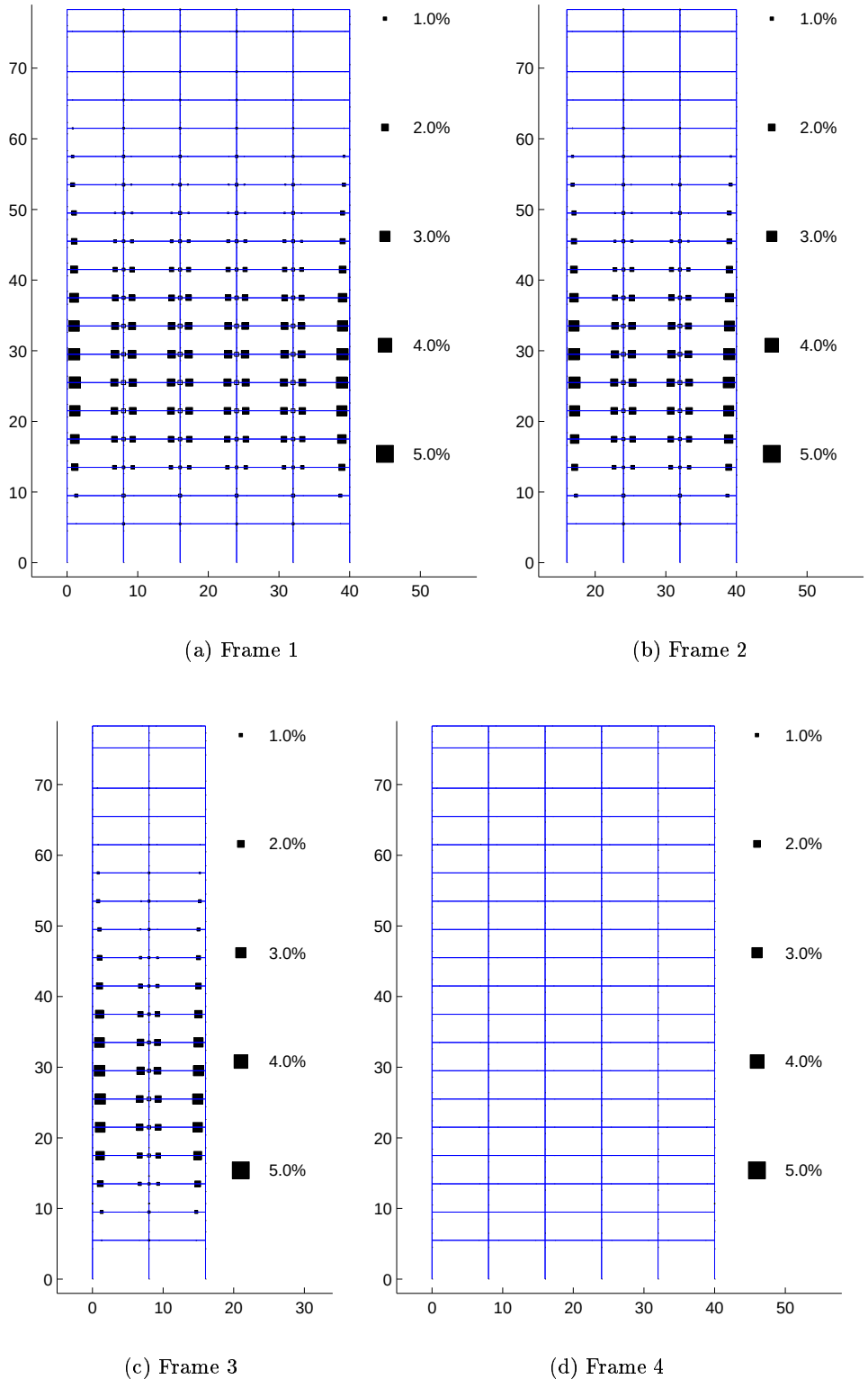

(a) Frame 1

(b) Frame 2

(c) Frame 3

(d) Frame 4

Figure E.11: Plastic Rotations (Black:Beam-Columns White:Panel Zones) at Ultimate Roof Displacement in Building 2A Frames 1-4: Pushover in X Direction

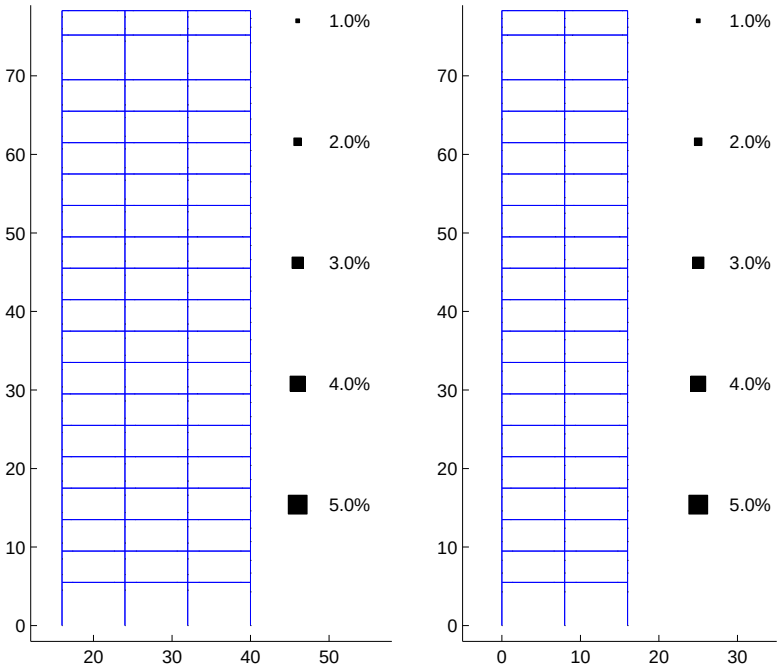

(a) Frame 5

(b) Frame 6

Figure E.12: Plastic Rotations (Black:Beam-Columns White:Panel Zones) at Ultimate Roof Displacement in Building 2A Frames 5-6: Pushover in X Direction

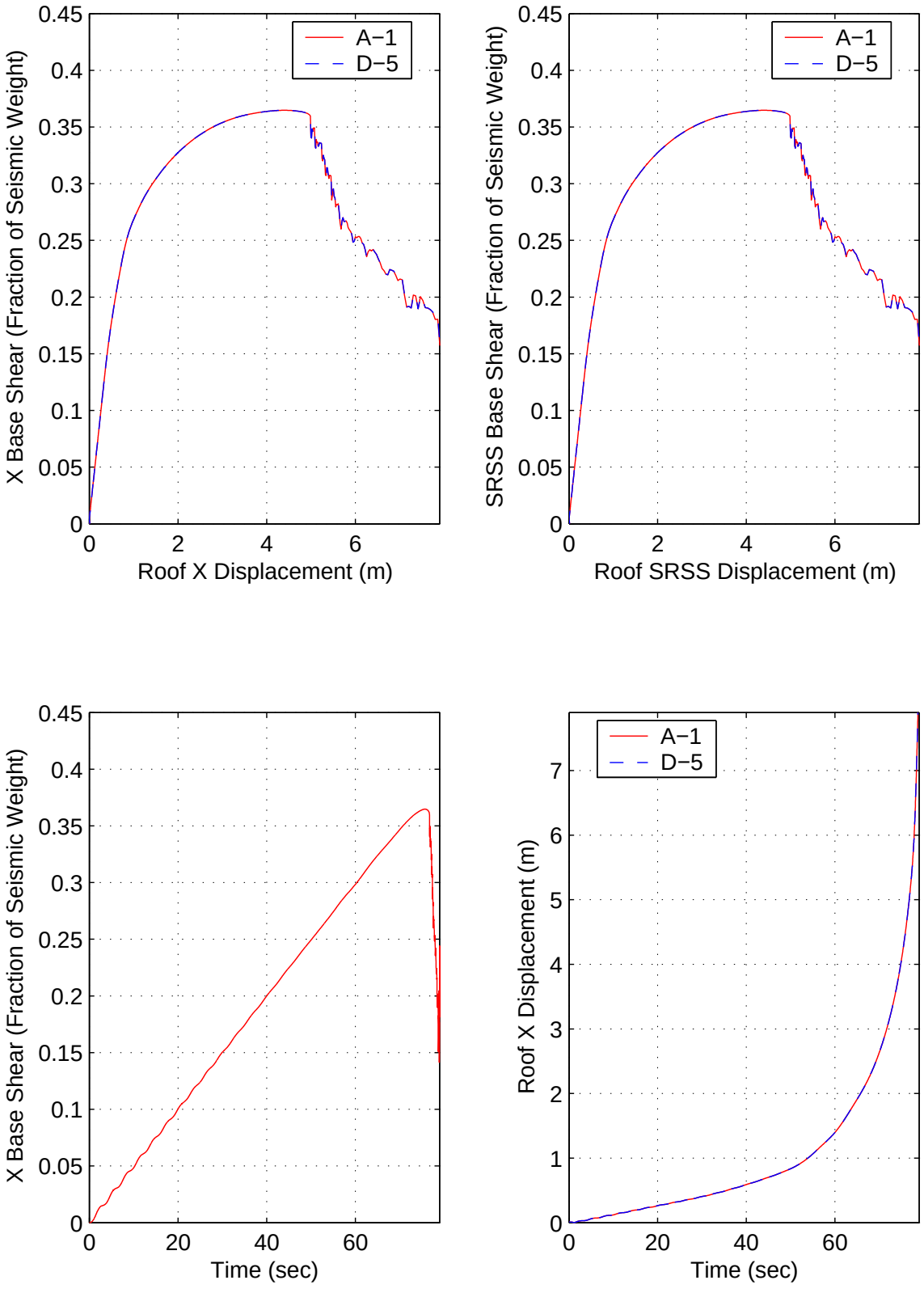

Figure E.13: Building 3 X-Direction Pushover Results

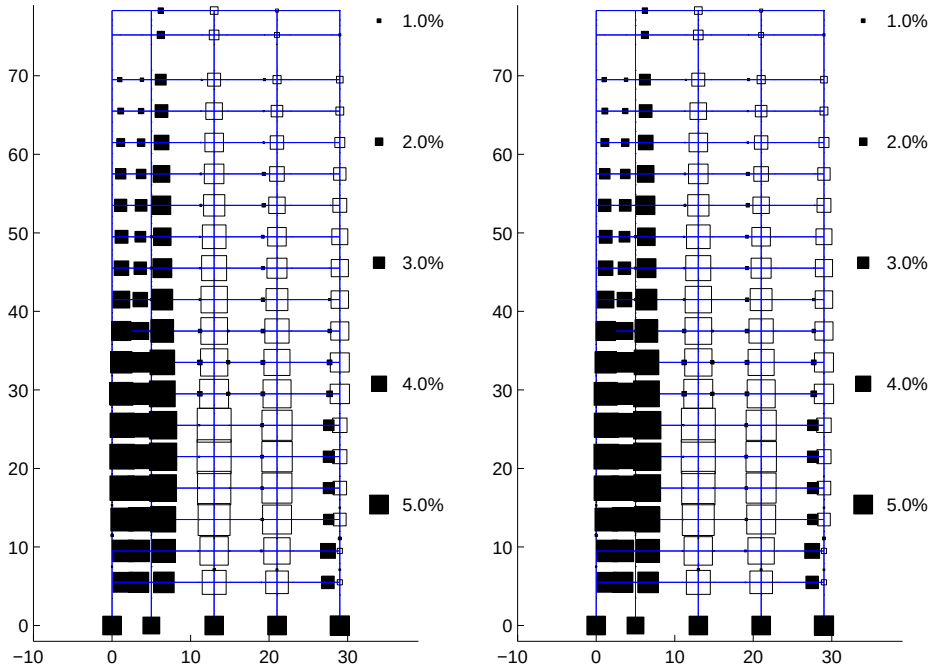

(a) Frame 1

(b) Frame 2

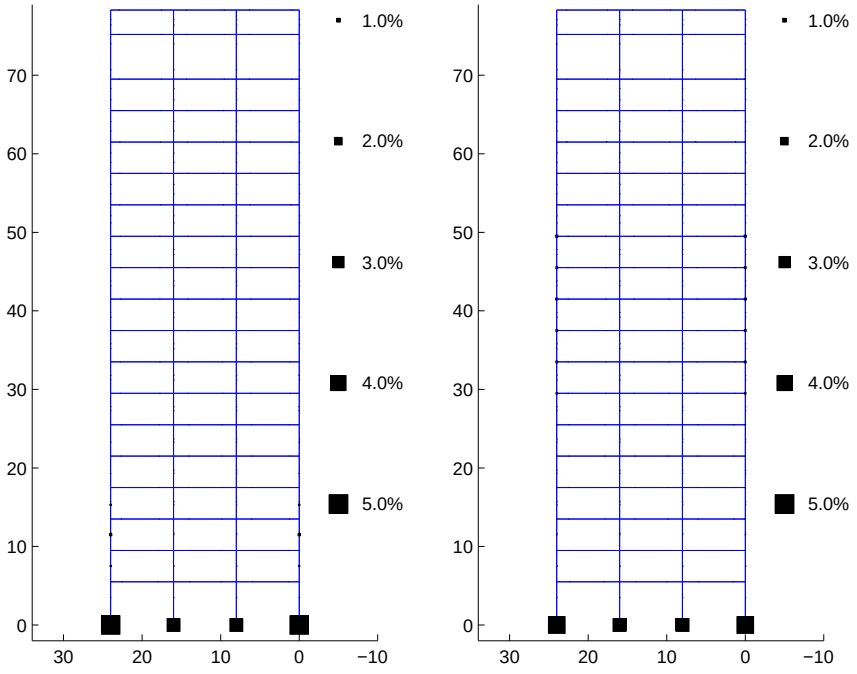

(c) Frame 3

(d) Frame 4

Figure E.14: Plastic Rotations (Black:Beam-Columns White:Panel Zones) at Ultimate Roof Displacement in Building 3 Frames 1-4: Pushover in X Direction

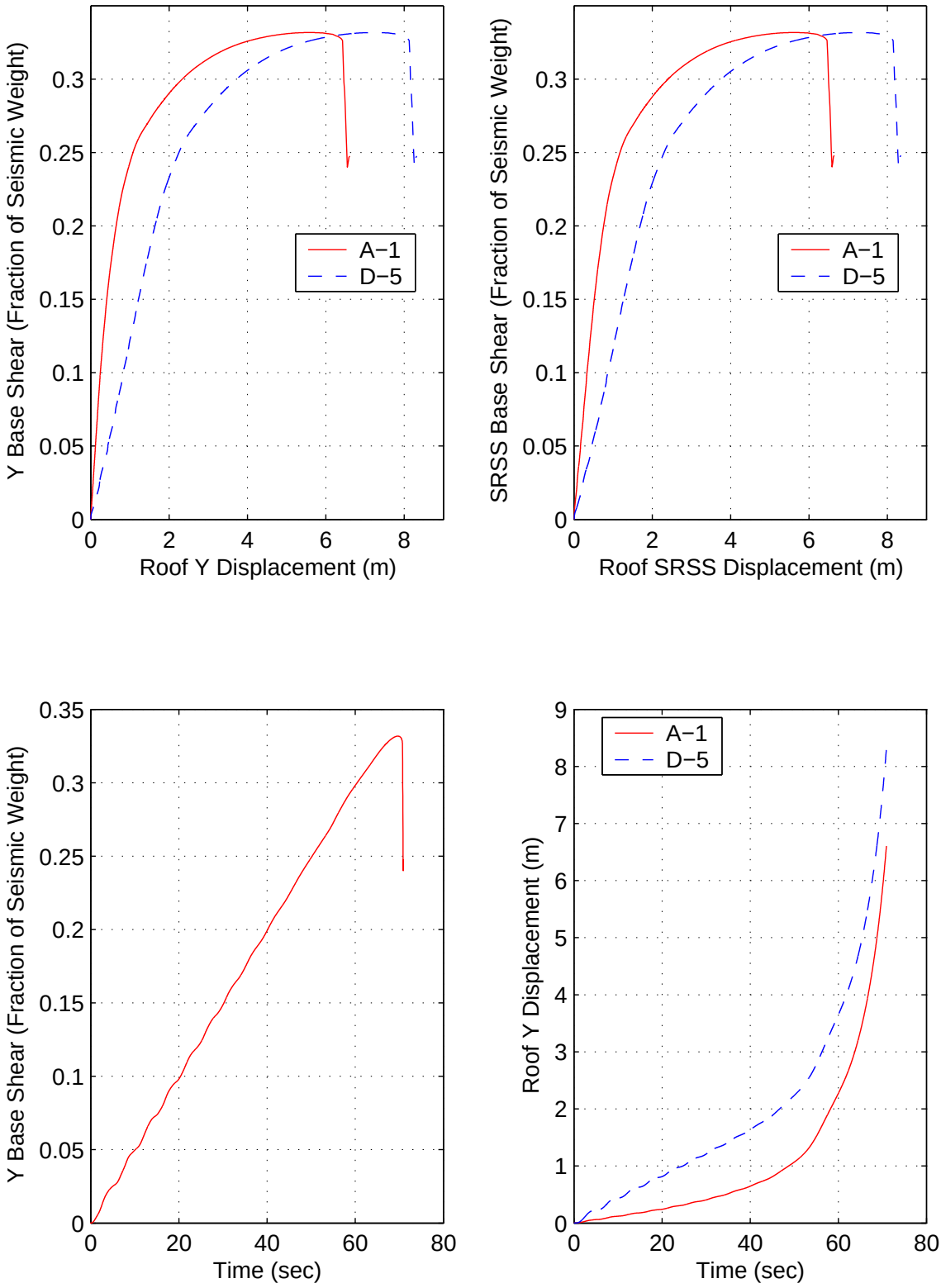

Figure E.15: Building 3 Y-Direction Pushover Results

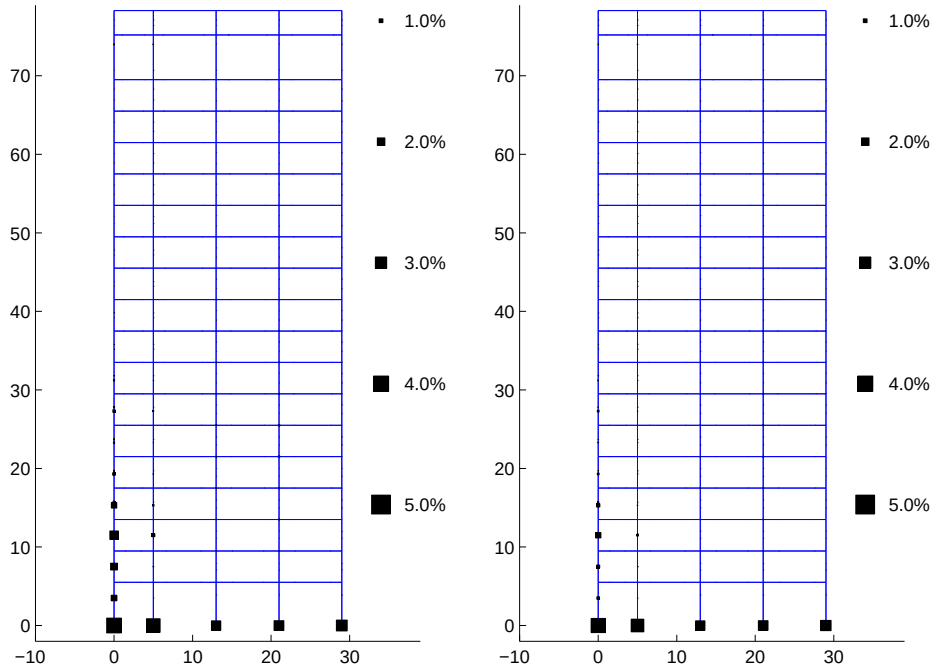

(a) Frame 1

(b) Frame 2

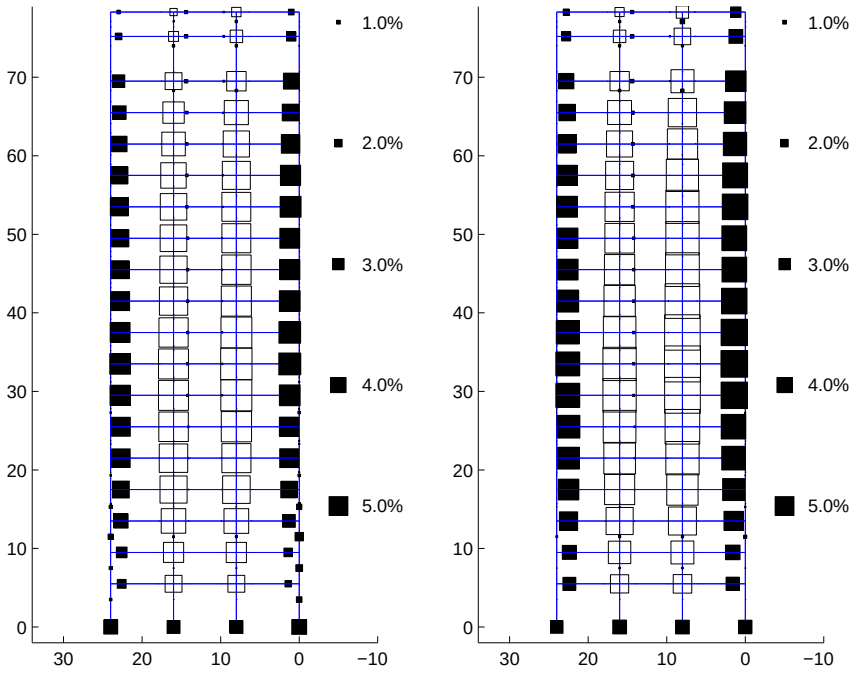

(c) Frame 3

(d) Frame 4

Figure E.16: Plastic Rotations (Black:Beam-Columns White:Panel Zones) at Ultimate Roof Displacement in Building 3 Frames 1-4: Pushover in Y Direction

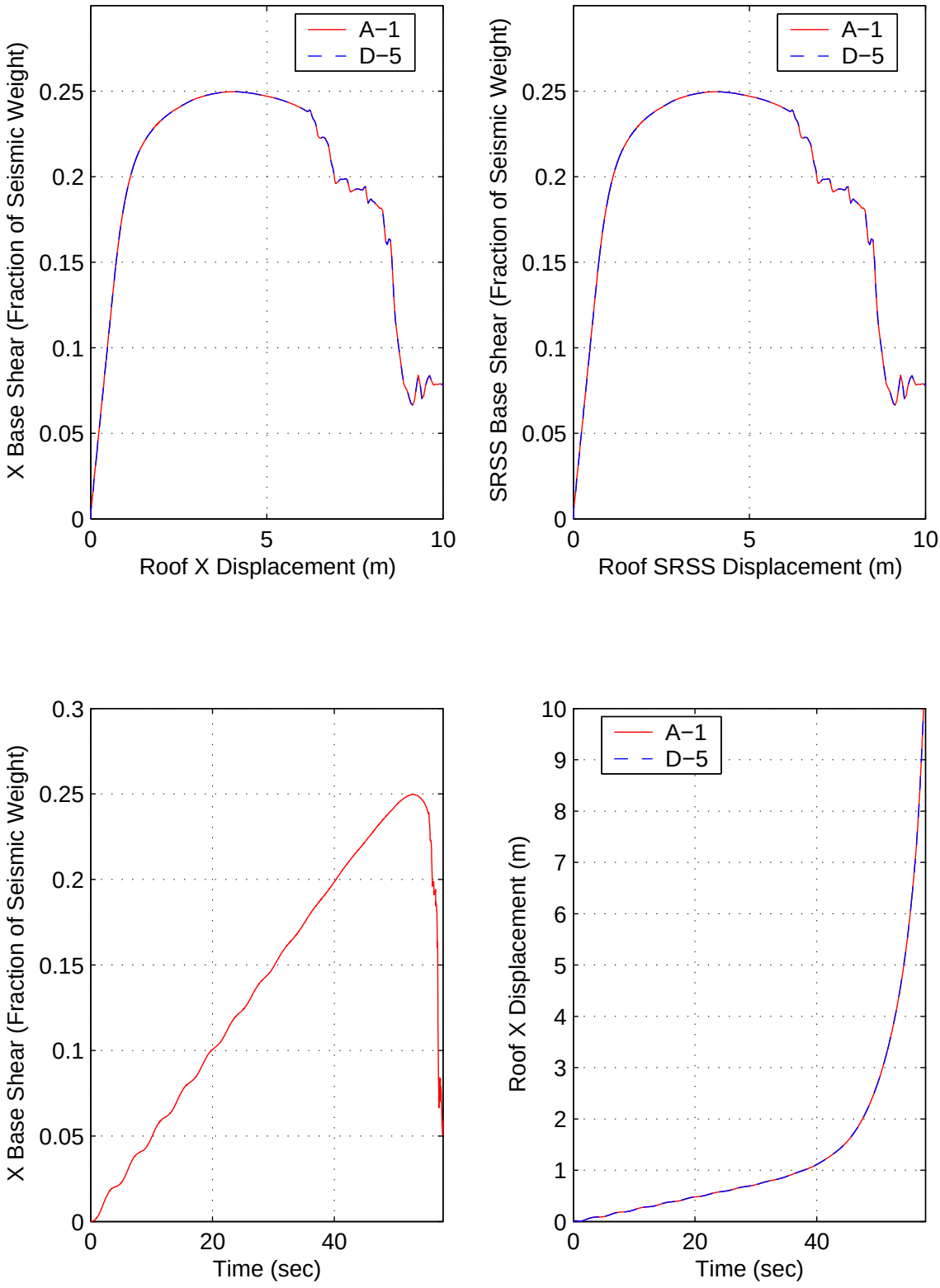

Figure E.17: Building 3A X-Direction Pushover Results

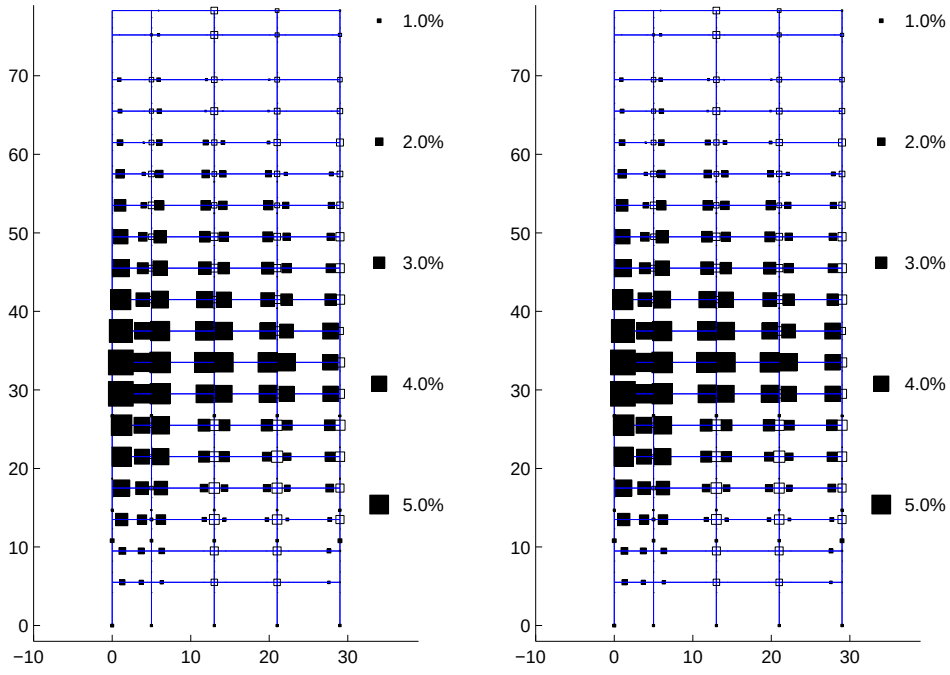

(a) Frame 1

(b) Frame 2

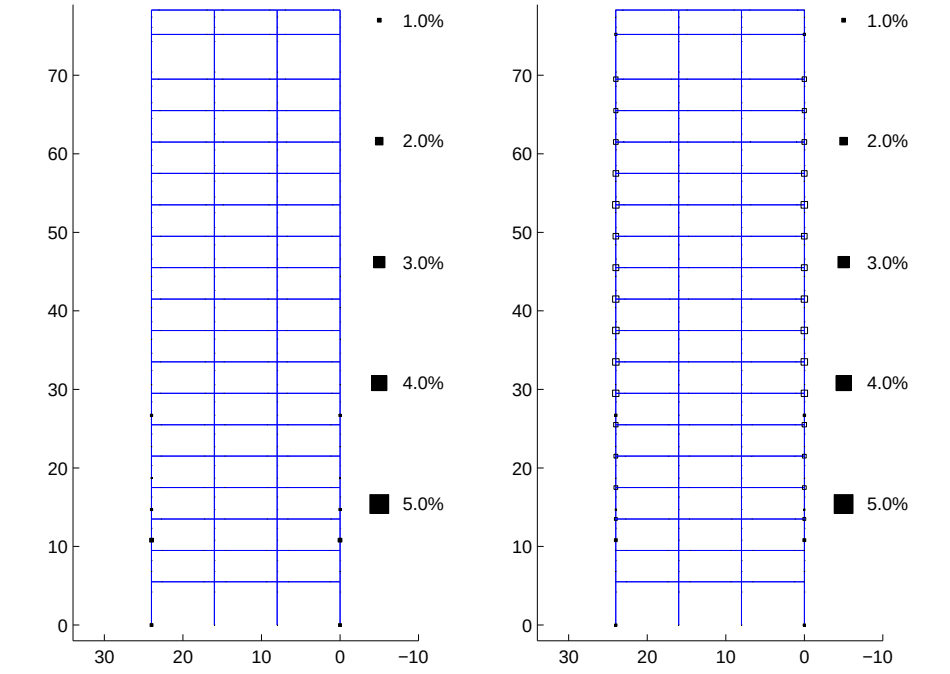

(c) Frame 3

(d) Frame 4

Figure E.18: Plastic Rotations (Black:Beam-Columns White:Panel Zones) at Ultimate Roof Displacement in Building 3A Frames 1-4: Pushover in X Direction

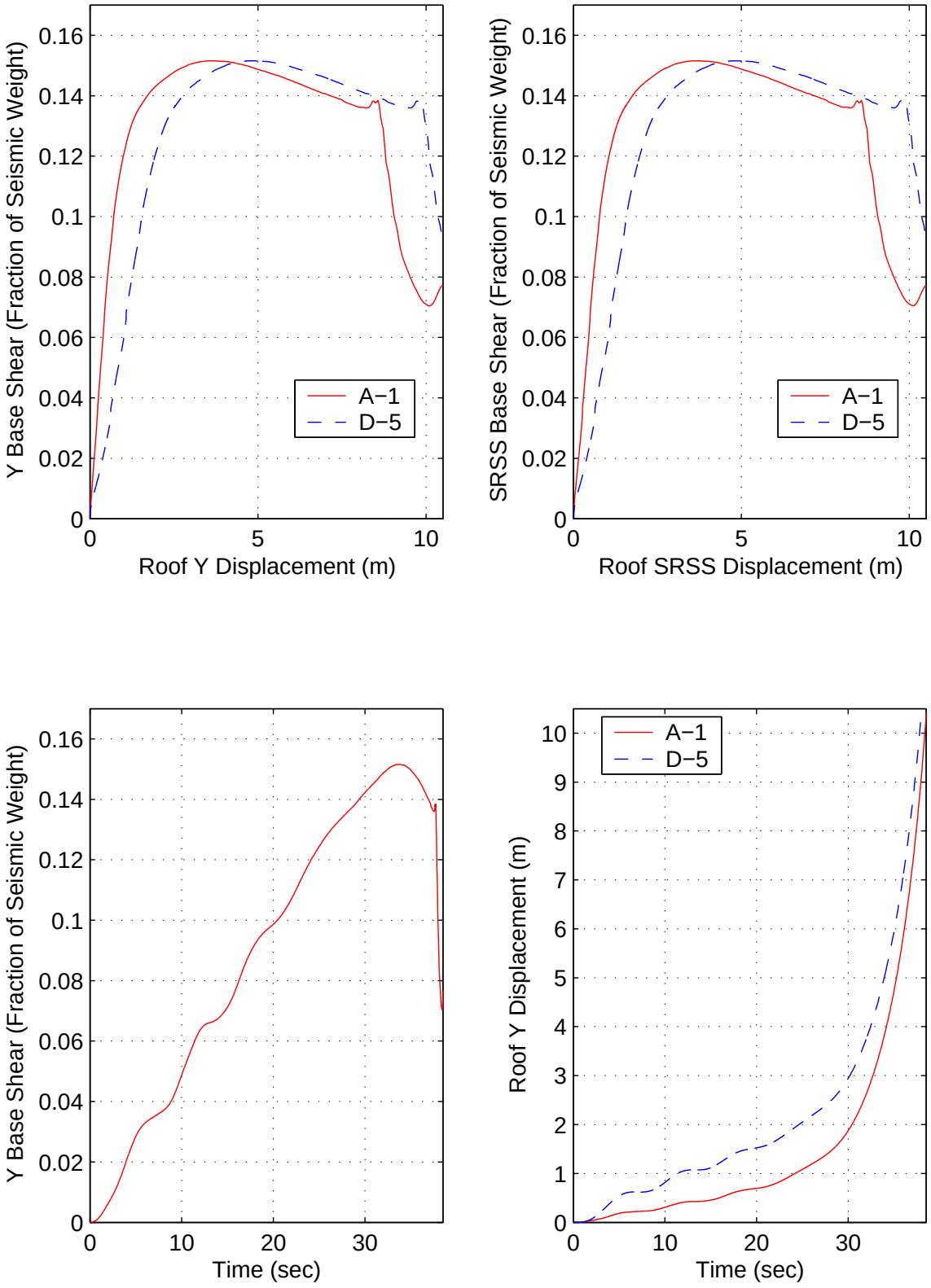

Figure E.19: Building 3A Y-Direction Pushover Results

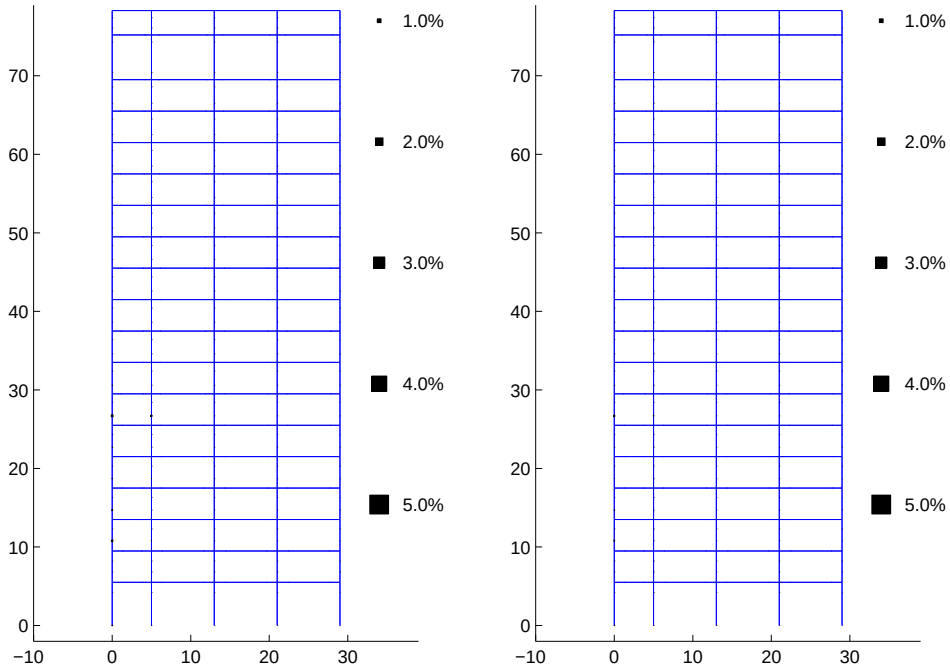

(a) Frame 1

(b) Frame 2

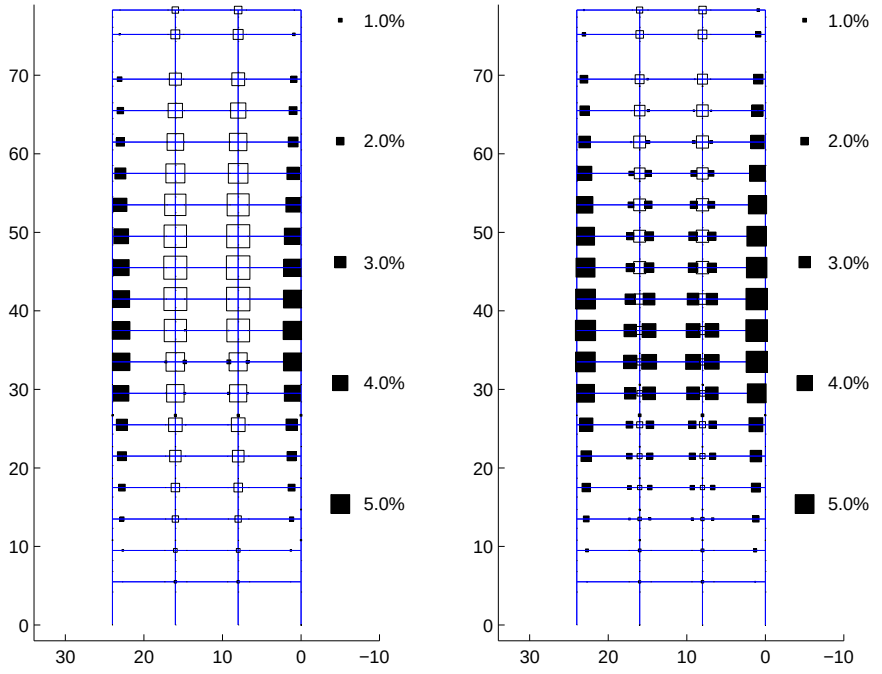

(c) Frame 3

(d) Frame 4

Figure E.20: Plastic Rotations (Black:Beam-Columns White:Panel Zones) at Ultimate Roof Displacement in Building 3A Frames 1-4: Pushover in Y Direction

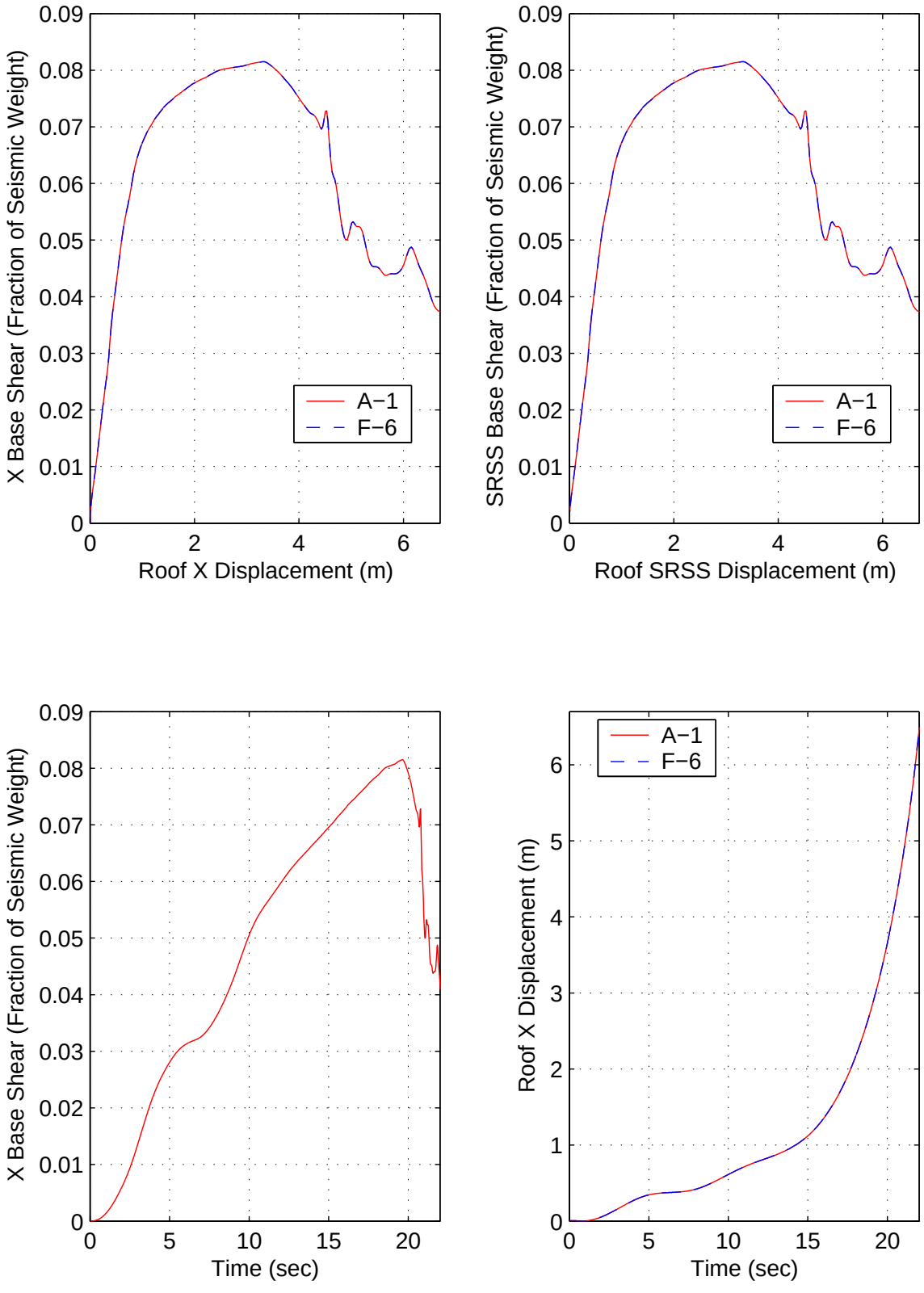

Figure E.21: Building 4 X-Direction Pushover Results

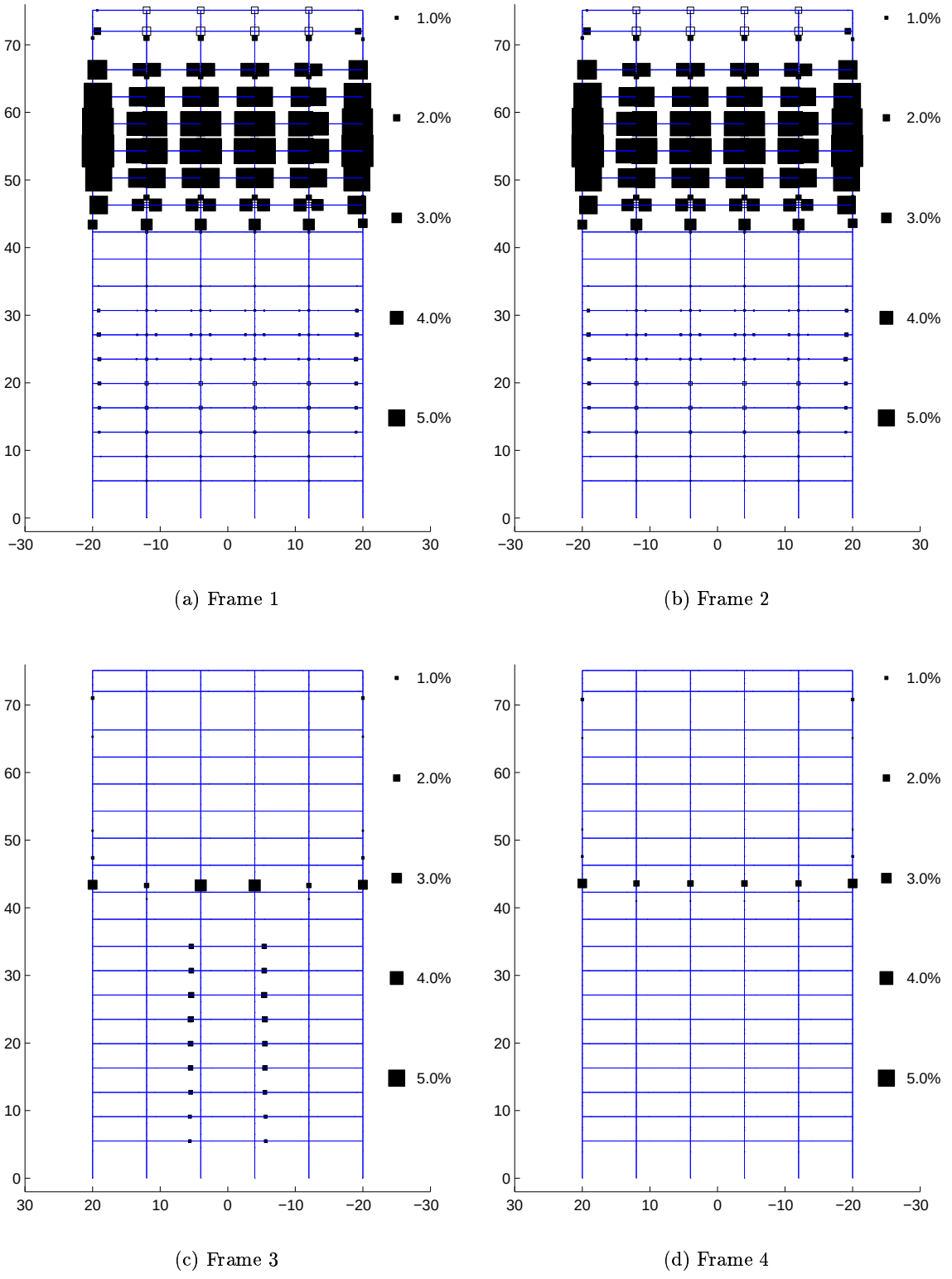

(a) Frame 1

(b) Frame 2

(c) Frame 3

(d) Frame 4

Figure E.22: Plastic Rotations (Black:Beam-Columns White:Panel Zones) at Ultimate Roof Displacement in Building 4 Frames 1-4: Pushover in X Direction

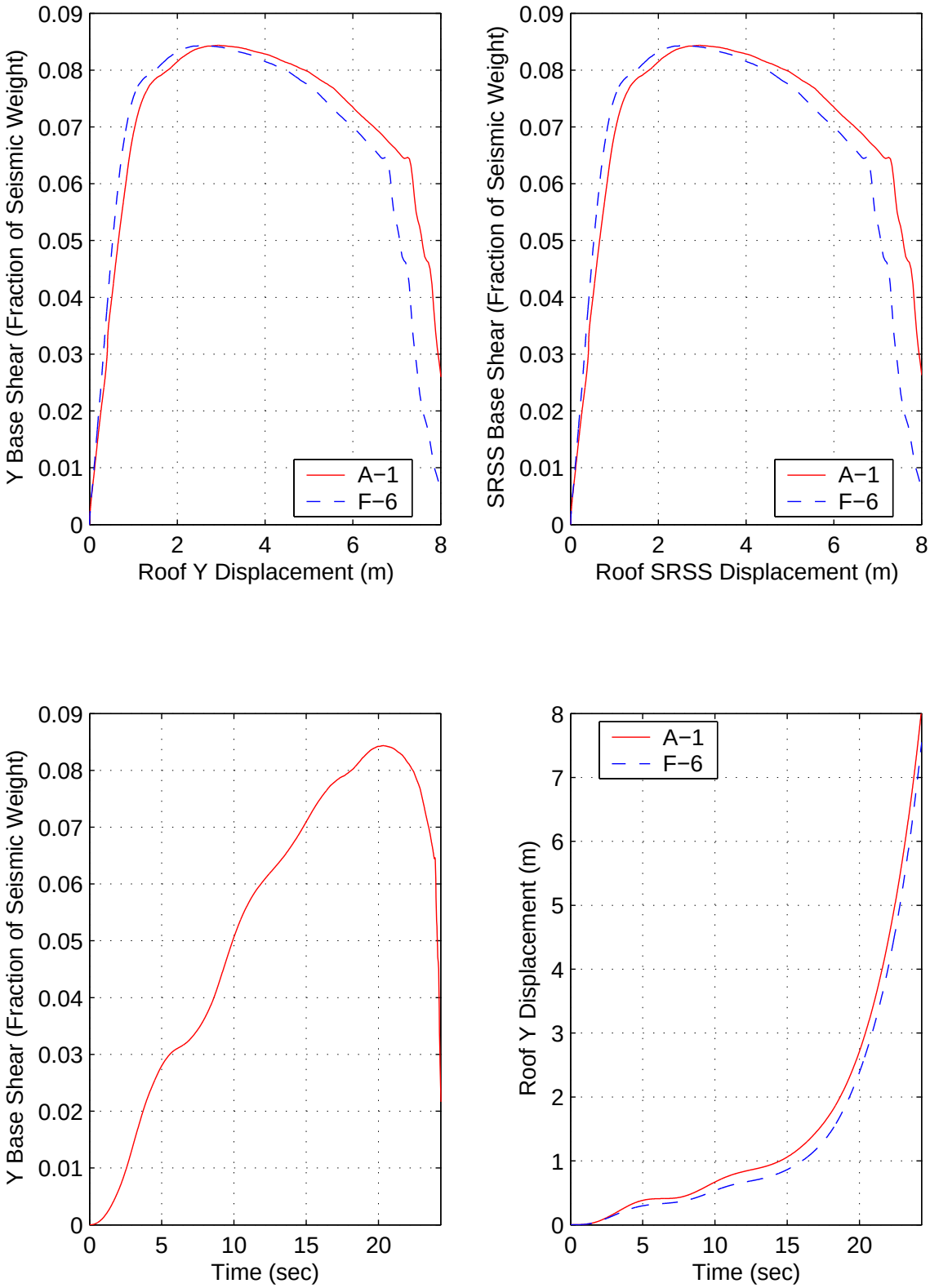

Figure E.23: Building 4 Y-Direction Pushover Results

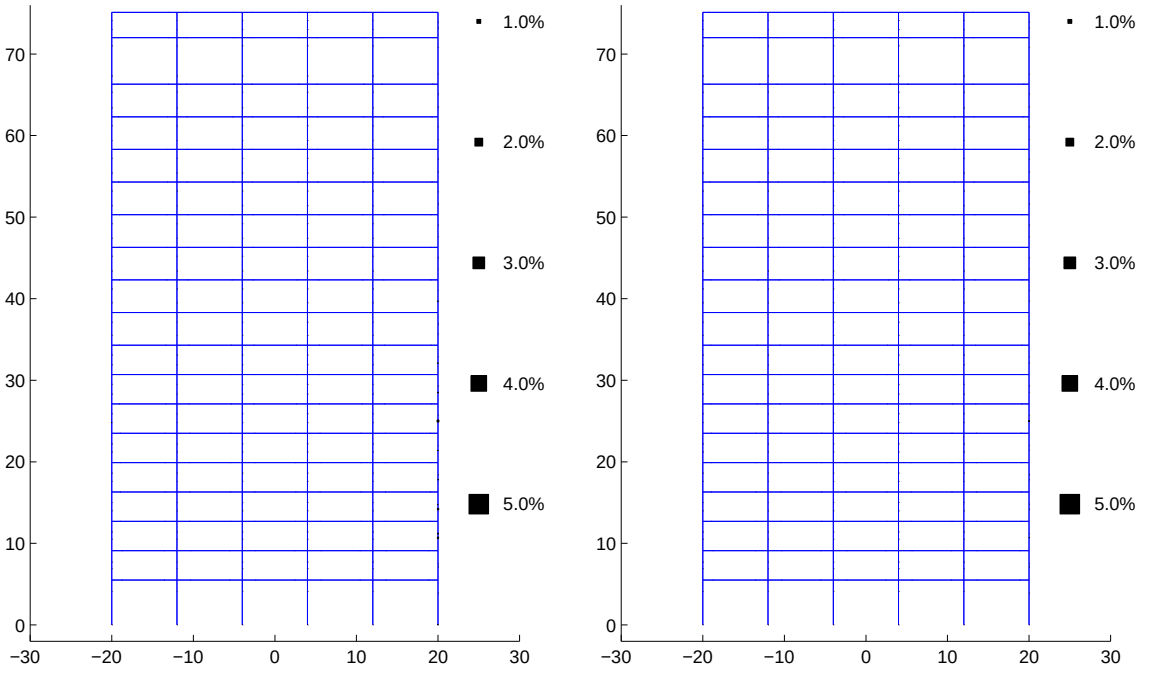

(a) Frame 1

(b) Frame 2

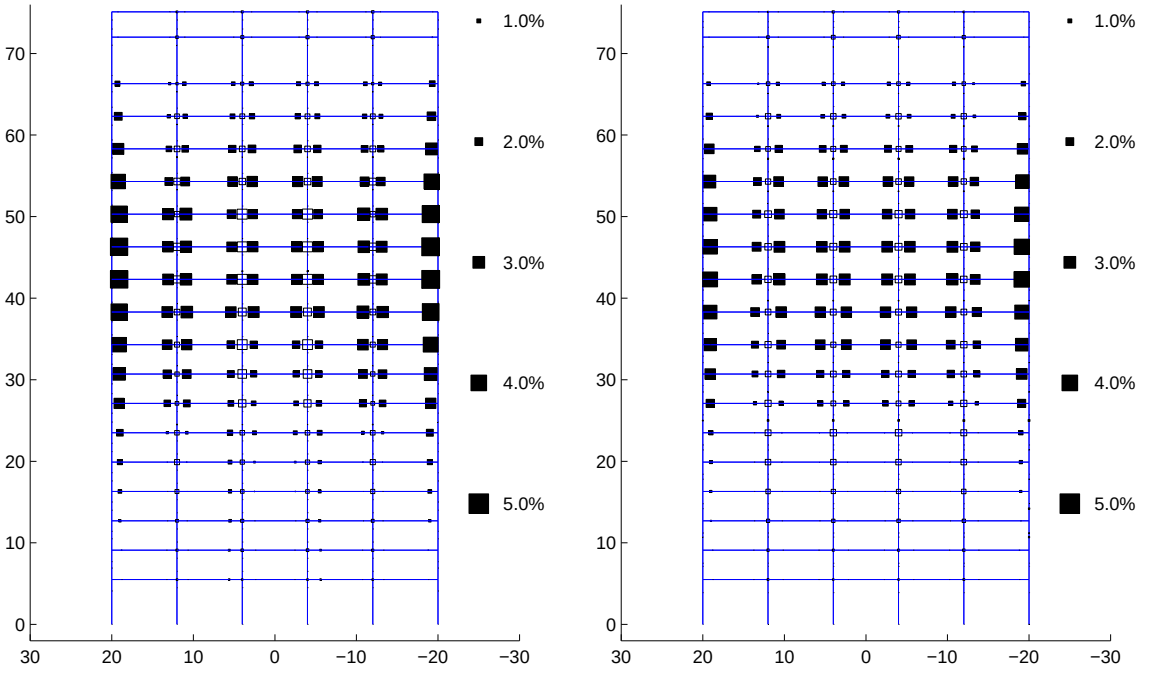

(c) Frame 3

(d) Frame 4

Figure E.24: Plastic Rotations (Black:Beam-Columns White:Panel Zones) at Ultimate Roof Displacement in Building 4 Frames 1-4: Pushover in Y Direction

Appendix F Ground Motion Analysis of Buildings: Displacement and Drift Time Histories

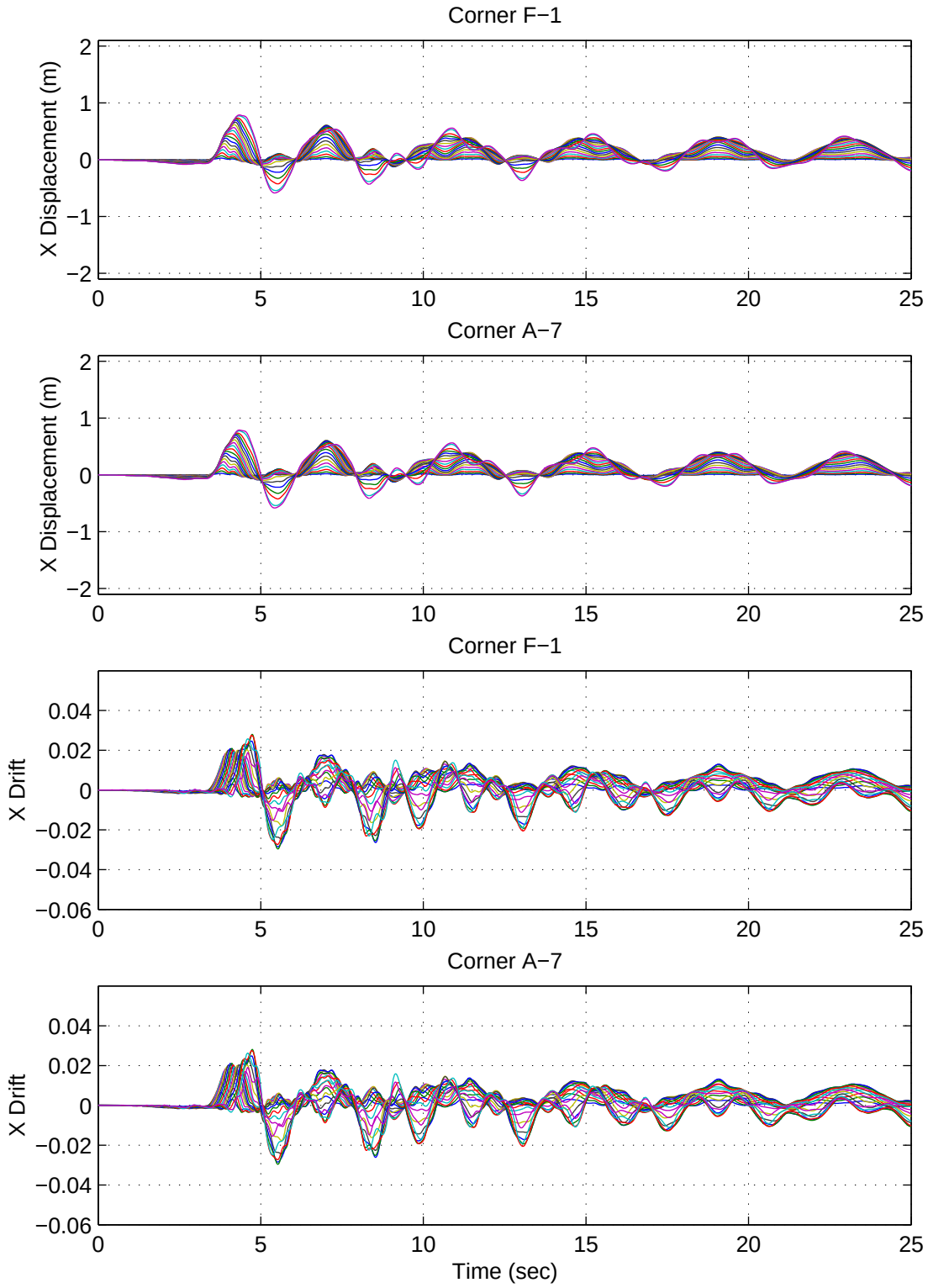

Figure F.1: Building 1 X-Direction Displacements & Drifts: Northridge Earthquake (Sylmar Record Strong Component in X Direction)

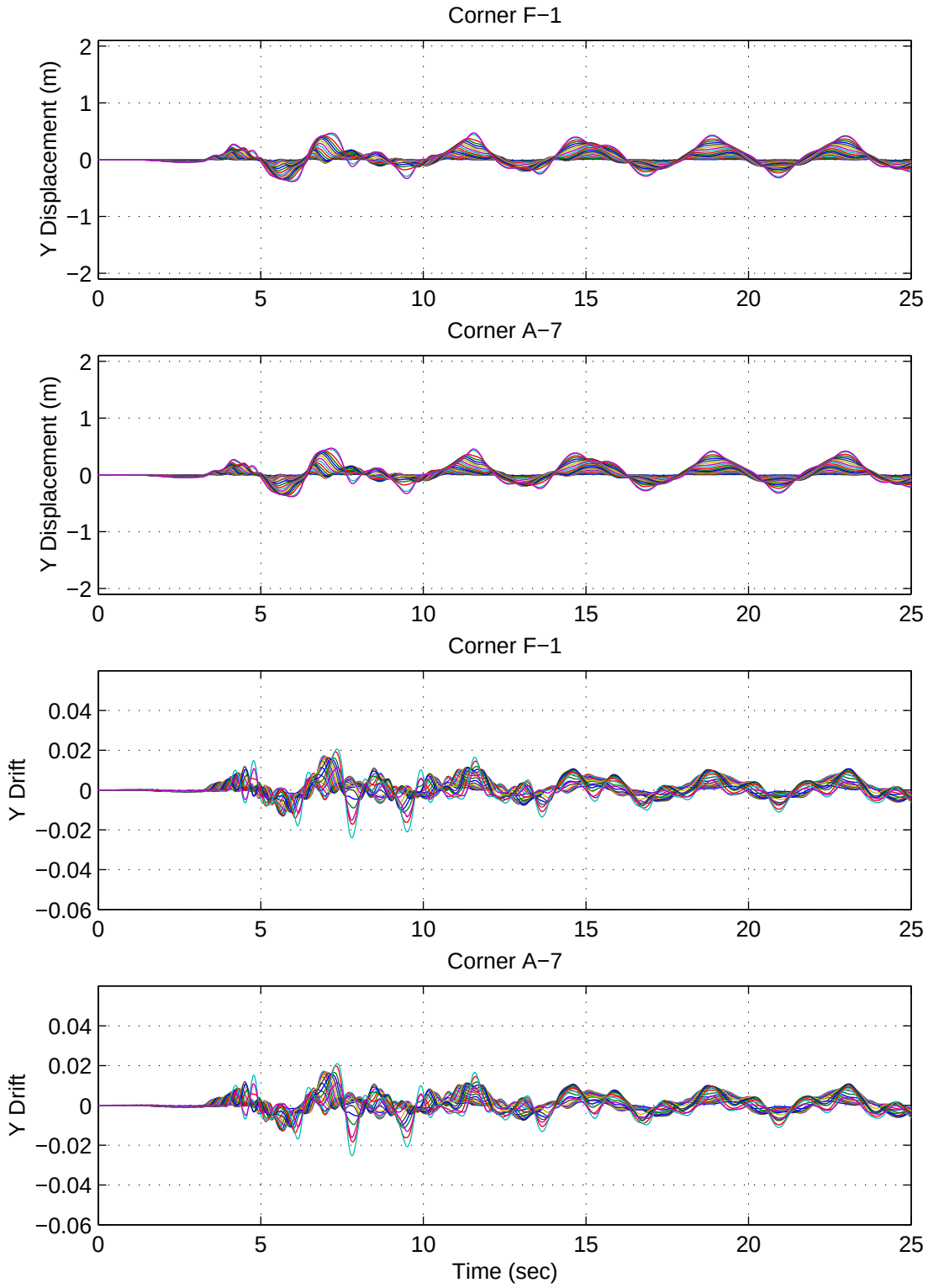

Figure F.2: Building 1 Y-Direction Displacements & Drifts: Northridge Earthquake (Sylmar Record Strong Component in X Direction)

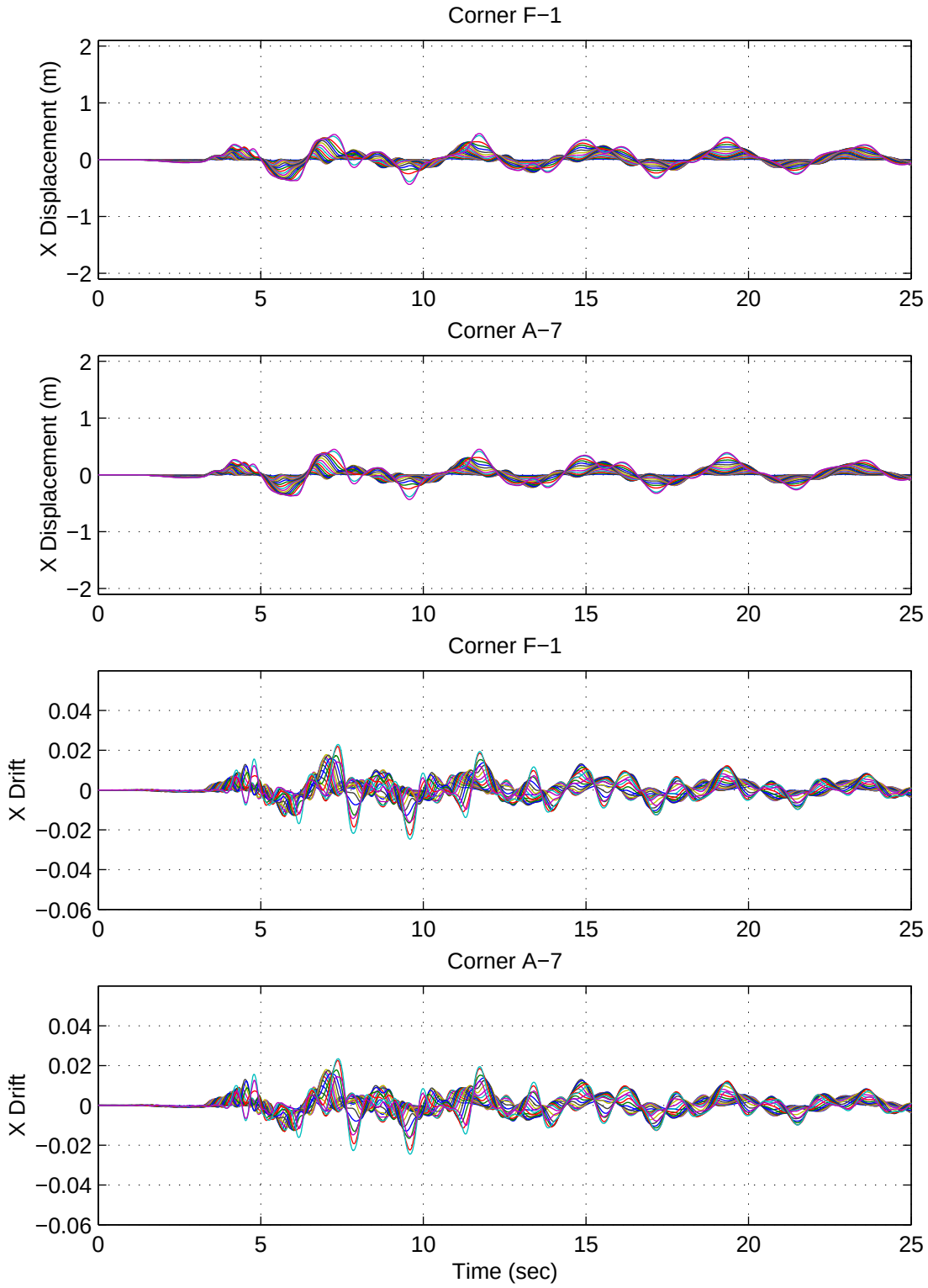

Figure F.3: Building 1 X-Direction Displacements & Drifts: Northridge Earthquake (Sylmar Record Strong Component in Y Direction)

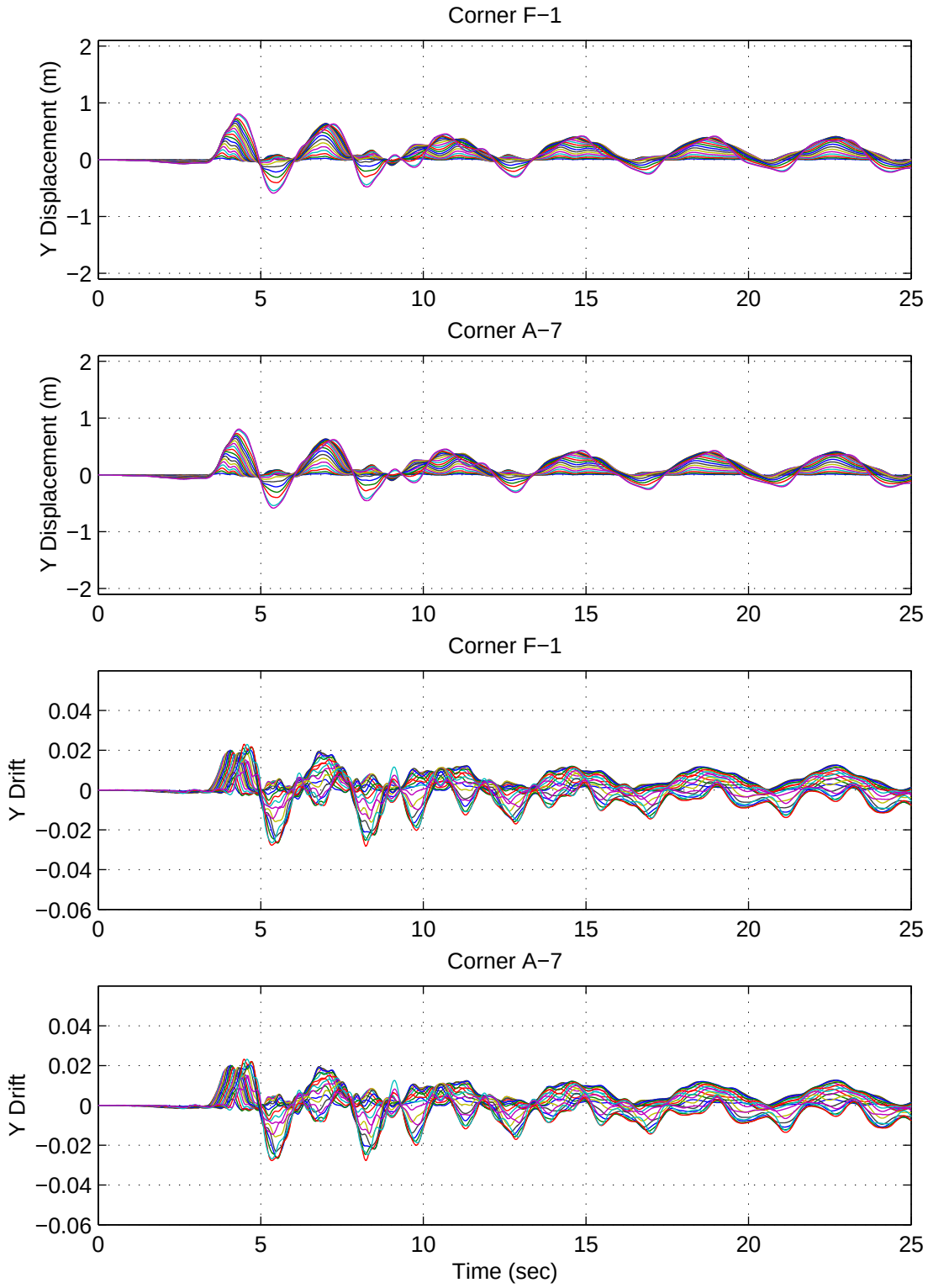

Figure F.4: Building 1 Y-Direction Displacements & Drifts: Northridge Earthquake (Sylmar Record Strong Component in Y Direction)

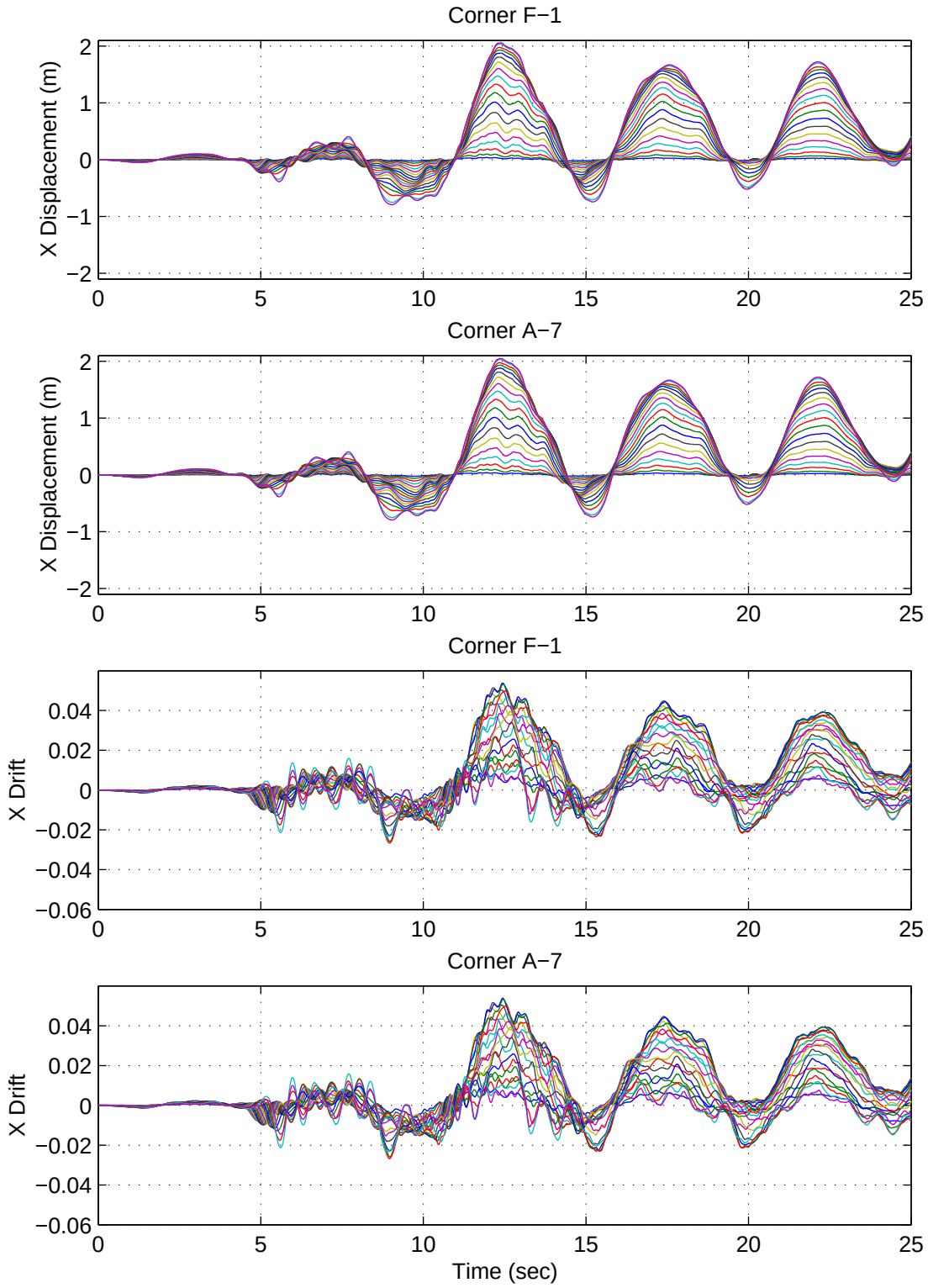

Figure F.5: Building 1 X-Direction Displacements & Drifts: Iran Earthquake (Tabas Record Strong Component in X Direction)

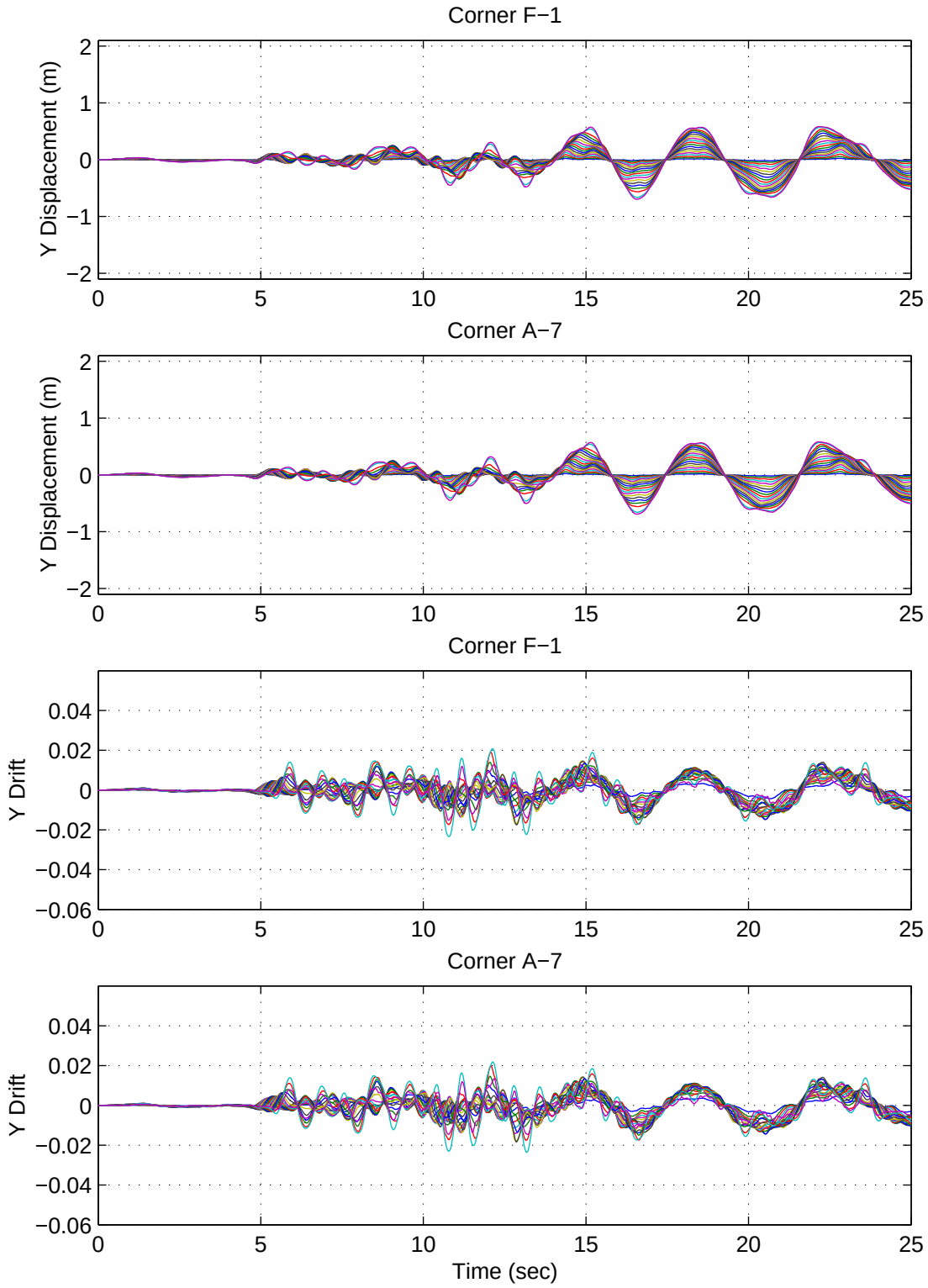

Figure F.6: Building 1 Y-Direction Displacements & Drifts: Iran Earthquake (Tabas Record Strong Component in X Direction)

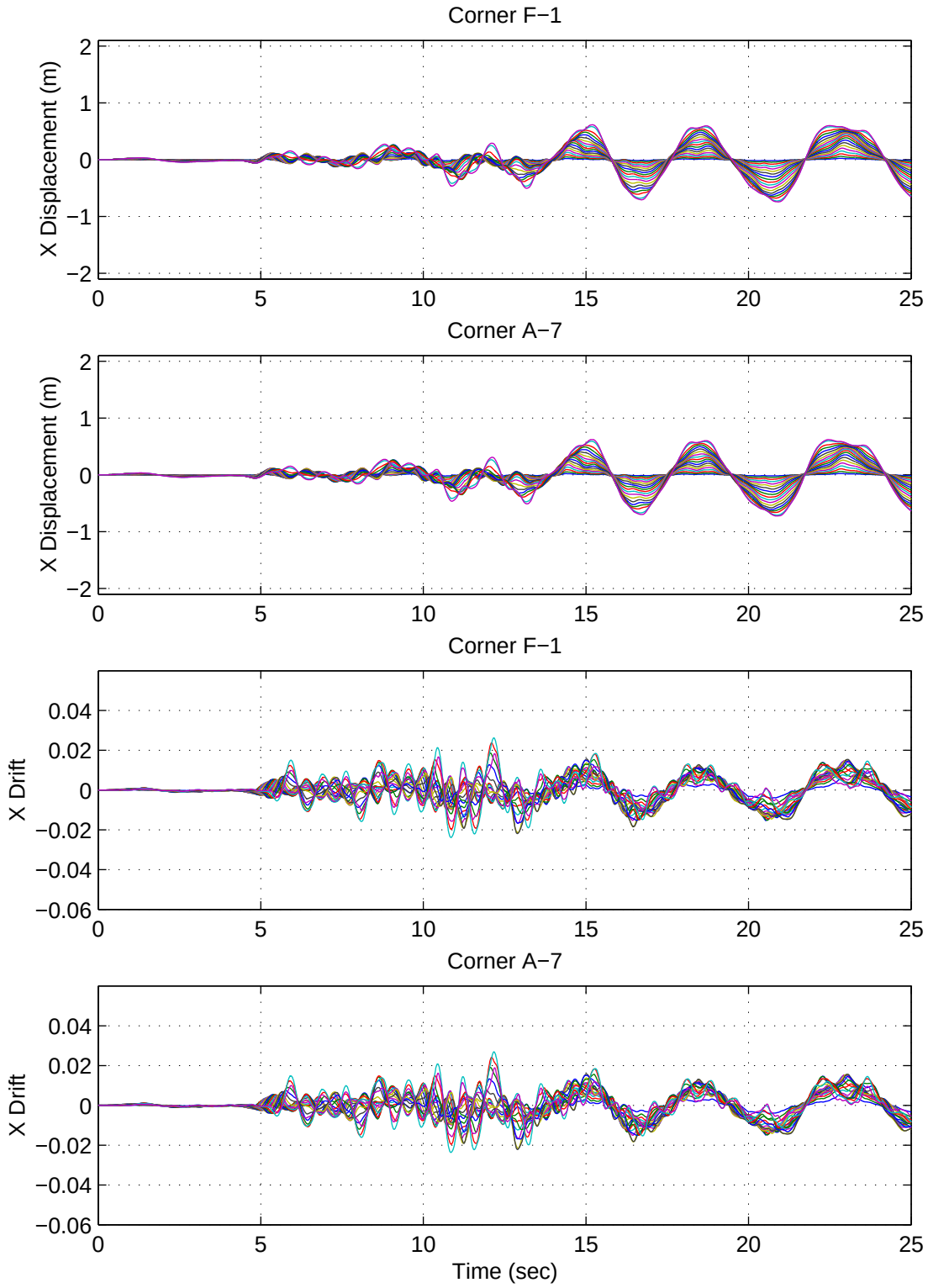

Figure F.7: Building 1 X-Direction Displacements & Drifts: Iran Earthquake (Tabas Record Strong Component in Y Direction)

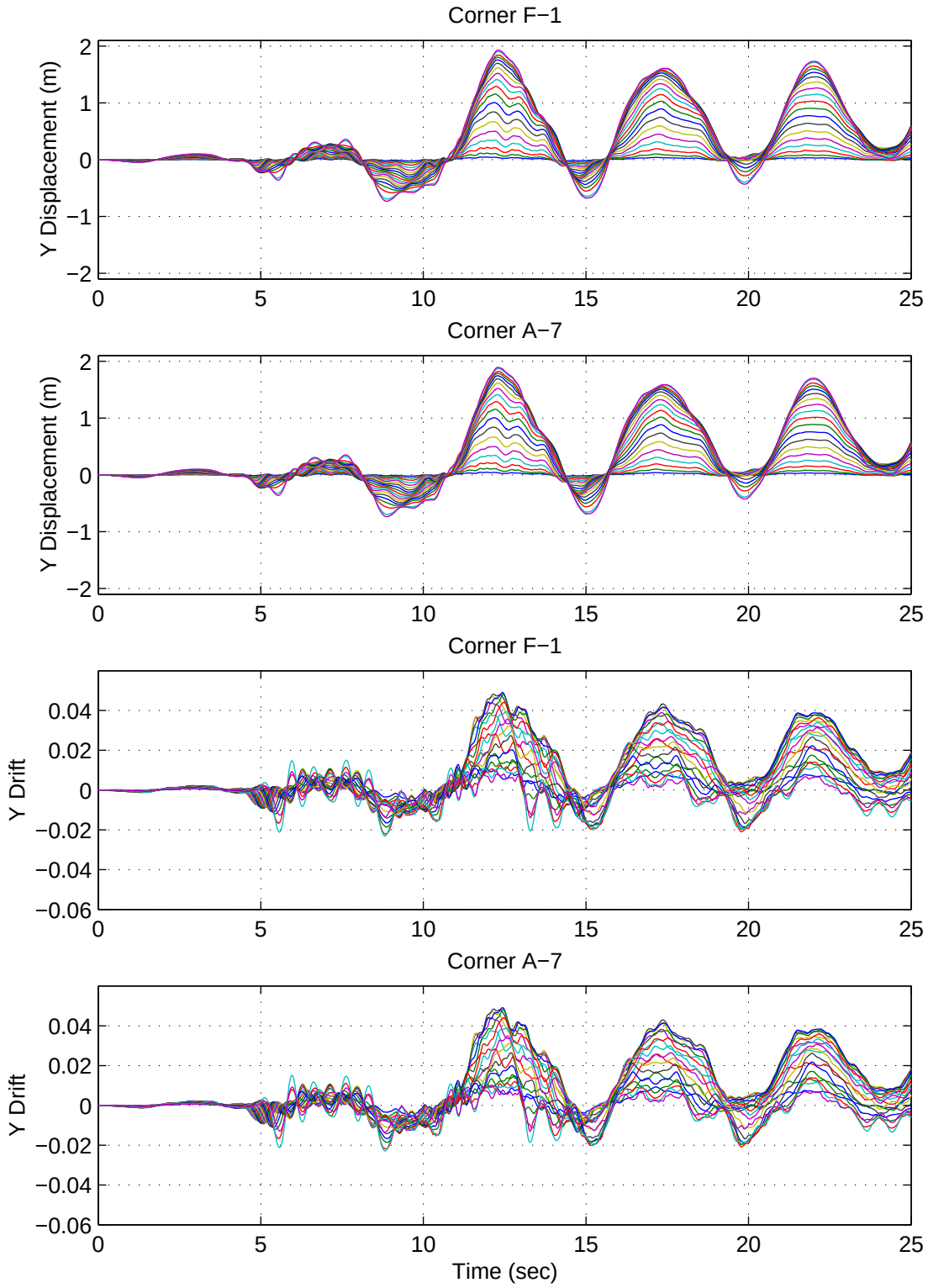

Figure F.8: Building 1 Y-Direction Displacements & Drifts: Iran Earthquake (Tabas Record Strong Component in Y Direction)

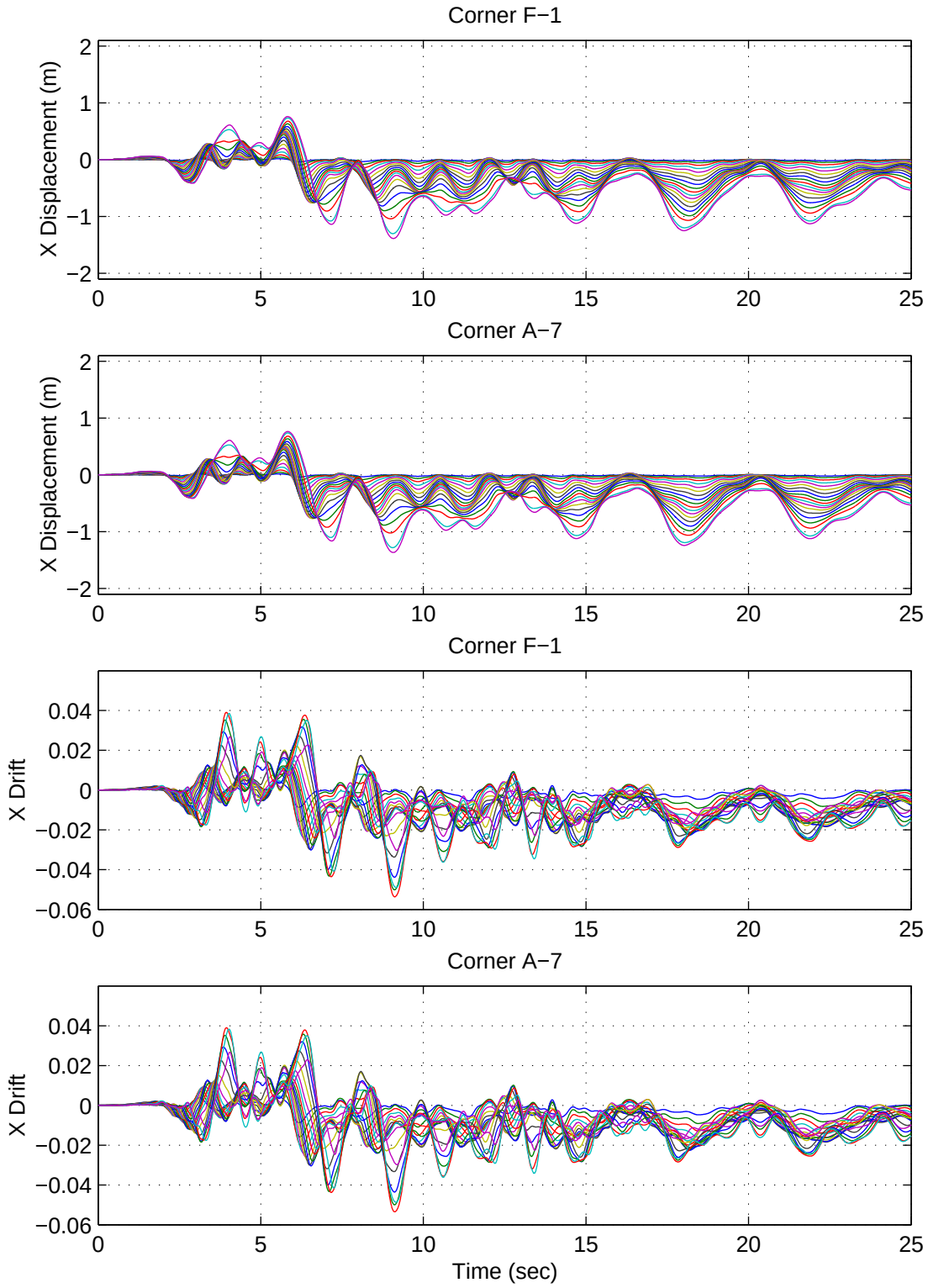

Figure F.9: Building 1 X-Direction Displacements & Drifts: Kobe Earthquake (Takatori Record Strong Component in X Direction)

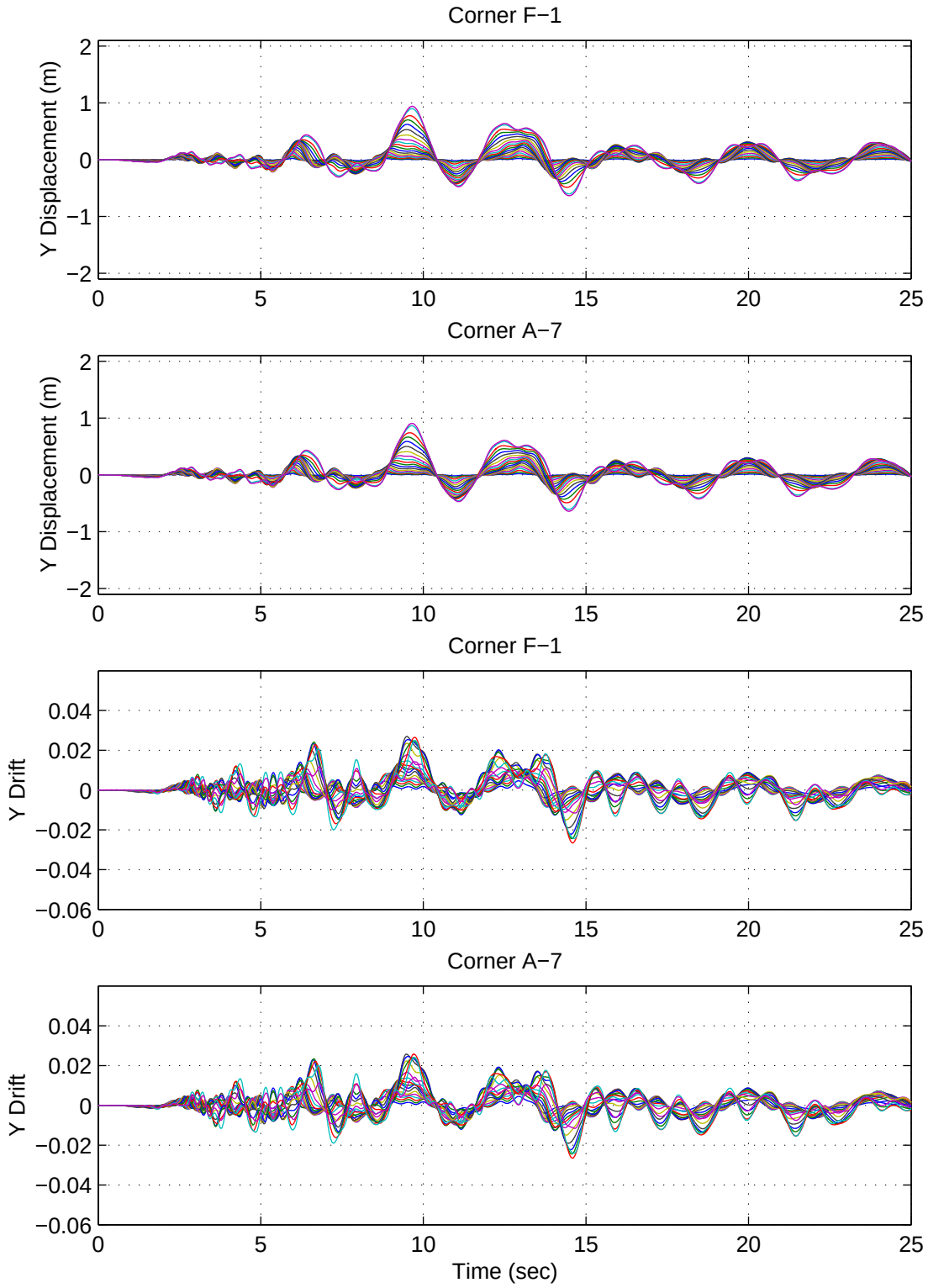

Figure F.10: Building 1 Y-Direction Displacements & Drifts: Kobe Earthquake (Takatori Record Strong Component in X Direction)

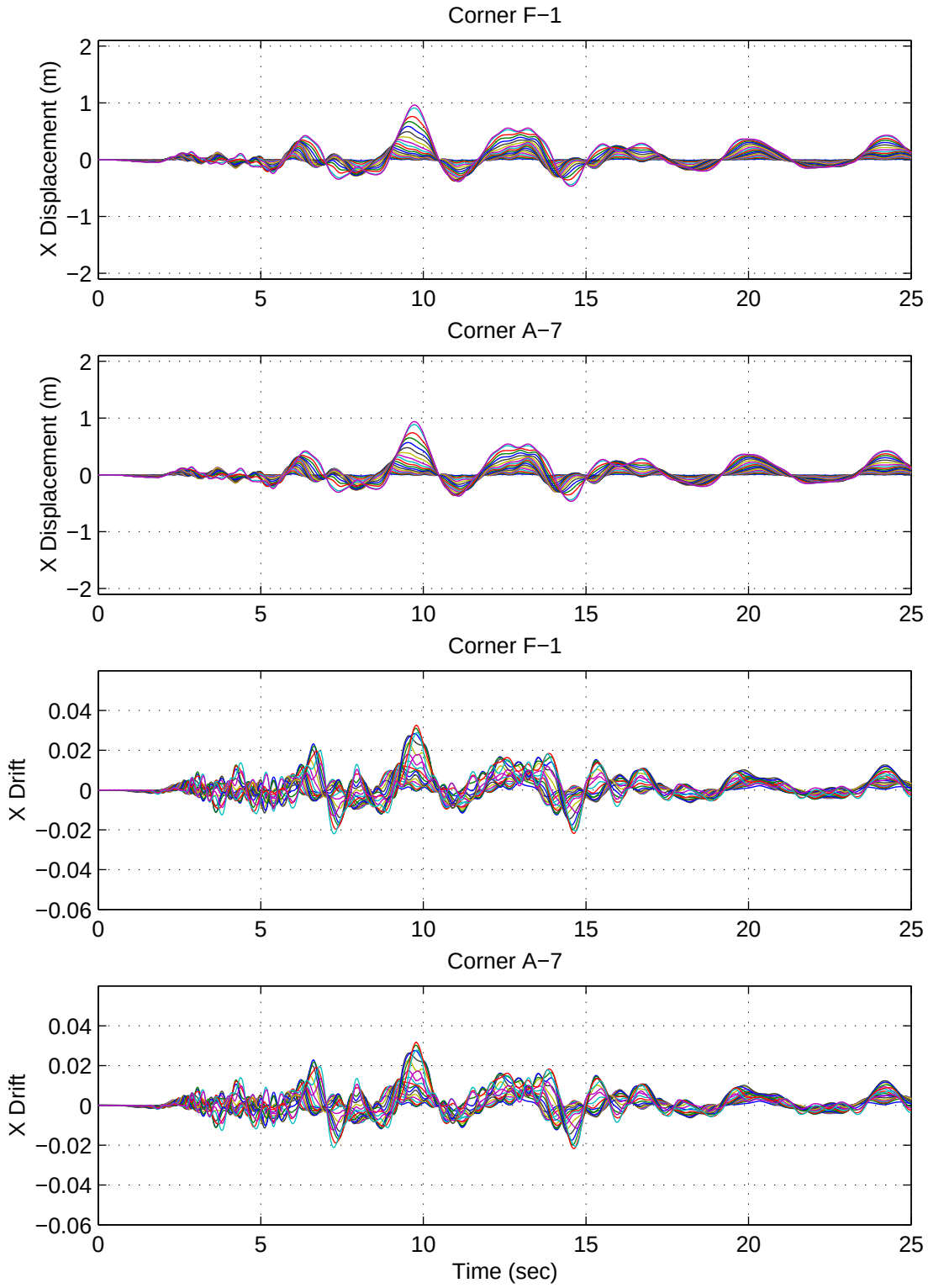

Figure F.11: Building 1 X-Direction Displacements & Drifts: Kobe Earthquake (Takatori Record Strong Component in Y Direction)

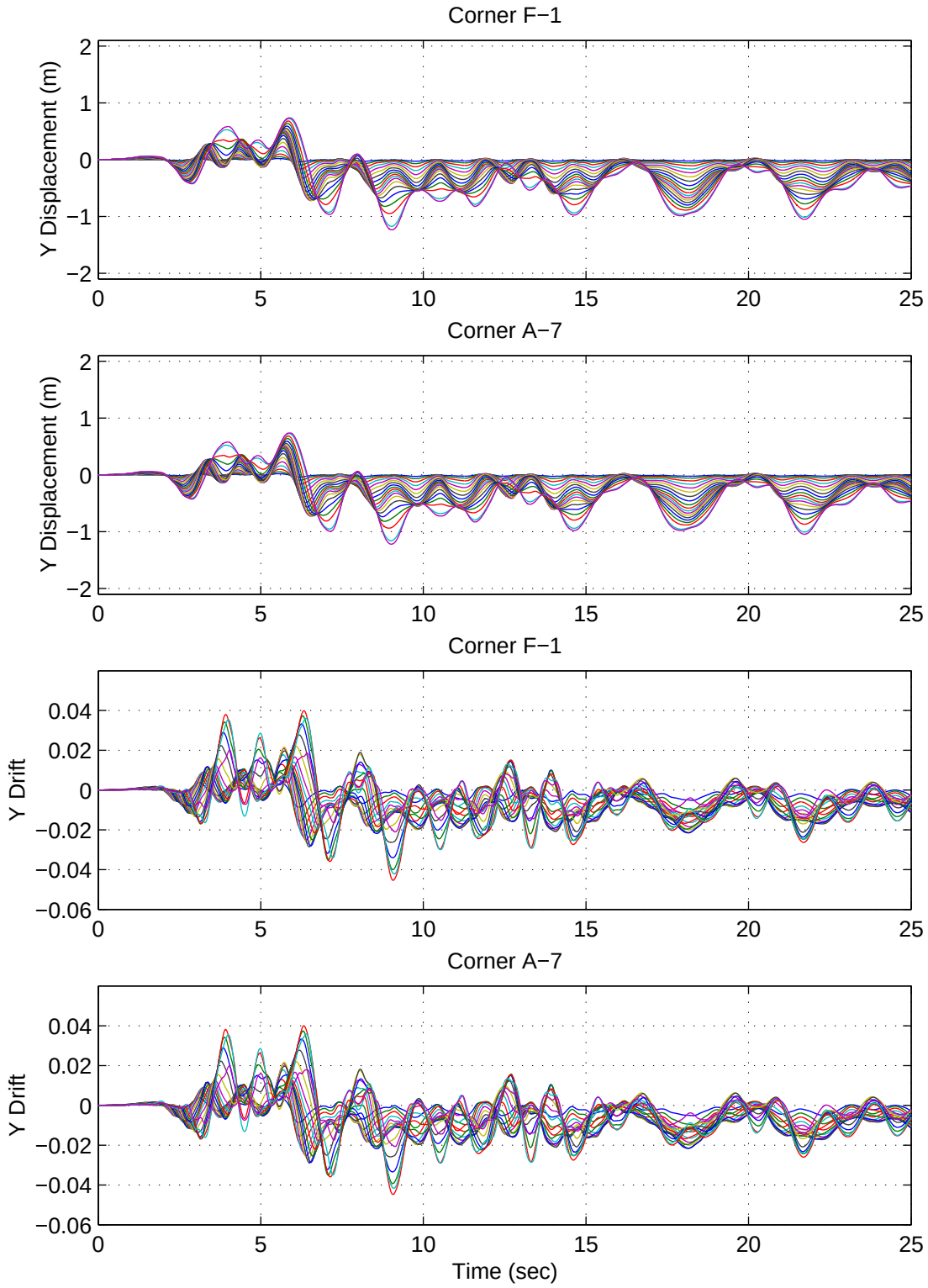

Figure F.12: Building 1 Y-Direction Displacements & Drifts: Kobe Earthquake (Takatori Record Strong Component in Y Direction)

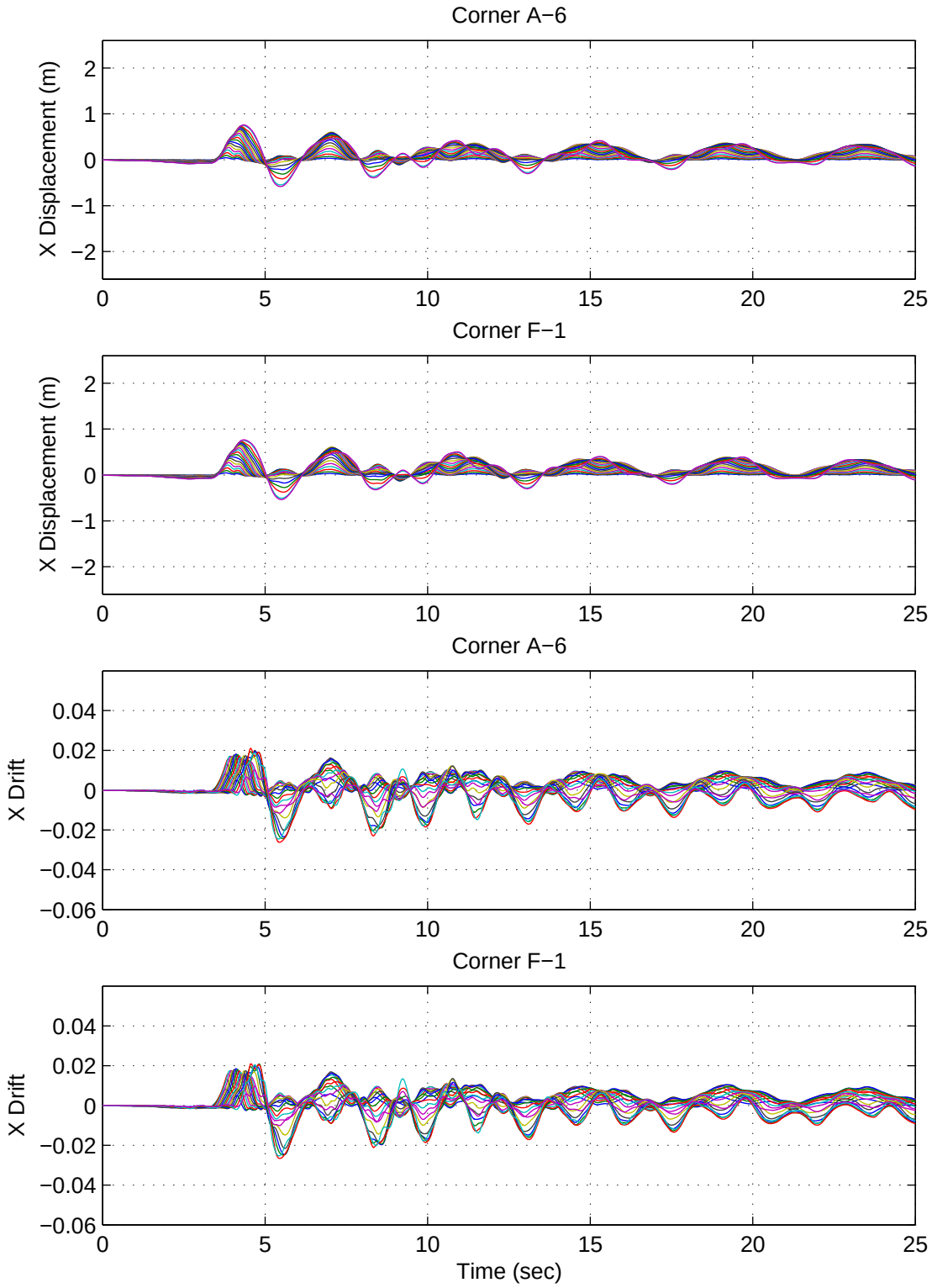

Figure F.13: Building 2 X-Direction Displacements & Drifts: Northridge Earthquake (Sylmar Record Strong Component in X Direction)

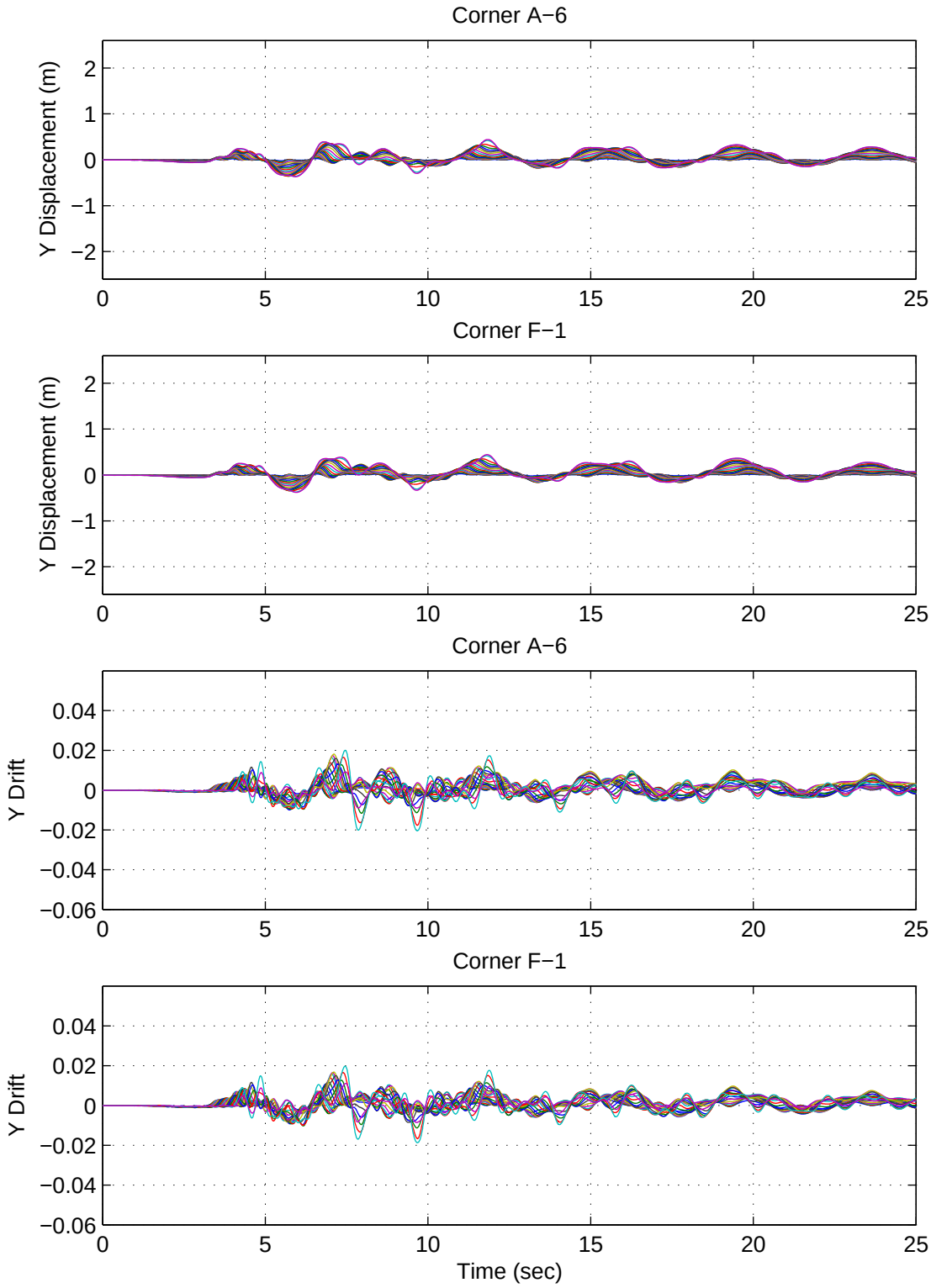

Figure F.14: Building 2 Y-Direction Displacements & Drifts: Northridge Earthquake (Sylmar Record Strong Component in X Direction)

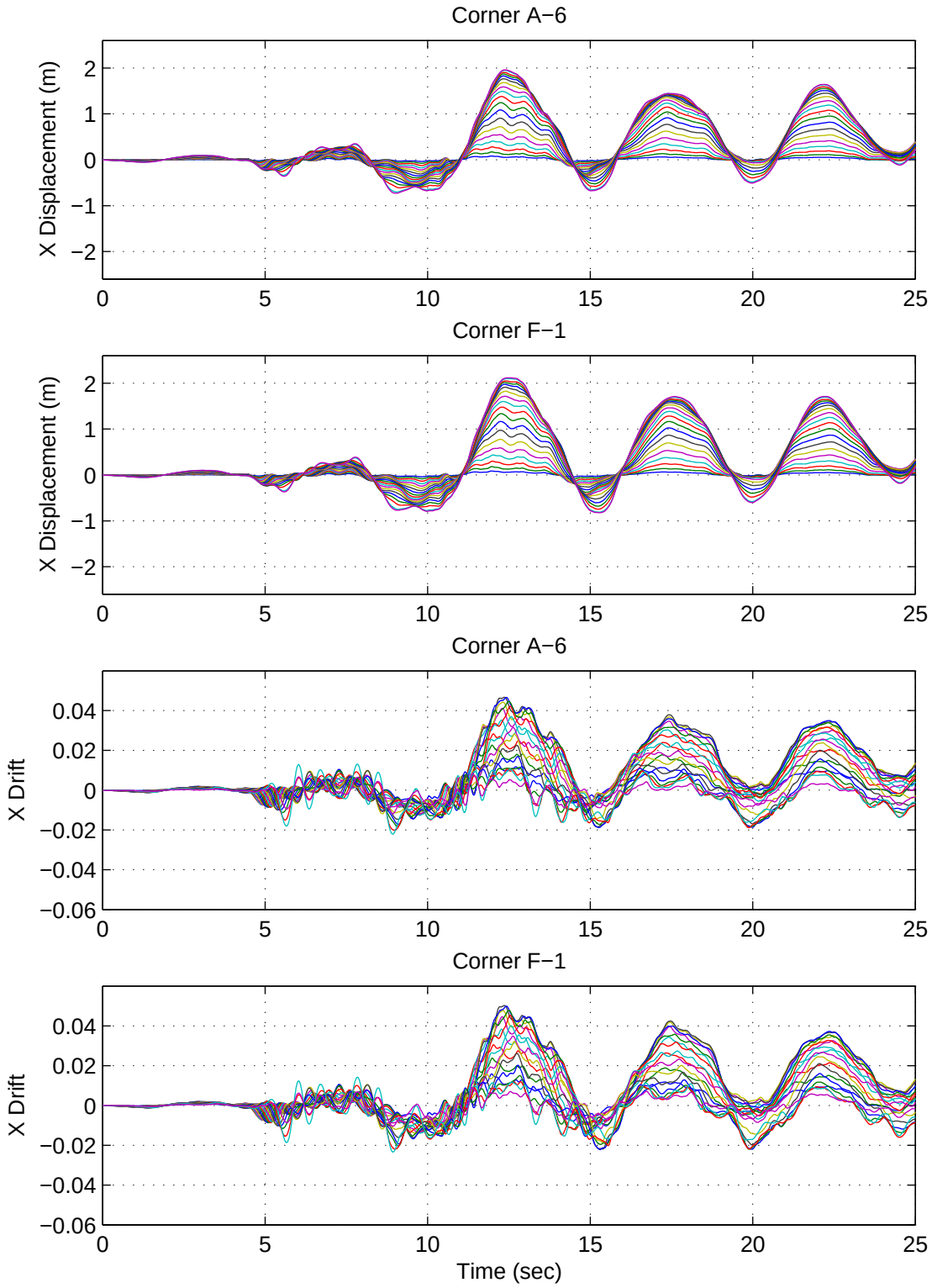

Figure F.15: Building 2 X-Direction Displacements & Drifts: Iran Earthquake (Tabas Record Strong Component in X Direction)

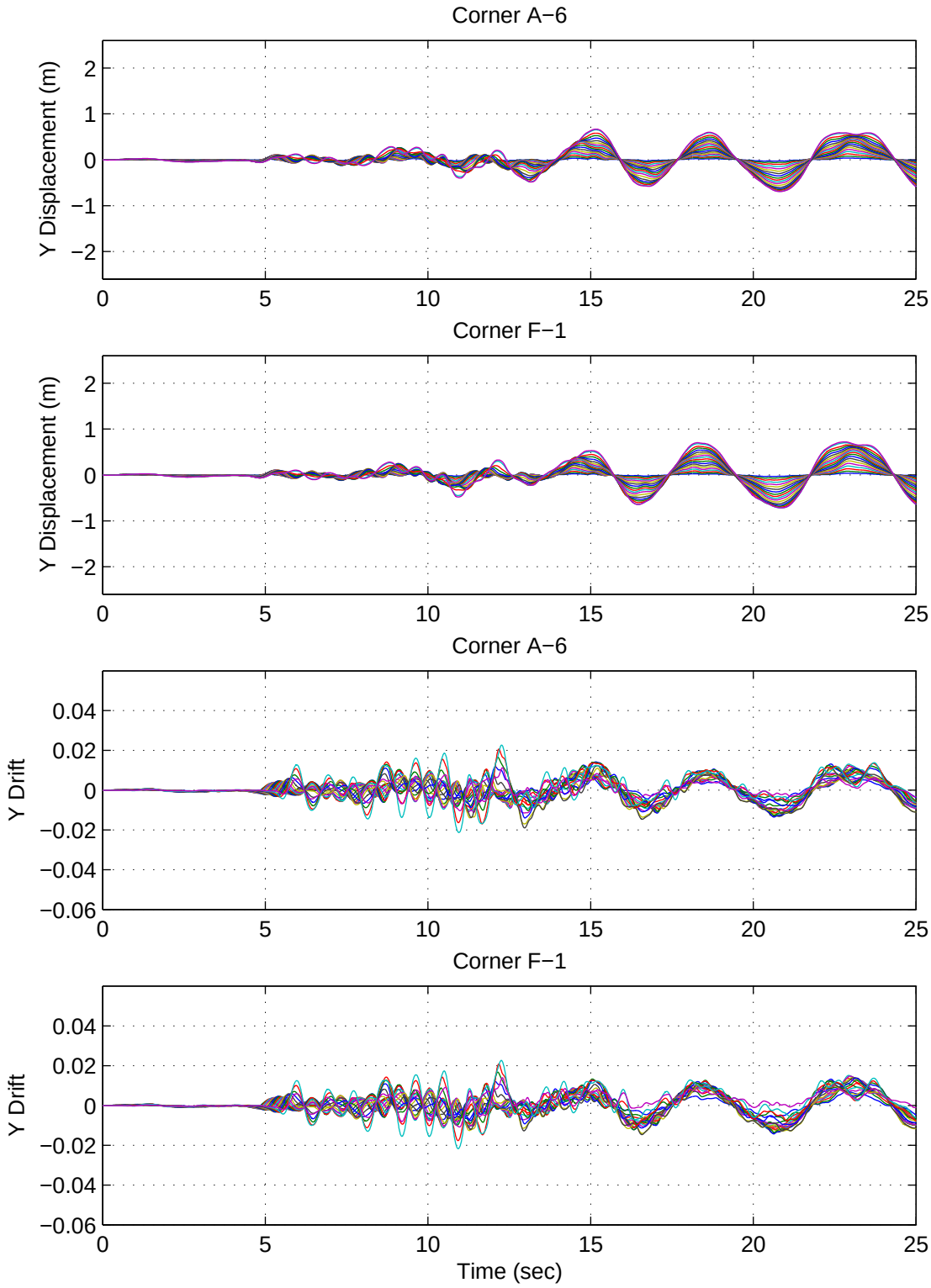

Figure F.16: Building 2 Y-Direction Displacements & Drifts: Iran Earthquake (Tabas Record Strong Component in X Direction)

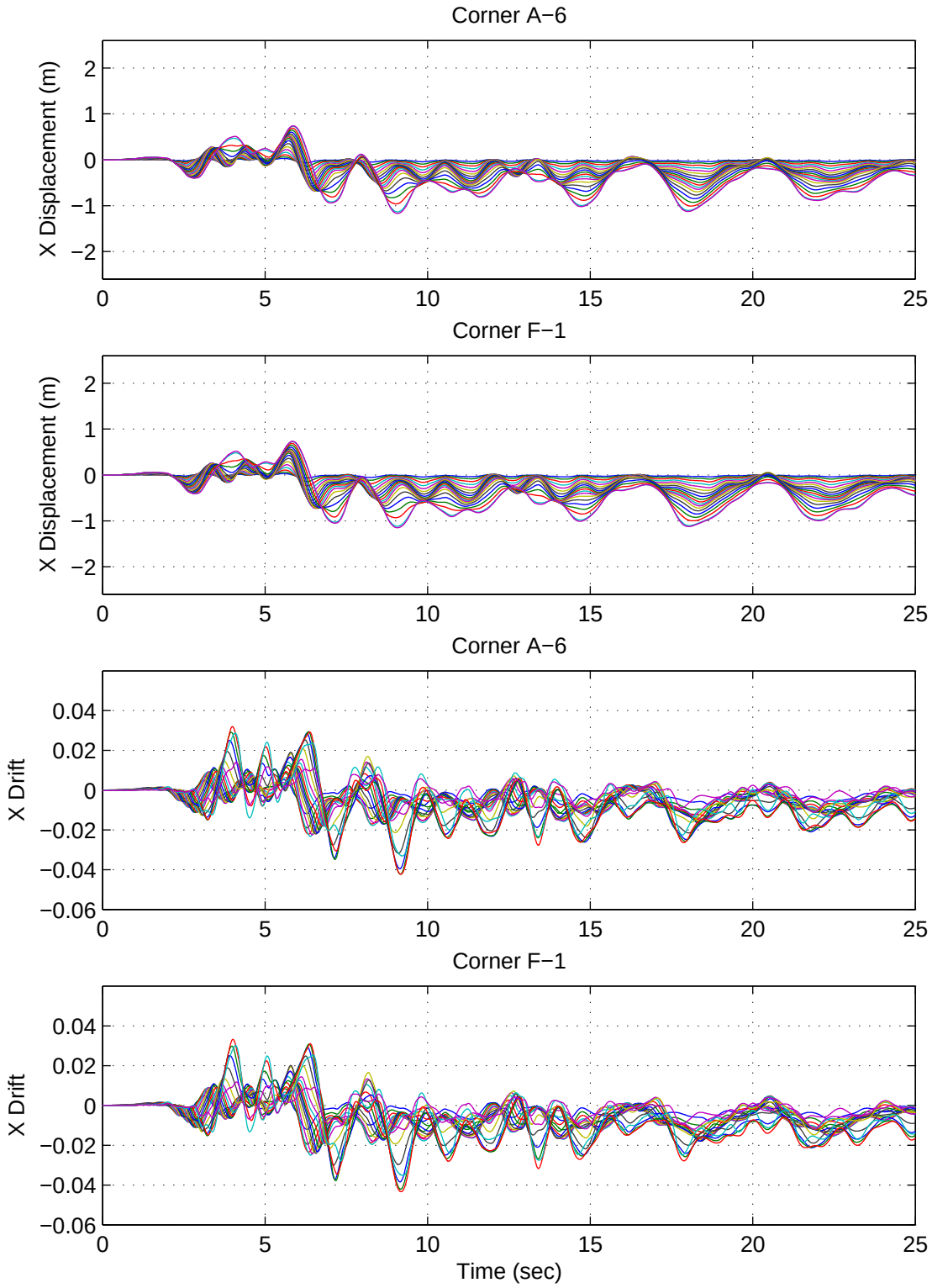

Figure F.17: Building 2 X-Direction Displacements & Drifts: Kobe Earthquake (Takatori Record Strong Component in X Direction)

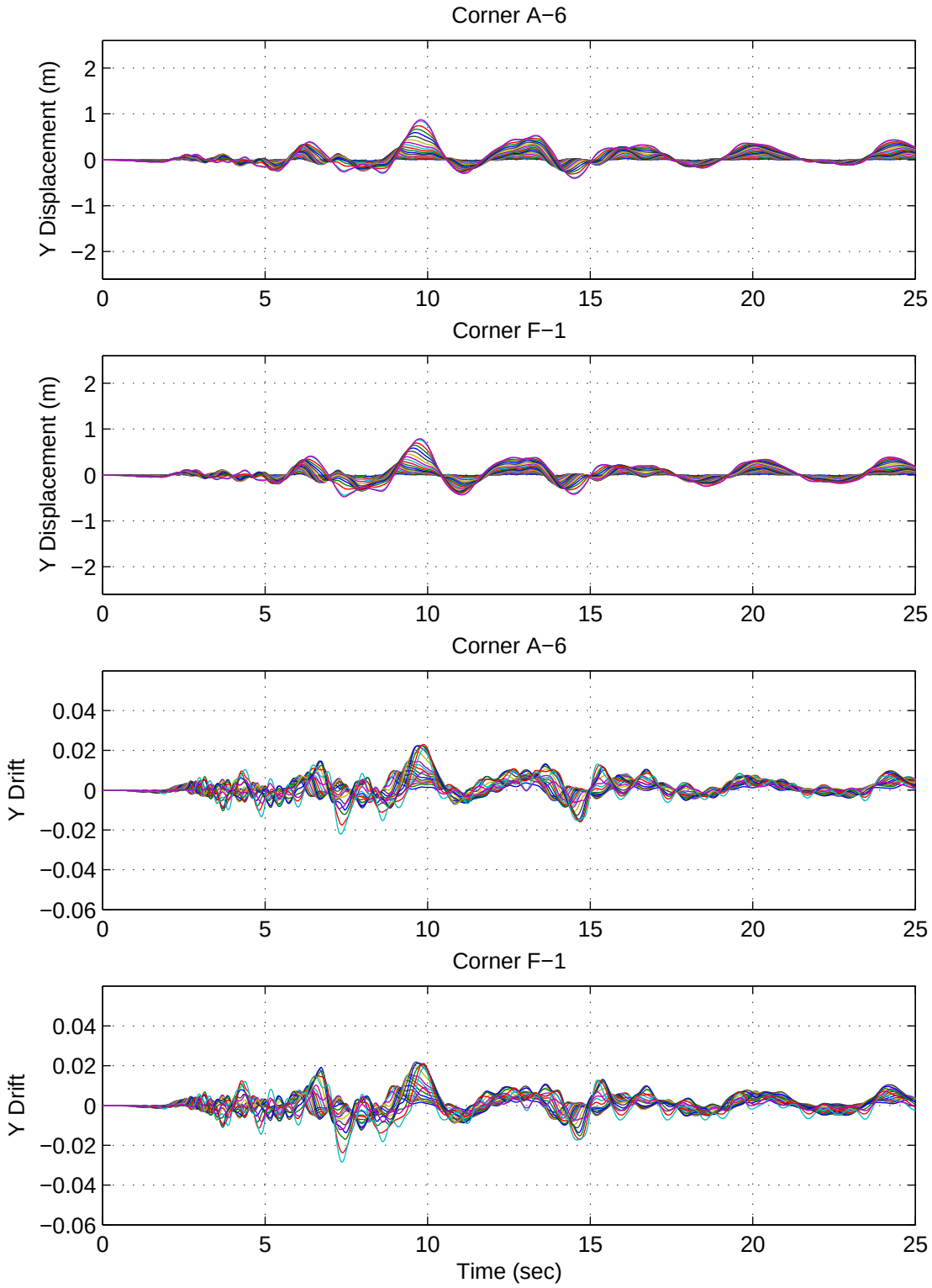

Figure F.18: Building 2 Y-Direction Displacements & Drifts: Kobe Earthquake (Takatori Record Strong Component in X Direction)

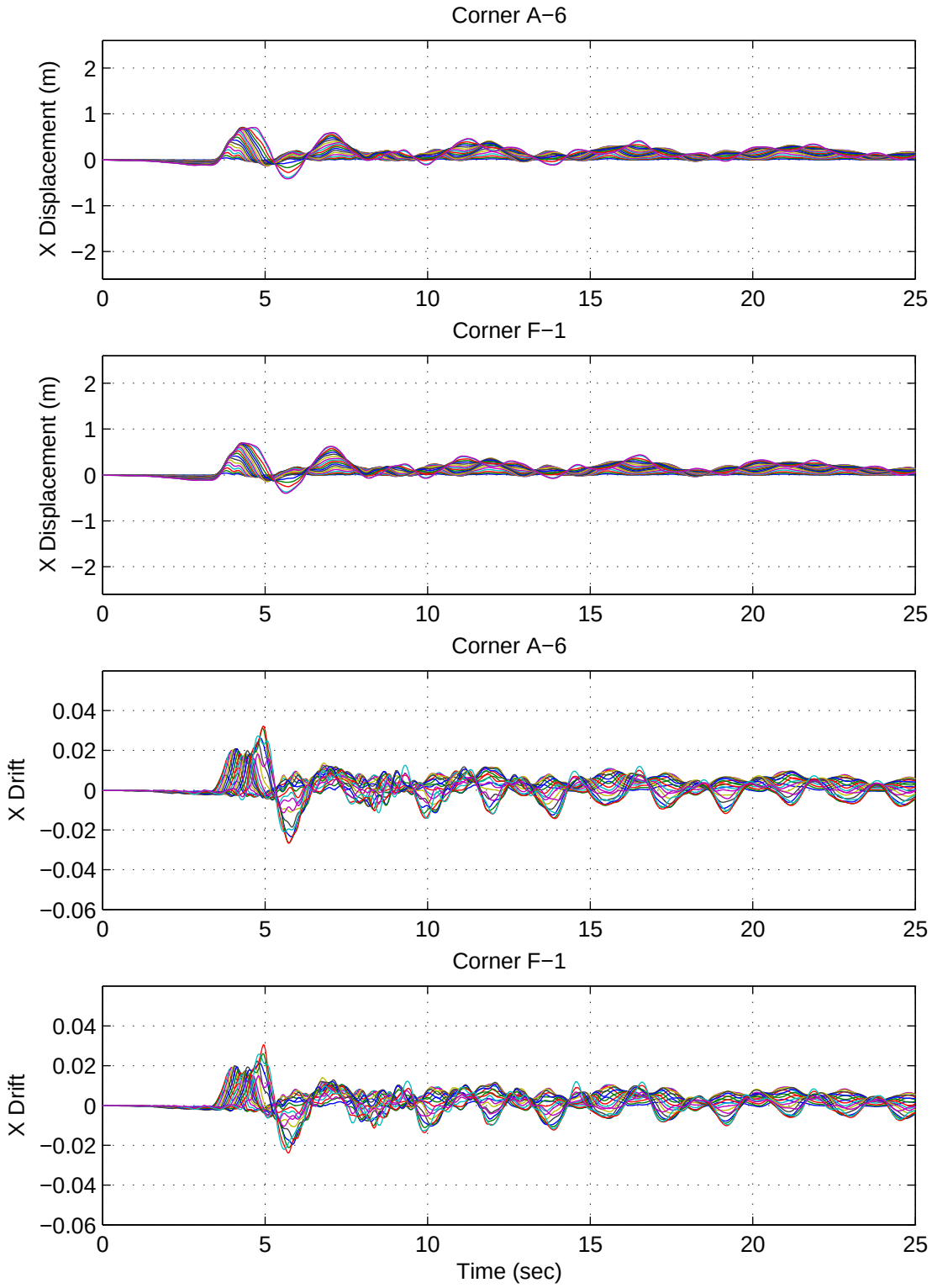

Figure F.19: Building 2A X-Direction Displacements & Drifts: Northridge Earthquake (Sylmar Record Strong Component in X Direction)

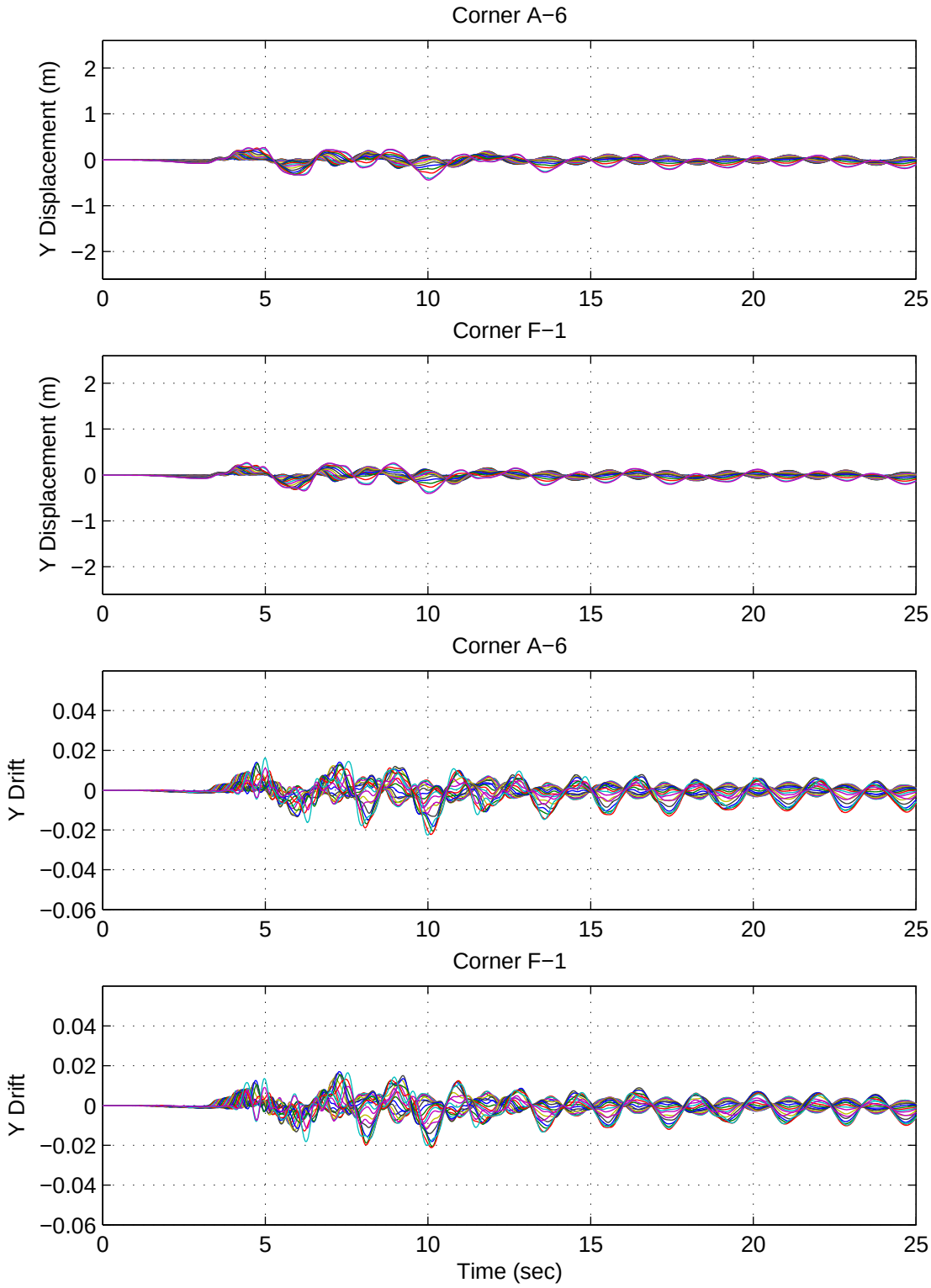

Figure F.20: Building 2A Y-Direction Displacements & Drifts: Northridge Earthquake (Sylmar Record Strong Component in X Direction)

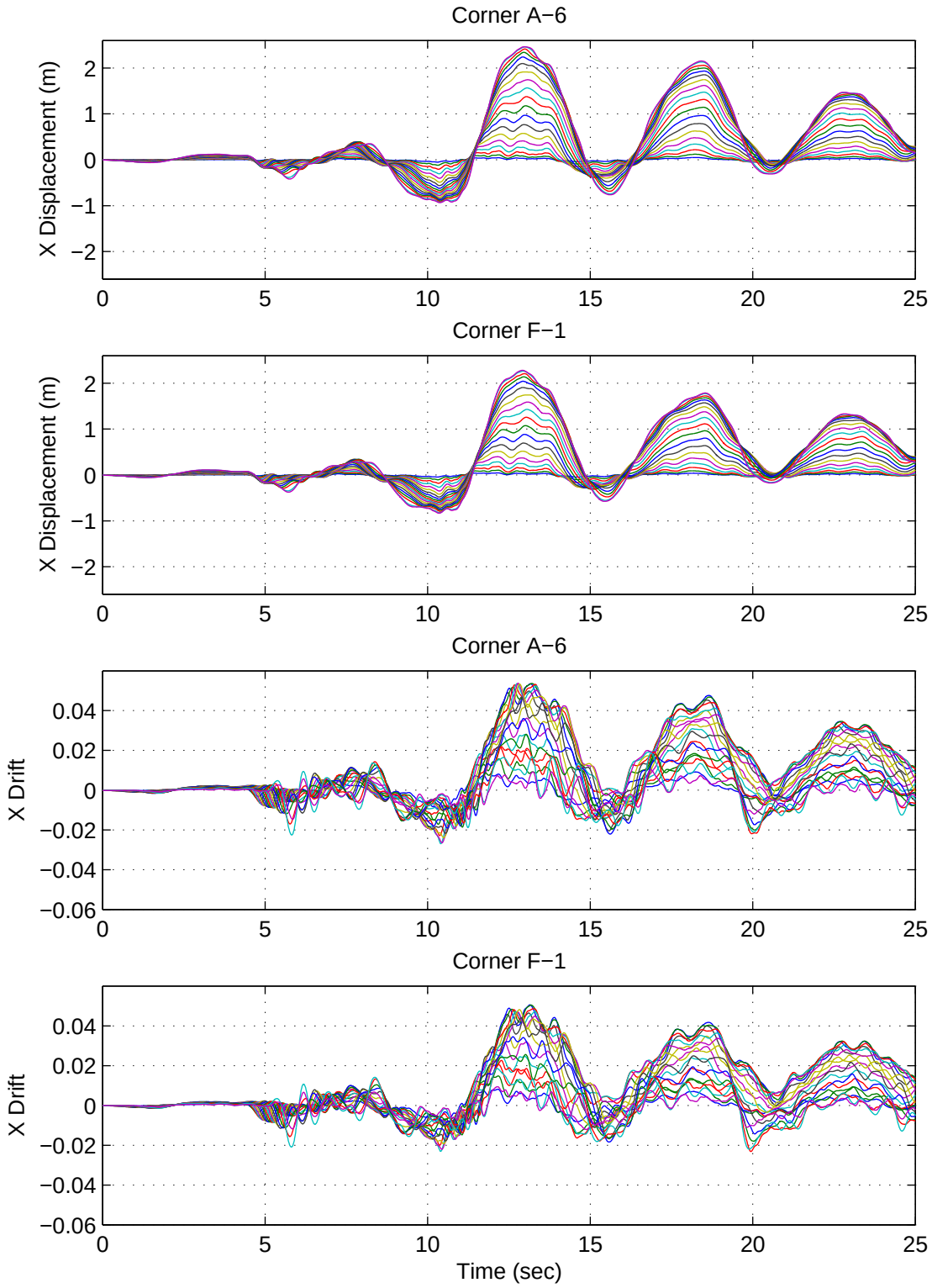

Figure F.21: Building 2A X-Direction Displacements & Drifts: Iran Earthquake (Tabas Record Strong Component in X Direction)

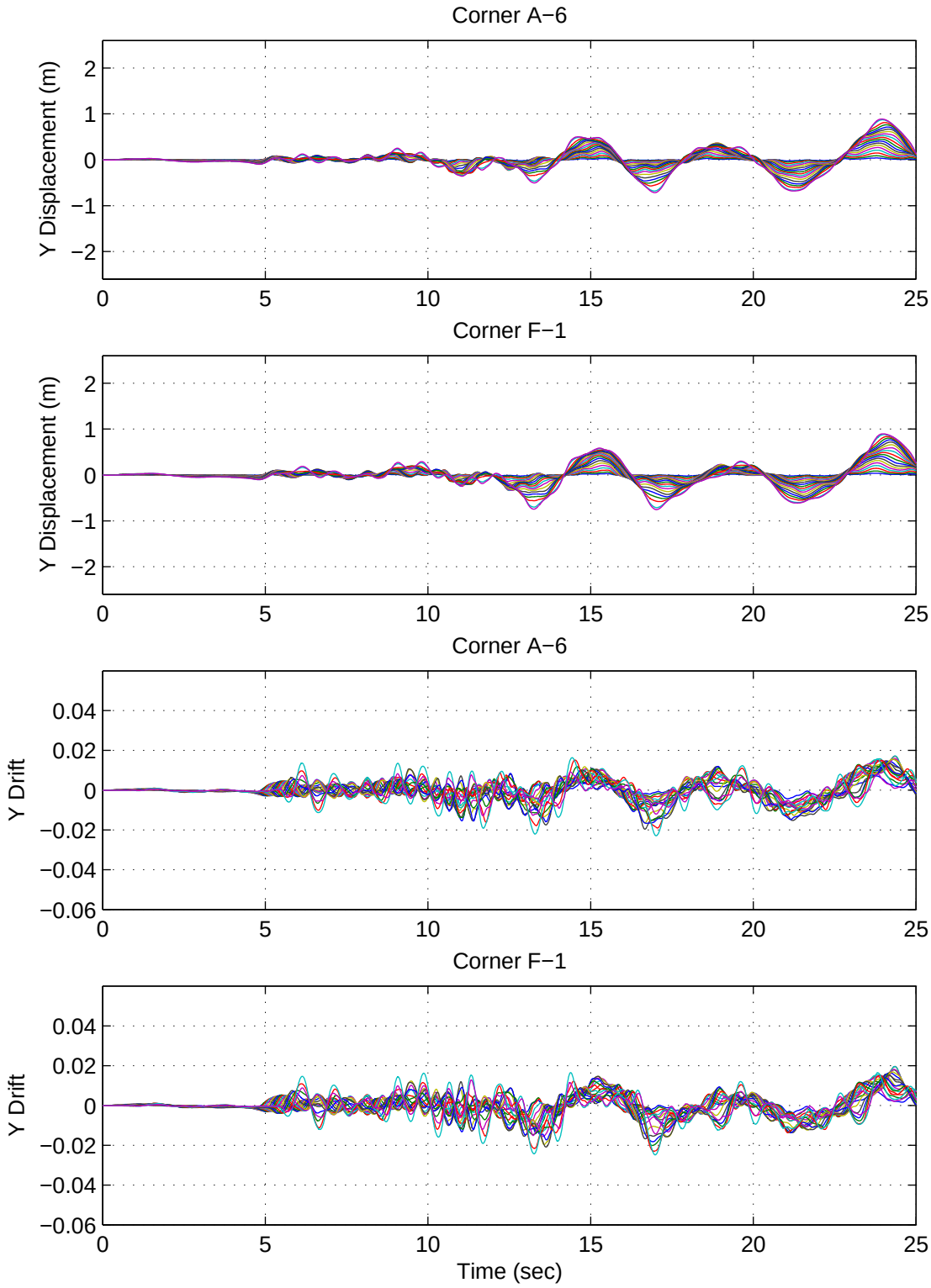

Figure F.22: Building 2A Y-Direction Displacements & Drifts: Iran Earthquake (Tabas Record Strong Component in X Direction)

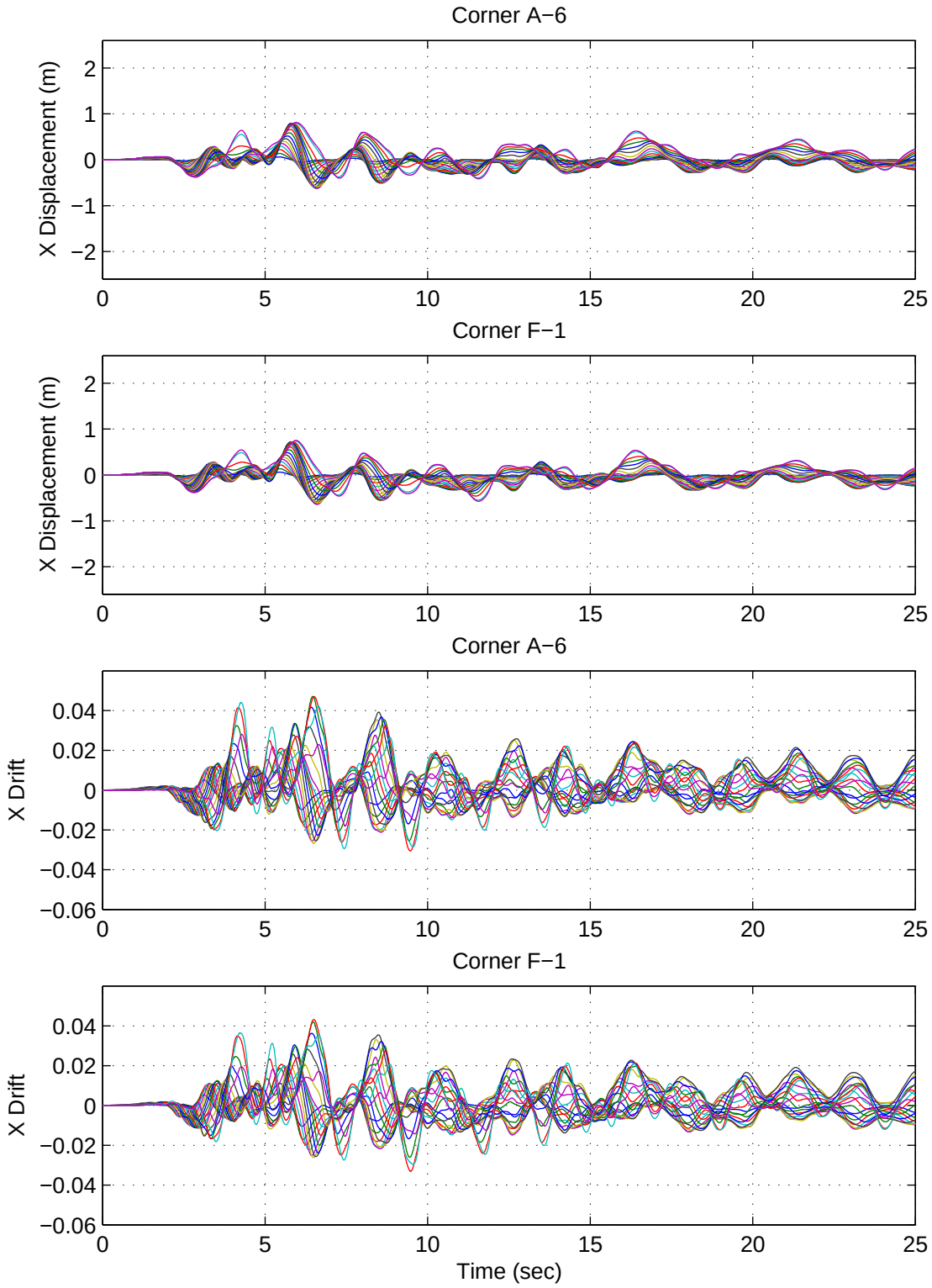

Figure F.23: Building 2A X-Direction Displacements & Drifts: Kobe Earthquake (Takatori Record Strong Component in X Direction)

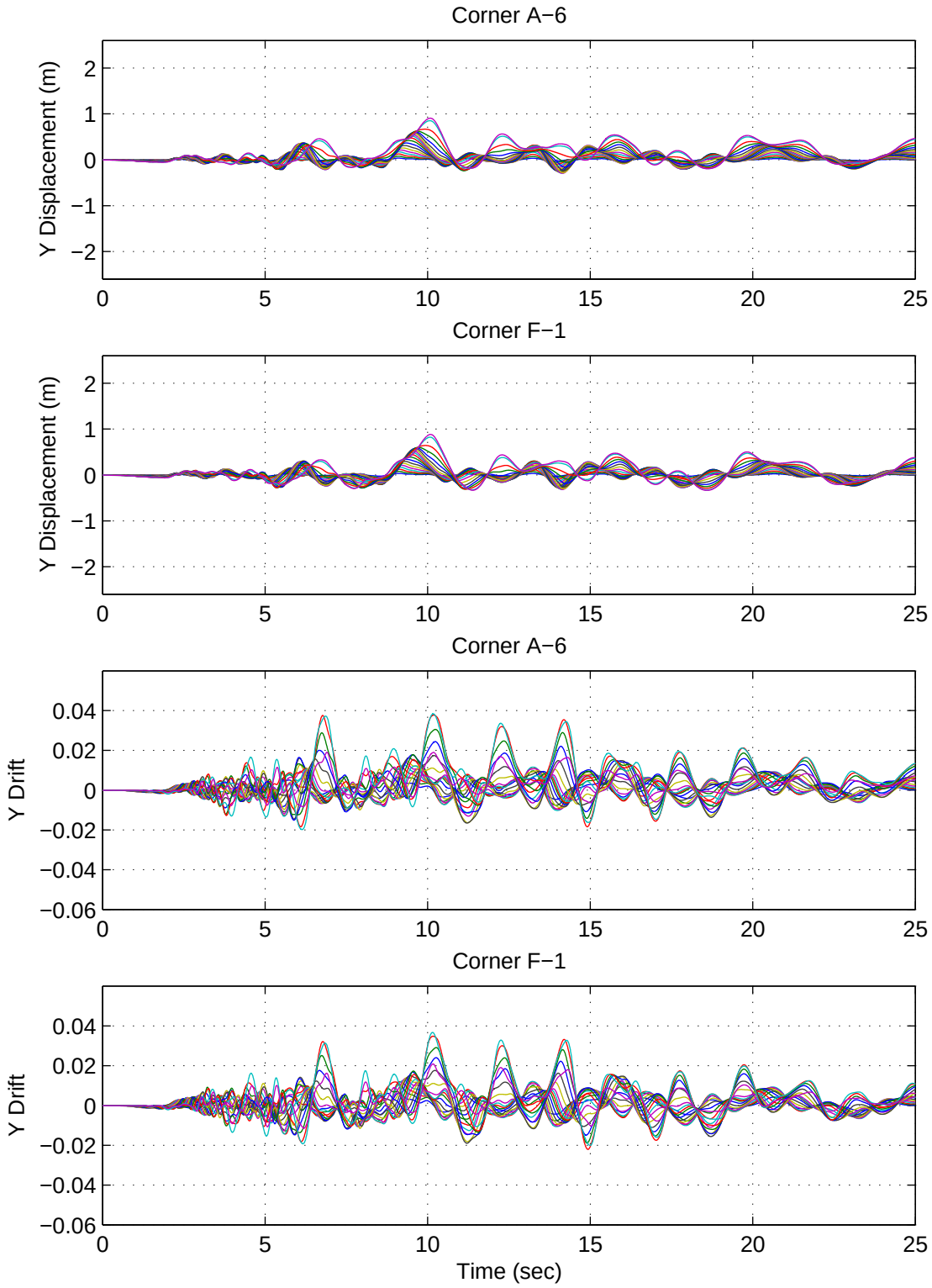

Figure F.24: Building 2A Y-Direction Displacements & Drifts: Kobe Earthquake (Takatori Record Strong Component in X Direction)

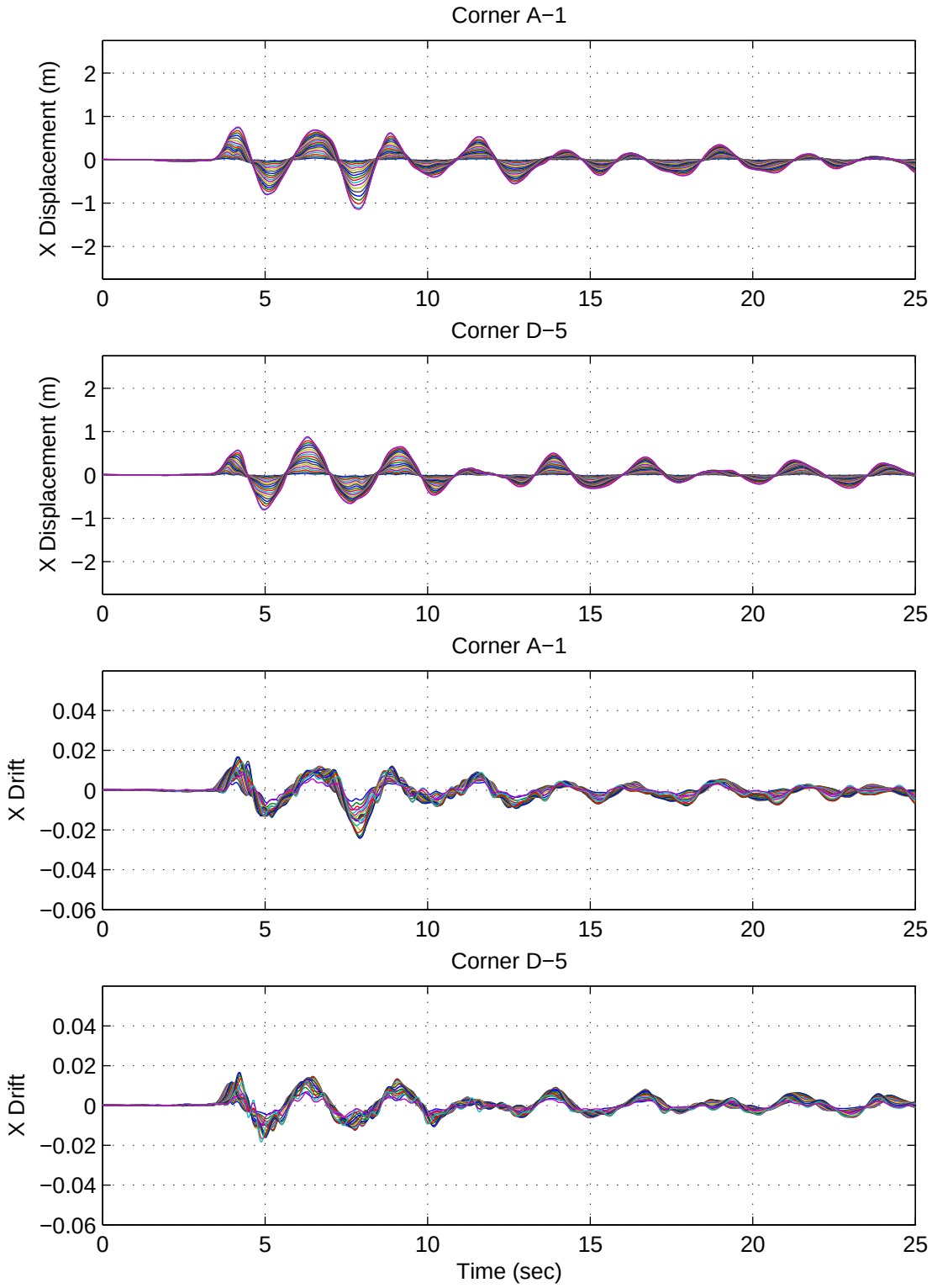

Figure F.25: Building 3 X-Direction Displacements & Drifts: Northridge Earthquake (Sylmar Record Strong Component in X Direction)

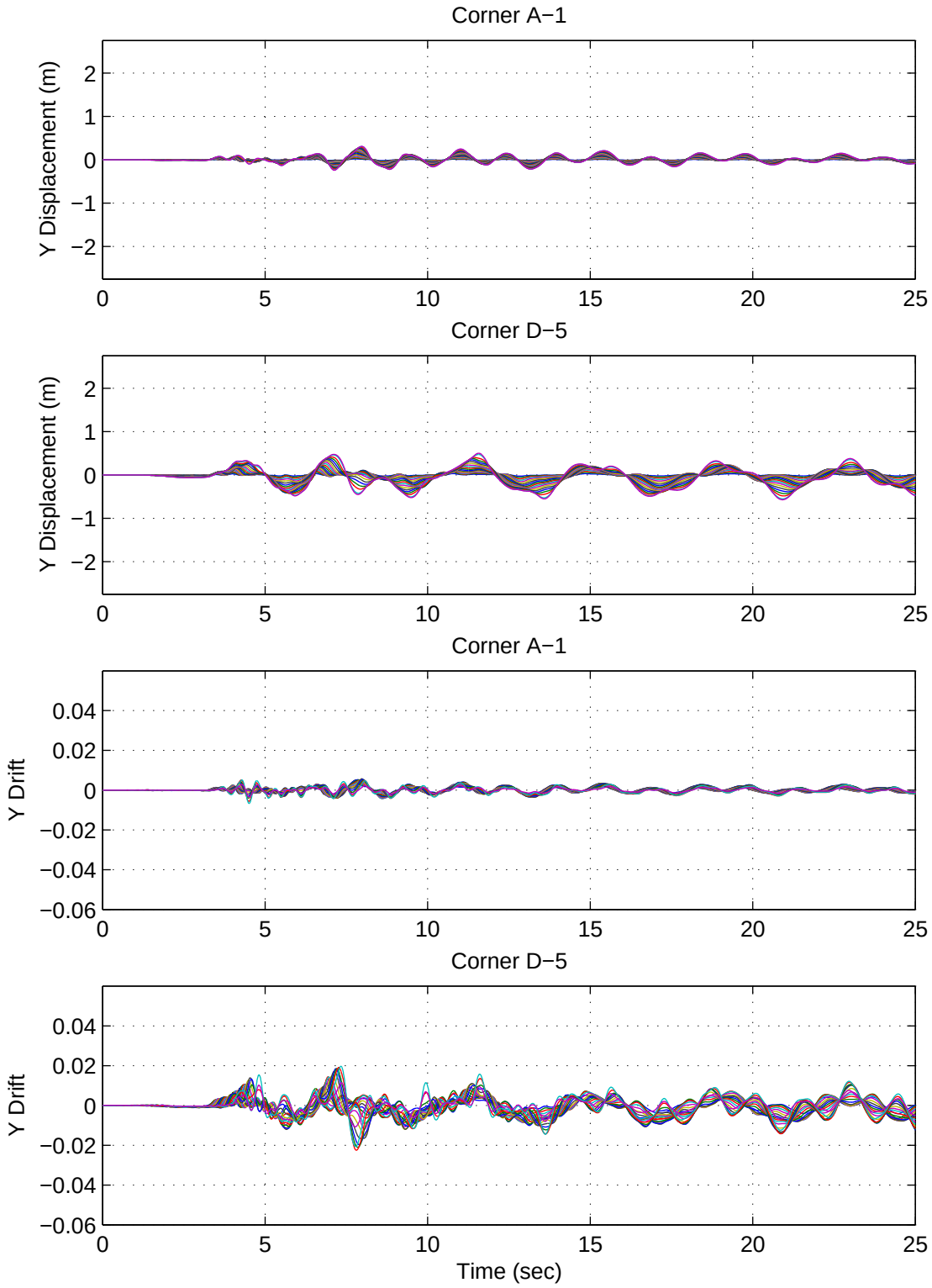

Figure F.26: Building 3 Y-Direction Displacements & Drifts: Northridge Earthquake (Sylmar Record Strong Component in X Direction)

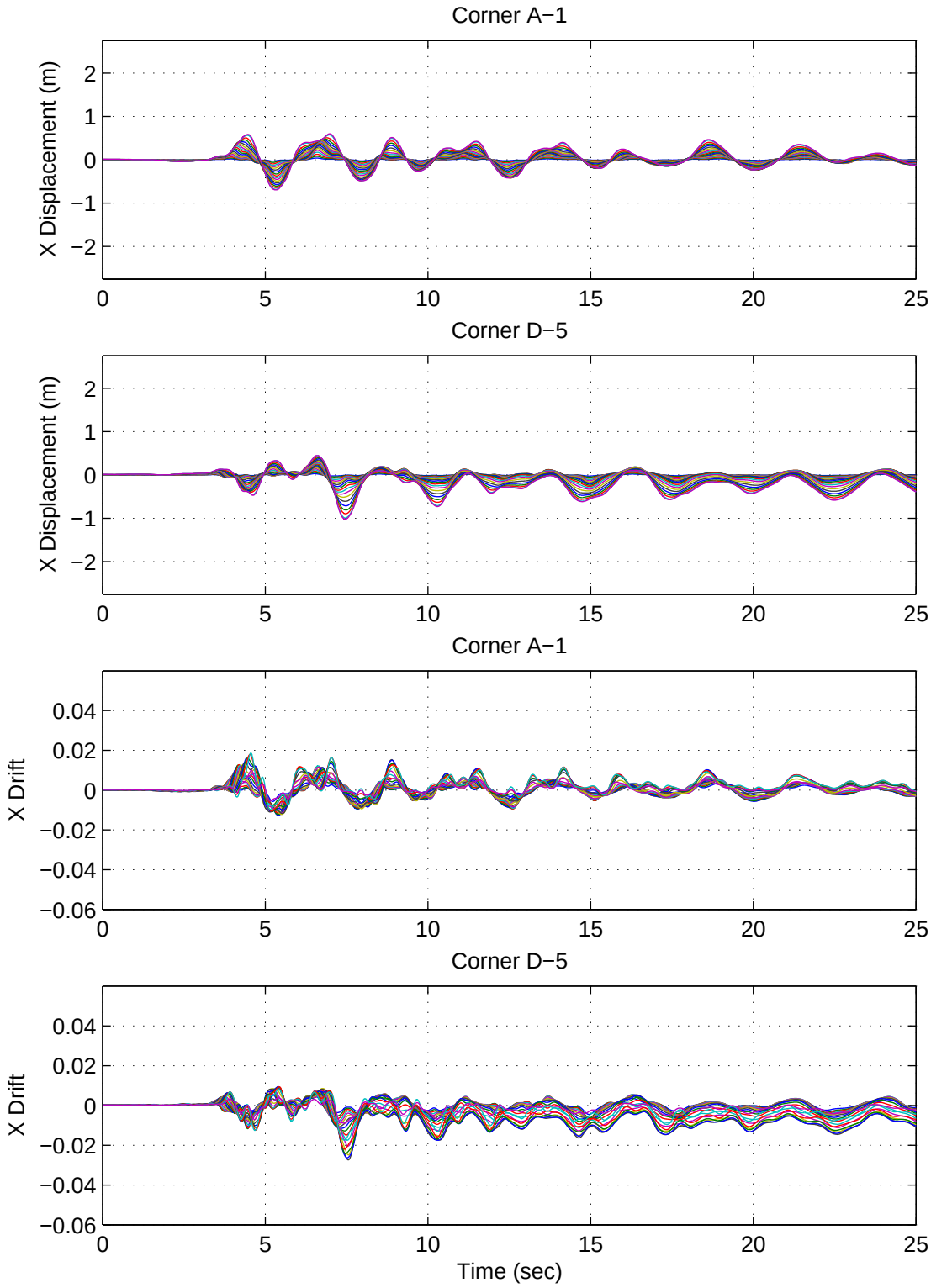

Figure F.27: Building 3 X-Direction Displacements & Drifts: Northridge Earthquake (Sylmar Record Strong Component in Y Direction)

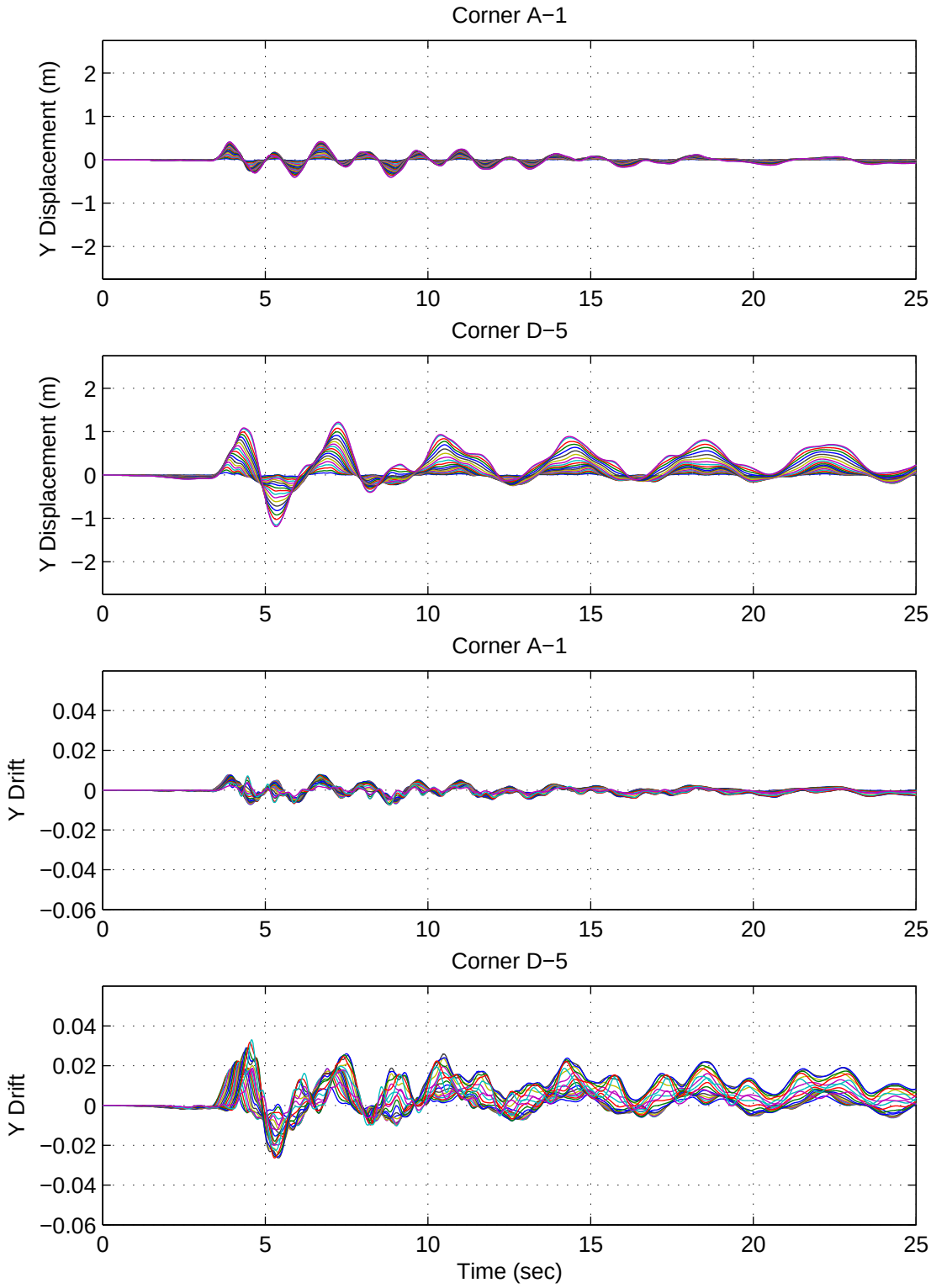

Figure F.28: Building 3 Y-Direction Displacements & Drifts: Northridge Earthquake (Sylmar Record Strong Component in Y Direction)

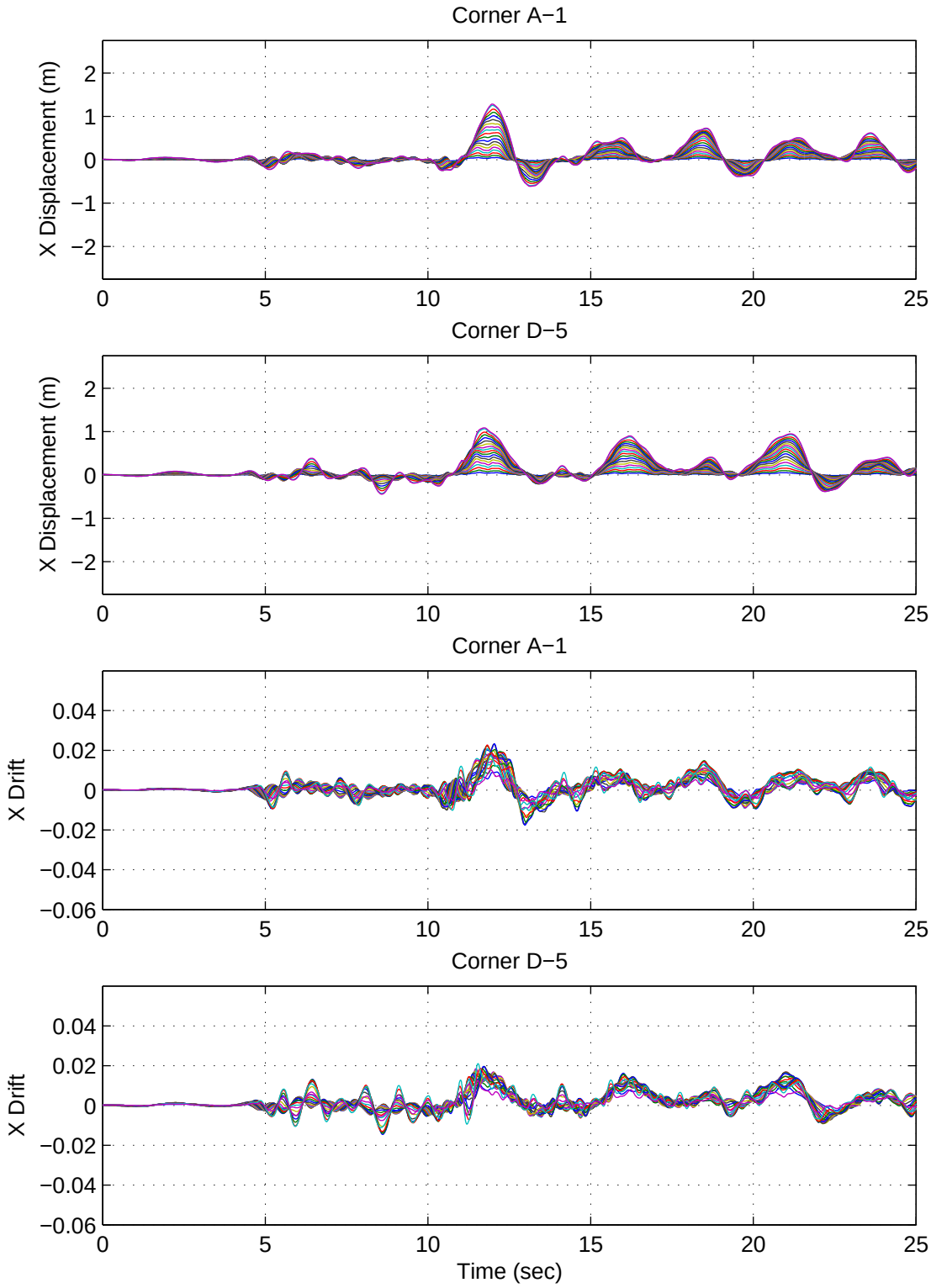

Figure F.29: Building 3 X-Direction Displacements & Drifts: Iran Earthquake (Tabas Record Strong Component in X Direction)

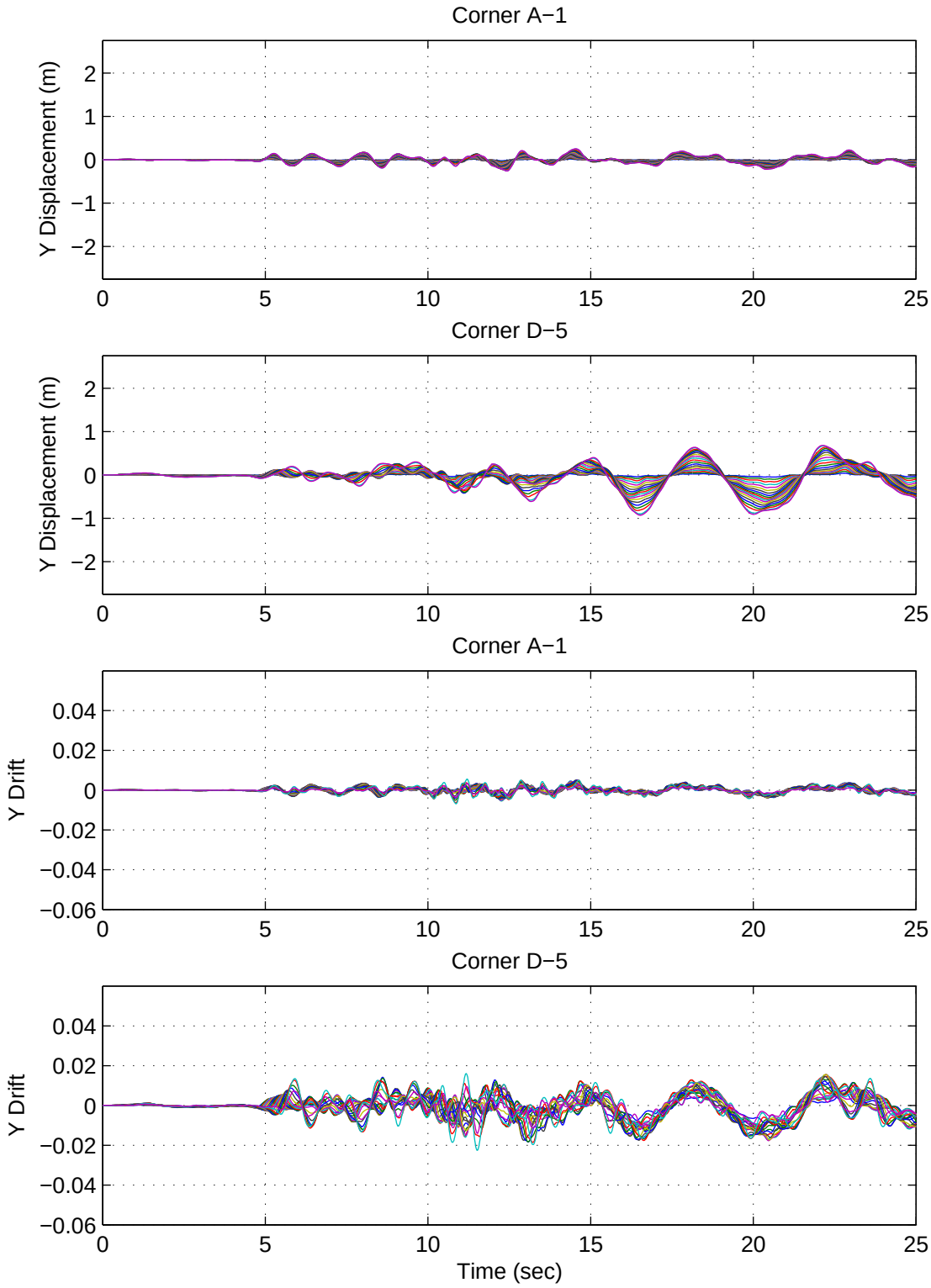

Figure F.30: Building 3 Y-Direction Displacements & Drifts: Iran Earthquake (Tabas Record Strong Component in X Direction)

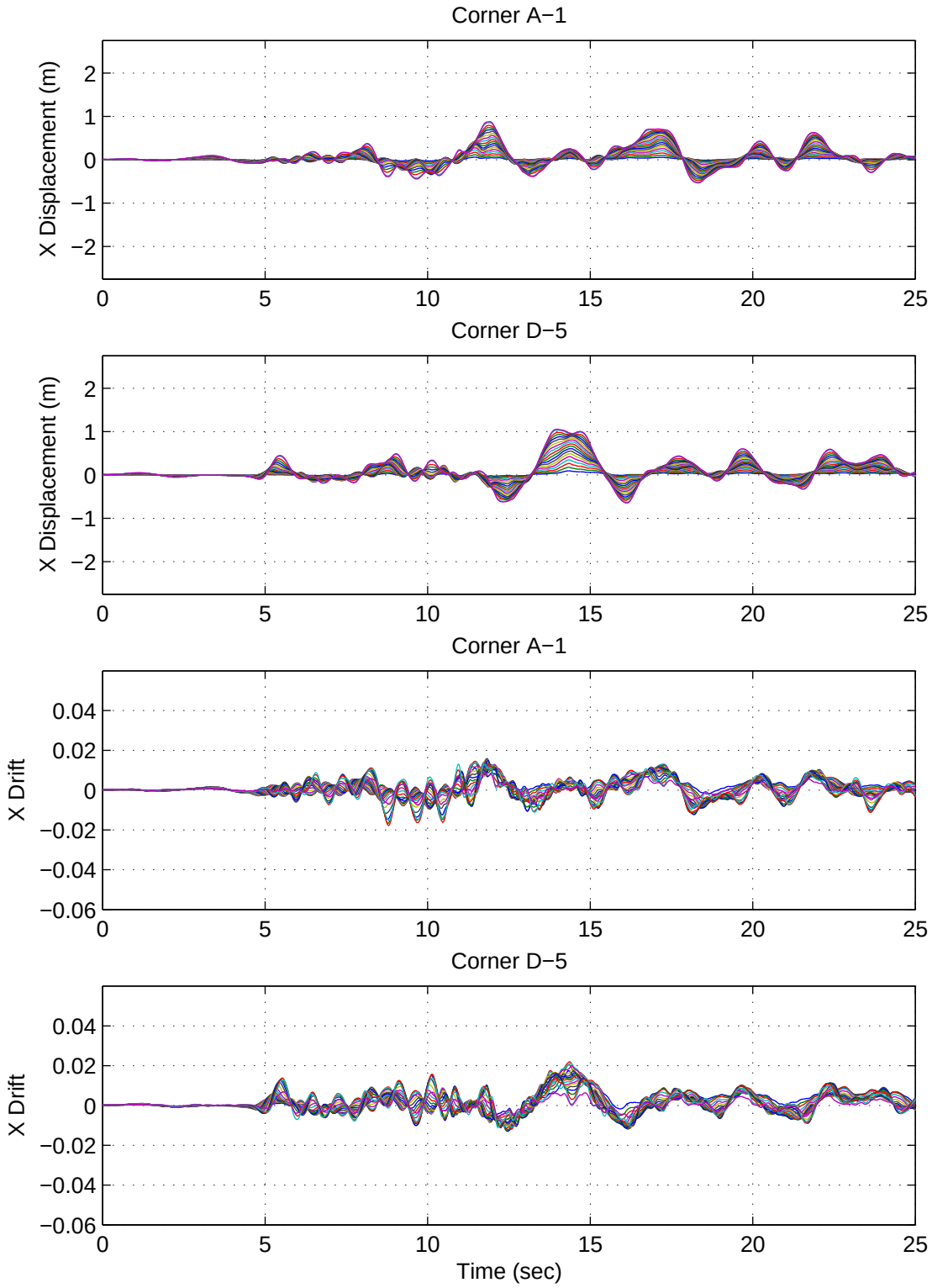

Figure F.31: Building 3 X-Direction Displacements & Drifts: Iran Earthquake (Tabas Record Strong Component in Y Direction)

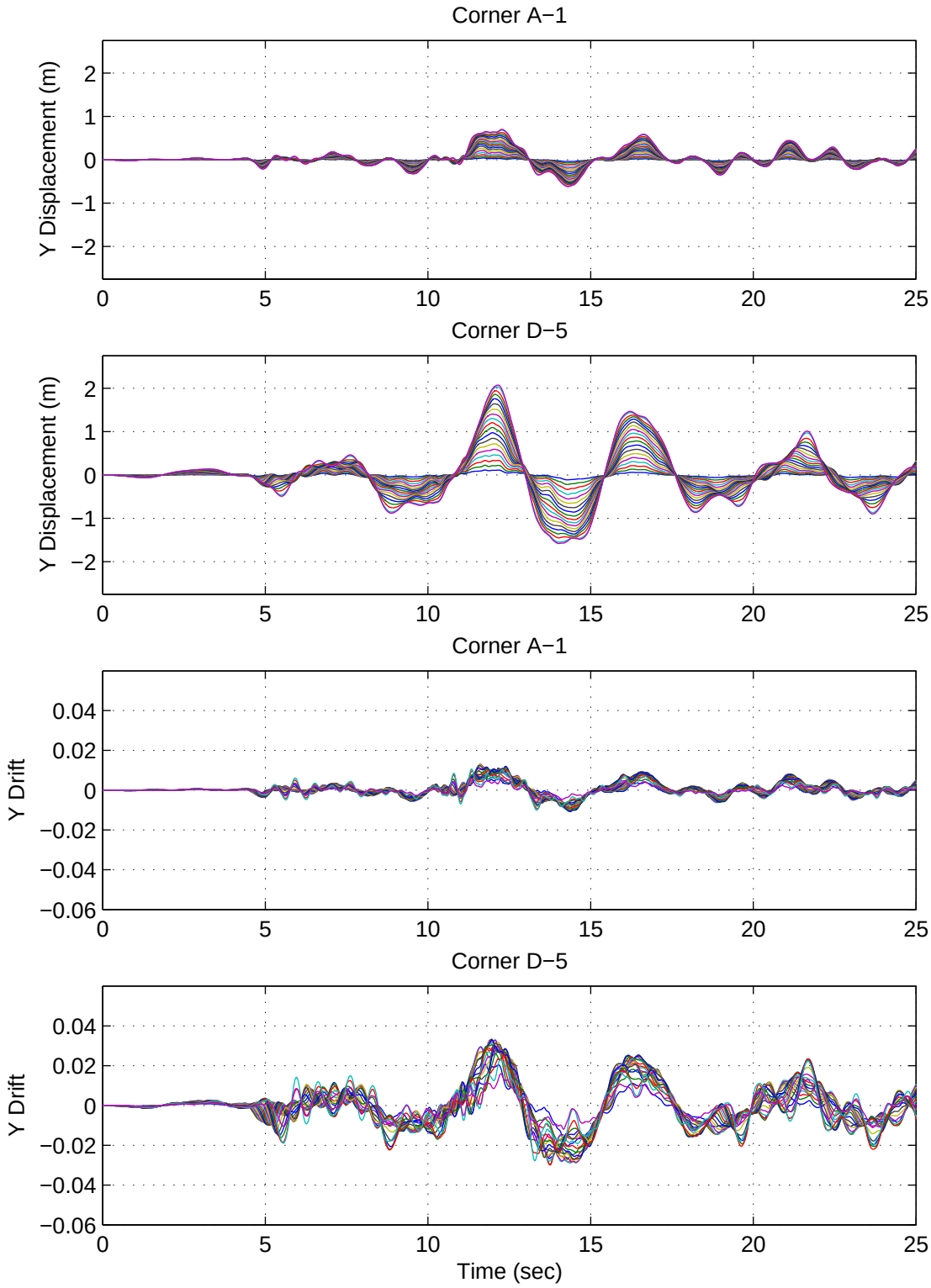

Figure F.32: Building 3 Y-Direction Displacements & Drifts: Iran Earthquake (Tabas Record Strong Component in Y Direction)

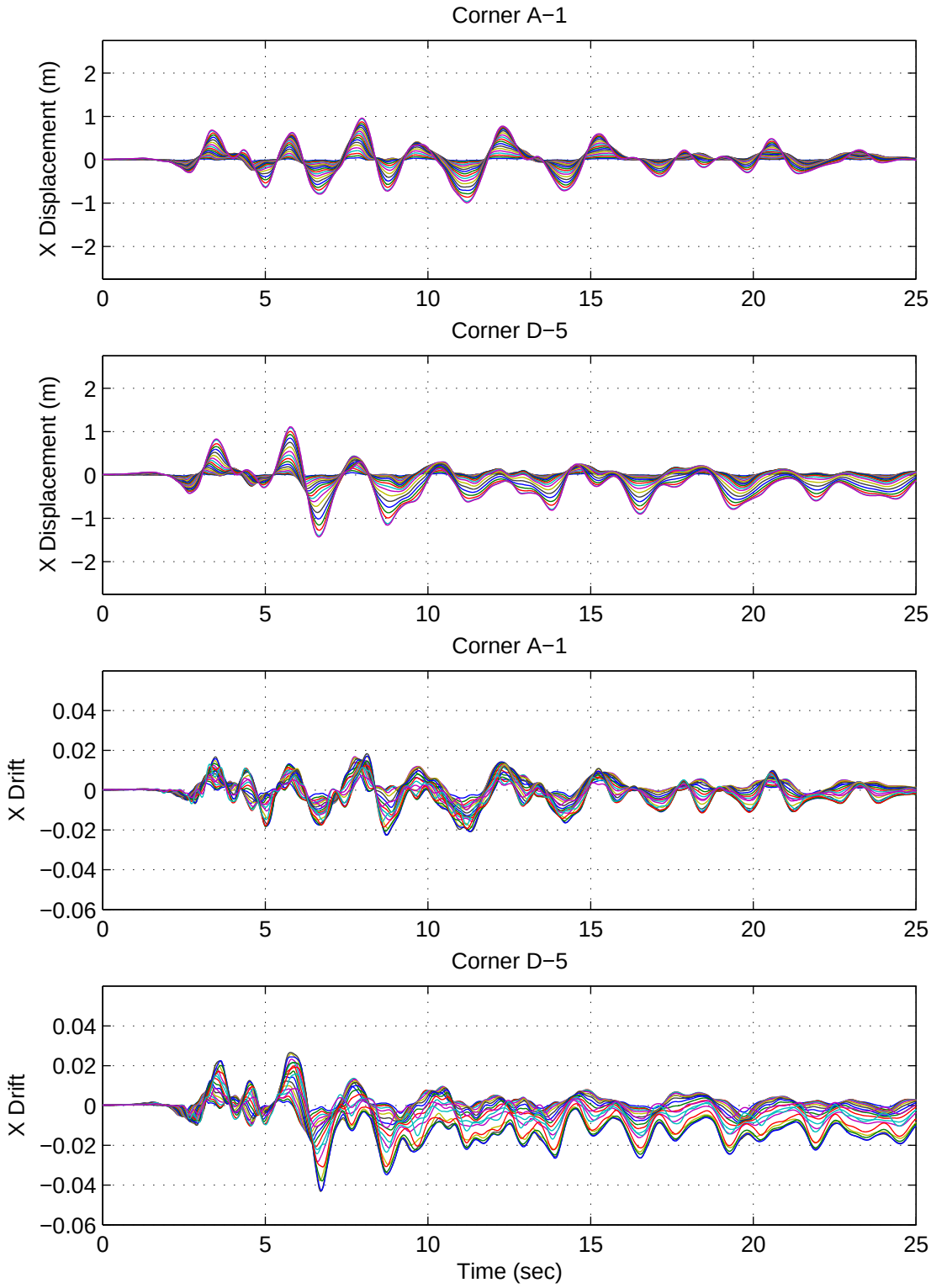

Figure F.33: Building 3 X-Direction Displacements & Drifts: Kobe Earthquake (Takatori Record Strong Component in X Direction)

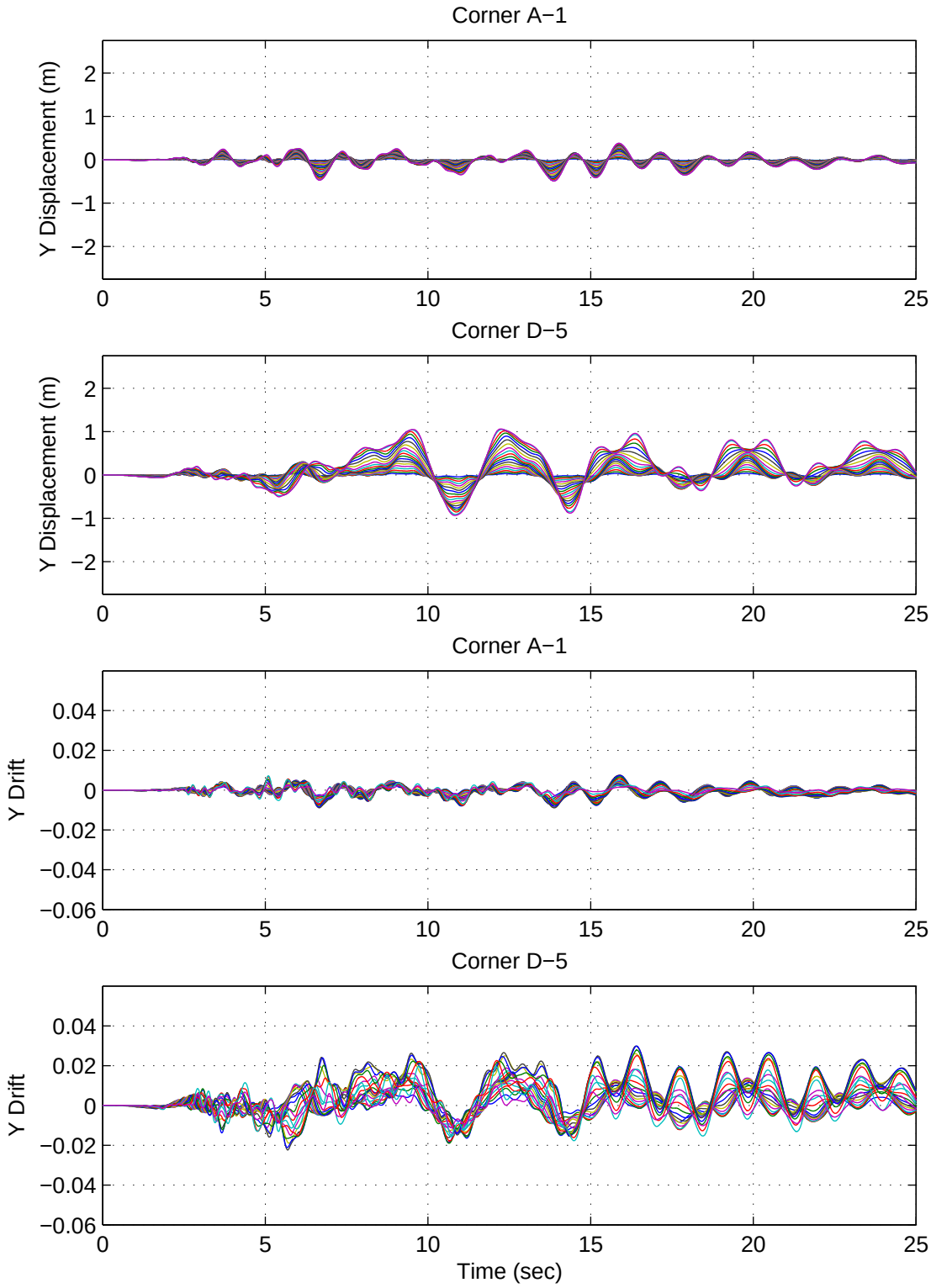

Figure F.34: Building 3 Y-Direction Displacements & Drifts: Kobe Earthquake (Takatori Record Strong Component in X Direction)

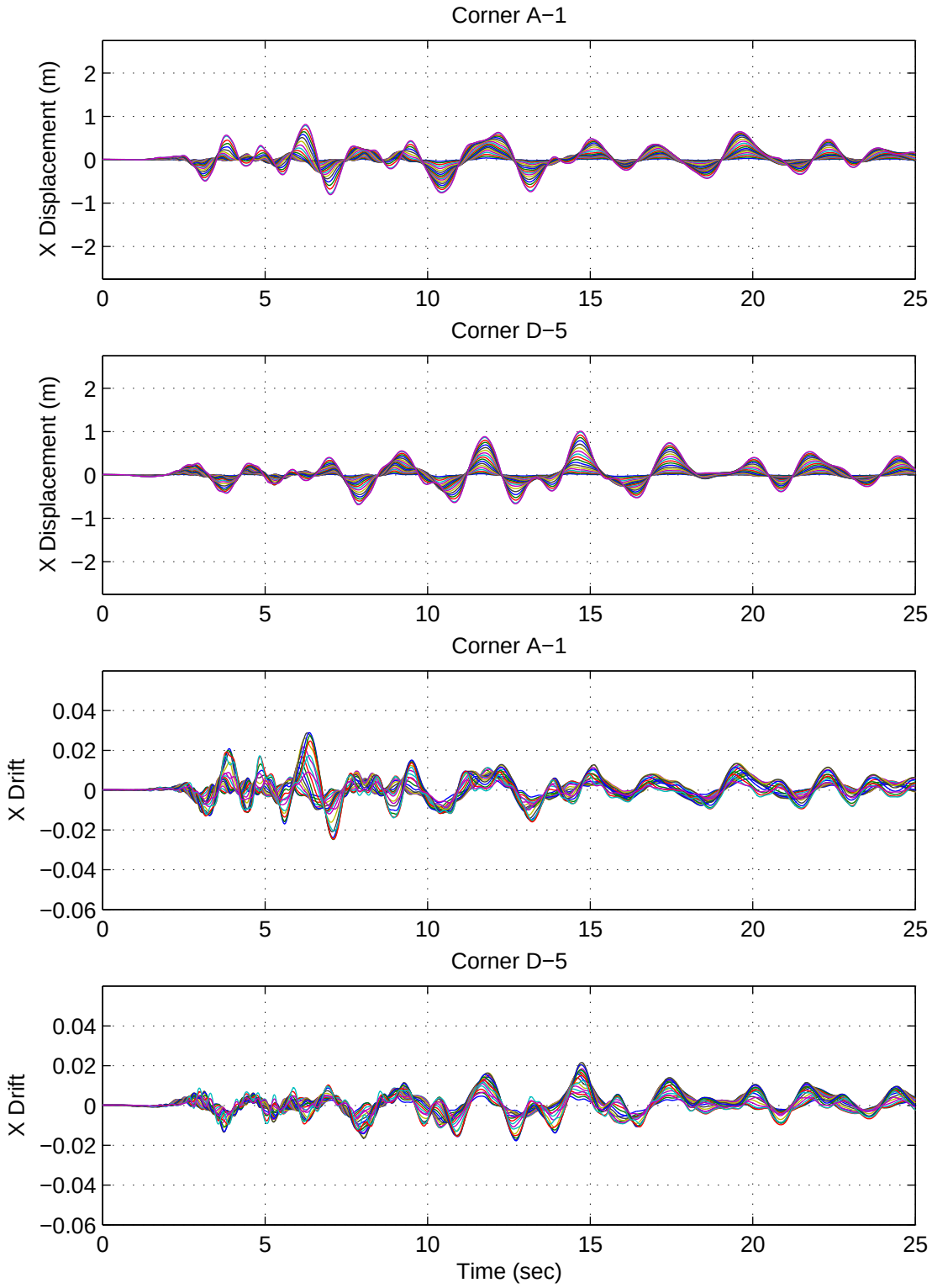

Figure F.35: Building 3 X-Direction Displacements & Drifts: Kobe Earthquake (Takatori Record Strong Component in Y Direction)

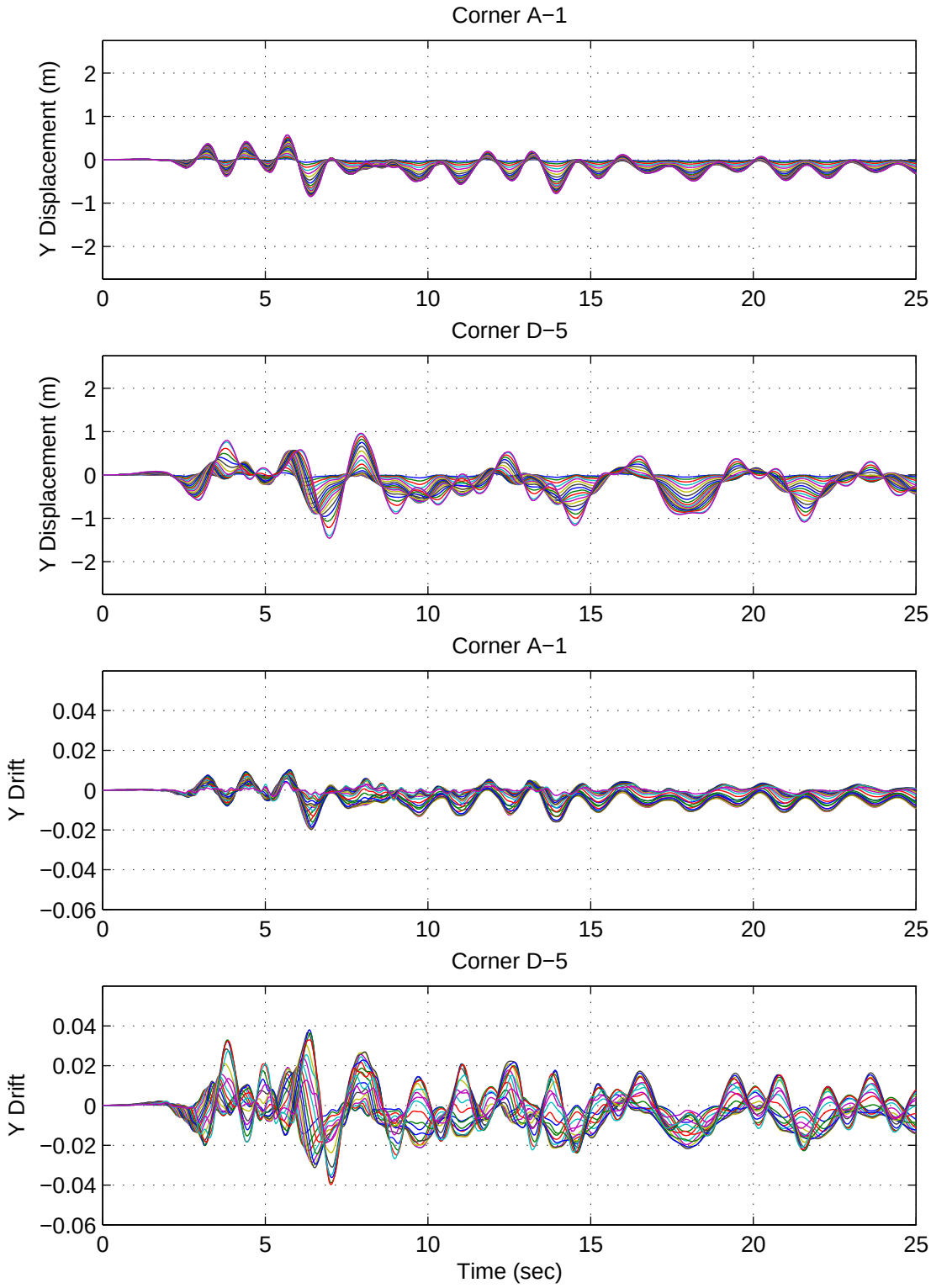

Figure F.36: Building 3 Y-Direction Displacements & Drifts: Kobe Earthquake (Takatori Record Strong Component in Y Direction)

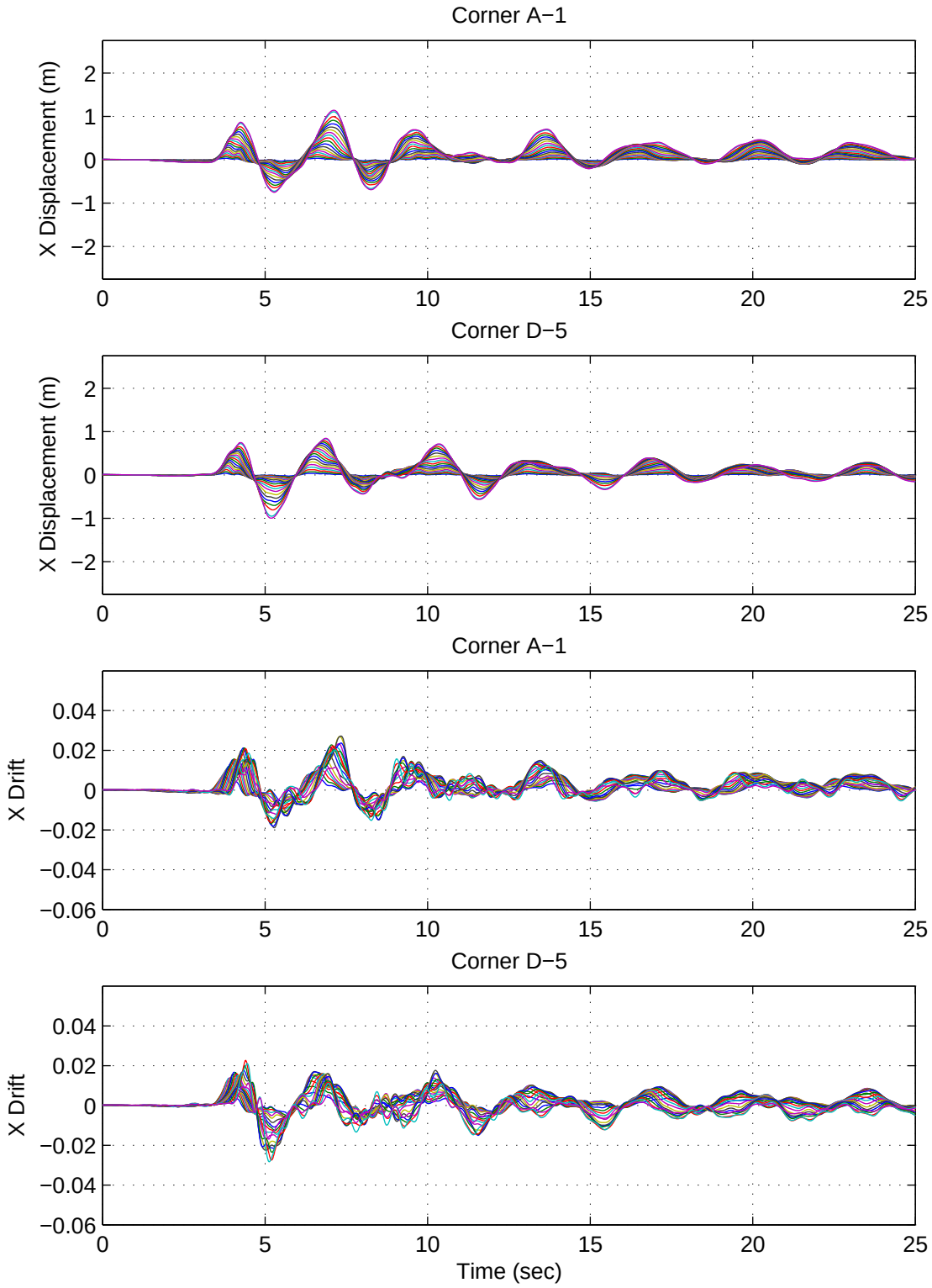

Figure F.37: Building 3A X-Direction Displacements & Drifts: Northridge Earthquake (Sylmar Record Strong Component in X Direction)

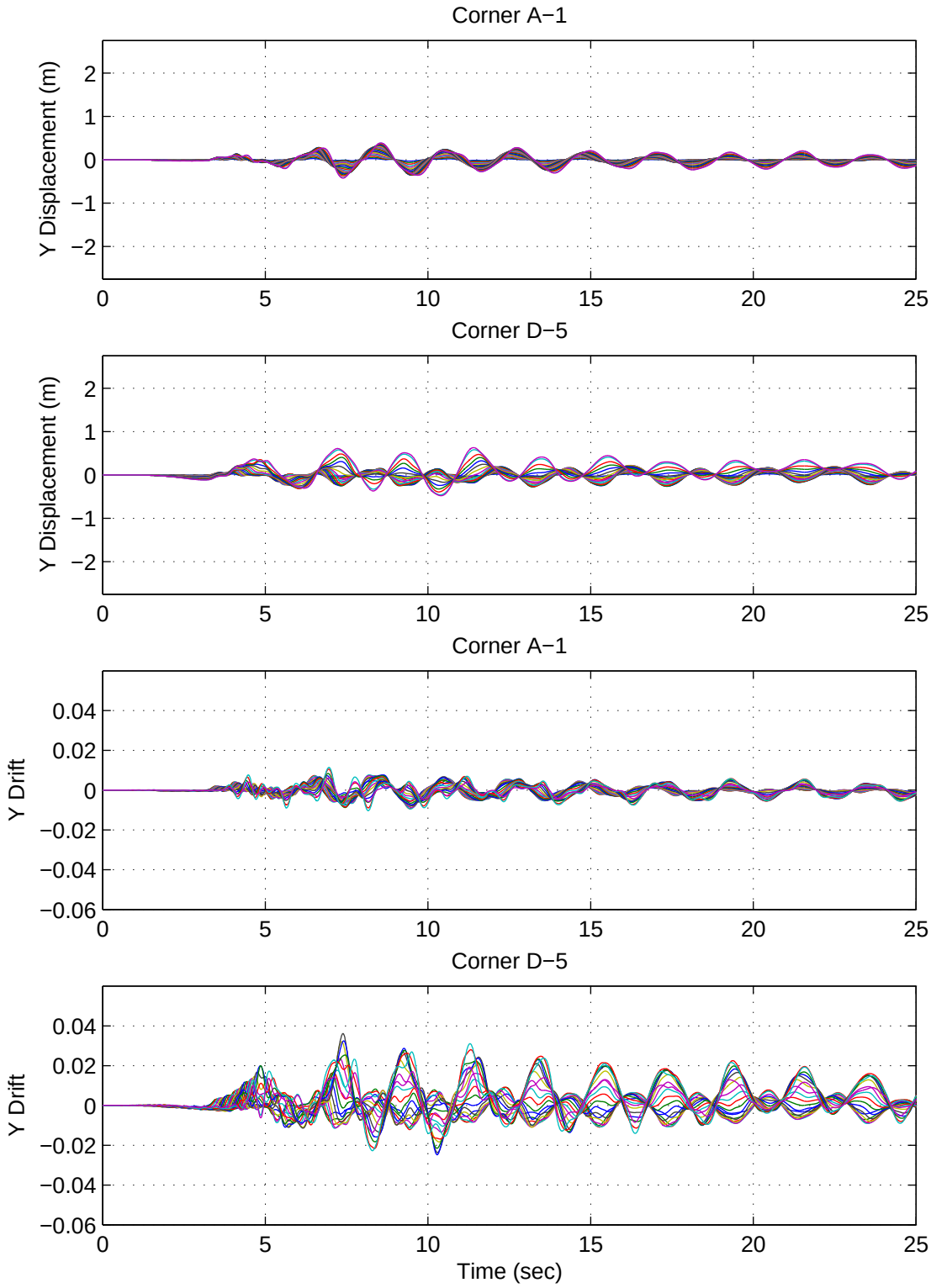

Figure F.38: Building 3A Y-Direction Displacements & Drifts: Northridge Earthquake (Sylmar Record Strong Component in X Direction)

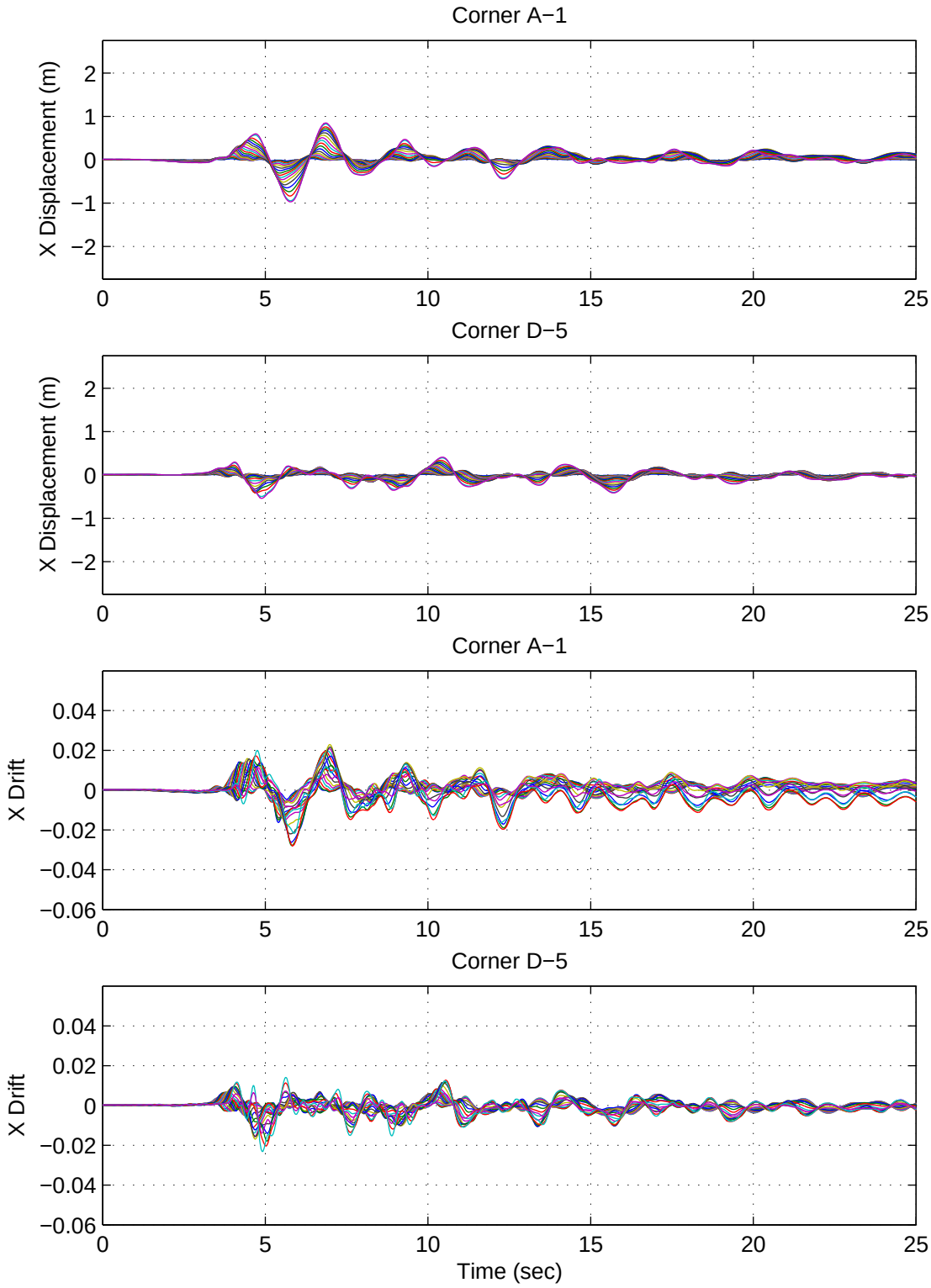

Figure F.39: Building 3A X-Direction Displacements & Drifts: Northridge Earthquake (Sylmar Record Strong Component in Y Direction)

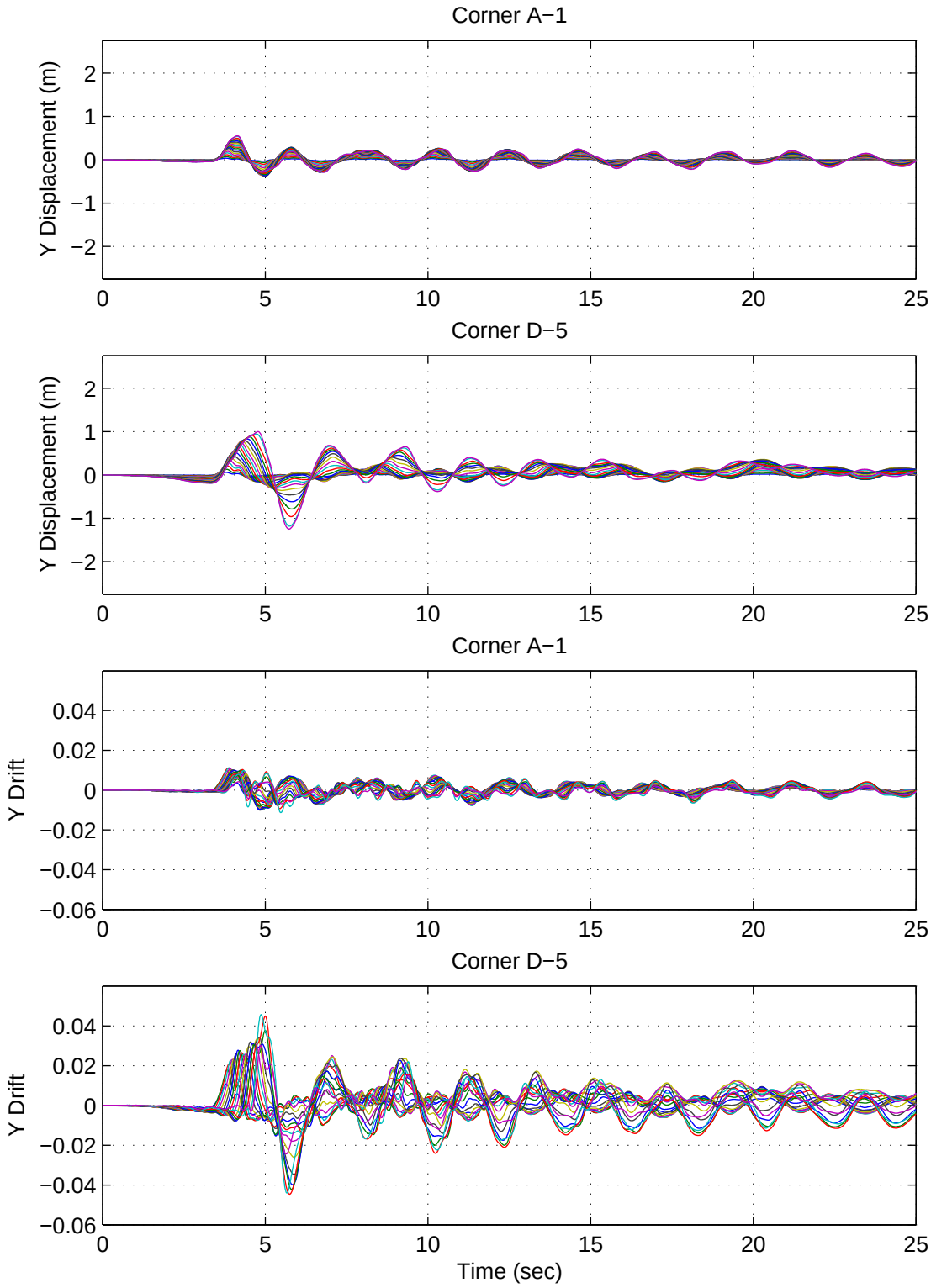

Figure F.40: Building 3A Y-Direction Displacements & Drifts: Northridge Earthquake (Sylmar Record Strong Component in Y Direction)

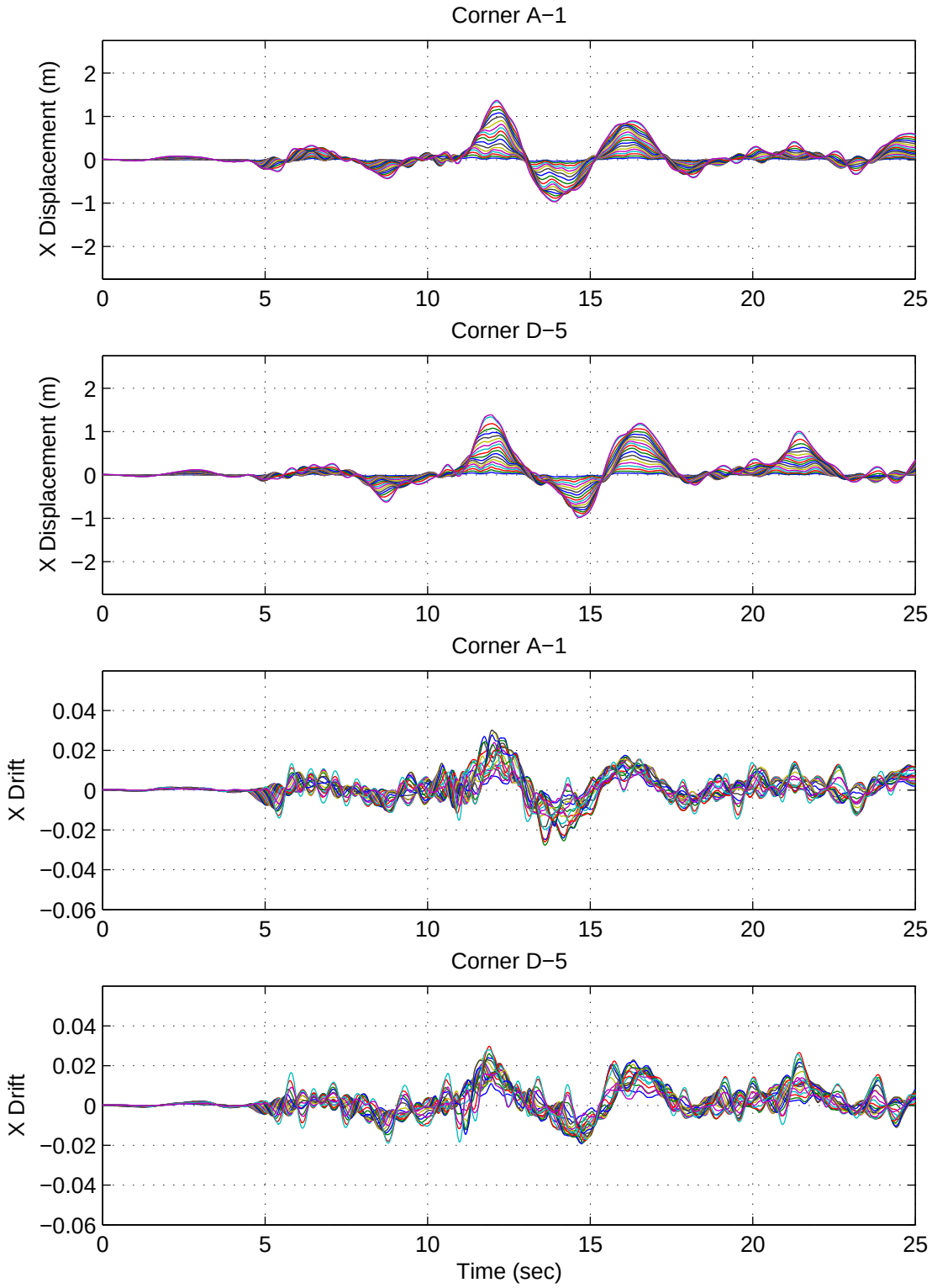

Figure F.41: Building 3A X-Direction Displacements & Drifts: Iran Earthquake (Tabas Record Strong Component in X Direction)

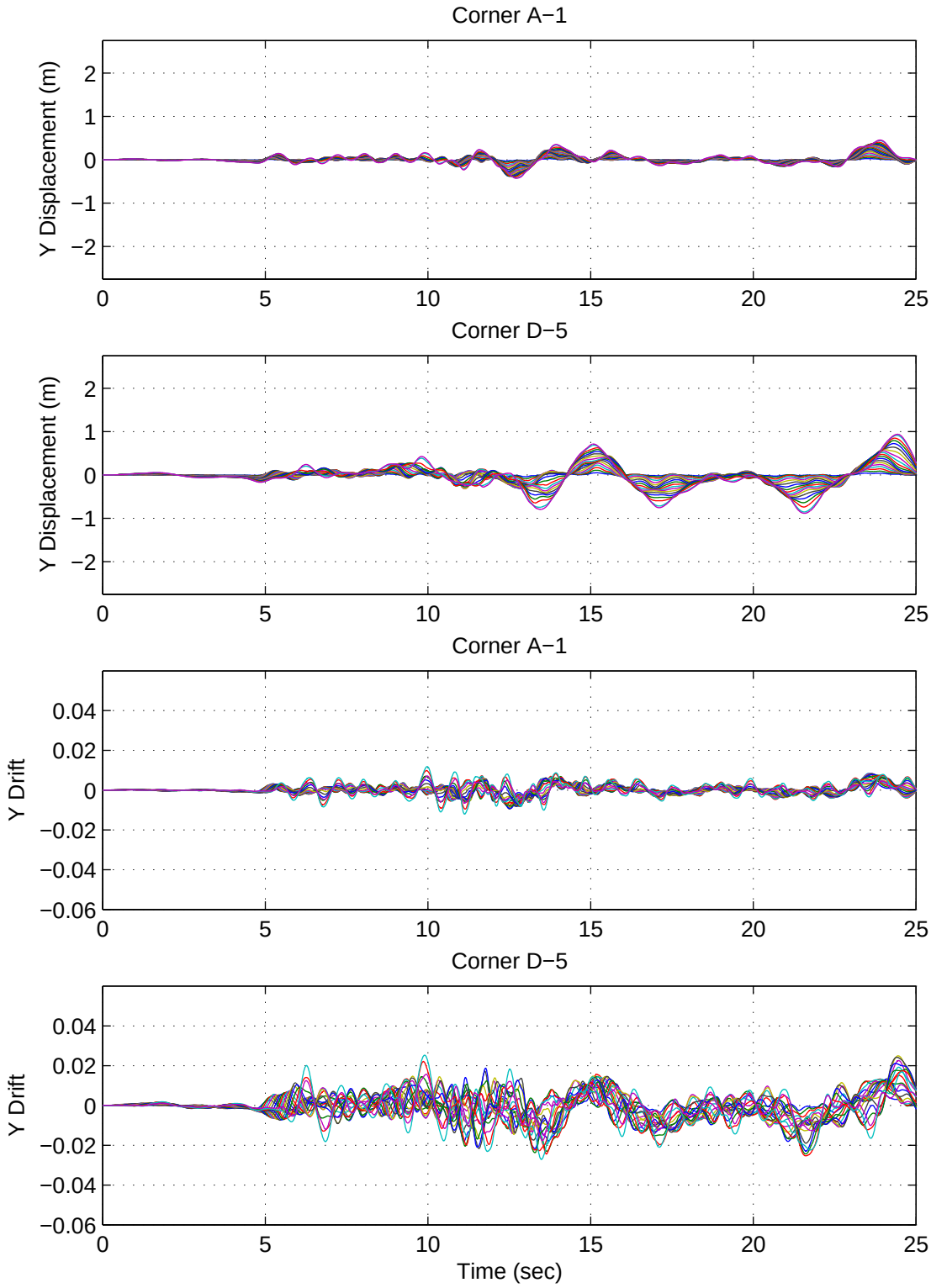

Figure F.42: Building 3A Y-Direction Displacements & Drifts: Iran Earthquake (Tabas Record Strong Component in X Direction)

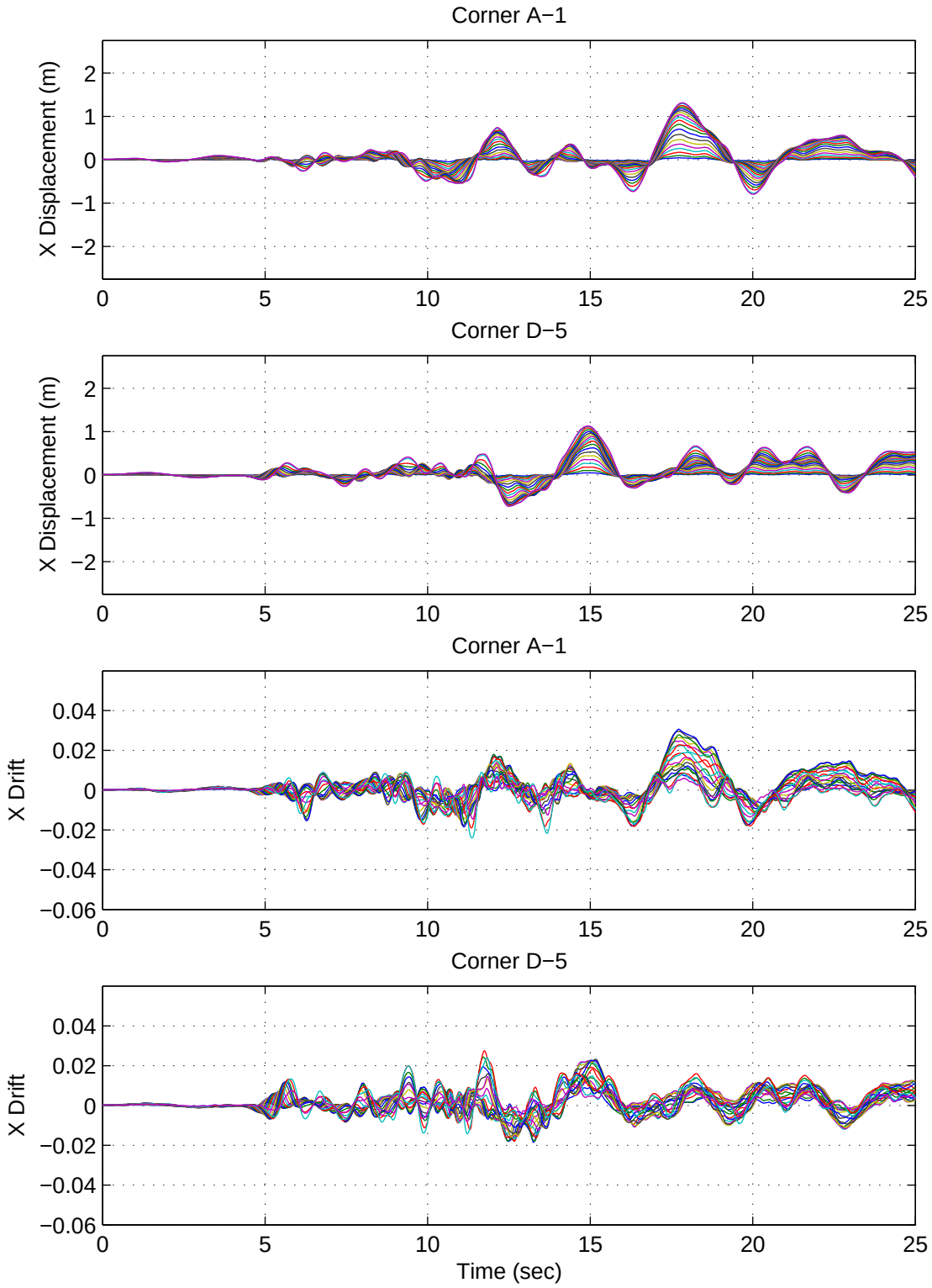

Figure F.43: Building 3A X-Direction Displacements & Drifts: Iran Earthquake (Tabas Record Strong Component in Y Direction)

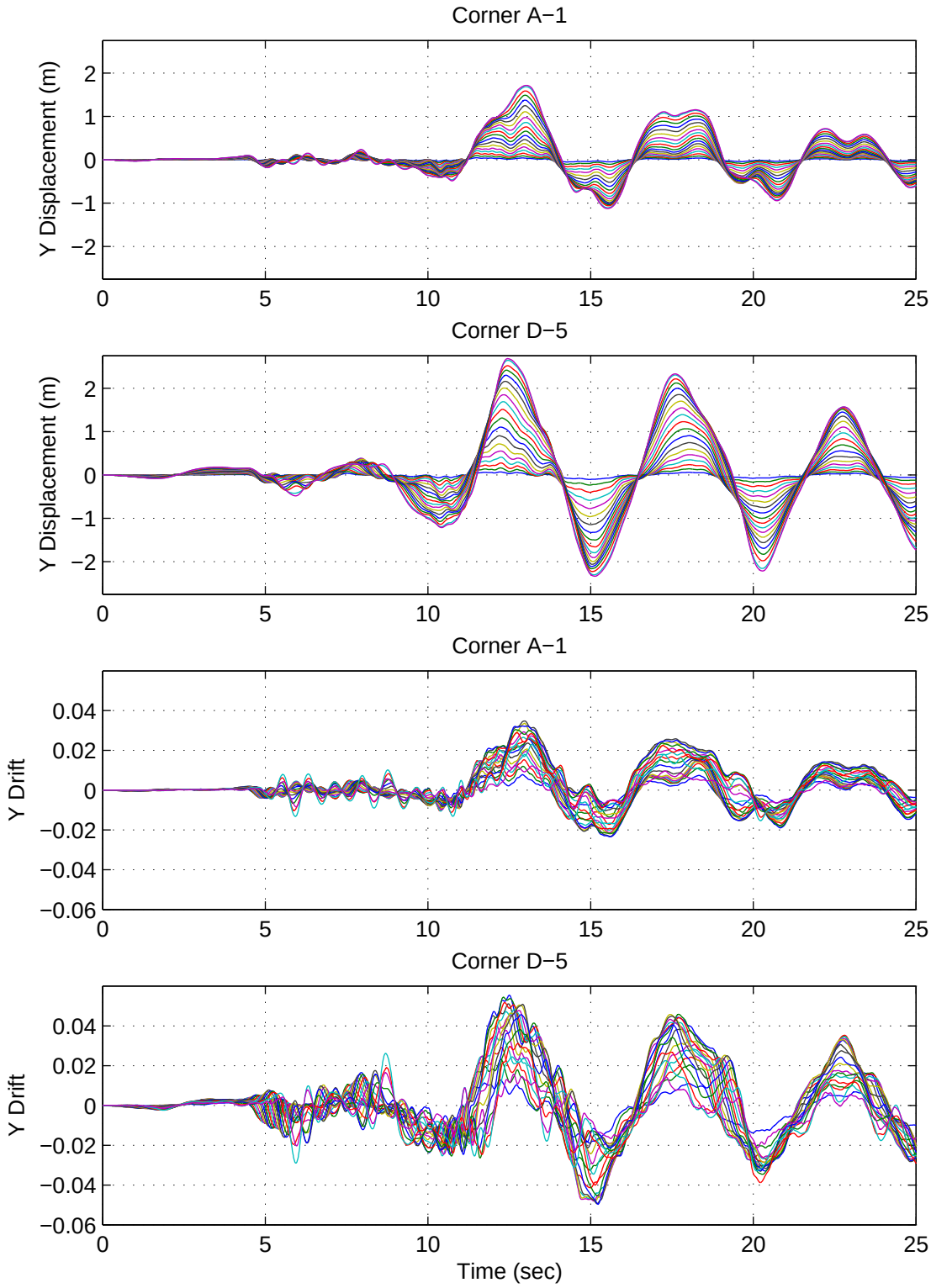

Figure F.44: Building 3A Y-Direction Displacements & Drifts: Iran Earthquake (Tabas Record Strong Component in Y Direction)

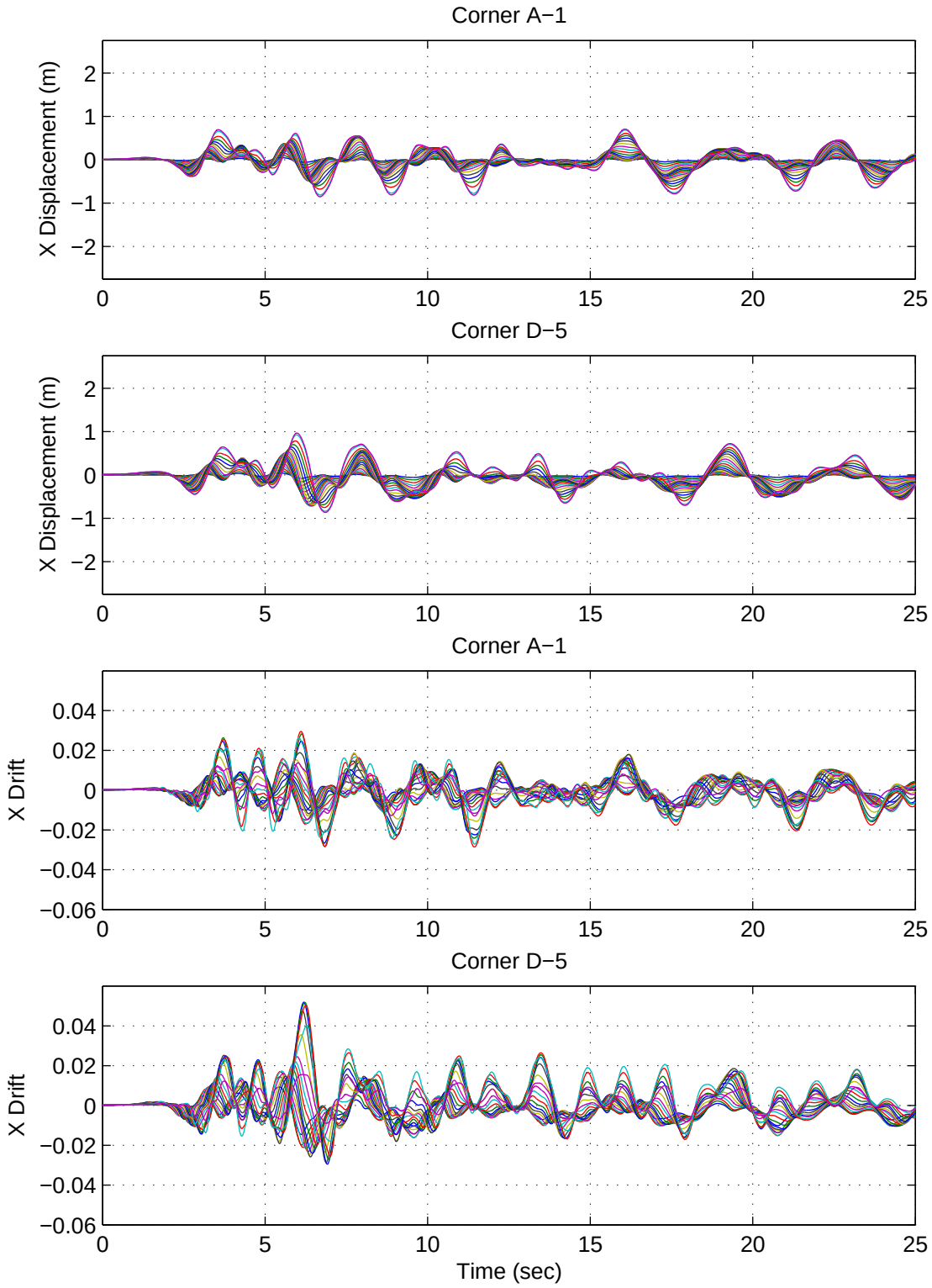

Figure F.45: Building 3A X-Direction Displacements & Drifts: Kobe Earthquake (Takatori Record Strong Component in X Direction)

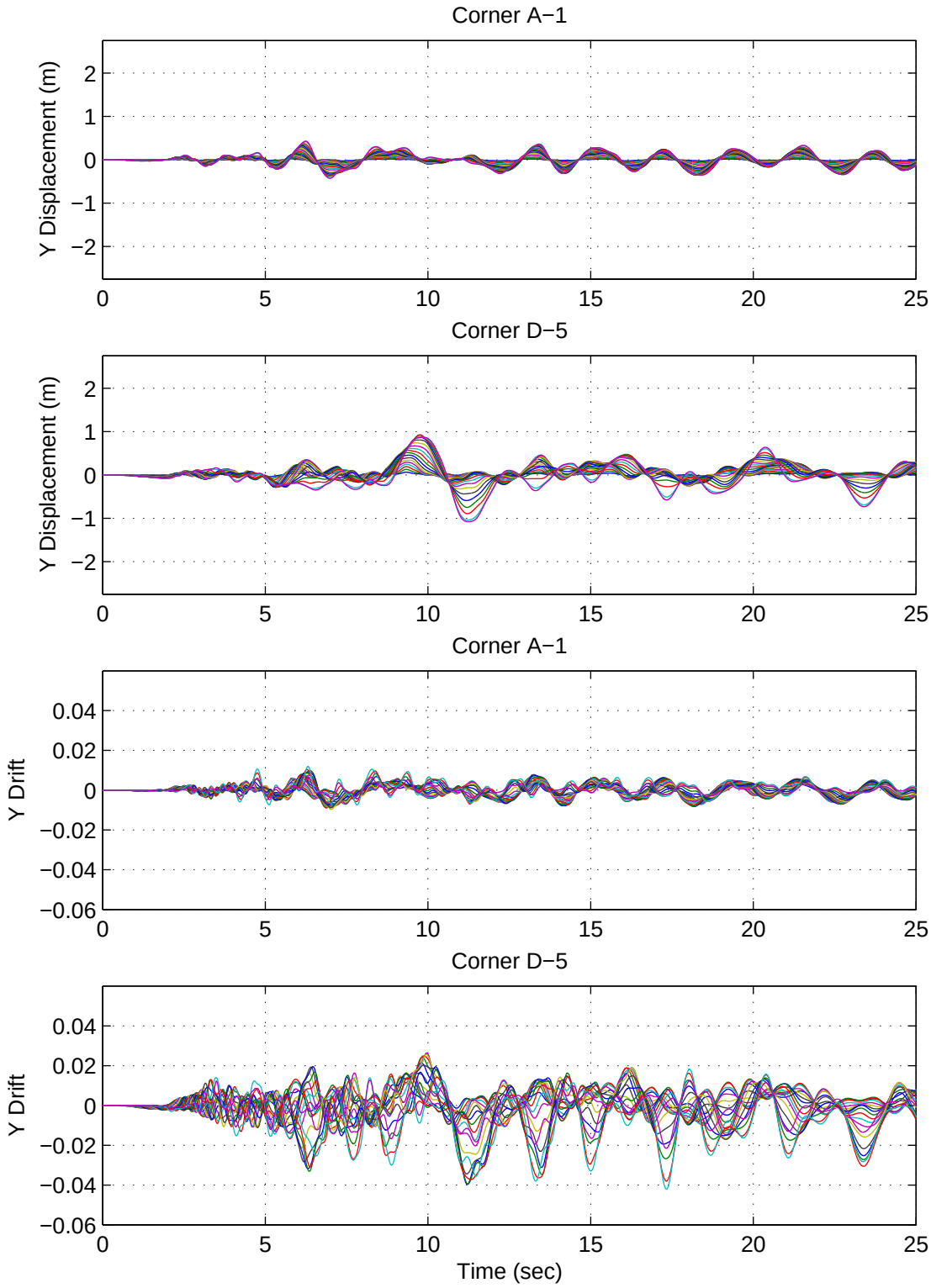

Figure F.46: Building 3A Y-Direction Displacements & Drifts: Kobe Earthquake (Takatori Record Strong Component in X Direction)

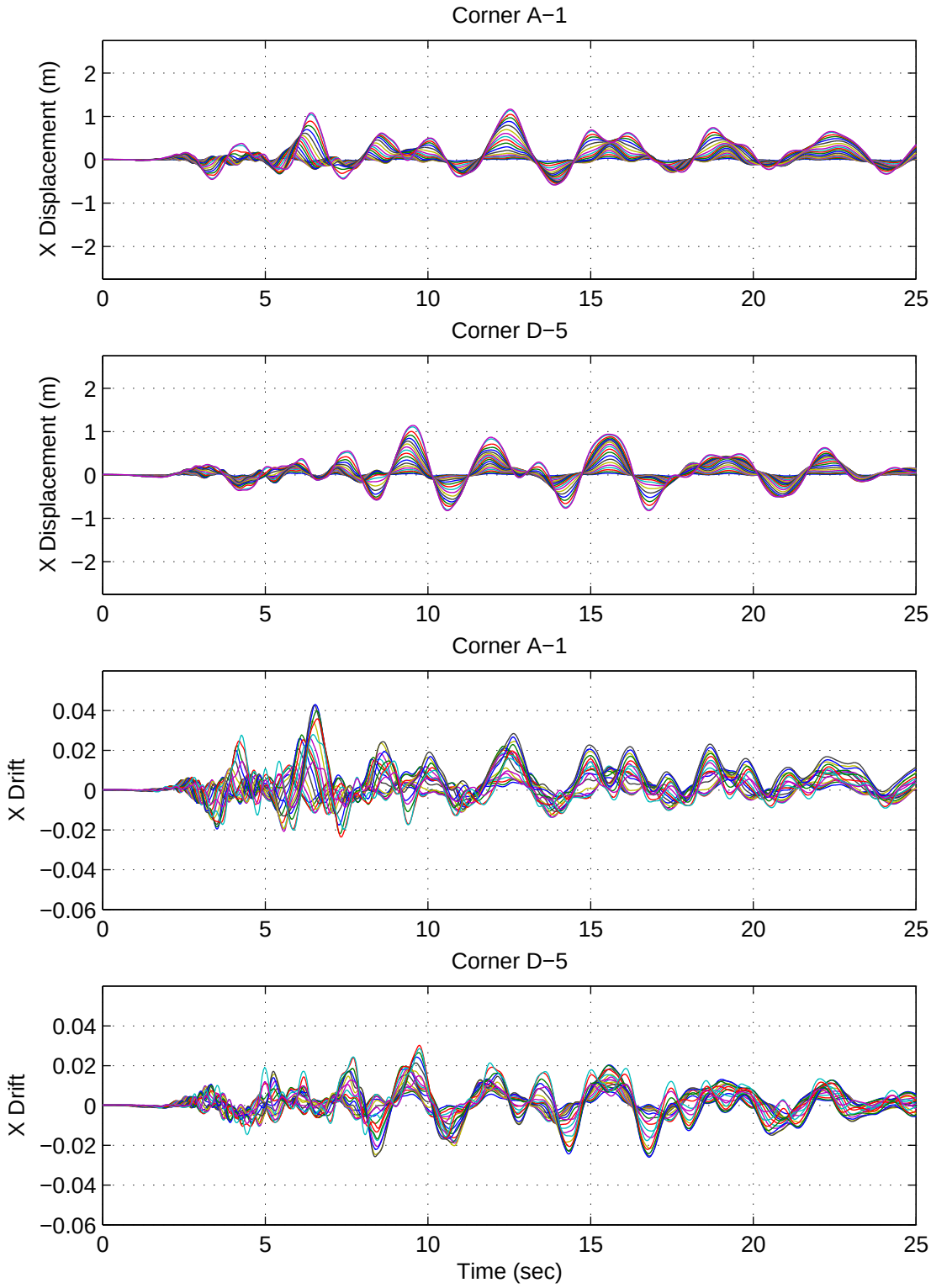

Figure F.47: Building 3A X-Direction Displacements & Drifts: Kobe Earthquake (Takatori Record Strong Component in Y Direction)

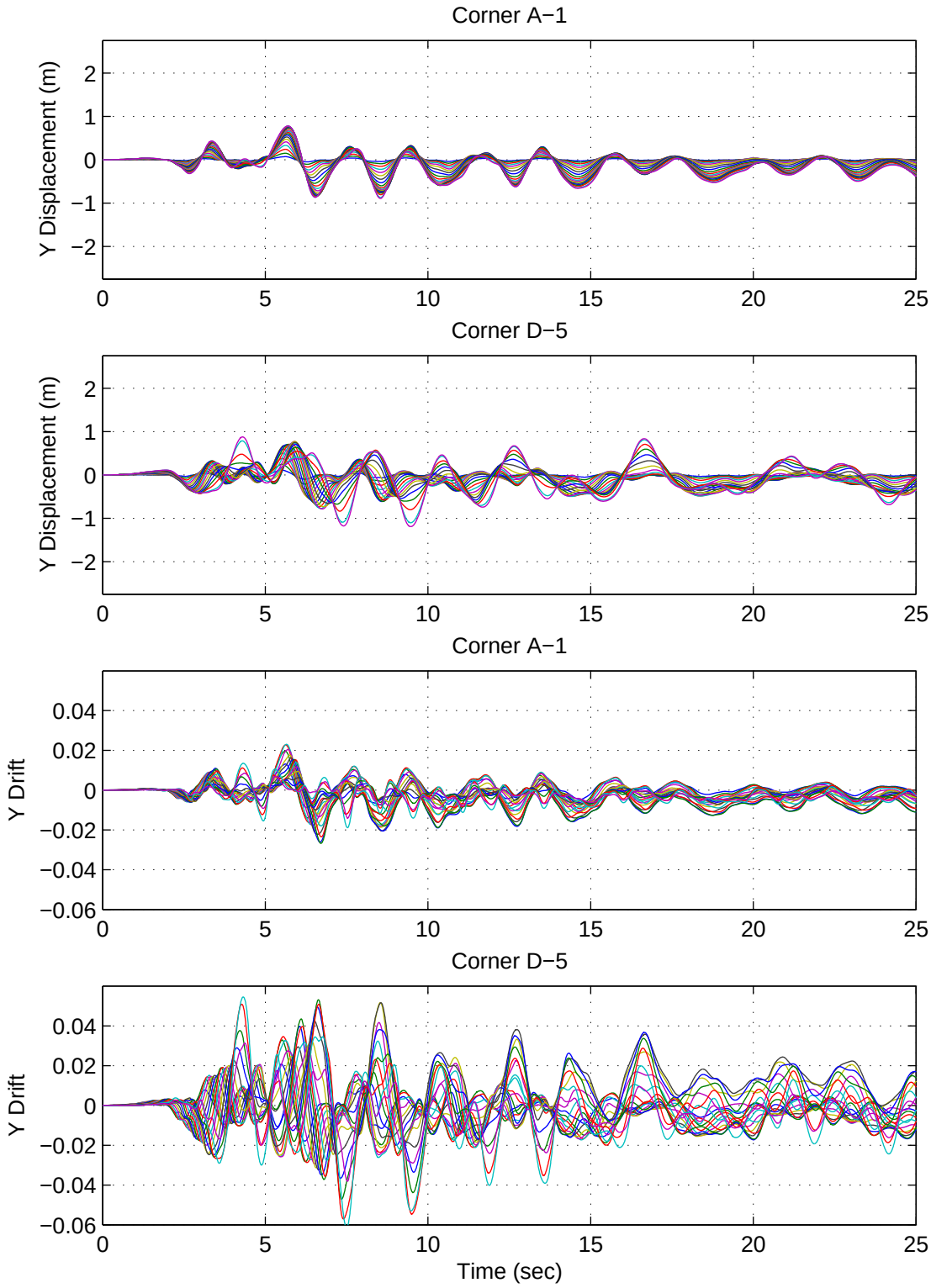

Figure F.48: Building 3A Y-Direction Displacements & Drifts: Kobe Earthquake (Takatori Record Strong Component in Y Direction)

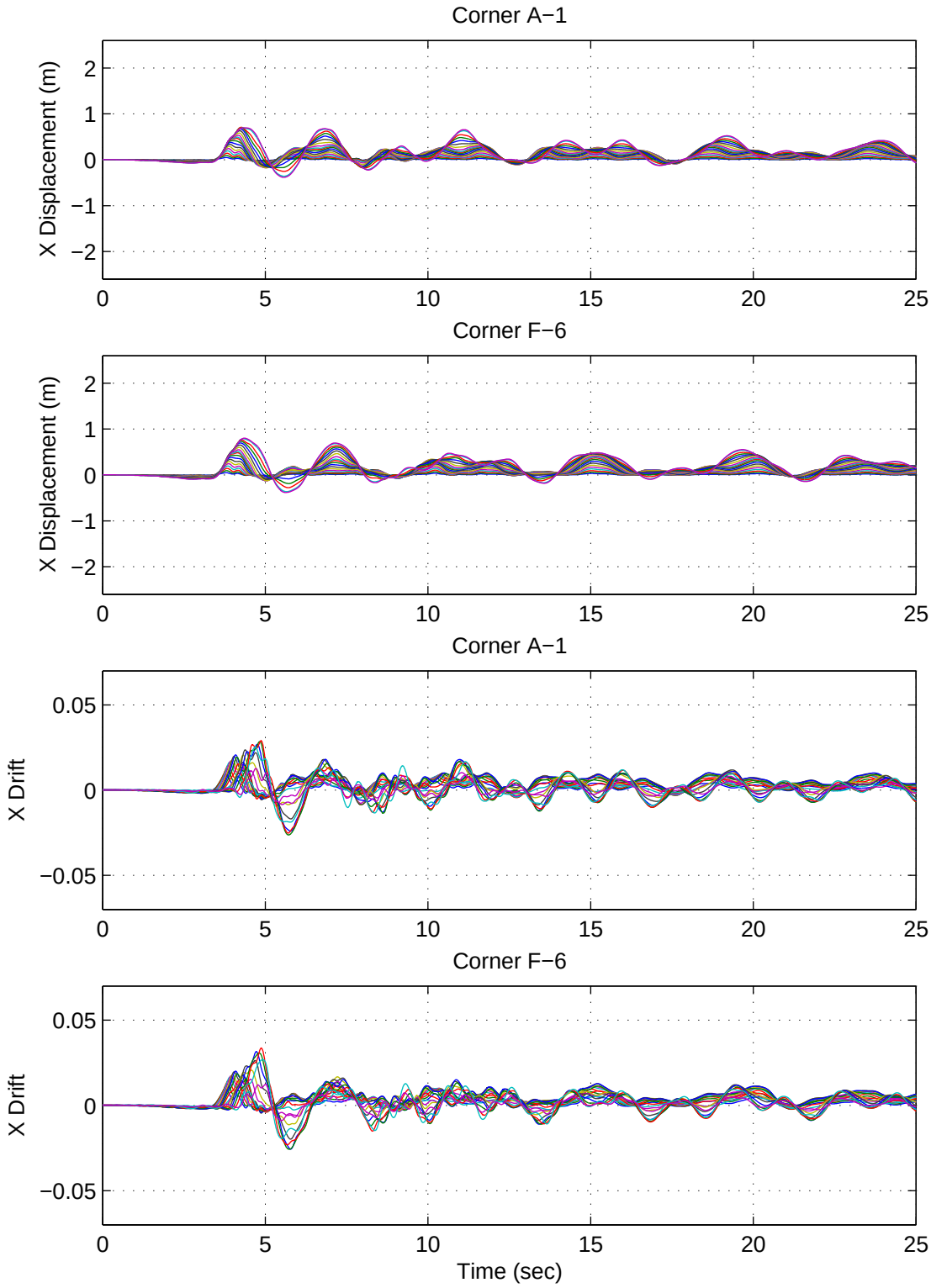

Figure F.49: Building 4 X-Direction Displacements & Drifts: Northridge Earthquake (Sylmar Record Strong Component in X Direction)

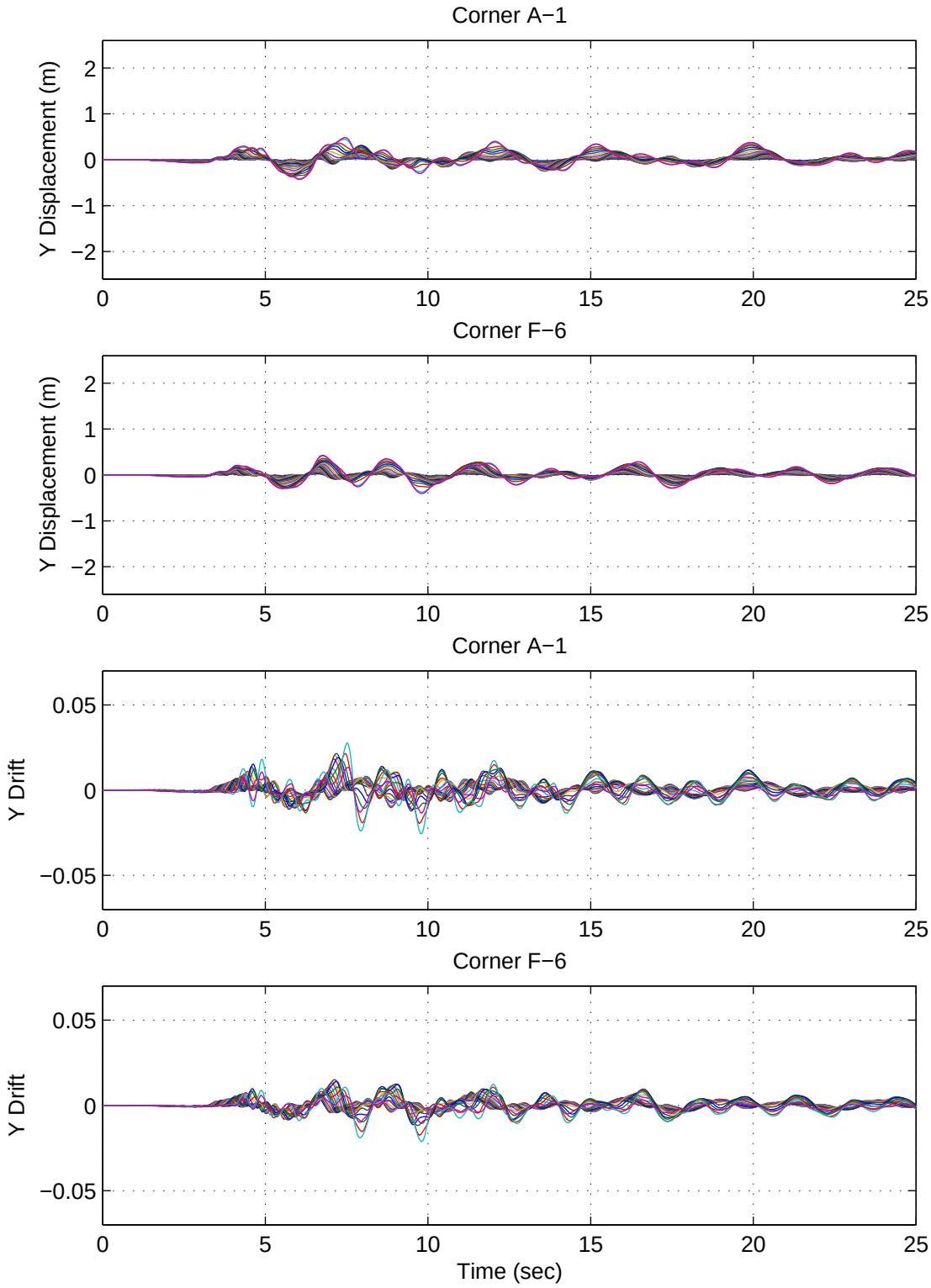

Figure F.50: Building 4 Y-Direction Displacements & Drifts: Northridge Earthquake (Sylmar Record Strong Component in X Direction)

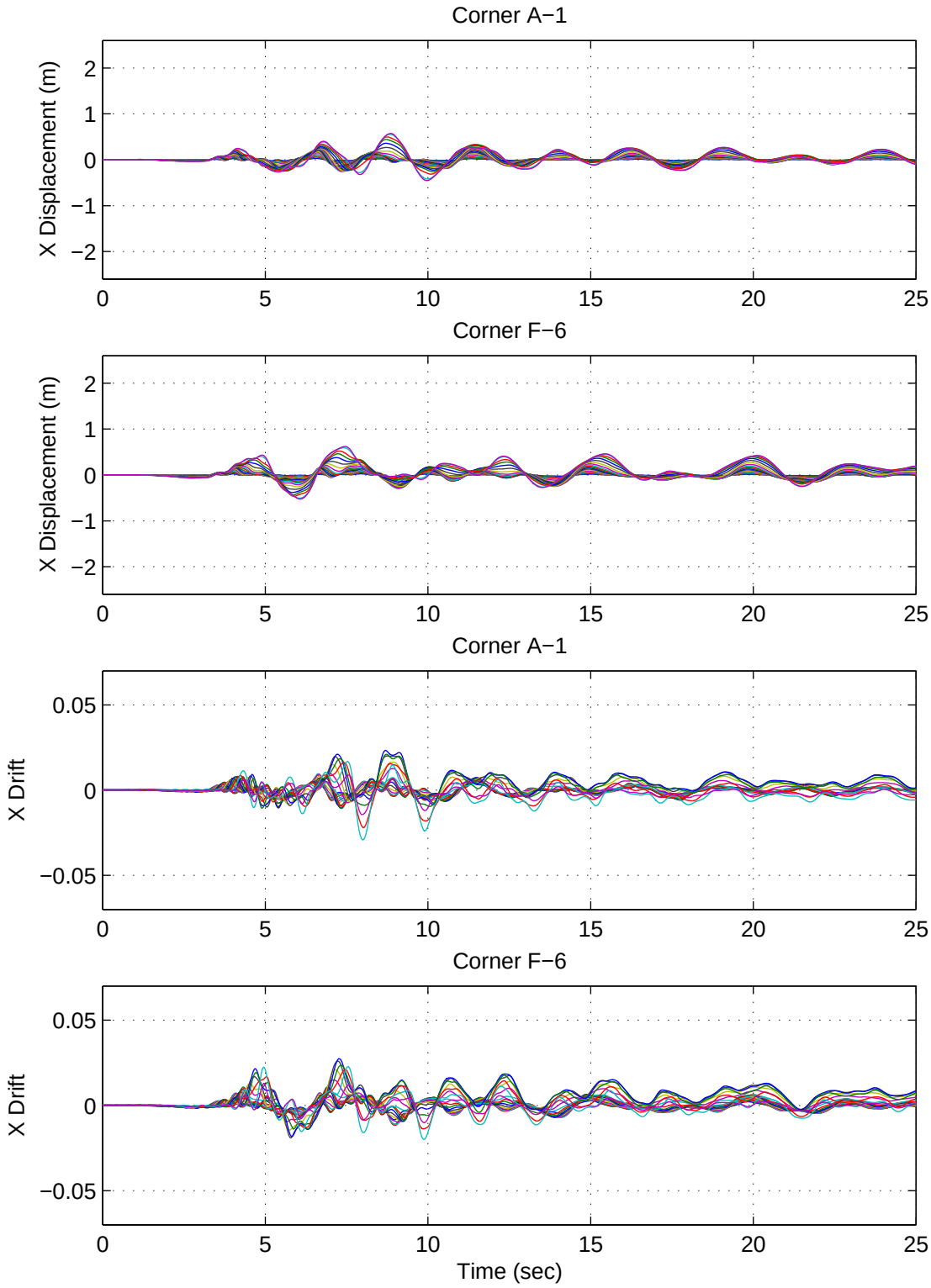

Figure F.51: Building 4 X-Direction Displacements & Drifts: Northridge Earthquake (Sylmar Record Strong Component in Y Direction)

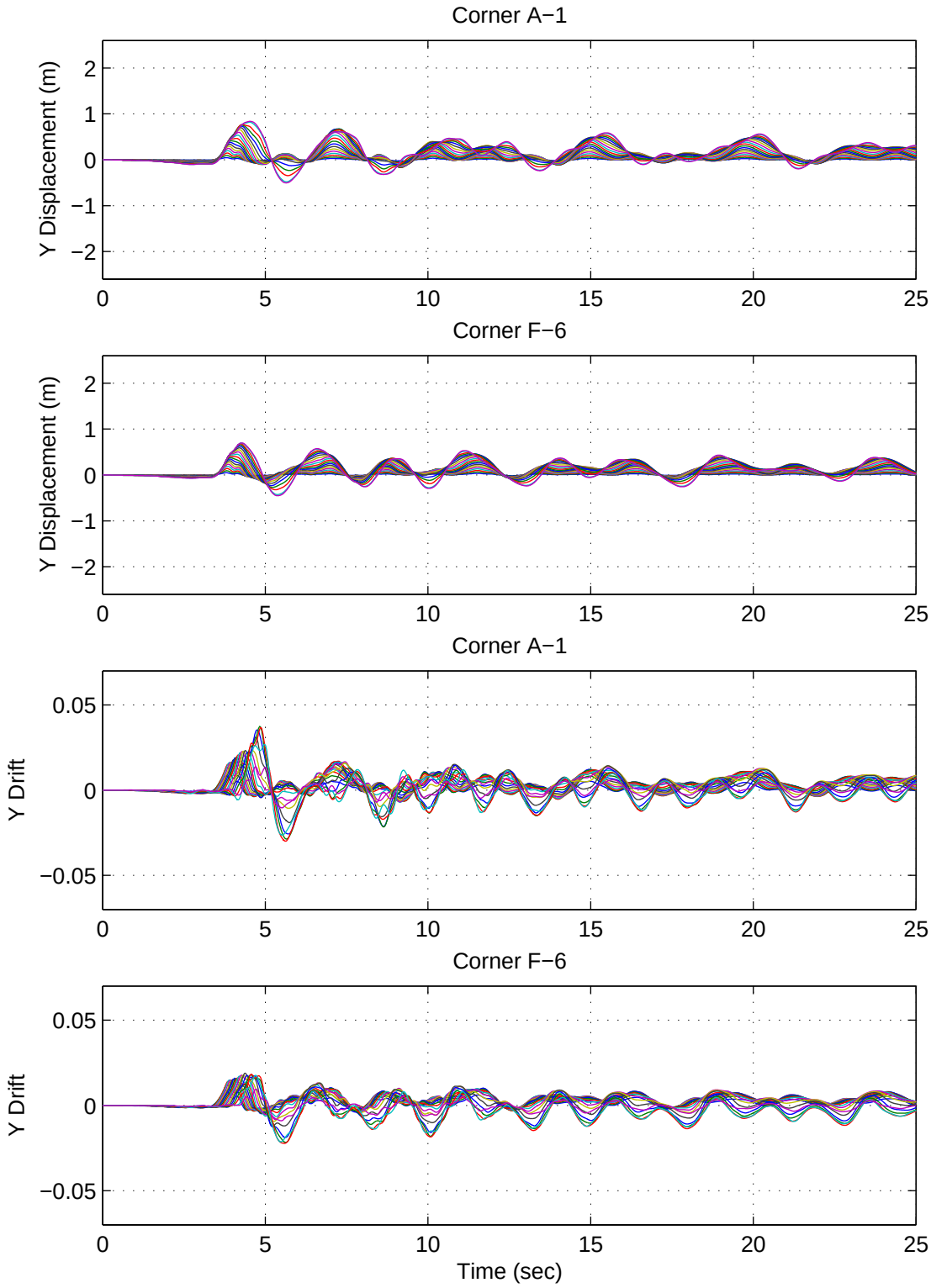

Figure F.52: Building 4 Y-Direction Displacements & Drifts: Northridge Earthquake (Sylmar Record Strong Component in Y Direction)

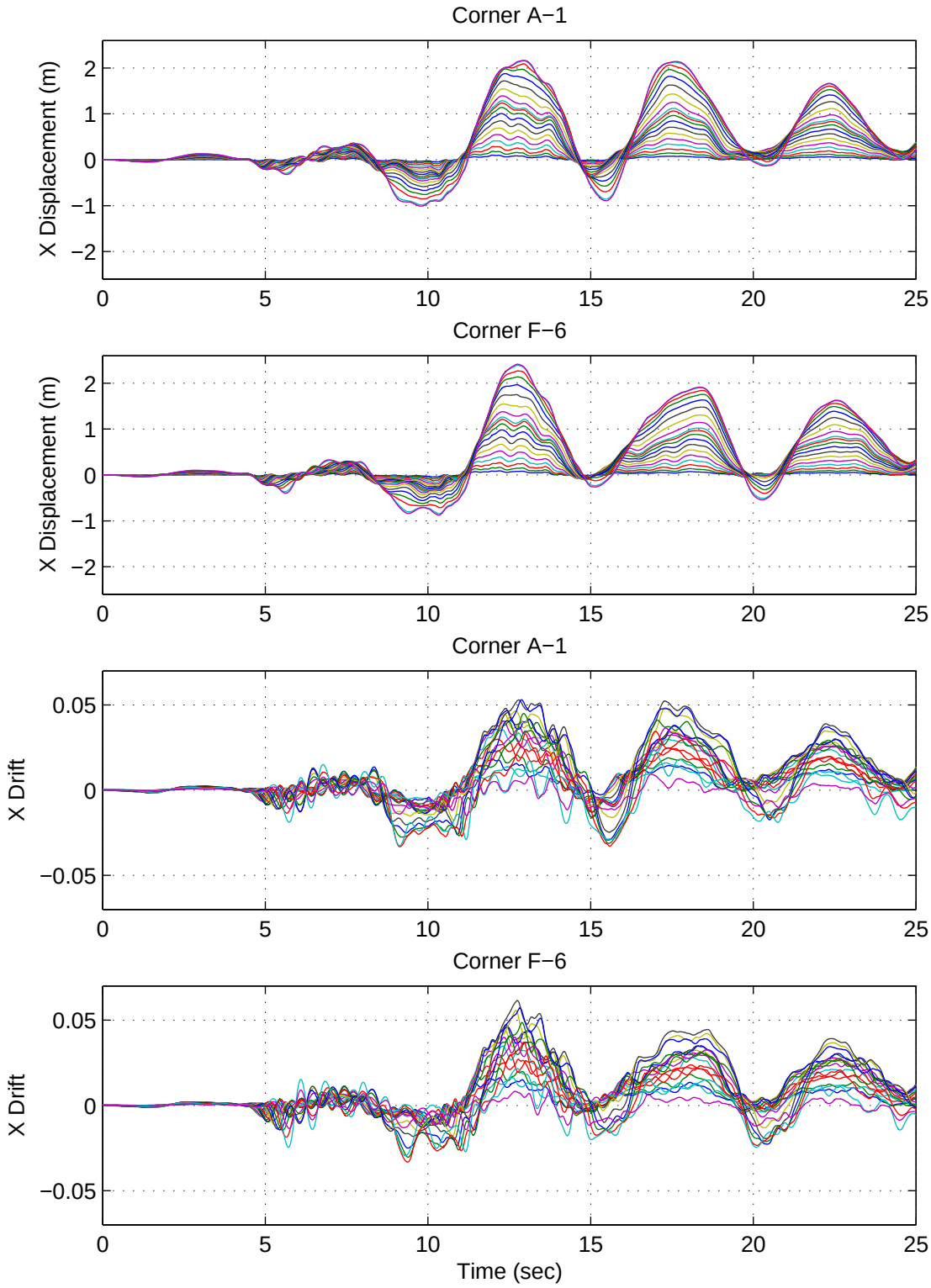

Figure F.53: Building 4 X-Direction Displacements & Drifts: Iran Earthquake (Tabas Record Strong Component in X Direction)

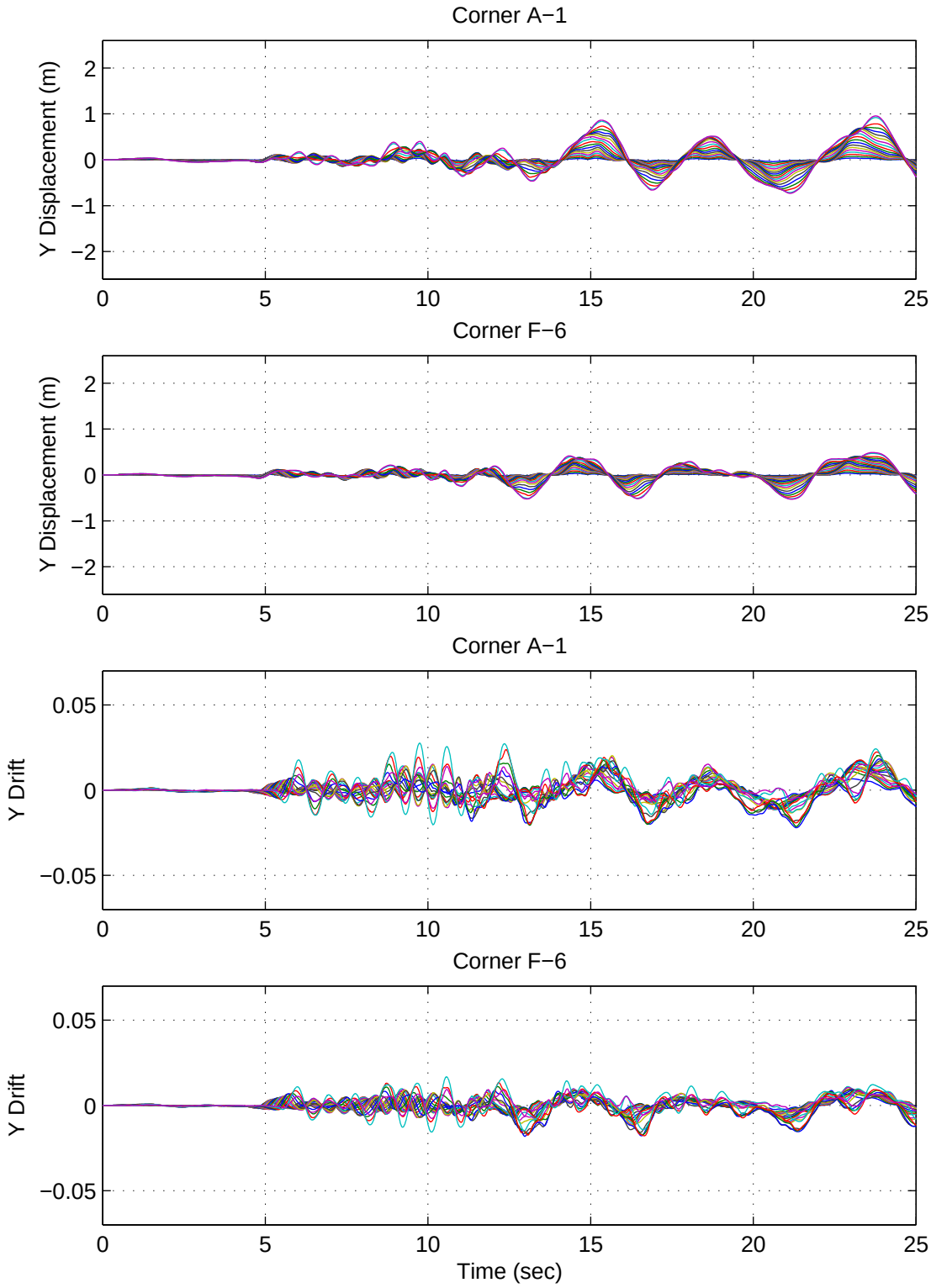

Figure F.54: Building 4 Y-Direction Displacements & Drifts: Iran Earthquake (Tabas Record Strong Component in X Direction)

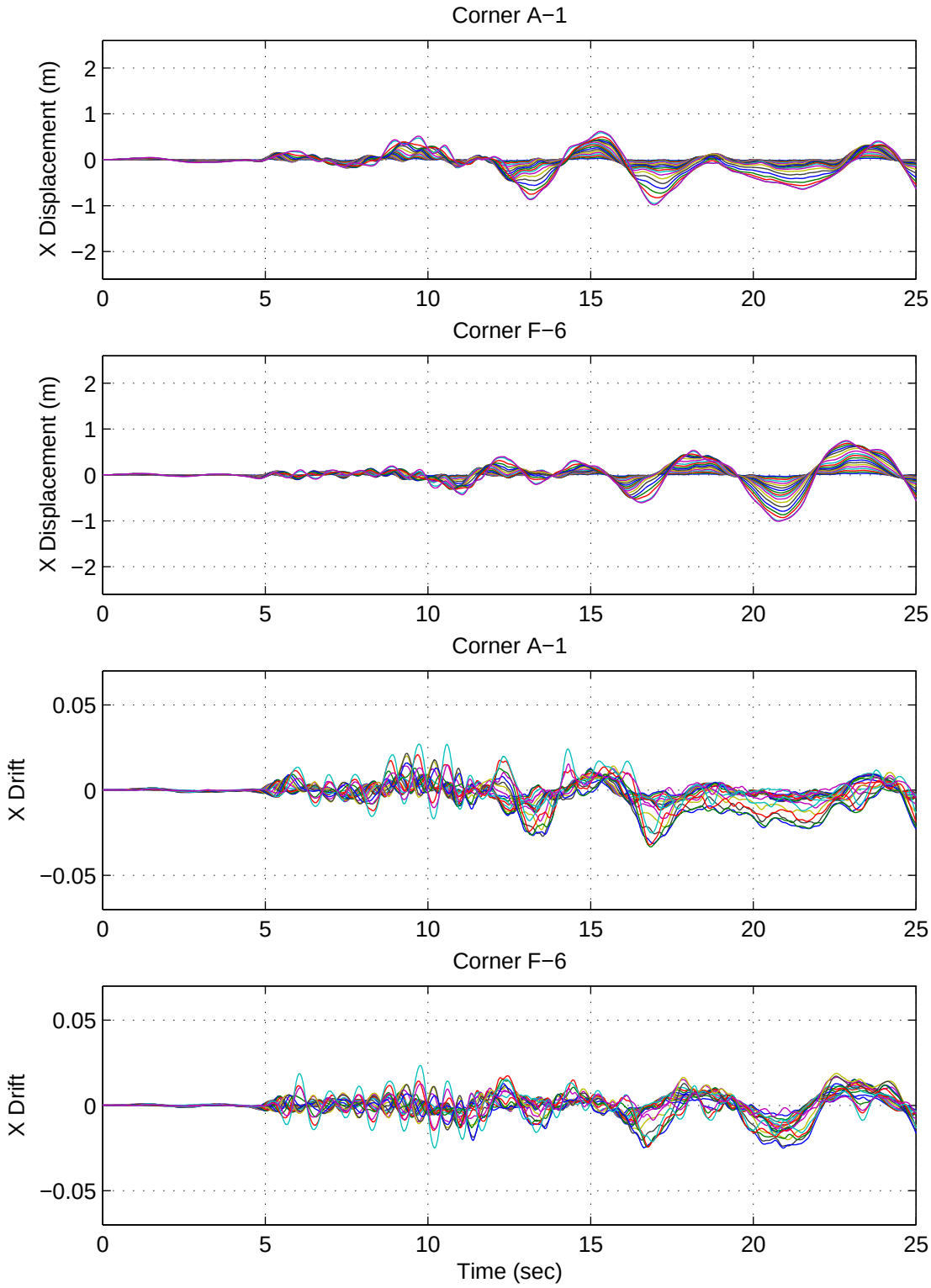

Figure F.55: Building 4 X-Direction Displacements & Drifts: Iran Earthquake (Tabas Record Strong Component in Y Direction)

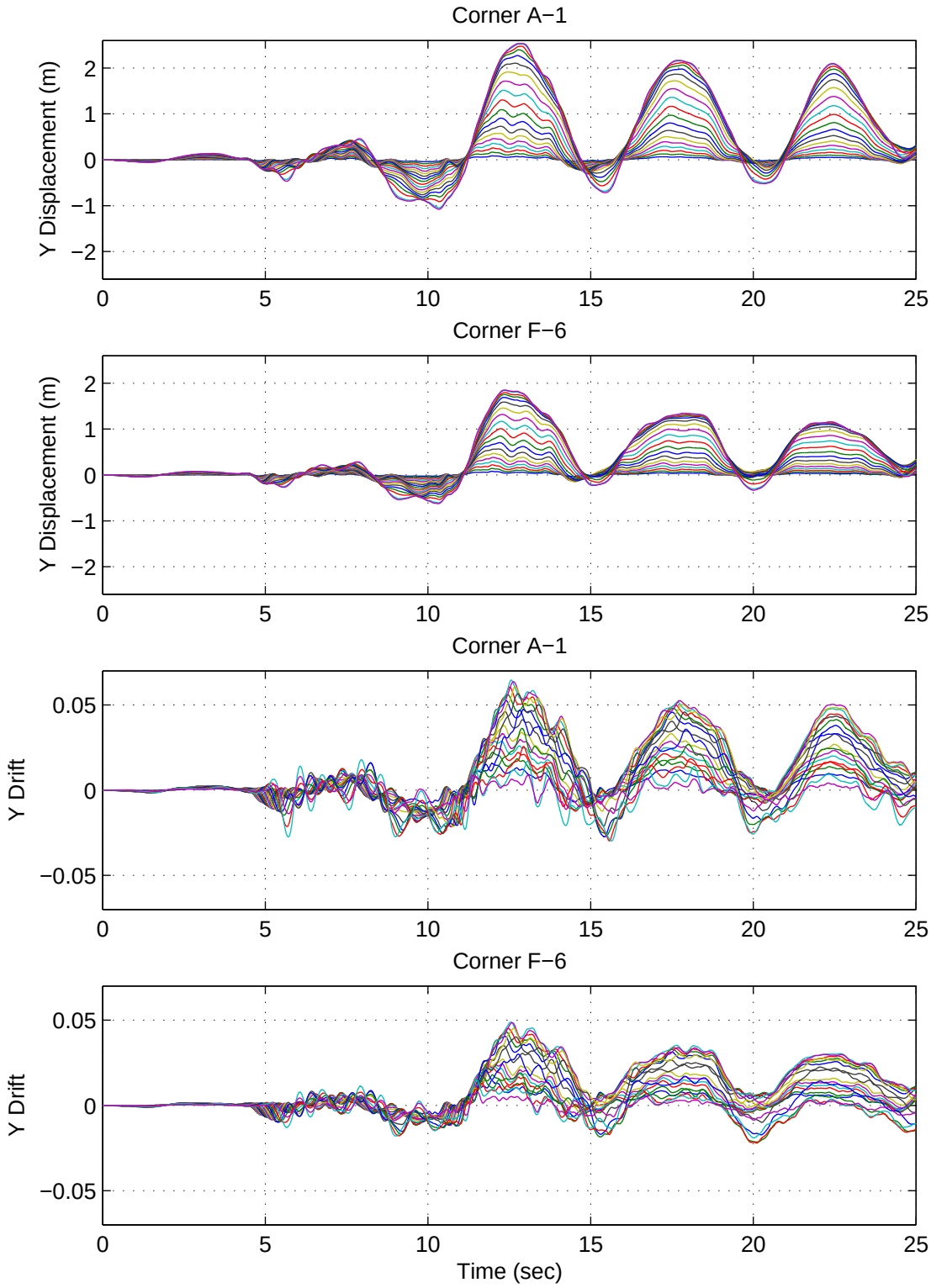

Figure F.56: Building 4 Y-Direction Displacements & Drifts: Iran Earthquake (Tabas Record Strong Component in Y Direction)

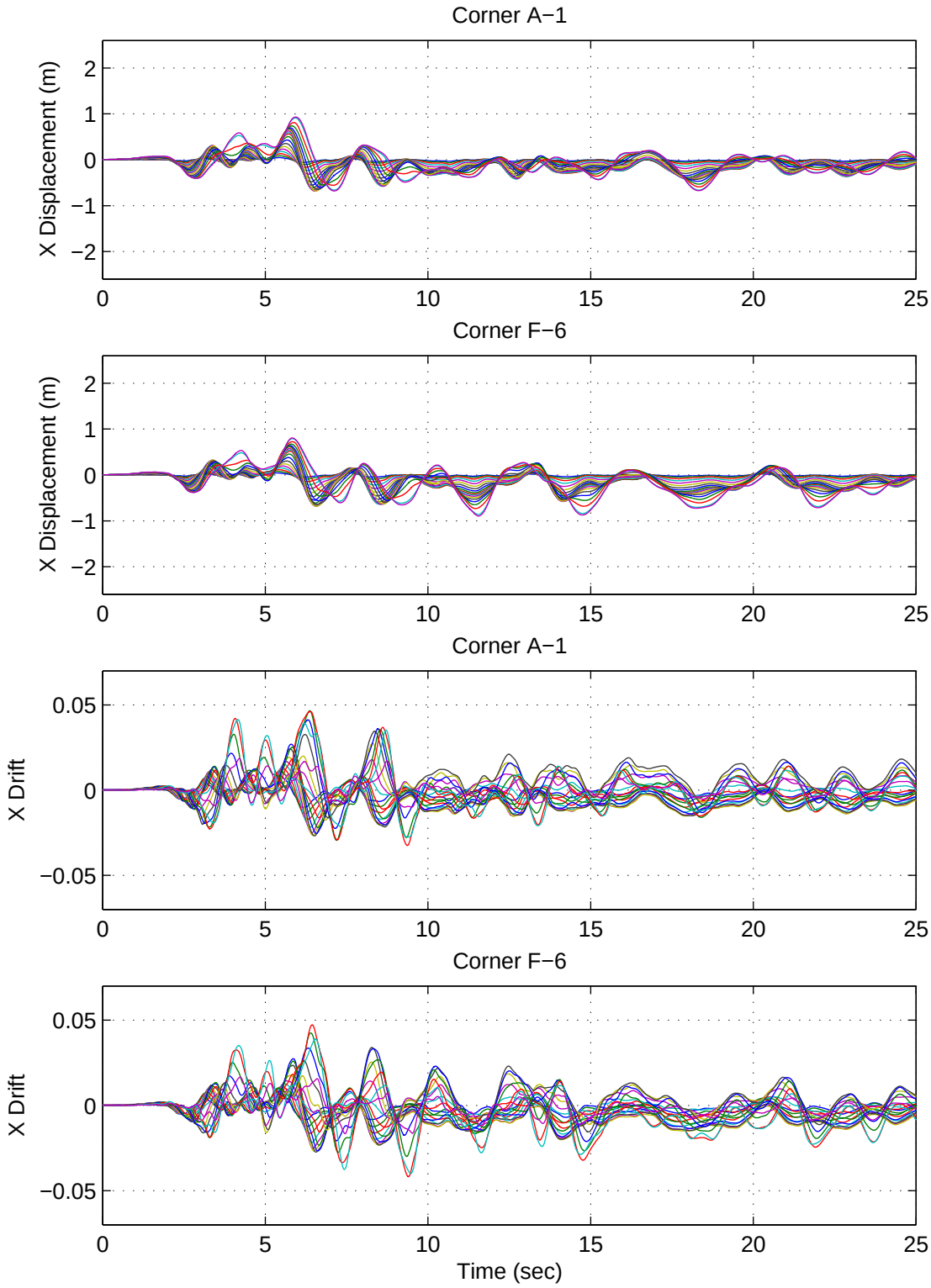

Figure F.57: Building 4 X-Direction Displacements & Drifts: Kobe Earthquake (Takatori Record Strong Component in X Direction)

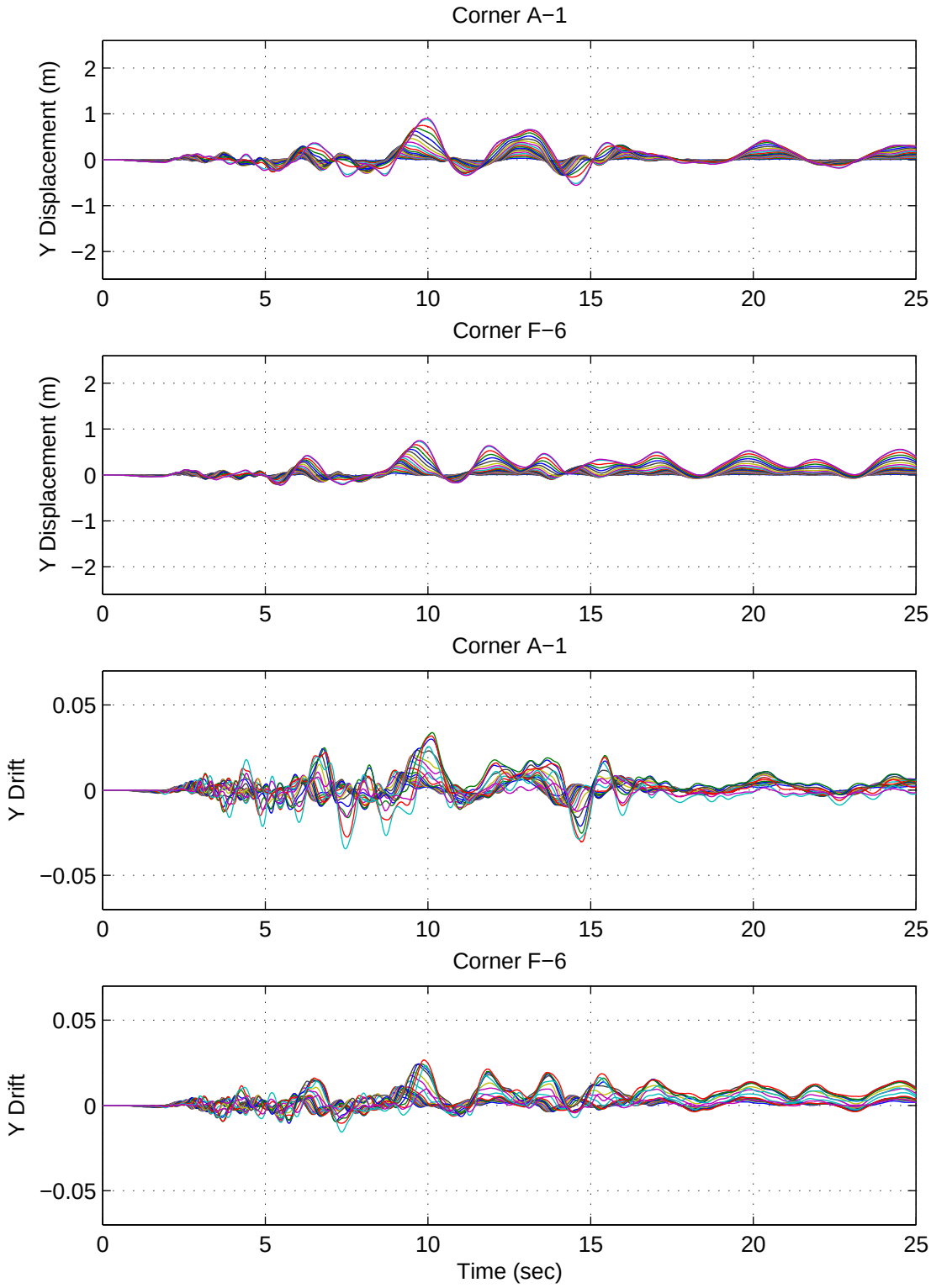

Figure F.58: Building 4 Y-Direction Displacements & Drifts: Kobe Earthquake (Takatori Record Strong Component in X Direction)

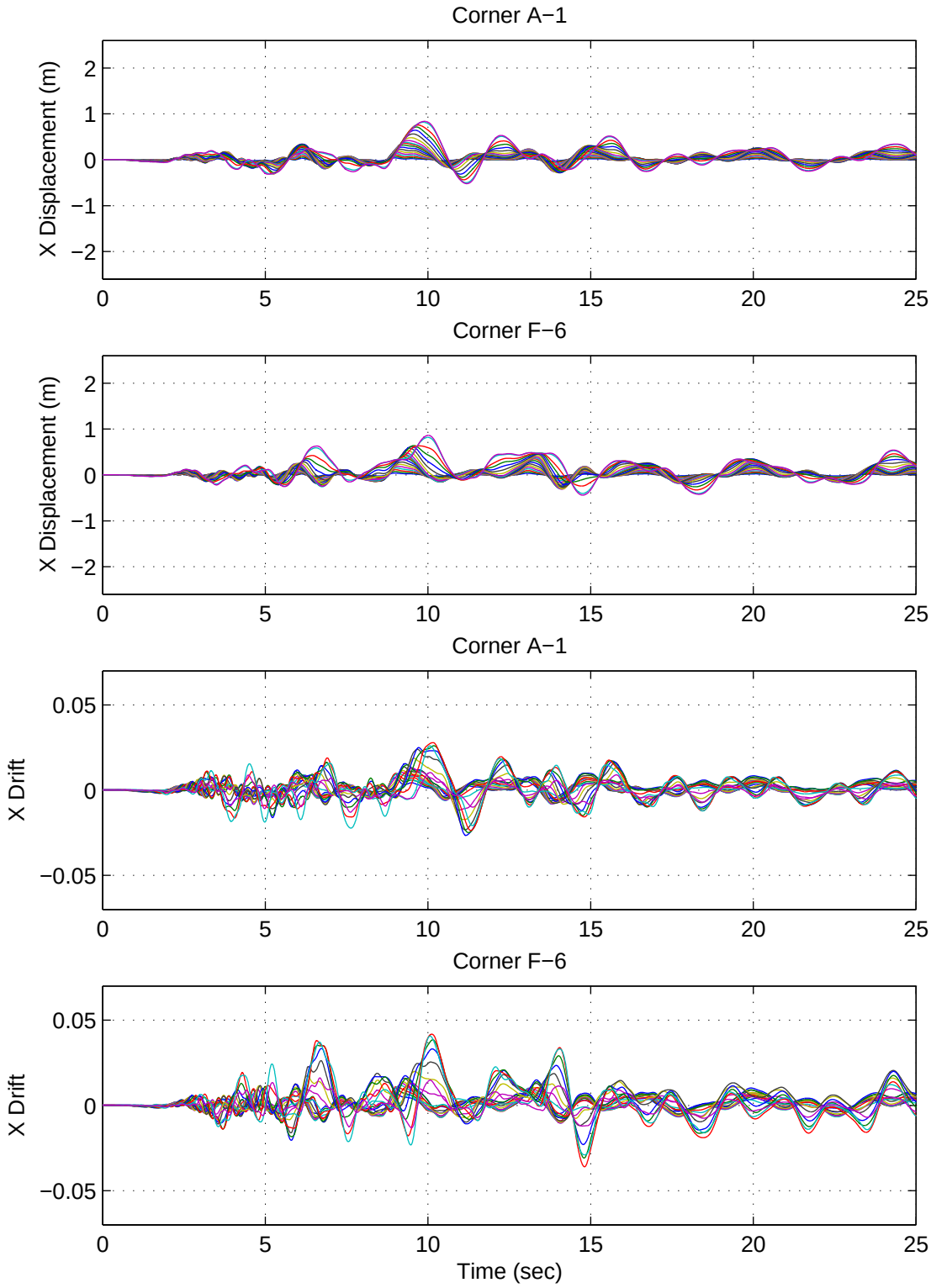

Figure F.59: Building 4 X-Direction Displacements & Drifts: Kobe Earthquake (Takatori Record Strong Component in Y Direction)

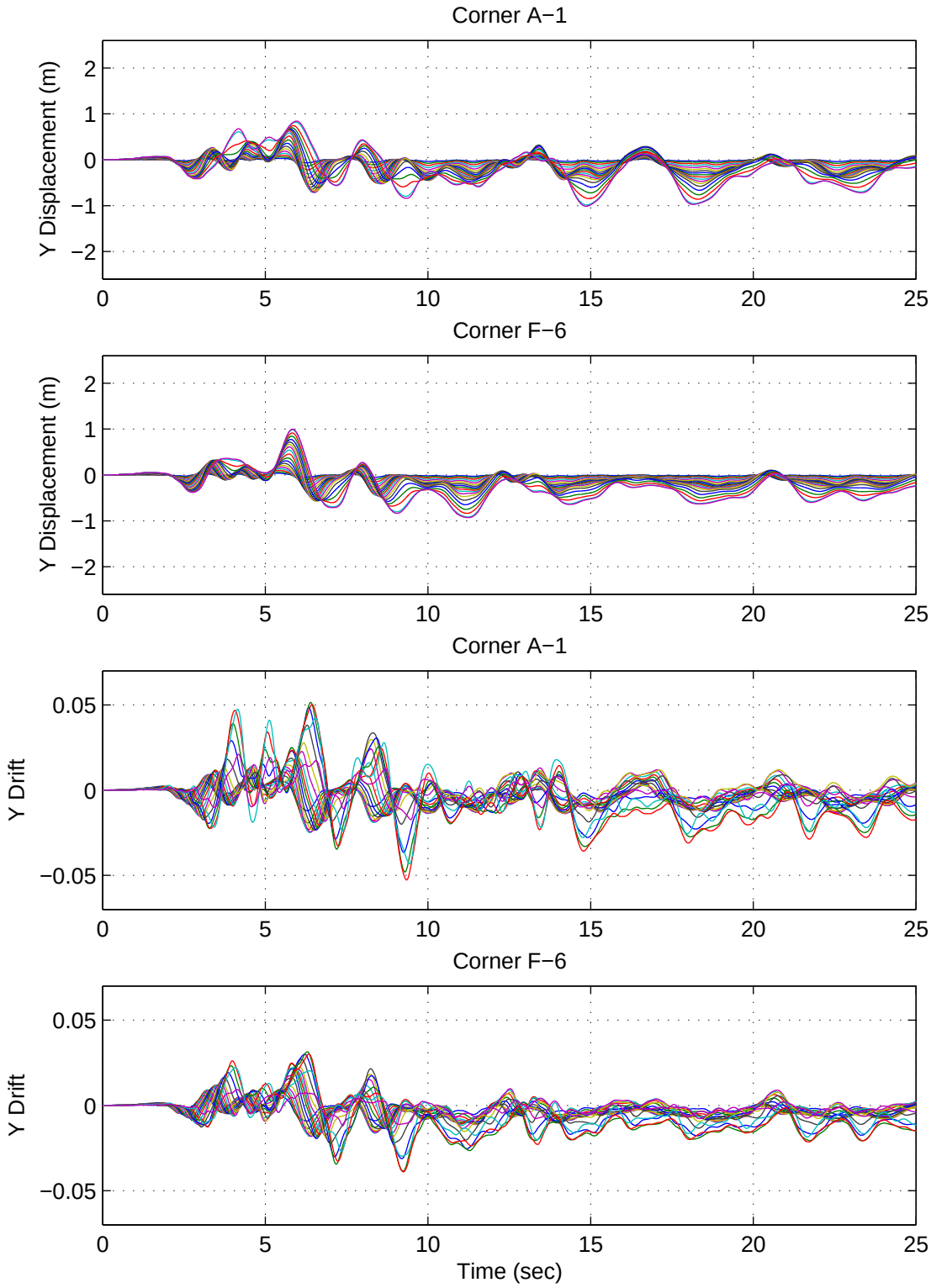

Figure F.60: Building 4 Y-Direction Displacements & Drifts: Kobe Earthquake (Takatori Record Strong Component in Y Direction)

Appendix G Ground Motion Analysis of Buildings: Bar Diagrams of Peak Drifts

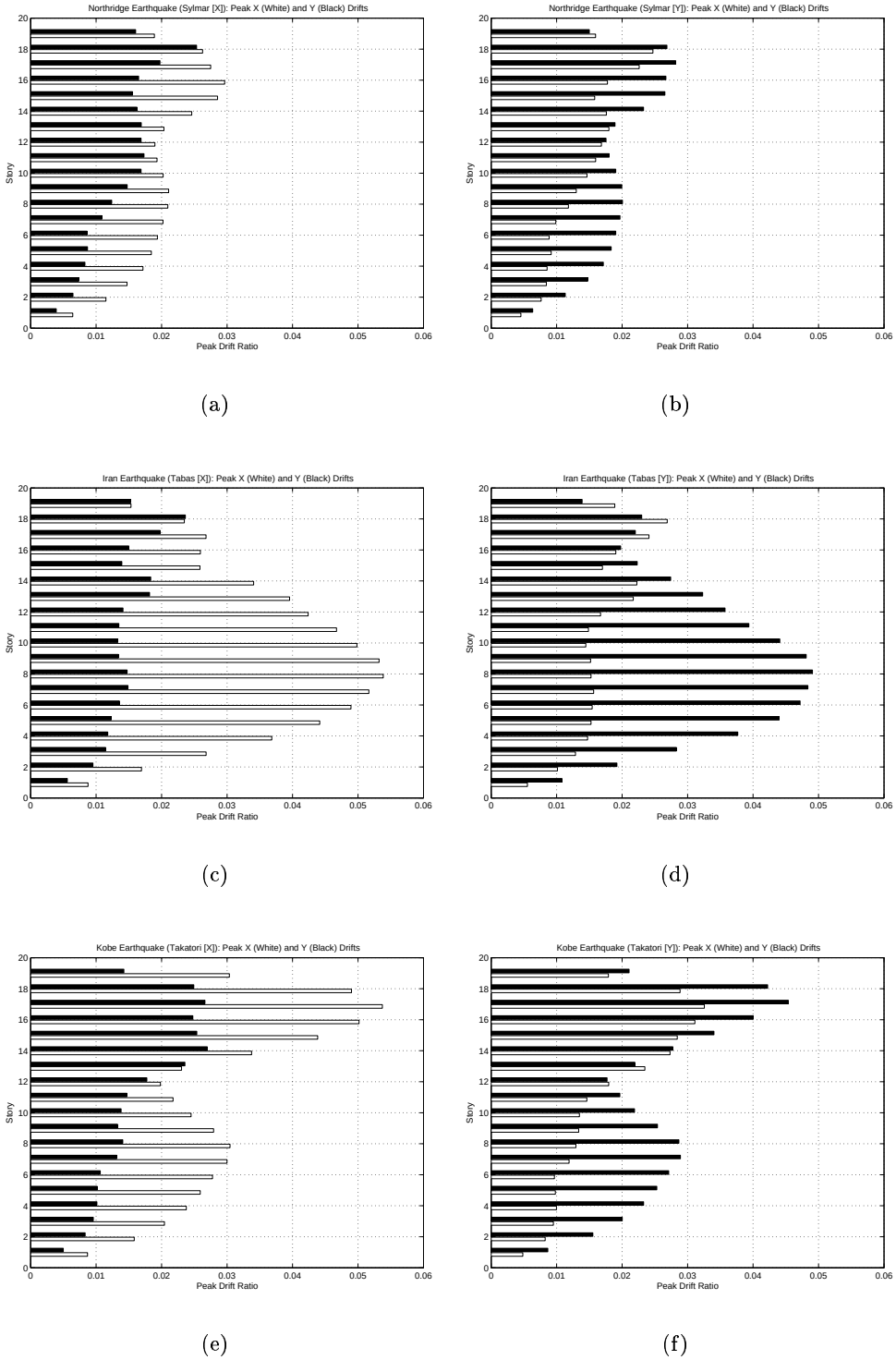

Figure G.1: Building 1 Peak Drifts During the Northridge, Iran and Kobe Earthquakes ([X] and [Y] indicate strong component in X and Y directions, respectively)

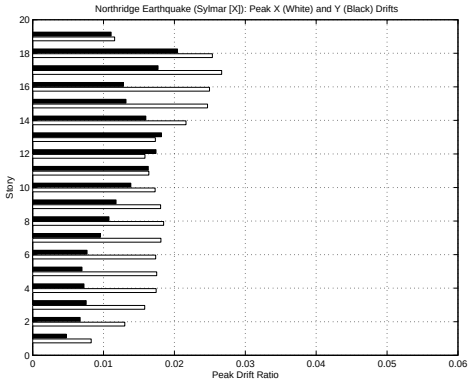

(a)

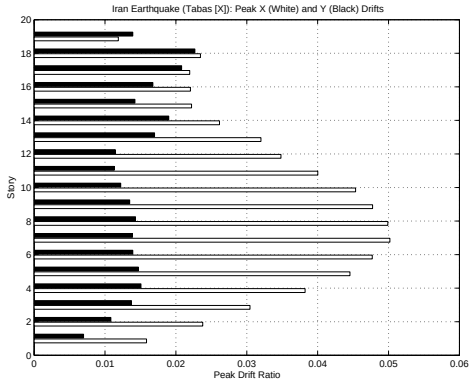

(b)

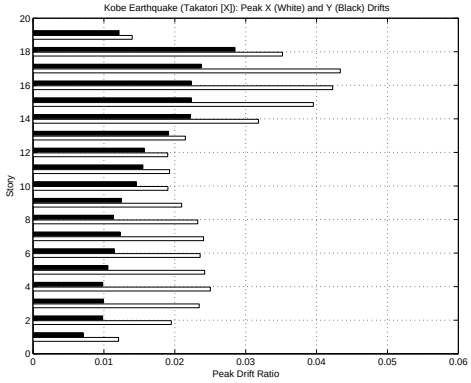

(c)

Figure G.2: Building 2 Peak Drifts During the Northridge, Iran and Kobe Earthquakes ([X] indicates strong component in X direction)

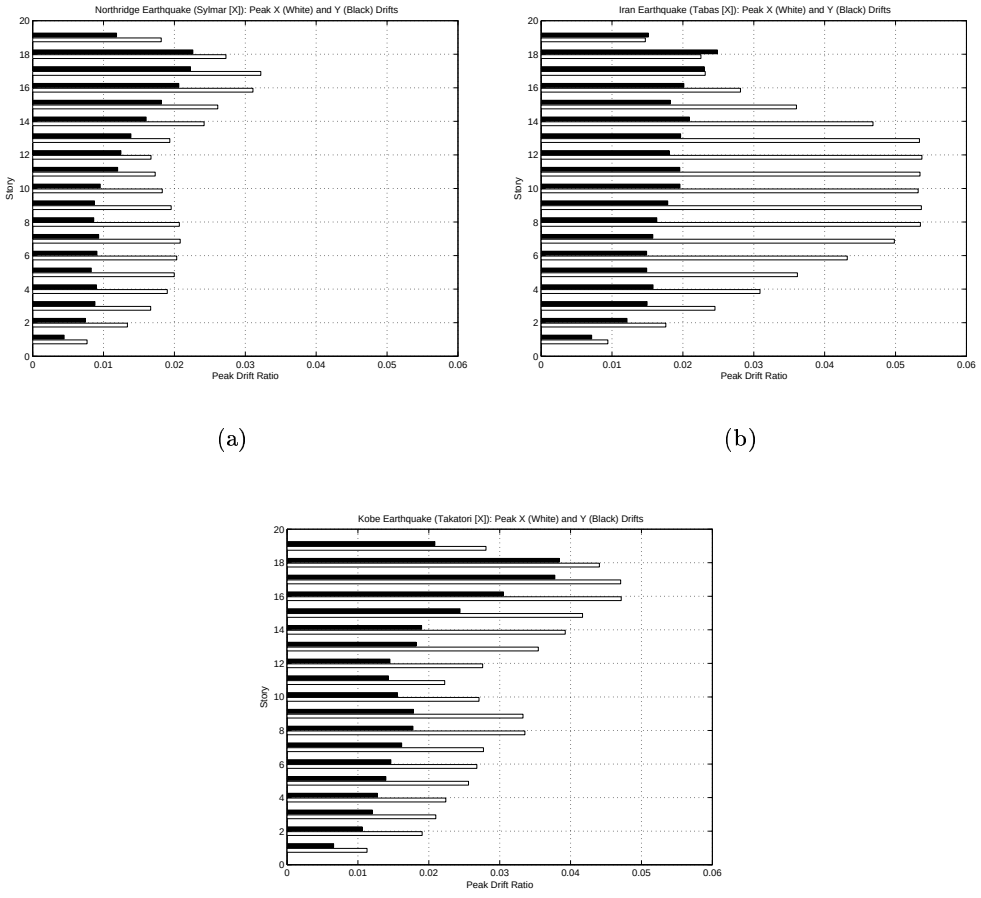

Figure G.3: Building 2A Peak Drifts During the Northridge, Iran and Kobe Earthquakes ([X] indicates strong component in X direction)

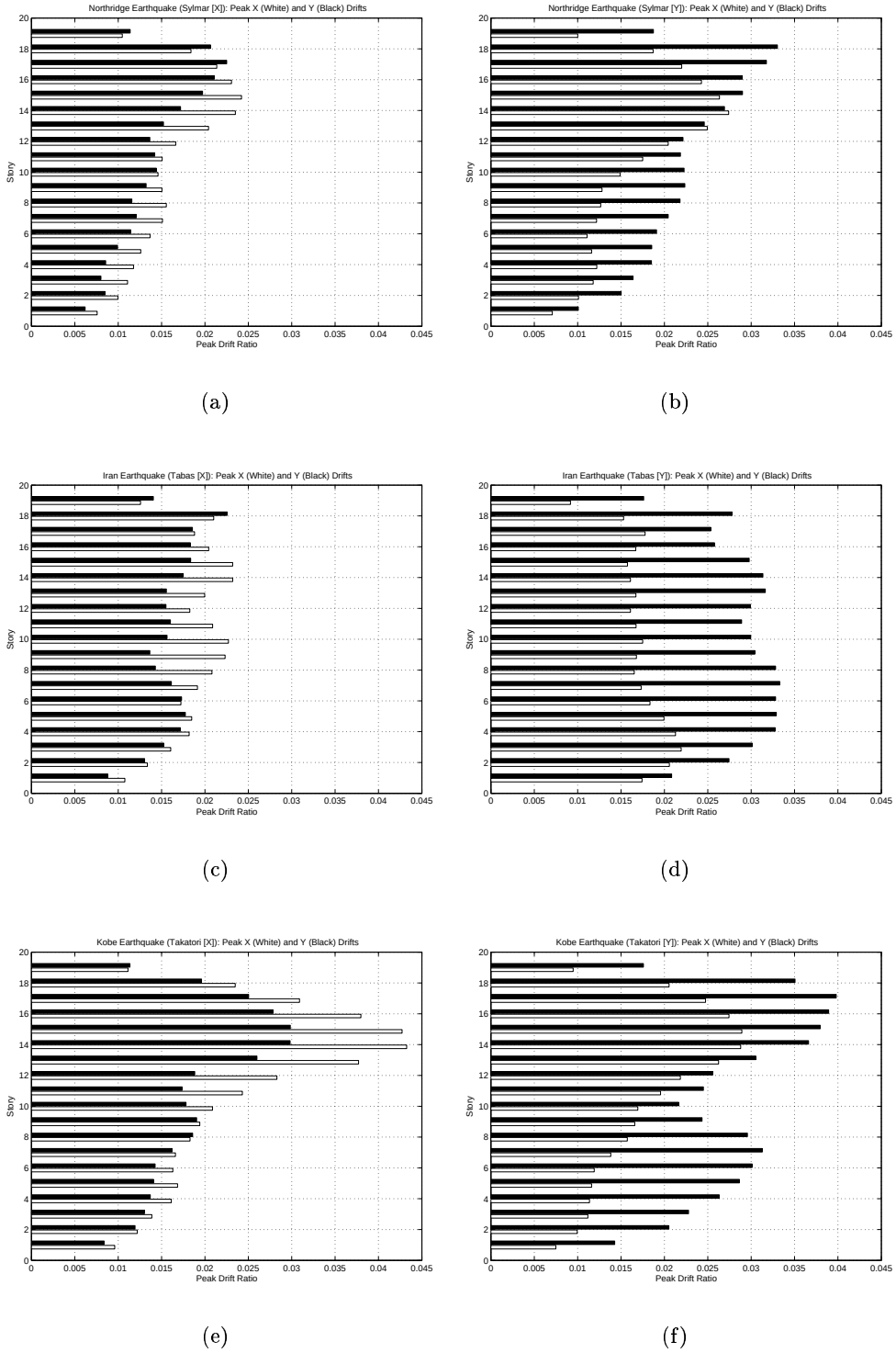

Figure G.4: Building 3 Peak Drifts During the Northridge, Iran and Kobe Earthquakes ([X] and [Y] indicate strong component in X and Y directions, respectively)

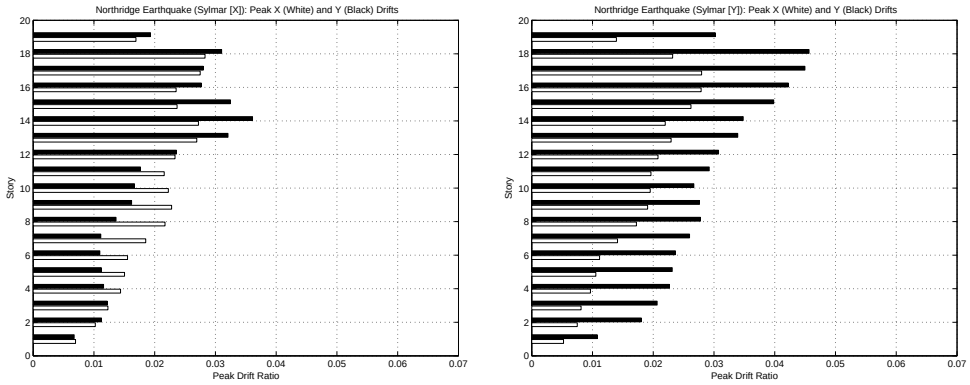

(a)

(b)

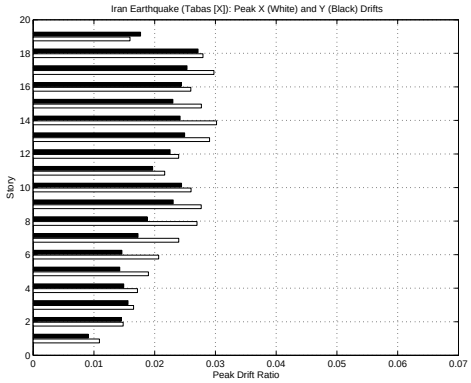

(c)

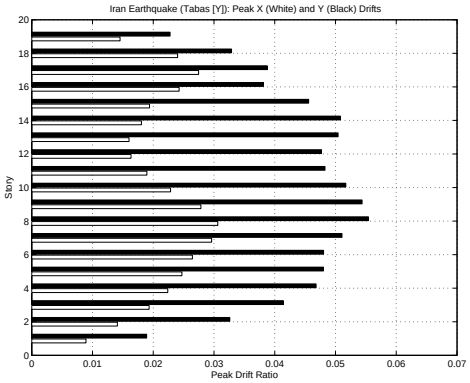

(d)

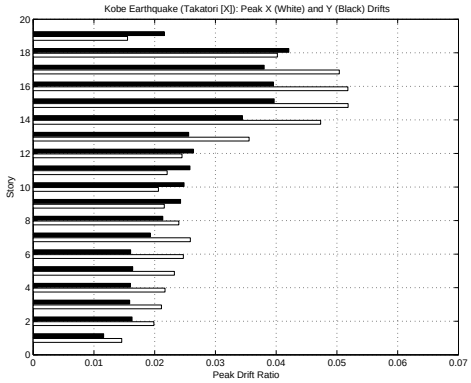

(e)

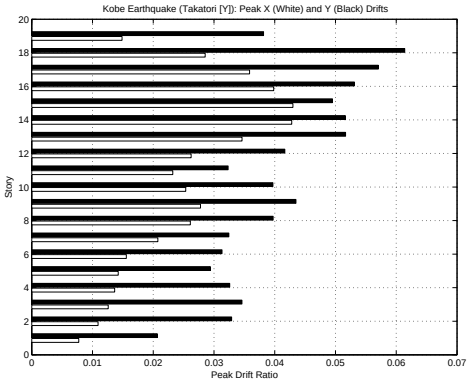

(f)

Figure G.5: Building 3A Peak Drifts During the Northridge, Iran and Kobe Earthquakes ([X] and [Y] indicate strong component in X and Y directions, respectively)

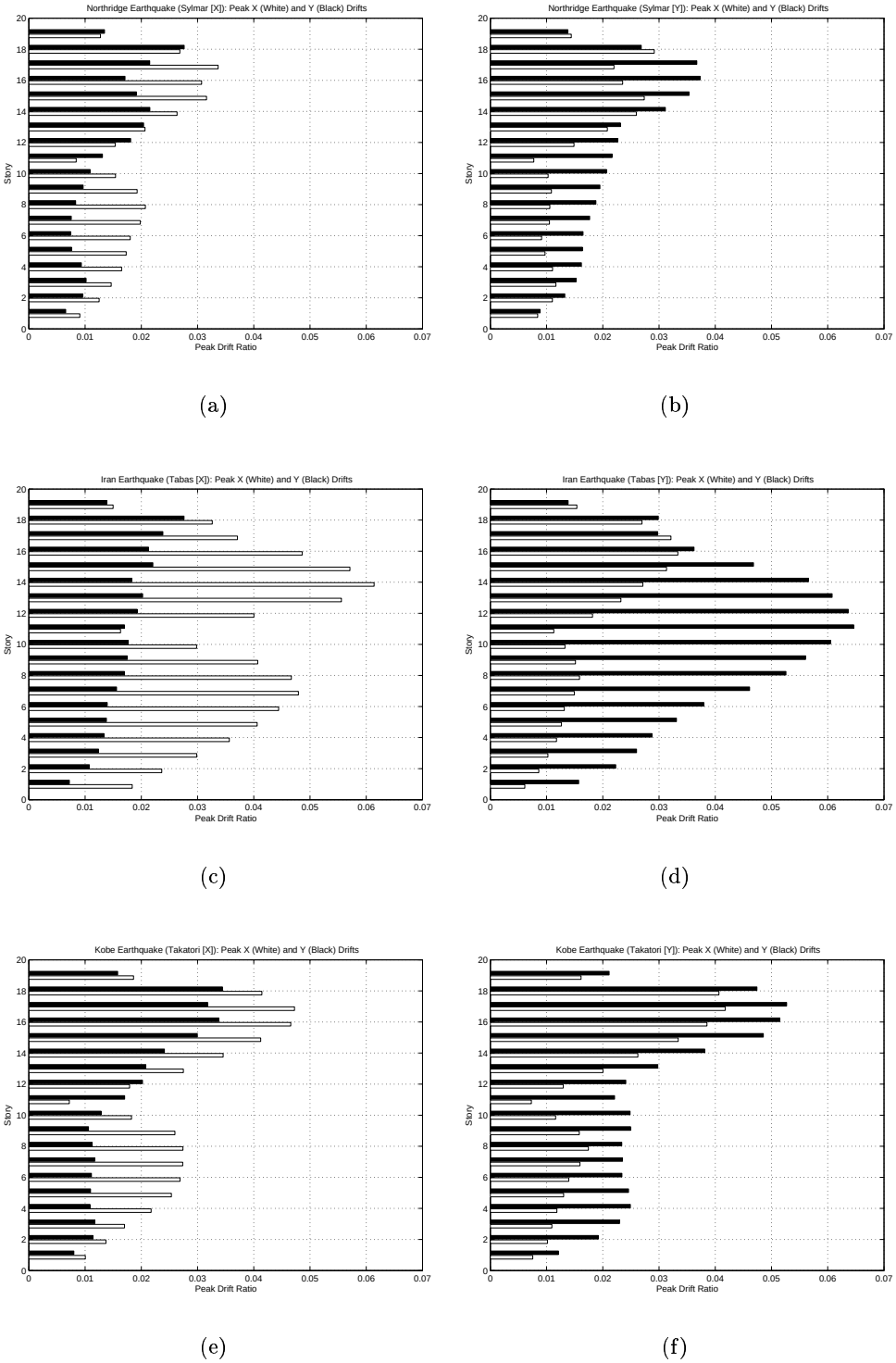

Figure G.6: Building 4 Peak Drifts During the Northridge, Iran and Kobe Earthquakes ([X] and [Y] indicate strong component in X and Y directions, respectively)

Appendix H Ground Motion Analysis of Buildings: Maps and Summary of Plastic Deformation in Beam-Columns and Joints

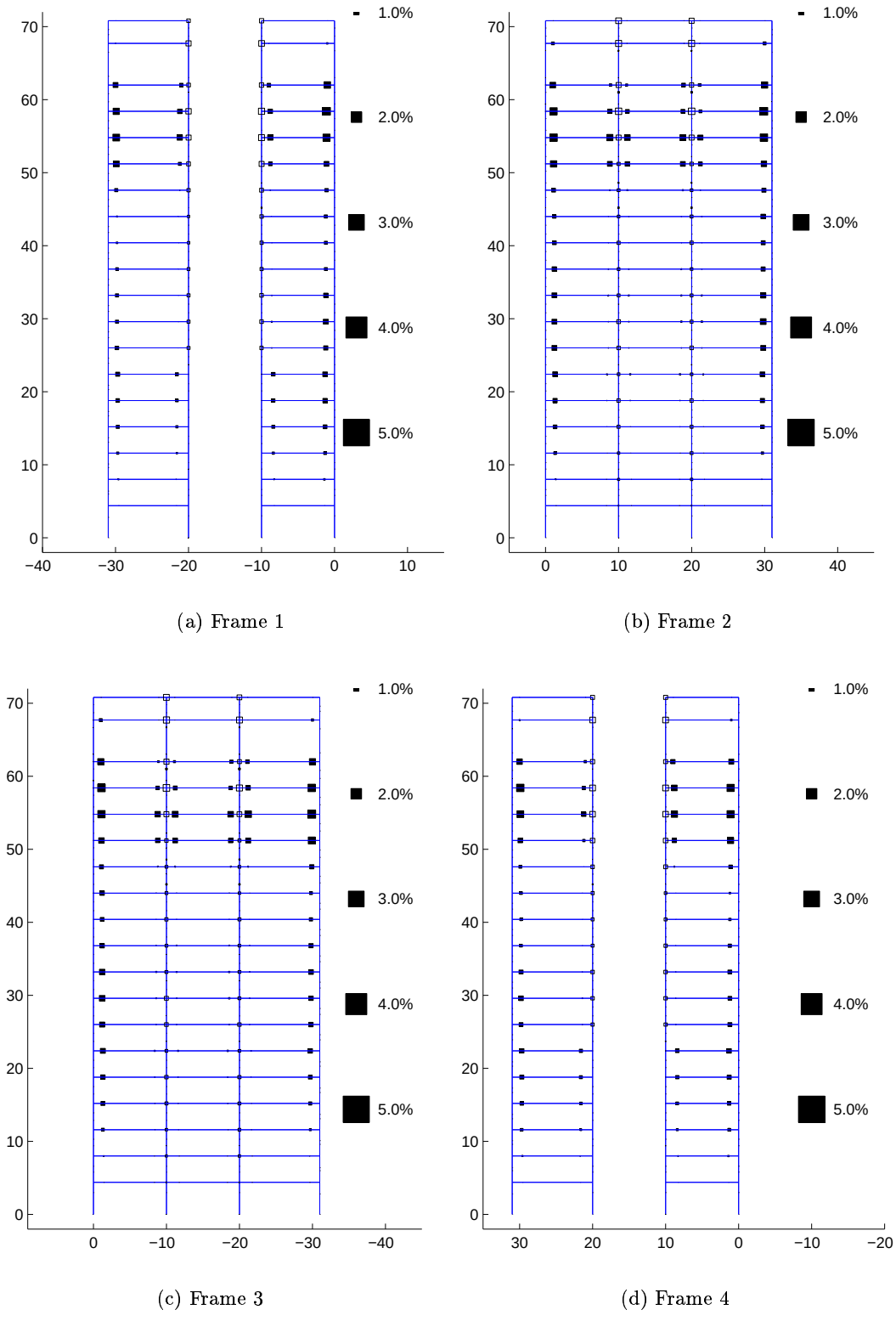

(a) Frame 1

(b) Frame 2

(c) Frame 3

(d) Frame 4

Figure H.1: Plastic Rotations (Black:Beam-Columns White:Panel Zones) in Building 1 Frames 1-4: Northridge Earthquake (Sylmar Record Strong Component in X Direction)

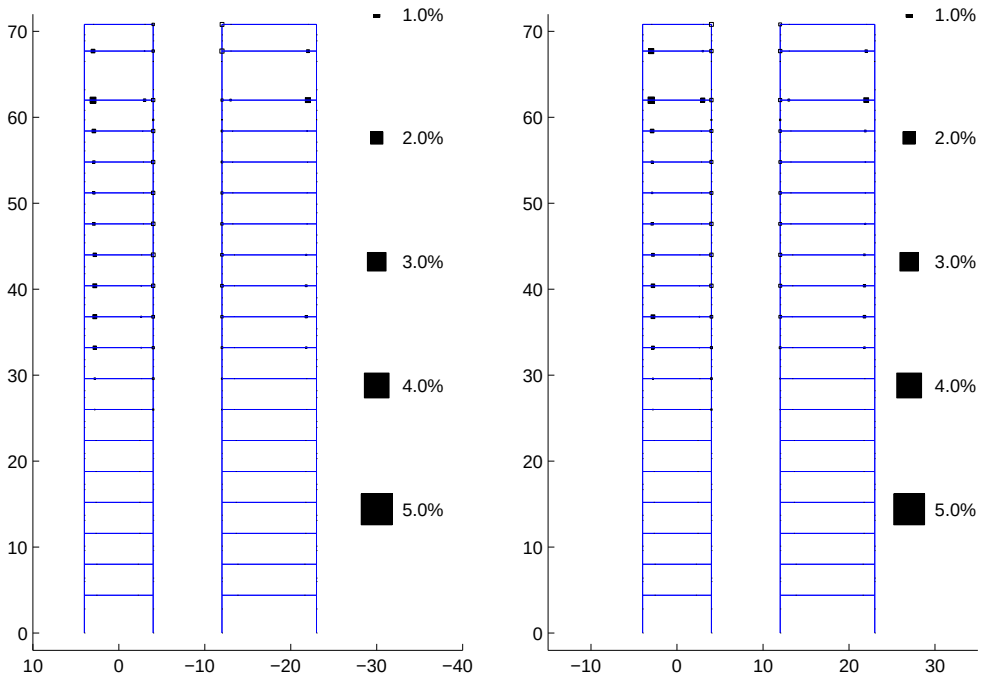

(a) Frame 5

(b) Frame 7

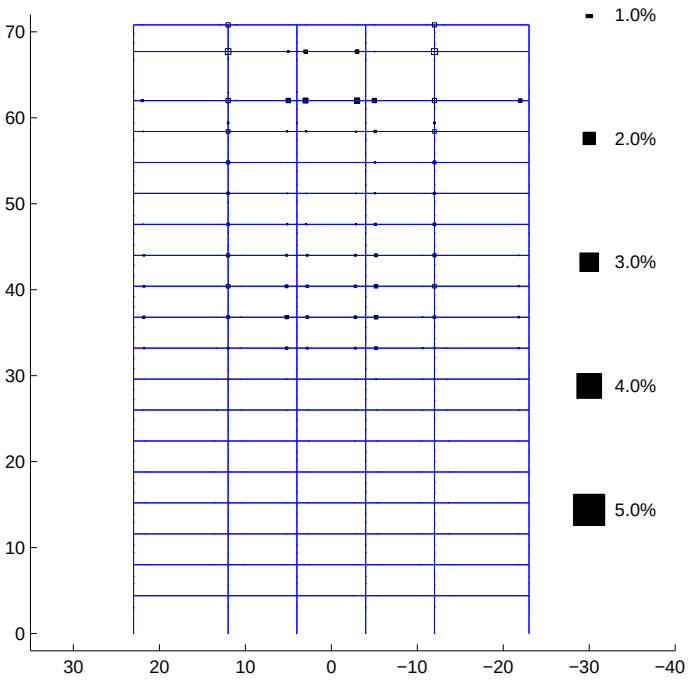

(c) Frame 6

Figure H.2: Plastic Rotations (Black:Beam-Columns White:Panel Zones) in Building 1 Frames 5-7: Northridge Earthquake (Sylmar Record Strong Component in X Direction)

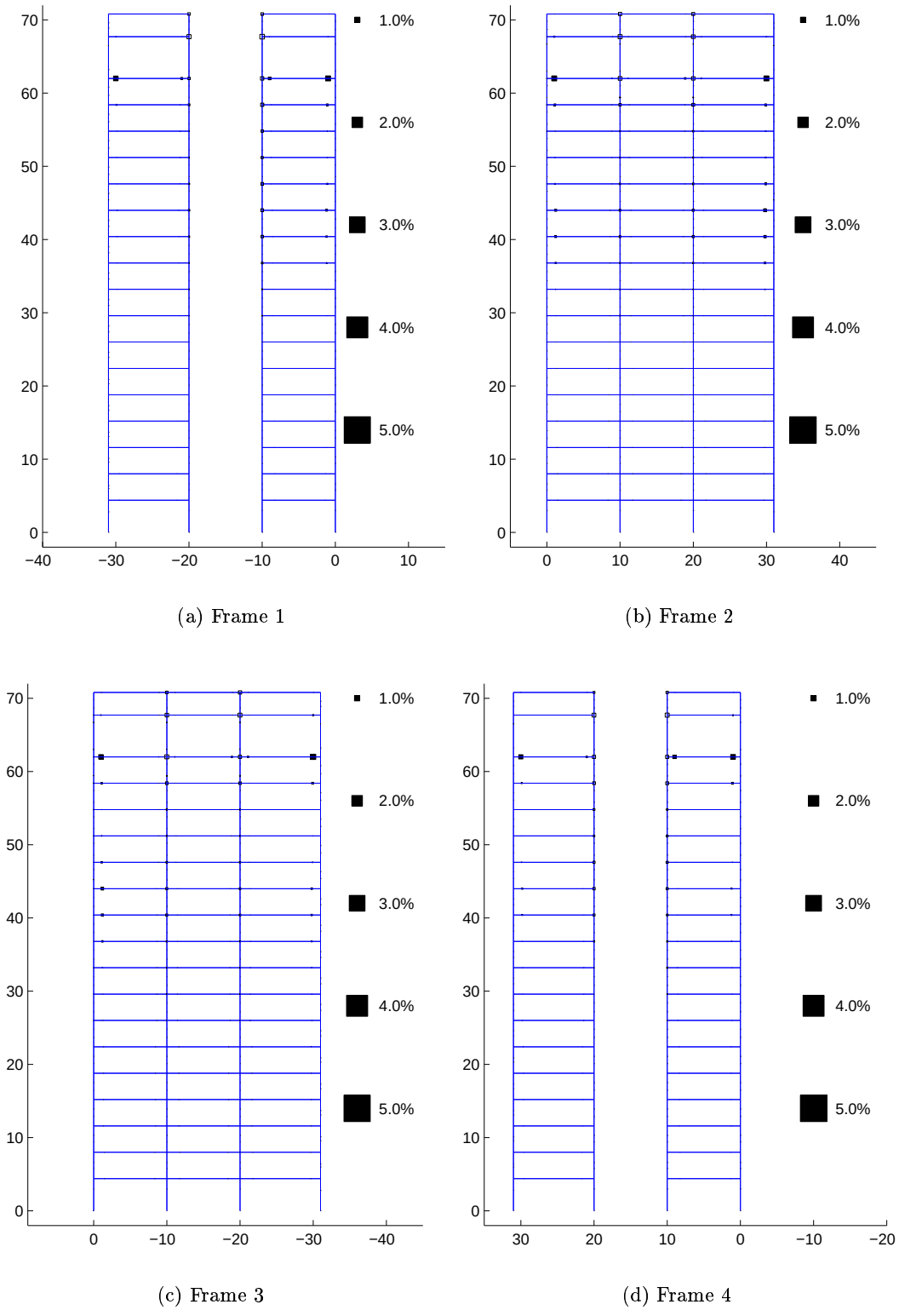

(a) Frame 1

(b) Frame 2

(c) Frame 3

(d) Frame 4

Figure H.3: Plastic Rotations (Black:Beam-Columns White:Panel Zones) in Building 1 Frames 1-4: Northridge Earthquake (Sylmar Record Strong Component in Y Direction)

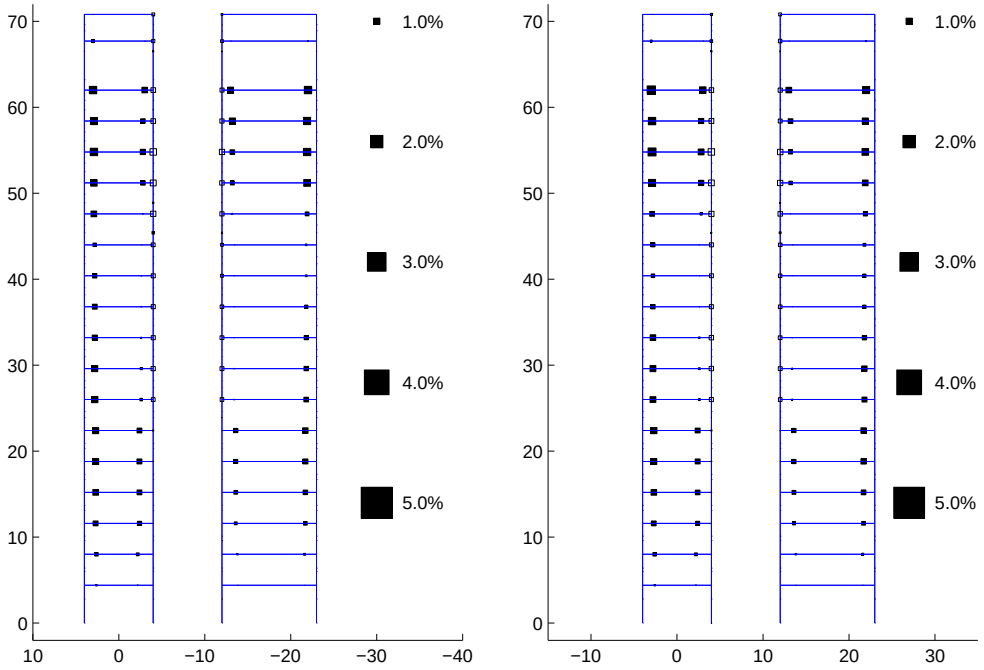

(a) Frame 5

(b) Frame 7

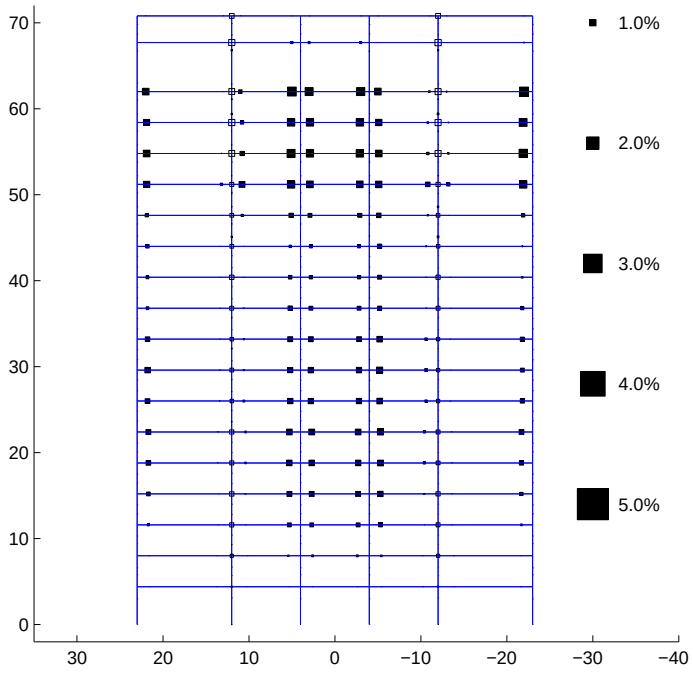

(c) Frame 6

Figure H.4: Plastic Rotations (Black:Beam-Columns White:Panel Zones) in Building 1 Frames 5-7: Northridge Earthquake (Sylmar Record Strong Component in Y Direction)

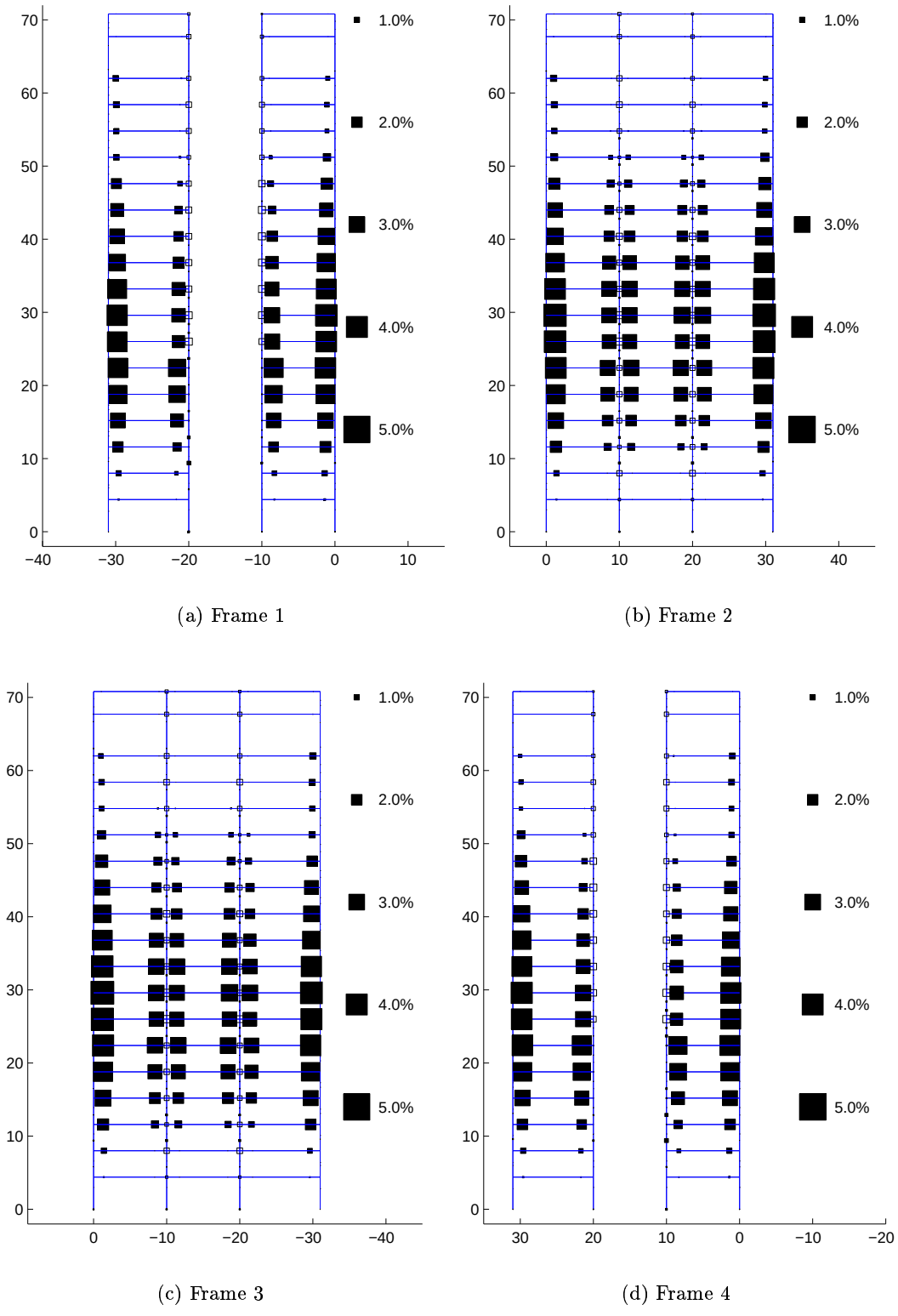

(a) Frame 1

(b) Frame 2

(c) Frame 3

(d) Frame 4

Figure H.5: Plastic Rotations (Black:Beam-Columns White:Panel Zones) in Building 1 Frames 1-4: Iran Earthquake (Tabas Record Strong Component in X Direction)

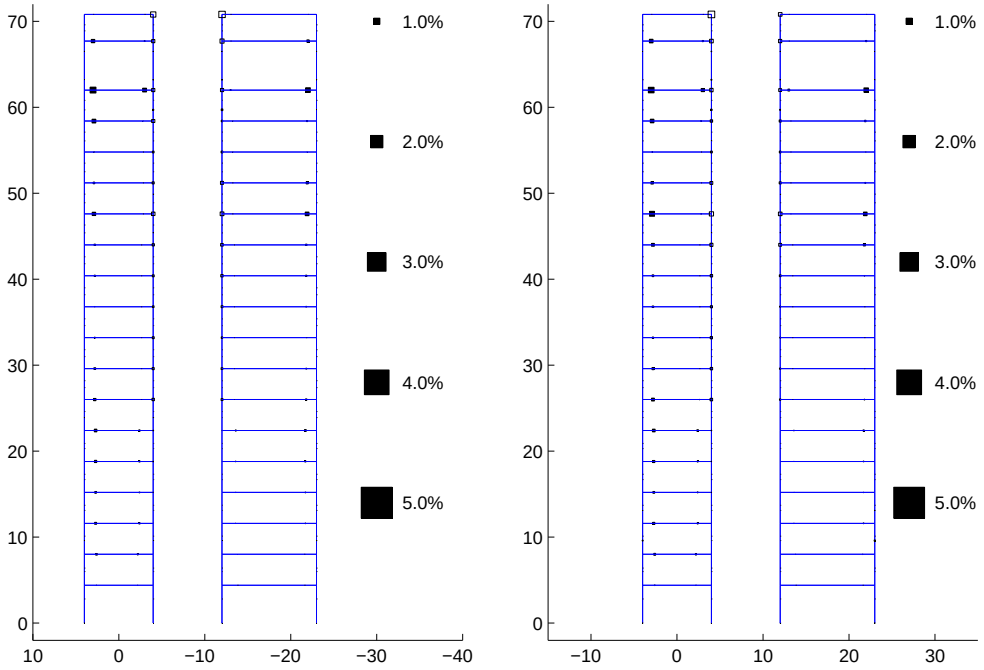

(a) Frame 5

(b) Frame 7

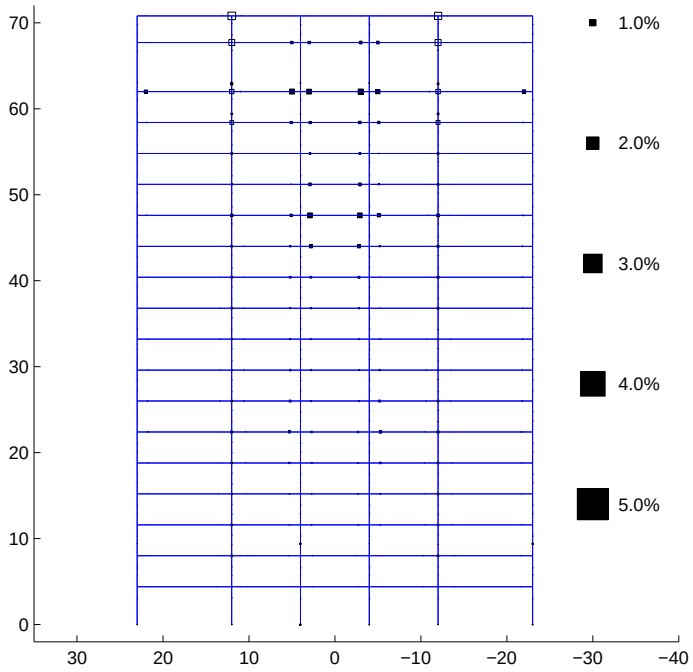

(c) Frame 6

Figure H.6: Plastic Rotations (Black:Beam-Columns White:Panel Zones) in Building 1 Frames 5-7: Iran Earthquake (Tabas Record Strong Component in X Direction)

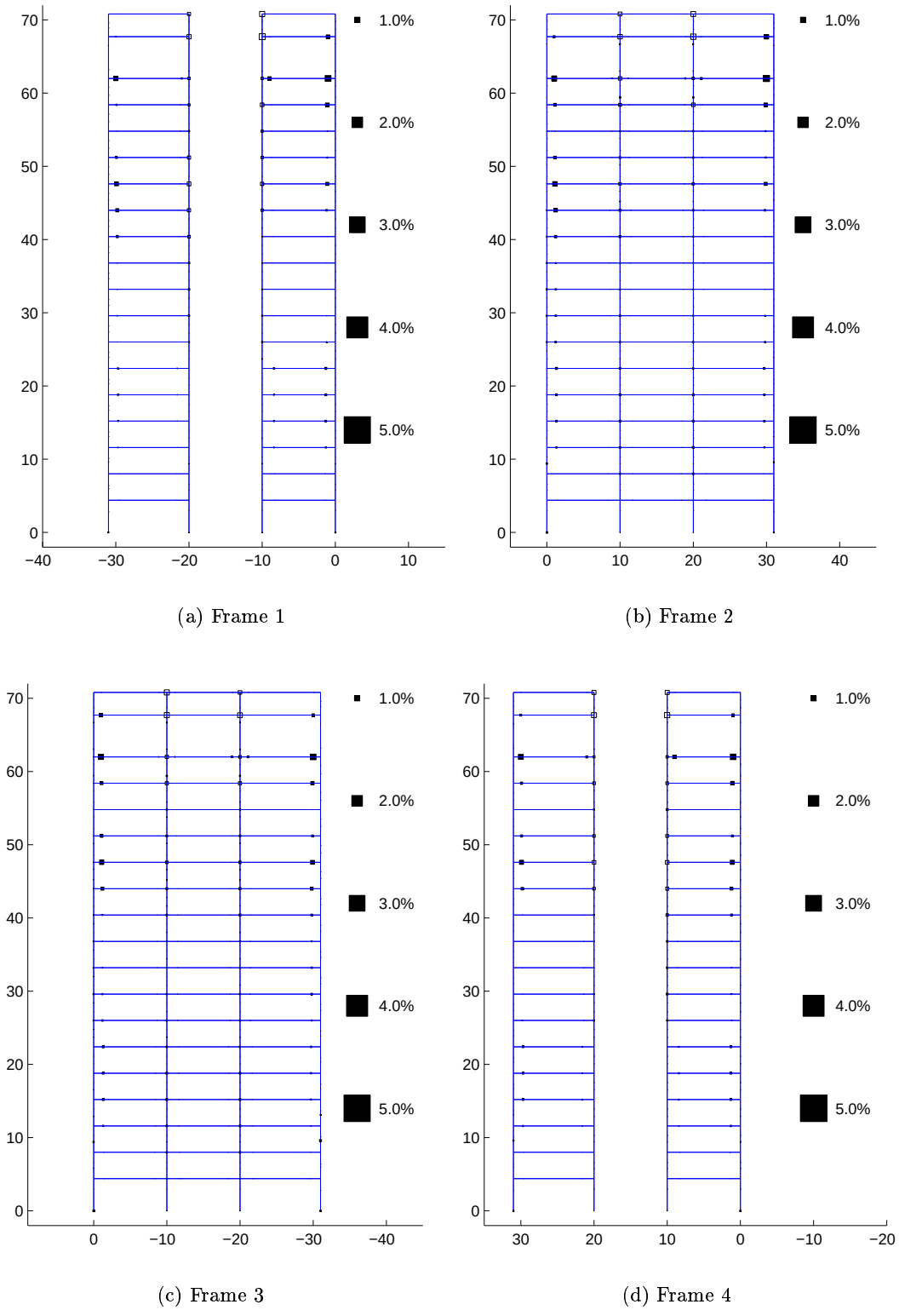

(a) Frame 1

(b) Frame 2

(c) Frame 3

(d) Frame 4

Figure H.7: Plastic Rotations (Black:Beam-Columns White:Panel Zones) in Building 1 Frames 1-4: Iran Earthquake (Tabas Record Strong Component in Y Direction)

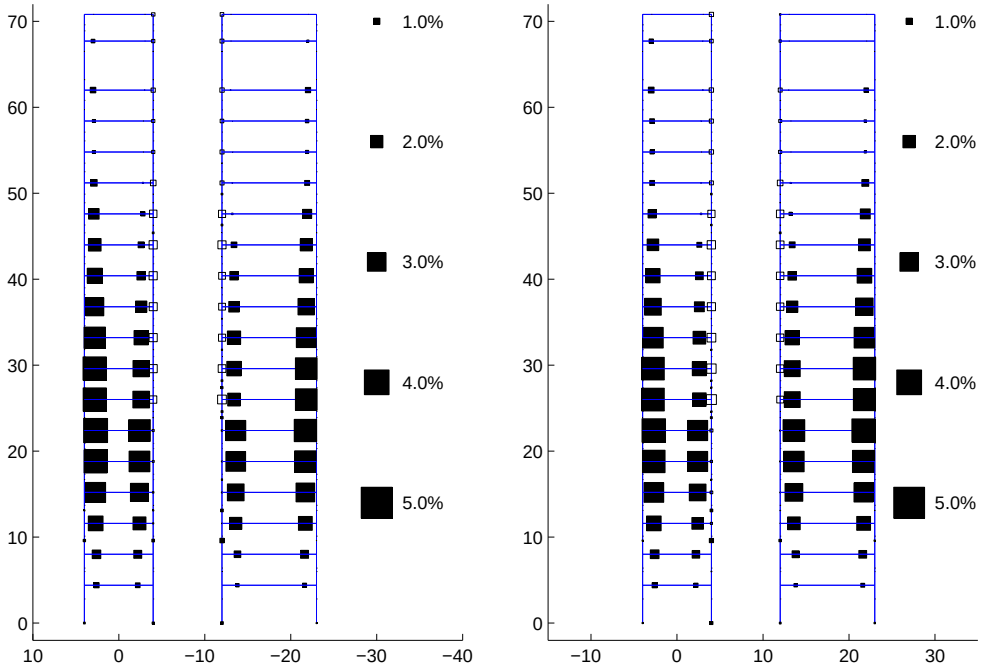

(a) Frame 5

(b) Frame 7

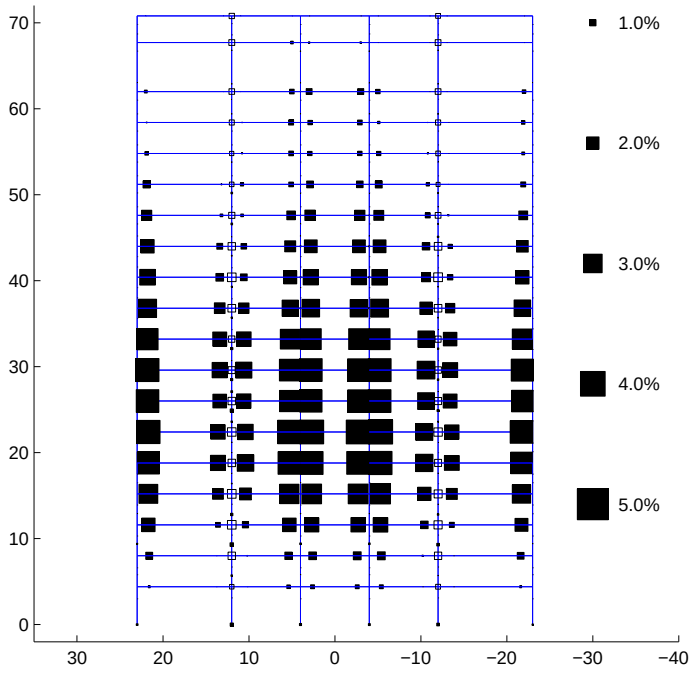

(c) Frame 6

Figure H.8: Plastic Rotations (Black:Beam-Columns White:Panel Zones) in Building 1 Frames 5-7: Iran Earthquake (Tabas Record Strong Component in Y Direction)

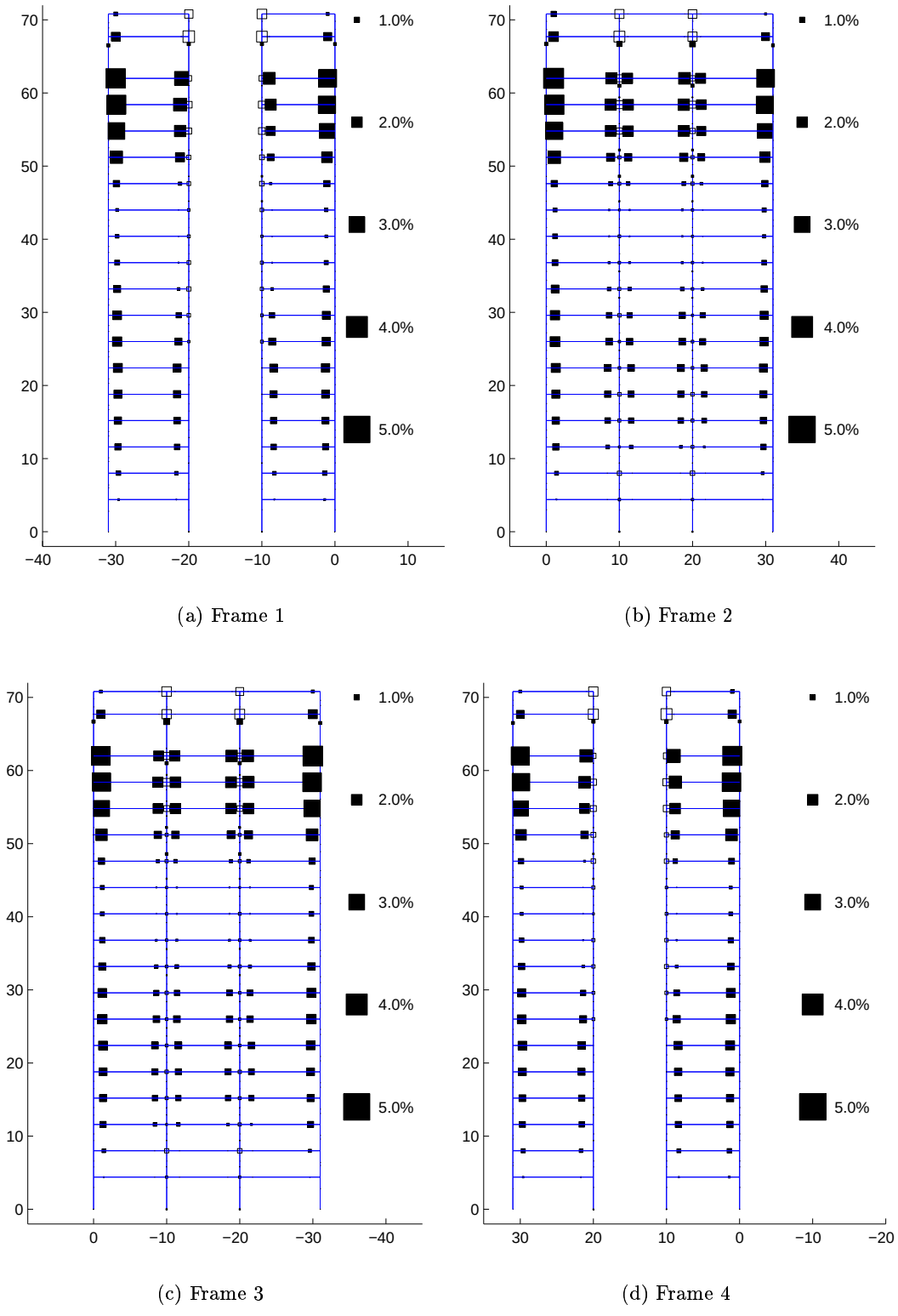

(a) Frame 1

(b) Frame 2

(c) Frame 3

(d) Frame 4

Figure H.9: Plastic Rotations (Black:Beam-Columns White:Panel Zones) in Building 1 Frames 1-4: Kobe Earthquake (Takatori Record Strong Component in X Direction)

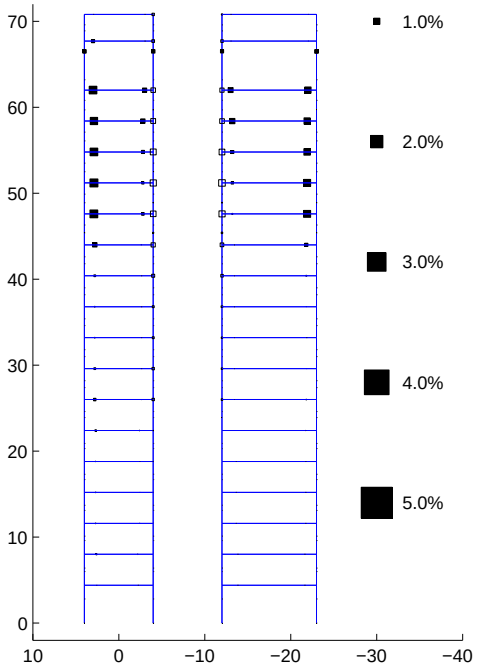

(a) Frame 5

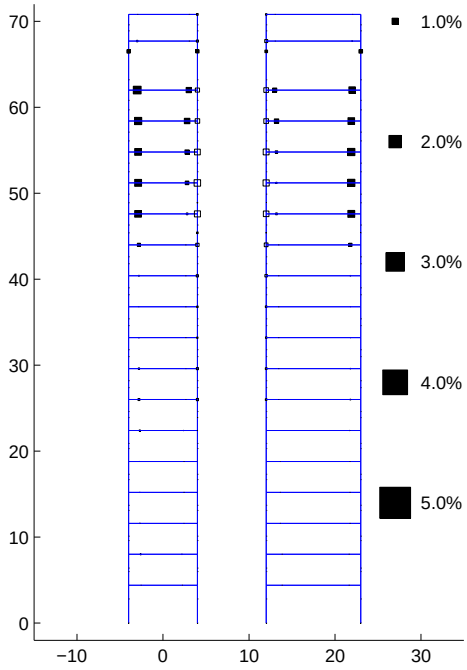

(b) Frame 7

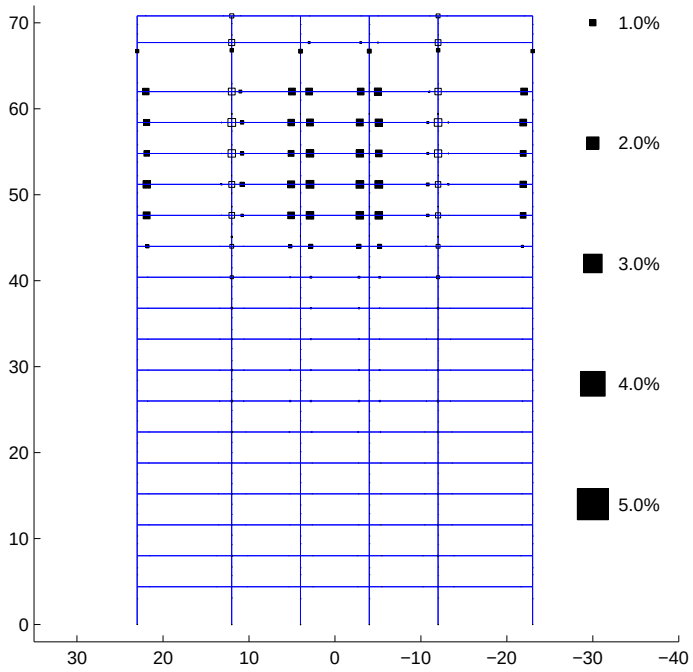

(c) Frame 6

Figure H.10: Plastic Rotations (Black:Beam-Columns White:Panel Zones) in Building 1 Frames 5-7: Kobe Earthquake (Takatori Record Strong Component in X Direction)

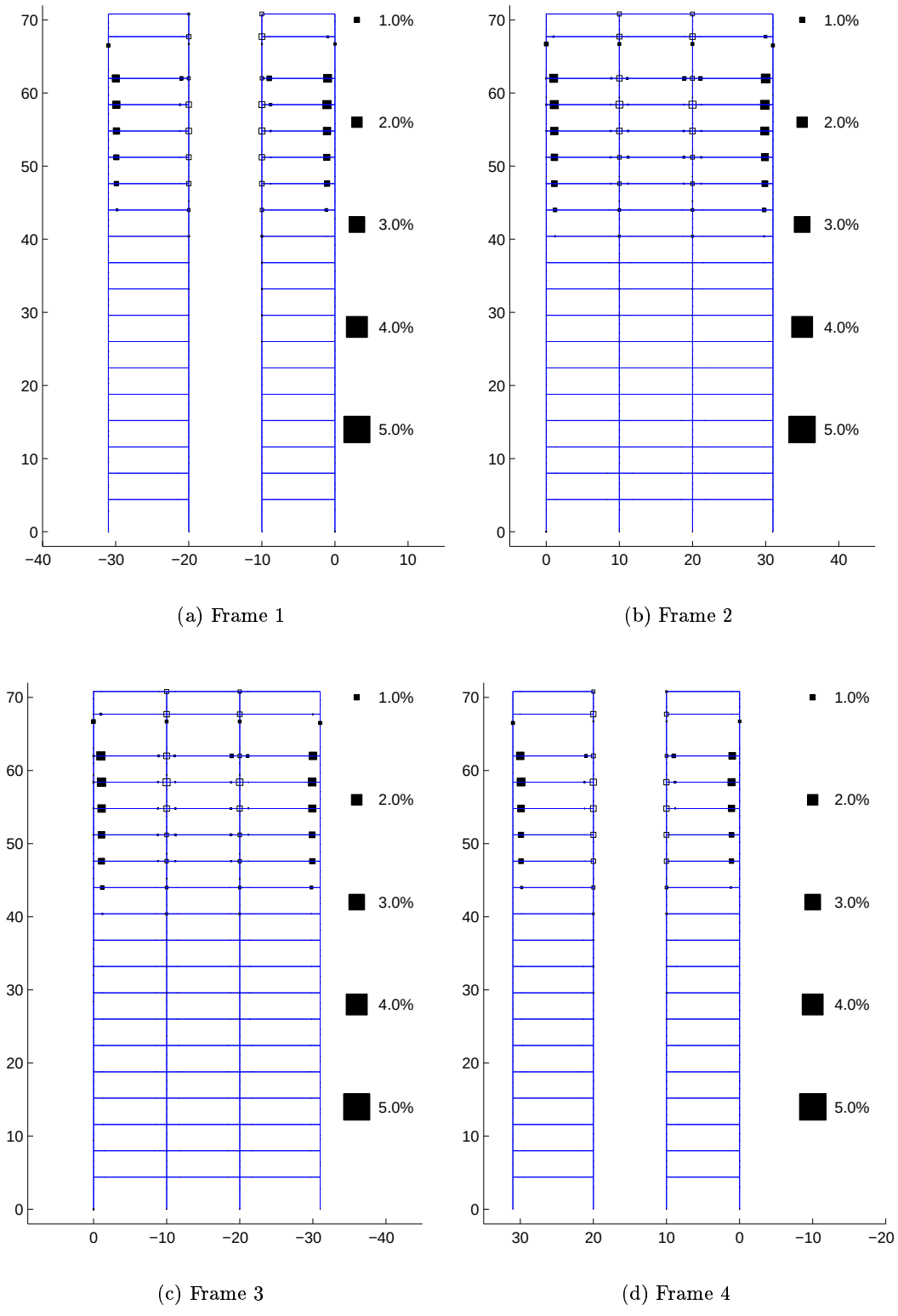

(a) Frame 1

(b) Frame 2

(c) Frame 3

(d) Frame 4

Figure H.11: Plastic Rotations (Black:Beam-Columns White:Panel Zones) in Building 1 Frames 1-4: Kobe Earthquake (Takatori Record Strong Component in Y Direction)

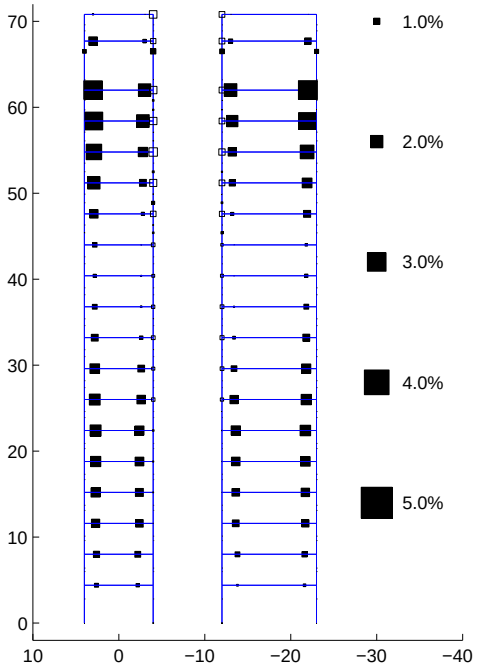

(a) Frame 5

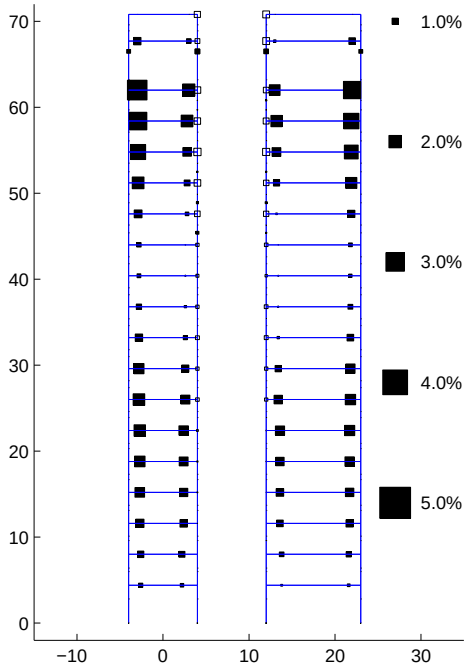

(b) Frame 7

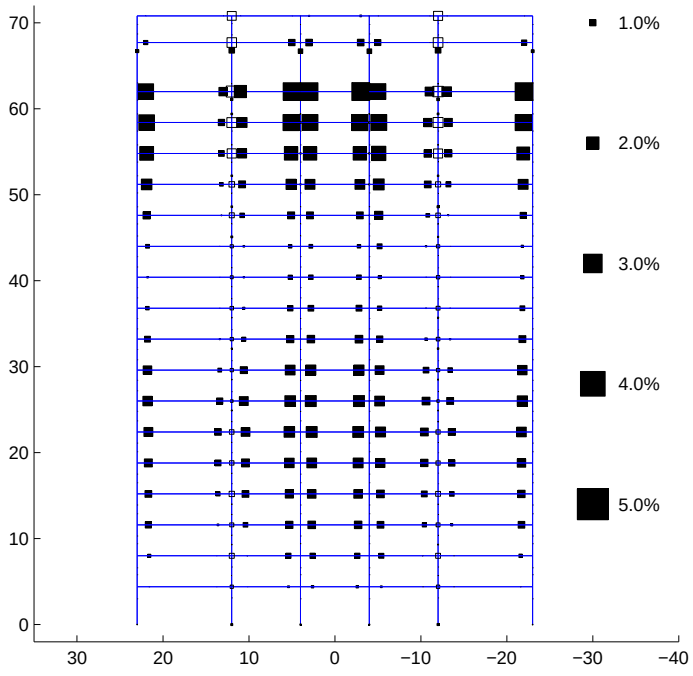

(c) Frame 6

Figure H.12: Plastic Rotations (Black:Beam-Columns White:Panel Zones) in Building 1 Frames 5-7: Kobe Earthquake (Takatori Record Strong Component in Y Direction)

Table H.1: Building 1 Moment Frame Beam Plastic Rotations (Major Axis Bending)

Ground Motion	**Moment Frame Beam Plastic Rotations (Major Axis Bending)**						
	$\leqslant$ 0.1%	**(0.1-1]%**	**(1-2]%**	**(2-3]%**	**(3-4]%**	**(4-5]%**	**(5-6]%**
Northridge Sylmar $[X]^*$	368	313	41	0	0	0	0
Northridge Sylmar $[Y]^{**}$	411	273	38	0	0	0	0
Iran Tabas $[X]^*$	289	194	70	104	52	13	0
Iran Tabas $[Y]^{**}$	308	211	61	75	67	0	0
Kobe Takatori $[X]^*$	260	203	207	31	21	0	0
Kobe Takatori $[Y]^{**}$	311	189	190	30	2	0	0

** Strong component in building X direction*
*** Strong component in building Y direction*

Table H.2: Building 1 Moment Frame Beam Plastic Rotations (Minor Axis Bending)

Ground Motion	**Moment Frame Beam Plastic Rotations (Minor Axis Bending)**						
	$\leqslant$ 0.1%	**(0.1-1]%**	**(1-2]%**	**(2-3]%**	**(3-4]%**	**(4-5]%**	**(5-6]%**
Northridge Sylmar $[X]^*$	689	33	0	0	0	0	0
Northridge Sylmar $[Y]^{**}$	703	19	0	0	0	0	0
Iran Tabas $[X]^*$	671	51	0	0	0	0	0
Iran Tabas $[Y]^{**}$	684	38	0	0	0	0	0
Kobe Takatori $[X]^*$	597	125	0	0	0	0	0
Kobe Takatori $[Y]^{**}$	642	80	0	0	0	0	0

** Strong component in building X direction*
*** Strong component in building Y direction*

Table H.3: Building 1 Column Plastic Rotations (Major Axis Bending)

Ground Motion	**Column Plastic Rotations (Major Axis Bending)**						
	$\leqslant$ 0.1%	**(0.1-1]%**	**(1-2]%**	**(2-3]%**	**(3-4]%**	**(4-5]%**	**(5-6]%**
Northridge Sylmar $[X]^*$	1424	20	0	0	0	0	0
Northridge Sylmar $[Y]^{**}$	1423	21	0	0	0	0	0
Iran Tabas $[X]^*$	1301	143	0	0	0	0	0
Iran Tabas $[Y]^{**}$	1363	81	0	0	0	0	0
Kobe Takatori $[X]^*$	1359	82	3	0	0	0	0
Kobe Takatori $[Y]^{**}$	1374	70	0	0	0	0	0

** Strong component in building X direction*
*** Strong component in building Y direction*

Table H.4: Building 1 Column Plastic Rotations (Minor Axis Bending)

Ground Motion	**Column Plastic Rotations (Minor Axis Bending)**						
	$\leqslant$ 0.1%	**(0.1-1]%**	**(1-2]%**	**(2-3]%**	**(3-4]%**	**(4-5]%**	**(5-6]%**
Northridge Sylmar $[X]^*$	826	10	0	0	0	0	0
Northridge Sylmar $[Y]^{**}$	826	10	0	0	0	0	0
Iran Tabas $[X]^*$	817	19	0	0	0	0	0
Iran Tabas $[Y]^{**}$	802	34	0	0	0	0	0
Kobe Takatori $[X]^*$	797	39	0	0	0	0	0
Kobe Takatori $[Y]^{**}$	814	22	0	0	0	0	0

** Strong component in building X direction*
*** Strong component in building Y direction*

Table H.5: Building 1 Panel Zone Plastic Rotations

Ground Motion	**Panel Zone Plastic Rotations**						
	$\leqslant$ 0.1%	**(0.1-1]%**	**(1-2]%**	**(2-3]%**	**(3-4]%**	**(4-5]%**	**(5-6]%**
Northridge Sylmar $[X]^{*}$	365	185	20	0	0	0	0
Northridge Sylmar $[Y]^{**}$	381	187	2	0	0	0	0
Iran Tabas $[X]^{*}$	341	171	58	0	0	0	0
Iran Tabas $[Y]^{**}$	328	191	51	0	0	0	0
Kobe Takatori $[X]^{*}$	357	167	42	4	0	0	0
Kobe Takatori $[Y]^{**}$	365	160	45	0	0	0	0

** Strong component in building X direction*
*** Strong component in building Y direction*

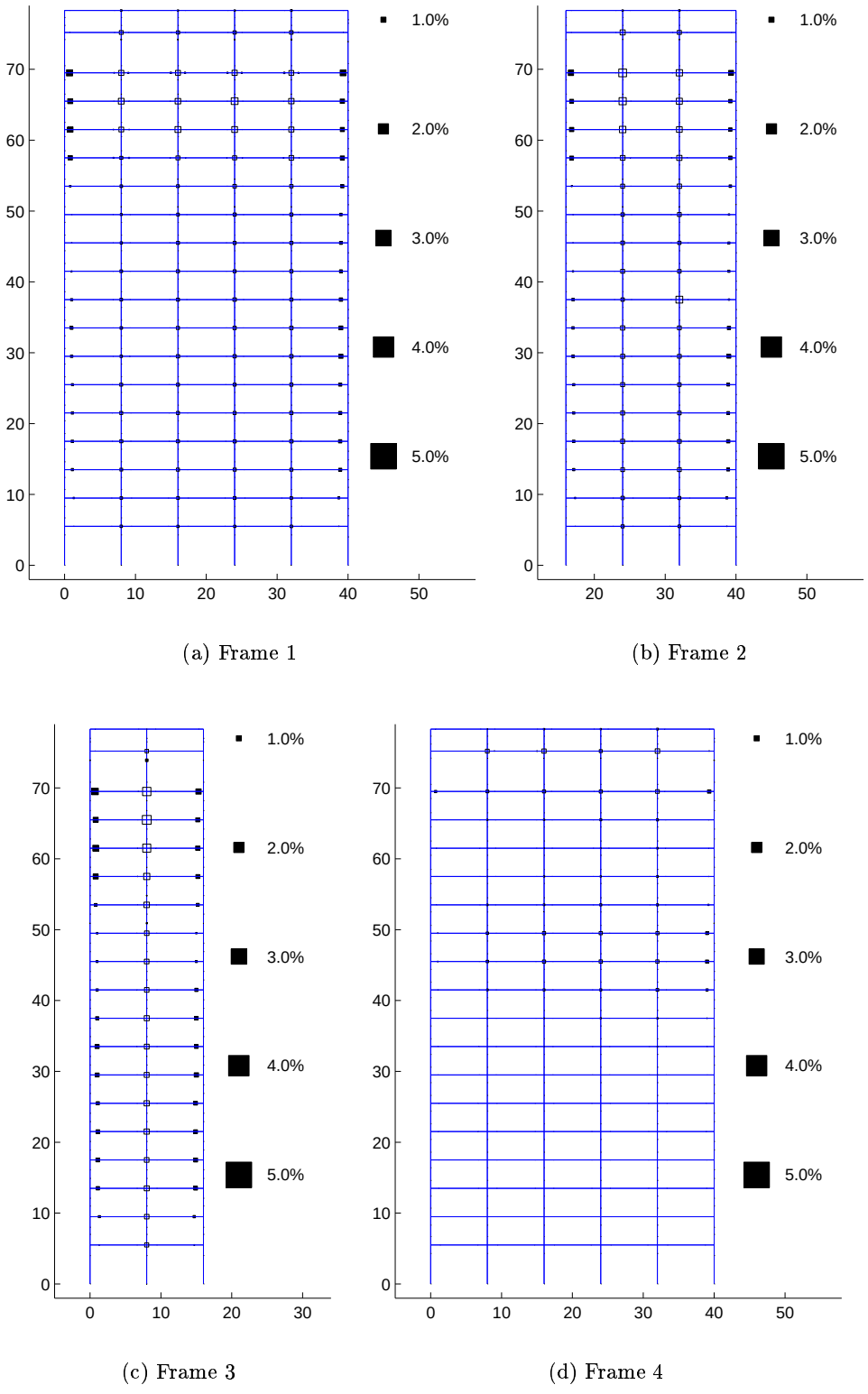

(a) Frame 1

(b) Frame 2

(c) Frame 3

(d) Frame 4

Figure H.13: Plastic Rotations (Black:Beam-Columns White:Panel Zones) in Building 2 Frames 1-4: Northridge Earthquake (Sylmar Record Strong Component in X Direction)

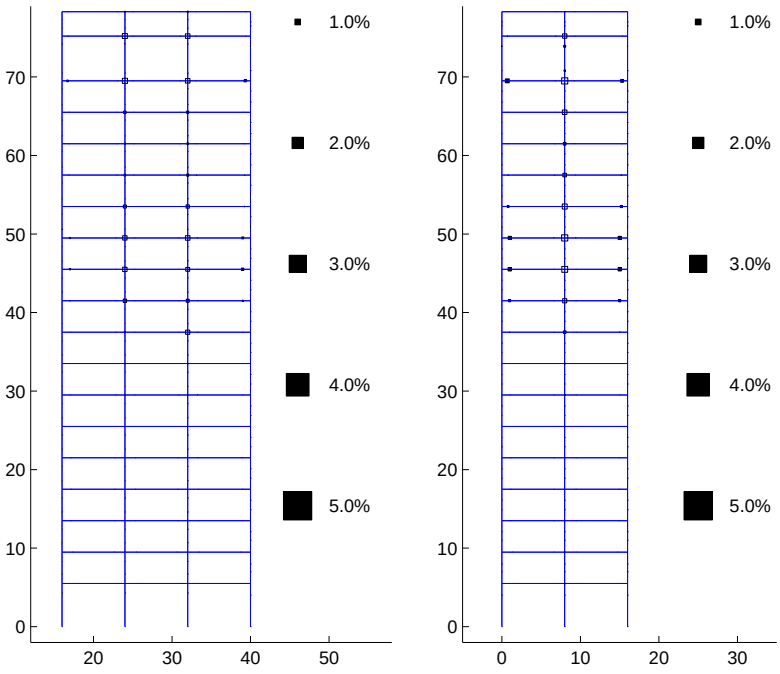

(a) Frame 5 (b) Frame 6

Figure H.14: Plastic Rotations (Black:Beam-Columns White:Panel Zones) in Building 2 Frames 5-6: Northridge Earthquake (Sylmar Record Strong Component in X Direction)

Table H.6: Building 2 Moment Frame Beam Plastic Rotations (Major Axis Bending)

Ground Motion	**Moment Frame Beam Plastic Rotations (Major Axis Bending)**						
	$\leqslant$ 0.1%	**(0.1-1]%**	**(1-2]%**	**(2-3]%**	**(3-4]%**	**(4-5]%**	**(5-6]%**
Northridge Sylmar $[X]^*$	620	133	7	0	0	0	0
Iran Tabas $[X]^*$	460	137	99	29	34	1	0
Kobe Takatori $[X]^*$	476	183	81	20	0	0	0

** Strong component in building X direction*

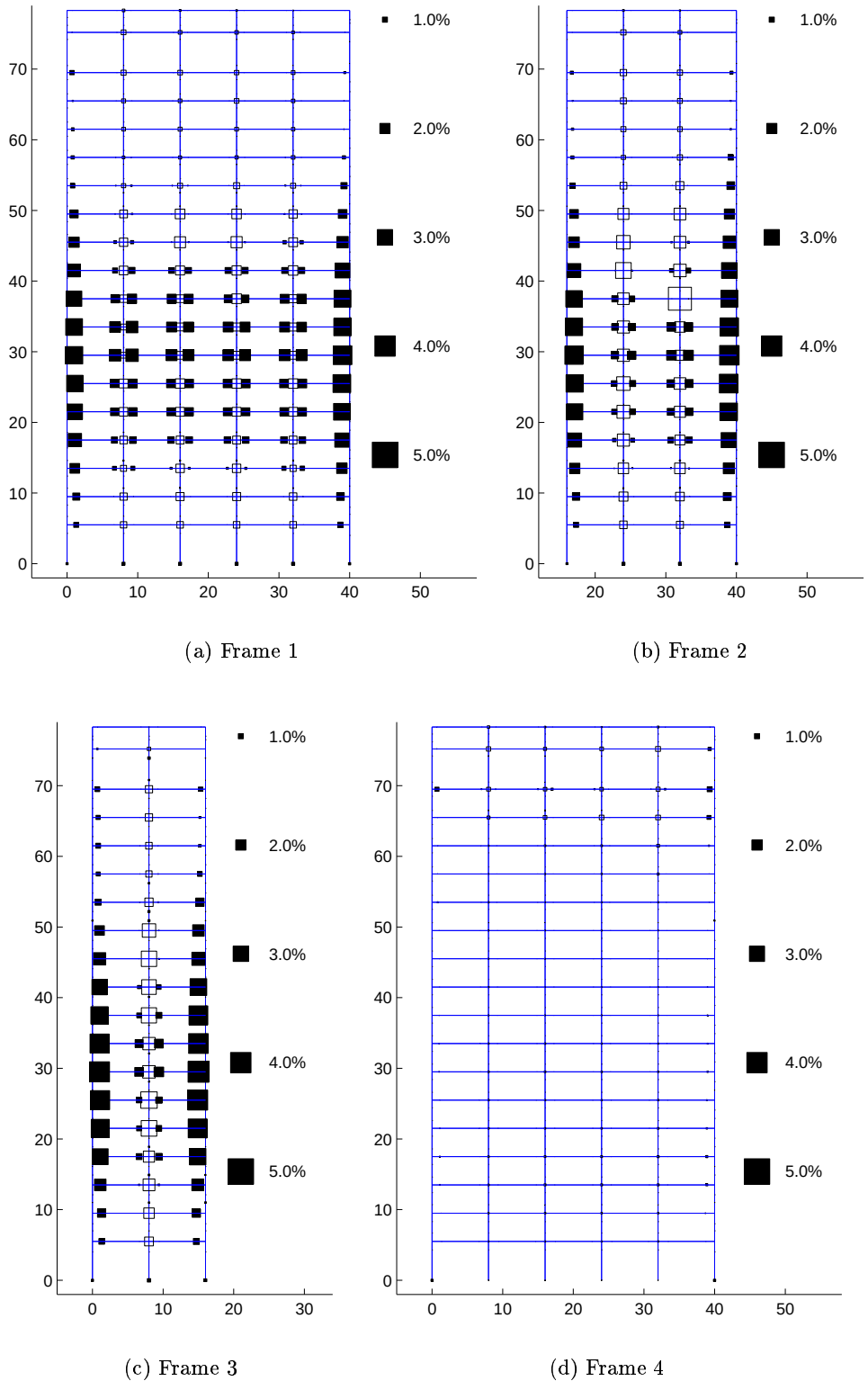

(a) Frame 1

(b) Frame 2

(c) Frame 3

(d) Frame 4

Figure H.15: Plastic Rotations (Black:Beam-Columns White:Panel Zones) in Building 2 Frames 1-4: Iran Earthquake (Tabas Record Strong Component in X Direction)

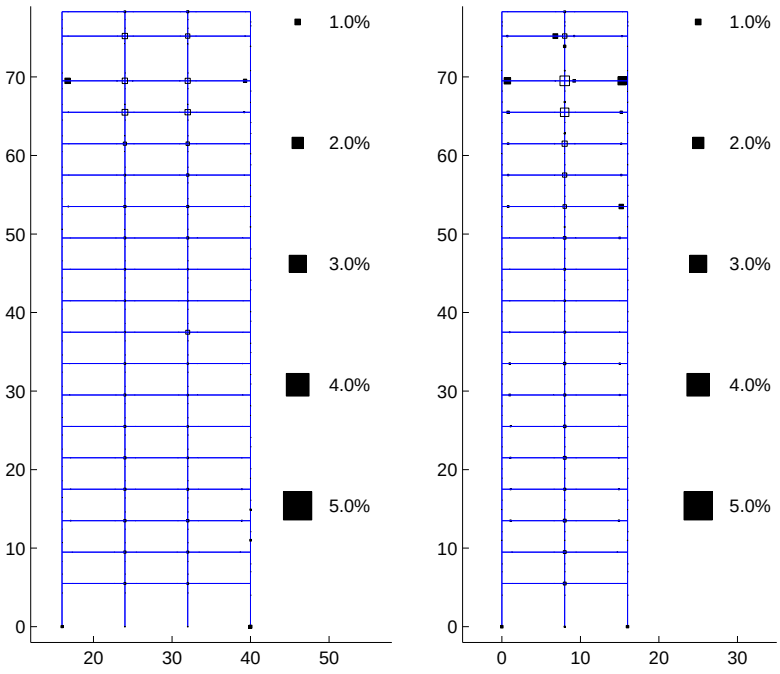

(a) Frame 5 (b) Frame 6

Figure H.16: Plastic Rotations (Black:Beam-Columns White:Panel Zones) in Building 2 Frames 5-6: Iran Earthquake (Tabas Record Strong Component in X Direction)

Table H.7: Building 2 Moment Frame Beam Plastic Rotations (Minor Axis Bending)

Ground Motion	**Moment Frame Beam Plastic Rotations (Minor Axis Bending)**						
	$\leqslant$ 0.1%	**(0.1-1]%**	**(1-2]%**	**(2-3]%**	**(3-4]%**	**(4-5]%**	**(5-6]%**
Northridge Sylmar $[X]^*$	754	6	0	0	0	0	0
Iran Tabas $[X]^*$	724	36	0	0	0	0	0
Kobe Takatori $[X]^*$	701	59	0	0	0	0	0

** Strong component in building X direction*

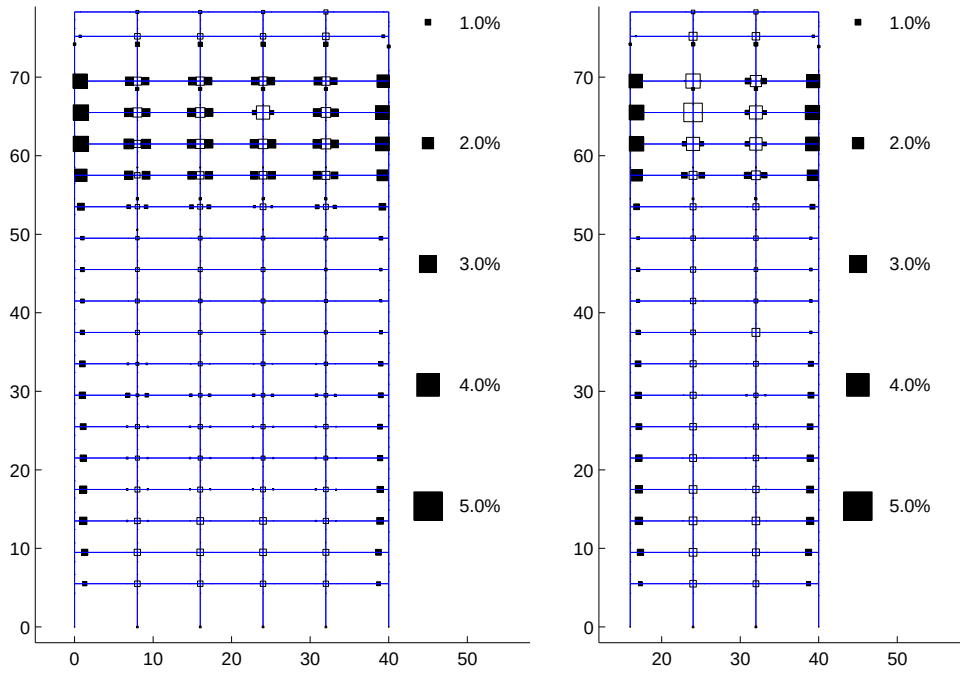

(a) Frame 1

(b) Frame 2

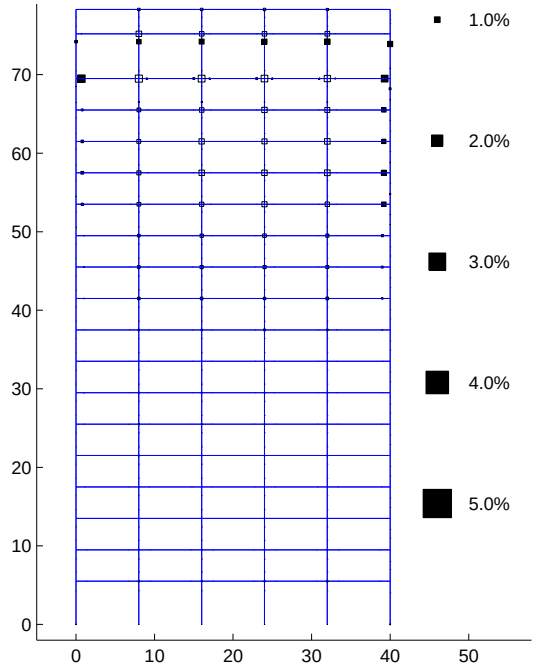

(c) Frame 3

(d) Frame 4

Figure H.17: Plastic Rotations (Black:Beam-Columns White:Panel Zones) in Building 2 Frames 1-4: Kobe Earthquake (Takatori Record Strong Component in X Direction)

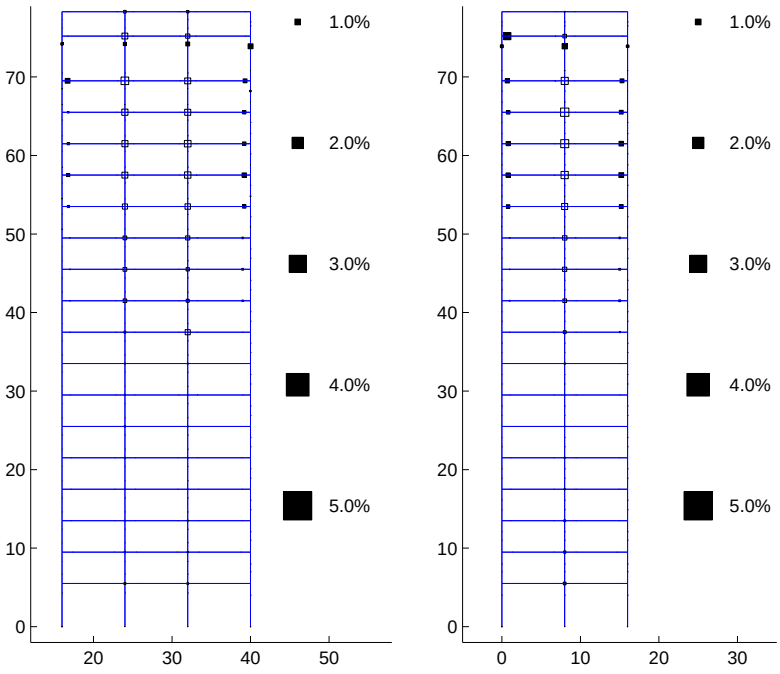

(a) Frame 5 (b) Frame 6

Figure H.18: Plastic Rotations (Black:Beam-Columns White:Panel Zones) in Building 2 Frames 5-6: Kobe Earthquake (Takatori Record Strong Component in X Direction)

Table H.8: Building 2 Column Plastic Rotations (Major Axis Bending)

Ground Motion	**Column Plastic Rotations (Major Axis Bending)**						
	$\leqslant$ 0.1%	**(0.1-1]%**	**(1-2]%**	**(2-3]%**	**(3-4]%**	**(4-5]%**	**(5-6]%**
Northridge Sylmar $[X]^*$	1247	7	0	0	0	0	0
Iran Tabas $[X]^*$	1185	69	0	0	0	0	0
Kobe Takatori $[X]^*$	1182	72	0	0	0	0	0

** Strong component in building X direction*

Table H.9: Building 2 Column Plastic Rotations (Minor Axis Bending)

Ground Motion	**Column Plastic Rotations (Minor Axis Bending)**						
	$\leqslant$ 0.1%	**(0.1-1]%**	**(1-2]%**	**(2-3]%**	**(3-4]%**	**(4-5]%**	**(5-6]%**
Northridge Sylmar $[X]^*$	789	9	0	0	0	0	0
Iran Tabas $[X]^*$	775	23	0	0	0	0	0
Kobe Takatori $[X]^*$	761	36	1	0	0	0	0

** Strong component in building X direction*

Table H.10: Building 2 Panel Zone Plastic Rotations

Ground Motion	**Panel Zone Plastic Rotations**						
	$\leqslant$ 0.1%	**(0.1-1]%**	**(1-2]%**	**(2-3]%**	**(3-4]%**	**(4-5]%**	**(5-6]%**
Northridge Sylmar $[X]^*$	278	193	23	0	0	0	0
Iran Tabas $[X]^*$	229	166	68	26	4	1	0
Kobe Takatori $[X]^*$	240	171	74	7	2	0	0

** Strong component in building X direction*

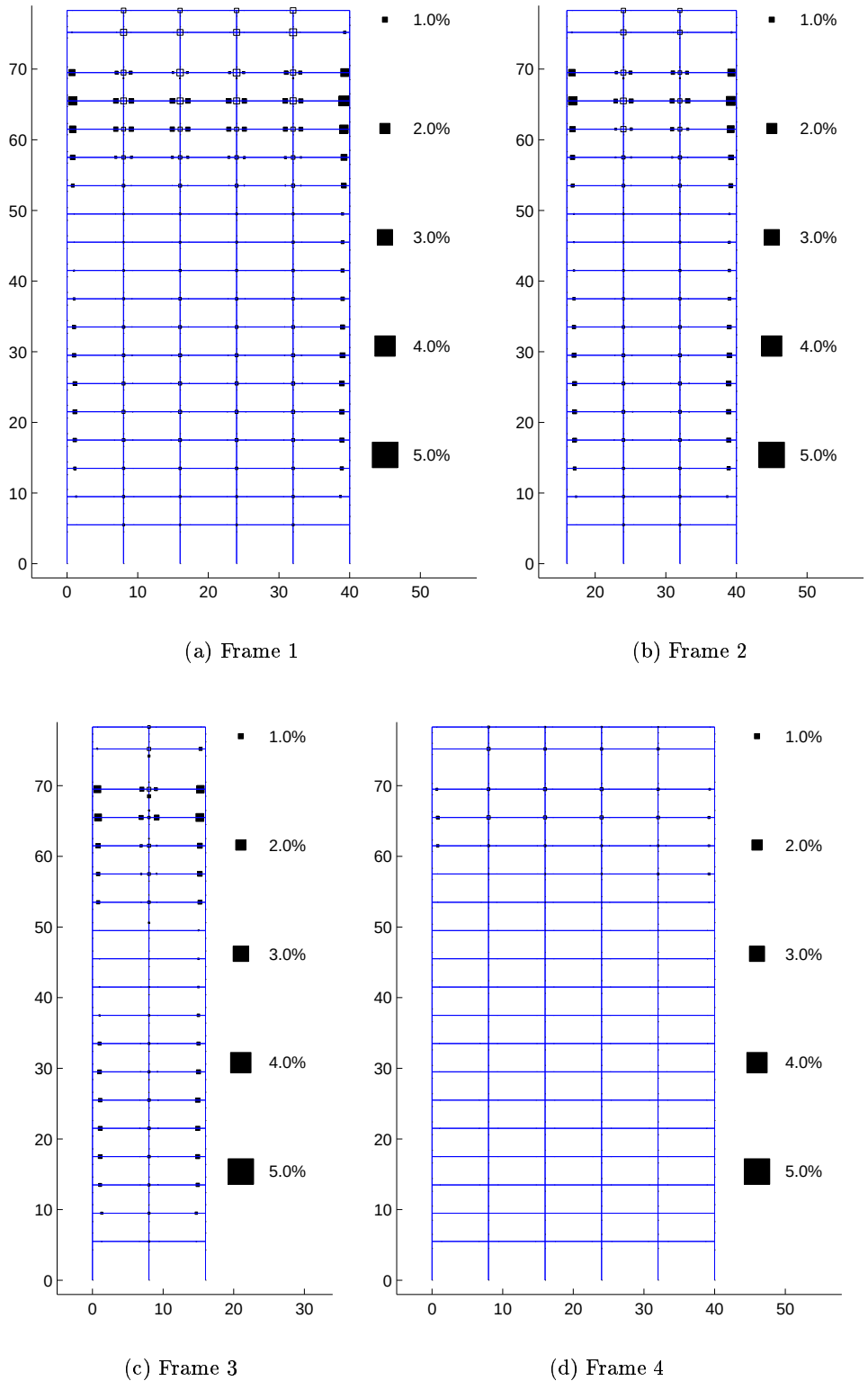

(a) Frame 1

(b) Frame 2

(c) Frame 3

(d) Frame 4

Figure H.19: Plastic Rotations (Black:Beam-Columns White:Panel Zones) in Building 2A Frames 1-4: Northridge Earthquake (Sylmar Record Strong Component in X Direction)

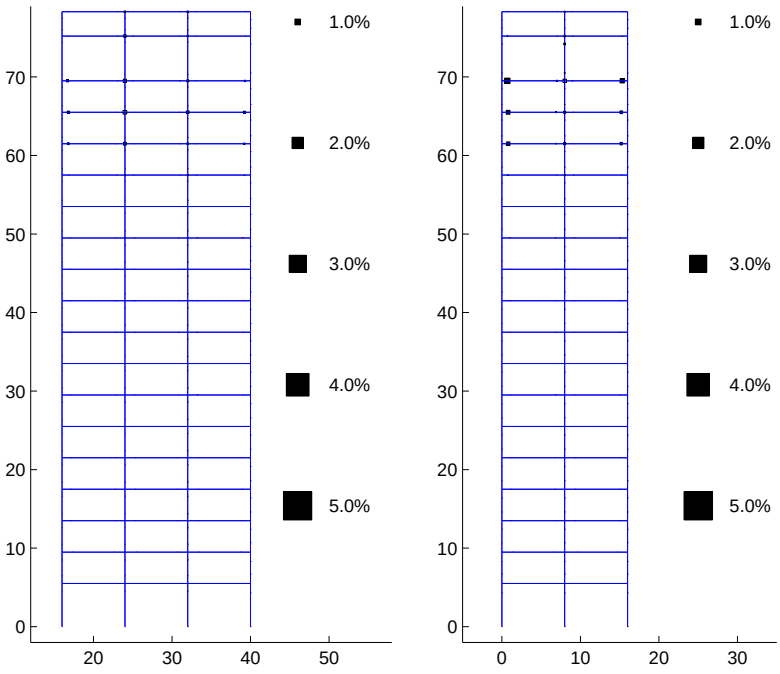

(a) Frame 5 (b) Frame 6

Figure H.20: Plastic Rotations (Black:Beam-Columns White:Panel Zones) in Building 2A Frames 5-6: Northridge Earthquake (Sylmar Record Strong Component in X Direction)

Table H.11: Building 2A Moment Frame Beam Plastic Rotations (Major Axis Bending)

Ground Motion	**Moment Frame Beam Plastic Rotations (Major Axis Bending)**						
	$\leqslant$ 0.1%	**(0.1-1]%**	**(1-2]%**	**(2-3]%**	**(3-4]%**	**(4-5]%**	**(5-6]%**
Northridge Sylmar $[X]^*$	557	186	17	0	0	0	0
Iran Tabas $[X]^*$	344	163	70	114	54	15	0
Kobe Takatori $[X]^*$	313	182	199	60	6	0	0

** Strong component in building X direction*

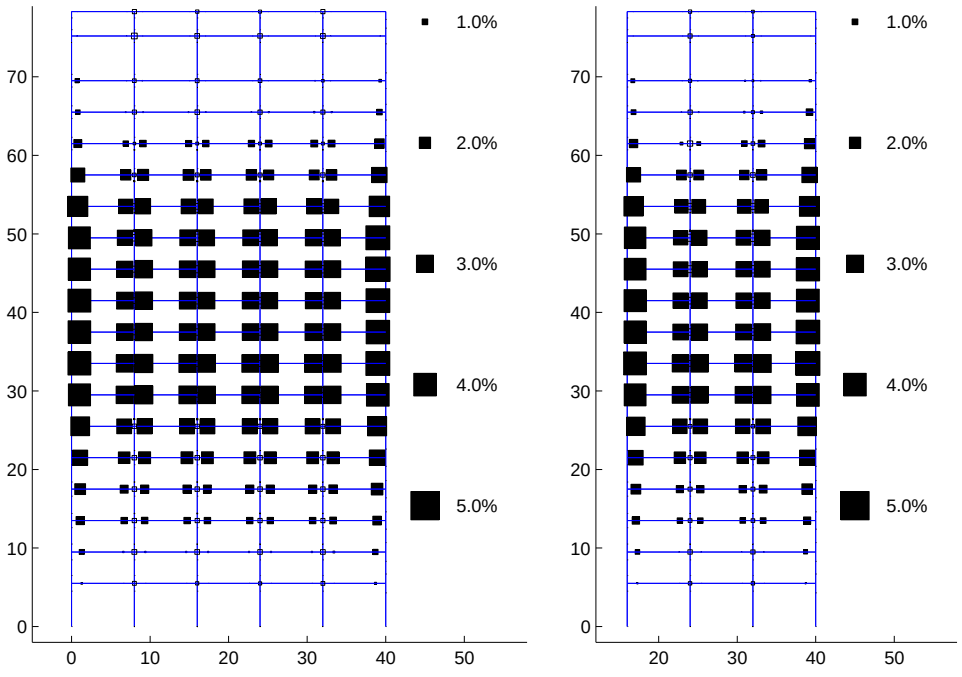

(a) Frame 1

(b) Frame 2

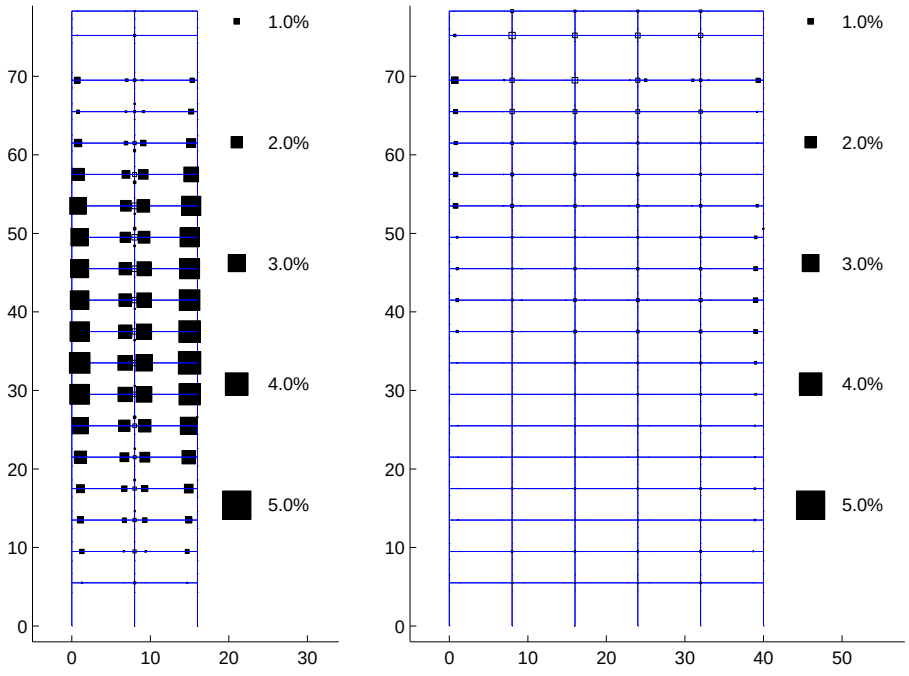

(c) Frame 3

(d) Frame 4

Figure H.21: Plastic Rotations (Black:Beam-Columns White:Panel Zones) in Building 2A Frames 1-4: Iran Earthquake (Tabas Record Strong Component in X Direction)

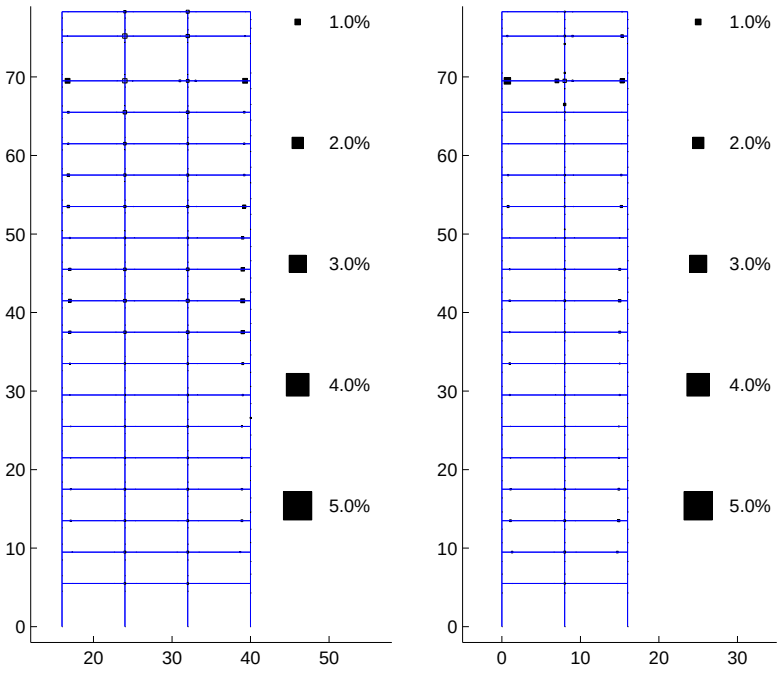

(a) Frame 5 (b) Frame 6

Figure H.22: Plastic Rotations (Black:Beam-Columns White:Panel Zones) in Building 2A Frames 5-6: Iran Earthquake (Tabas Record Strong Component in X Direction)

Table H.12: Building 2A Moment Frame Beam Plastic Rotations (Minor Axis Bending)

Ground Motion	**Moment Frame Beam Plastic Rotations (Minor Axis Bending)**						
	$\leqslant$ 0.1%	**(0.1-1]%**	**(1-2]%**	**(2-3]%**	**(3-4]%**	**(4-5]%**	**(5-6]%**
Northridge Sylmar $[X]^*$	723	37	0	0	0	0	0
Iran Tabas $[X]^*$	724	36	0	0	0	0	0
Kobe Takatori $[X]^*$	612	148	0	0	0	0	0

** Strong component in building X direction*

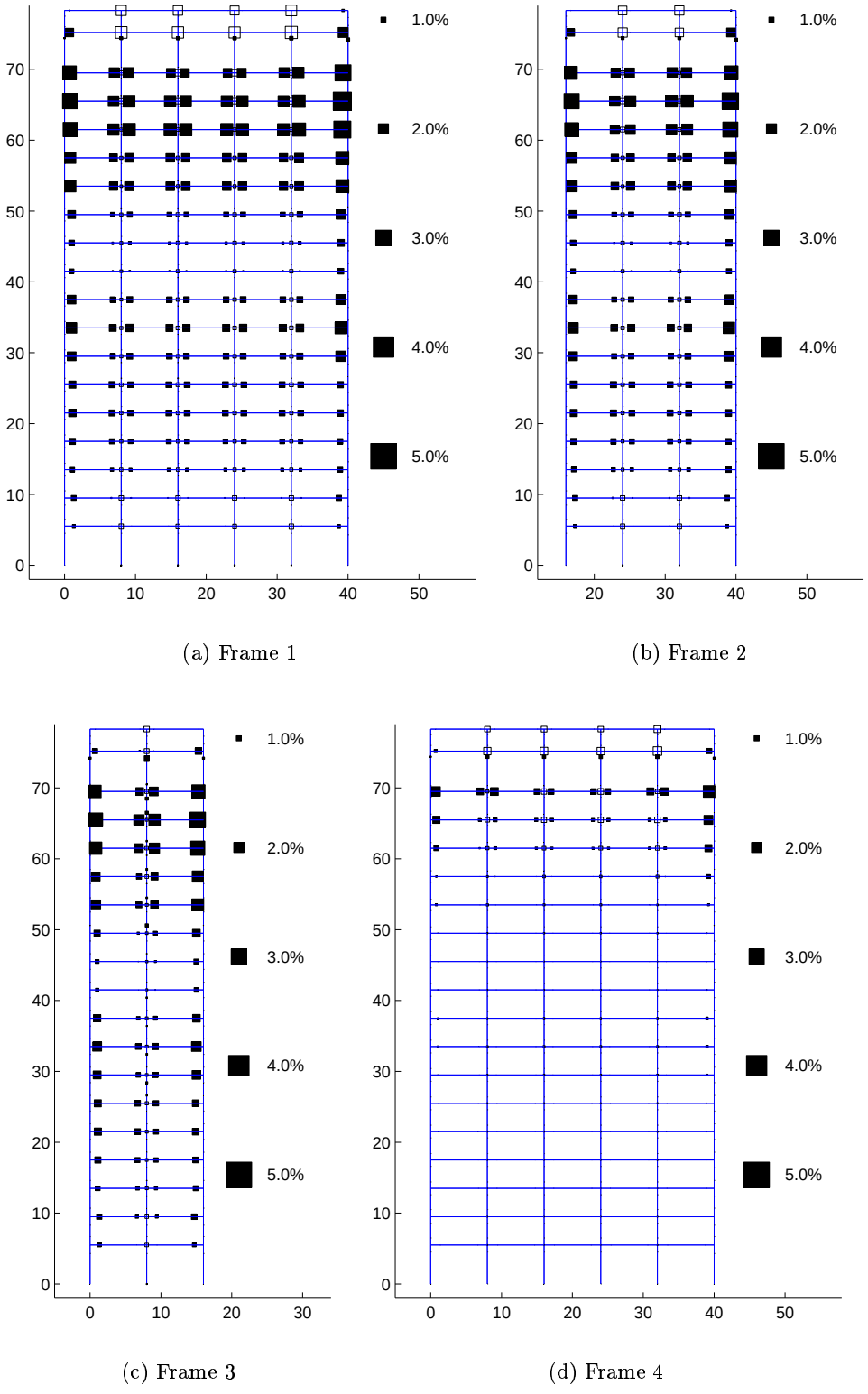

(a) Frame 1

(b) Frame 2

(c) Frame 3

(d) Frame 4

Figure H.23: Plastic Rotations (Black:Beam-Columns White:Panel Zones) in Building 2A Frames 1-4: Kobe Earthquake (Takatori Record Strong Component in X Direction)

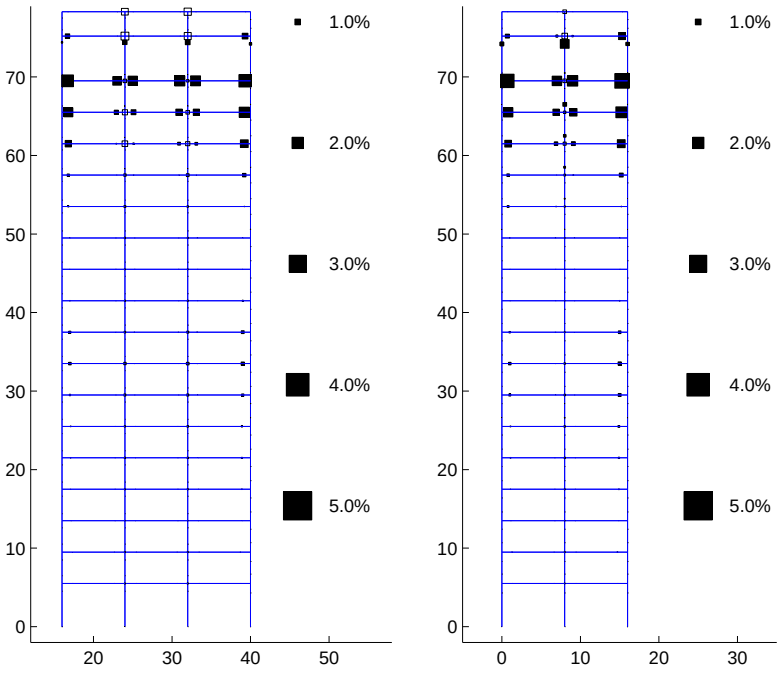

(a) Frame 5 (b) Frame 6

Figure H.24: Plastic Rotations (Black:Beam-Columns White:Panel Zones) in Building 2A Frames 5-6: Kobe Earthquake (Takatori Record Strong Component in X Direction)

Table H.13: Building 2A Column Plastic Rotations (Major Axis Bending)

Ground Motion	**Column Plastic Rotations (Major Axis Bending)**						
	$\leqslant$ 0.1%	**(0.1-1]%**	**(1-2]%**	**(2-3]%**	**(3-4]%**	**(4-5]%**	**(5-6]%**
Northridge Sylmar $[X]^*$	1247	7	0	0	0	0	0
Iran Tabas $[X]^*$	1212	42	0	0	0	0	0
Kobe Takatori $[X]^*$	1190	64	0	0	0	0	0

** Strong component in building X direction*

Table H.14: Building 2A Column Plastic Rotations (Minor Axis Bending)

Ground Motion	**Column Plastic Rotations (Minor Axis Bending)**						
	$\leqslant$ 0.1%	**(0.1-1]%**	**(1-2]%**	**(2-3]%**	**(3-4]%**	**(4-5]%**	**(5-6]%**
Northridge Sylmar $[X]^*$	786	12	0	0	0	0	0
Iran Tabas $[X]^*$	789	9	0	0	0	0	0
Kobe Takatori $[X]^*$	763	34	1	0	0	0	0

** Strong component in building X direction*

Table H.15: Building 2A Panel Zone Plastic Rotations

Ground Motion	**Panel Zone Plastic Rotations**						
	$\leqslant$ 0.1%	**(0.1-1]%**	**(1-2]%**	**(2-3]%**	**(3-4]%**	**(4-5]%**	**(5-6]%**
Northridge Sylmar $[X]^*$	314	165	15	0	0	0	0
Iran Tabas $[X]^*$	228	232	34	0	0	0	0
Kobe Takatori $[X]^*$	234	225	30	5	0	0	0

** Strong component in building X direction*

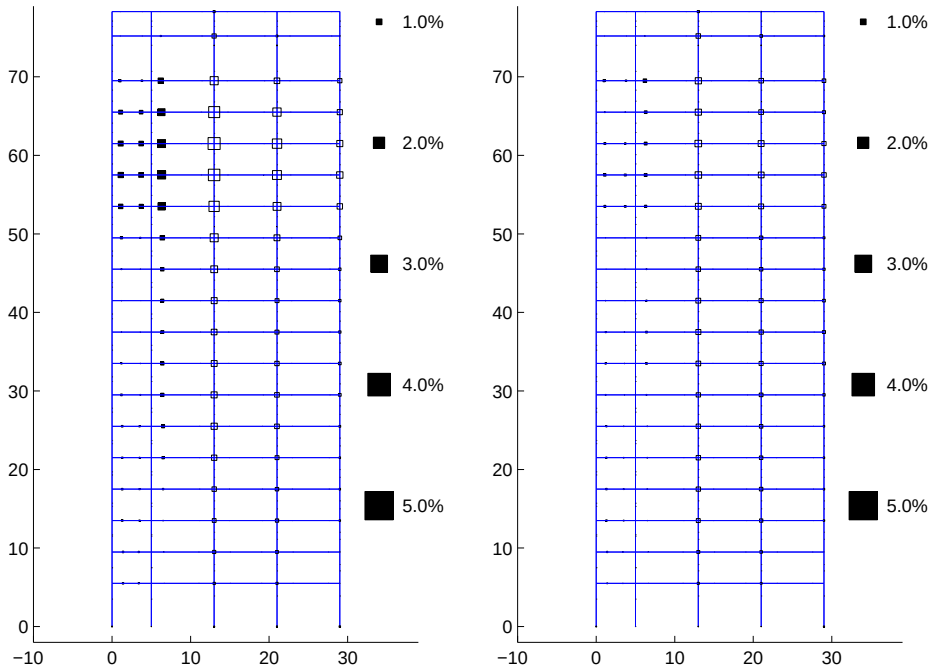

(a) Frame 1

(b) Frame 2

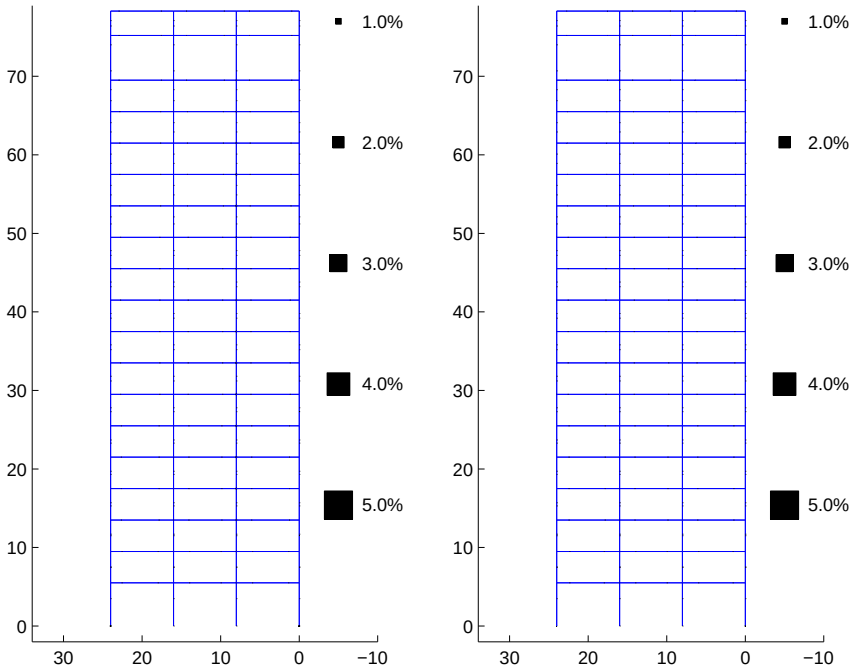

(c) Frame 3

(d) Frame 4

Figure H.25: Plastic Rotations (Black:Beam-Columns White:Panel Zones) in Building 3 Frames 1-4: Northridge Earthquake (Sylmar Record Strong Component in X Direction)

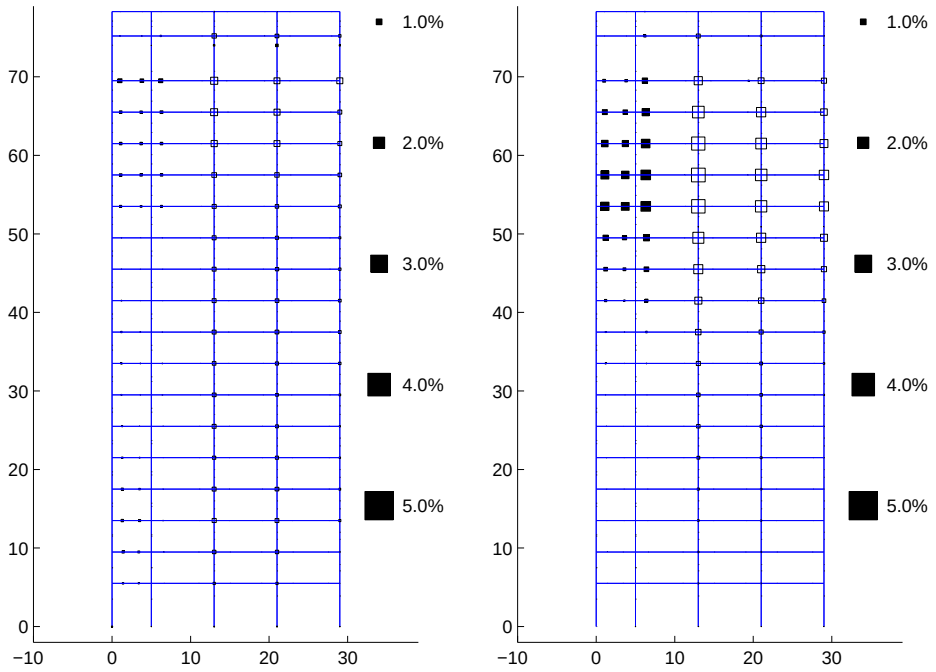

(a) Frame 1

(b) Frame 2

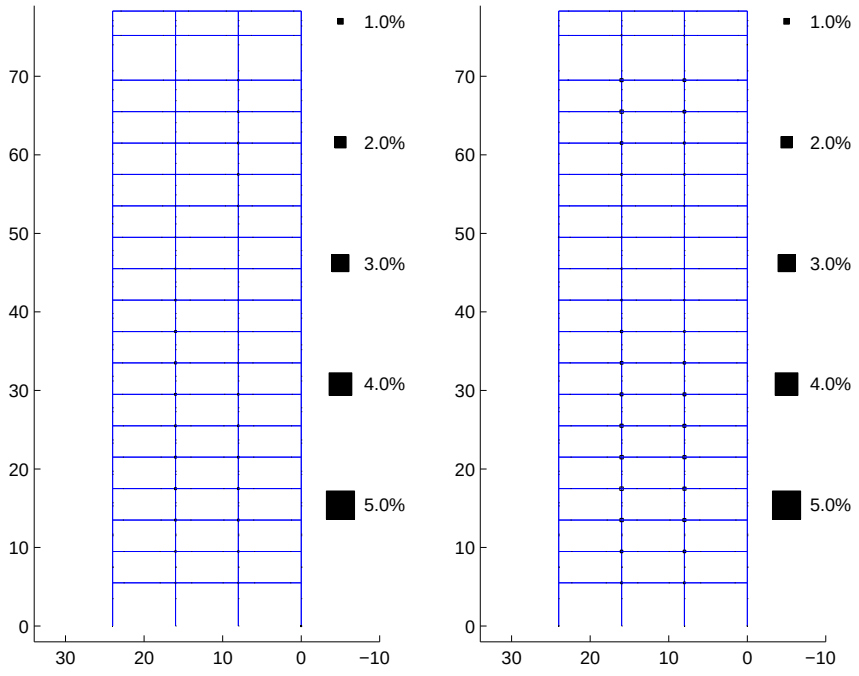

(c) Frame 3

(d) Frame 4

Figure H.26: Plastic Rotations (Black:Beam-Columns White:Panel Zones) in Building 3 Frames 1-4: Northridge Earthquake (Sylmar Record Strong Component in Y Direction)

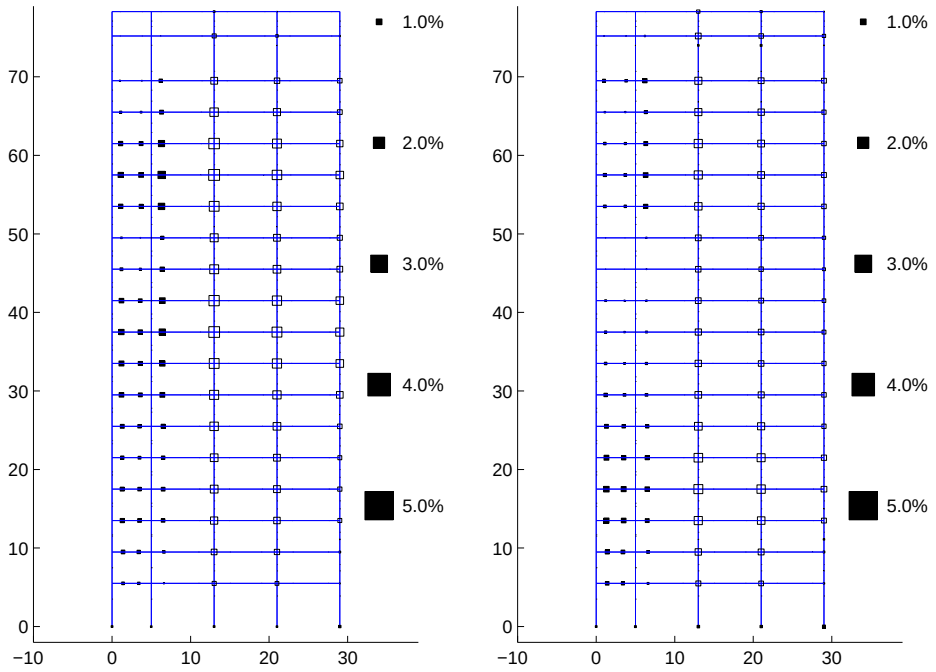

(a) Frame 1

(b) Frame 2

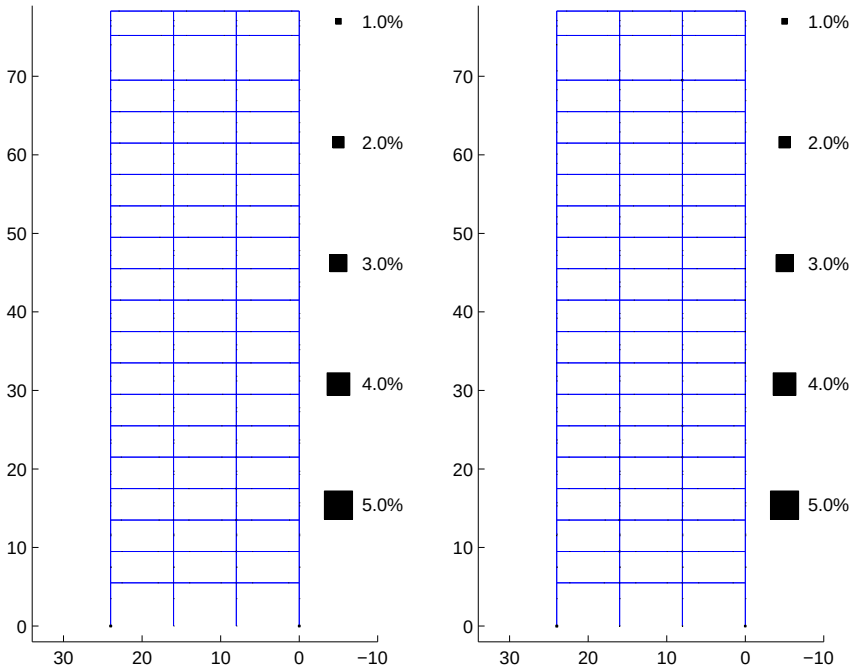

(c) Frame 3

(d) Frame 4

Figure H.27: Plastic Rotations (Black:Beam-Columns White:Panel Zones) in Building 3 Frames 1-4: Iran Earthquake (Tabas Record Strong Component in X Direction)

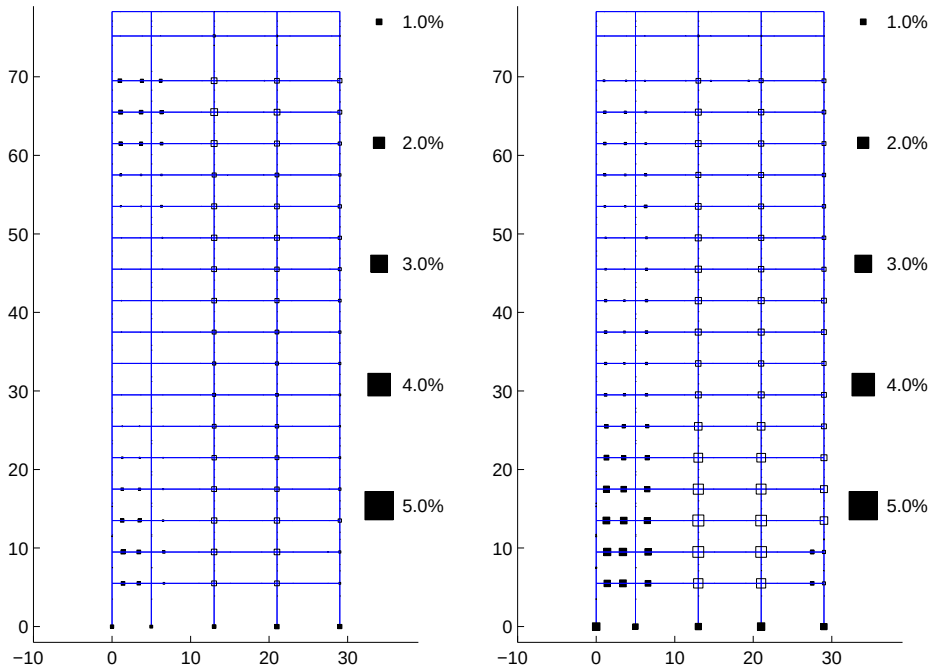

(a) Frame 1

(b) Frame 2

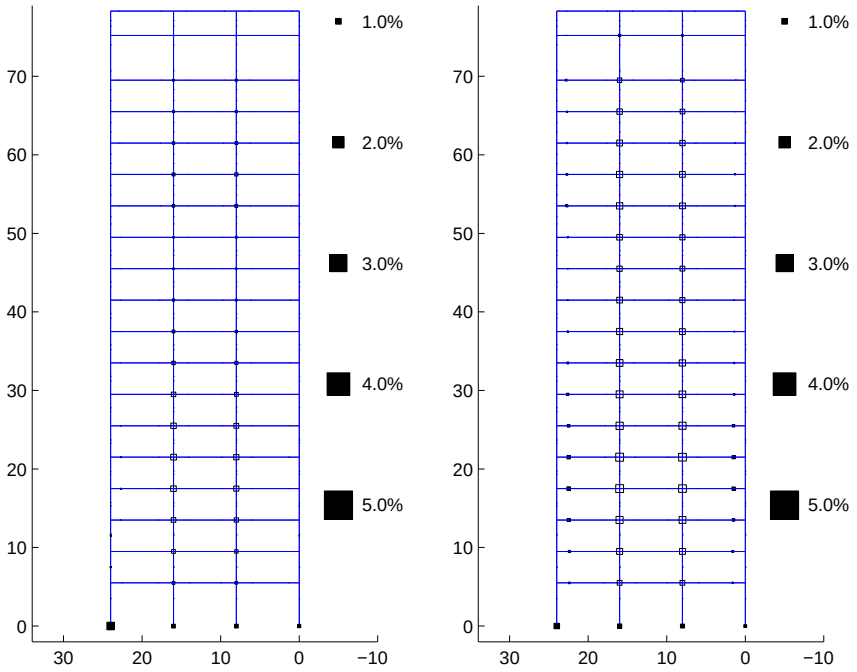

(c) Frame 3

(d) Frame 4

Figure H.28: Plastic Rotations (Black:Beam-Columns White:Panel Zones) in Building 3 Frames 1-4: Iran Earthquake (Tabas Record Strong Component in Y Direction)

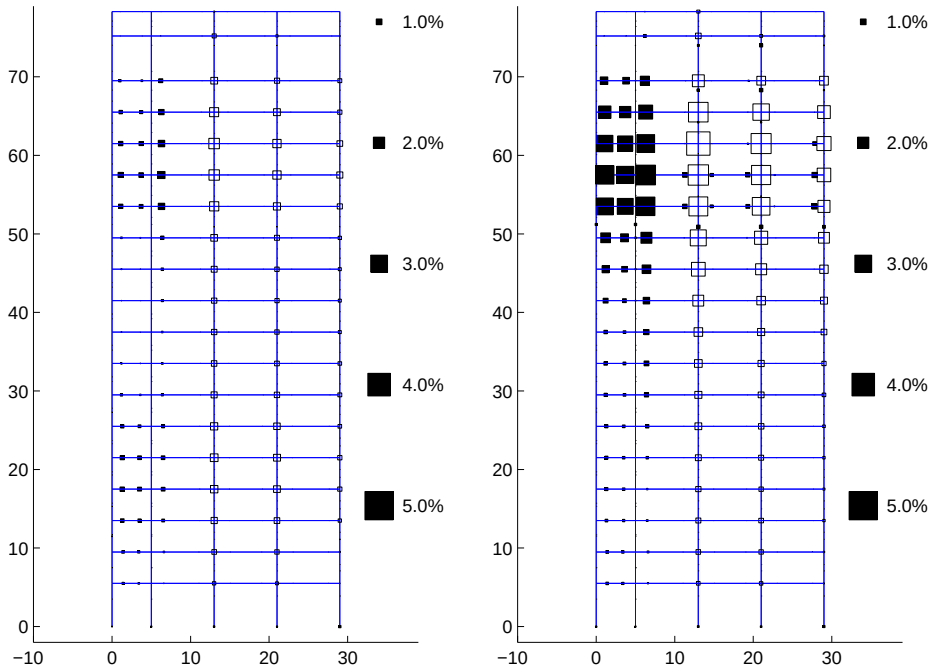

(a) Frame 1

(b) Frame 2

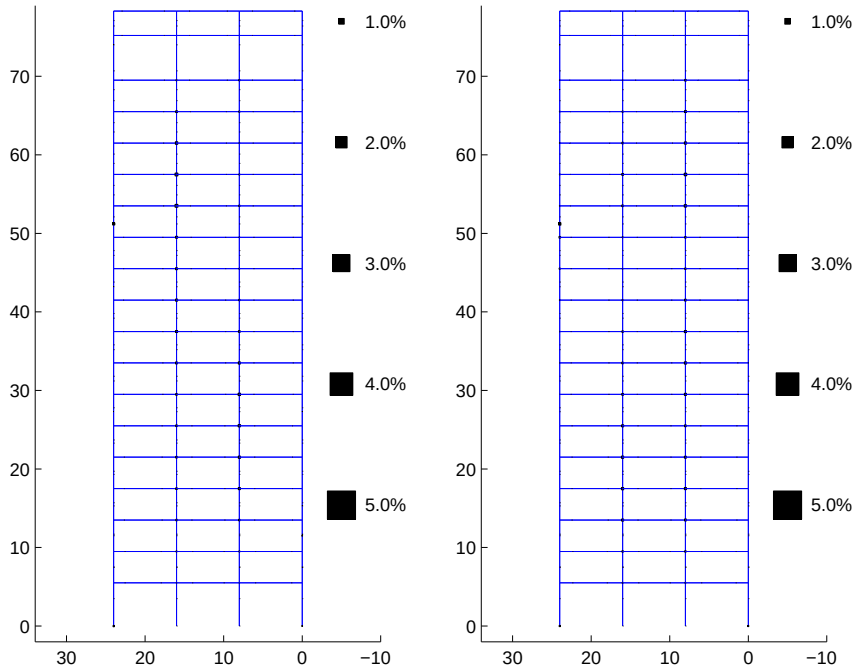

(c) Frame 3

(d) Frame 4

Figure H.29: Plastic Rotations (Black:Beam-Columns White:Panel Zones) in Building 3 Frames 1-4: Kobe Earthquake (Takatori Record Strong Component in X Direction)

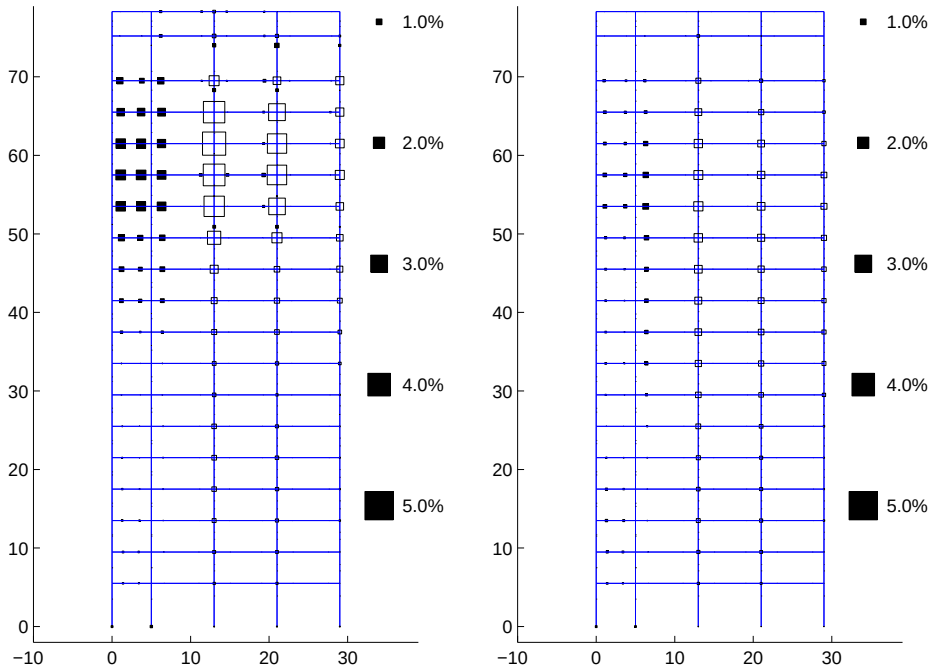

(a) Frame 1

(b) Frame 2

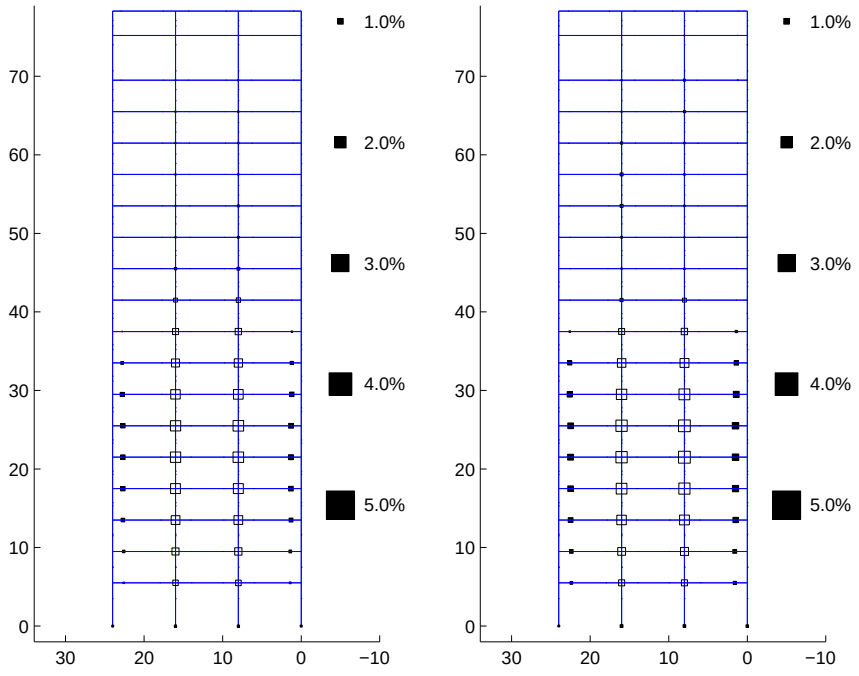

(c) Frame 3

(d) Frame 4

Figure H.30: Plastic Rotations (Black:Beam-Columns White:Panel Zones) in Building 3 Frames 1-4: Kobe Earthquake (Takatori Record Strong Component in Y Direction)

Table H.16: Building 3 Moment Frame Beam Plastic Rotations (Major Axis Bending)

Ground Motion	**Moment Frame Beam Plastic Rotations (Major Axis Bending)**						
	$\leqslant$ 0.1%	**(0.1-1]%**	**(1-2]%**	**(2-3]%**	**(3-4]%**	**(4-5]%**	**(5-6]%**
Northridge Sylmar $[X]^*$	451	77	4	0	0	0	0
Northridge Sylmar $[Y]^{**}$	463	58	11	0	0	0	0
Iran Tabas $[X]^*$	432	95	5	0	0	0	0
Iran Tabas $[Y]^{**}$	412	110	10	0	0	0	0
Kobe Takatori $[X]^*$	421	87	13	6	5	0	0
Kobe Takatori $[Y]^{**}$	389	121	22	0	0	0	0

** Strong component in building X direction*
*** Strong component in building Y direction*

Table H.17: Building 3 Moment Frame Beam Plastic Rotations (Minor Axis Bending)

Ground Motion	**Moment Frame Beam Plastic Rotations (Minor Axis Bending)**						
	$\leqslant$ 0.1%	**(0.1-1]%**	**(1-2]%**	**(2-3]%**	**(3-4]%**	**(4-5]%**	**(5-6]%**
Northridge Sylmar $[X]^*$	527	5	0	0	0	0	0
Northridge Sylmar $[Y]^{**}$	522	10	0	0	0	0	0
Iran Tabas $[X]^*$	521	11	0	0	0	0	0
Iran Tabas $[Y]^{**}$	515	17	0	0	0	0	0
Kobe Takatori $[X]^*$	506	26	0	0	0	0	0
Kobe Takatori $[Y]^{**}$	500	32	0	0	0	0	0

** Strong component in building X direction*
*** Strong component in building Y direction*

Table H.18: Building 3 Column Plastic Rotations (Major Axis Bending)

Ground Motion	**Column Plastic Rotations (Major Axis Bending)**						
	$\leqslant$ 0.1%	**(0.1-1]%**	**(1-2]%**	**(2-3]%**	**(3-4]%**	**(4-5]%**	**(5-6]%**
Northridge Sylmar $[X]^*$	906	6	0	0	0	0	0
Northridge Sylmar $[Y]^{**}$	909	3	0	0	0	0	0
Iran Tabas $[X]^*$	894	18	0	0	0	0	0
Iran Tabas $[Y]^{**}$	884	24	4	0	0	0	0
Kobe Takatori $[X]^*$	889	23	0	0	0	0	0
Kobe Takatori $[Y]^{**}$	889	23	0	0	0	0	0

** Strong component in building X direction*
*** Strong component in building Y direction*

Table H.19: Building 3 Column Plastic Rotations (Minor Axis Bending)

Ground Motion	**Column Plastic Rotations (Minor Axis Bending)**						
	$\leqslant$ 0.1%	**(0.1-1]%**	**(1-2]%**	**(2-3]%**	**(3-4]%**	**(4-5]%**	**(5-6]%**
Northridge Sylmar $[X]^*$	604	4	0	0	0	0	0
Northridge Sylmar $[Y]^{**}$	603	5	0	0	0	0	0
Iran Tabas $[X]^*$	602	6	0	0	0	0	0
Iran Tabas $[Y]^{**}$	592	13	3	0	0	0	0
Kobe Takatori $[X]^*$	595	13	0	0	0	0	0
Kobe Takatori $[Y]^{**}$	594	14	0	0	0	0	0

** Strong component in building X direction*
*** Strong component in building Y direction*

Table H.20: Building 3 Panel Zone Plastic Rotations

Ground Motion	**Panel Zone Plastic Rotations**						
	$\leqslant$ 0.1%	**(0.1-1]%**	**(1-2]%**	**(2-3]%**	**(3-4]%**	**(4-5]%**	**(5-6]%**
Northridge Sylmar $[X]^{*}$	221	96	23	2	0	0	0
Northridge Sylmar $[Y]^{**}$	174	141	22	5	0	0	0
Iran Tabas $[X]^{*}$	208	70	64	0	0	0	0
Iran Tabas $[Y]^{**}$	163	128	51	0	0	0	0
Kobe Takatori $[X]^{*}$	157	133	36	9	6	1	0
Kobe Takatori $[Y]^{**}$	165	106	60	5	5	1	0

** Strong component in building X direction*
*** Strong component in building Y direction*

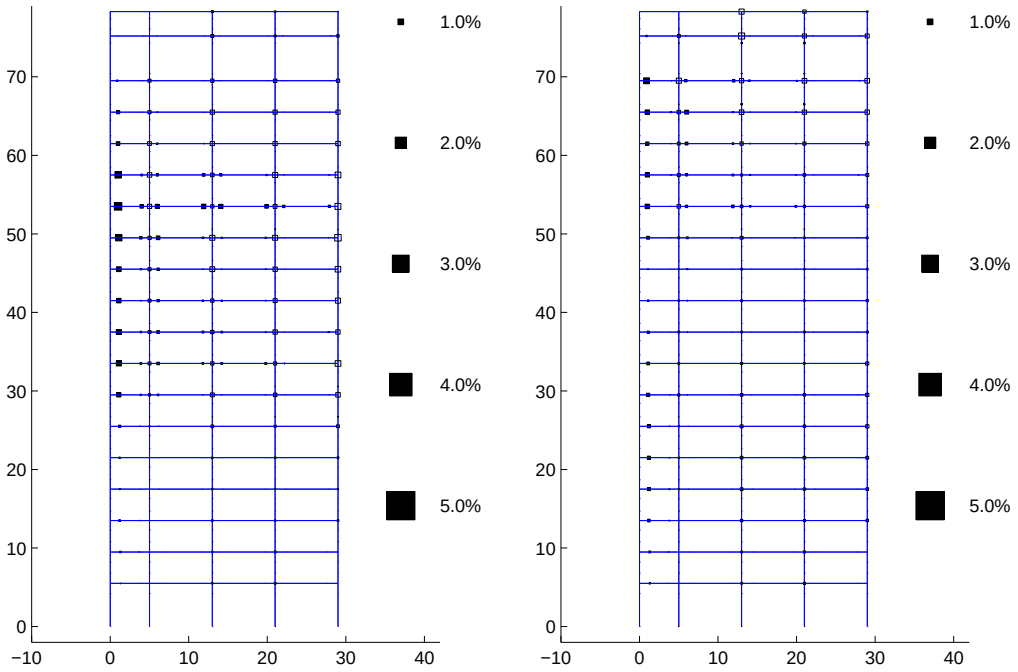

(a) Frame 1

(b) Frame 2

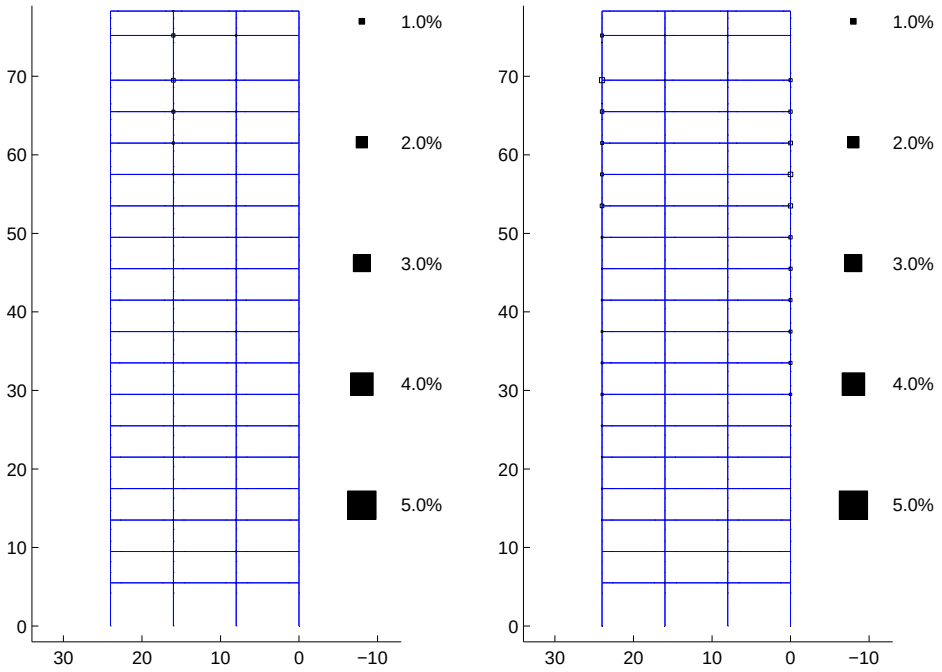

(c) Frame 3

(d) Frame 4

Figure H.31: Plastic Rotations (Black:Beam-Columns White:Panel Zones) in Building 3A Frames 1-4: Northridge Earthquake (Sylmar Record Strong Component in X Direction)

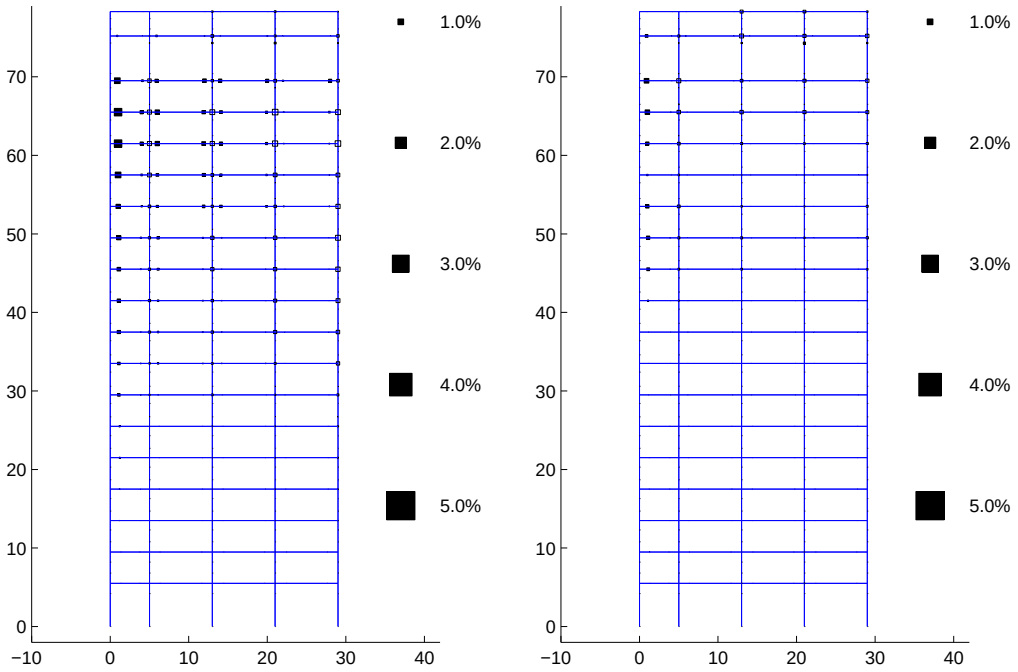

(a) Frame 1

(b) Frame 2

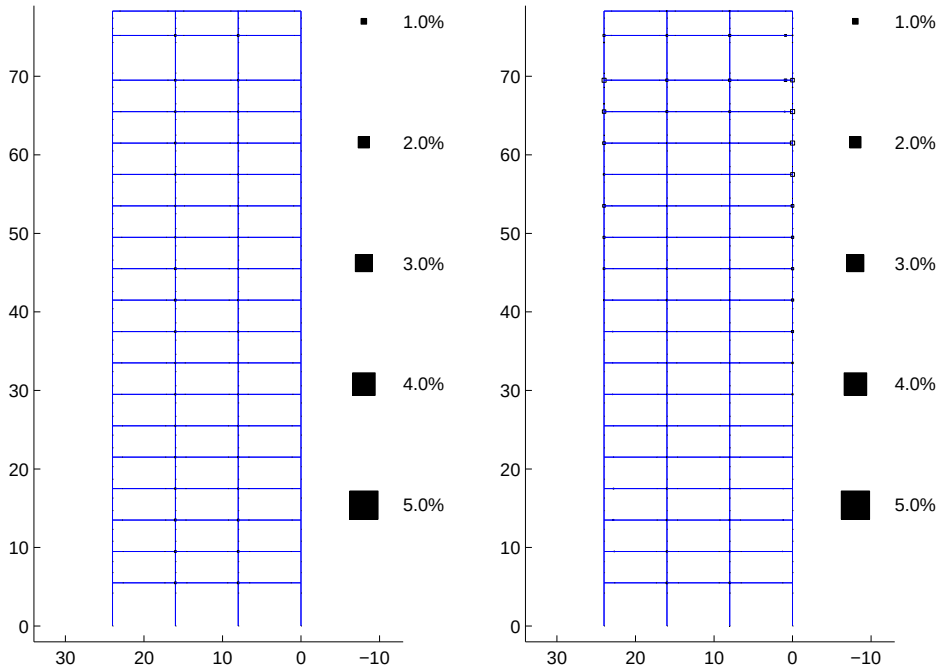

(c) Frame 3

(d) Frame 4

Figure H.32: Plastic Rotations (Black:Beam-Columns White:Panel Zones) in Building 3A Frames 1-4: Northridge Earthquake (Sylmar Record Strong Component in Y Direction)

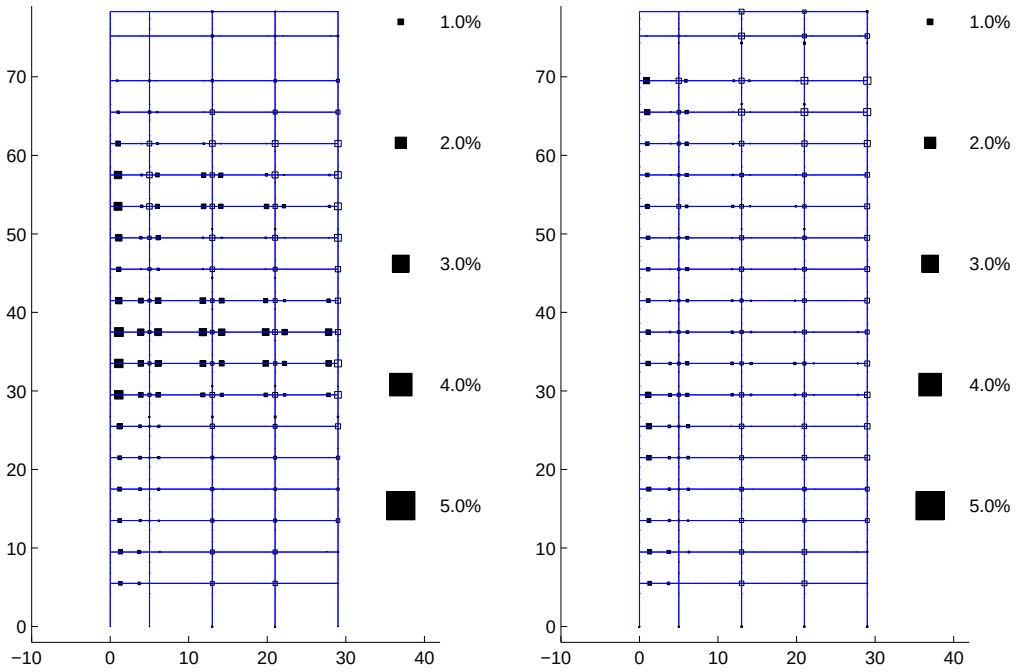

(a) Frame 1

(b) Frame 2

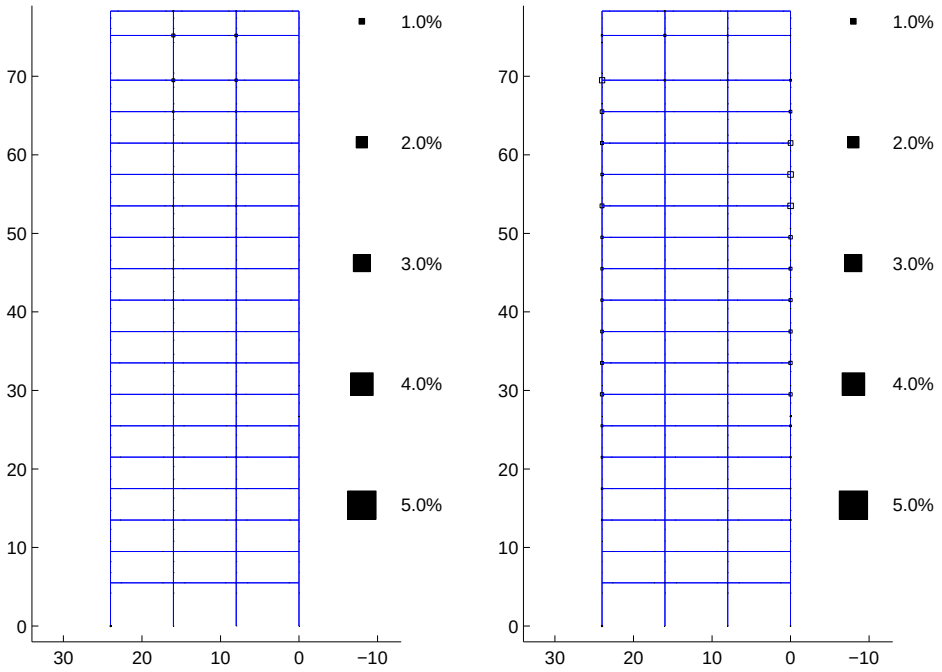

(c) Frame 3

(d) Frame 4

Figure H.33: Plastic Rotations (Black:Beam-Columns White:Panel Zones) in Building 3A Frames 1-4: Iran Earthquake (Tabas Record Strong Component in X Direction)

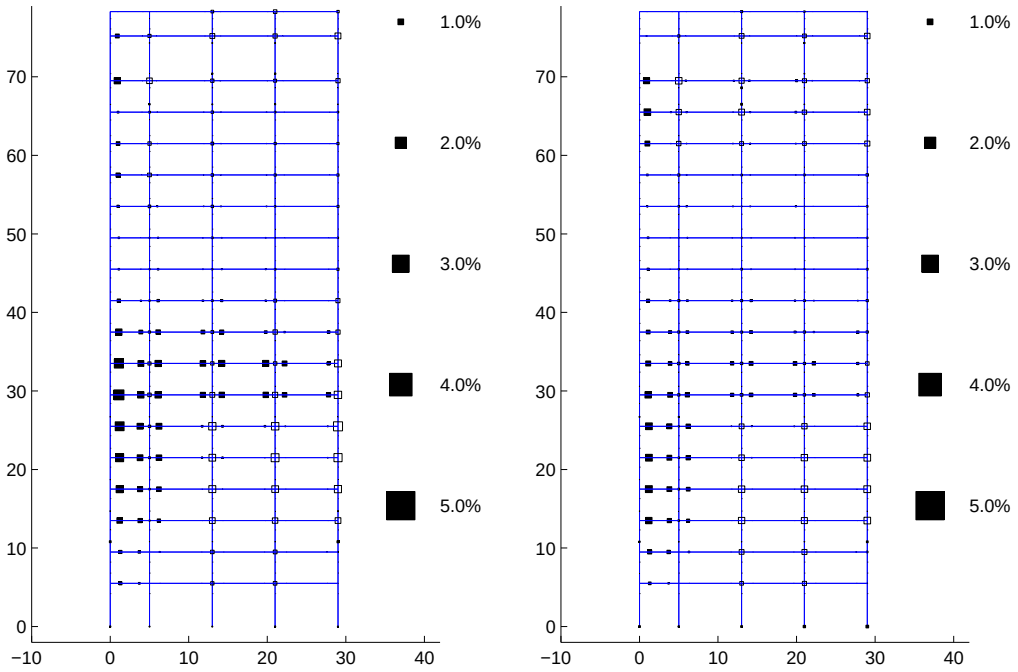

(a) Frame 1

(b) Frame 2

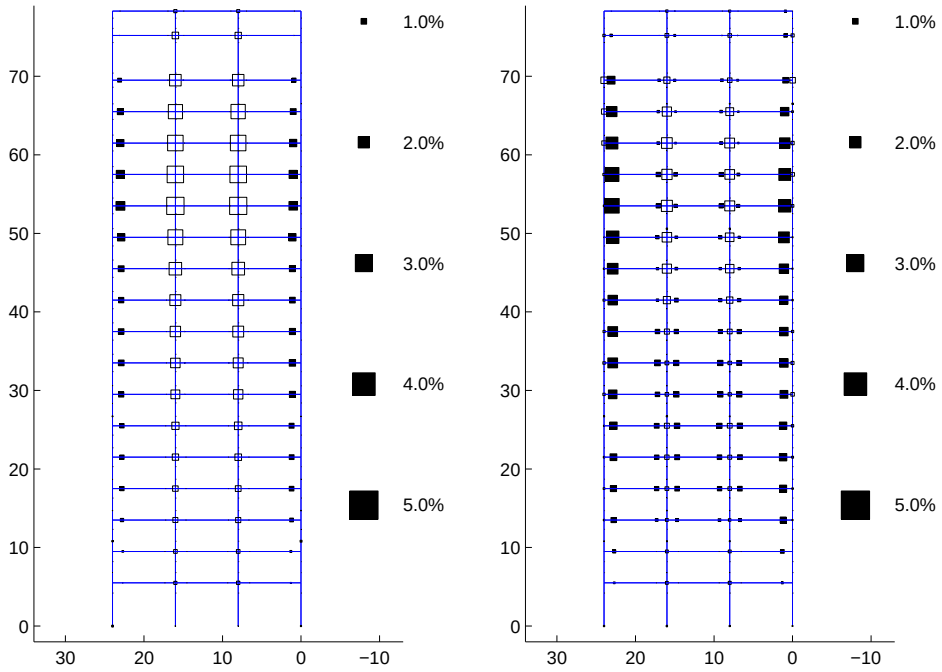

(c) Frame 3

(d) Frame 4

Figure H.34: Plastic Rotations (Black:Beam-Columns White:Panel Zones) in Building 3A Frames 1-4: Iran Earthquake (Tabas Record Strong Component in Y Direction)

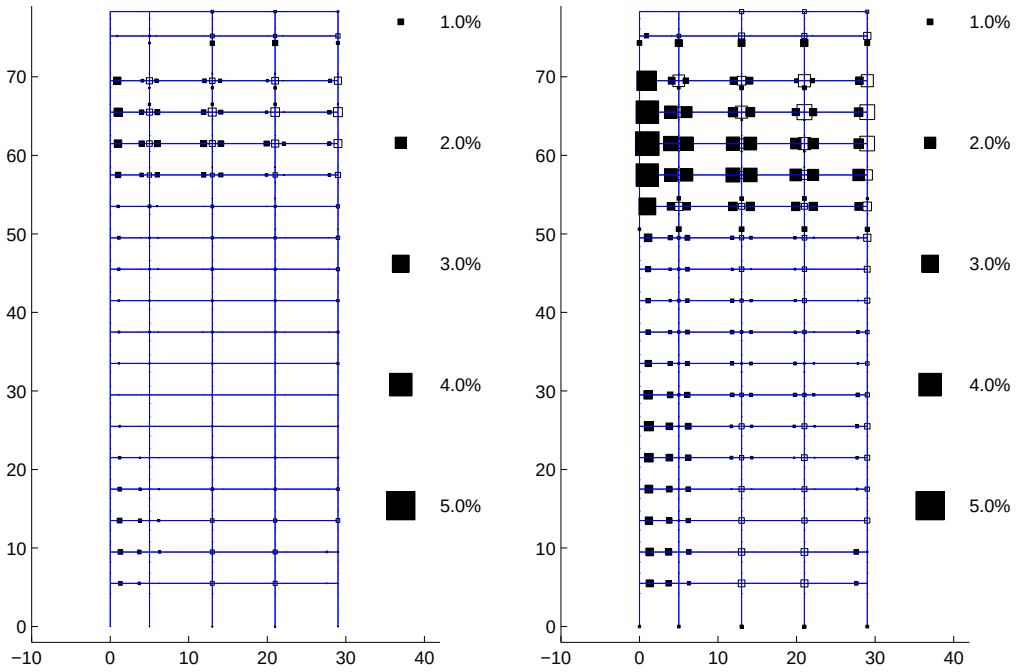

(a) Frame 1

(b) Frame 2

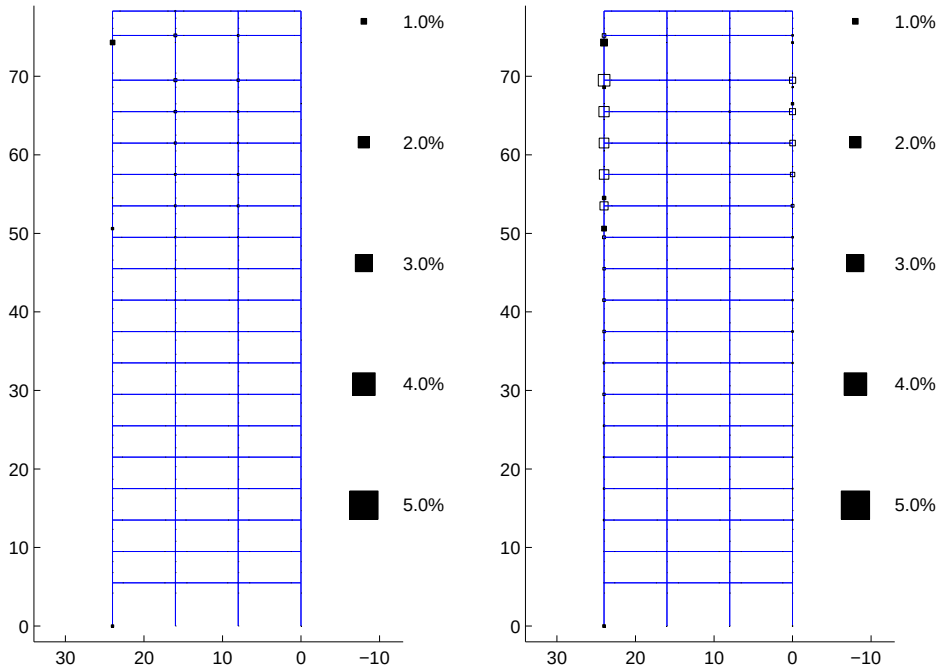

(c) Frame 3

(d) Frame 4

Figure H.35: Plastic Rotations (Black:Beam-Columns White:Panel Zones) in Building 3A Frames 1-4: Kobe Earthquake (Takatori Record Strong Component in X Direction)

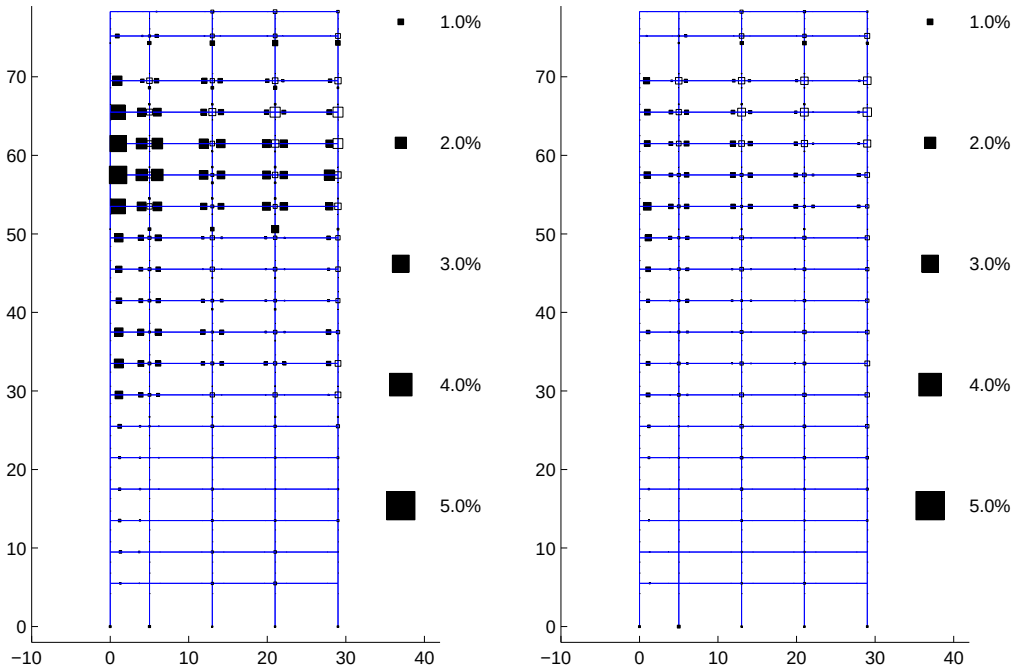

(a) Frame 1

(b) Frame 2

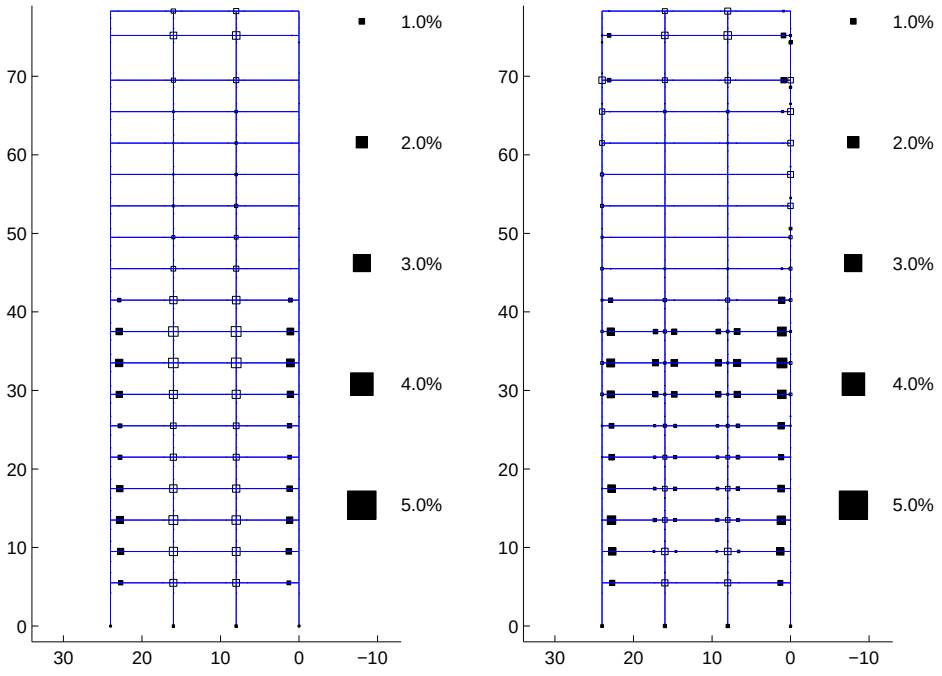

(c) Frame 3

(d) Frame 4

Figure H.36: Plastic Rotations (Black:Beam-Columns White:Panel Zones) in Building 3A Frames 1-4: Kobe Earthquake (Takatori Record Strong Component in Y Direction)

Table H.21: Building 3A Moment Frame Beam Plastic Rotations (Major Axis Bending)

Ground Motion	**Moment Frame Beam Plastic Rotations (Major Axis Bending)**						
	$\leqslant$ 0.1%	**(0.1-1]%**	**(1-2]%**	**(2-3]%**	**(3-4]%**	**(4-5]%**	**(5-6]%**
Northridge Sylmar $[X]^*$	421	107	4	0	0	0	0
Northridge Sylmar $[Y]^{**}$	446	82	4	0	0	0	0
Iran Tabas $[X]^*$	360	154	18	0	0	0	0
Iran Tabas $[Y]^{**}$	236	227	63	6	0	0	0
Kobe Takatori $[X]^*$	355	120	41	12	3	1	0
Kobe Takatori $[Y]^{**}$	272	185	69	5	1	0	0

** Strong component in building X direction*
*** Strong component in building Y direction*

Table H.22: Building 3A Moment Frame Beam Plastic Rotations (Minor Axis Bending)

Ground Motion	**Moment Frame Beam Plastic Rotations (Minor Axis Bending)**						
	$\leqslant$ 0.1%	**(0.1-1]%**	**(1-2]%**	**(2-3]%**	**(3-4]%**	**(4-5]%**	**(5-6]%**
Northridge Sylmar $[X]^*$	524	8	0	0	0	0	0
Northridge Sylmar $[Y]^{**}$	522	10	0	0	0	0	0
Iran Tabas $[X]^*$	481	51	0	0	0	0	0
Iran Tabas $[Y]^{**}$	412	120	0	0	0	0	0
Kobe Takatori $[X]^*$	439	93	0	0	0	0	0
Kobe Takatori $[Y]^{**}$	405	127	0	0	0	0	0

** Strong component in building X direction*
*** Strong component in building Y direction*

Table H.23: Building 3A Column Plastic Rotations (Major Axis Bending)

Ground Motion	**Column Plastic Rotations (Major Axis Bending)**						
	$\leqslant$ 0.1%	**(0.1-1]%**	**(1-2]%**	**(2-3]%**	**(3-4]%**	**(4-5]%**	**(5-6]%**
Northridge Sylmar $[X]^*$	905	7	0	0	0	0	0
Northridge Sylmar $[Y]^{**}$	907	5	0	0	0	0	0
Iran Tabas $[X]^*$	884	28	0	0	0	0	0
Iran Tabas $[Y]^{**}$	874	38	0	0	0	0	0
Kobe Takatori $[X]^*$	865	44	3	0	0	0	0
Kobe Takatori $[Y]^{**}$	845	66	1	0	0	0	0

** Strong component in building X direction*
*** Strong component in building Y direction*

Table H.24: Building 3A Column Plastic Rotations (Minor Axis Bending)

Ground Motion	**Column Plastic Rotations (Minor Axis Bending)**						
	$\leqslant$ 0.1%	**(0.1-1]%**	**(1-2]%**	**(2-3]%**	**(3-4]%**	**(4-5]%**	**(5-6]%**
Northridge Sylmar $[X]^*$	601	7	0	0	0	0	0
Northridge Sylmar $[Y]^{**}$	602	6	0	0	0	0	0
Iran Tabas $[X]^*$	596	12	0	0	0	0	0
Iran Tabas $[Y]^{**}$	587	21	0	0	0	0	0
Kobe Takatori $[X]^*$	575	33	0	0	0	0	0
Kobe Takatori $[Y]^{**}$	559	49	0	0	0	0	0

** Strong component in building X direction*
*** Strong component in building Y direction*

Table H.25: Building 3A Panel Zone Plastic Rotations

Ground Motion	**Panel Zone Plastic Rotations**						
	$\leqslant$ 0.1%	**(0.1-1]%**	**(1-2]%**	**(2-3]%**	**(3-4]%**	**(4-5]%**	**(5-6]%**
Northridge Sylmar $[X]^{*}$	174	164	4	0	0	0	0
Northridge Sylmar $[Y]^{**}$	178	164	0	0	0	0	0
Iran Tabas $[X]^{*}$	166	161	15	0	0	0	0
Iran Tabas $[Y]^{**}$	122	152	54	12	2	0	0
Kobe Takatori $[X]^{*}$	173	130	31	8	0	0	0
Kobe Takatori $[Y]^{**}$	134	159	49	0	0	0	0

** Strong component in building X direction*
*** Strong component in building Y direction*

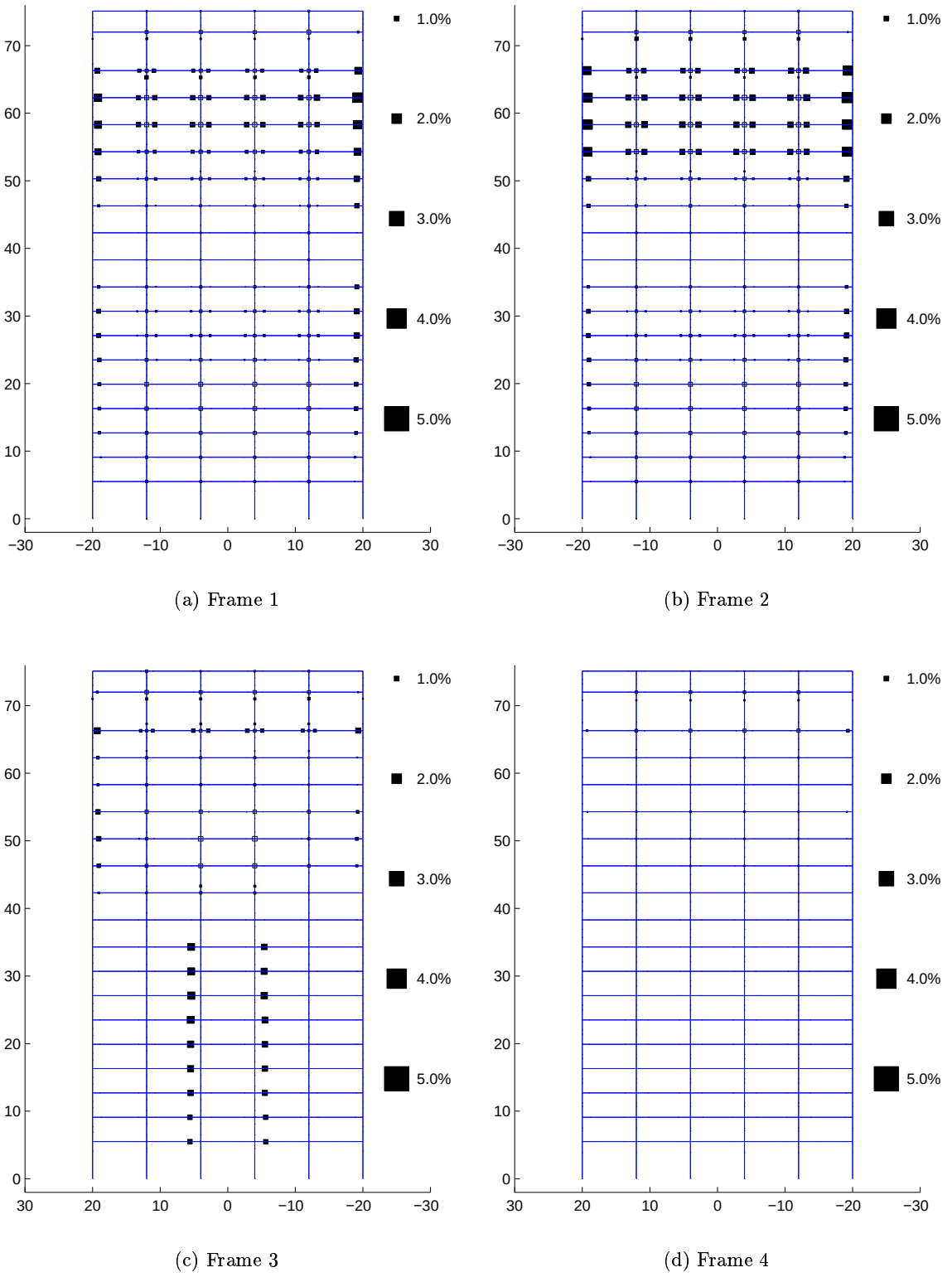

(a) Frame 1

(b) Frame 2

(c) Frame 3

(d) Frame 4

Figure H.37: Plastic Rotations (Black:Beam-Columns White:Panel Zones) in Building 4 Frames 1-4: Northridge Earthquake (Sylmar Record Strong Component in X Direction)

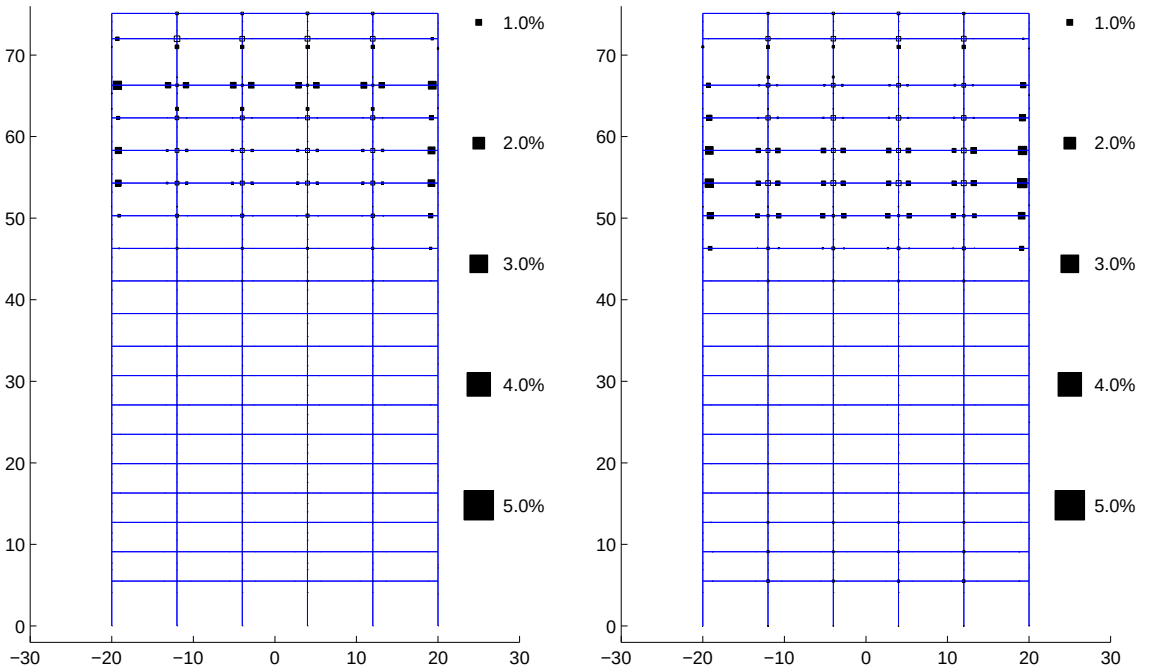

(a) Frame 1

(b) Frame 2

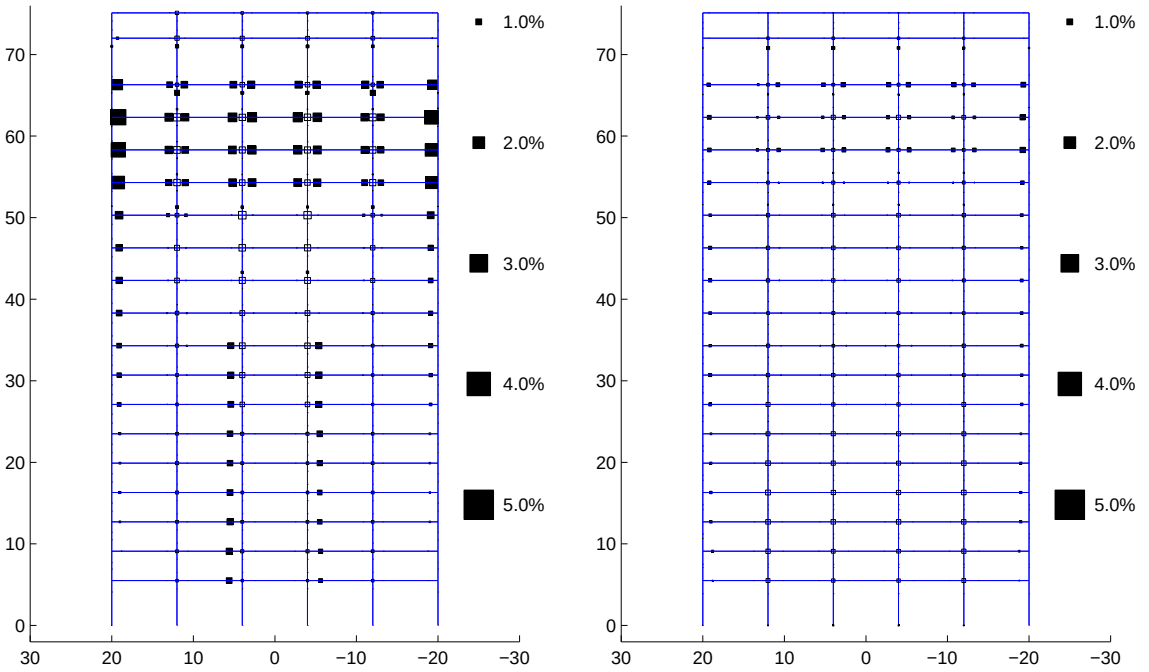

(c) Frame 3

(d) Frame 4

Figure H.38: Plastic Rotations (Black:Beam-Columns White:Panel Zones) in Building 4 Frames 1-4: Northridge Earthquake (Sylmar Record Strong Component in Y Direction)

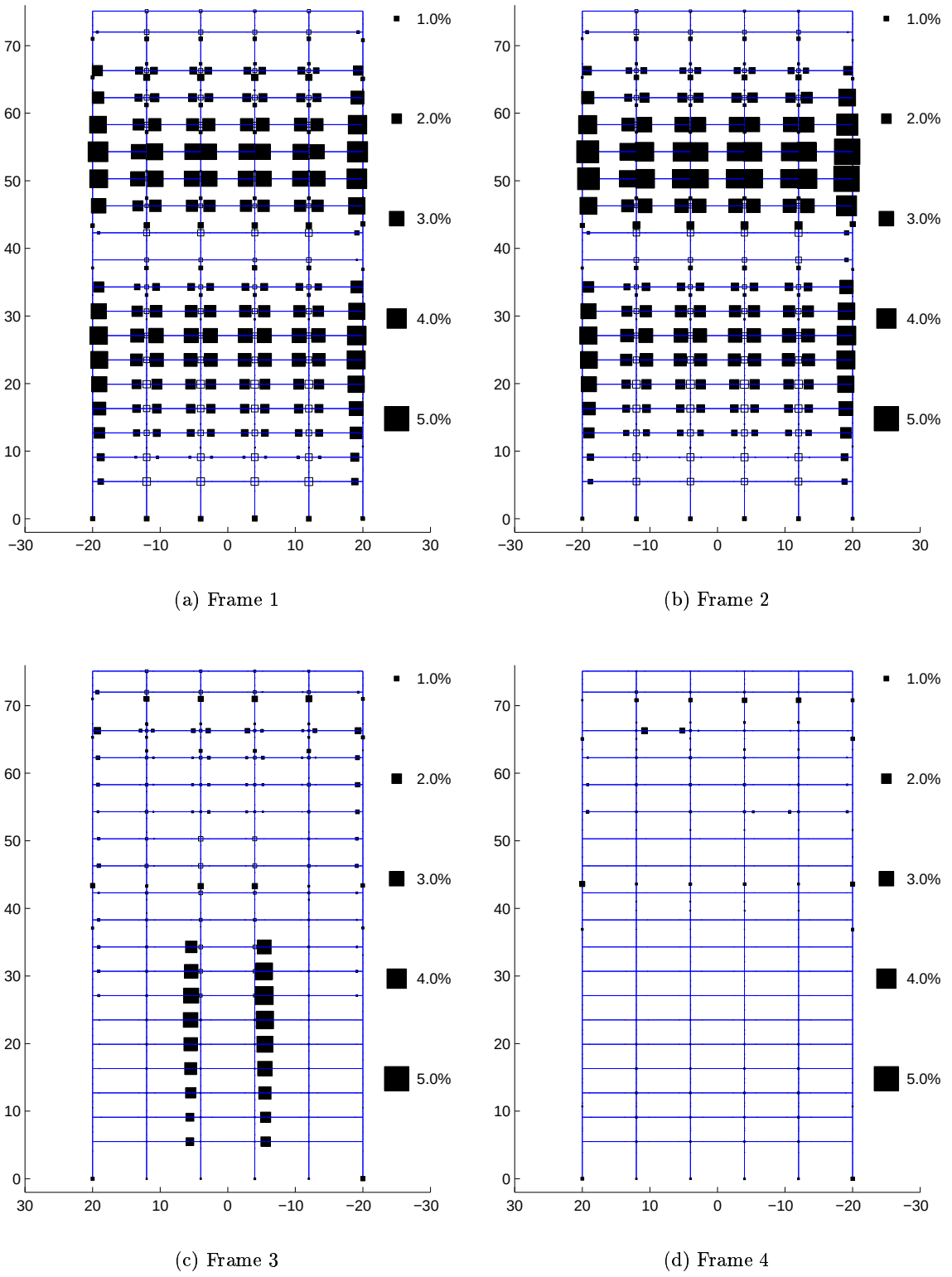

(a) Frame 1

(b) Frame 2

(c) Frame 3

(d) Frame 4

Figure H.39: Plastic Rotations (Black:Beam-Columns White:Panel Zones) in Building 4 Frames 1-4: Iran Earthquake (Tabas Record Strong Component in X Direction)

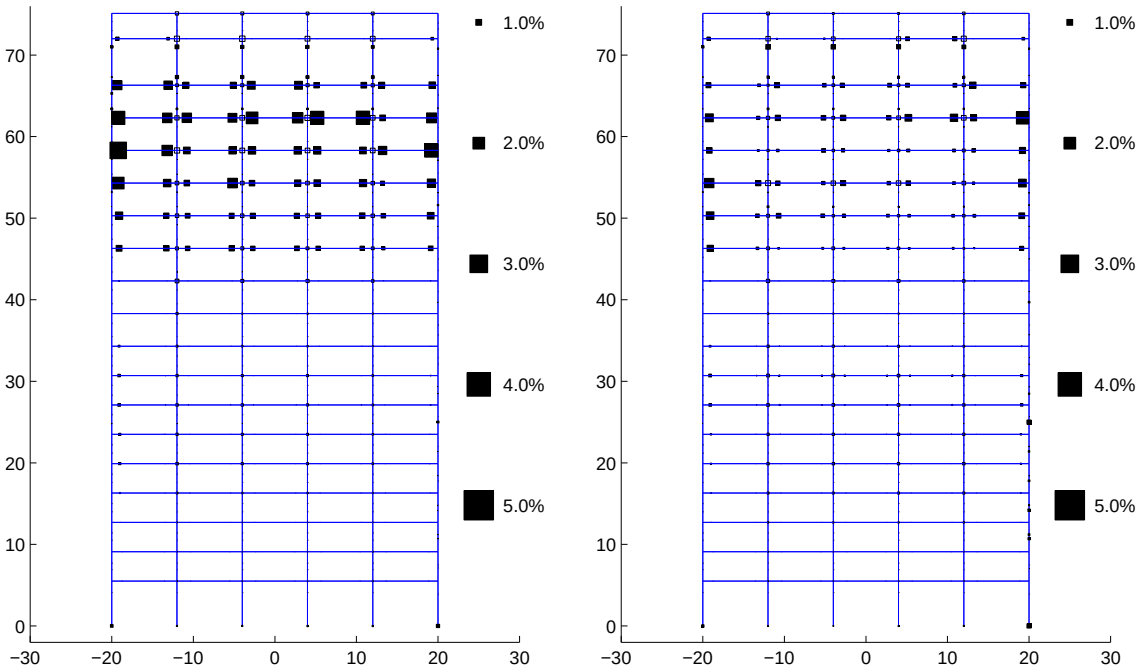

(a) Frame 1

(b) Frame 2

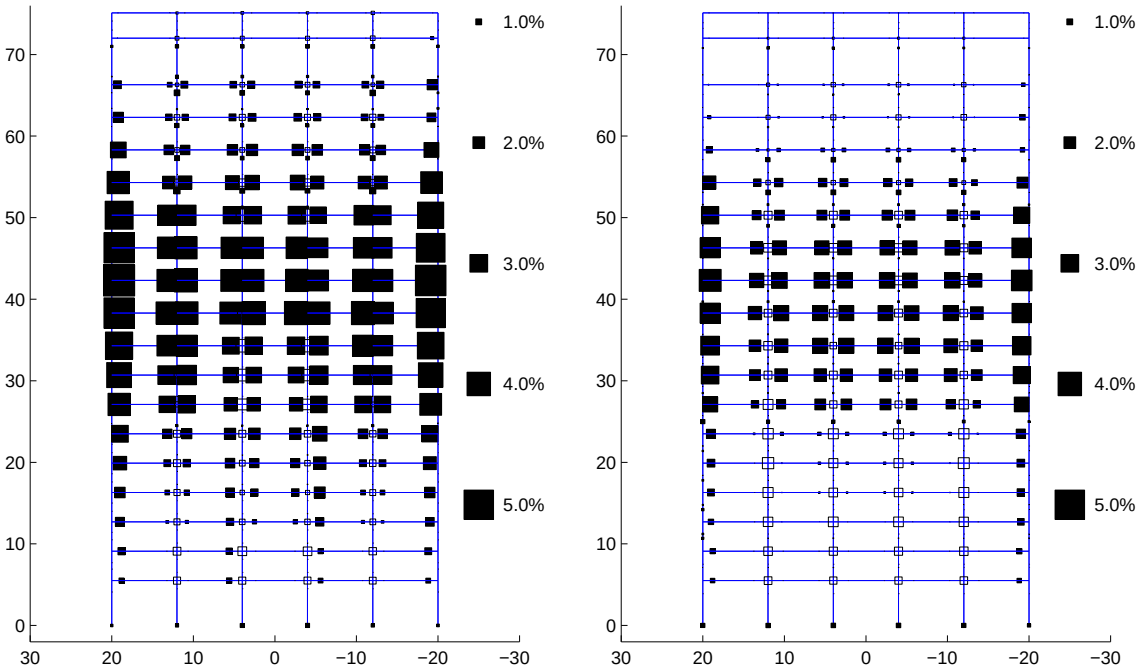

(c) Frame 3

(d) Frame 4

Figure H.40: Plastic Rotations (Black:Beam-Columns White:Panel Zones) in Building 4 Frames 1-4: Iran Earthquake (Tabas Record Strong Component in Y Direction)

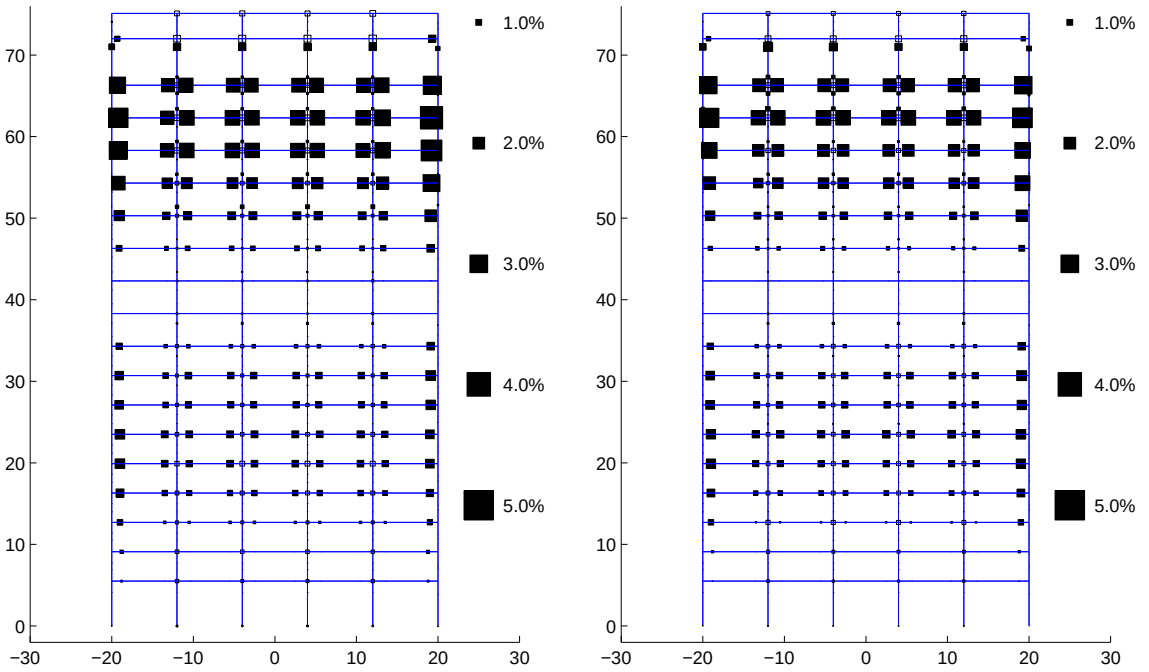

(a) Frame 1

(b) Frame 2

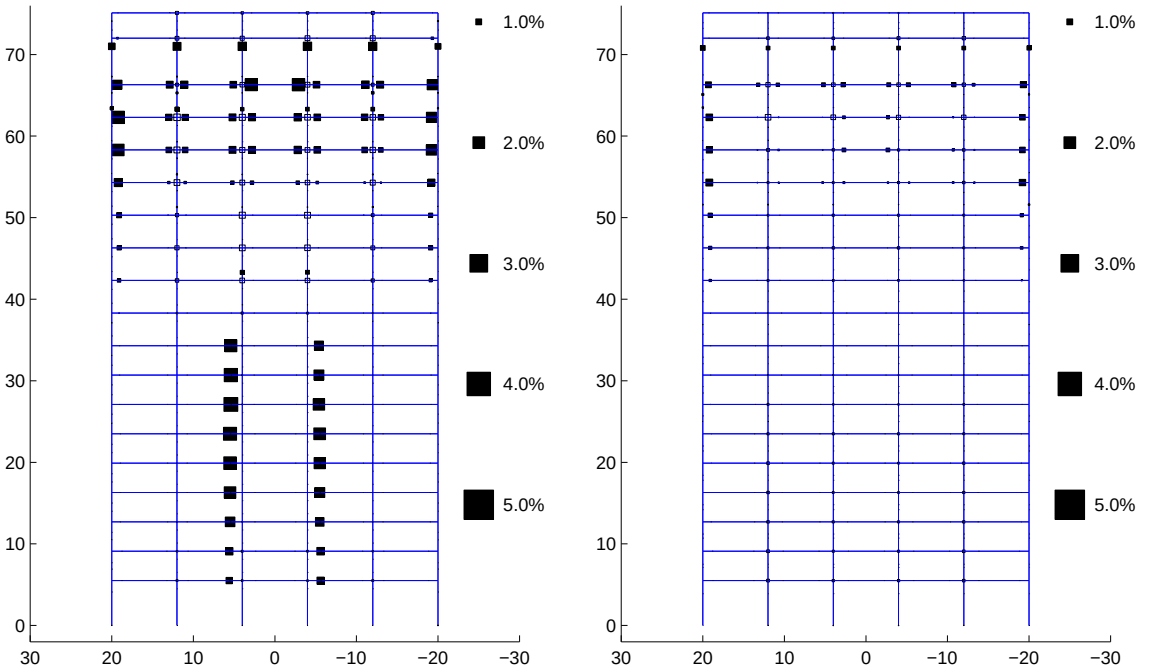

(c) Frame 3

(d) Frame 4

Figure H.41: Plastic Rotations (Black:Beam-Columns White:Panel Zones) in Building 4 Frames 1-4: Kobe Earthquake (Takatori Record Strong Component in X Direction)

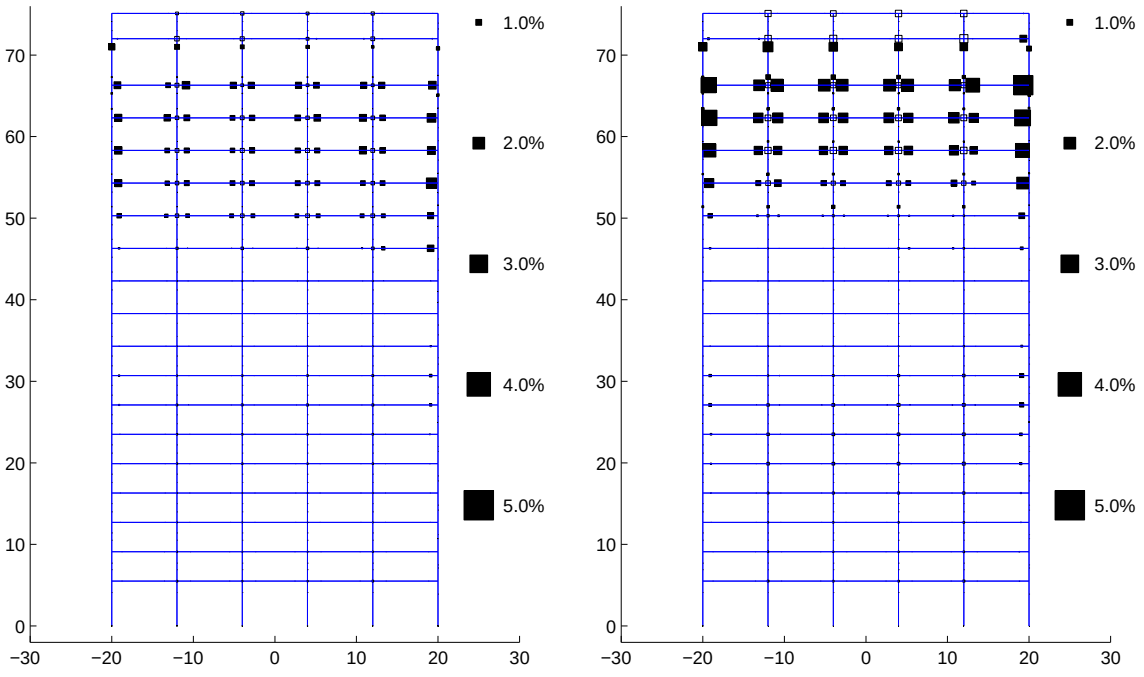

(a) Frame 1

(b) Frame 2

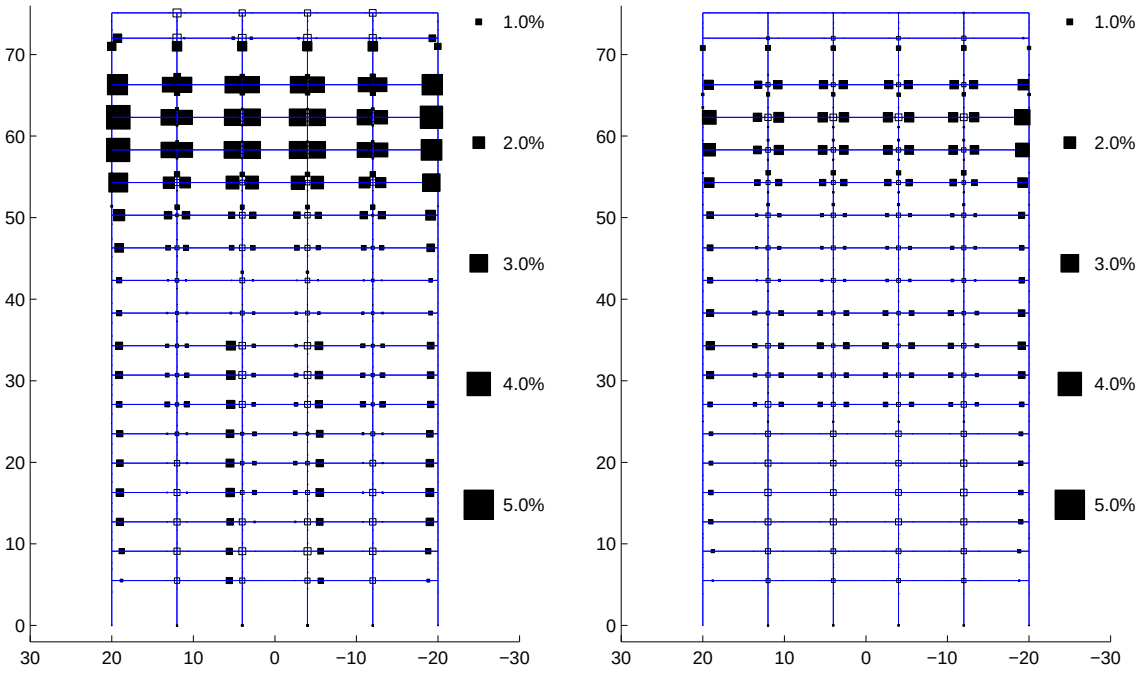

(c) Frame 3

(d) Frame 4

Figure H.42: Plastic Rotations (Black:Beam-Columns White:Panel Zones) in Building 4 Frames 1-4: Kobe Earthquake (Takatori Record Strong Component in Y Direction)

Table H.26: Building 4 Moment Frame Beam Plastic Rotations (Major Axis Bending)

Ground Motion	**Moment Frame Beam Plastic Rotations (Major Axis Bending)**						
	$\leqslant$ 0.1%	**(0.1-1]%**	**(1-2]%**	**(2-3]%**	**(3-4]%**	**(4-5]%**	**(5-6]%**
Northridge Sylmar $[X]^{*}$	515	194	50	1	0	0	0
Northridge Sylmar $[Y]^{**}$	493	213	48	6	0	0	0
Iran Tabas $[X]^{*}$	397	92	103	105	54	7	2
Iran Tabas $[Y]^{**}$	305	183	128	82	50	8	4
Kobe Takatori $[X]^{*}$	396	143	159	55	7	0	0
Kobe Takatori $[Y]^{**}$	351	238	119	44	7	1	0

** Strong component in building X direction*
*** Strong component in building Y direction*

Table H.27: Building 4 Moment Frame Beam Plastic Rotations (Minor Axis Bending)

Ground Motion	**Moment Frame Beam Plastic Rotations (Minor Axis Bending)**						
	$\leqslant$ 0.1%	**(0.1-1]%**	**(1-2]%**	**(2-3]%**	**(3-4]%**	**(4-5]%**	**(5-6]%**
Northridge Sylmar $[X]^{*}$	681	79	0	0	0	0	0
Northridge Sylmar $[Y]^{**}$	627	133	0	0	0	0	0
Iran Tabas $[X]^{*}$	559	201	0	0	0	0	0
Iran Tabas $[Y]^{**}$	454	306	0	0	0	0	0
Kobe Takatori $[X]^{*}$	574	186	0	0	0	0	0
Kobe Takatori $[Y]^{**}$	511	249	0	0	0	0	0

** Strong component in building X direction*
*** Strong component in building Y direction*

Table H.28: Building 4 Column Plastic Rotations (Major Axis Bending)

Ground Motion	**Column Plastic Rotations (Major Axis Bending)**						
	$\leqslant$ 0.1%	**(0.1-1]%**	**(1-2]%**	**(2-3]%**	**(3-4]%**	**(4-5]%**	**(5-6]%**
Northridge Sylmar $[X]^*$	1420	52	0	0	0	0	0
Northridge Sylmar $[Y]^{**}$	1419	53	0	0	0	0	0
Iran Tabas $[X]^*$	1276	180	16	0	0	0	0
Iran Tabas $[Y]^{**}$	1286	184	2	0	0	0	0
Kobe Takatori $[X]^*$	1321	140	11	0	0	0	0
Kobe Takatori $[Y]^{**}$	1336	125	11	0	0	0	0

** Strong component in building X direction*
*** Strong component in building Y direction*

Table H.29: Building 4 Column Plastic Rotations (Minor Axis Bending)

Ground Motion	**Column Plastic Rotations (Minor Axis Bending)**						
	$\leqslant$ 0.1%	**(0.1-1]%**	**(1-2]%**	**(2-3]%**	**(3-4]%**	**(4-5]%**	**(5-6]%**
Northridge Sylmar $[X]^*$	1130	38	0	0	0	0	0
Northridge Sylmar $[Y]^{**}$	1116	52	0	0	0	0	0
Iran Tabas $[X]^*$	998	162	8	0	0	0	0
Iran Tabas $[Y]^{**}$	1048	120	0	0	0	0	0
Kobe Takatori $[X]^*$	1055	106	7	0	0	0	0
Kobe Takatori $[Y]^{**}$	1045	117	6	0	0	0	0

** Strong component in building X direction*
*** Strong component in building Y direction*

Table H.30: Building 4 Panel Zone Plastic Rotations

Ground Motion	**Panel Zone Plastic Rotations**						
	$\leqslant$ 0.1%	**(0.1-1]%**	**(1-2]%**	**(2-3]%**	**(3-4]%**	**(4-5]%**	**(5-6]%**
Northridge Sylmar $[X]^{*}$	224	232	0	0	0	0	0
Northridge Sylmar $[Y]^{**}$	207	234	15	0	0	0	0
Iran Tabas $[X]^{*}$	171	198	87	0	0	0	0
Iran Tabas $[Y]^{**}$	159	199	93	5	0	0	0
Kobe Takatori $[X]^{*}$	177	270	9	0	0	0	0
Kobe Takatori $[Y]^{**}$	163	236	57	0	0	0	0

** Strong component in building X direction*
*** Strong component in building Y direction*

Appendix I Ground Motion Analysis of Buildings: Floor Diaphragm Stress Maps

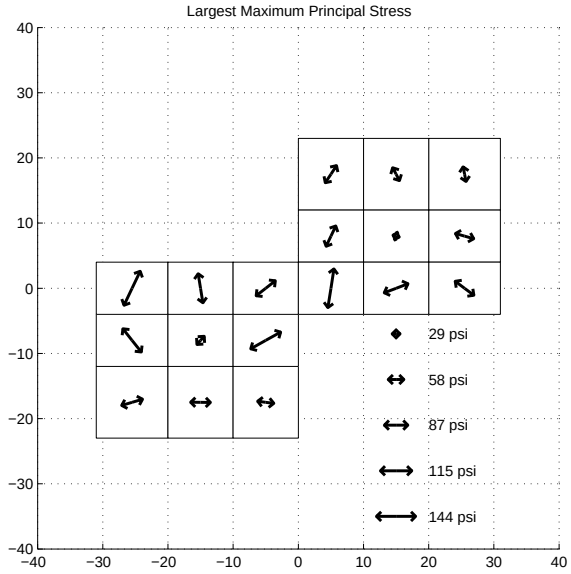

(a) Maximum Principal Stress (Tension)

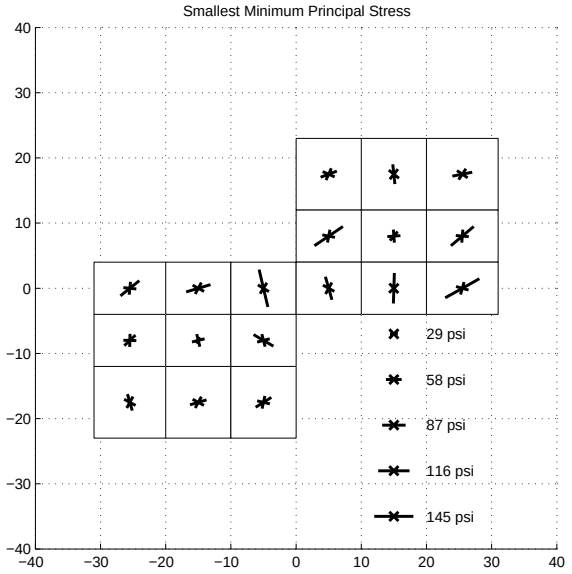

(b) Maximum Principal Stress (Compression)

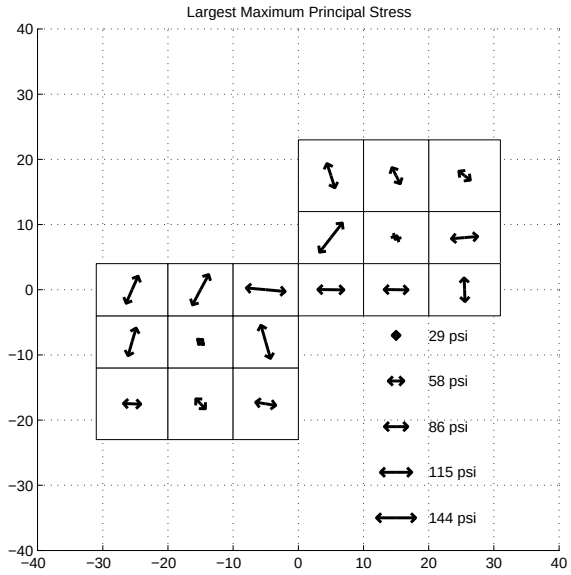

(c) Maximum Principal Stress (Tension)

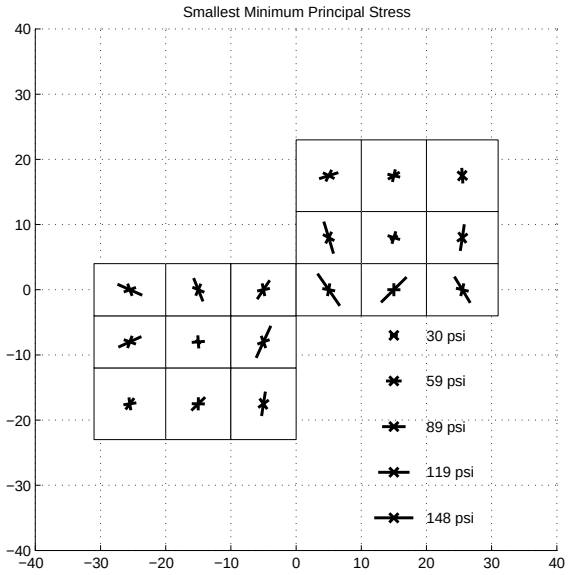

(d) Maximum Principal Stress (Compression)

Figure I.1: Floor Diaphragm Peak Stresses in Building 1, Second Floor (a) & (b) and Ninth Floor (c) & (d): Northridge Earthquake (Sylmar Record Strong Component in X Direction)

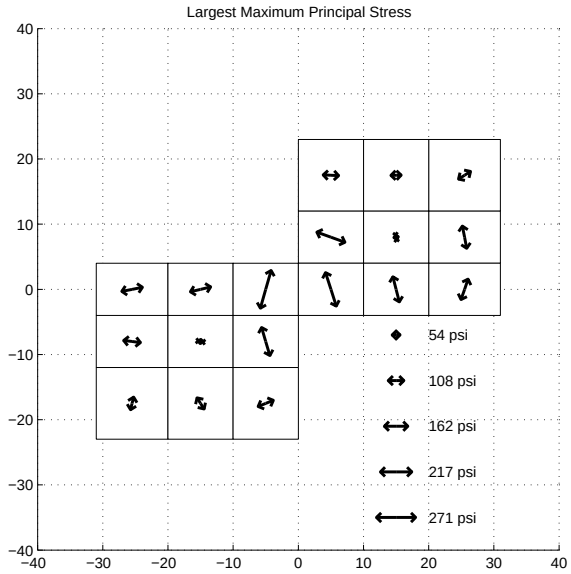

(a) Maximum Principal Stress (Tension)

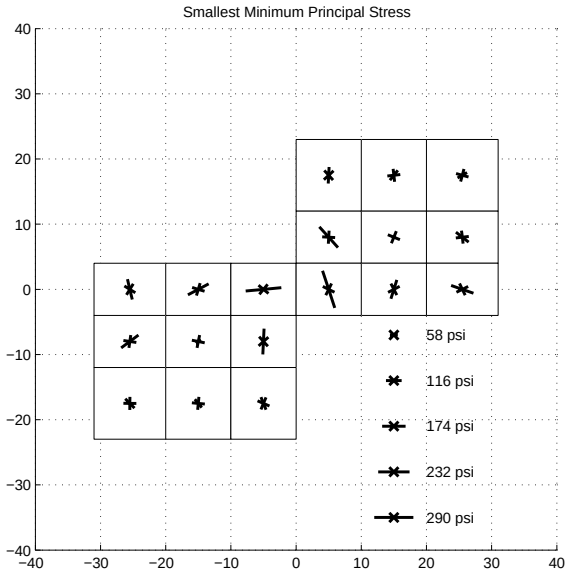

(b) Maximum Principal Stress (Compression)

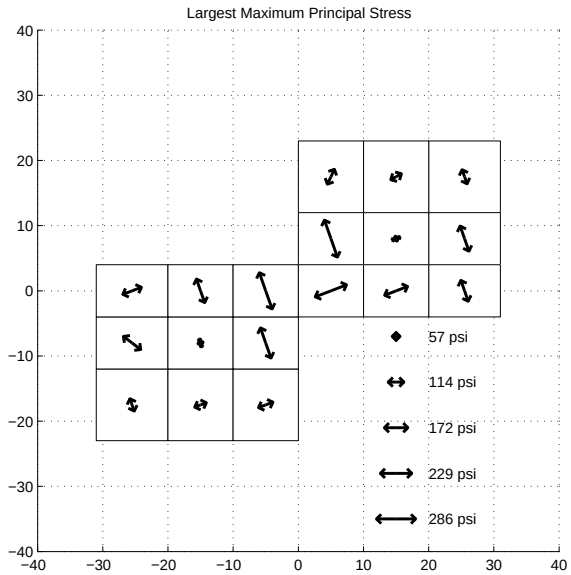

(c) Maximum Principal Stress (Tension)

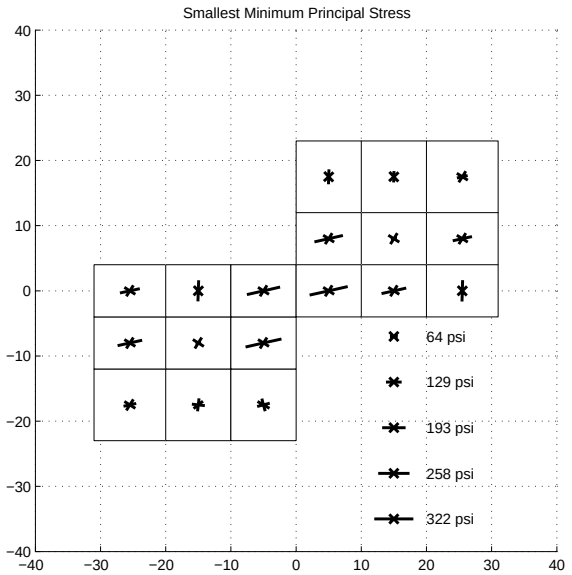

(d) Maximum Principal Stress (Compression)

Figure I.2: Floor Diaphragm Peak Stresses in Building 1, Lower Mechanical Floor (a) & (b) and All Floors (c) & (d): Northridge Earthquake (Sylmar Record Strong Component in X Direction)

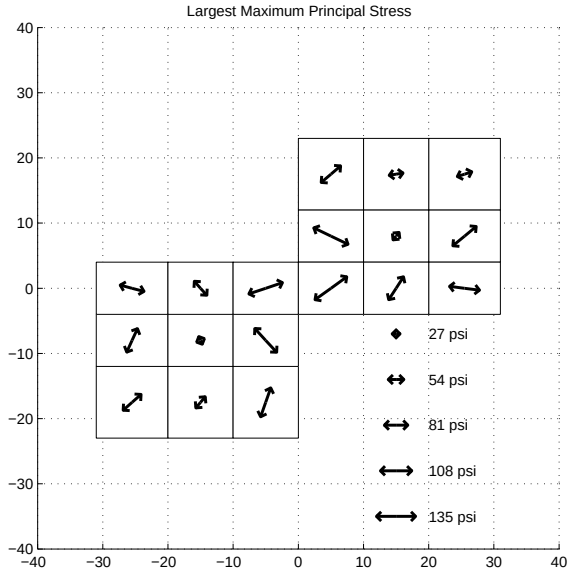

(a) Maximum Principal Stress (Tension)

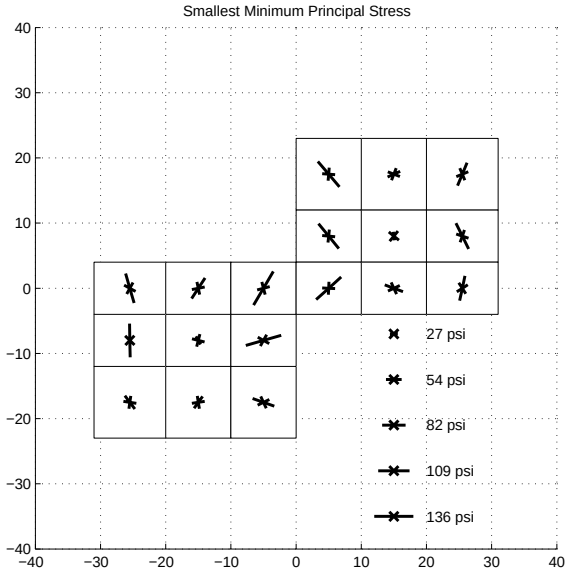

(b) Maximum Principal Stress (Compression)

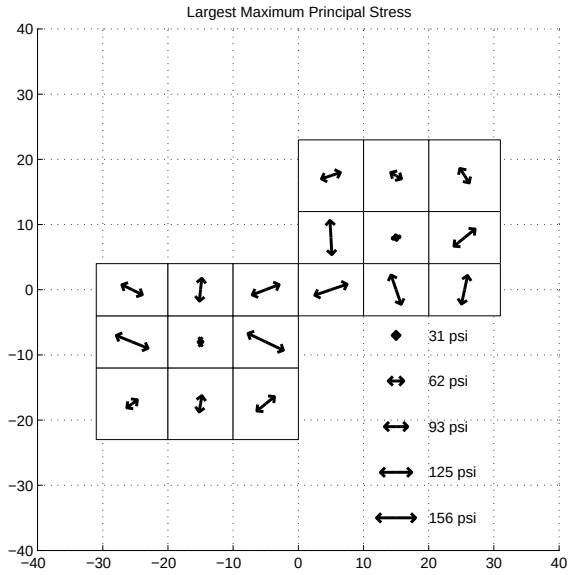

(c) Maximum Principal Stress (Tension)

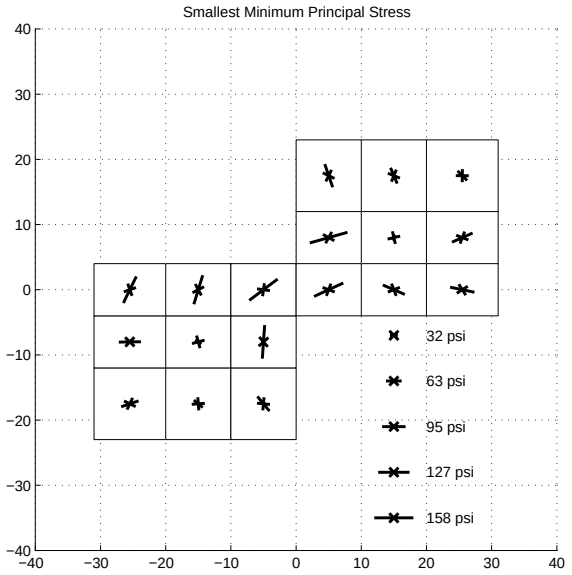

(d) Maximum Principal Stress (Compression)

Figure I.3: Floor Diaphragm Peak Stresses in Building 1, Second Floor (a) & (b) and Ninth Floor (c) & (d): Northridge Earthquake (Sylmar Record Strong Component in Y Direction)

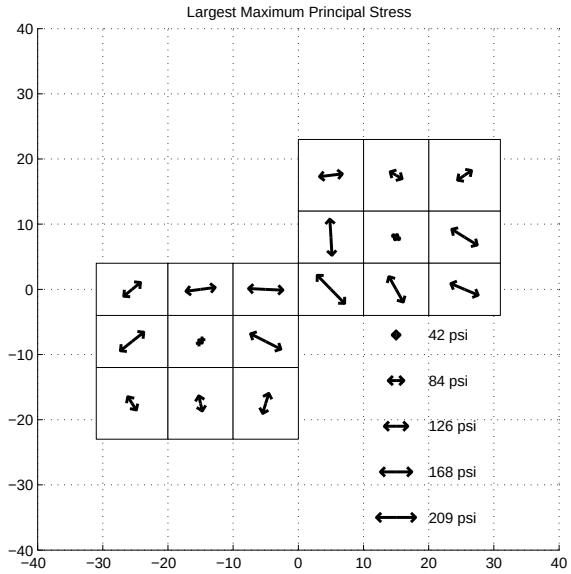

(a) Maximum Principal Stress (Tension)

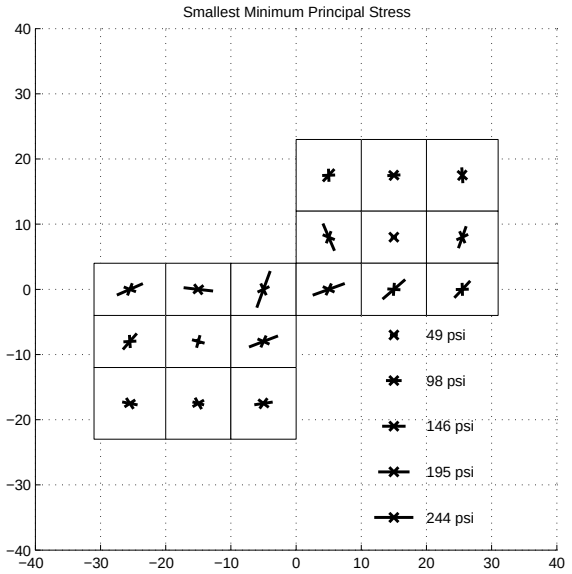

(b) Maximum Principal Stress (Compression)

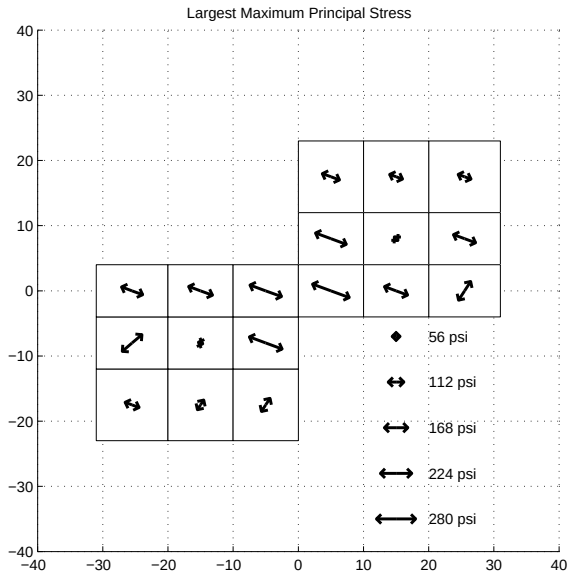

(c) Maximum Principal Stress (Tension)

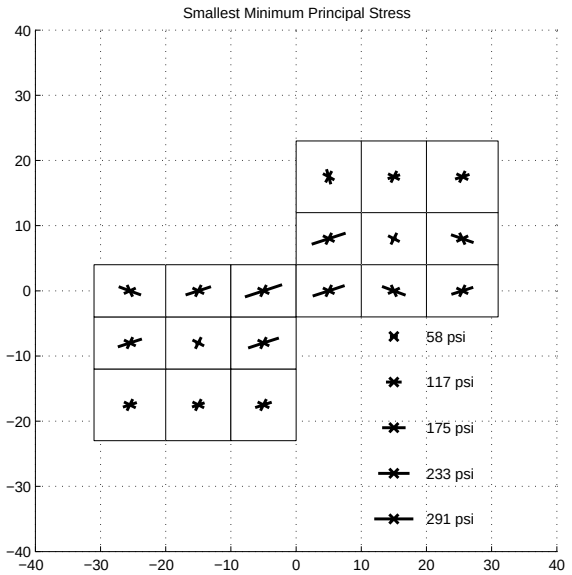

(d) Maximum Principal Stress (Compression)

Figure I.4: Floor Diaphragm Peak Stresses in Building 1, Lower Mechanical Floor (a) & (b) and All Floors (c) & (d): Northridge Earthquake (Sylmar Record Strong Component in Y Direction)

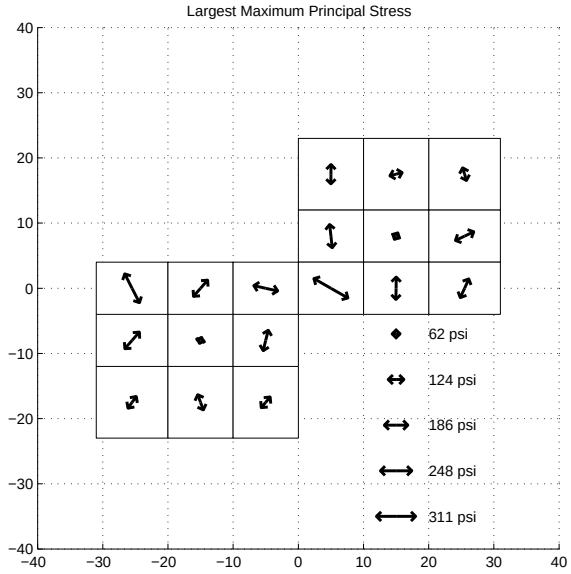

(a) Maximum Principal Stress (Tension)

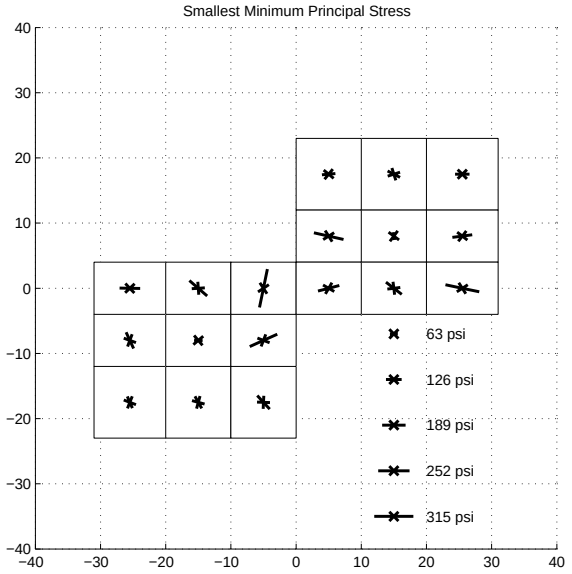

(b) Maximum Principal Stress (Compression)

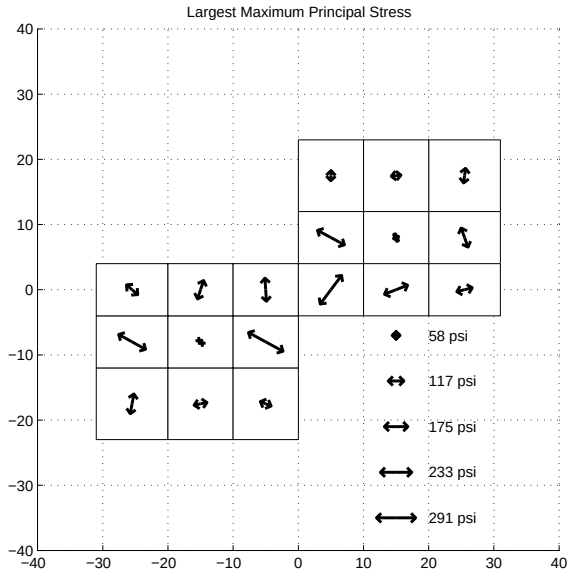

(c) Maximum Principal Stress (Tension)

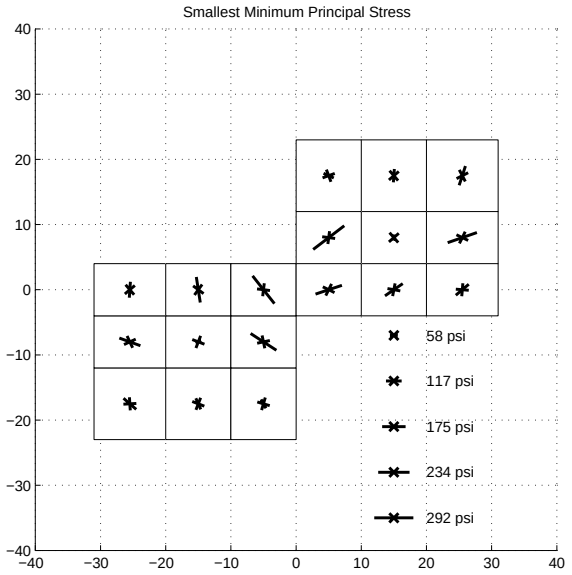

(d) Maximum Principal Stress (Compression)

Figure I.5: Floor Diaphragm Peak Stresses in Building 1, Second Floor (a) & (b) and Ninth Floor (c) & (d): Iran Earthquake (Tabas Record Strong Component in X Direction)

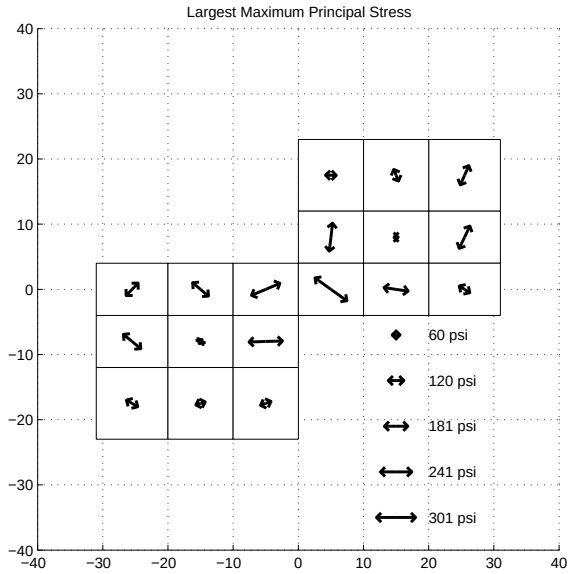

(a) Maximum Principal Stress (Tension)

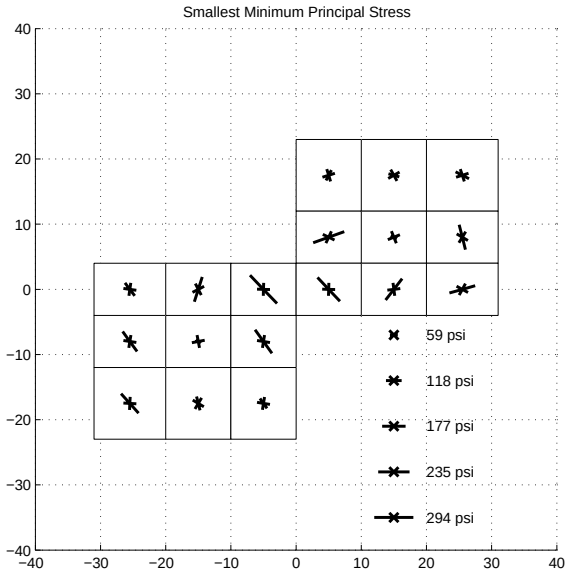

(b) Maximum Principal Stress (Compression)

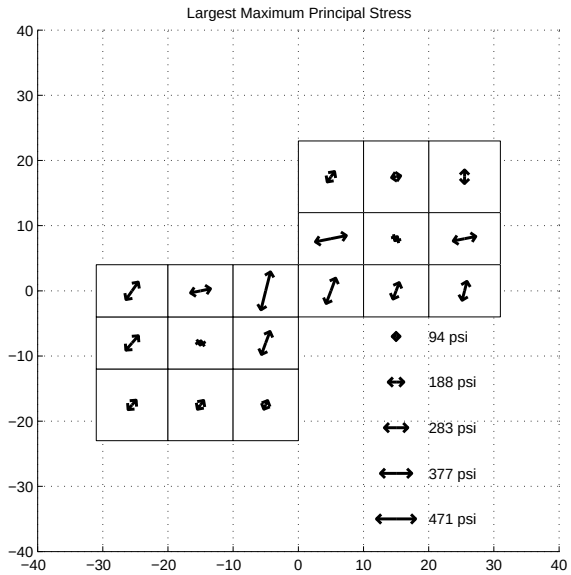

(c) Maximum Principal Stress (Tension)

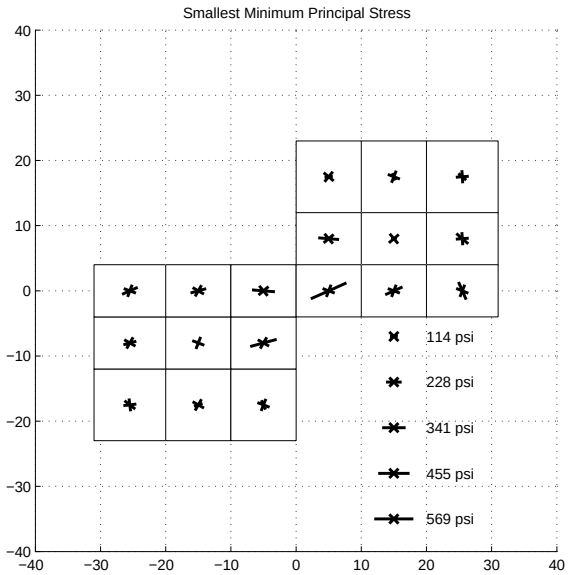

(d) Maximum Principal Stress (Compression)

Figure I.6: Floor Diaphragm Peak Stresses in Building 1, Lower Mechanical Floor (a) & (b) and All Floors (c) & (d): Iran Earthquake (Tabas Record Strong Component in X Direction)

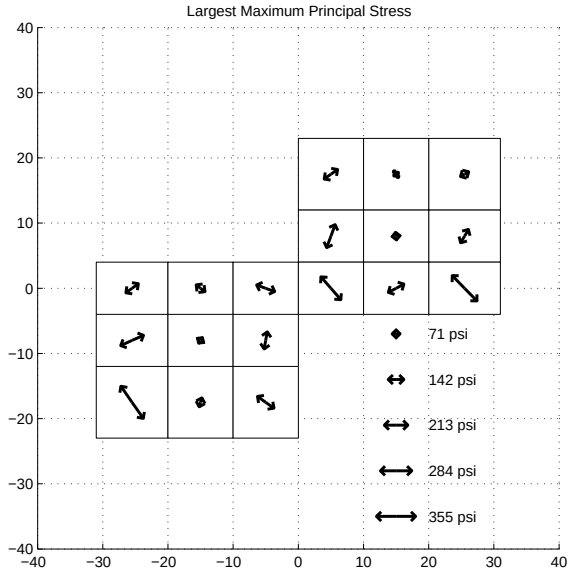

(a) Maximum Principal Stress (Tension)

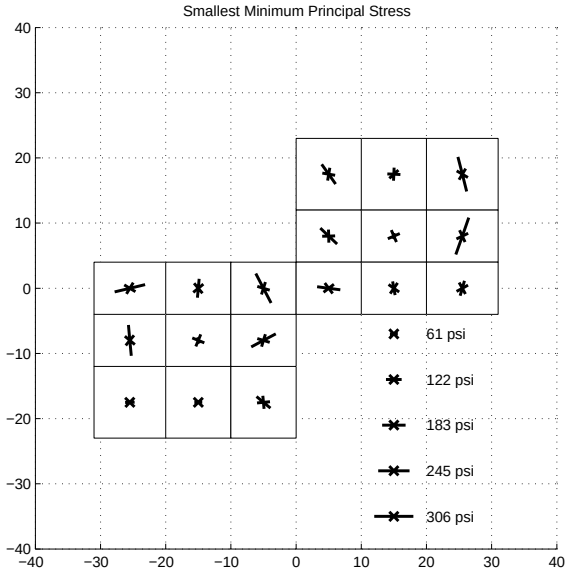

(b) Maximum Principal Stress (Compression)

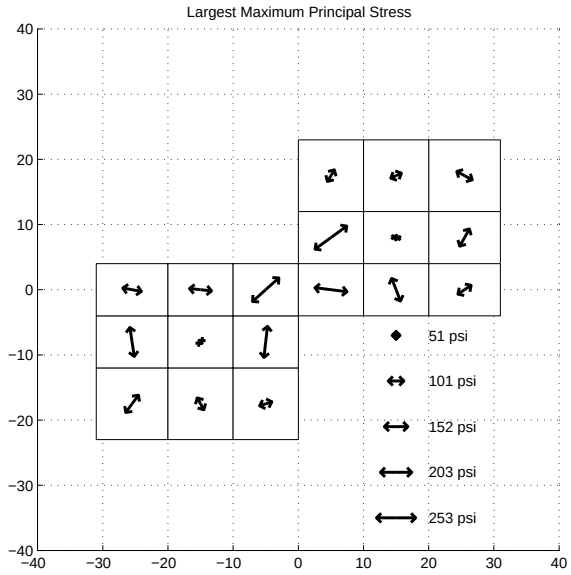

(c) Maximum Principal Stress (Tension)

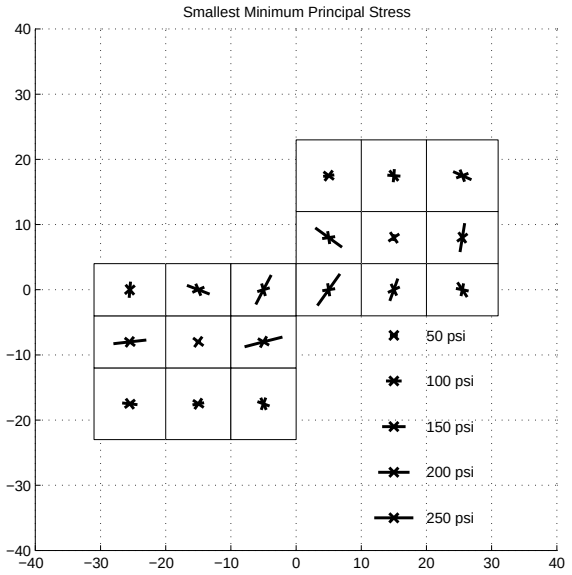

(d) Maximum Principal Stress (Compression)

Figure I.7: Floor Diaphragm Peak Stresses in Building 1, Second Floor (a) & (b) and Ninth Floor (c) & (d): Iran Earthquake (Tabas Record Strong Component in Y Direction)

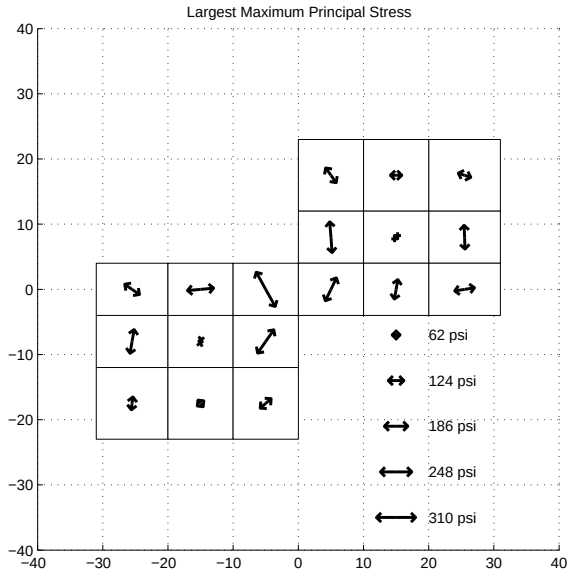

(a) Maximum Principal Stress (Tension)

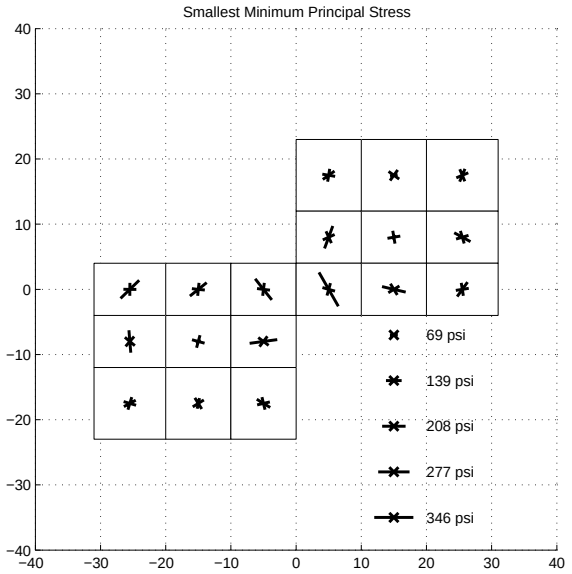

(b) Maximum Principal Stress (Compression)

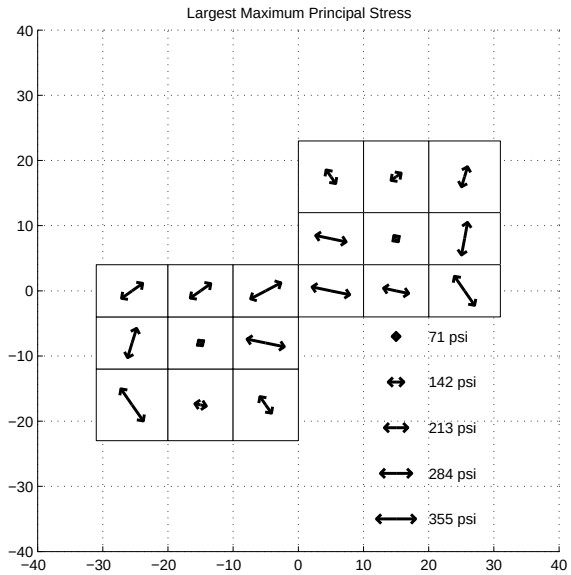

(c) Maximum Principal Stress (Tension)

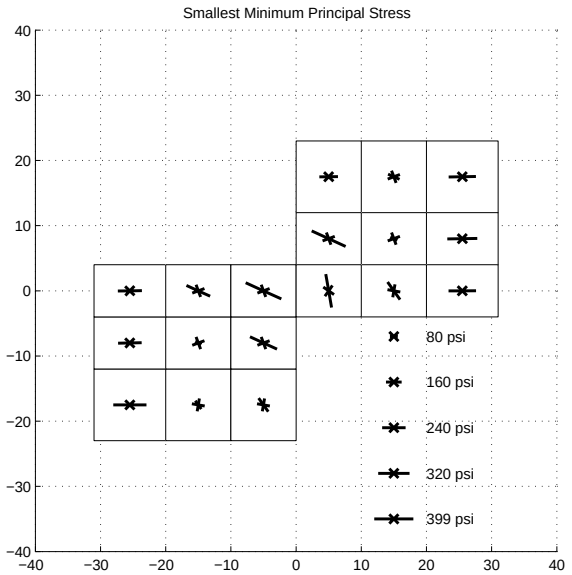

(d) Maximum Principal Stress (Compression)

Figure I.8: Floor Diaphragm Peak Stresses in Building 1, Lower Mechanical Floor (a) & (b) and All Floors (c) & (d): Iran Earthquake (Tabas Record Strong Component in Y Direction)

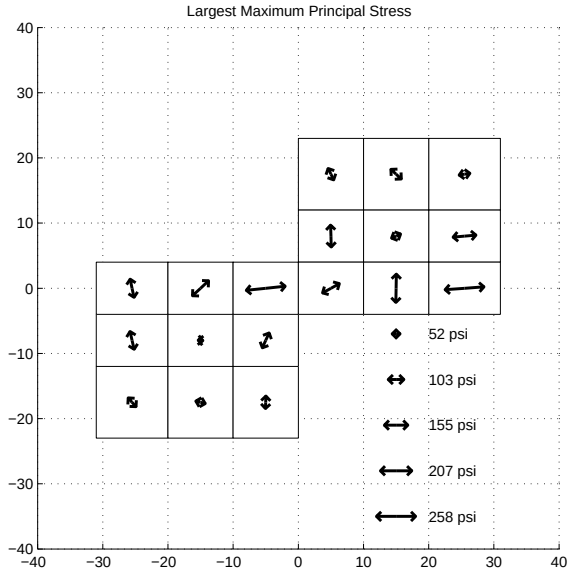

(a) Maximum Principal Stress (Tension)

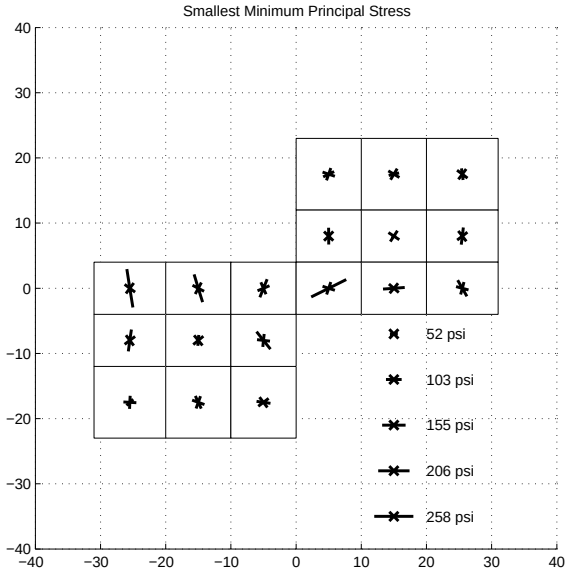

(b) Maximum Principal Stress (Compression)

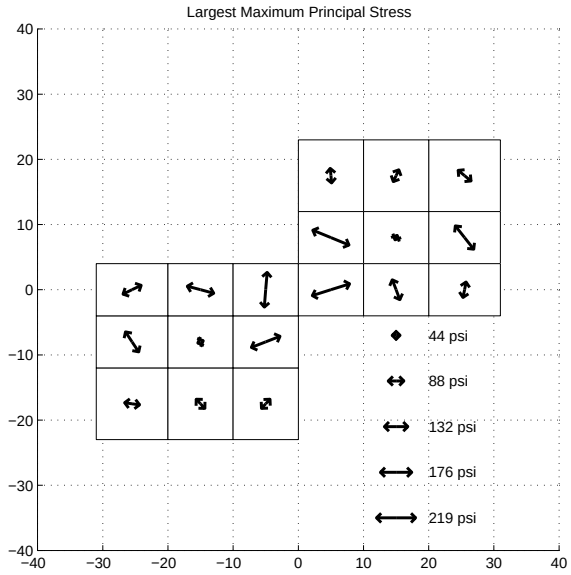

(c) Maximum Principal Stress (Tension)

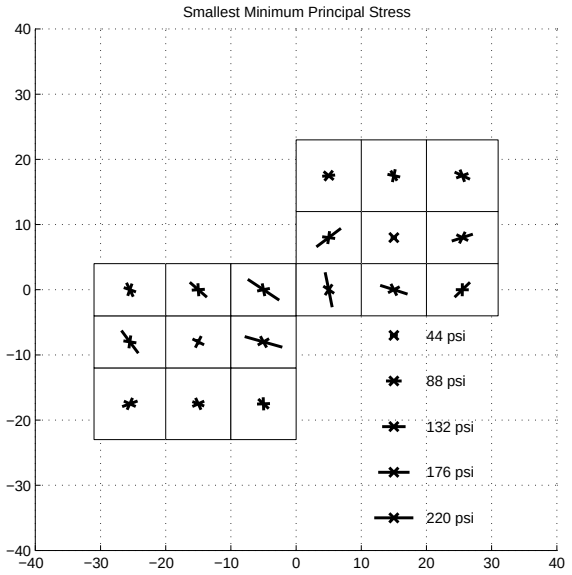

(d) Maximum Principal Stress (Compression)

Figure I.9: Floor Diaphragm Peak Stresses in Building 1, Second Floor (a) & (b) and Ninth Floor (c) & (d): Kobe Earthquake (Takatori Record Strong Component in X Direction)

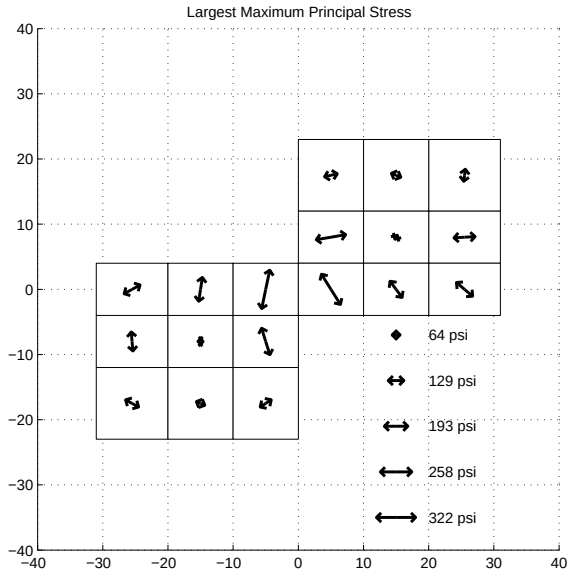

(a) Maximum Principal Stress (Tension)

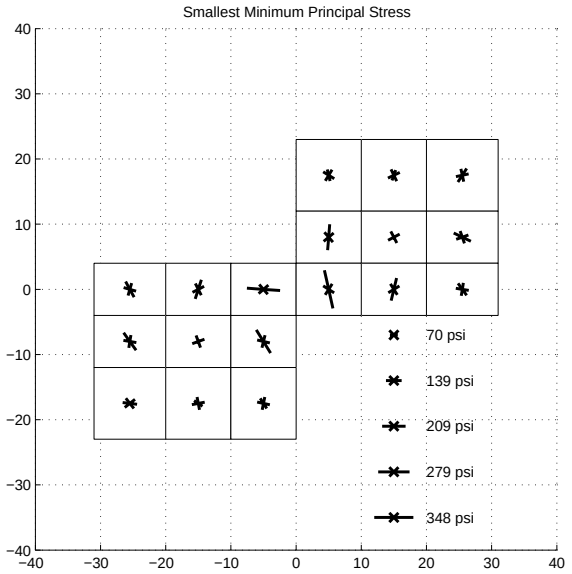

(b) Maximum Principal Stress (Compression)

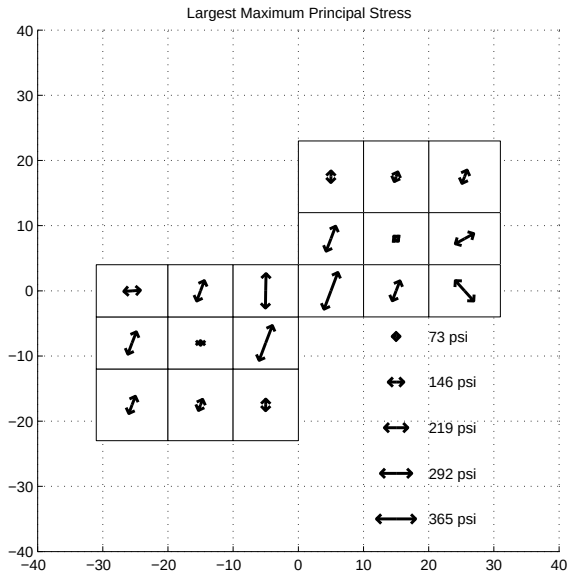

(c) Maximum Principal Stress (Tension)

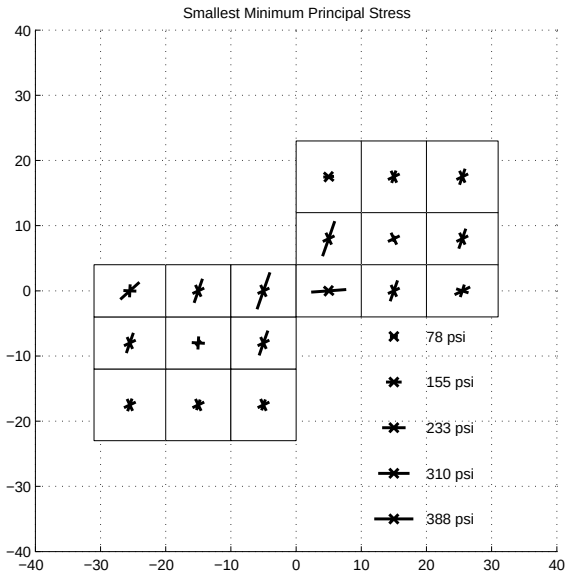

(d) Maximum Principal Stress (Compression)

Figure I.10: Floor Diaphragm Peak Stresses in Building 1, Lower Mechanical Floor (a) & (b) and All Floors (c) & (d): Kobe Earthquake (Takatori Record Strong Component in X Direction)

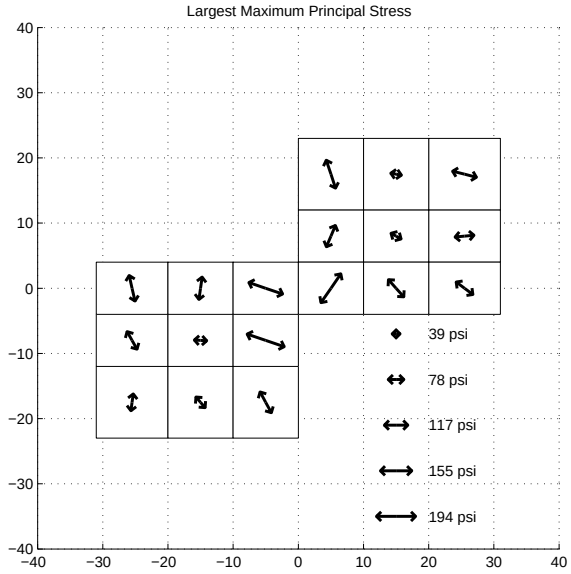

(a) Maximum Principal Stress (Tension)

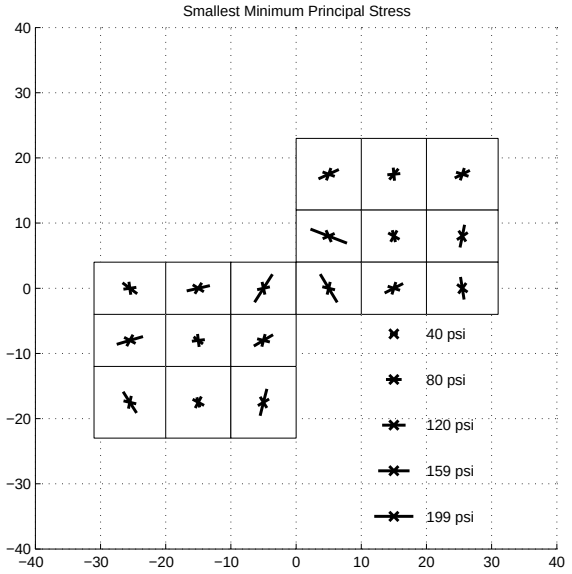

(b) Maximum Principal Stress (Compression)

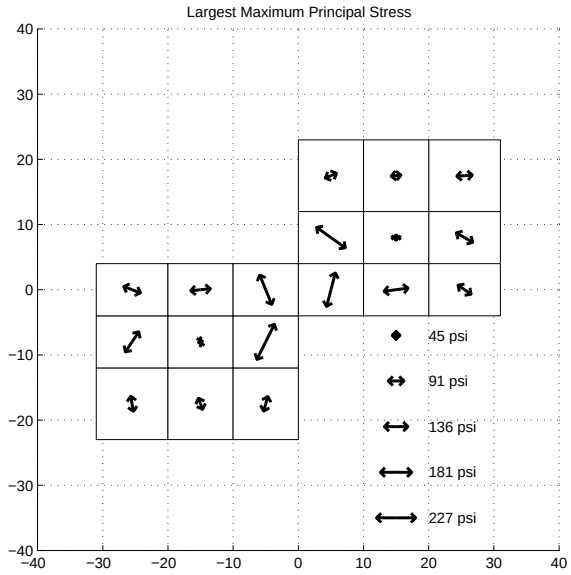

(c) Maximum Principal Stress (Tension)

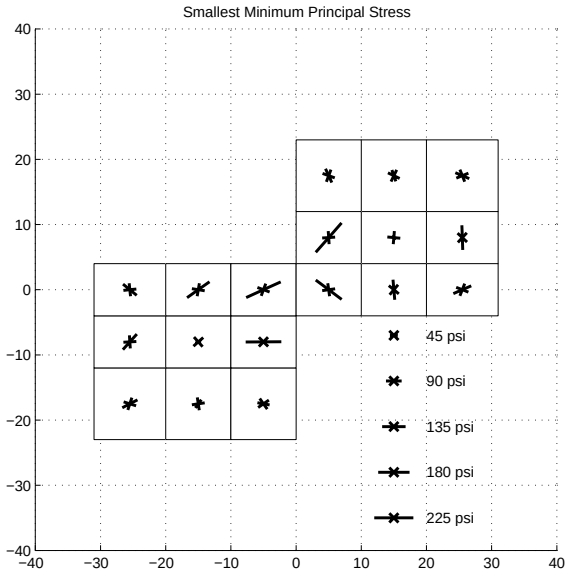

(d) Maximum Principal Stress (Compression)

Figure I.11: Floor Diaphragm Peak Stresses in Building 1, Second Floor (a) & (b) and Ninth Floor (c) & (d): Kobe Earthquake (Takatori Record Strong Component in Y Direction)

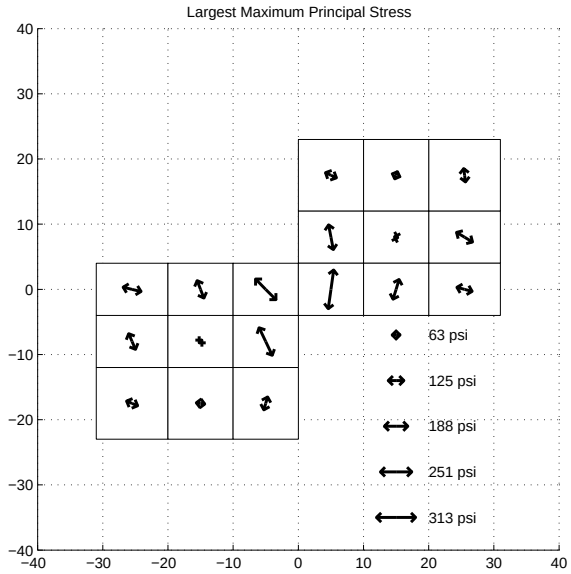

(a) Maximum Principal Stress (Tension)

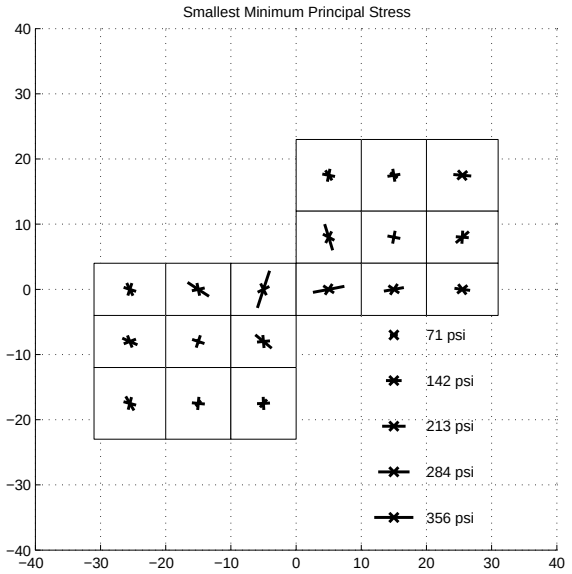

(b) Maximum Principal Stress (Compression)

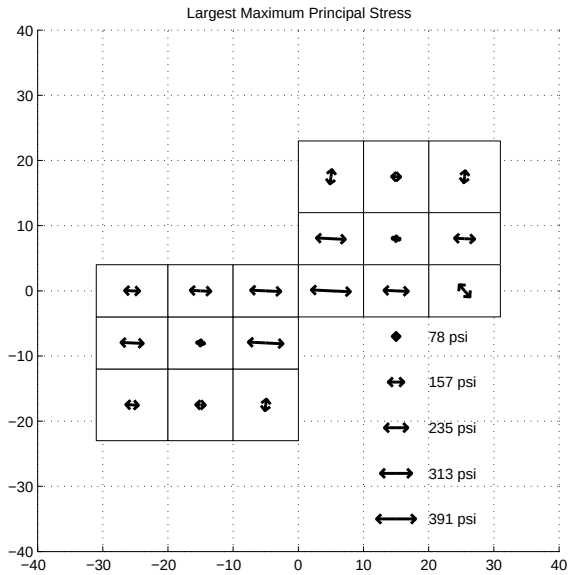

(c) Maximum Principal Stress (Tension)

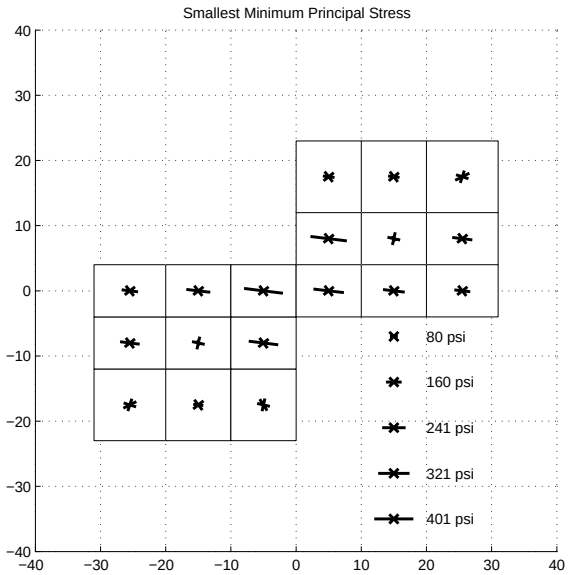

(d) Maximum Principal Stress (Compression)

Figure I.12: Floor Diaphragm Peak Stresses in Building 1, Lower Mechanical Floor (a) & (b) and All Floors (c) & (d): Kobe Earthquake (Takatori Record Strong Component in Y Direction)

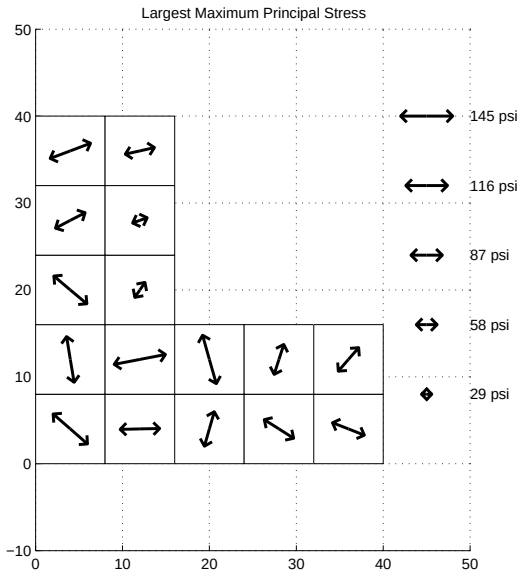

(a) Maximum Principal Stress (Tension)

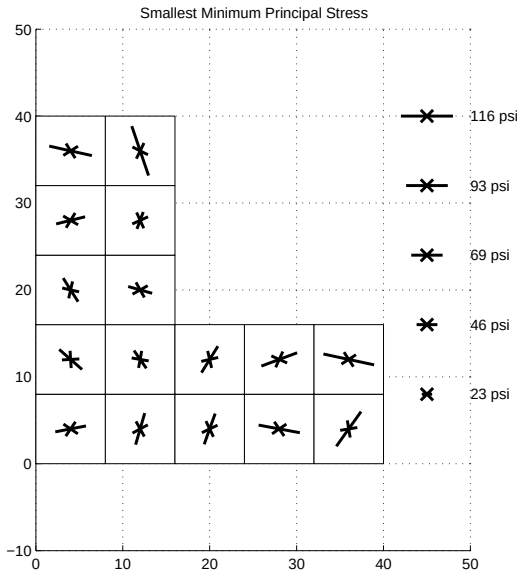

(b) Maximum Principal Stress (Compression)

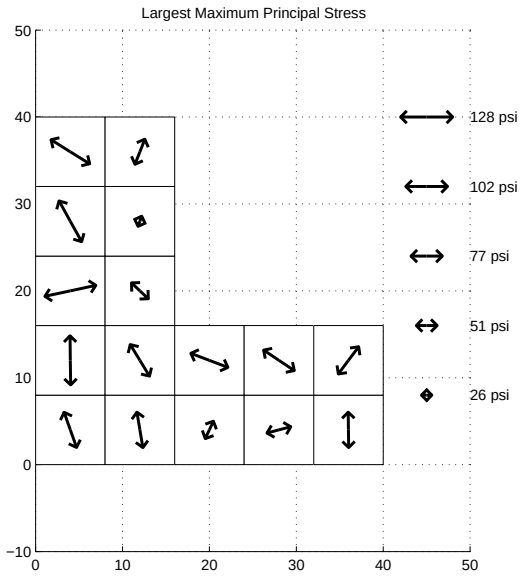

(c) Maximum Principal Stress (Tension)

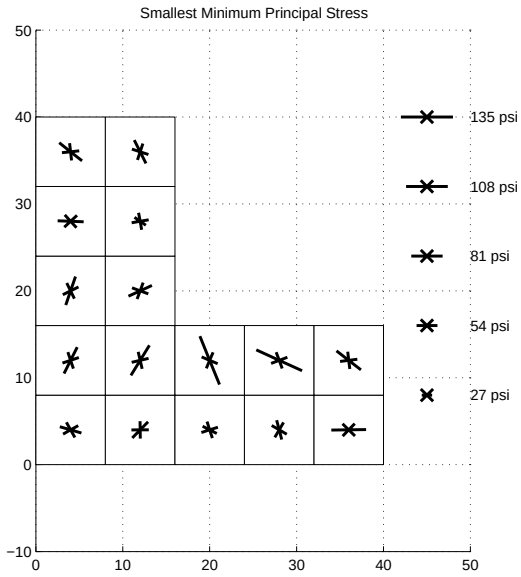

(d) Maximum Principal Stress (Compression)

Figure I.13: Floor Diaphragm Peak Stresses in Building 2, Second Floor (a) & (b) and Ninth Floor (c) & (d): Northridge Earthquake (Sylmar Record Strong Component in X Direction)

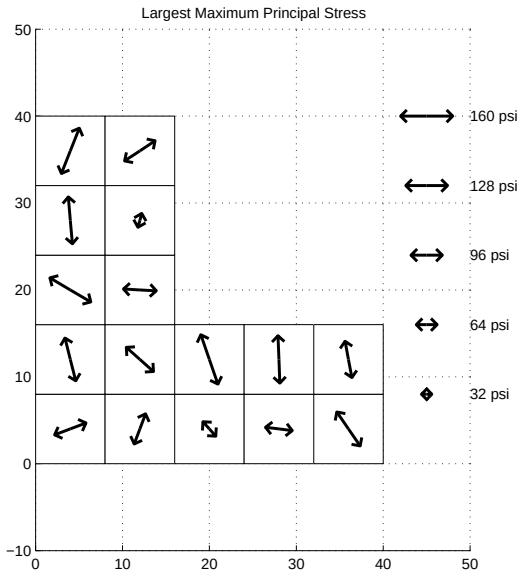

(a) Maximum Principal Stress (Tension)

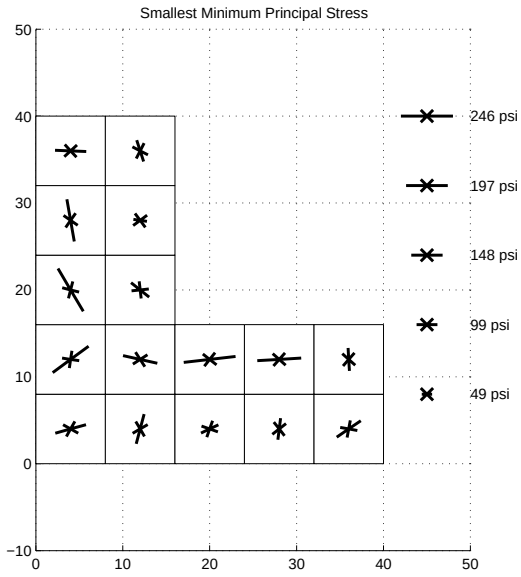

(b) Maximum Principal Stress (Compression)

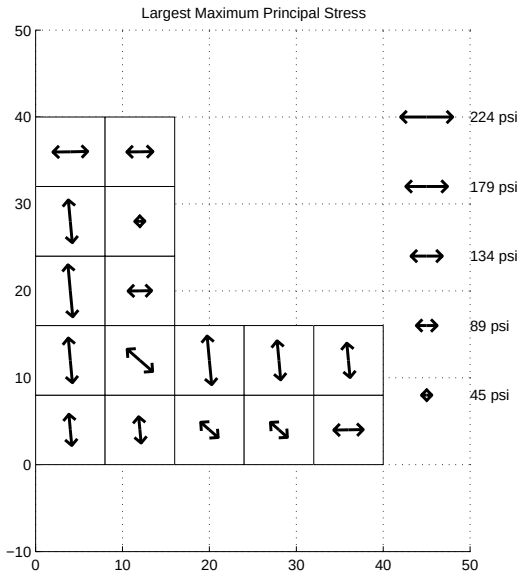

(c) Maximum Principal Stress (Tension)

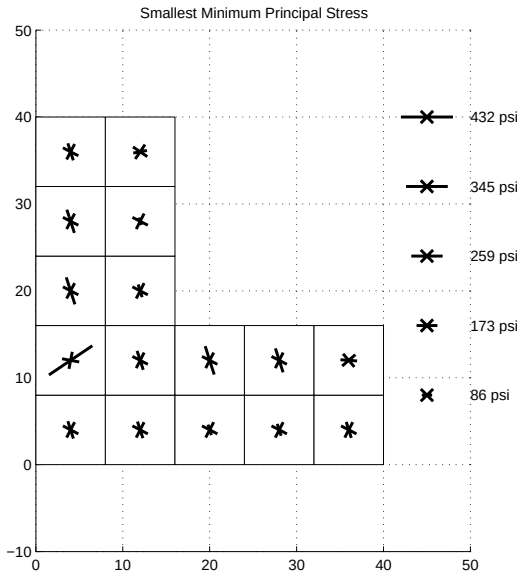

(d) Maximum Principal Stress (Compression)

Figure I.14: Floor Diaphragm Peak Stresses in Building 2, Lower Mechanical Floor (a) & (b) and All Floors (c) & (d): Northridge Earthquake (Sylmar Record Strong Component in X Direction)

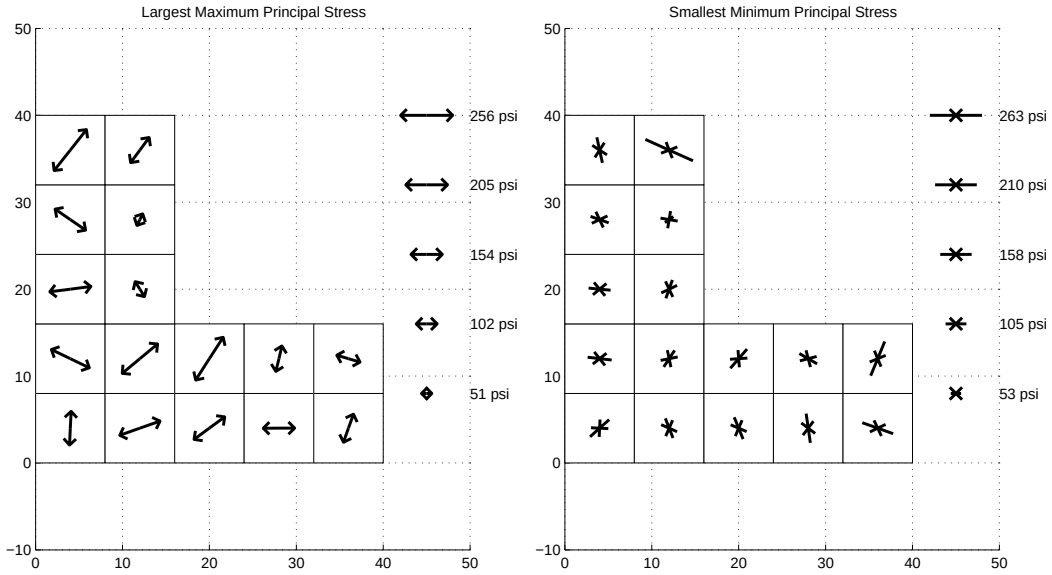

(a) Maximum Principal Stress (Tension)

(b) Maximum Principal Stress (Compression)

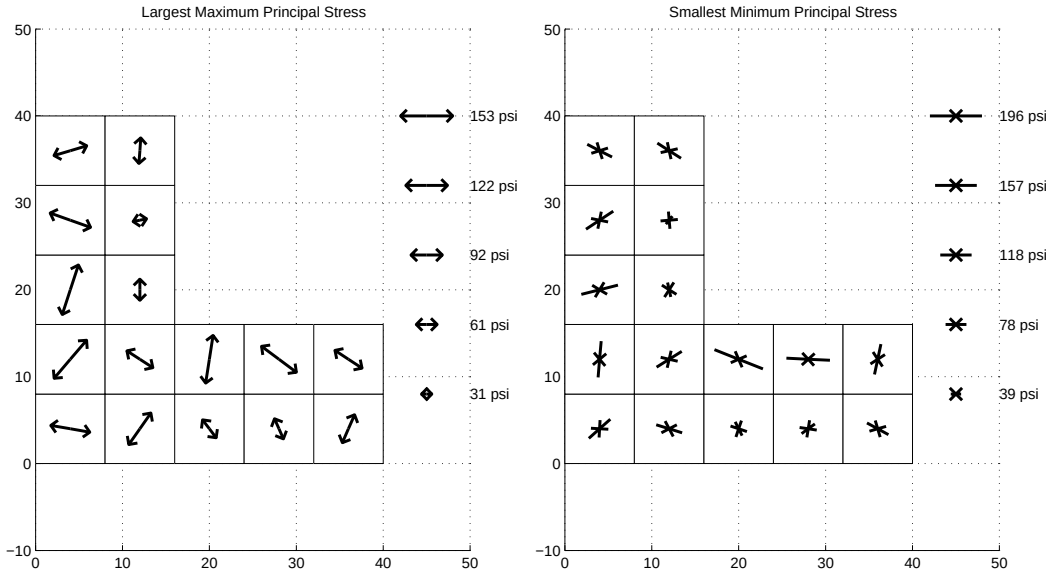

(c) Maximum Principal Stress (Tension)

(d) Maximum Principal Stress (Compression)

Figure I.15: Floor Diaphragm Peak Stresses in Building 2, Second Floor (a) & (b) and Ninth Floor (c) & (d): Iran Earthquake (Tabas Record Strong Component in X Direction)

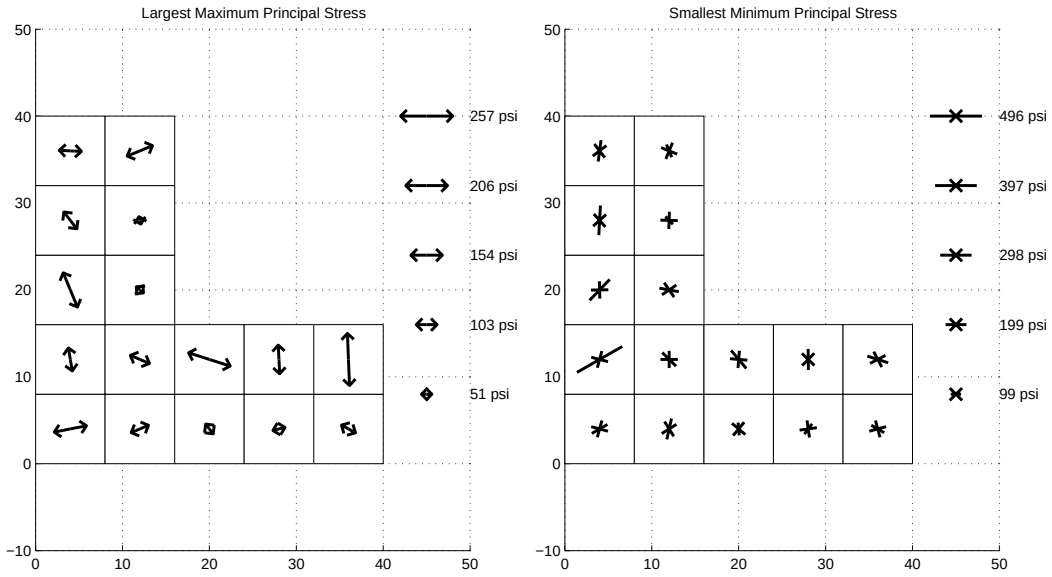

(a) Maximum Principal Stress (Tension)

(b) Maximum Principal Stress (Compression)

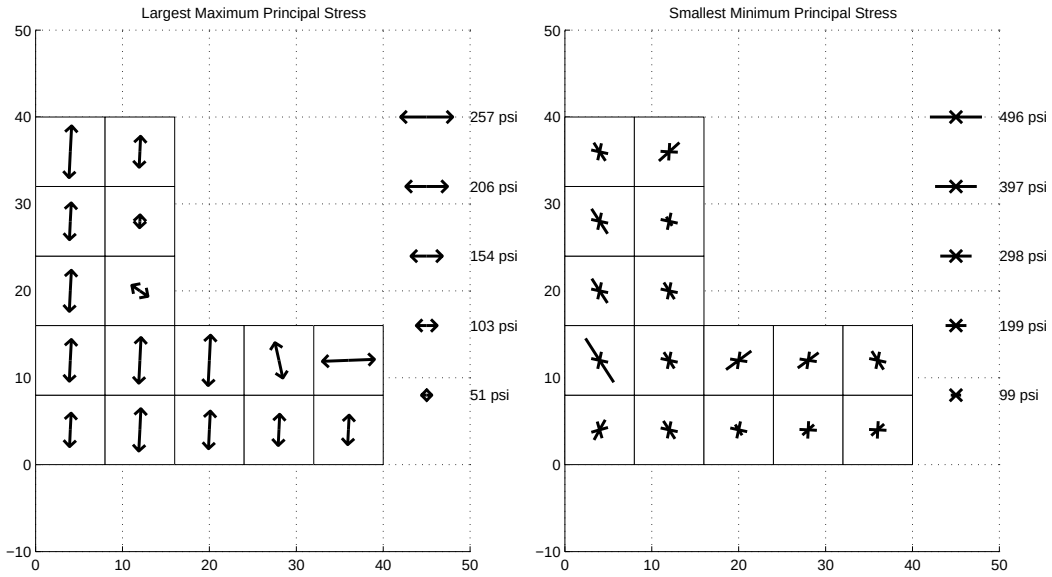

(c) Maximum Principal Stress (Tension)

(d) Maximum Principal Stress (Compression)

Figure I.16: Floor Diaphragm Peak Stresses in Building 2, Lower Mechanical Floor (a) & (b) and All Floors (c) & (d): Iran Earthquake (Tabas Record Strong Component in X Direction)

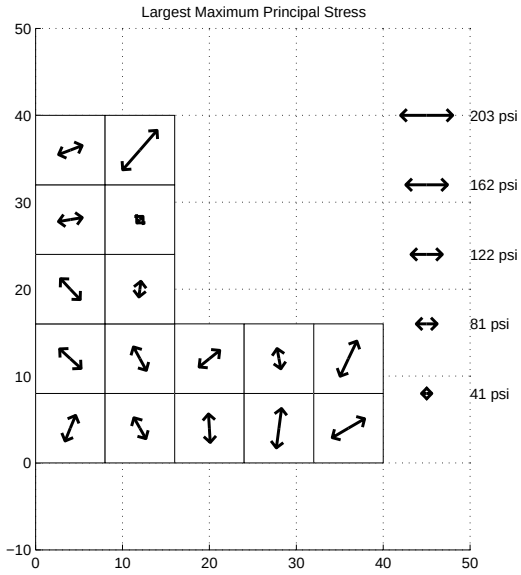

(a) Maximum Principal Stress (Tension)

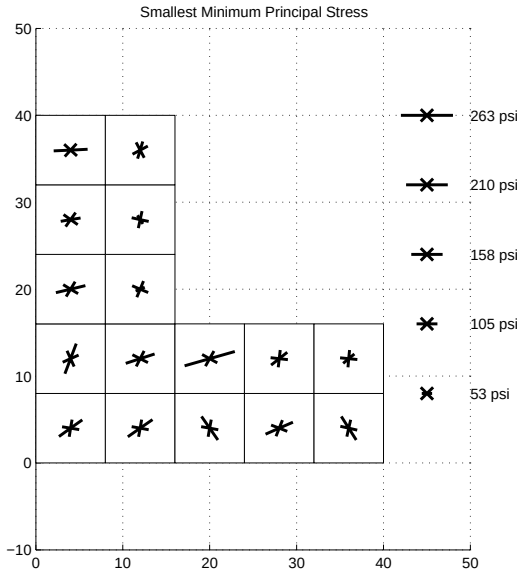

(b) Maximum Principal Stress (Compression)

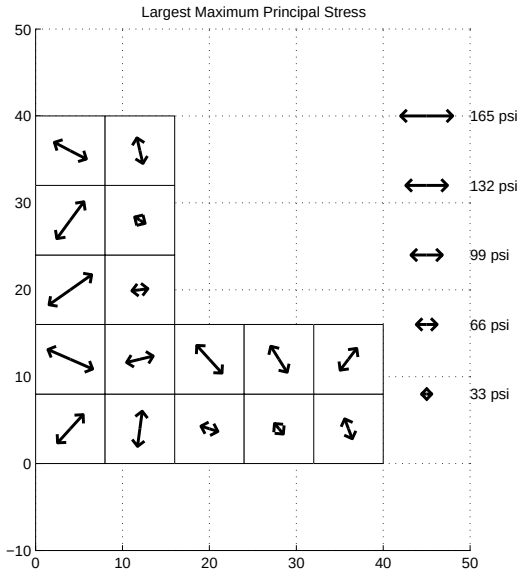

(c) Maximum Principal Stress (Tension)

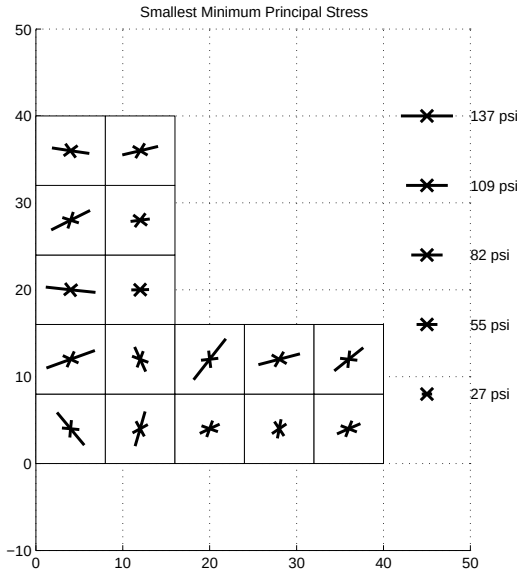

(d) Maximum Principal Stress (Compression)

Figure I.17: Floor Diaphragm Peak Stresses in Building 2, Second Floor (a) & (b) and Ninth Floor (c) & (d): Kobe Earthquake (Takatori Record Strong Component in X Direction)

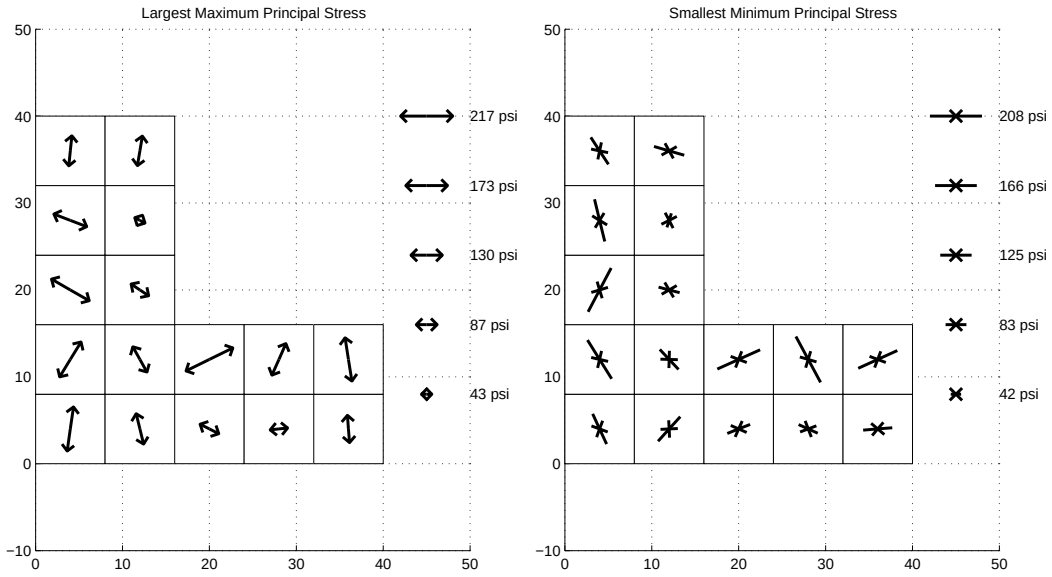

(a) Maximum Principal Stress (Tension)

(b) Maximum Principal Stress (Compression)

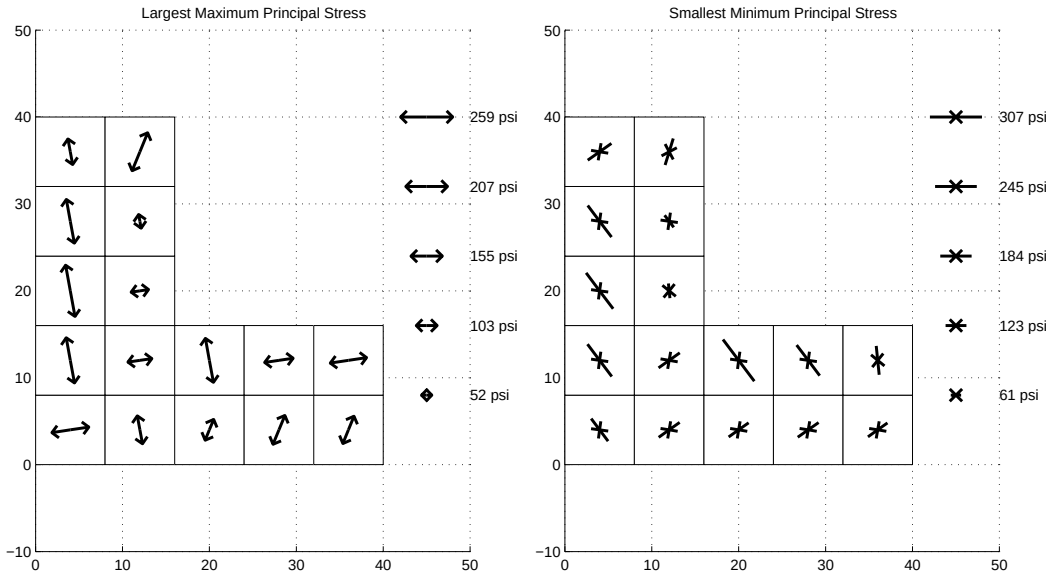

(c) Maximum Principal Stress (Tension)

(d) Maximum Principal Stress (Compression)

Figure I.18: Floor Diaphragm Peak Stresses in Building 2, Lower Mechanical Floor (a) & (b) and All Floors (c) & (d): Kobe Earthquake (Takatori Record Strong Component in X Direction)

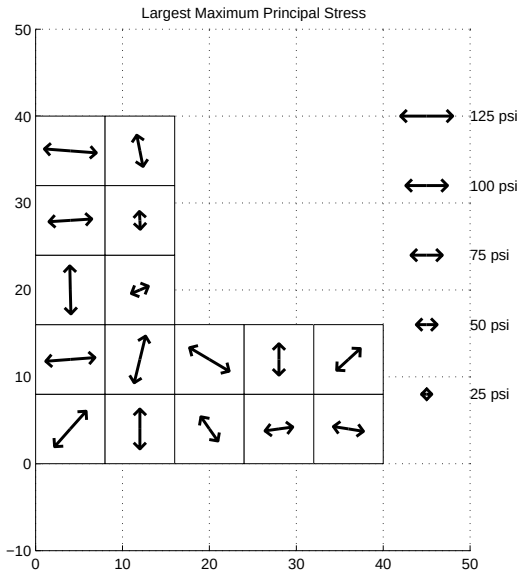

(a) Maximum Principal Stress (Tension)

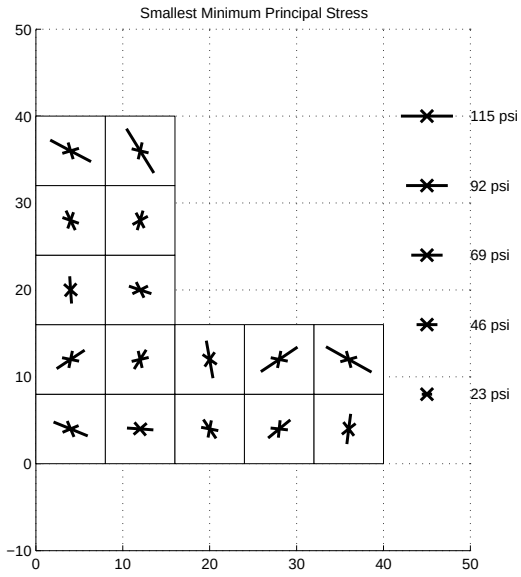

(b) Maximum Principal Stress (Compression)

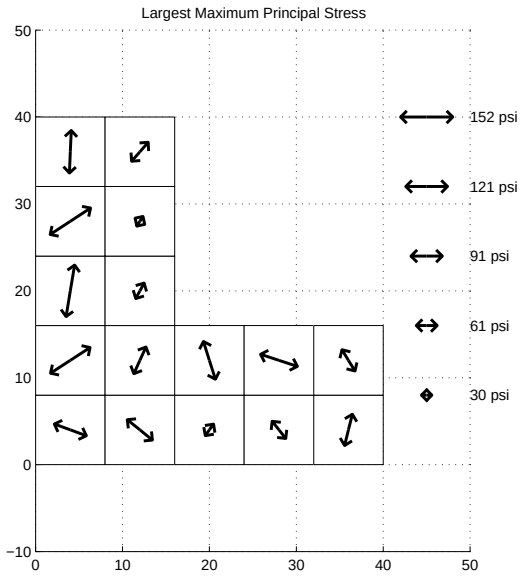

(c) Maximum Principal Stress (Tension)

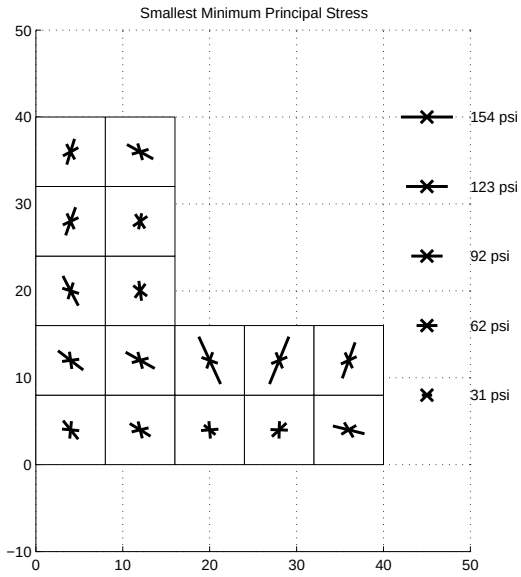

(d) Maximum Principal Stress (Compression)

Figure I.19: Floor Diaphragm Peak Stresses in Building 2A, Second Floor (a) & (b) and Ninth Floor (c) & (d): Northridge Earthquake (Sylmar Record Strong Component in X Direction)

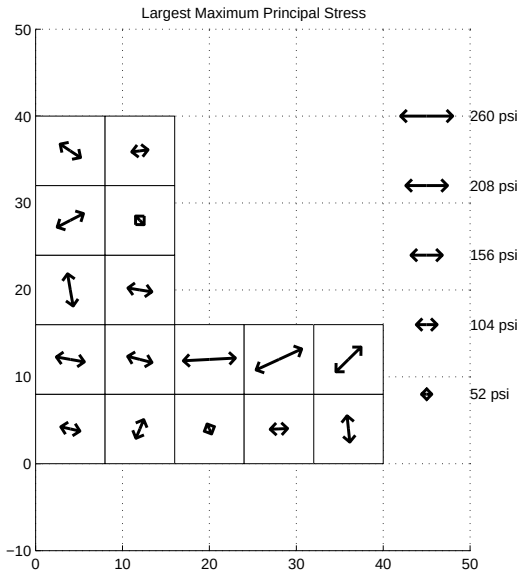

(a) Maximum Principal Stress (Tension)

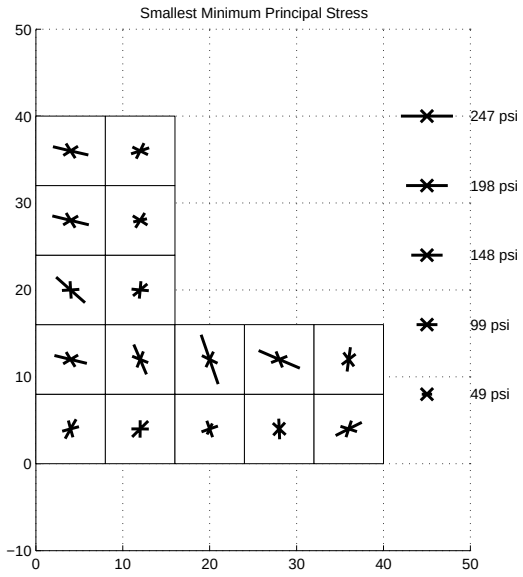

(b) Maximum Principal Stress (Compression)

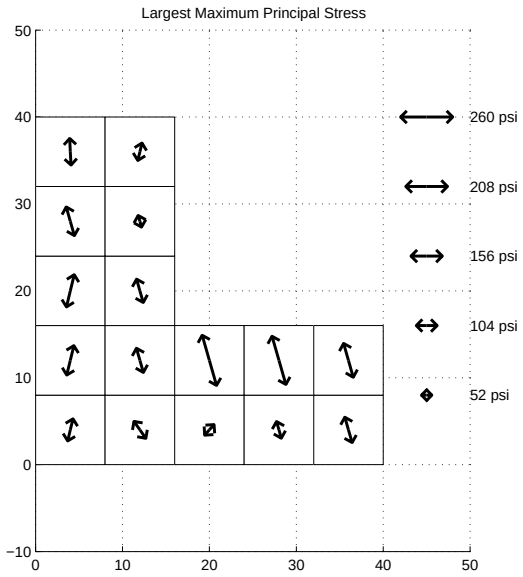

(c) Maximum Principal Stress (Tension)

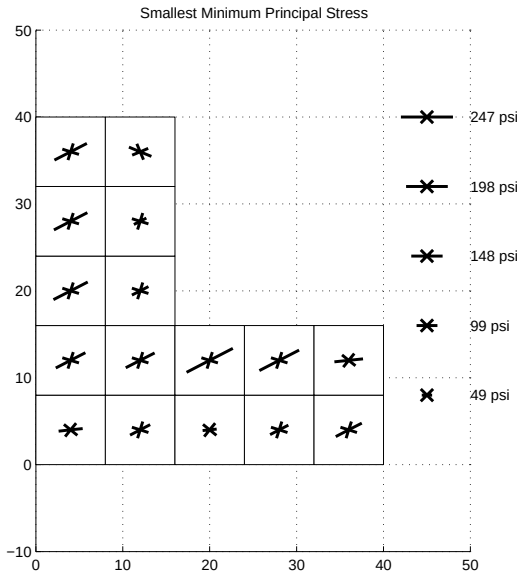

(d) Maximum Principal Stress (Compression)

Figure I.20: Floor Diaphragm Peak Stresses in Building 2A, Lower Mechanical Floor (a) & (b) and All Floors (c) & (d): Northridge Earthquake (Sylmar Record Strong Component in X Direction)

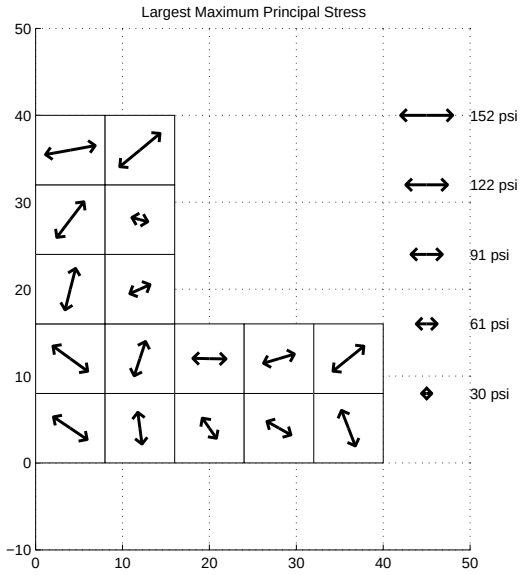

(a) Maximum Principal Stress (Tension)

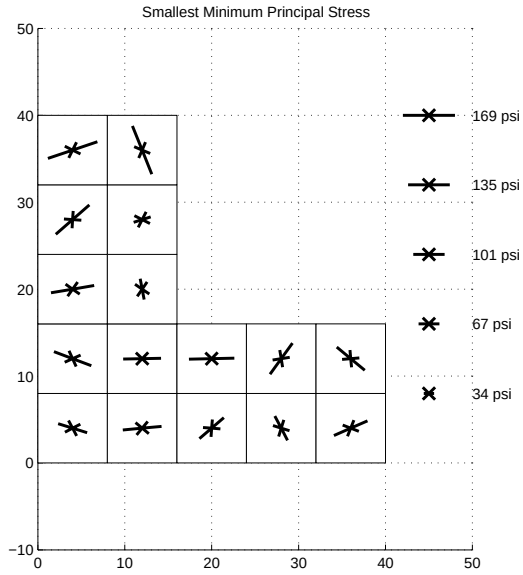

(b) Maximum Principal Stress (Compression)

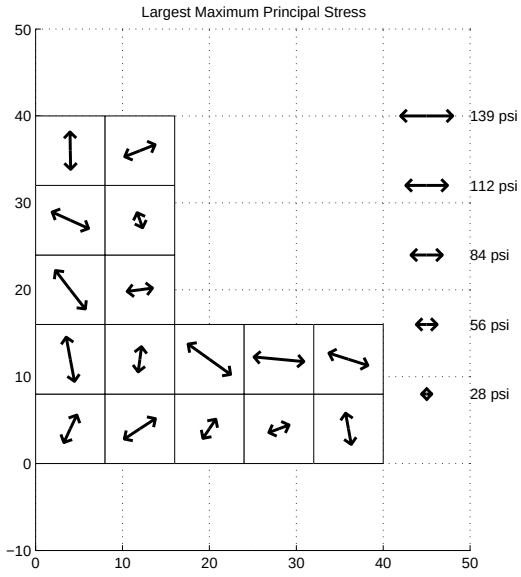

(c) Maximum Principal Stress (Tension)

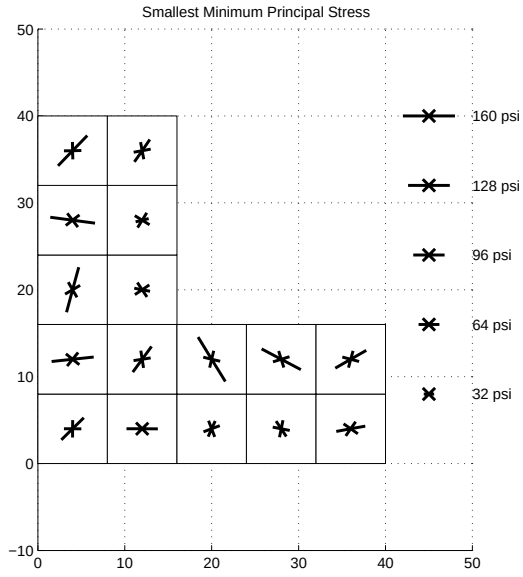

(d) Maximum Principal Stress (Compression)

Figure I.21: Floor Diaphragm Peak Stresses in Building 2A, Second Floor (a) & (b) and Ninth Floor (c) & (d): Iran Earthquake (Tabas Record Strong Component in X Direction)

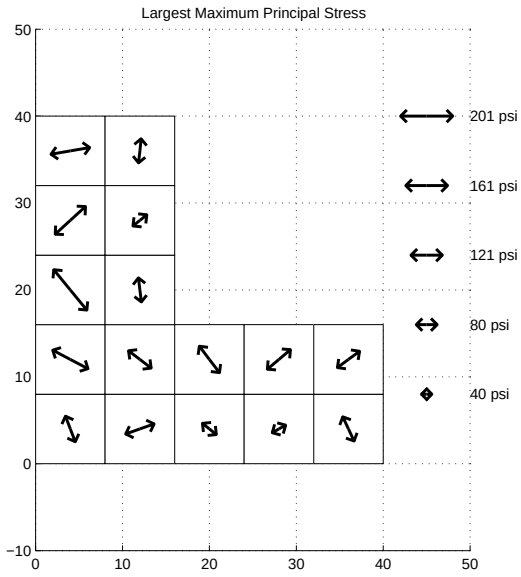

(a) Maximum Principal Stress (Tension)

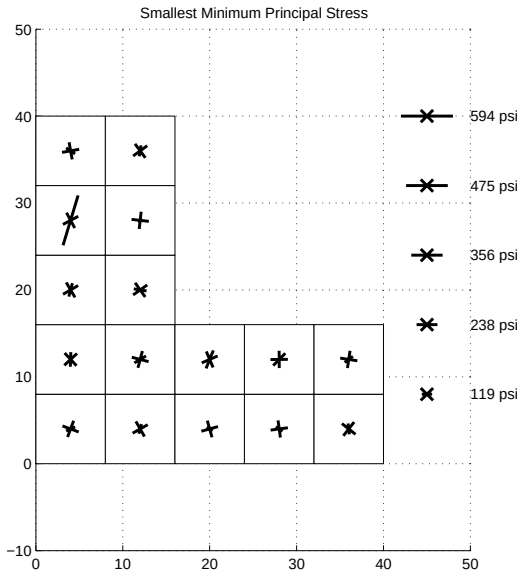

(b) Maximum Principal Stress (Compression)

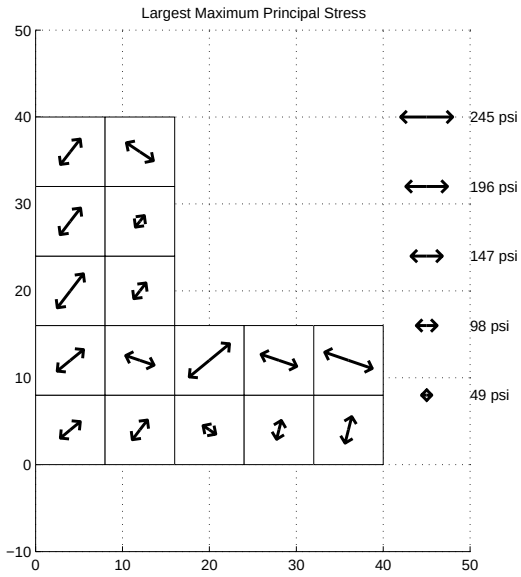

(c) Maximum Principal Stress (Tension)

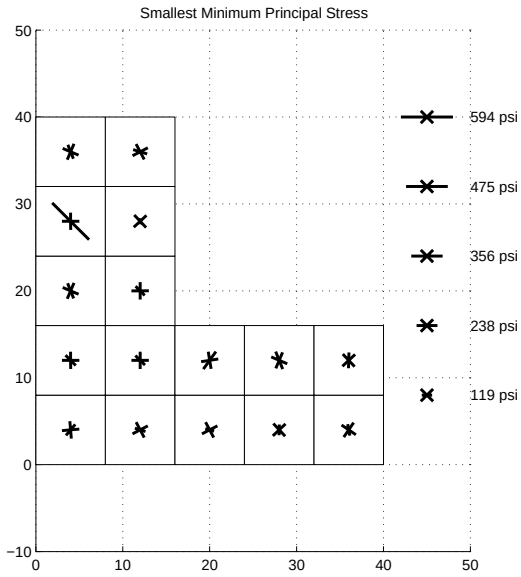

(d) Maximum Principal Stress (Compression)

Figure I.22: Floor Diaphragm Peak Stresses in Building 2A, Lower Mechanical Floor (a) & (b) and All Floors (c) & (d): Iran Earthquake (Tabas Record Strong Component in X Direction)

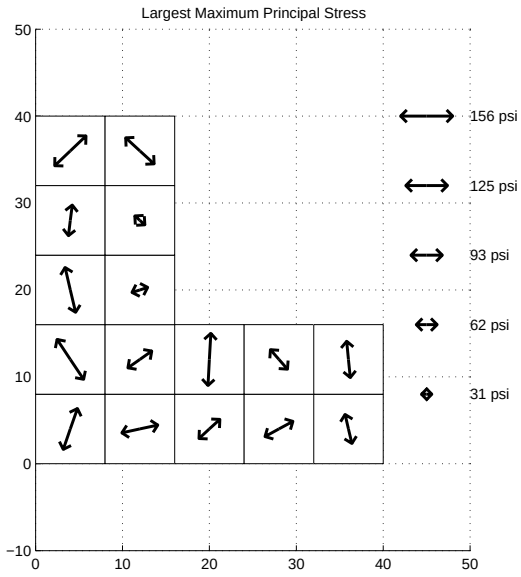

(a) Maximum Principal Stress (Tension)

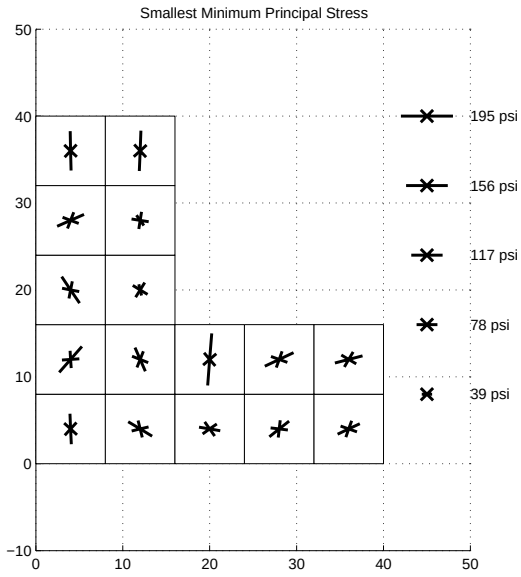

(b) Maximum Principal Stress (Compression)

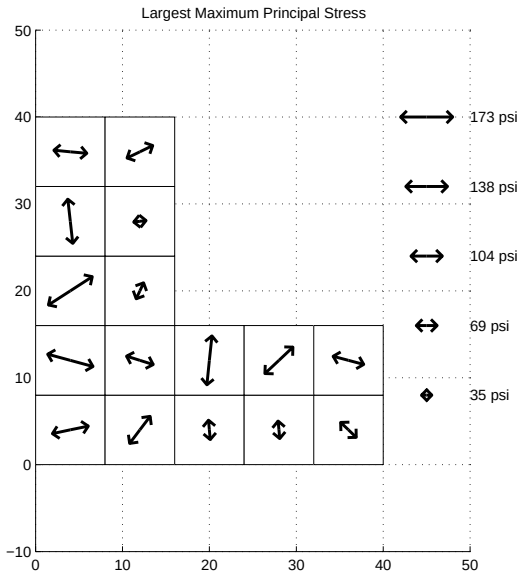

(c) Maximum Principal Stress (Tension)

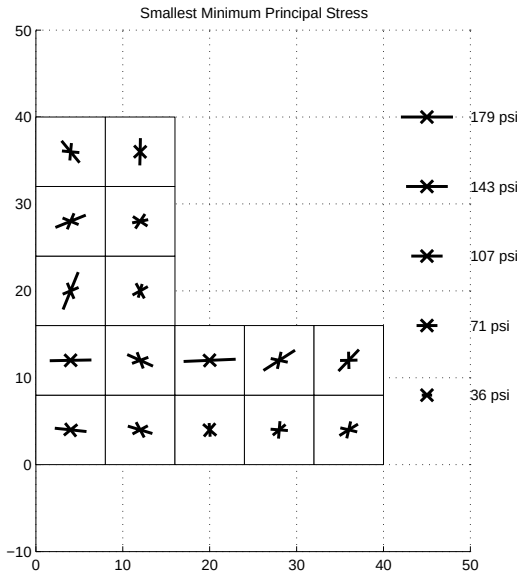

(d) Maximum Principal Stress (Compression)

Figure I.23: Floor Diaphragm Peak Stresses in Building 2A, Second Floor (a) & (b) and Ninth Floor (c) & (d): Kobe Earthquake (Takatori Record Strong Component in X Direction)

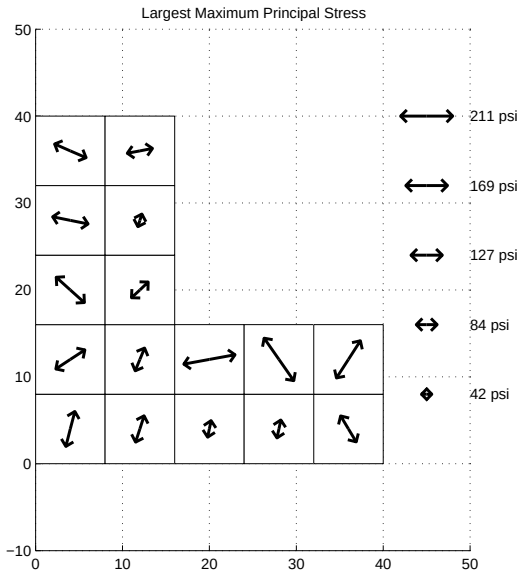

(a) Maximum Principal Stress (Tension)

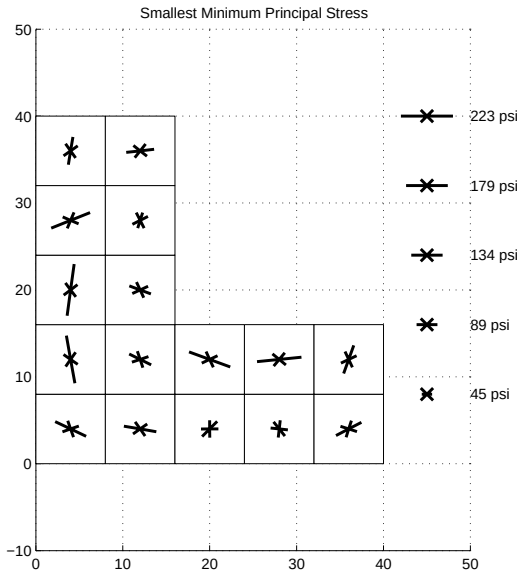

(b) Maximum Principal Stress (Compression)

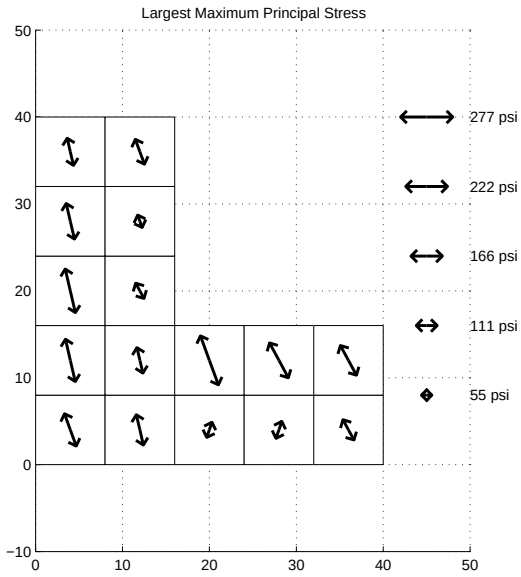

(c) Maximum Principal Stress (Tension)

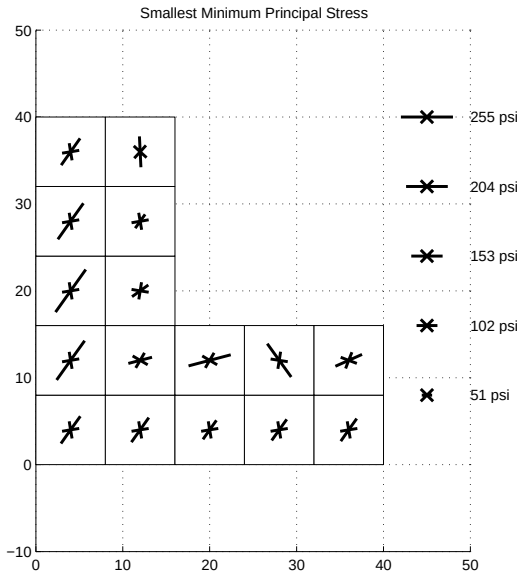

(d) Maximum Principal Stress (Compression)

Figure I.24: Floor Diaphragm Peak Stresses in Building 2A, Lower Mechanical Floor (a) & (b) and All Floors (c) & (d): Kobe Earthquake (Takatori Record Strong Component in X Direction)

Appendix J Ground Motion Analysis of Buildings: Element Response Histories

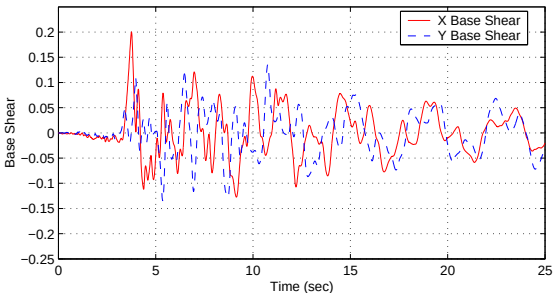

(a) Sylmar Strong Component in X Direction

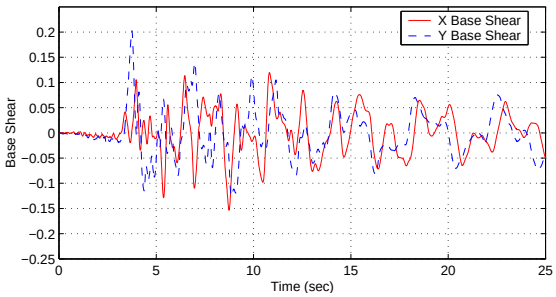

(b) Sylmar Strong Component in Y Direction

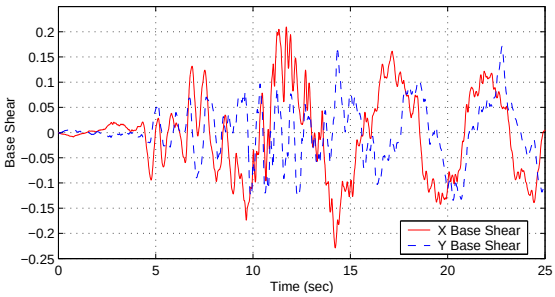

(c) Tabas Strong Component in X Direction

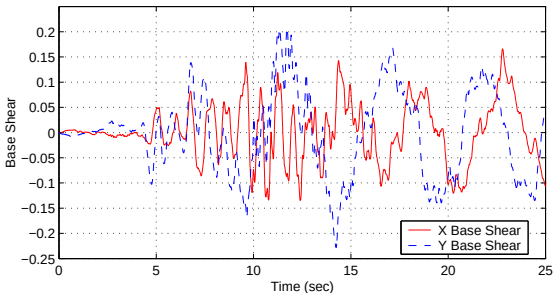

(d) Tabas Strong Component in Y Direction

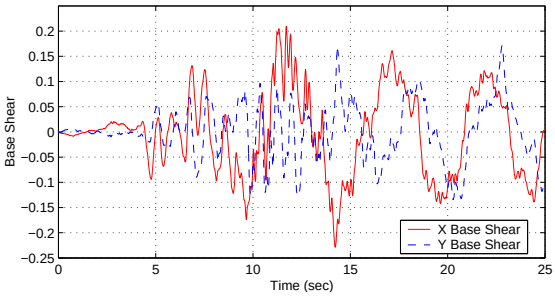

(e) Takatori Strong Component in X Direction

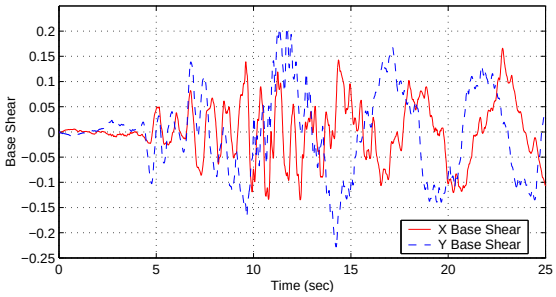

(f) Takatori Strong Component in Y Direction

Figure J.1: Building 1 Base Shear History: Northridge (Sylmar), Iran (Tabas) and Kobe (Takatori) Earthquakes

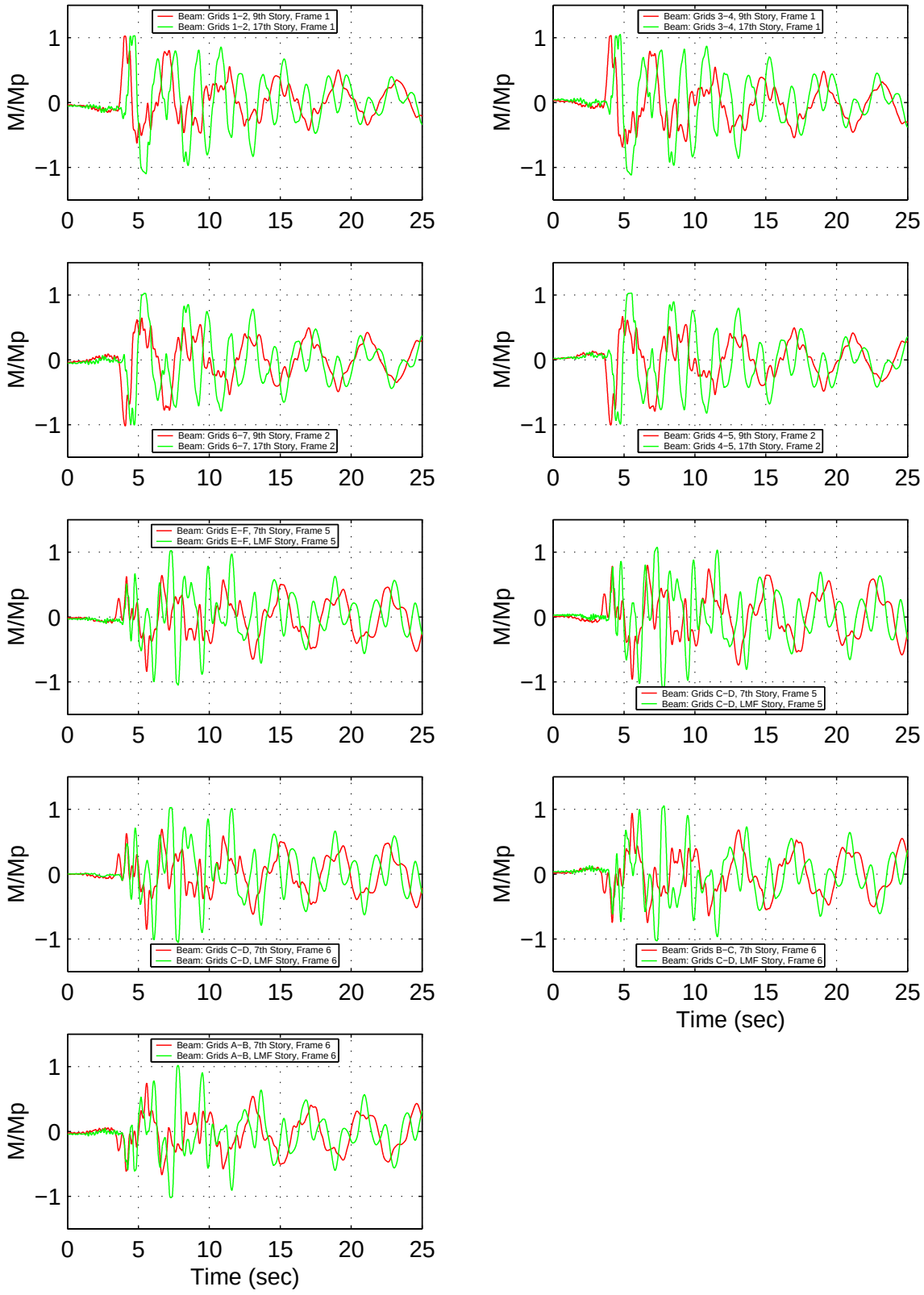

Figure J.2: Building 1: Beam-Column End Moment Histories - Northridge Earthquake (Sylmar Record Strong Component in X Direction)

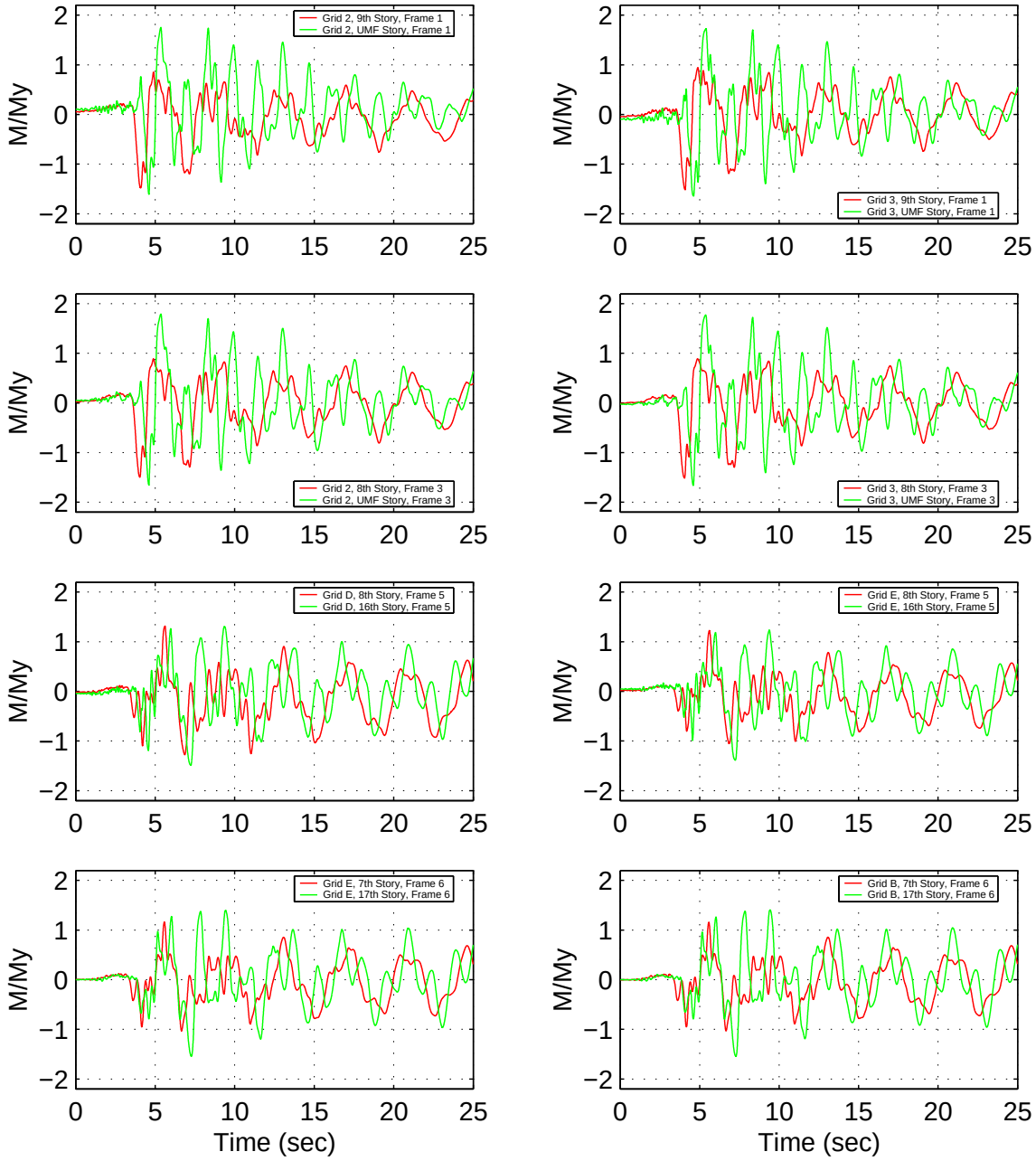

Figure J.3: Building 1: Panel Zone Moment Histories - Northridge Earthquake (Sylmar Record Strong Component in X Direction)

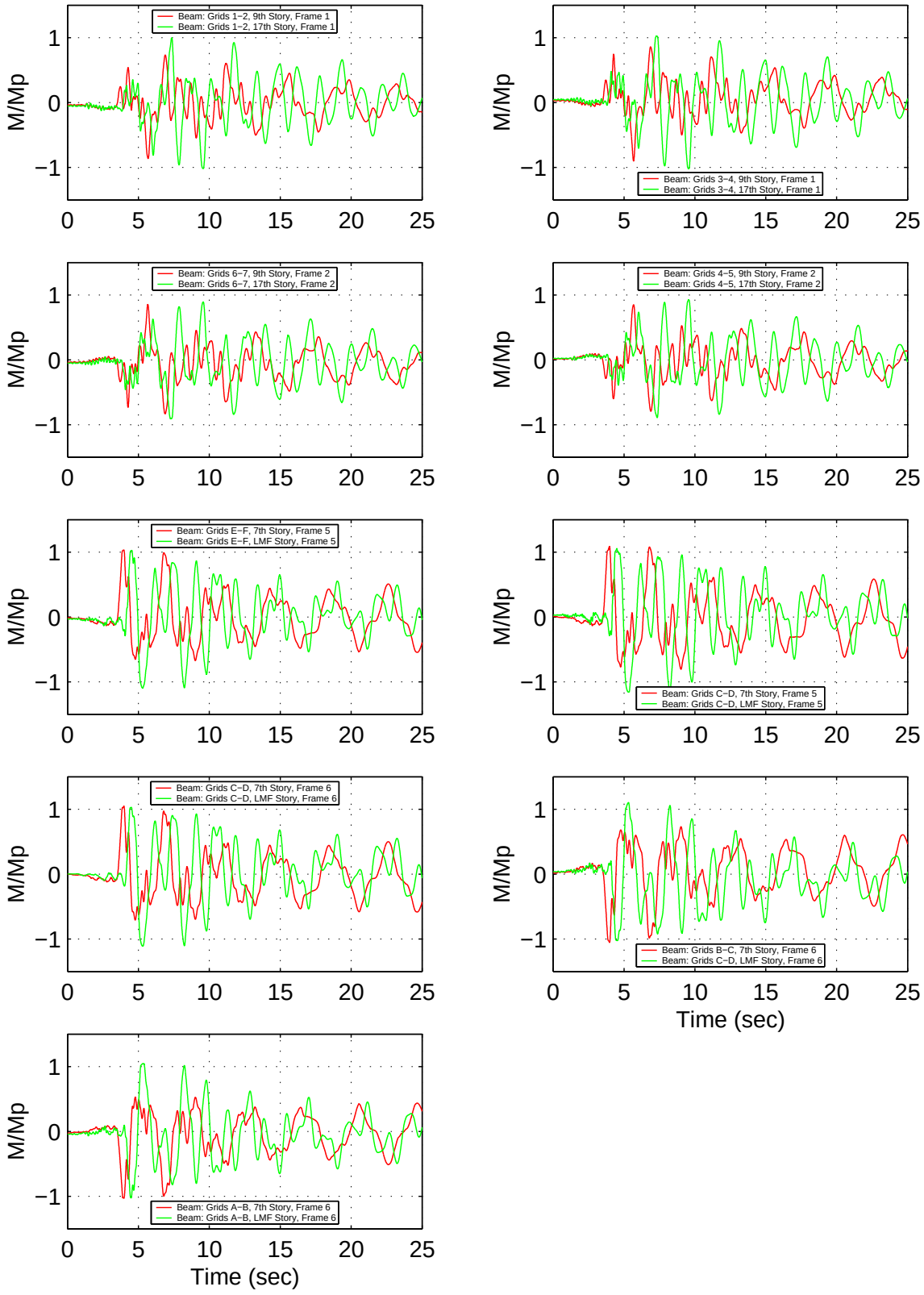

Figure J.4: Building 1: Beam-Column End Moment Histories - Northridge Earthquake (Sylmar Record Strong Component in Y Direction)

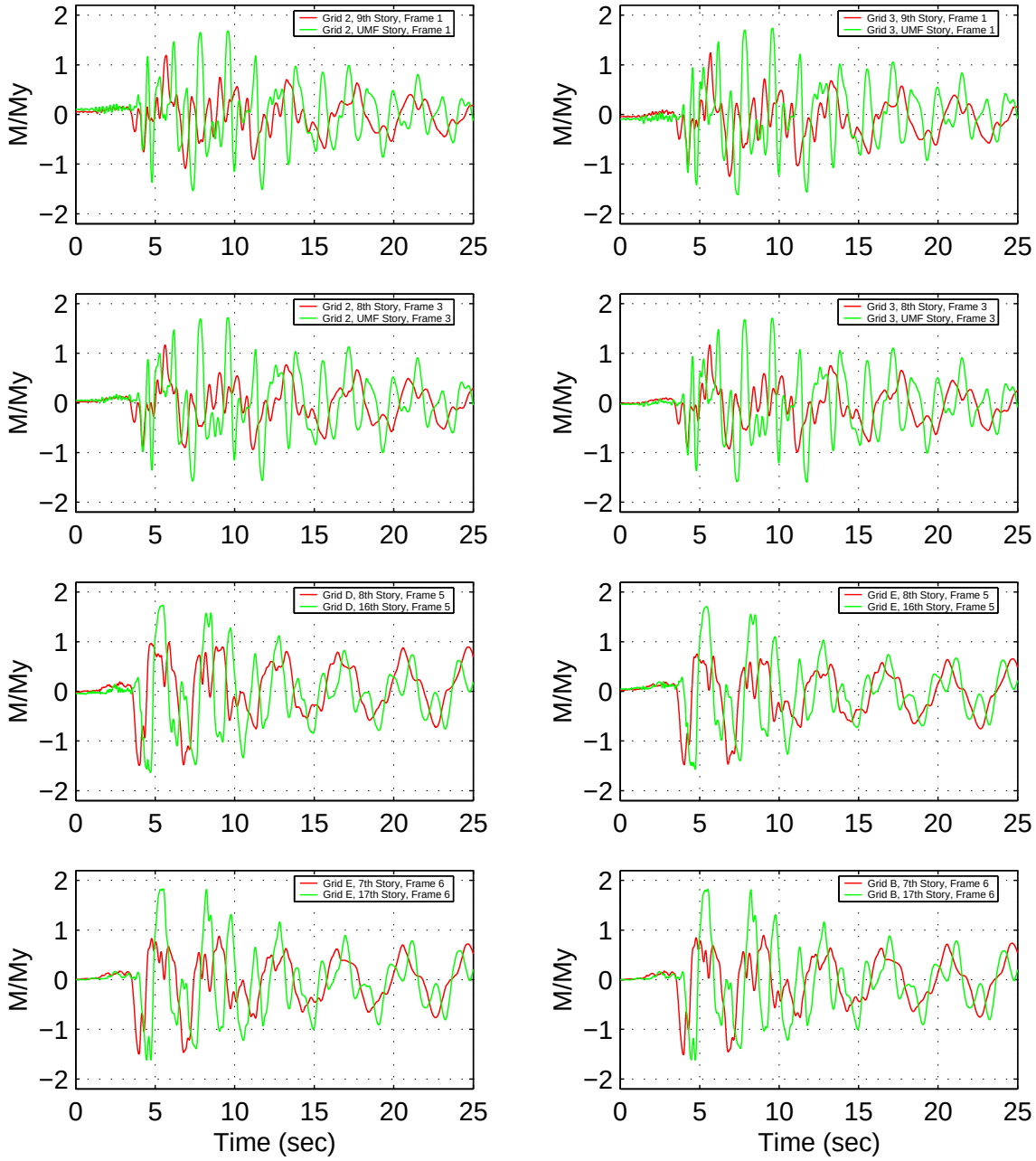

Figure J.5: Building 1: Panel Zone Moment Histories - Northridge Earthquake (Sylmar Record Strong Component in Y Direction)

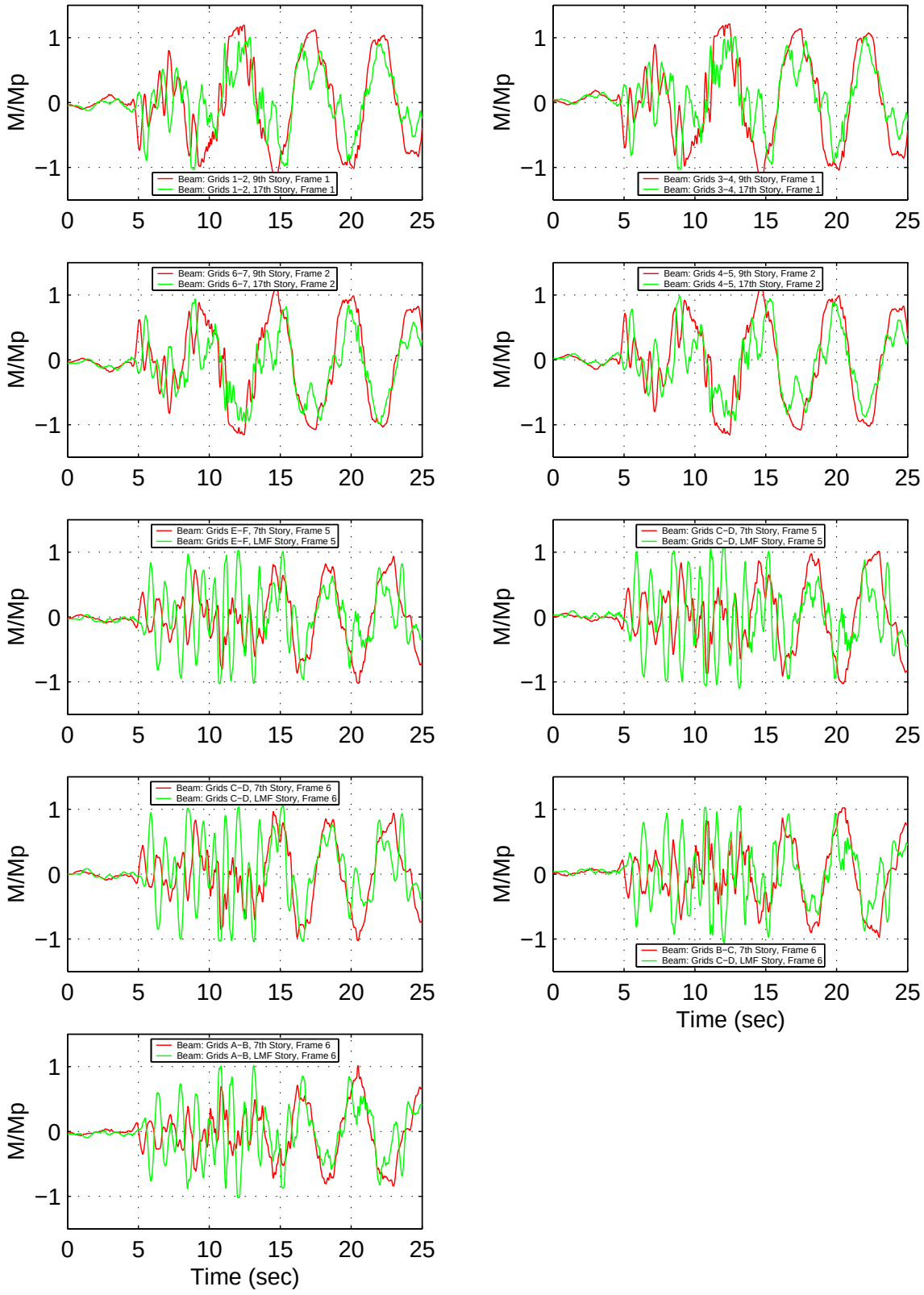

Figure J.6: Building 1: Beam-Column End Moment Histories - Iran Earthquake (Tabas Record Strong Component in X Direction)

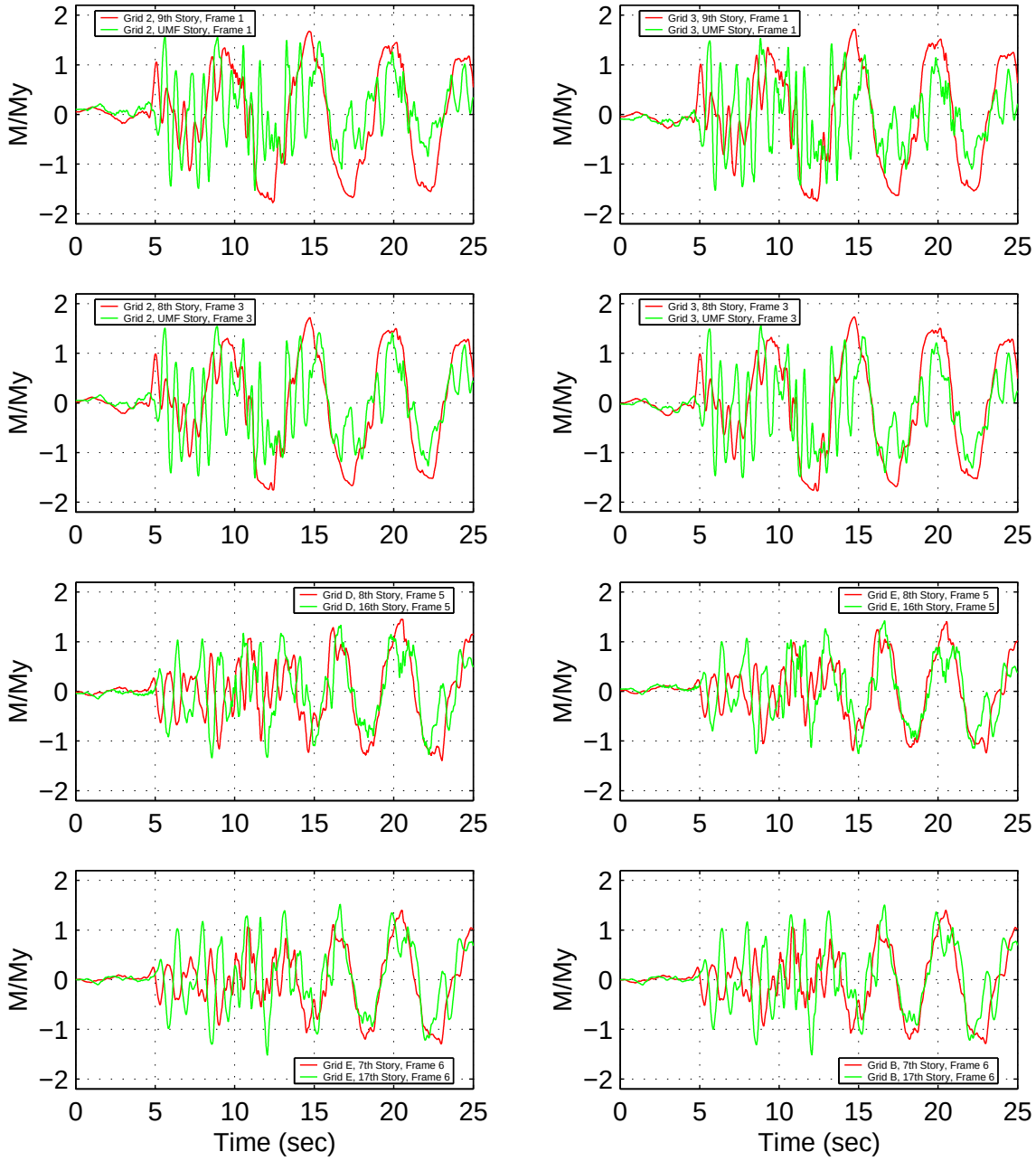

Figure J.7: Building 1: Panel Zone Moment Histories - Iran Earthquake (Tabas Record Strong Component in X Direction)

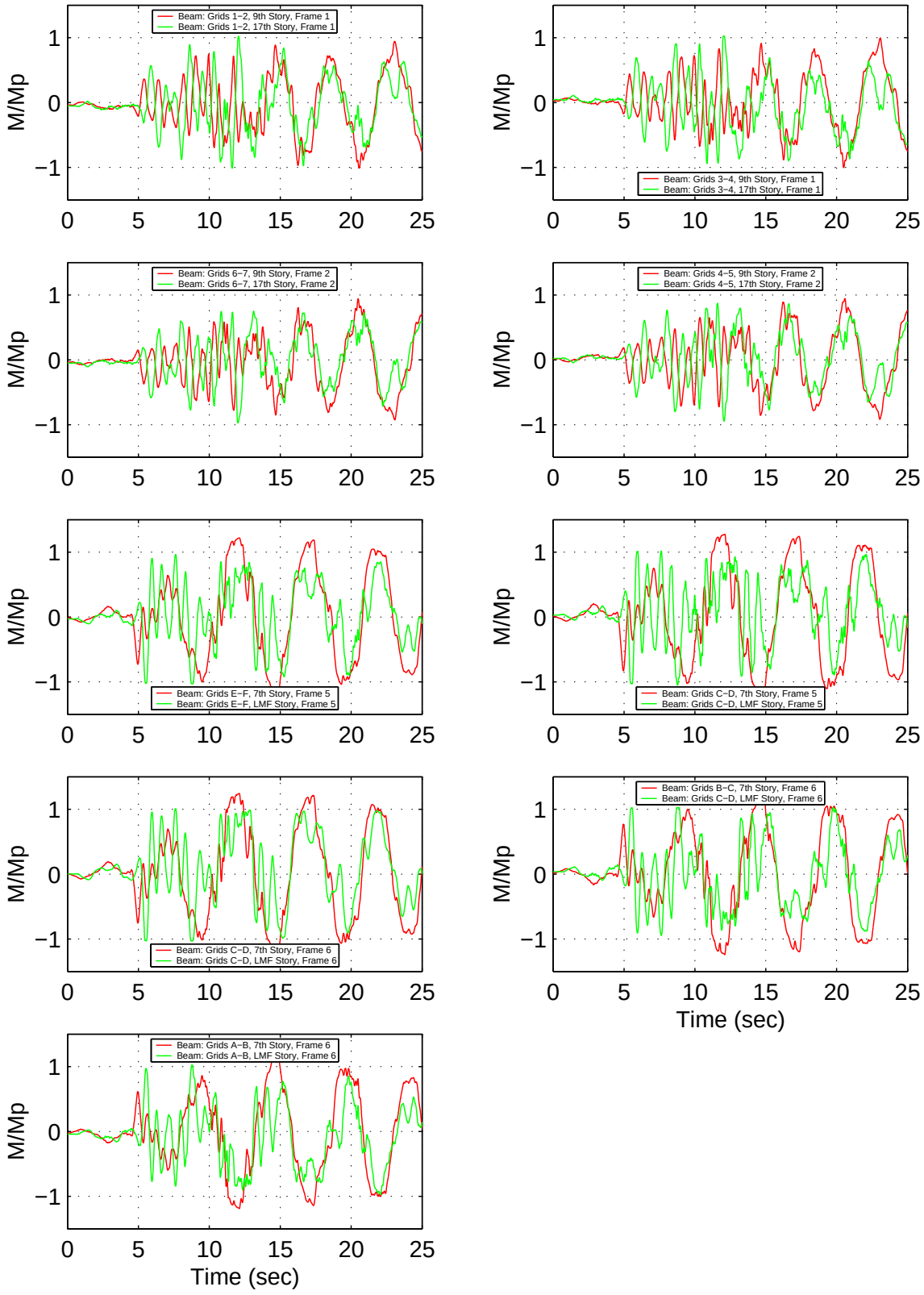

Figure J.8: Building 1: Beam-Column End Moment Histories - Iran Earthquake (Tabas Record Strong Component in Y Direction)

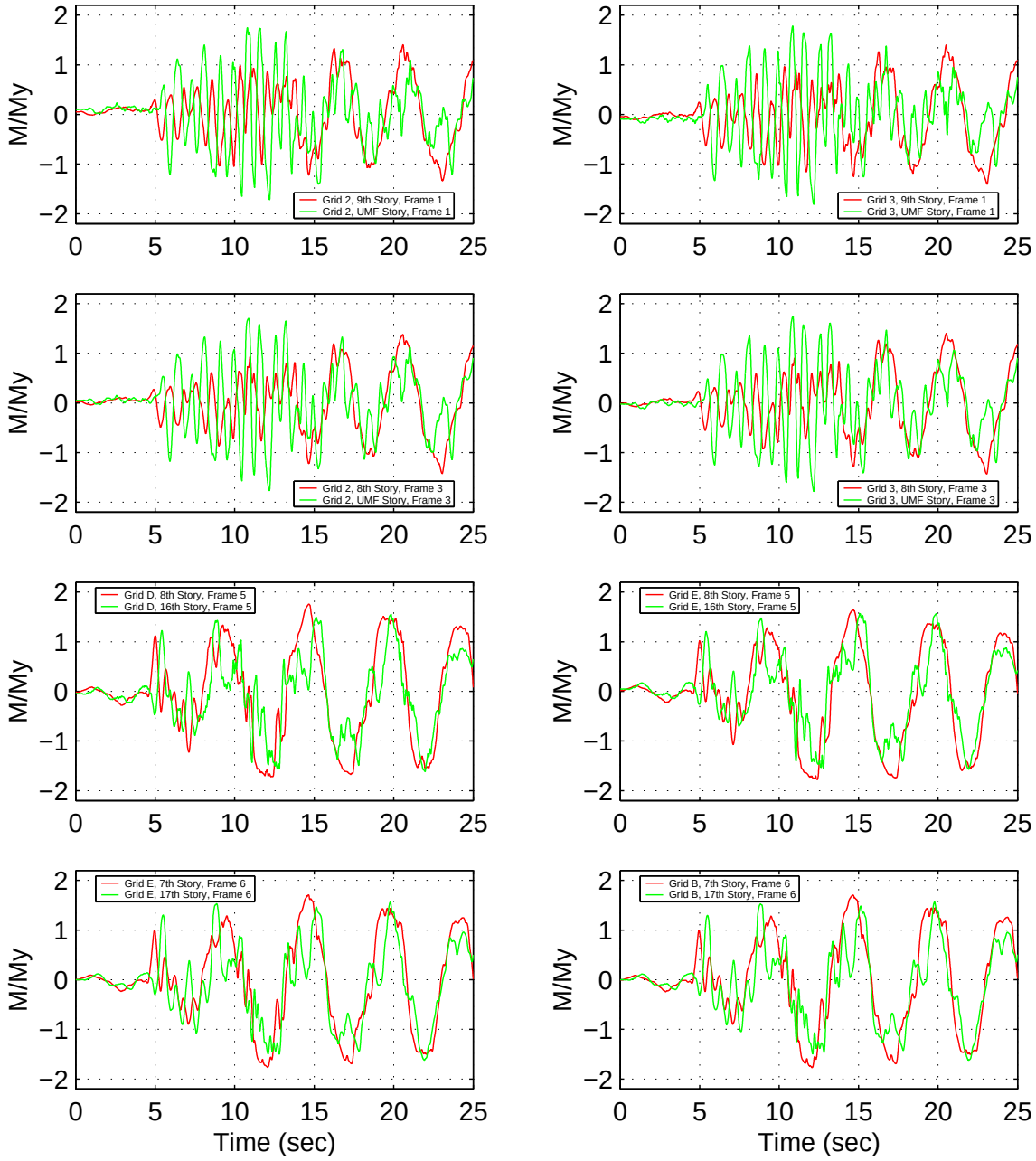

Figure J.9: Building 1: Panel Zone Moment Histories - Iran Earthquake (Tabas Record Strong Component in Y Direction)

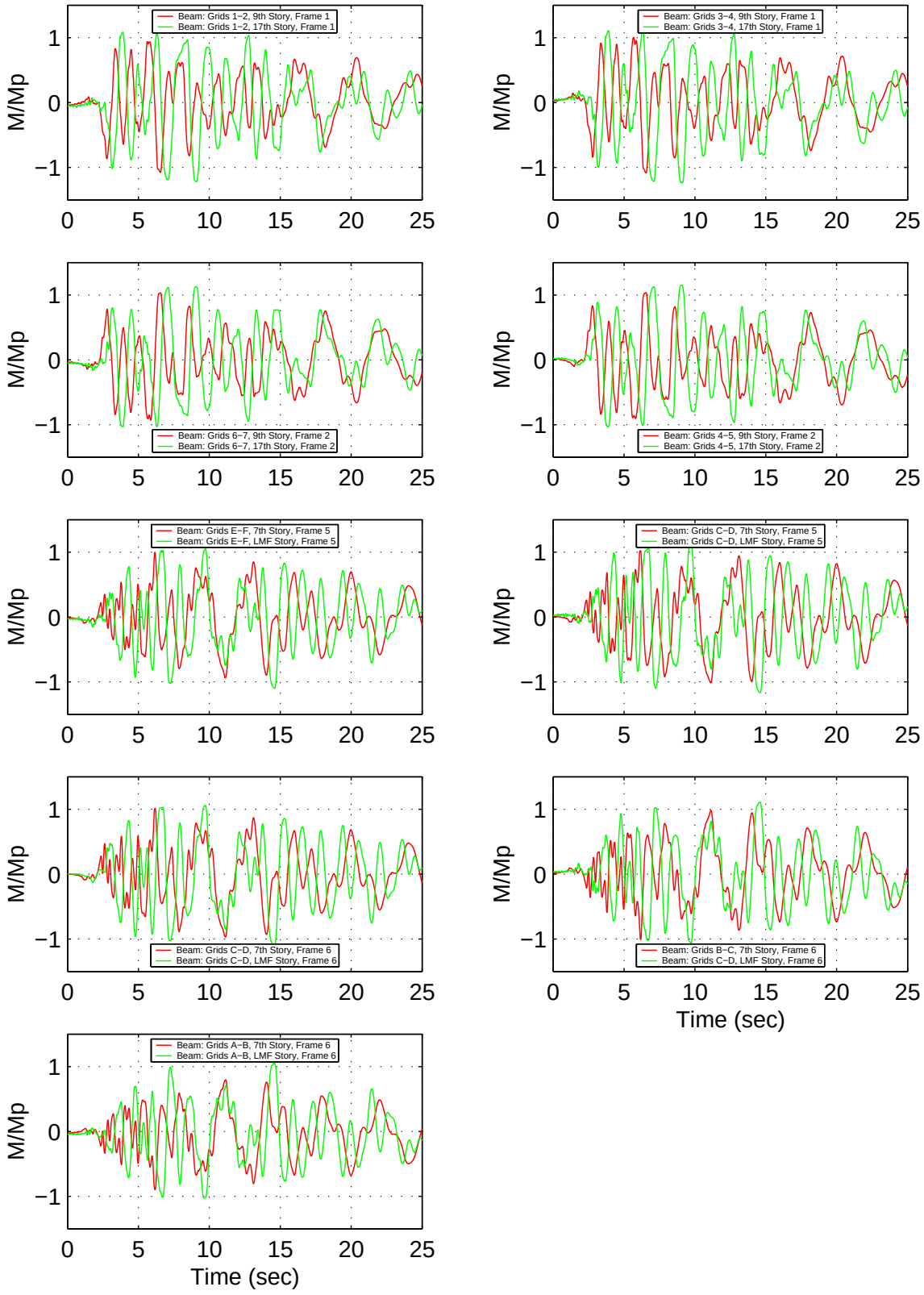

Figure J.10: Building 1: Beam-Column End Moment Histories - Kobe Earthquake (Takatori Record Strong Component in X Direction)

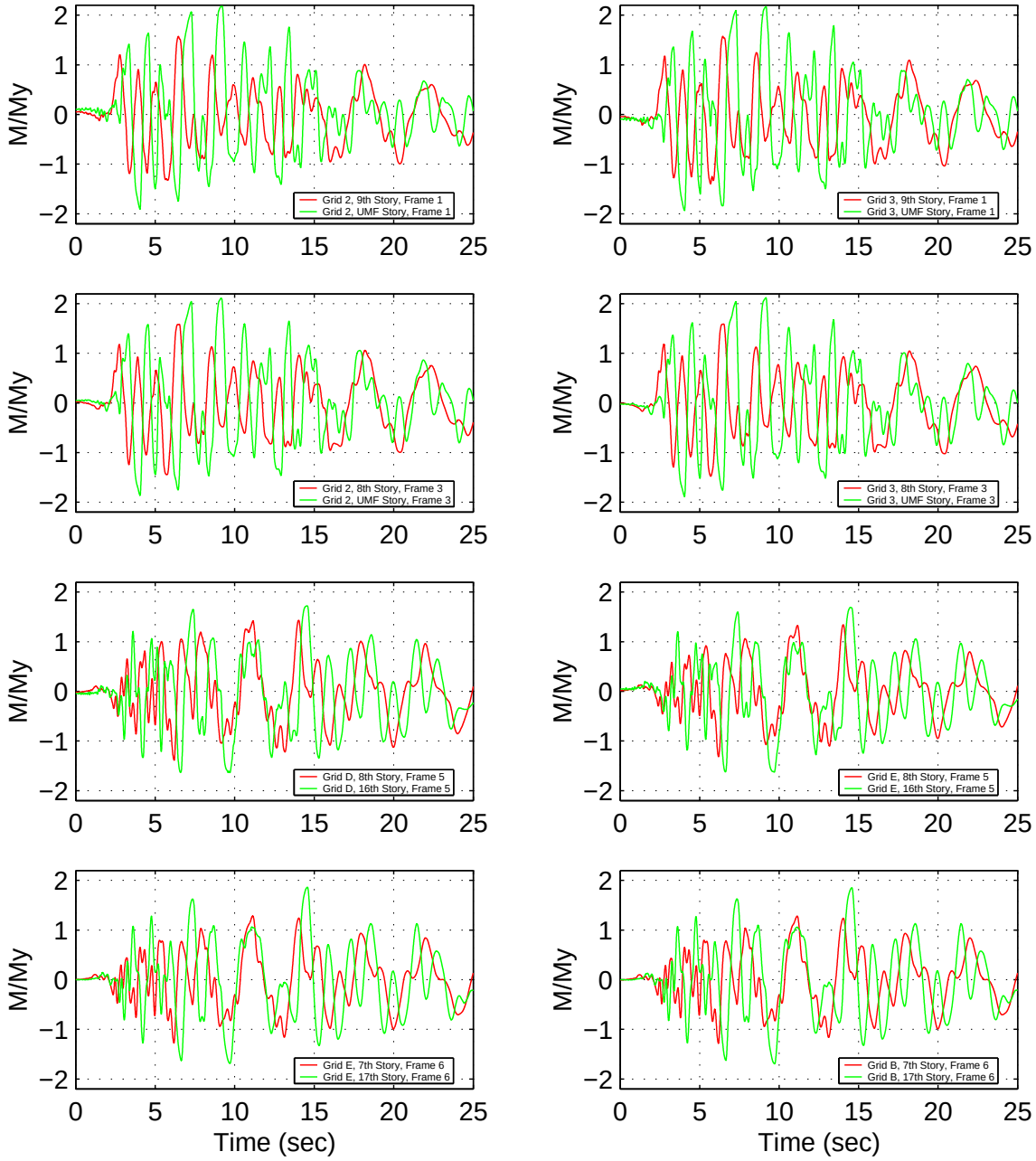

Figure J.11: Building 1: Panel Zone Moment Histories - Kobe Earthquake (Takatori Record Strong Component in X Direction)

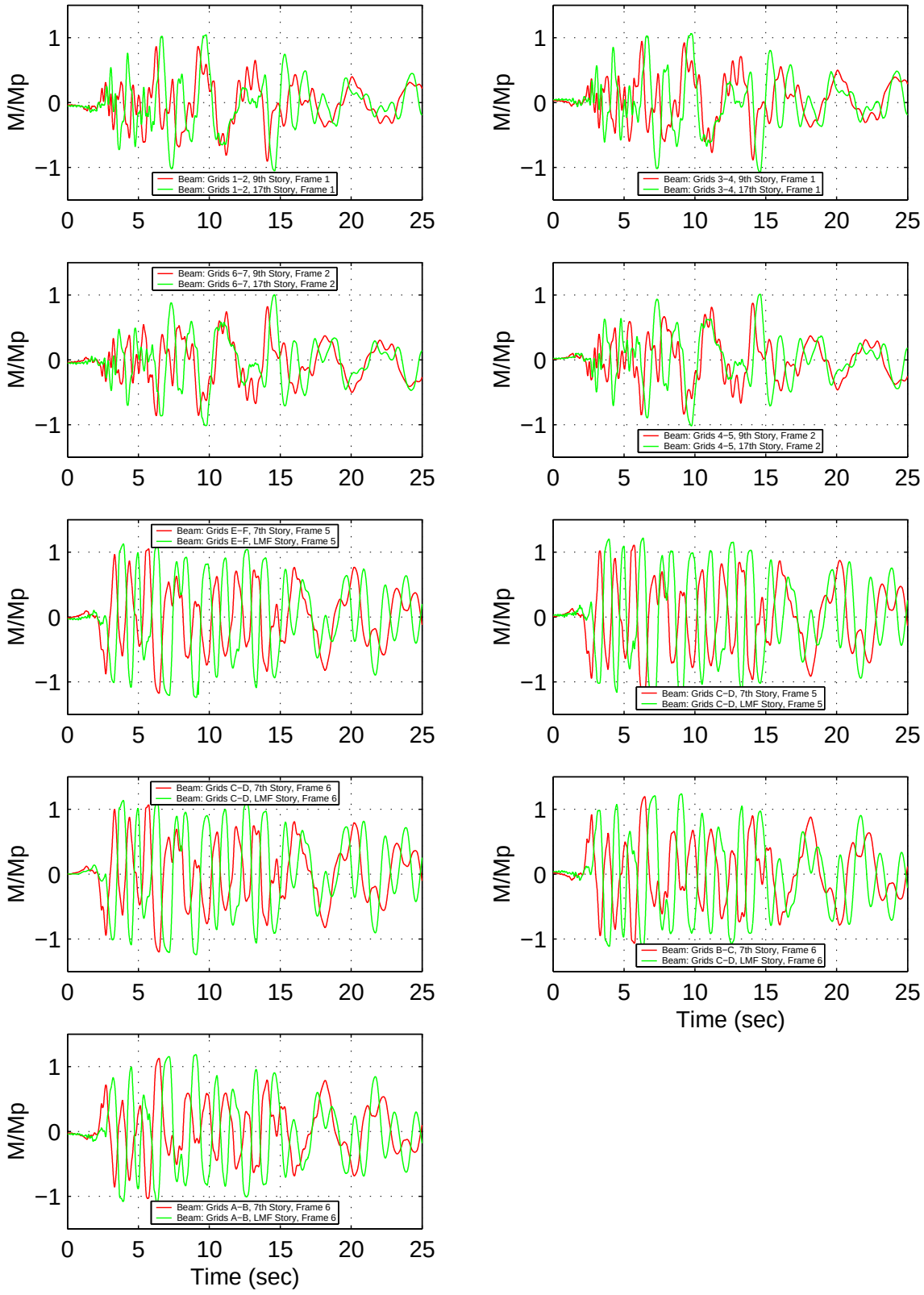

Figure J.12: Building 1: Beam-Column End Moment Histories - Kobe Earthquake (Takatori Record Strong Component in Y Direction)

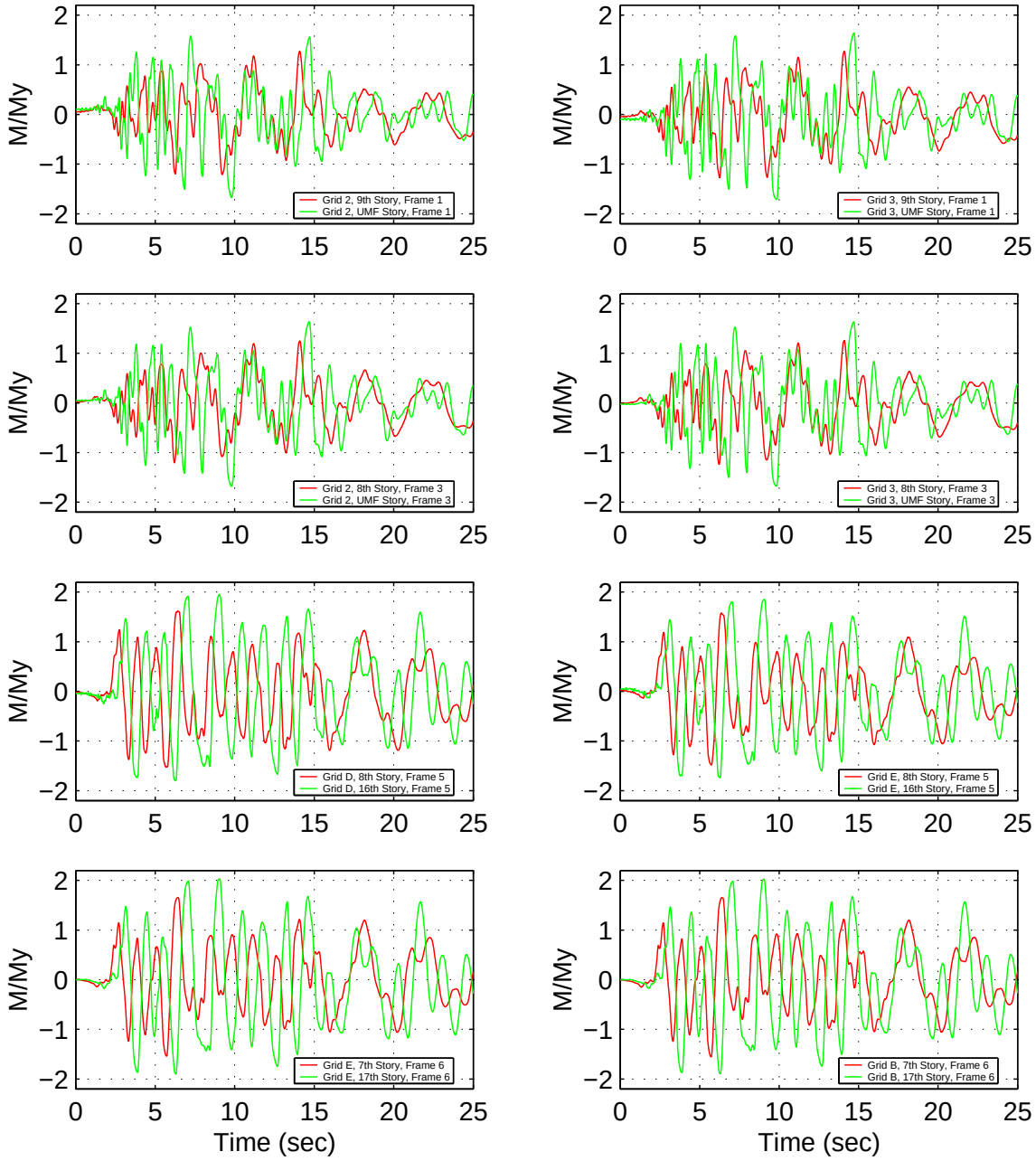

Figure J.13: Building 1: Panel Zone Moment Histories - Kobe Earthquake (Takatori Record Strong Component in Y Direction)

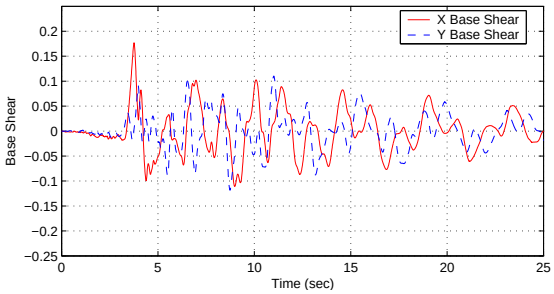

(a) Sylmar Strong Component in X Direction

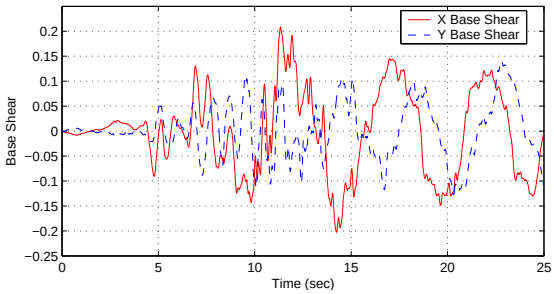

(b) Tabas Strong Component in X Direction

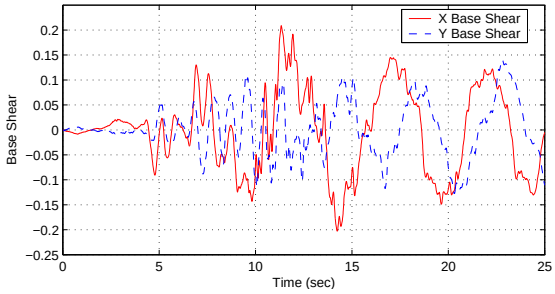

(c) Takatori Strong Component in X Direction

Figure J.14: Building 2 Base Shear History: Northridge (Sylmar), Iran (Tabas) and Kobe (Takatori) Earthquakes

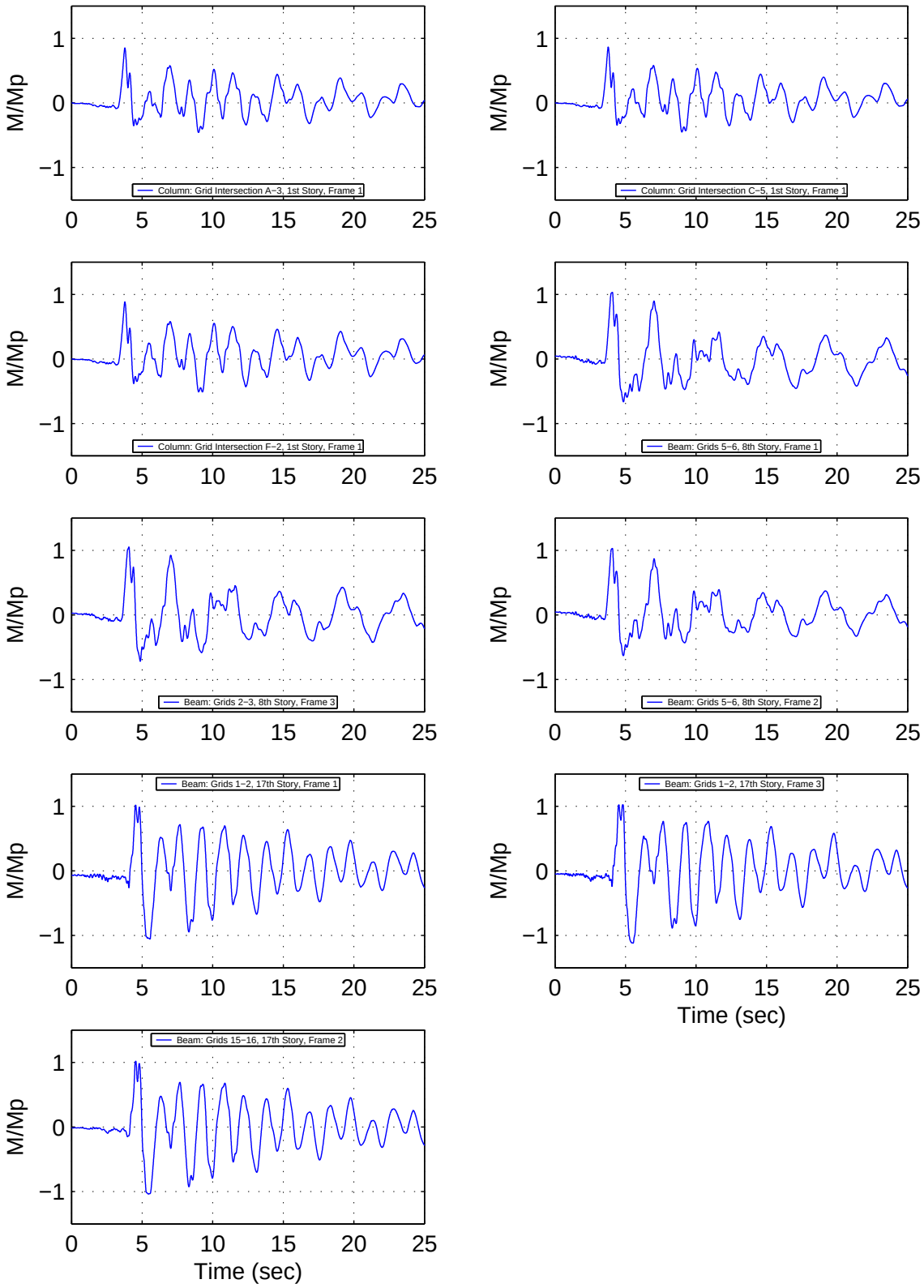

Figure J.15: Building 2: Beam-Column End Moment Histories - Northridge Earthquake (Sylmar Record Strong Component in X Direction)

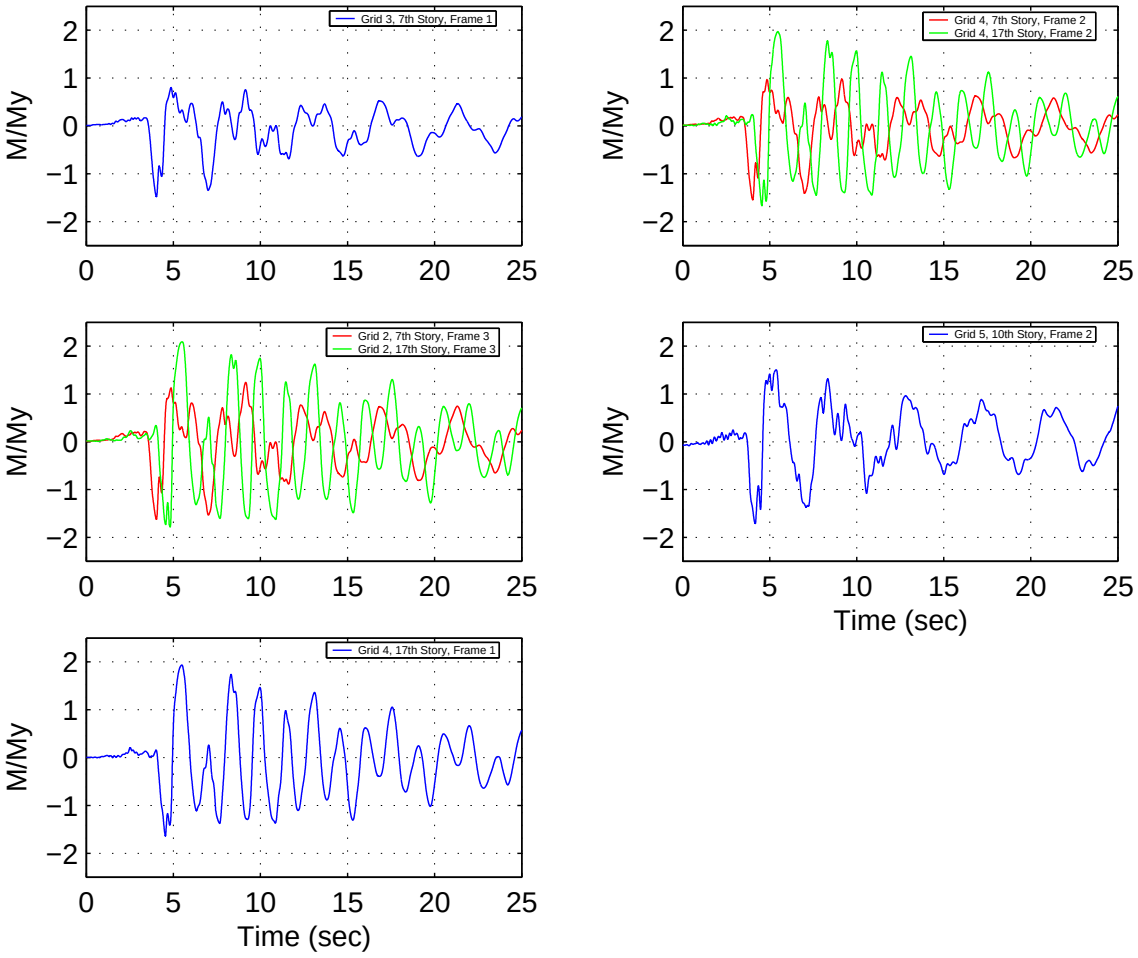

Figure J.16: Building 2: Panel Zone Moment Histories - Northridge Earthquake (Sylmar Record Strong Component in X Direction)

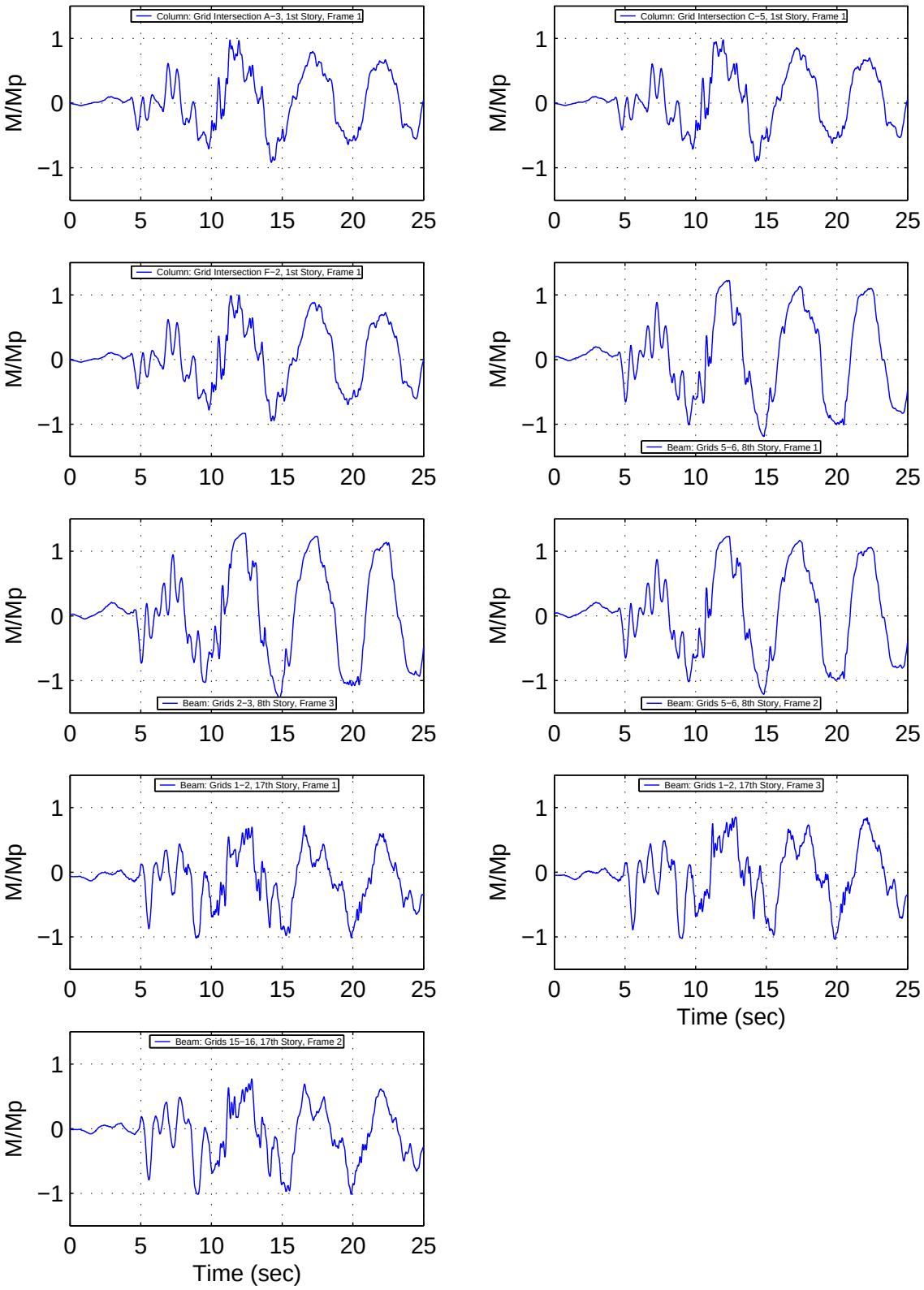

Figure J.17: Building 2: Beam-Column End Moment Histories - Iran Earthquake (Tabas Record Strong Component in X Direction)

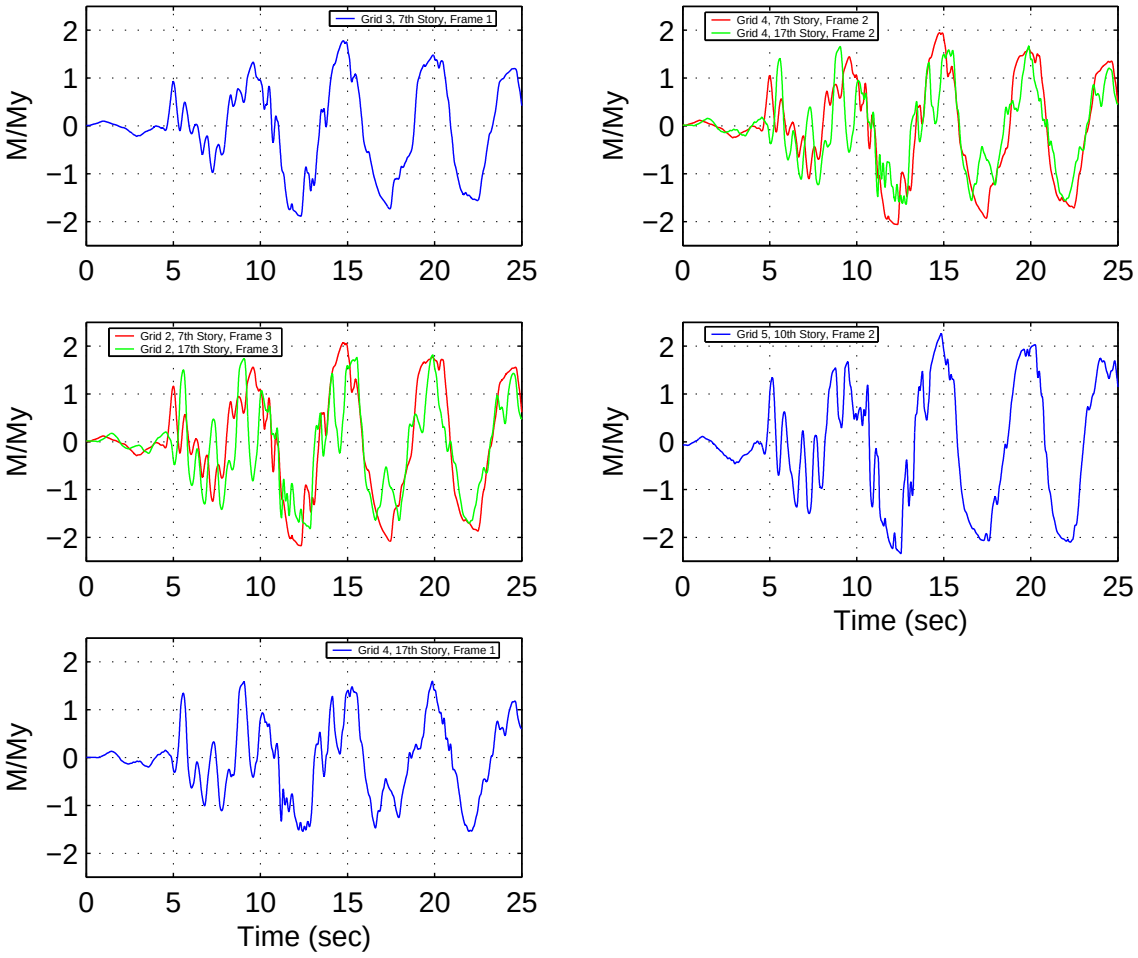

Figure J.18: Building 2: Panel Zone Moment Histories - Iran Earthquake (Tabas Record Strong Component in X Direction)

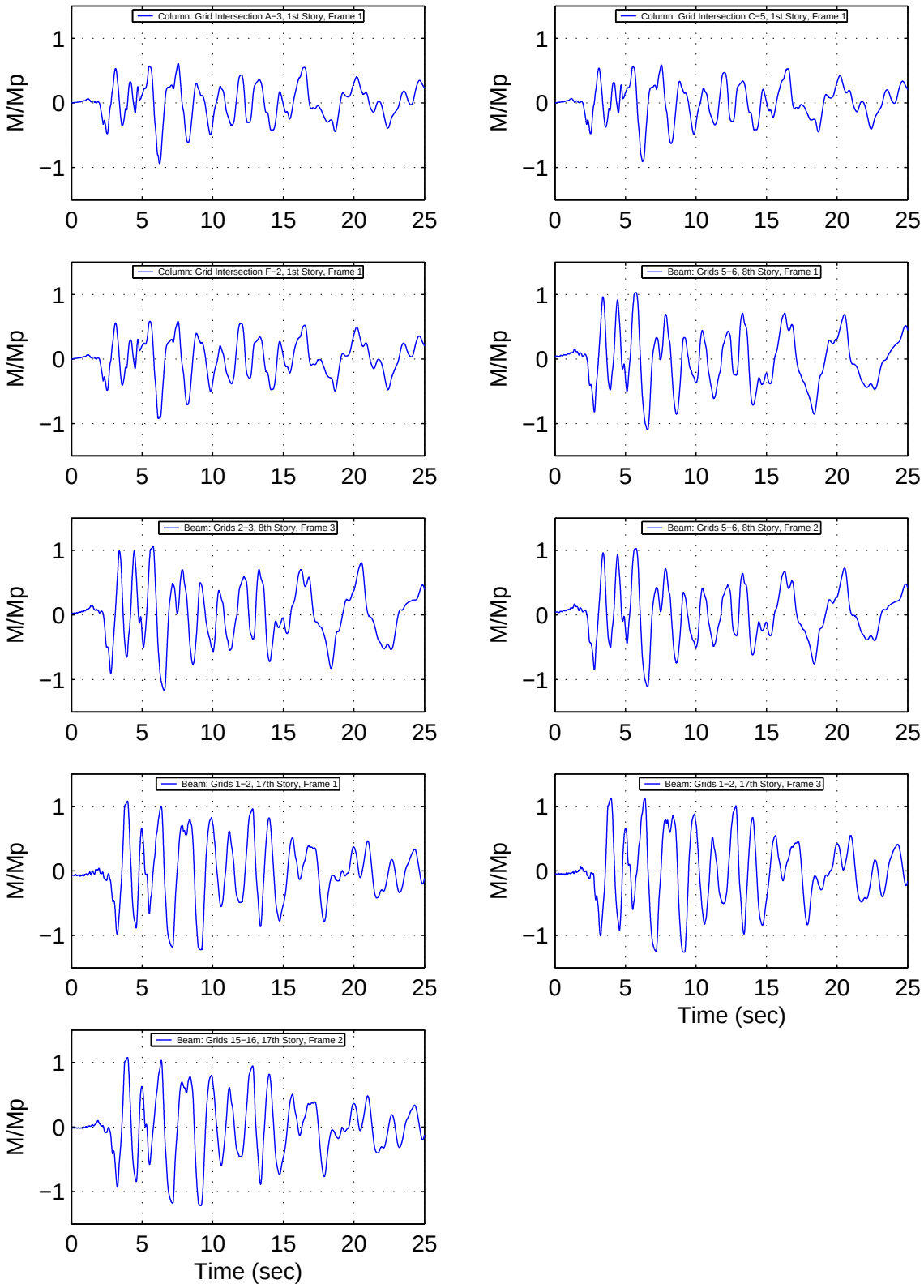

Figure J.19: Building 2: Beam-Column End Moment Histories - Kobe Earthquake (Takatori Record Strong Component in X Direction)

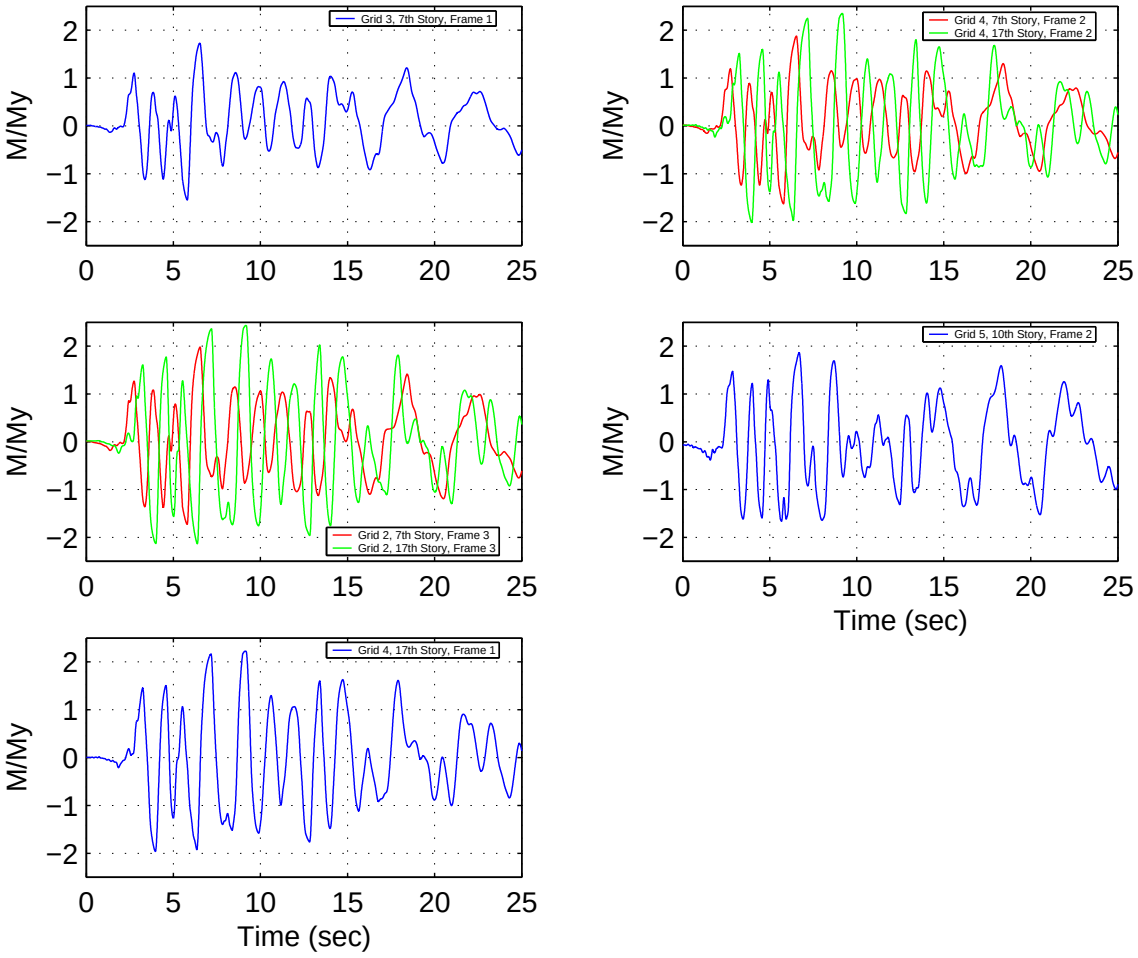

Figure J.20: Building 2: Panel Zone Moment Histories - Kobe Earthquake (Takatori Record Strong Component in X Direction)

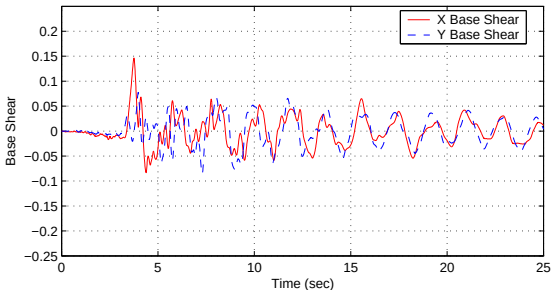

(a) Sylmar Strong Component in X Direction

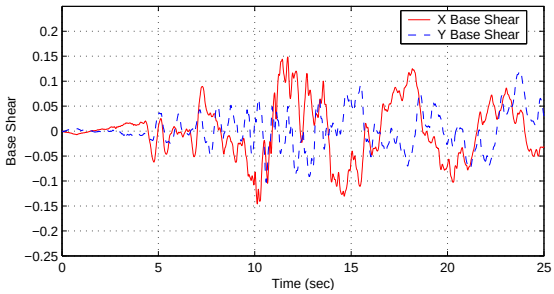

(b) Tabas Strong Component in X Direction

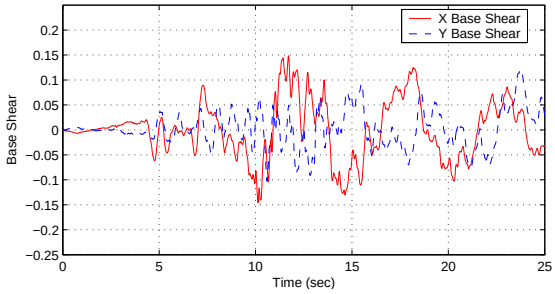

(c) Takatori Strong Component in X Direction

Figure J.21: Building 2A Base Shear History: Northridge (Sylmar), Iran (Tabas) and Kobe (Takatori) Earthquakes

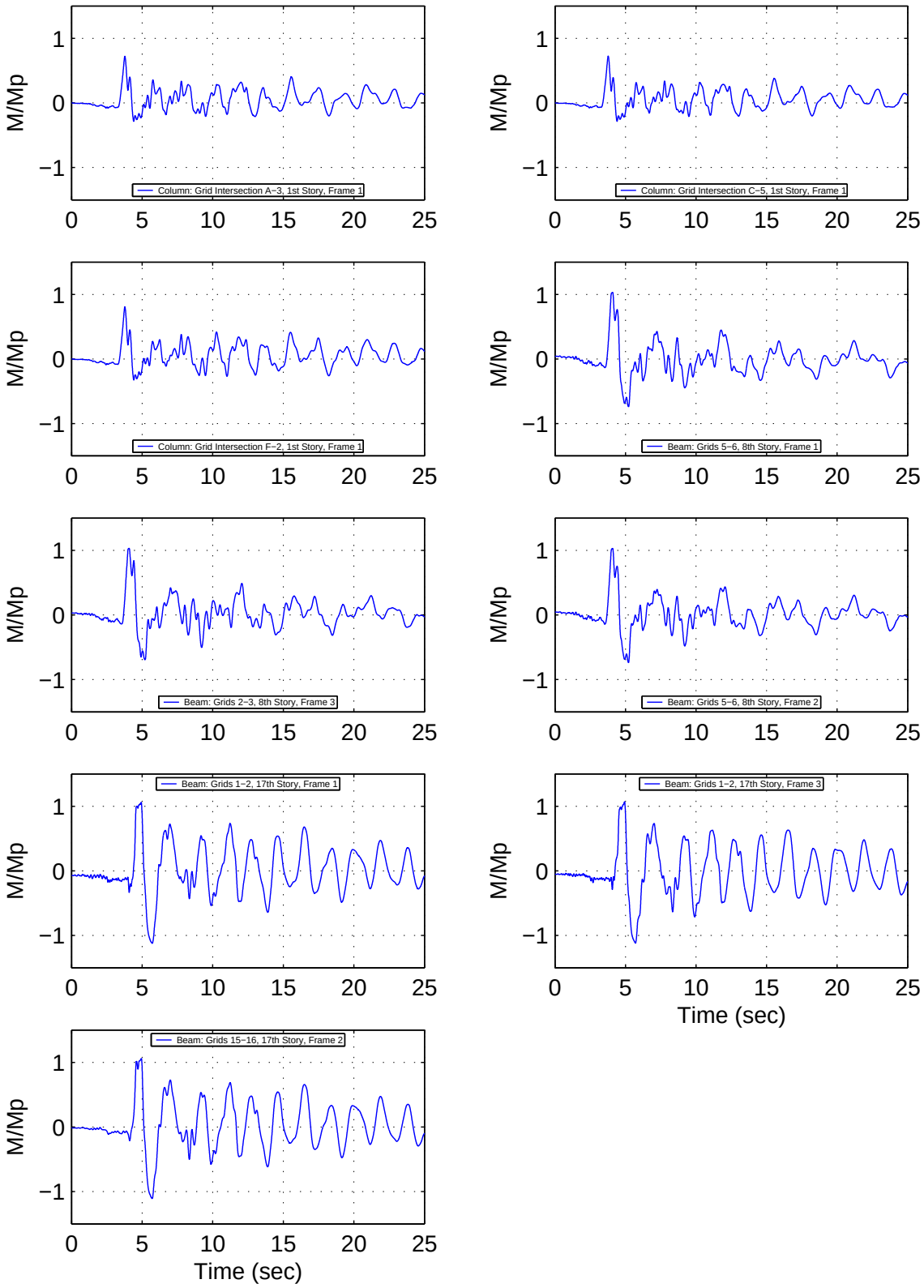

Figure J.22: Building 2A: Beam-Column End Moment Histories - Northridge Earthquake (Sylmar Record Strong Component in X Direction)

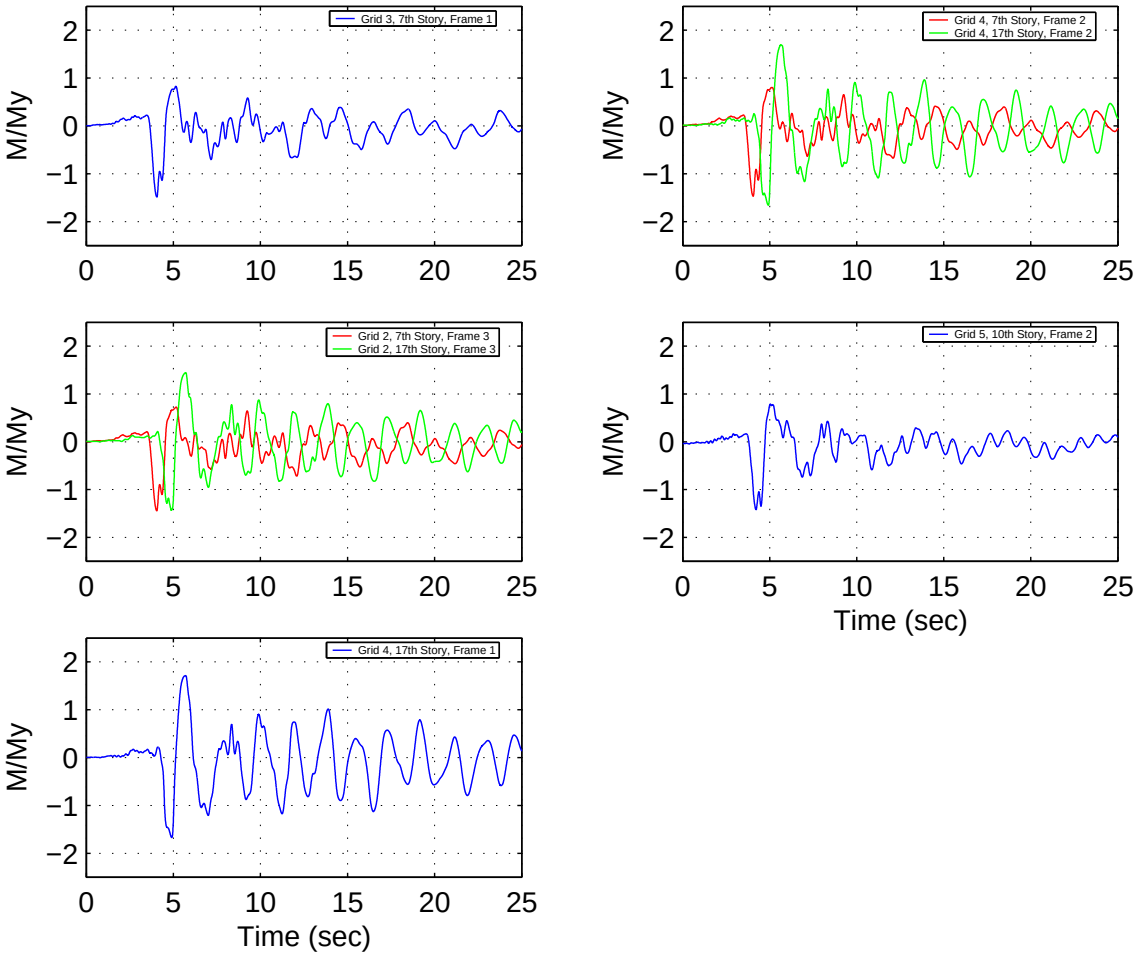

Figure J.23: Building 2A: Panel Zone Moment Histories - Northridge Earthquake (Sylmar Record Strong Component in X Direction)

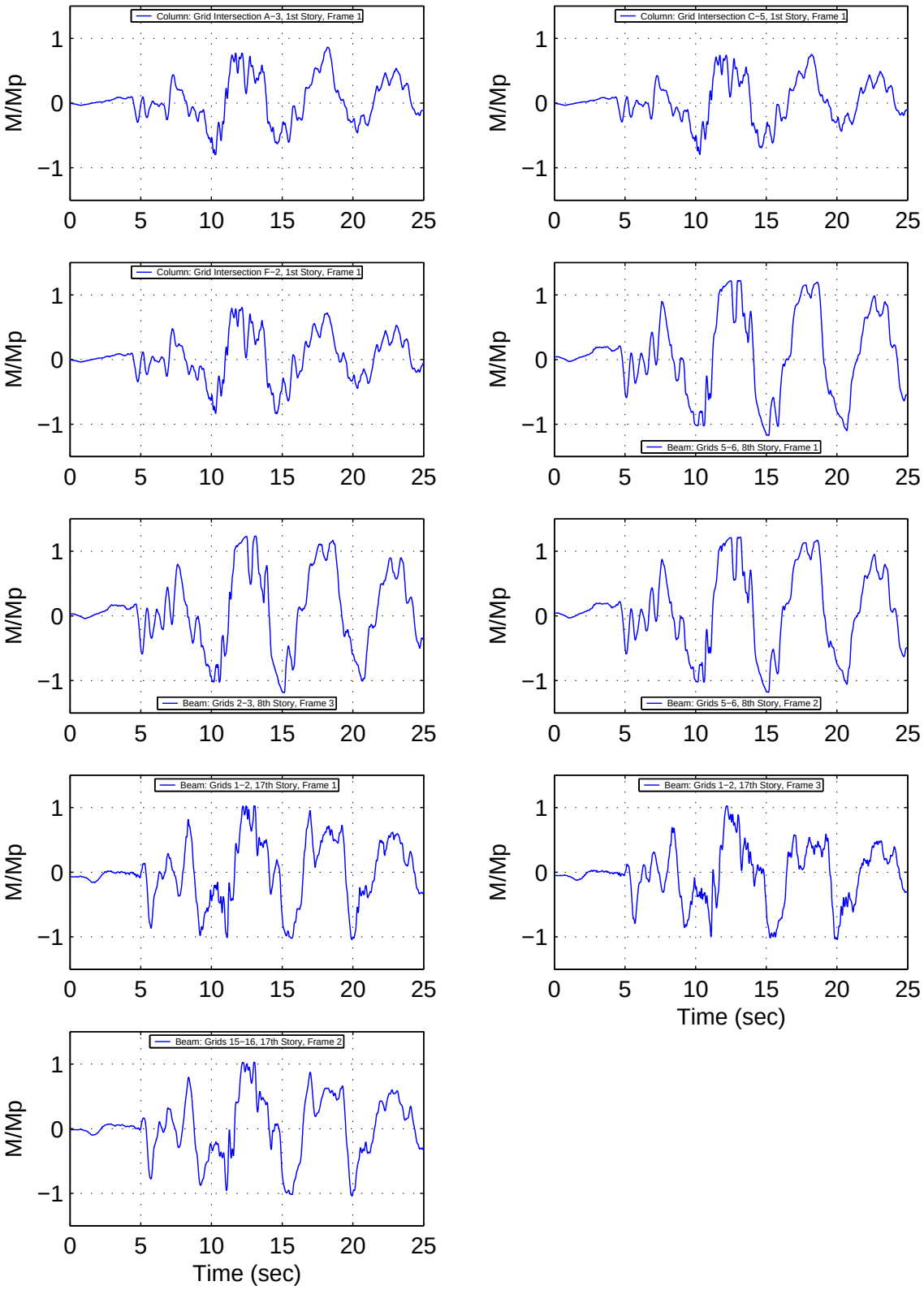

Figure J.24: Building 2A: Beam-Column End Moment Histories - Iran Earthquake (Tabas Record Strong Component in X Direction)

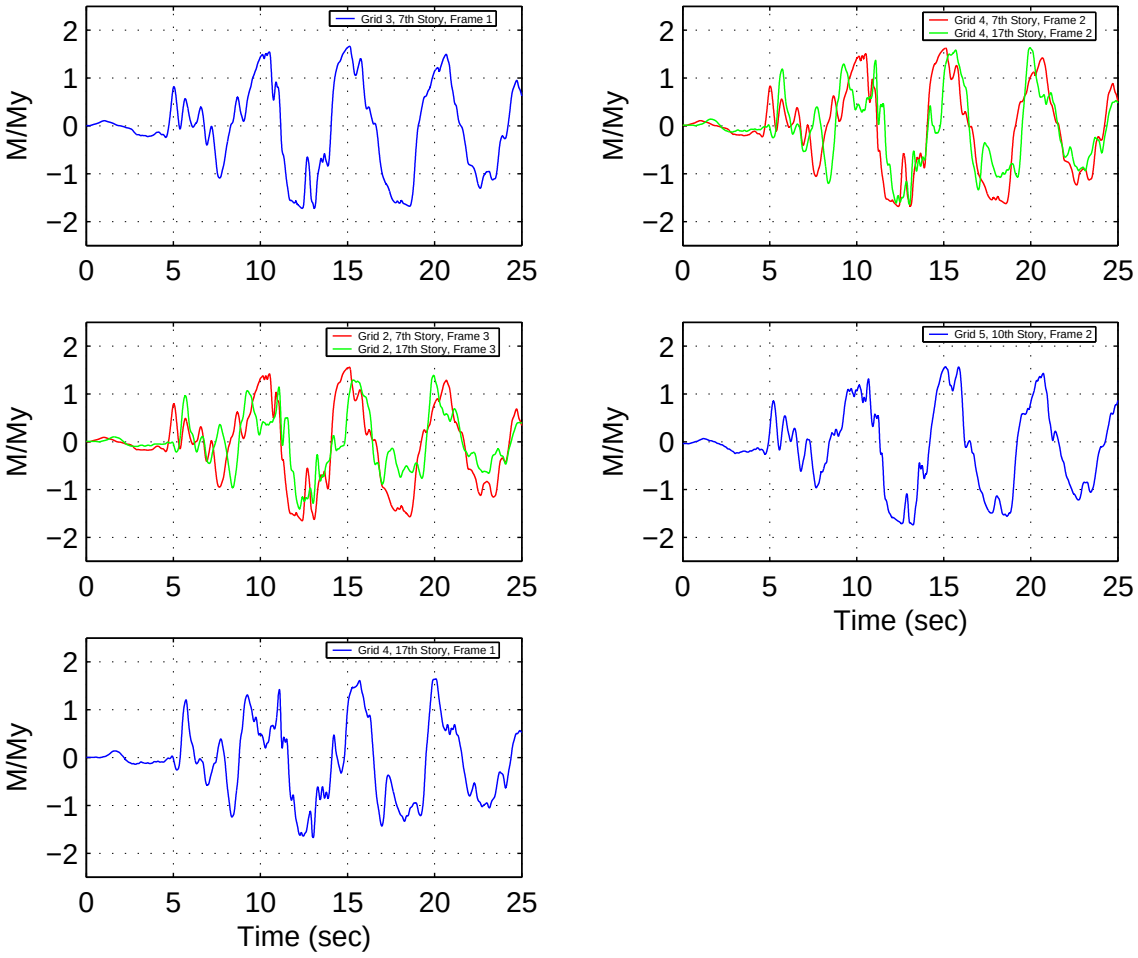

Figure J.25: Building 2A: Panel Zone Moment Histories - Iran Earthquake (Tabas Record Strong Component in X Direction)

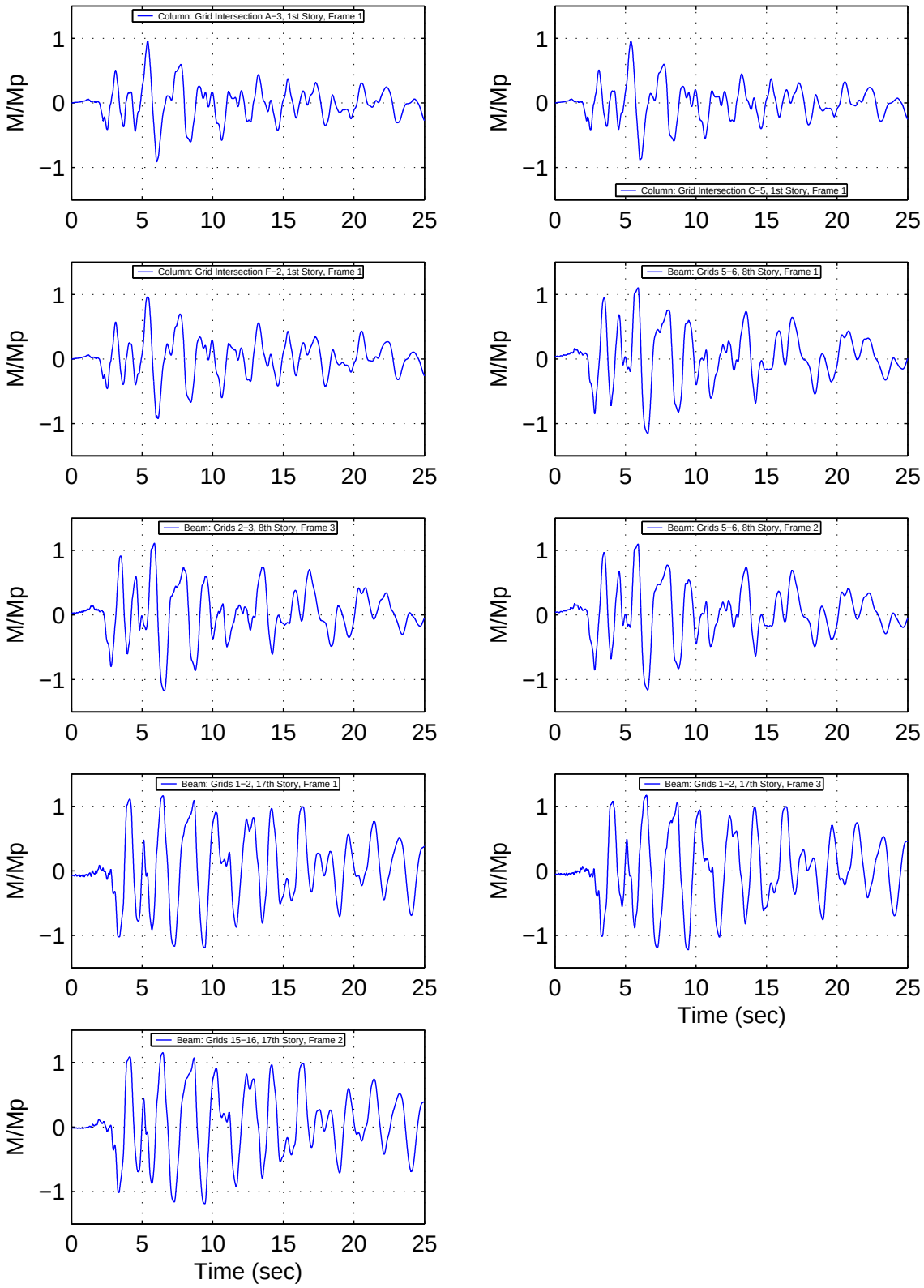

Figure J.26: Building 2A: Beam-Column End Moment Histories - Kobe Earthquake (Takatori Record Strong Component in X Direction)

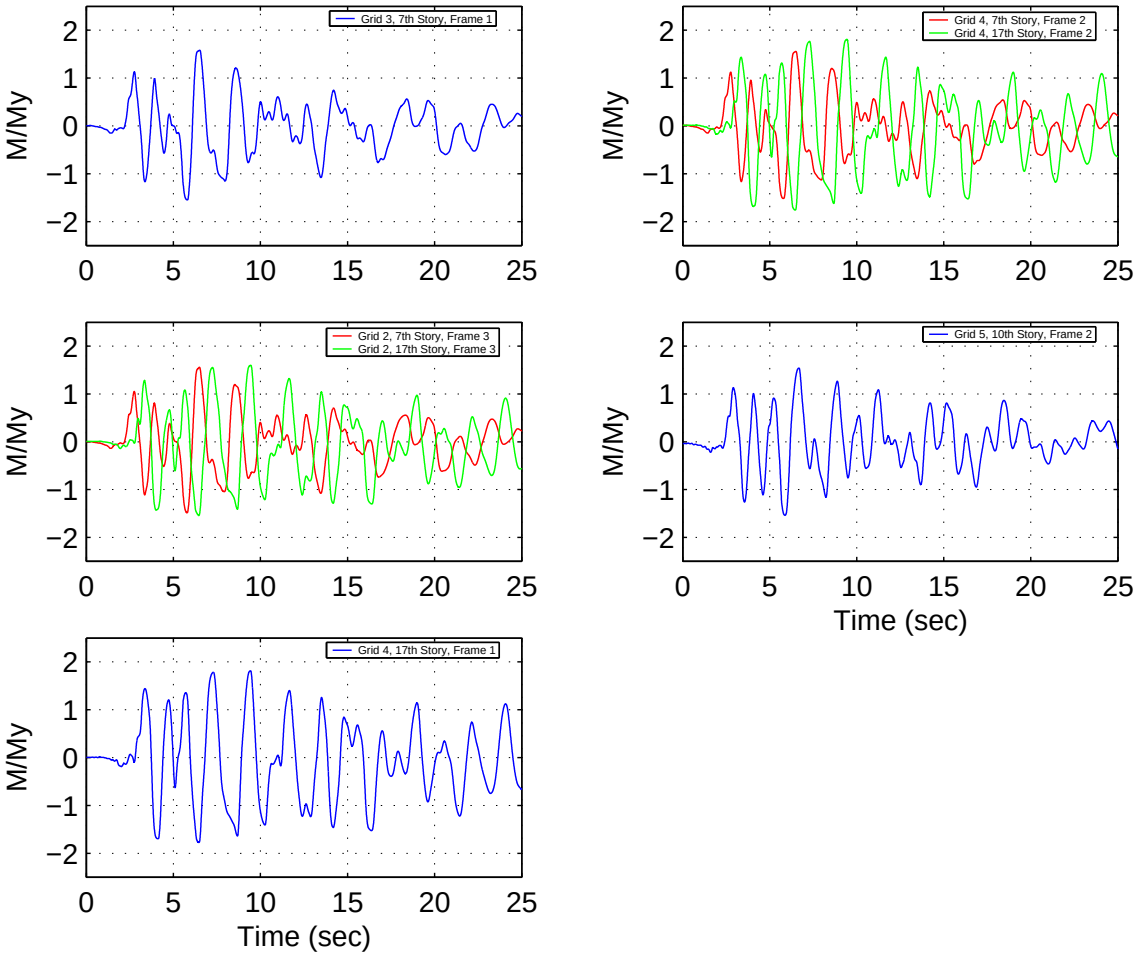

Figure J.27: Building 2A: Panel Zone Moment Histories - Kobe Earthquake (Takatori Record Strong Component in X Direction)

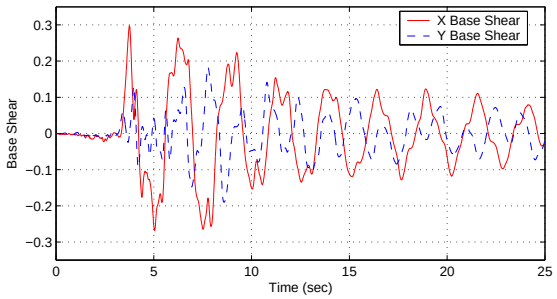

(a) Sylmar Strong Component in X Direction

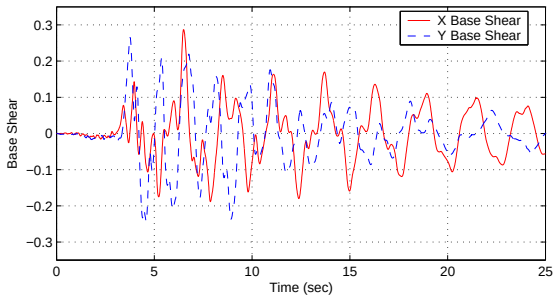

(b) Sylmar Strong Component in Y Direction

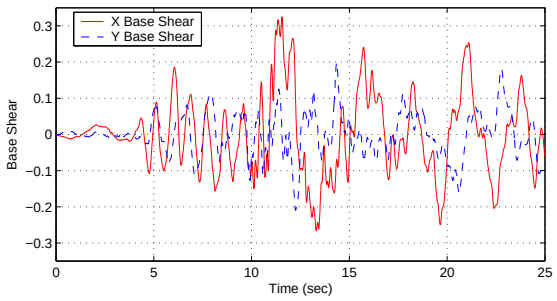

(c) Tabas Strong Component in X Direction

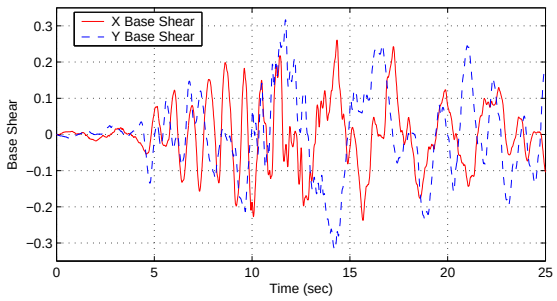

(d) Tabas Strong Component in Y Direction

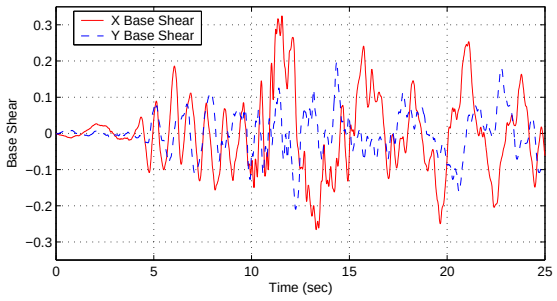

(e) Takatori Strong Component in X Direction

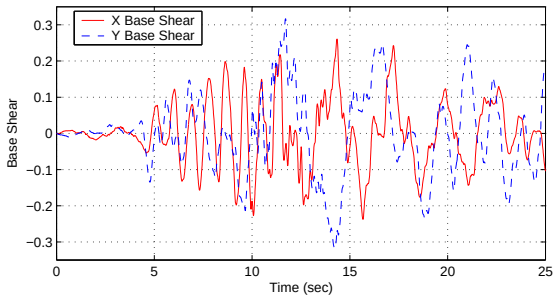

(f) Takatori Strong Component in Y Direction

Figure J.28: Building 3 Base Shear History: Northridge (Sylmar), Iran (Tabas) and Kobe (Takatori) Earthquakes

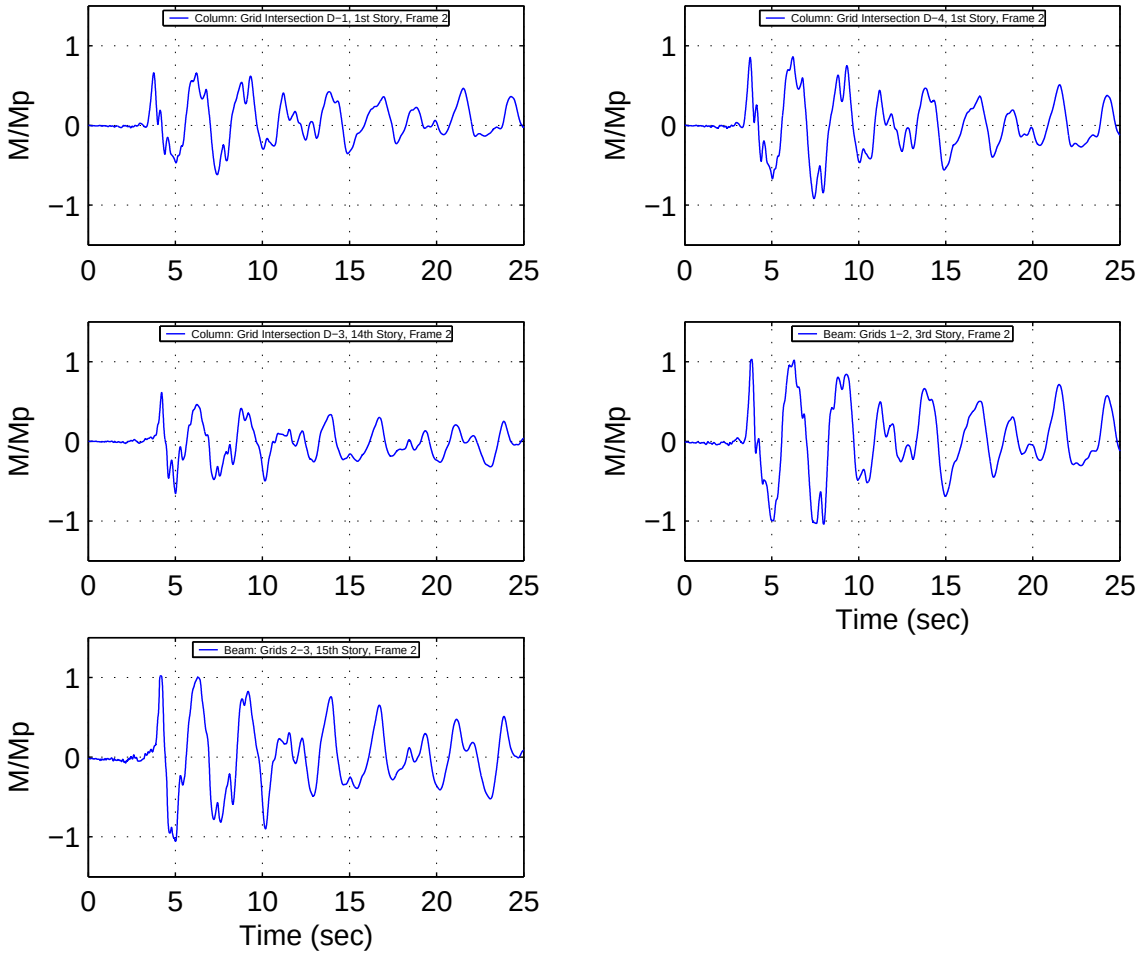

Figure J.29: Building 3: Beam-Column End Moment Histories - Northridge Earthquake (Sylmar Record Strong Component in X Direction)

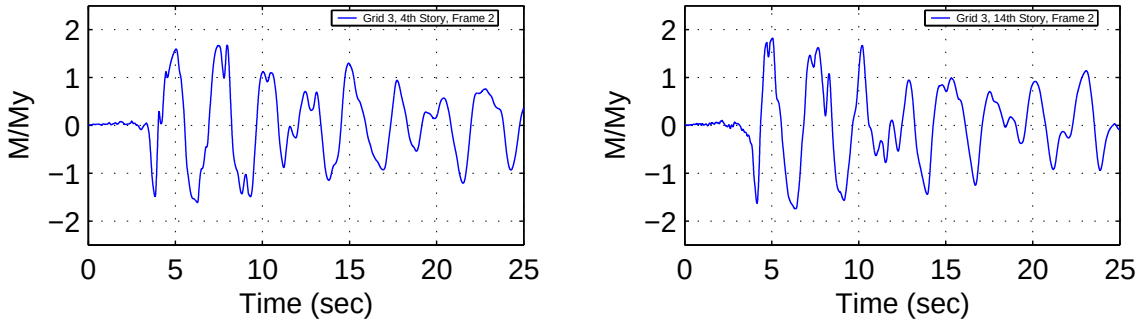

Figure J.30: Building 3: Panel Zone Moment Histories - Northridge Earthquake (Sylmar Record Strong Component in X Direction)

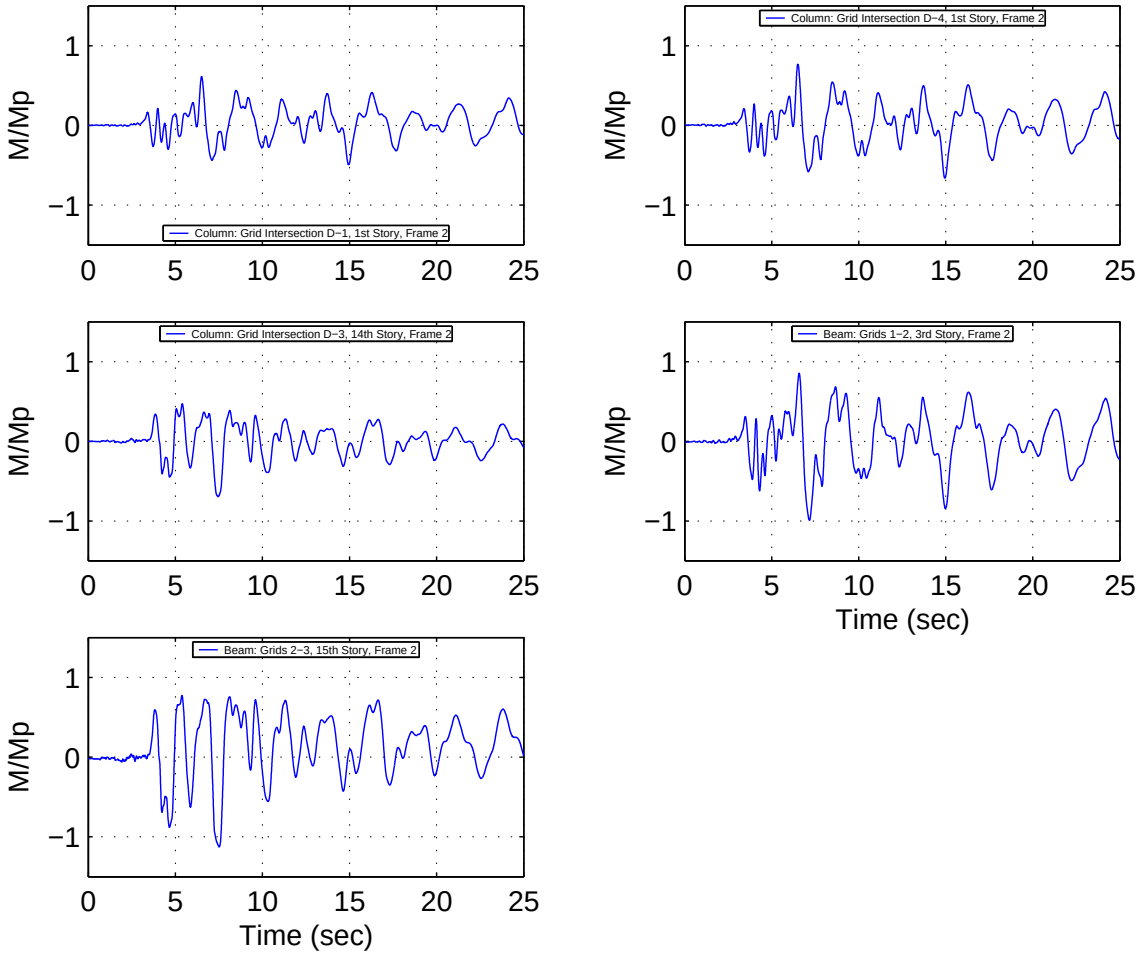

Figure J.31: Building 3: Beam-Column End Moment Histories - Northridge Earthquake (Sylmar Record Strong Component in Y Direction)

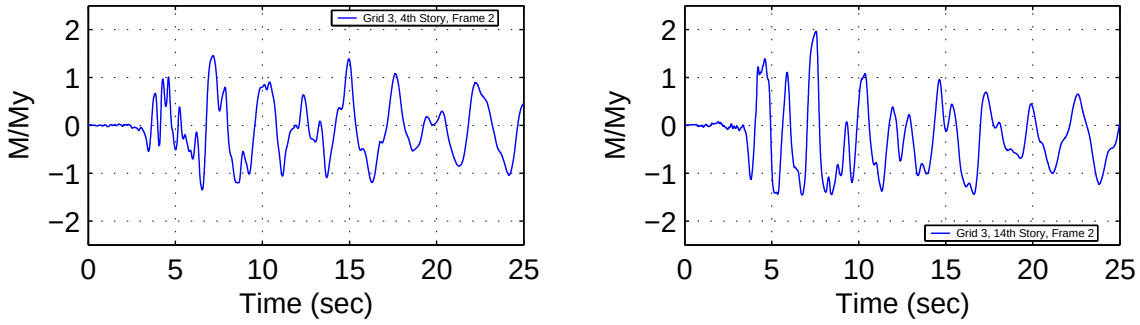

Figure J.32: Building 3: Panel Zone Moment Histories - Northridge Earthquake (Sylmar Record Strong Component in Y Direction)

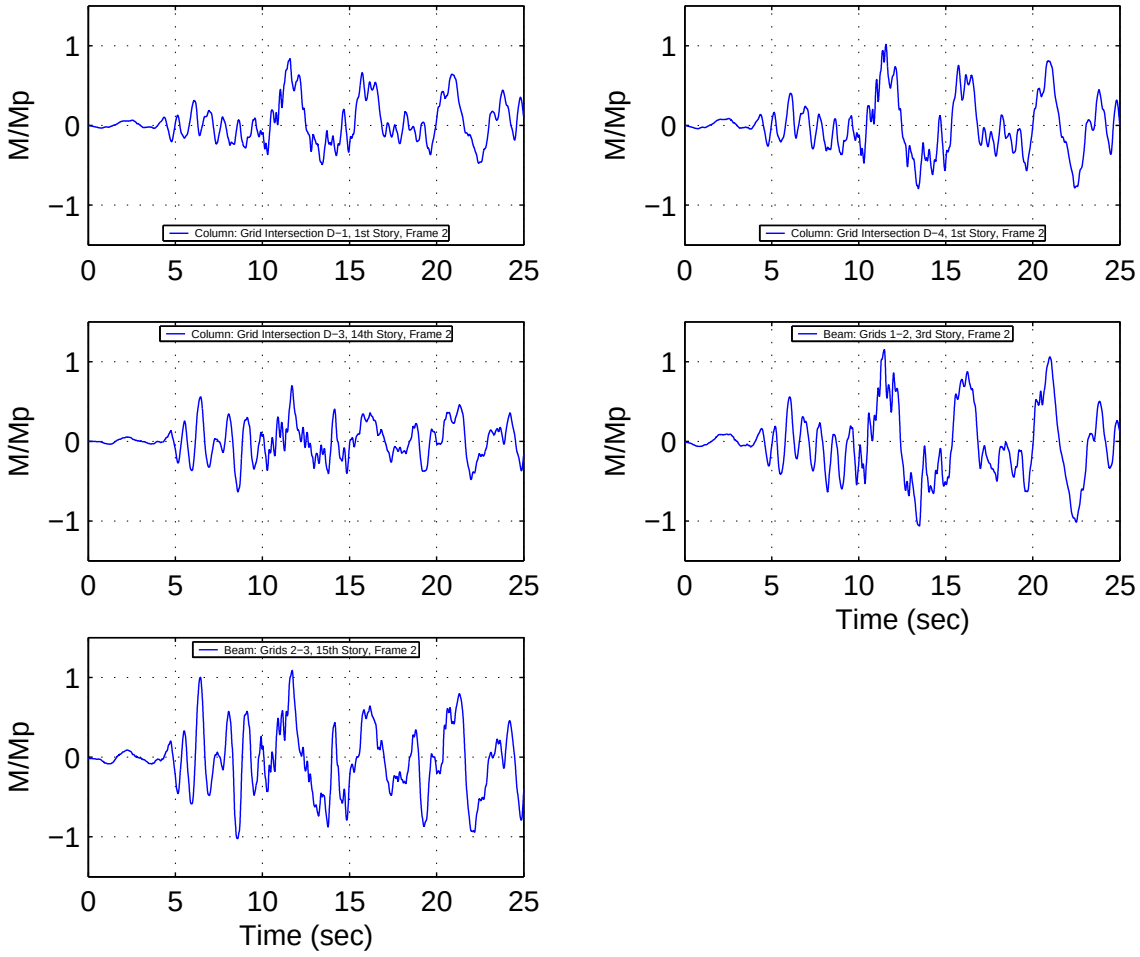

Figure J.33: Building 3: Beam-Column End Moment Histories - Iran Earthquake (Tabas Record Strong Component in X Direction)

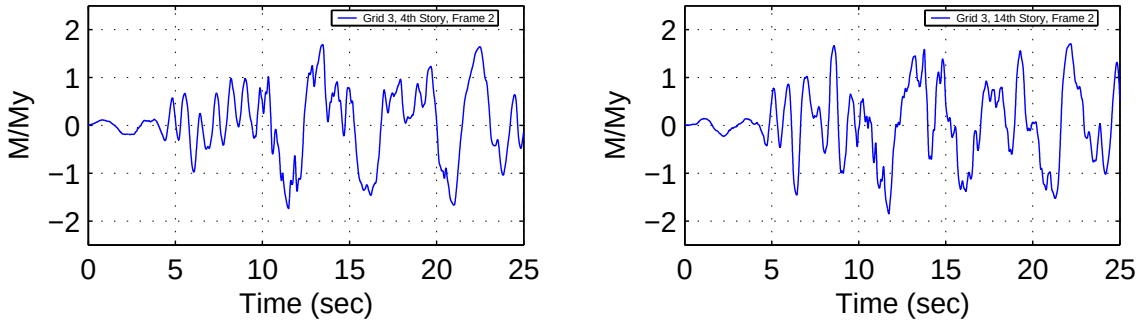

Figure J.34: Building 3: Panel Zone Moment Histories - Iran Earthquake (Tabas Record Strong Component in X Direction)

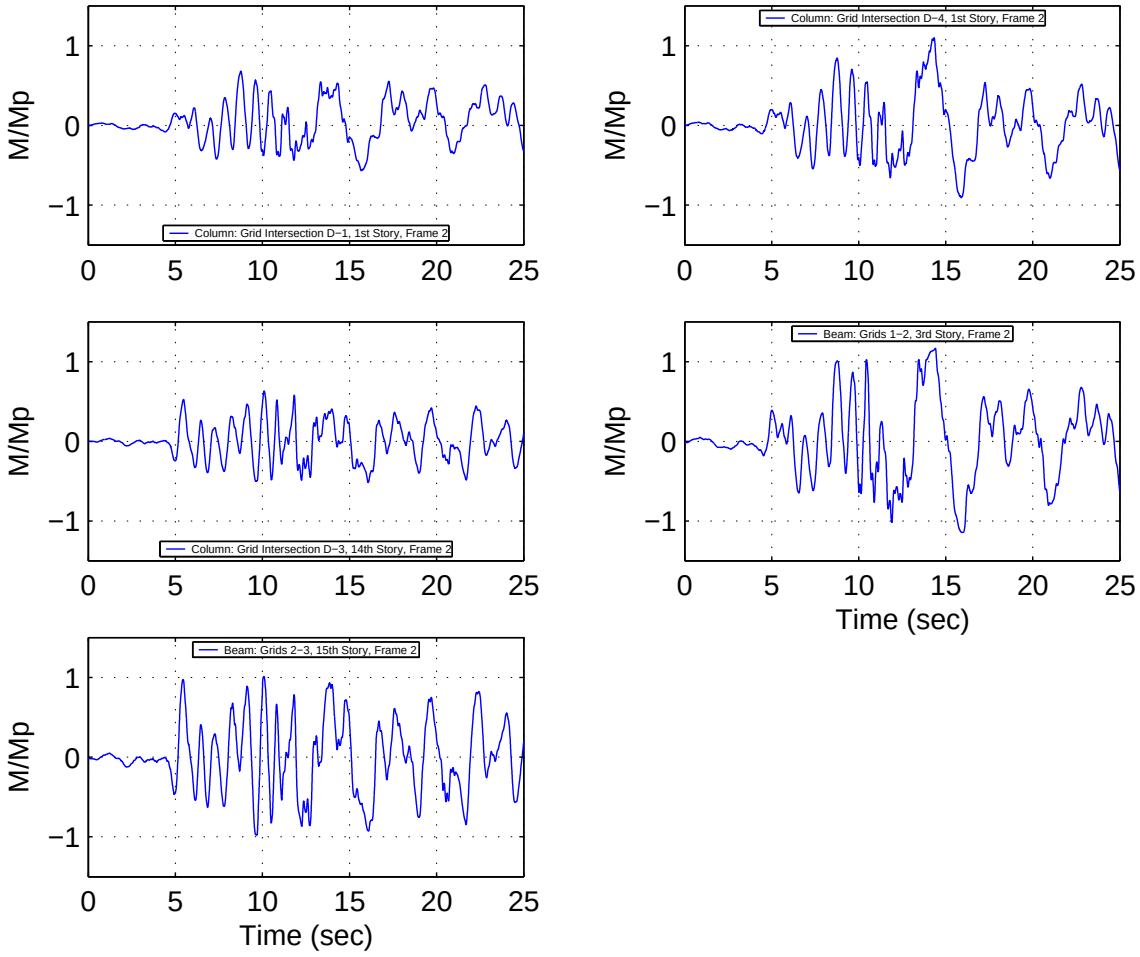

Figure J.35: Building 3: Beam-Column End Moment Histories - Iran Earthquake (Tabas Record Strong Component in Y Direction)

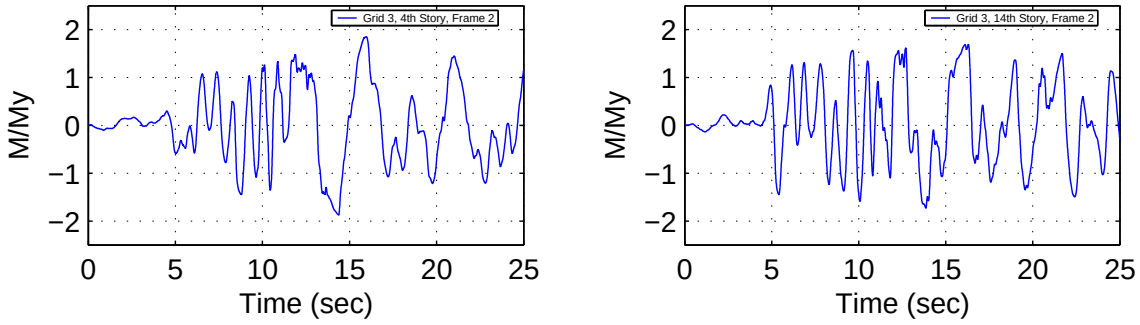

Figure J.36: Building 3: Panel Zone Moment Histories - Iran Earthquake (Tabas Record Strong Component in Y Direction)

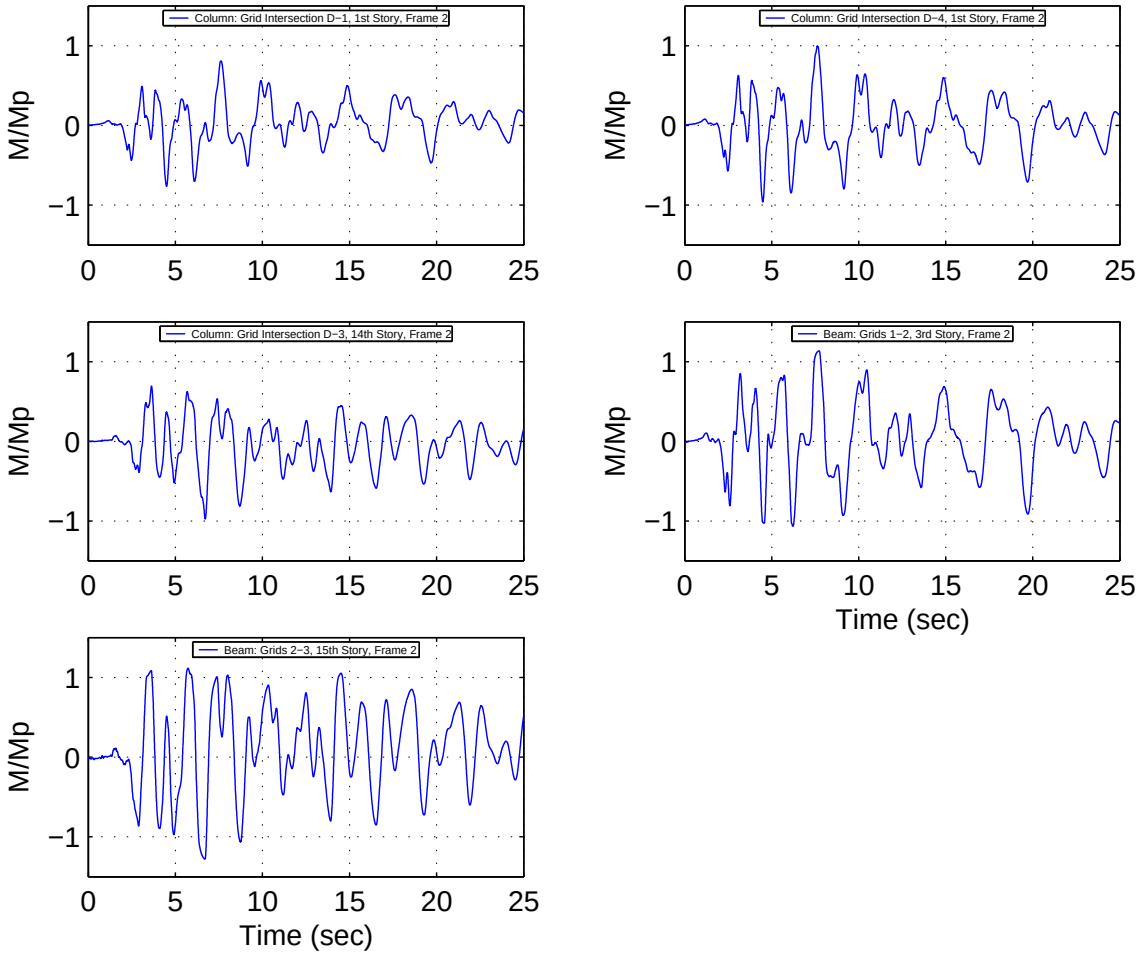

Figure J.37: Building 3: Beam-Column End Moment Histories - Kobe Earthquake (Takatori Record Strong Component in X Direction)

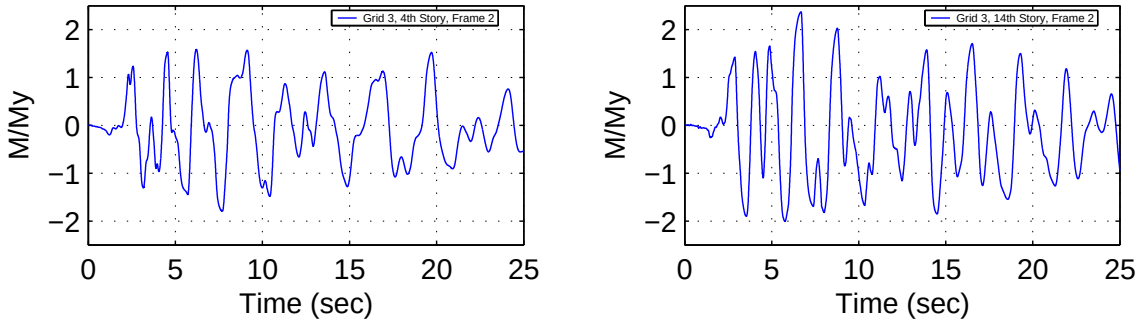

Figure J.38: Building 3: Panel Zone Moment Histories - Kobe Earthquake (Takatori Record Strong Component in X Direction)

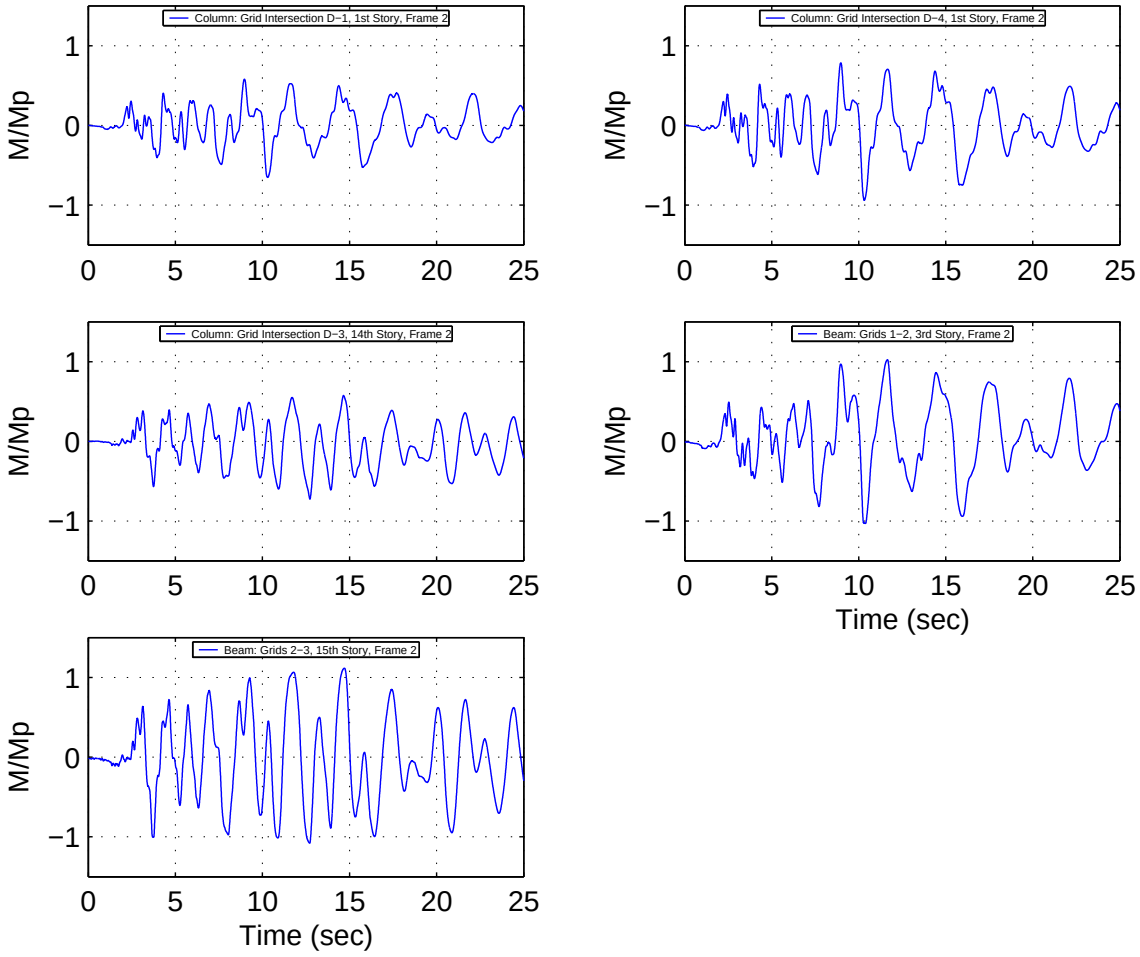

Figure J.39: Building 3: Beam-Column End Moment Histories - Kobe Earthquake (Takatori Record Strong Component in Y Direction)

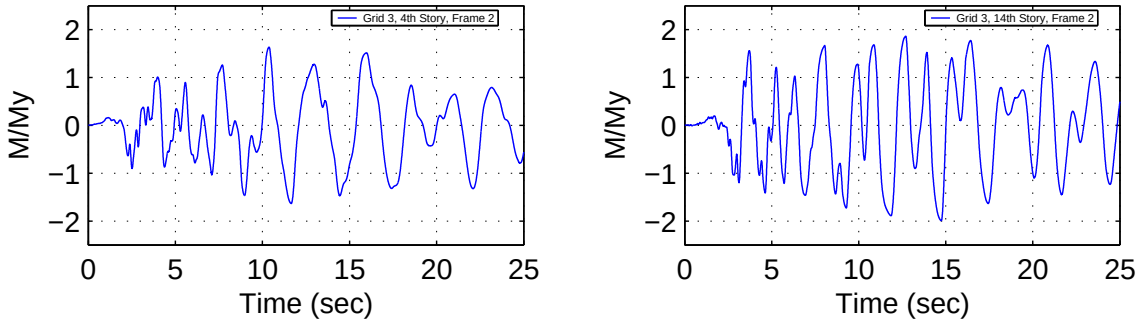

Figure J.40: Building 3: Panel Zone Moment Histories - Kobe Earthquake (Takatori Record Strong Component in Y Direction)

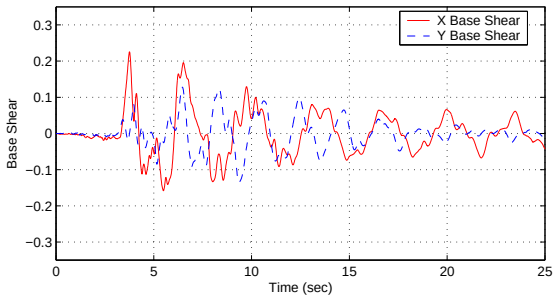

(a) Sylmar Strong Component in X Direction

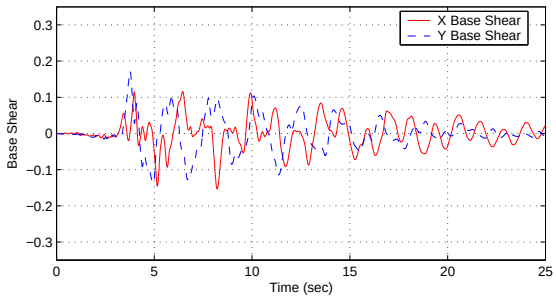

(b) Sylmar Strong Component in Y Direction

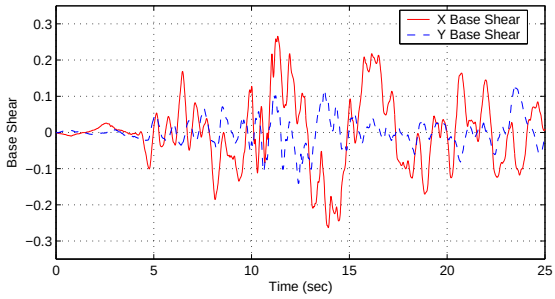

(c) Tabas Strong Component in X Direction

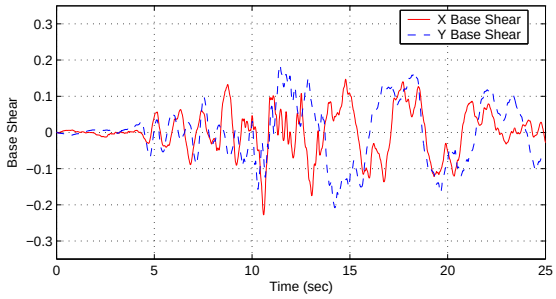

(d) Tabas Strong Component in Y Direction

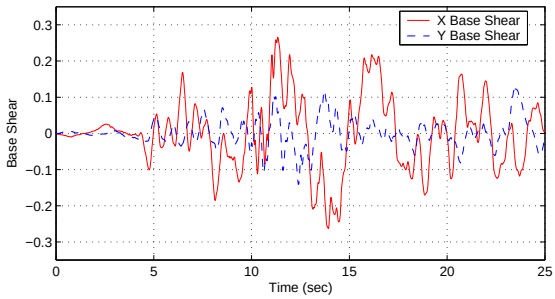

(e) Takatori Strong Component in X Direction

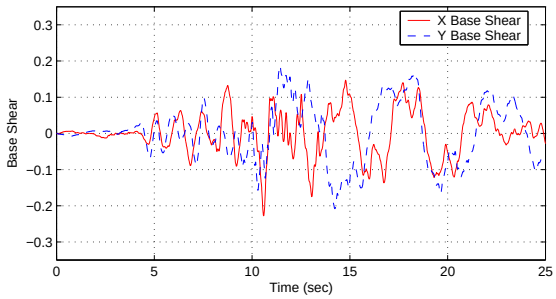

(f) Takatori Strong Component in Y Direction

Figure J.41: Building 3A Base Shear History: Northridge (Sylmar), Iran (Tabas) and Kobe (Takatori) Earthquakes

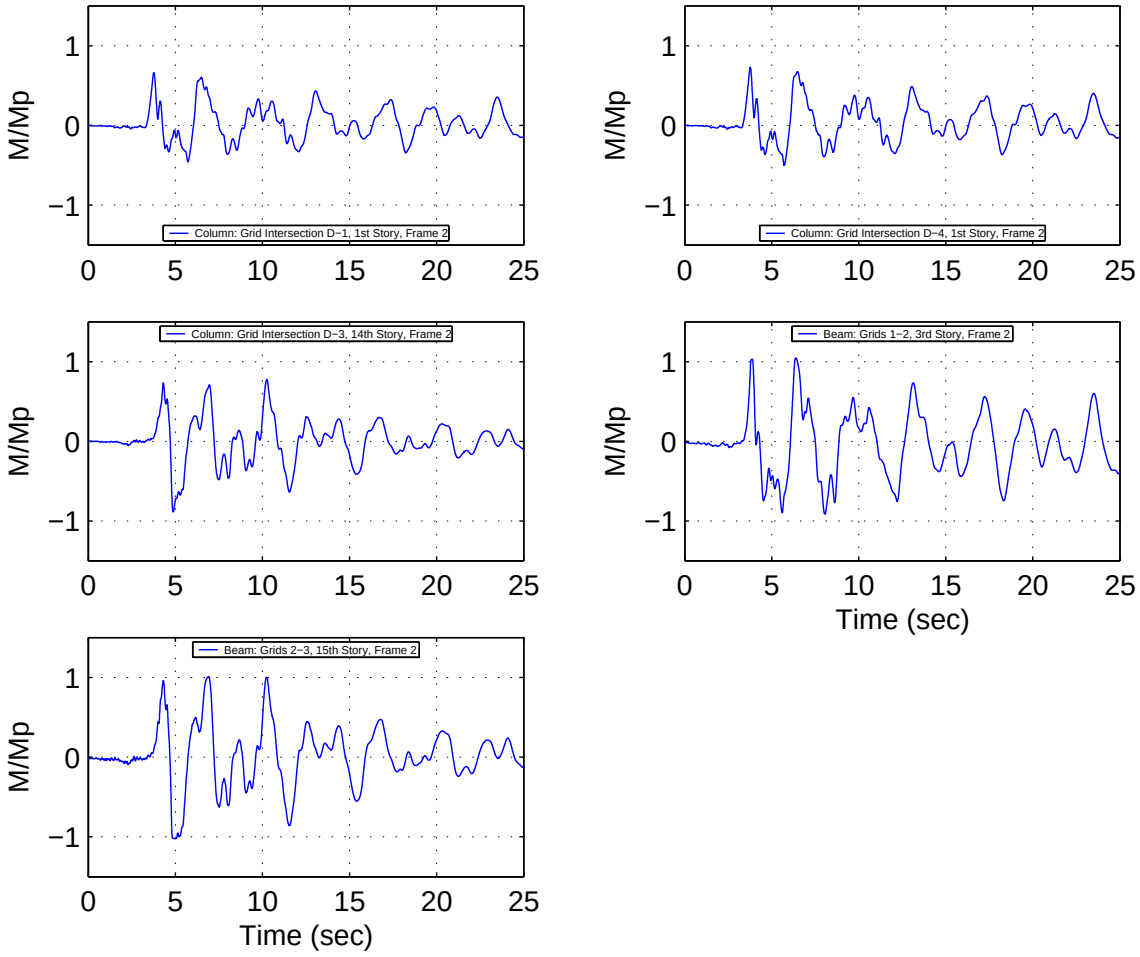

Figure J.42: Building 3A: Beam-Column End Moment Histories - Northridge Earthquake (Sylmar Record Strong Component in X Direction)

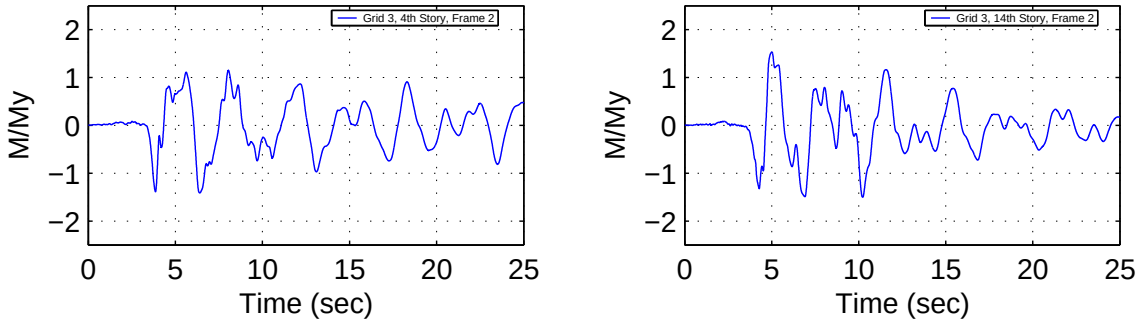

Figure J.43: Building 3A: Panel Zone Moment Histories - Northridge Earthquake (Sylmar Record Strong Component in X Direction)

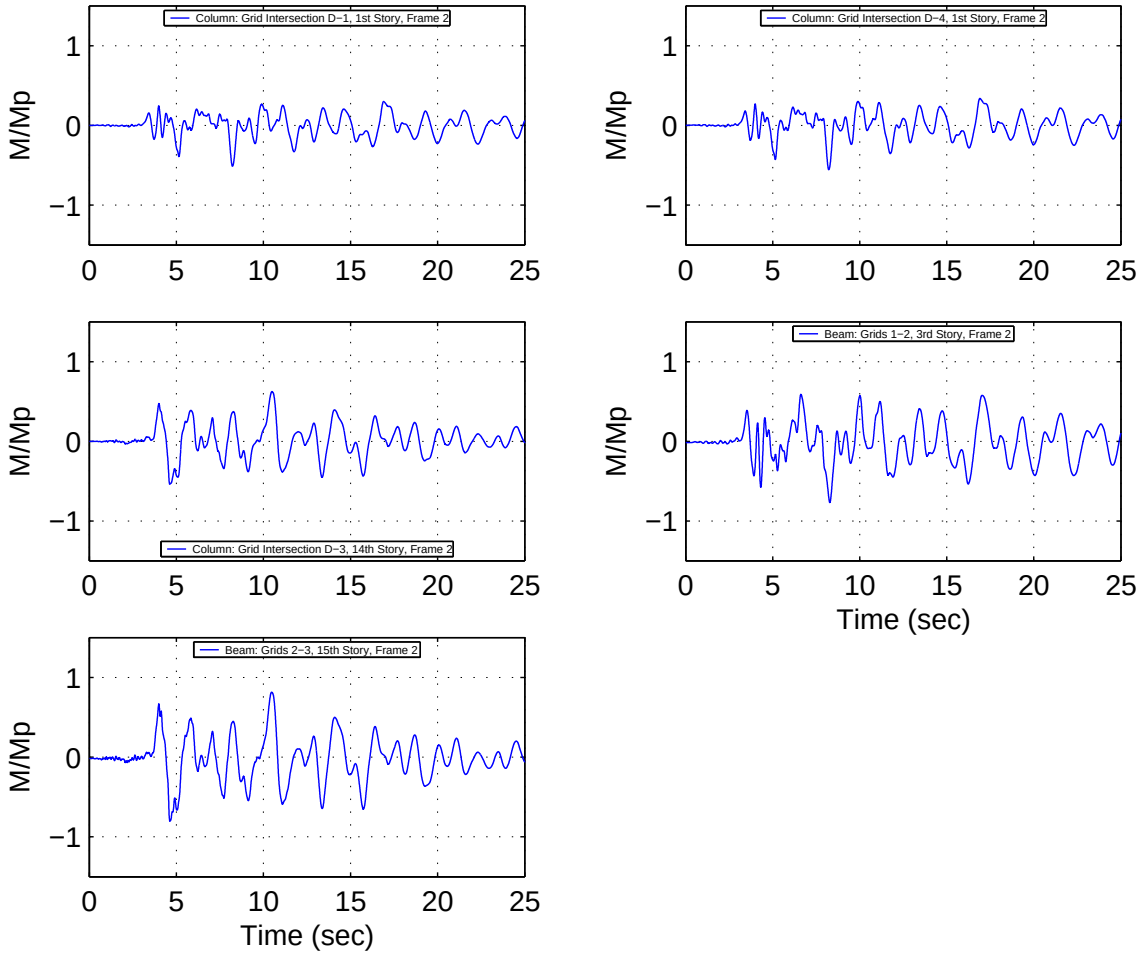

Figure J.44: Building 3A: Beam-Column End Moment Histories - Northridge Earthquake (Sylmar Record Strong Component in Y Direction)

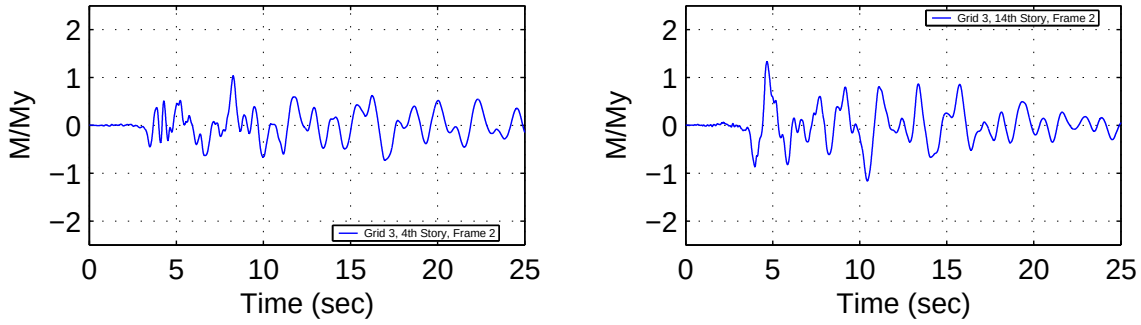

Figure J.45: Building 3A: Panel Zone Moment Histories - Northridge Earthquake (Sylmar Record Strong Component in Y Direction)

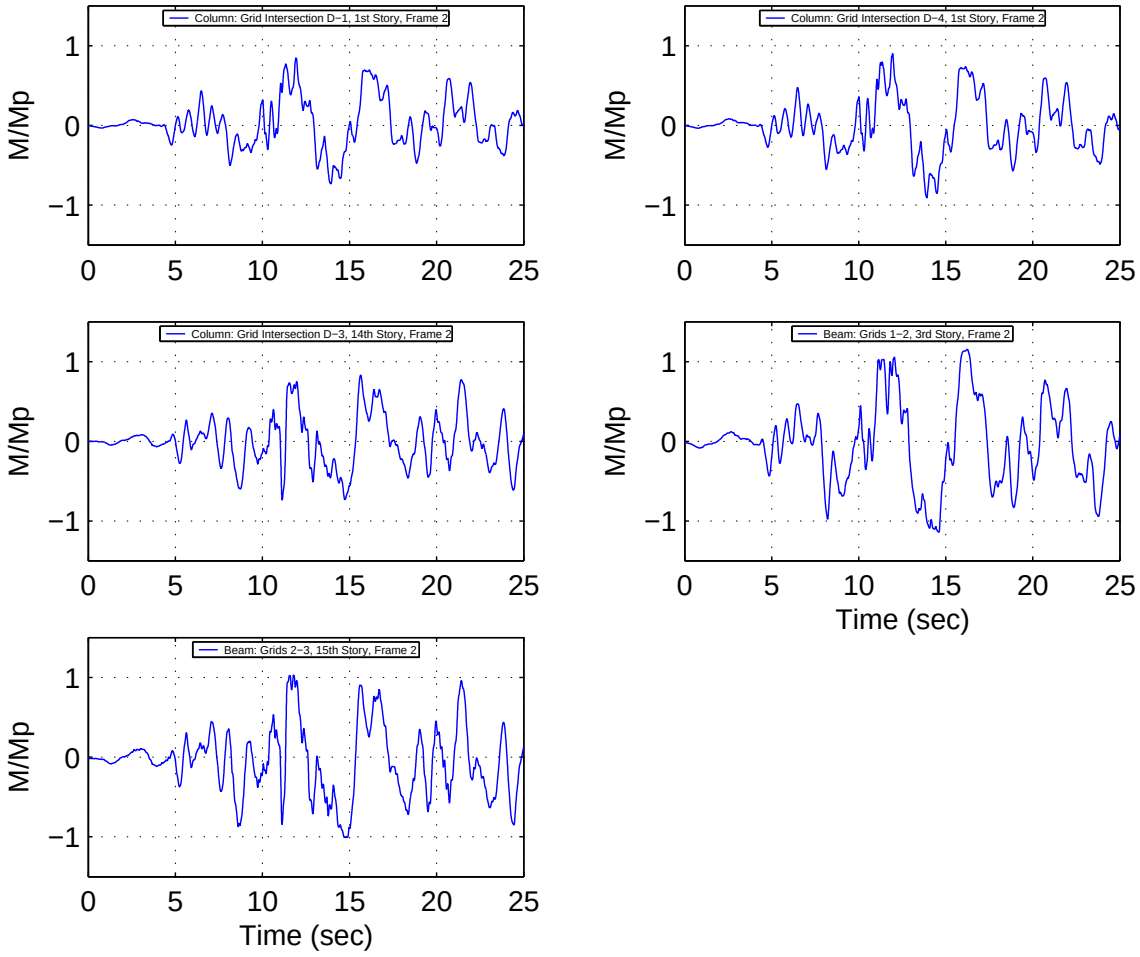

Figure J.46: Building 3A: Beam-Column End Moment Histories - Iran Earthquake (Tabas Record Strong Component in X Direction)

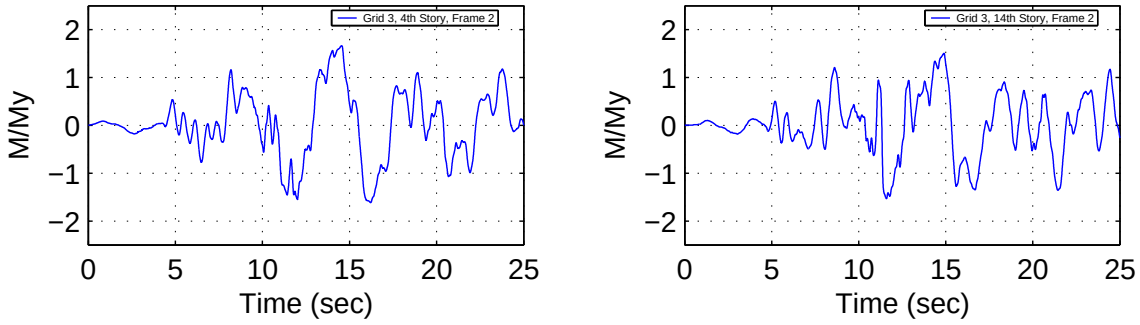

Figure J.47: Building 3A: Panel Zone Moment Histories - Iran Earthquake (Tabas Record Strong Component in X Direction)

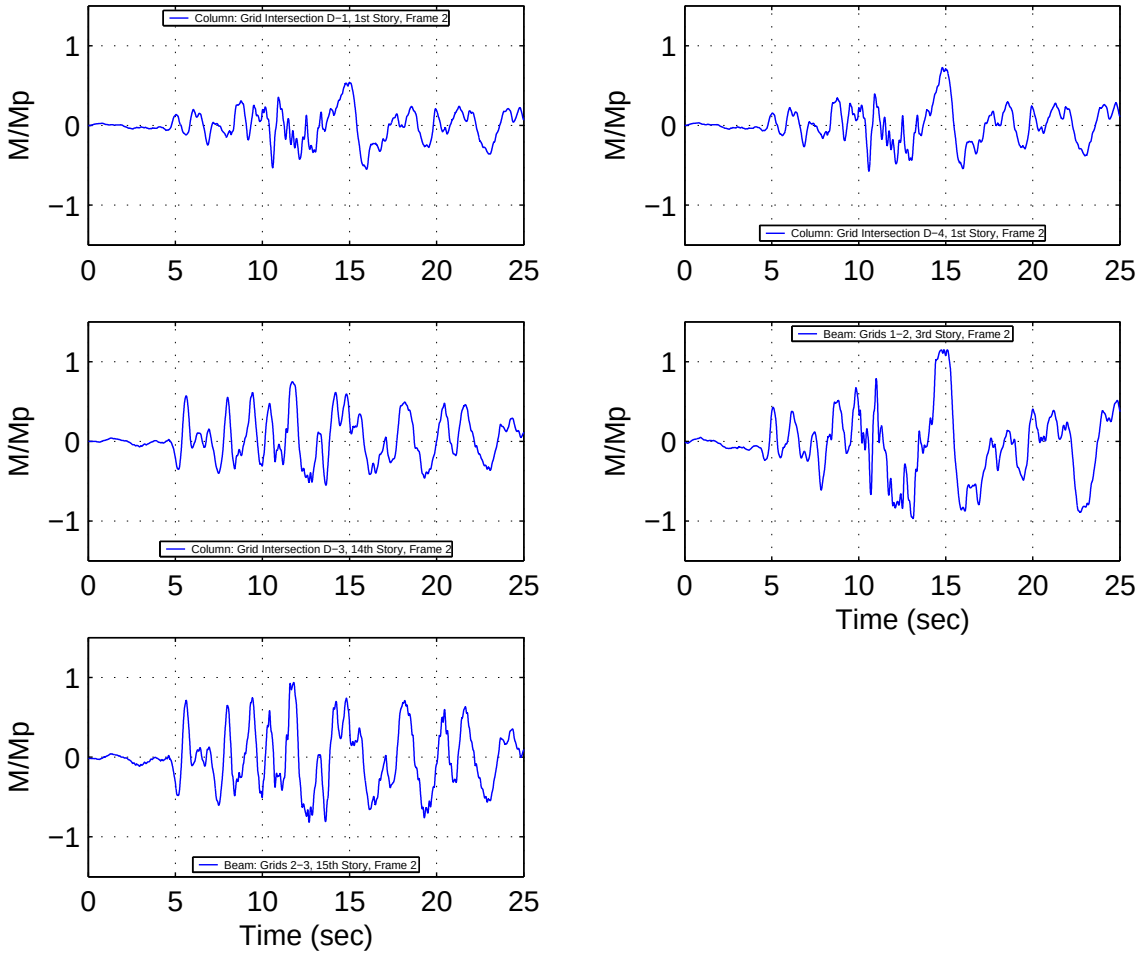

Figure J.48: Building 3A: Beam-Column End Moment Histories - Iran Earthquake (Tabas Record Strong Component in Y Direction)

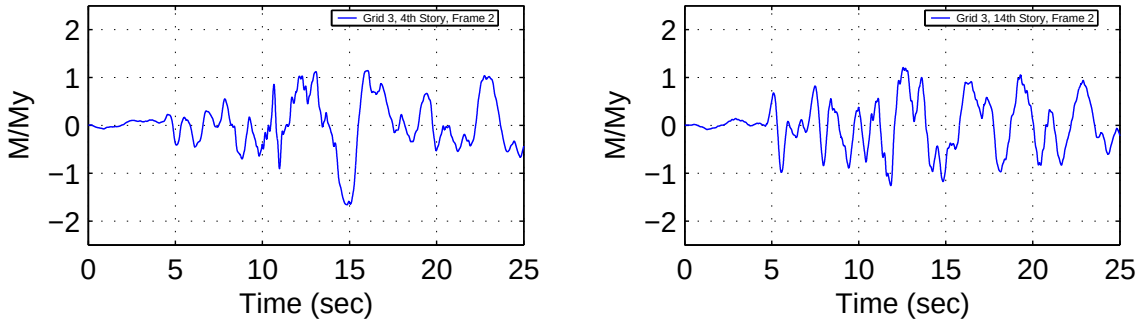

Figure J.49: Building 3A: Panel Zone Moment Histories - Iran Earthquake (Tabas Record Strong Component in Y Direction)

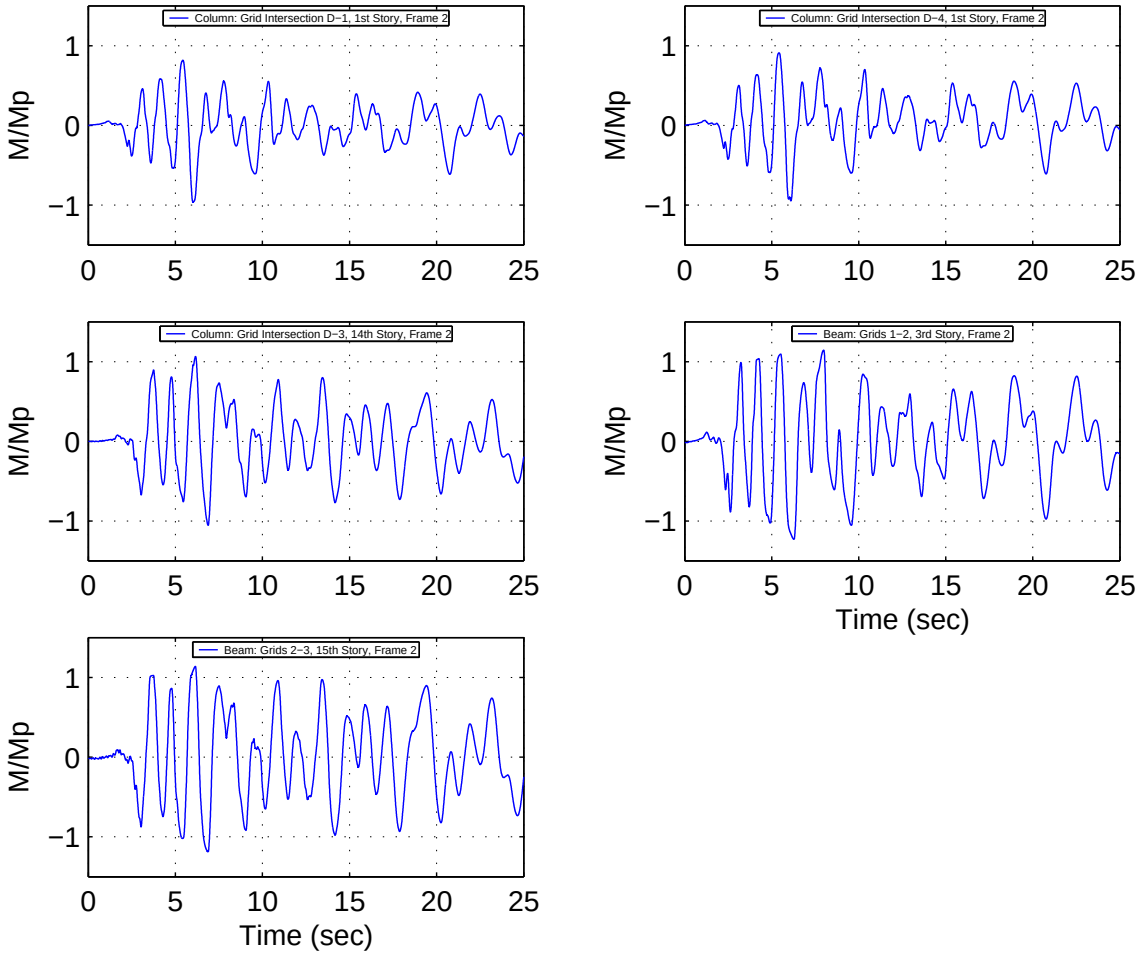

Figure J.50: Building 3A: Beam-Column End Moment Histories - Kobe Earthquake (Takatori Record Strong Component in X Direction)

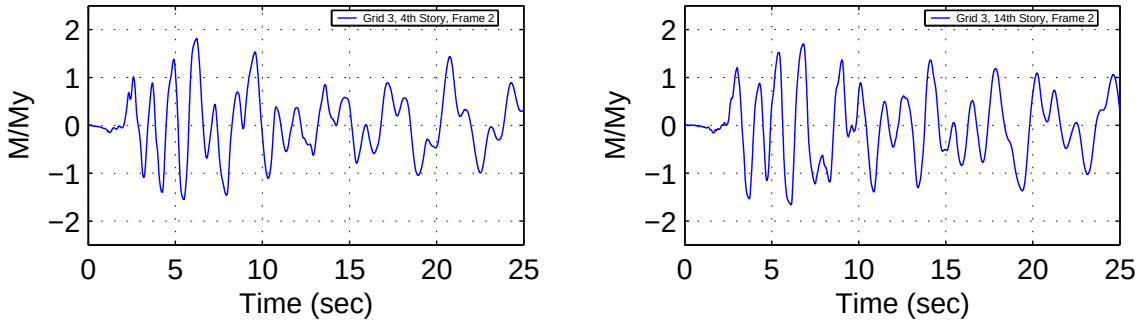

Figure J.51: Building 3A: Panel Zone Moment Histories - Kobe Earthquake (Takatori Record Strong Component in X Direction)

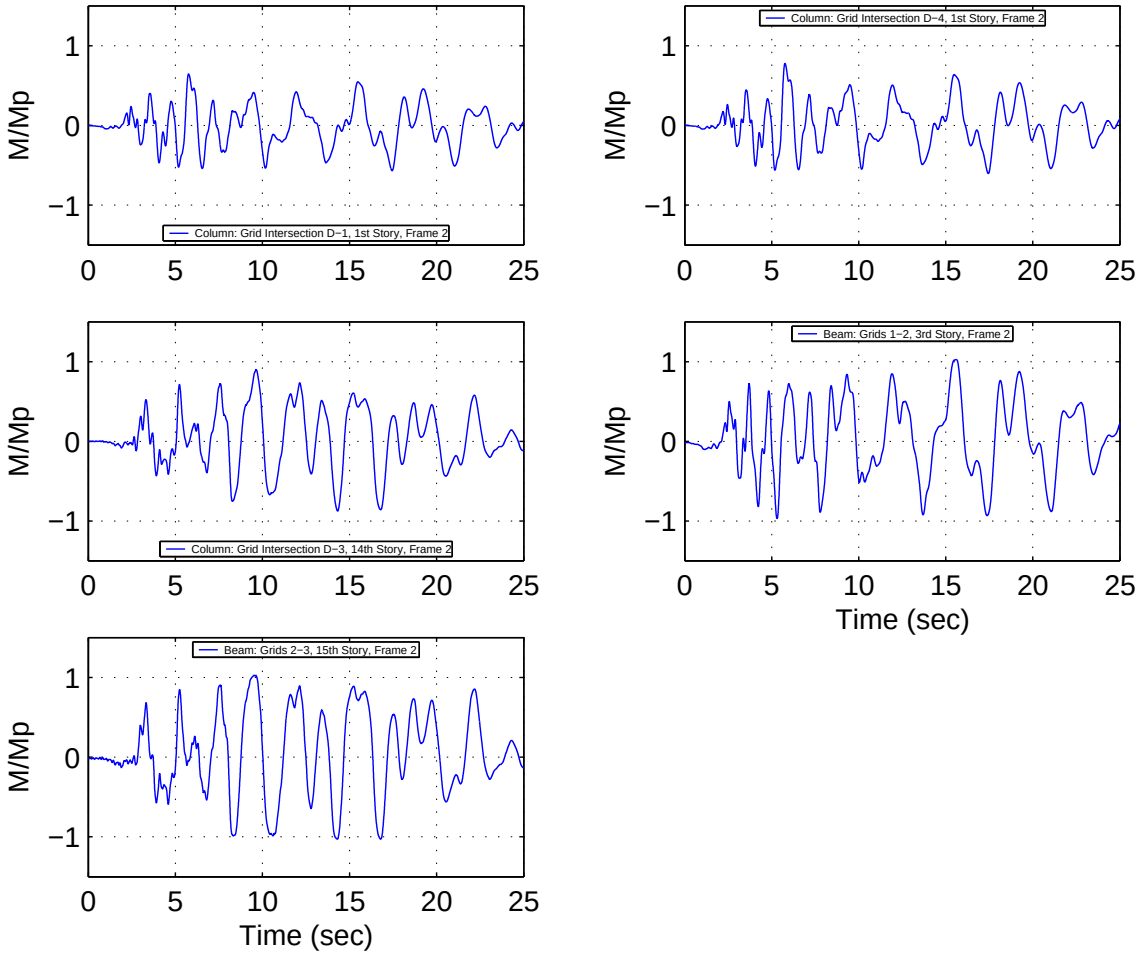

Figure J.52: Building 3A: Beam-Column End Moment Histories - Kobe Earthquake (Takatori Record Strong Component in Y Direction)

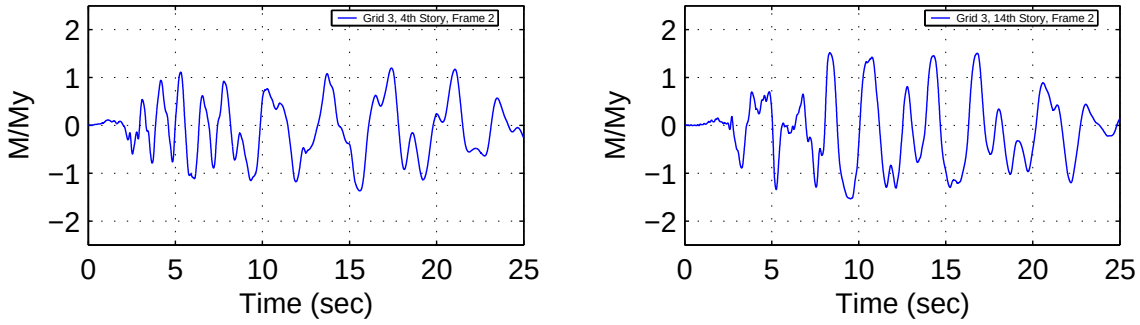

Figure J.53: Building 3A: Panel Zone Moment Histories - Kobe Earthquake (Takatori Record Strong Component in Y Direction)

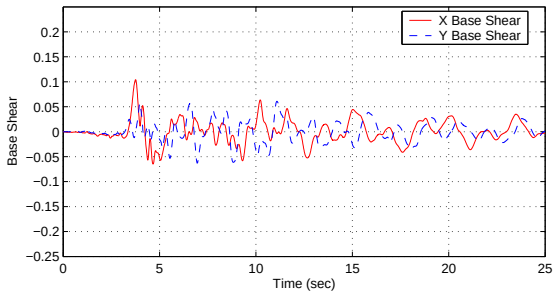

(a) Sylmar Strong Component in X Direction

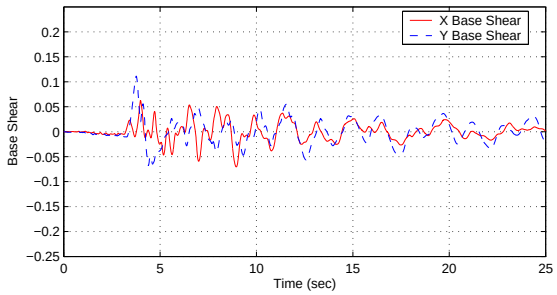

(b) Sylmar Strong Component in Y Direction

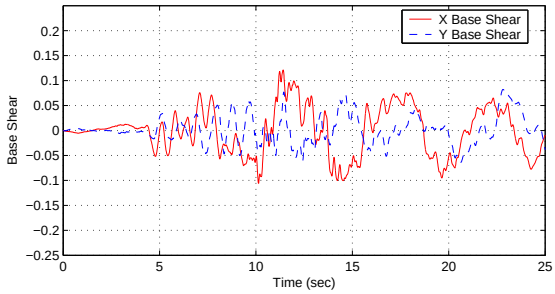

(c) Tabas Strong Component in X Direction

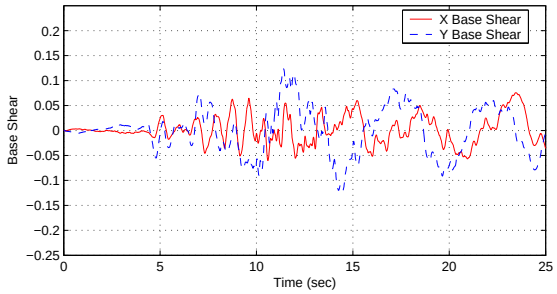

(d) Tabas Strong Component in Y Direction

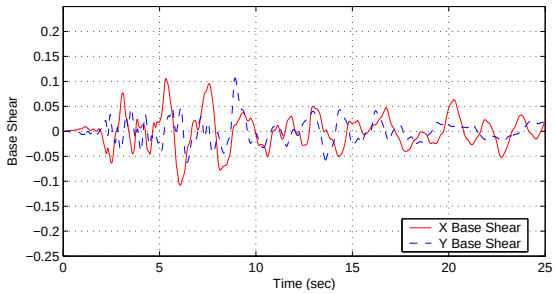

(e) Takatori Strong Component in X Direction

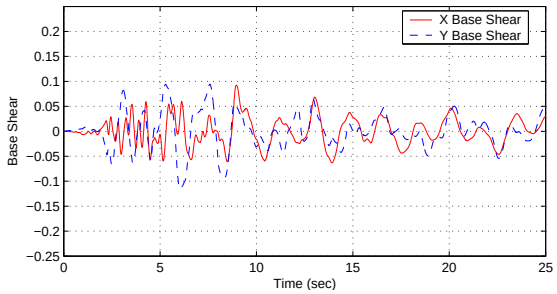

(f) Takatori Strong Component in Y Direction

Figure J.54: Building 4 Base Shear History: Northridge (Sylmar), Iran (Tabas) and Kobe (Takatori) Earthquakes

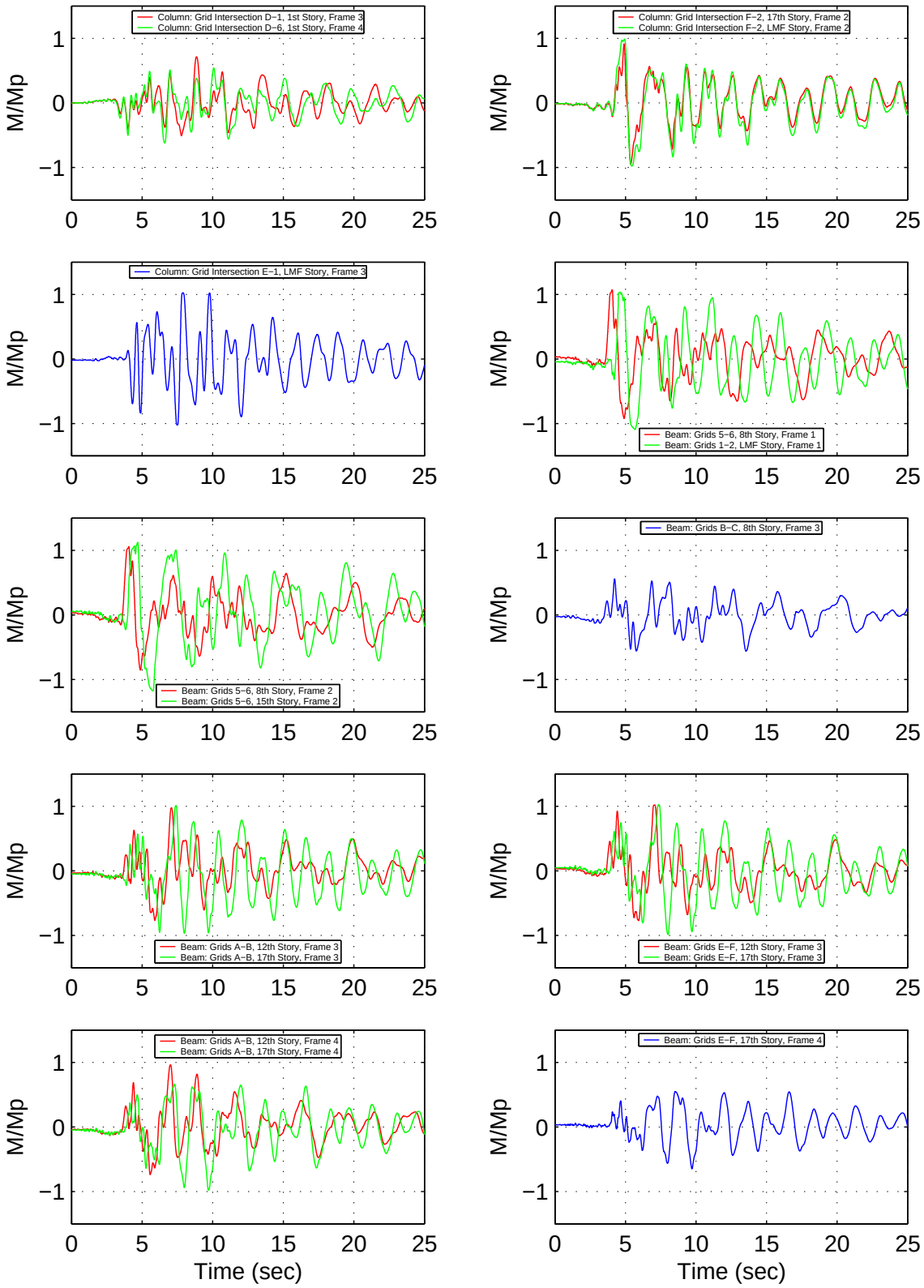

Figure J.55: Building 4: Beam-Column End Moment Histories - Northridge Earthquake (Sylmar Record Strong Component in X Direction)

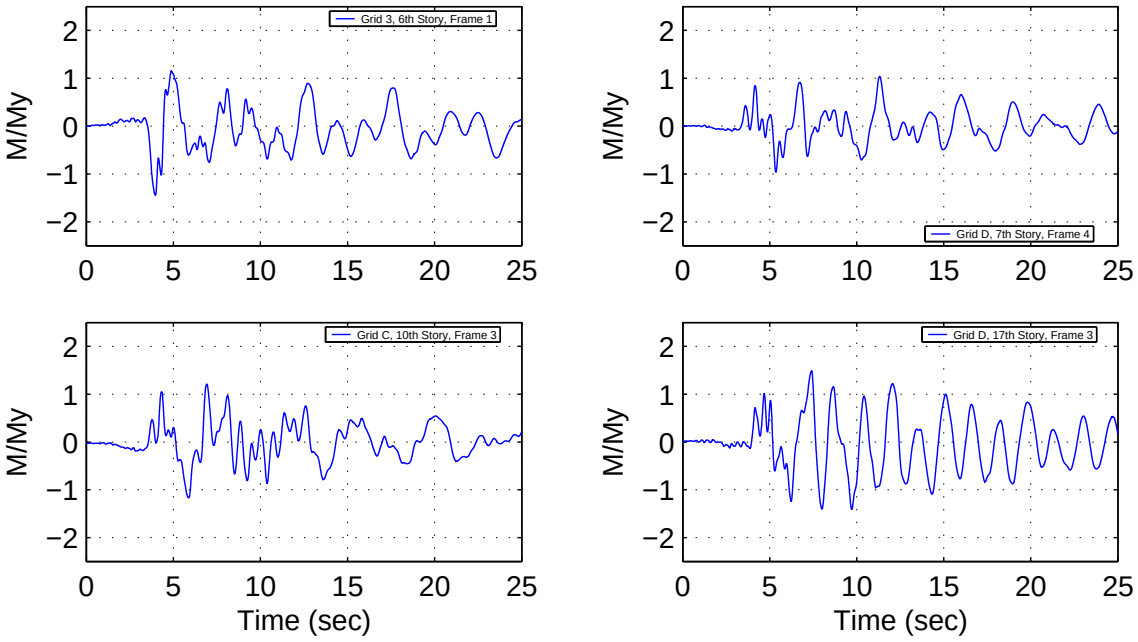

Figure J.56: Building 4: Panel Zone Moment Histories - Northridge Earthquake (Sylmar Record Strong Component in X Direction)

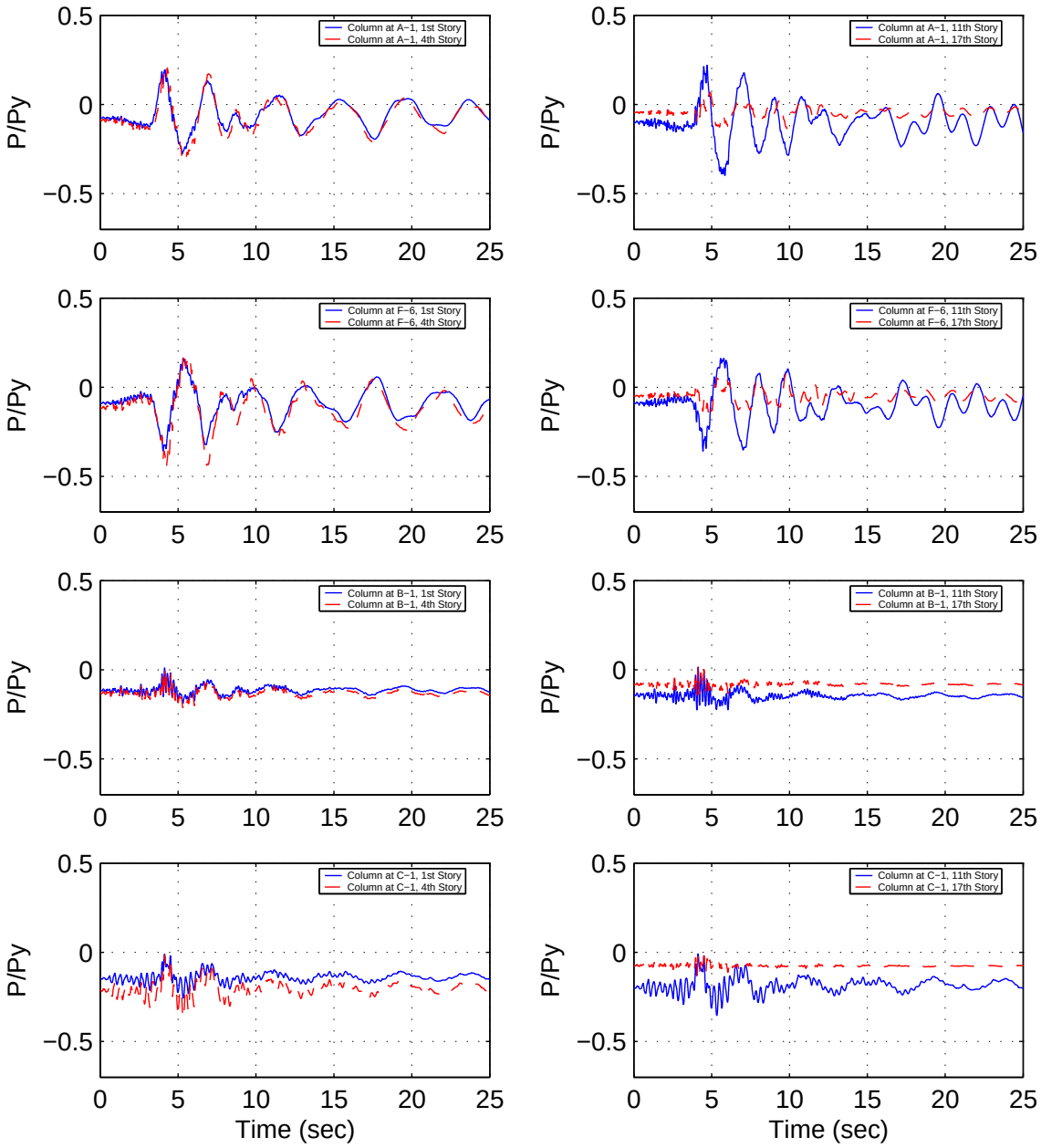

Figure J.57: Building 4: Column Axial Force Histories - Northridge Earthquake (Sylmar Record Strong Component in X Direction)

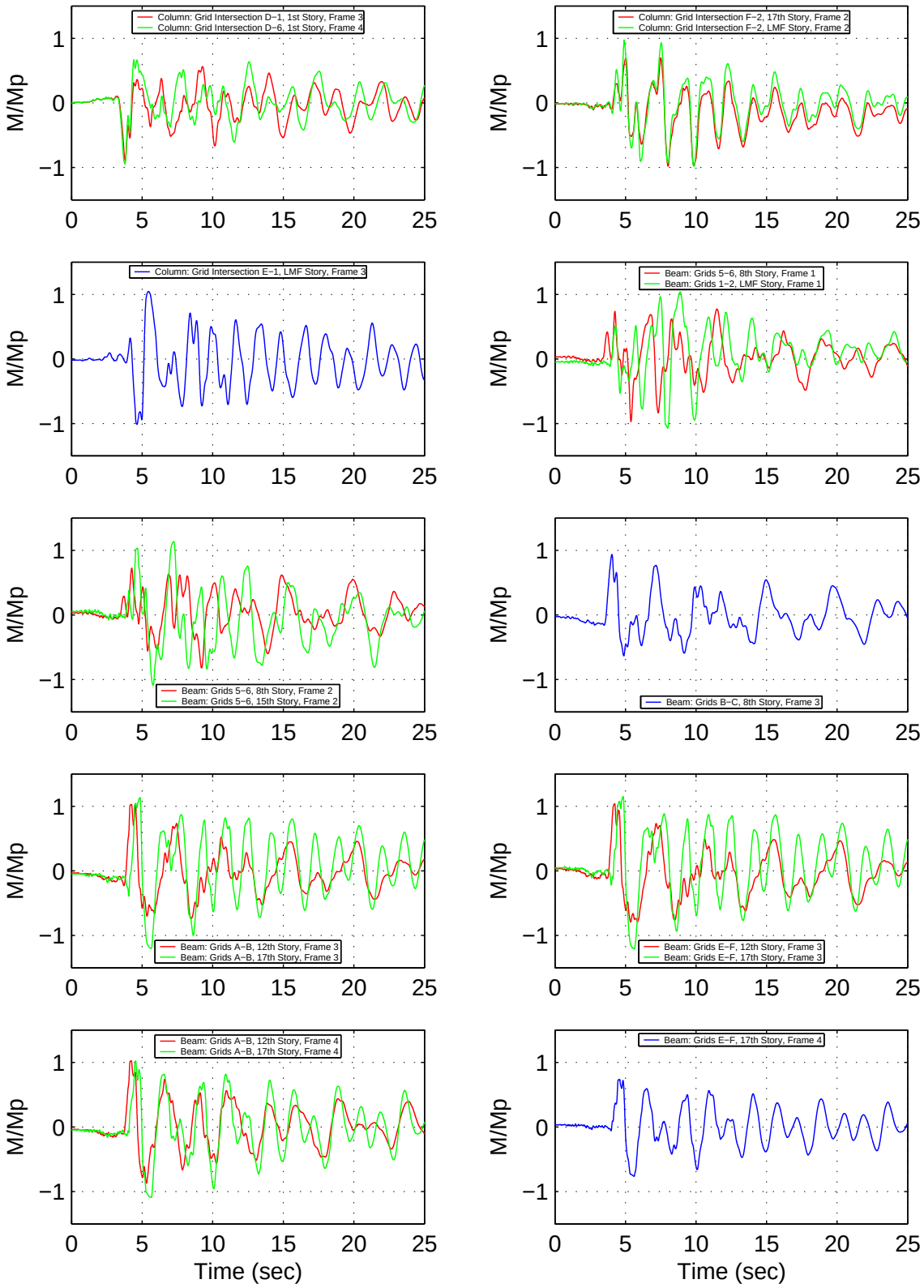

Figure J.58: Building 4: Beam-Column End Moment Histories - Northridge Earthquake (Sylmar Record Strong Component in Y Direction)

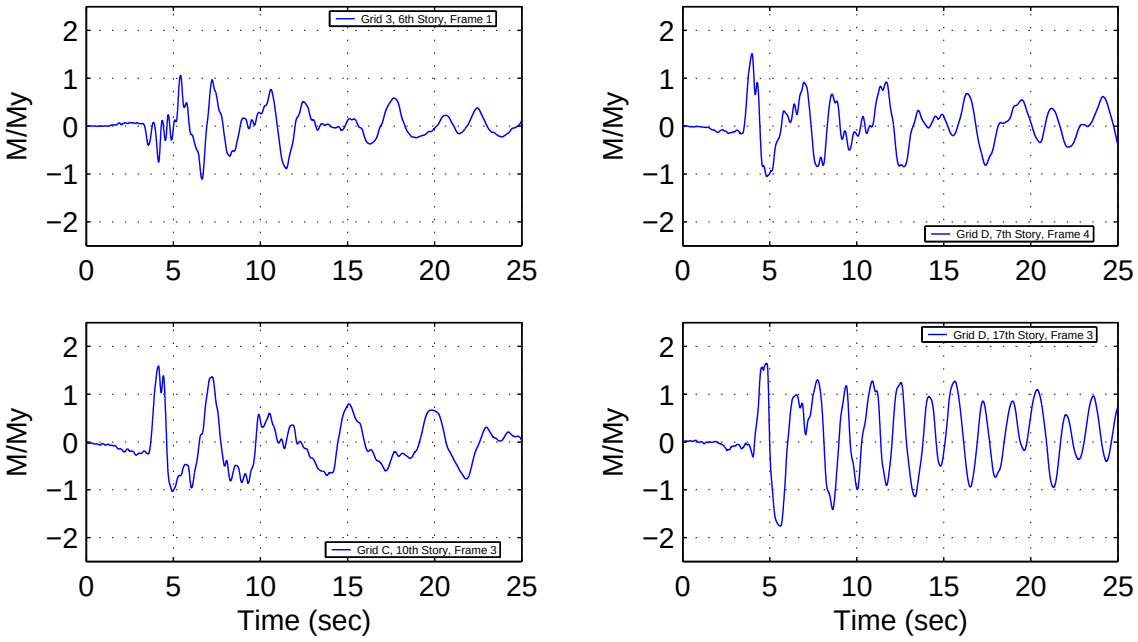

Figure J.59: Building 4: Panel Zone Moment Histories - Northridge Earthquake (Sylmar Record Strong Component in Y Direction)

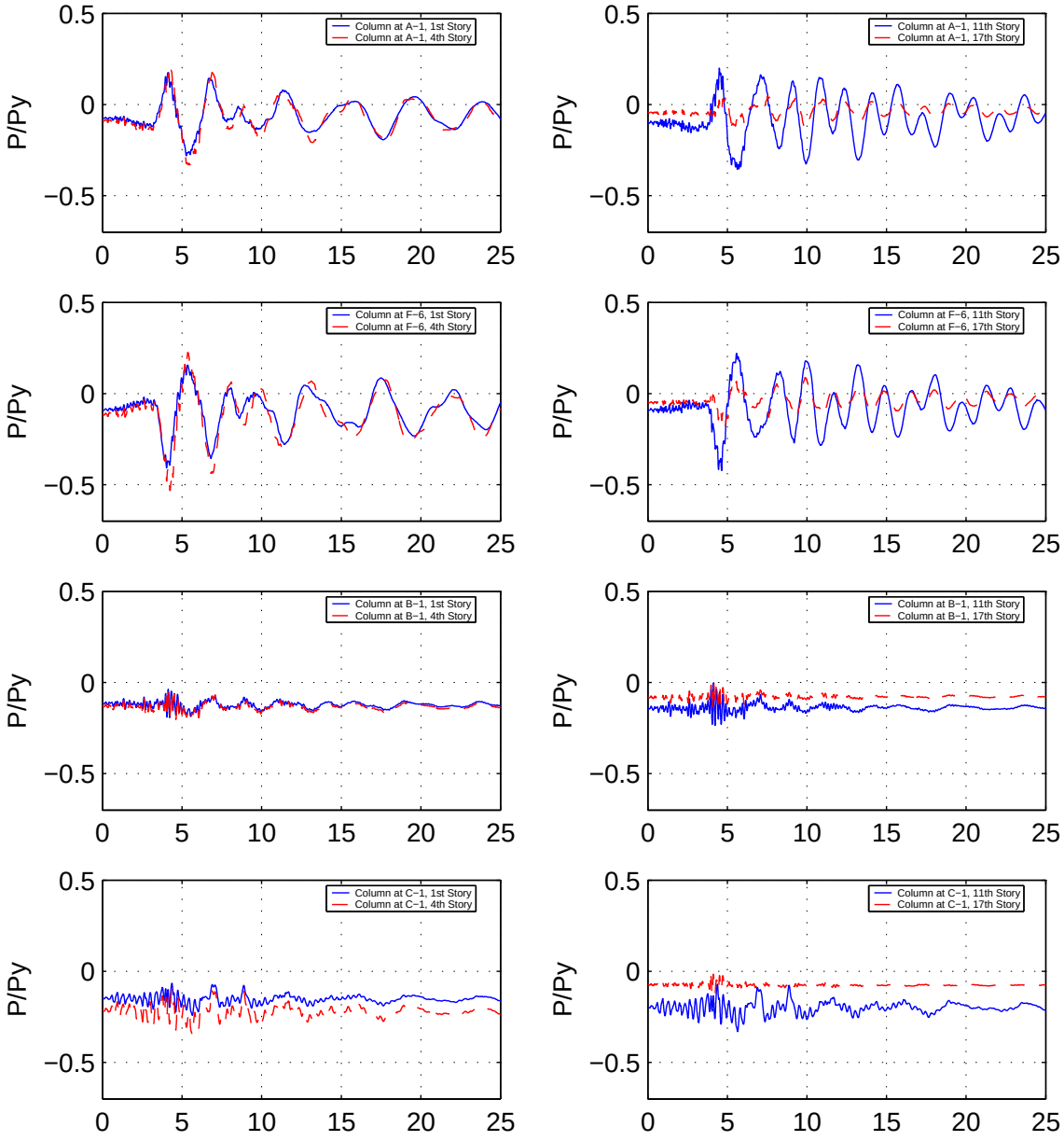

Figure J.60: Building 4: Column Axial Force Histories - Northridge Earthquake (Sylmar Record Strong Component in Y Direction)

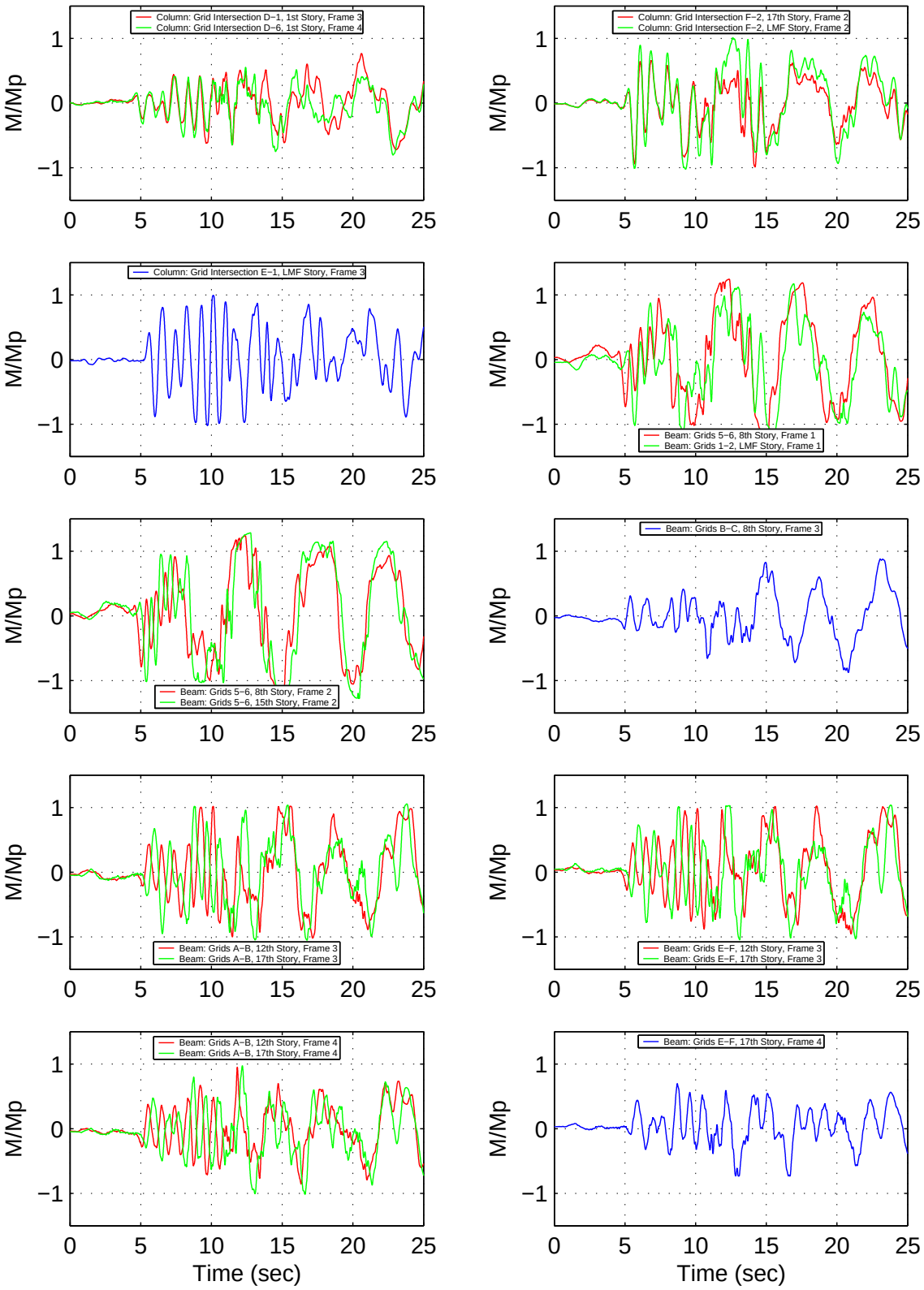

Figure J.61: Building 4: Beam-Column End Moment Histories - Iran Earthquake (Tabas Record Strong Component in X Direction)

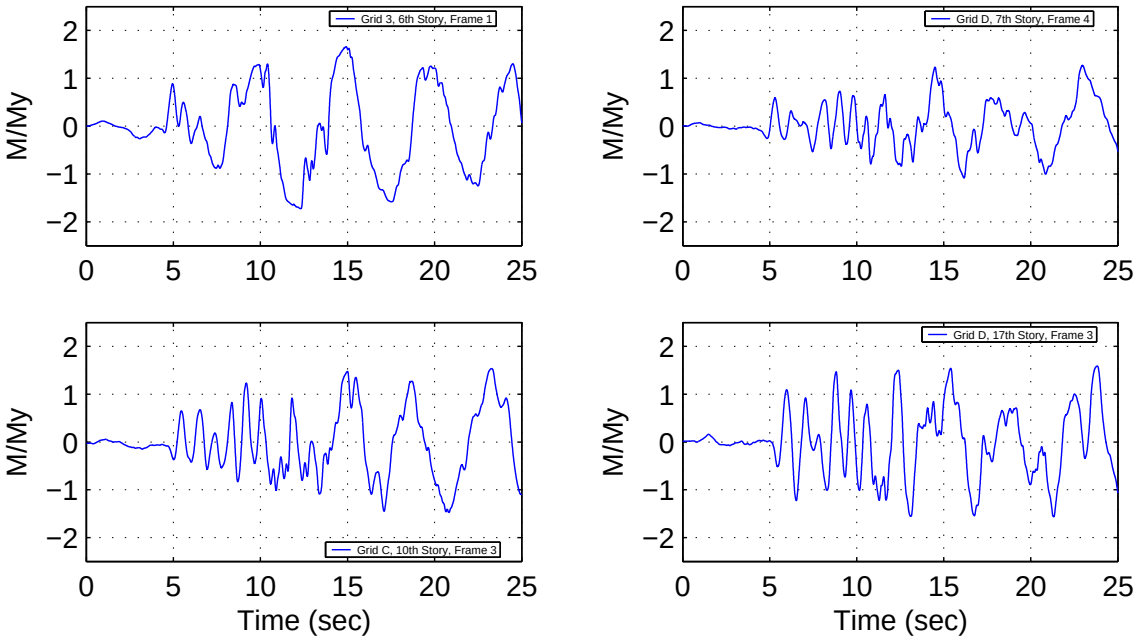

Figure J.62: Building 4: Panel Zone Moment Histories - Iran Earthquake (Tabas Record Strong Component in X Direction)

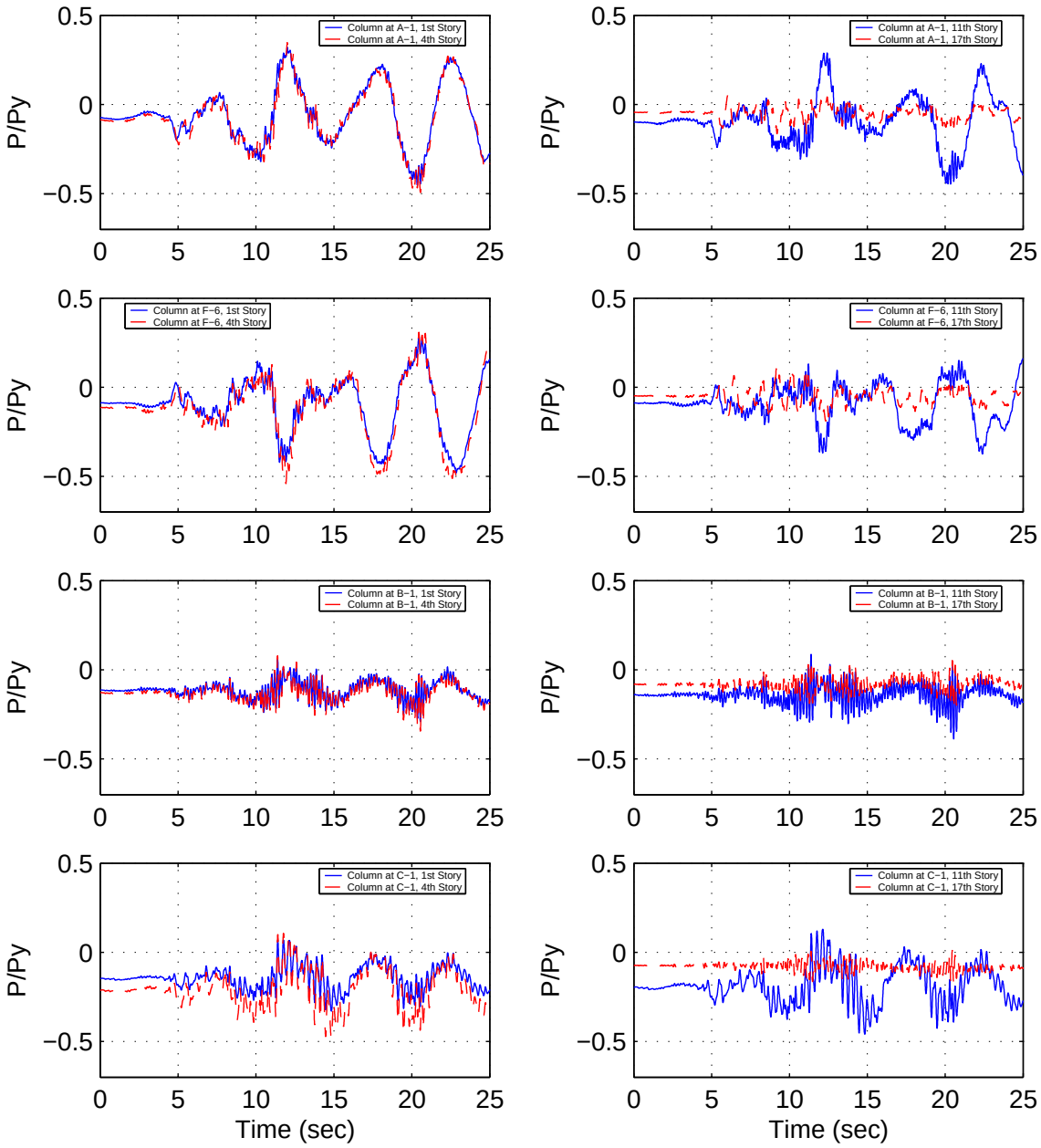

Figure J.63: Building 4: Column Axial Force Histories - Iran Earthquake (Tabas Record Strong Component in X Direction)

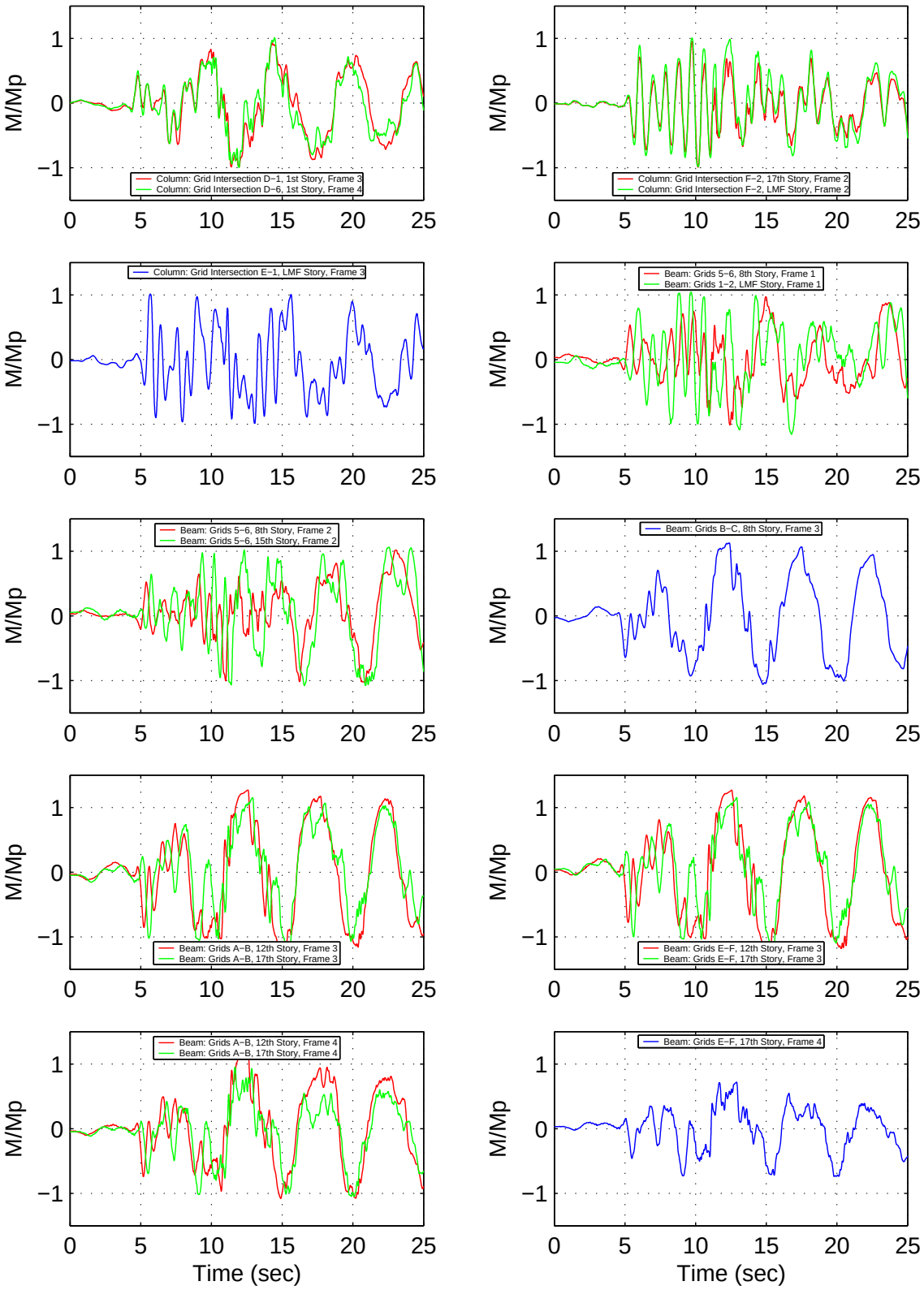

Figure J.64: Building 4: Beam-Column End Moment Histories - Iran Earthquake (Tabas Record Strong Component in Y Direction)

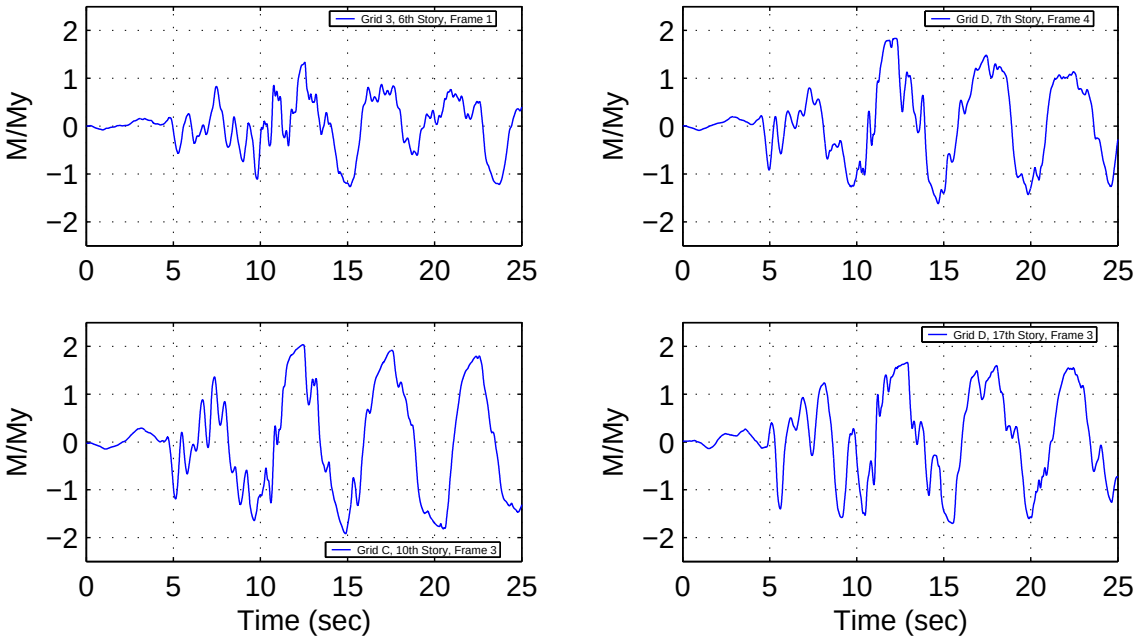

Figure J.65: Building 4: Panel Zone Moment Histories - Iran Earthquake (Tabas Record Strong Component in Y Direction)

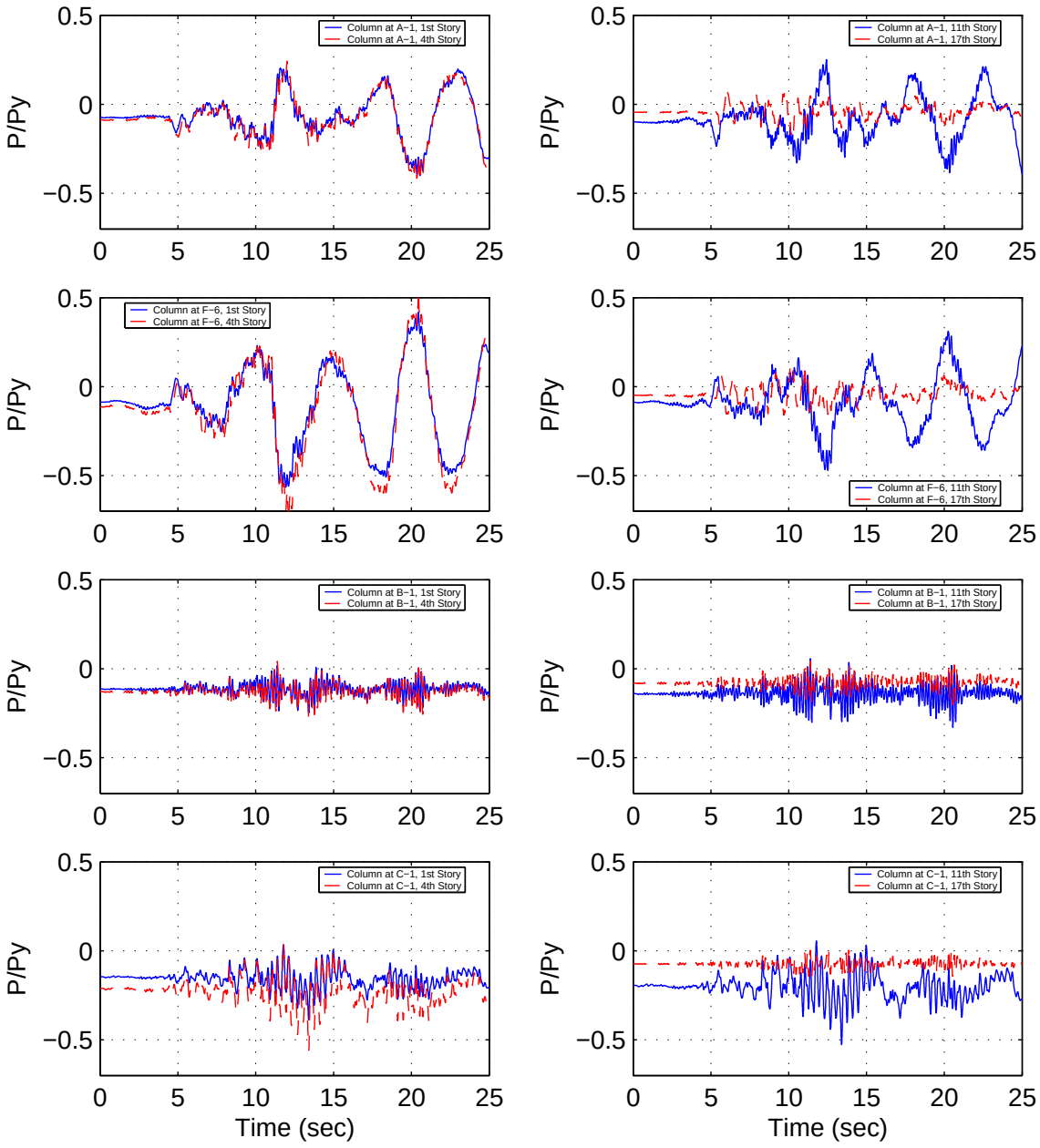

Figure J.66: Building 4: Column Axial Force Histories - Iran Earthquake (Tabas Record Strong Component in Y Direction)

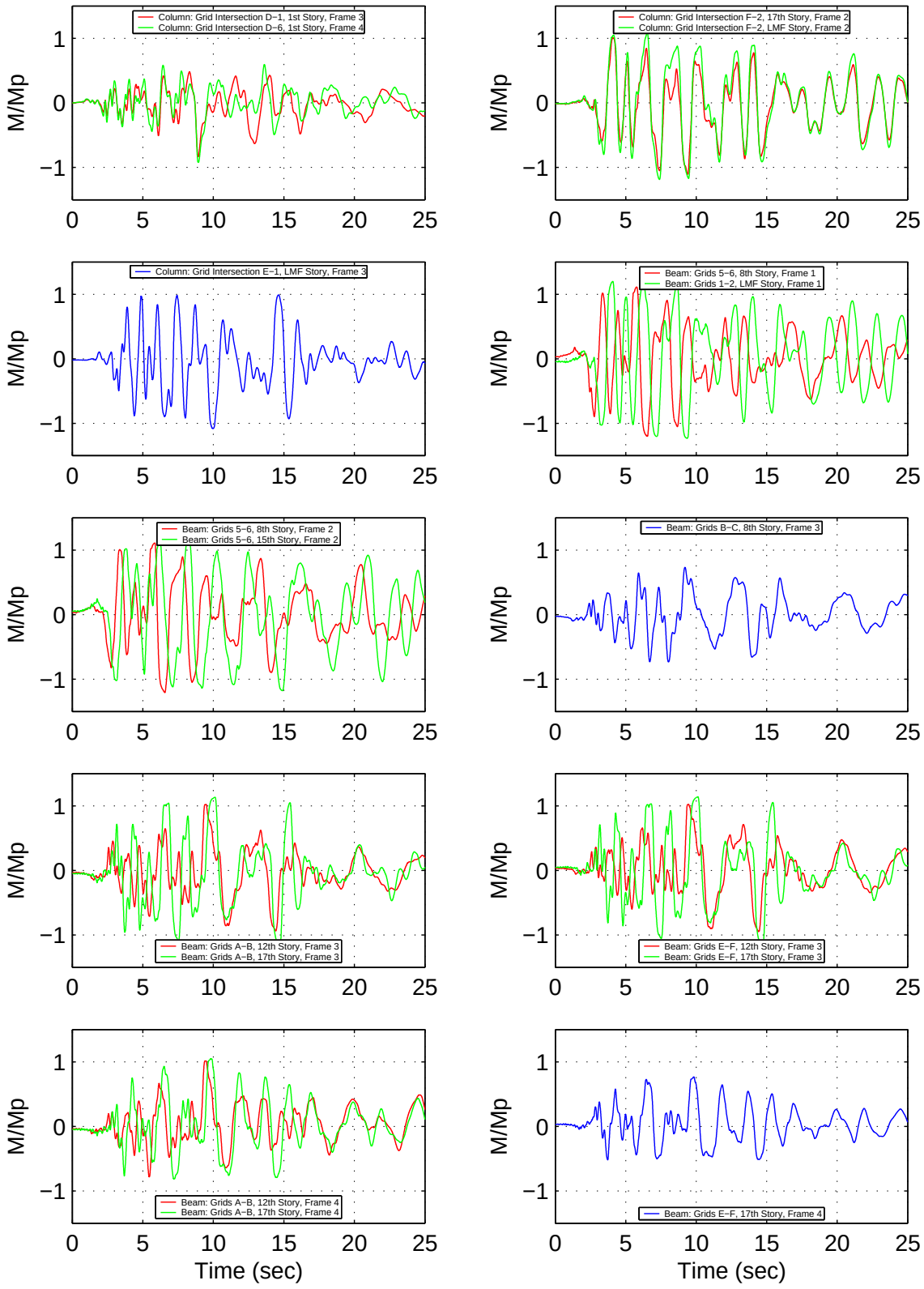

Figure J.67: Building 4: Beam-Column End Moment Histories - Kobe Earthquake (Takatori Record Strong Component in X Direction)

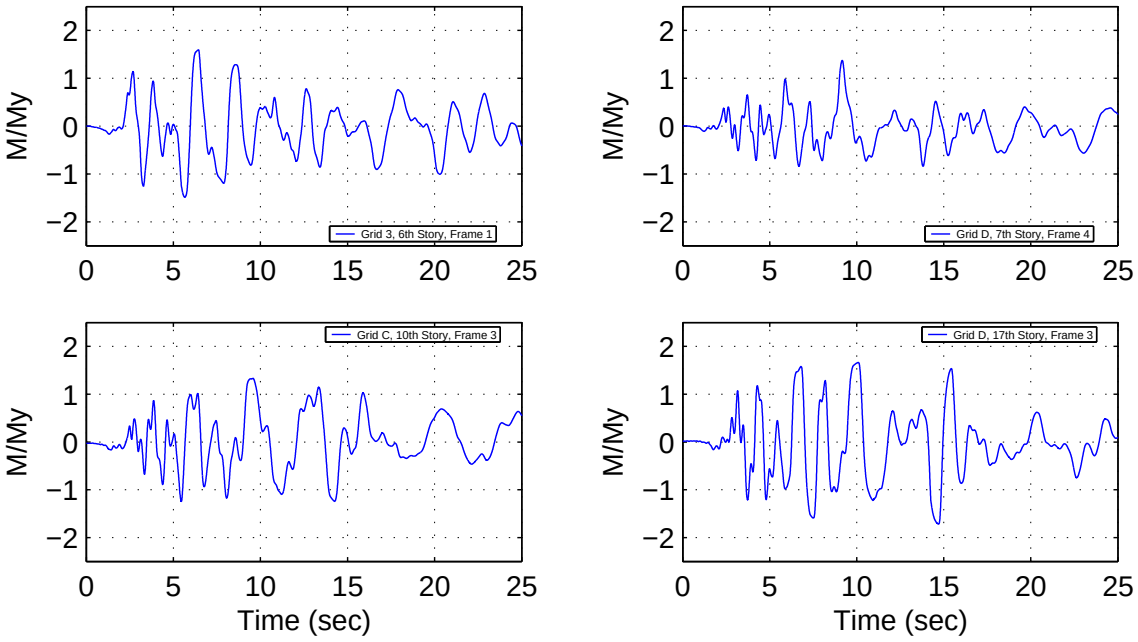

Figure J.68: Building 4: Panel Zone Moment Histories - Kobe Earthquake (Takatori Record Strong Component in X Direction)

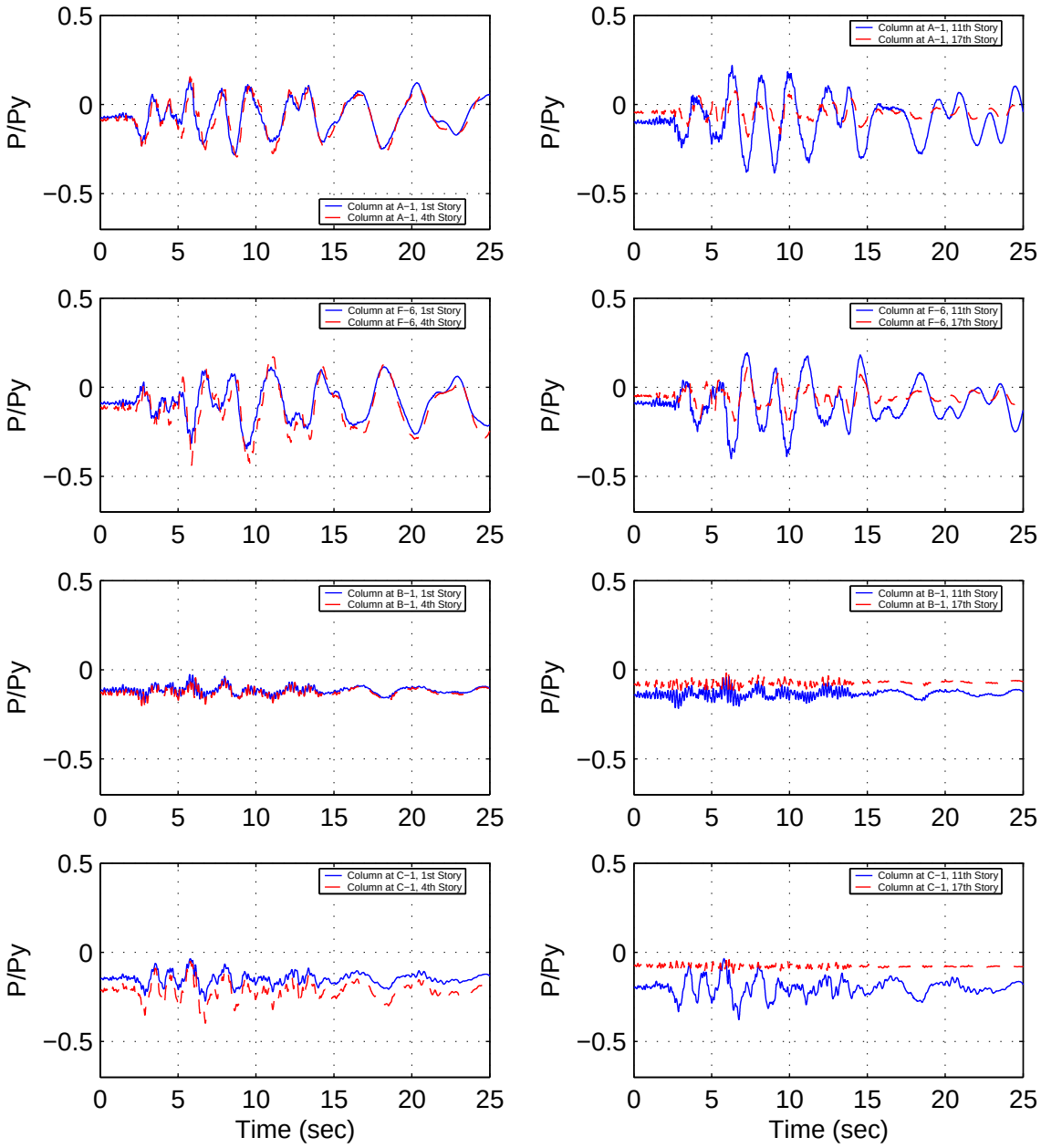

Figure J.69: Building 4: Column Axial Force Histories - Kobe Earthquake (Takatori Record Strong Component in X Direction)

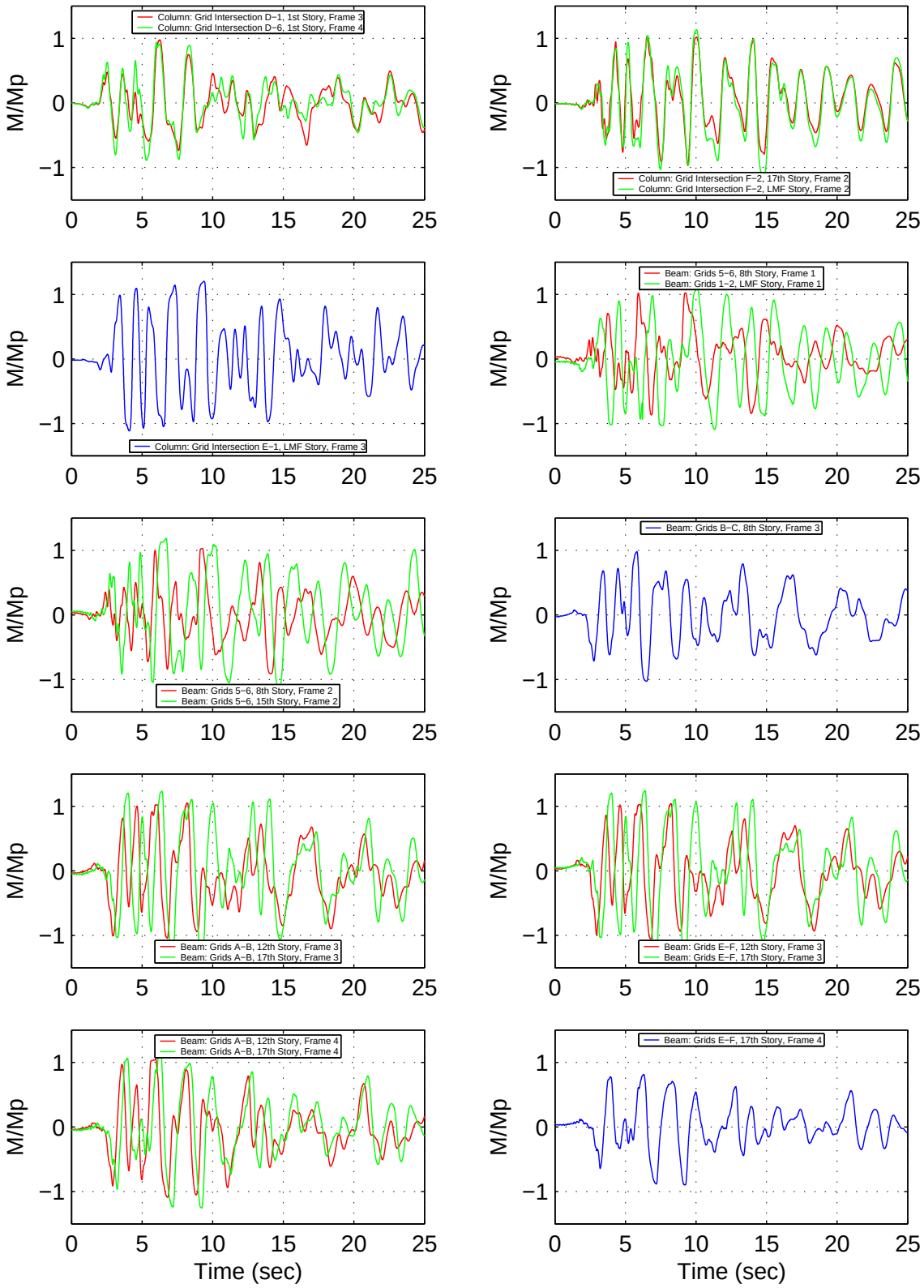

Figure J.70: Building 4: Beam-Column End Moment Histories - Kobe Earthquake (Takatori Record Strong Component in Y Direction)

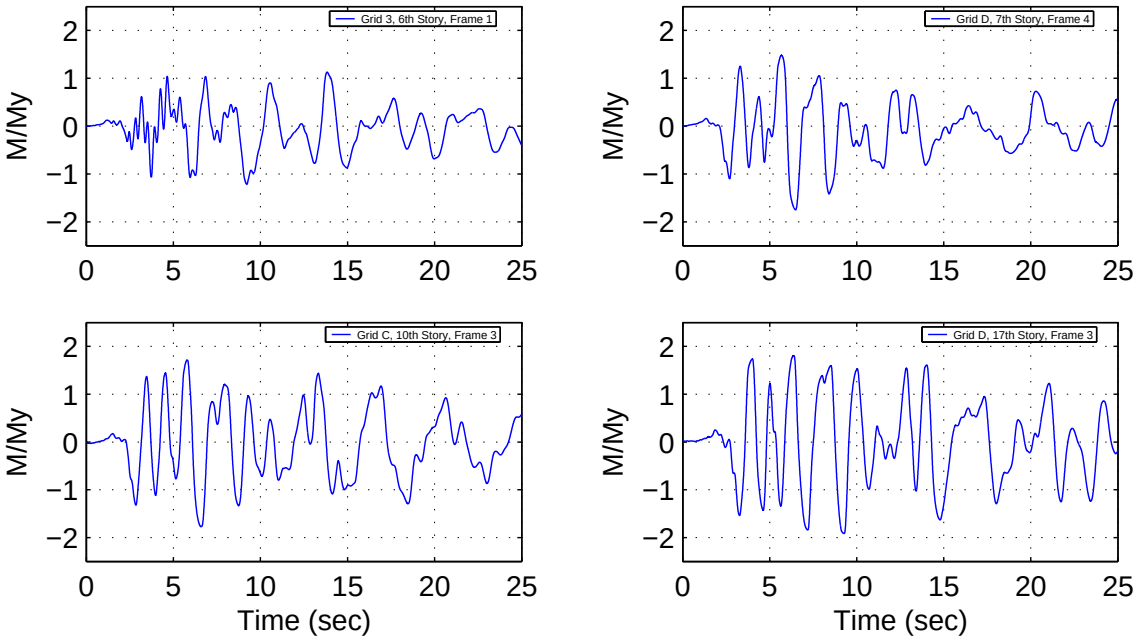

Figure J.71: Building 4: Panel Zone Moment Histories - Kobe Earthquake (Takatori Record Strong Component in Y Direction)

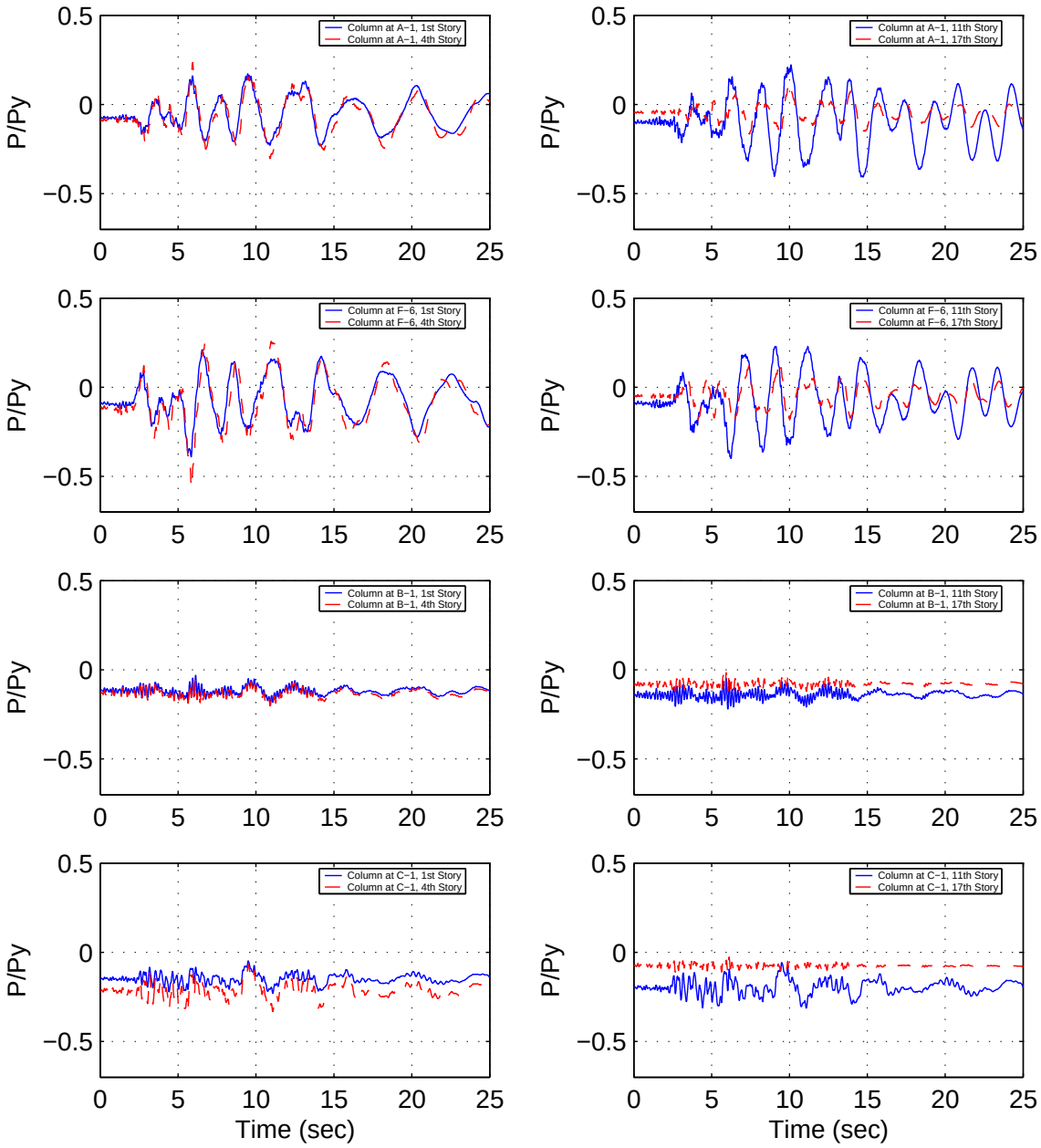

Figure J.72: Building 4: Column Axial Force Histories - Kobe Earthquake (Takatori Record Strong Component in Y Direction)

Bibliography

[1] AISC. *Manual of Steel Construction, Allowable Stress Design (Ninth Edition).* American Institute of Steel Construction, Inc., 1989.

[2] Algermissien, S., and Perkins, D. A probabilistic estimate of maximum acceleration in rock in the contiguous united states. Tech. Rep. 76-416, U.S. Geological Survey, 1976.

[3] Allahabadi, R., and Powell, G. H. DRAIN-2DX user guide. Tech. Rep. UCB/EERC-88-06, Earthquake Engineering Research Center, University of California, Berkeley, 1988.

[4] ATC. *Tentative Provisions for the Development of Seismic Regulations for Buildings.* ATC 3-06. Applied Technology Council, Redwood, CA, 1978.

[5] Attala, M. R., Deierlein, G. G., and McGuire, W. Spread of plasticity: Quasi-plastic-hinge approach. *Journal of the Structural Division, ASCE 120*, 8 (1994), 2451–2473.

[6] Bathe, K.-J. *Finite Element Procedures.* Prentice-Hall of India Private Limited, New Delhi, 1996.

[7] Bertero, V. V., Popov, E. P., and Krawinkler, H. Beam-column subassemblages under repeated loading. *Journal of the Structural Division, ASCE 98*, ST5 (1972), 1137–1159.

[8] Carlson, A. Three-dimensional nonlinear inelastic analysis of steel moment-frame buildings damaged by earthquake excitations. Tech. Rep. EERL 99-02, Earthquake Engineering Research Laboratory, California Institute of Technology, 1999.

[9] Carol, I., and Murcia, J. Nonlinear time-dependent analysis of planar frames using an 'exact' formulation - i. theory. *Computers and Structures 33*, 1 (1989), 79–87.

[10] Carol, I., and Murcia, J. Nonlinear time-dependent analysis of planar frames using an 'exact' formulation - ii. computer implementation. *Computers and Structures 33*, 1 (1989), 89–102.

[11] Challa, V. R. M. Nonlinear seismic behavior of steel planar moment-resisting frames. Tech. Rep. EERL 92-01, Earthquake Engineering Research Laboratory, California Institute of Technology, 1992.

[12] Challa, V. R. M., and Hall, J. F. Earthquake collapse analysis of steel frames. *Earthquake Engineering and Structural Dynamics 23*, 11 (1994), 1199–1218.

[13] Chopra, A. K. *Dynamics of Structures - Theory and Applications to Earthquake Engineering.* Prentice Hall, 1995.

[14] Clough, R. W., and Penzien, J. *Dynamics of Structures (Second Edition).* McGraw-Hill, Inc., 1993.

[15] Committee, S. *Recommended Lateral Force Requirements and Commentary.* Sixth Edition. Structural Engineers Association of California, 1996.

[16] Cook, R. D., Malkus, D. S., and Plesha, M. E. *Concepts and Applications of Finite Element Analysis (Third Edition).* John Wiley and Sons, 1989.

[17] El-Tawil, S., and Deierlein, G. G. Inelastic dynamic analysis of mixed steel-concrete space frames. Tech. Rep. Structural Engineering 96-05, Cornell University, 1996.

[18] Engelhardt, M. D., and Husain, A. S. Cyclic tests on large-scale steel moment connections. Tech. Rep. Res. Rep. PMFSEL 92-2, Dept. of Civil Engineering, University of Texas, Austin, 1992.

[19] Engelhardt, M. D., and Husain, A. S. Cyclic-loading performance of welded flange-bolted web connections. *Journal of Structural Engineering, ASCE 119*, 12 (1993), 3537–3550.

[20] FEMA. *NEHRP Commentary on the Guidelines for the Seismic Rehabilitation of Buildings.* FEMA-274. Federal Emergency Management Agency, 1997.

[21] FEMA. *NEHRP Guidelines for the Seismic Rehabilitation of Buildings.* FEMA-273. Federal Emergency Management Agency, 1997.

[22] FEMA. *Prestandard and Commentary for the Seismic Rehabilitation of Buildings.* FEMA-356. Federal Emergency Management Agency, 2000.

[23] Fielding, D. J., and Chen, W. F. Steel frame analysis and connection shear deformation. *Journal of the Structural Division, ASCE 99*, ST1 (1973), 1–18.

[24] Filippou, F., and Romero, M. L. Nonlinear and dynamic analysis from research to practice. In *Structural Engineering World Wide 1998* (1998), N. K. Srivatsava, Ed., Elsevier Science Ltd., pp. T101–3.

[25] Frankel, A., Mueller, C., Barnhard, T., Perkins, D., Leyendecker, E., Dickman, N., Hanson, S., and Hopper, M. Interim national seismic hazard maps: Documentation. Tech. rep., U.S. Geological Survey, Denver Colorado, Draft: January 18, 1996.

[26] Hall, J. F. Parameter study of the response of moment-resisting steel frame buildings to near-source ground motions. Tech. Rep. EERL 95-08, Earthquake Engineering Research Laboratory, California Institute of Technology, 1995.

[27] Hall, J. F. Seismic response of steel frame buildings to near-source ground motions. Tech. Rep. EERL 97-05, Earthquake Engineering Research Laboratory, California Institute of Technology, 1997.

[28] Hall, J. F. Seismic response of steel frame buildings to near-source ground motions. *Earthquake Engineering and Structural Dynamics 27* (1998), 1445–1464.

[29] Hall, J. F., and Challa, V. R. M. Beam-column modeling. *Journal of Engineering Mechanics 121*, 12 (1995), 1284–1291.

[30] Hall, J. F., Heaton, T. H., Halling, M. W., and Wald, D. J. Near-source ground motion and its effects on flexible buildings. *Earthquake Spectra 11*, 4 (1995), 569–605.

[31] Heaton, T. H. Evidence for and implications of self-healing pulse of slip in earthquake rupture. *Physics of Earth and Planetary Interiors 64* (1990), 1–20.

[32] ICBO. *1994 Uniform Building Code*. Volume 2. International Conference of Building Officials, Whittier, CA, 1994.

[33] ICBO. *1997 Uniform Building Code*. Volume 2. International Conference of Building Officials, Whittier, CA, 1997.

[34] Iwan, W. D. Near-field considerations in specification of seismic design motions for structures. In *Proceedings of the Tenth European Conference on Earthquake Engineering, Vienna, Austria* (August 28-September 2, 1994).

[35] Kaba, S., and Mahin, S. A. Refined modeling of reinforced concrete columns for seismic analysis. Tech. Rep. UCB/EERC-84-03, Earthquake Engineering Research Center, University of California, Berkeley, 1984.

[36] Kassimali, A. Large deformation analysis of elastic-plastic frames. *Journal of the Structural Division, ASCE 109*, 8 (1983), 1869–1886.

[37] Kato, B. Beam-to-column connection research in japan. *Journal of the Structural Division, ASCE 108*, ST2 (1982), 343–360.

[38] Kim, K. D., and Engelhardt, M. D. Beam-column element for nonlinear seismic analysis of steel frames. *Journal of Structural Engineering, ASCE 126*, 8 (2000), 916–925.

[39] Krawinkler, H., Bertero, V. V., and Popov, E. P. Shear behavior of steel frame joints. *Journal of the Structural Division, ASCE 101*, ST11 (1975), 2317–2336.

[40] Krawinkler, H., and Popov, E. P. Shear behavior of moment connections and joints. *Journal of the Structural Division, ASCE 108*, ST2 (1982), 373–391.

[41] Krishnan, S. FRAME3D - a program for three-dimensional nonlinear time-history analysis of steel buildings: User guide. Tech. Rep. EERL 2003-03, Earthquake Engineering Research Laboratory, California Institute of Technology, 2003.

[42] Kunnath, S. K. Enhancements to program IDARC: Modeling inelastic behavior of welded connections in steel moment-resisting frames. Tech. Rep. NIST GCR 95-673, Building and Fire Research Laboratory, National Institute of Standards and Technology, Gaithersburg, Maryland, 1995.

[43] Kunnath, S. K., Reinhorn, A. M., and Lobo, R. IDARC Version 3.0: A program for the inelastic damage analysis of reinforced concrete structures. Tech. Rep. NCEER-92-0022, National Center for Earthquake Engineering Research, State University of New York at Buffalo, 1992.

[44] Lobo, R. IDARC3D: Inelastic damage analysis of reinforced concrete structures in three dimensions. Tech. rep., National Center for Earthquake Engineering Research, State University of New York at Buffalo, 1994.

[45] Lobo, R. F., Skokan, M. J., Huang, S. C., and Hart, G. C. Three-dimensional analysis of a 13-story steel building with weld connection damage. In *Structural Engineering World Wide 1998* (1998), N. K. Srivatsava, Ed., Elsevier Science Ltd., pp. T114–2.

[46] Mark, K. M. S. Nonlinear dynamic response of reinforced concrete frames. Tech. Rep. R76-38, Department of Civil Engineering, Massachusetts Institute of Technology, 1976.

[47] Mattiasson, K. Numerical results from large deflection beam and frame problems analyzed by means of elliptic integrals. *International Journal for Numerical Methods in Engineering 17*, (1) (1980), 145–153.

[48] Neuenhofer, A., and Filippou, F. C. Evaluation of nonlinear frame finite-element models. *Journal of Structural Engineering, ASCE 123*, 7 (1997), 958–966.

[49] Neuenhofer, A., and Filippou, F. C. Geometrically nonlinear flexibility-based frame finite-element. *Journal of Structural Engineering, ASCE 124*, 6 (1998), 704–711.

[50] Oran, C. Tangent stiffness in plane frames. *Journal of the Structural Division, ASCE 99*, 6 (1973), 973–985.

[51] Oran, C. Tangent stiffness in space frames. *Journal of the Structural Division, ASCE 99*, 6 (1973), 987–1001.

[52] Park, Y. J., Reinhorn, A. M., and Kunnath, S. K. IDARC: Inelastic damage analysis of reinforced concrete frame-shearwall structures. Tech. Rep. NCEER-87-0008, National Center for Earthquake Engineering Research, State University of New York at Buffalo, 1987.

[53] Pinkney, R. B. Cyclic plastic analysis of structural steel joints. Tech. Rep. UCB/EERC-73-15, Earthquake Engineering Research Center, University of California, Berkeley, 1973.

[54] Popov, E. P., and Petersson, H. Cyclic metal plasticity: Experiments and theory. *Journal of the Engineering Mechanics Division, ASCE 104*, EM6 (1978), 1371–1388.

[55] Powell, G. H., and Campbell, S. DRAIN-3DX element description and user guide for element type01, type05, type08, type09, type15, and type17. Tech. Rep. UCB/SEMM-94/08, Structural Engineering Mechanics and Materials, University of California, Berkeley, 1994.

[56] Prakash, V., Powell, G. H., and Campbell, S. DRAIN-3DX base program description and user guide, Version 1.10. Tech. Rep. UCB/SEMM-94/07, Structural Engineering Mechanics and Materials, University of California, Berkeley, 1994.

[57] Przemeniecki, J. *Theory of Matrix Structural Analysis.* McGraw-Hill Book Co., New York, NY, 1968.

[58] Roeder, C. Inelastic dynamic analysis of two 8-story moment frames. Tech. rep., Report to Structural Engineers Association of Washington, 1987.

[59] Salmon, C. G., and Johnson, J. E. *Steel Structures - Design and Behavior.* Second Edition. Harper & Row, Publishers, New York, NY, 1980.

[60] Simeonov, V. K., Sivaselvan, M. V., and Reinhorn, A. M. Nonlinear analysis of structural frame systems by the state-space approach. *Computer-Aided Civil and Infrastructure Engineering 15* (2000), 76–89.

[61] Sivaselvan, M. V., and Reinhorn, A. M. Collapse analysis: Large inelastic deformations analysis of planar frames. *Journal of Structural Engineering, ASCE 128*, 12 (2002), 1575–1583.

[62] Spacone, E., Ciampi, V., and Filippou, F. C. Mixed formulation of nonlinear beam finite element. *Computers and Structures 58*, 1 (1996), 71–83.

[63] Spacone, E., Filippou, F. C., and Taucer, F. F. Fibre beam-column model for nonlinear analysis of r/c frames: Part i. formulation. *Earthquake Engineering and Structural Dynamics 25* (1996), 711–725.

[64] Spacone, E., Filippou, F. C., and Taucer, F. F. Fibre beam-column model for nonlinear analysis of r/c frames: Part ii. applications. *Earthquake Engineering and Structural Dynamics 25* (1996), 727–742.

[65] Stratta, J. *Manual of Seismic Design.* Prentice-Hall Inc., Englewood Cliffs, New Jersey, 1987.

[66] Tsai, K. C., and Popov, E. P. Steel beam-column joints in seismic moment resisting frames. Tech. Rep. UCB/EERC-88-19, Earthquake Engineering Research Center, University of California, Berkeley, 1988.

[67] Wilson, E., Der Kiureghian, A., and Bayo, E. A replacement for the srss method. *Earthquake Engineering and Structural Dynamics 9* (1981).

[68] Zeris, C. A., and Mahin, S. Analysis of reinforced concrete beam-columns under uniaxial excitation. *Journal of Structural Engineering, ASCE 114*, ST4 (1988), 804–820.

[69] Zeris, C. A., and Mahin, S. Behavior of reinforced concrete structures subjected to biaxial excitation. *Journal of Structural Engineering, ASCE 117*, ST9 (1991), 2657–2673.

[70] Zienkiewicz, O., and Taylor, R. *The Finite Element Method.* Volume 1, Fourth Edition. McGraw-Hill Book Co., New York, NY, 1989.

[71] Zienkiewicz, O., and Taylor, R. *The Finite Element Method.* Volume 2, Fourth Edition. McGraw-Hill Book Co., New York, NY, 1991.